JULY 1, 1989

Analytical CHEMISTRY

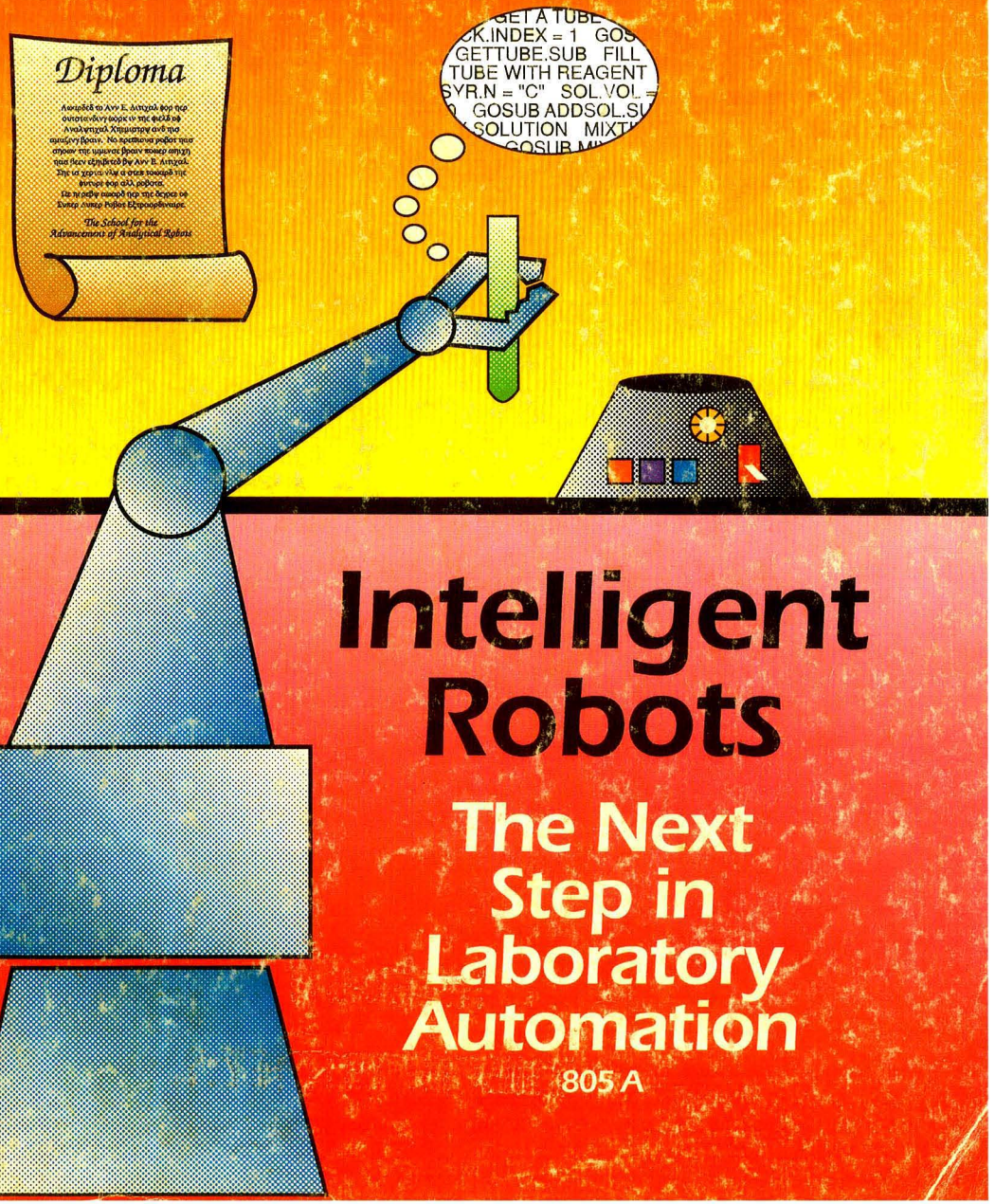

Intelligent Robots

The Next Step in Laboratory Automation

805 A

Seven precise reasons why your first capillary electrophoresis system should be a Dionex.

Get it right the first time.

Not all capillary electrophoresis systems are created equal. Which one should you get? The one that gives you the greatest flexibility and value.

That's precisely what the Dionex CES I does:

1. Fully programmable, dual polarity power supply with 3 control modes *and* gradients allows you to wield total control over each run.

2. Three automatic sample injection methods let you match the sampling technique to the sample—*any* sample.

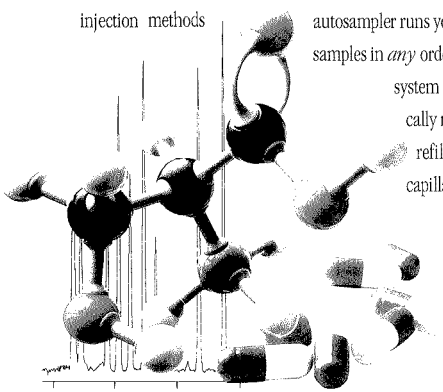

3. Our smart, 40-position autosampler runs your samples in *any* order. The system automatically rinses and refills vials and capillaries at each run for reproducible results. It also changes buffers—even during a run—*and* automates methods development.

4. Two detection modes are standard—UV/Vis with fiber optic-based remote cell for low noise *and* fluorescence with photo multiplier tube for femtomole sensitivity.

5. Easy, menu-driven programming of all instrument parameters from a single keyboard for effortless operation.

6. Forced-air cooling assures ideal conditions for your analyses.

7. Committed support by *the leader* in polar and ionic separations—from applications expertise and responsive service to complete automation capabilities.

Find out why your first capillary electrophoresis system should be a Dionex. Contact your local Dionex representative or (in U.S.A.) call **1-800-227-1817, ext. 42** today.

Capillary Electrophoresis System I

DIONEX
A BETTER SOLUTION

Dionex Corporation, P.O. Box 3603, Sunnyvale, CA 94088-3603. **Canada** Dionex Canada, Ltd., (416) 620-0077, **England** Dionex (UK) Ltd., (276) 691122, **West Germany** Dionex GmbH, (612) 66036, **France** Dionex S.A., (1) 4621-6666, **Italy** Dionex S.r.l., (06) 5792984, **Netherlands** Dionex B.V. (76) 714800.

MODEL 305
Modular HPLC Pump

The new Gilson Model 305 Master Pump. For analytical or preparative HPLC in the isocratic, binary or ternary modes.

The Pump.

Now you can program gradients without a computer. Upgrade your isocratic system without major expense. Switch from analytical to preparative and back again. Use the special dispense mode for repetitive injection in automatic preparative systems.

The heads.

For micro-analytical up to laboratory preparative scale (0.025 - 200 mL/min). For aqueous or salt-concentrated solutions. In titanium for ion-free work. All completely interchangeable so you can choose the optimum combination for your separation.

This compact new pump (only 32 cm wide) can handle any HPLC application.

To find out more about Gilson's new Master Pump, please contact your nearest Gilson representative.

THE MASTER PUMP

with built-in gradient controller

GILSON

U.S.A. - Box 27, 3000 West Beltline Hwy - Middleton, WI 53562 - Tel. : 608-836-1551
Tlx : 26-5478 - Fax : 608-831-4451 - FRANCE - BP 45 - 95400 Villiers-le-Bel - Tel. : (1) 34 29 50 00
Tlx : 606 682 - Fax : (1) 39 94 51 83

CIRCLE 61 ON READER SERVICE CARD

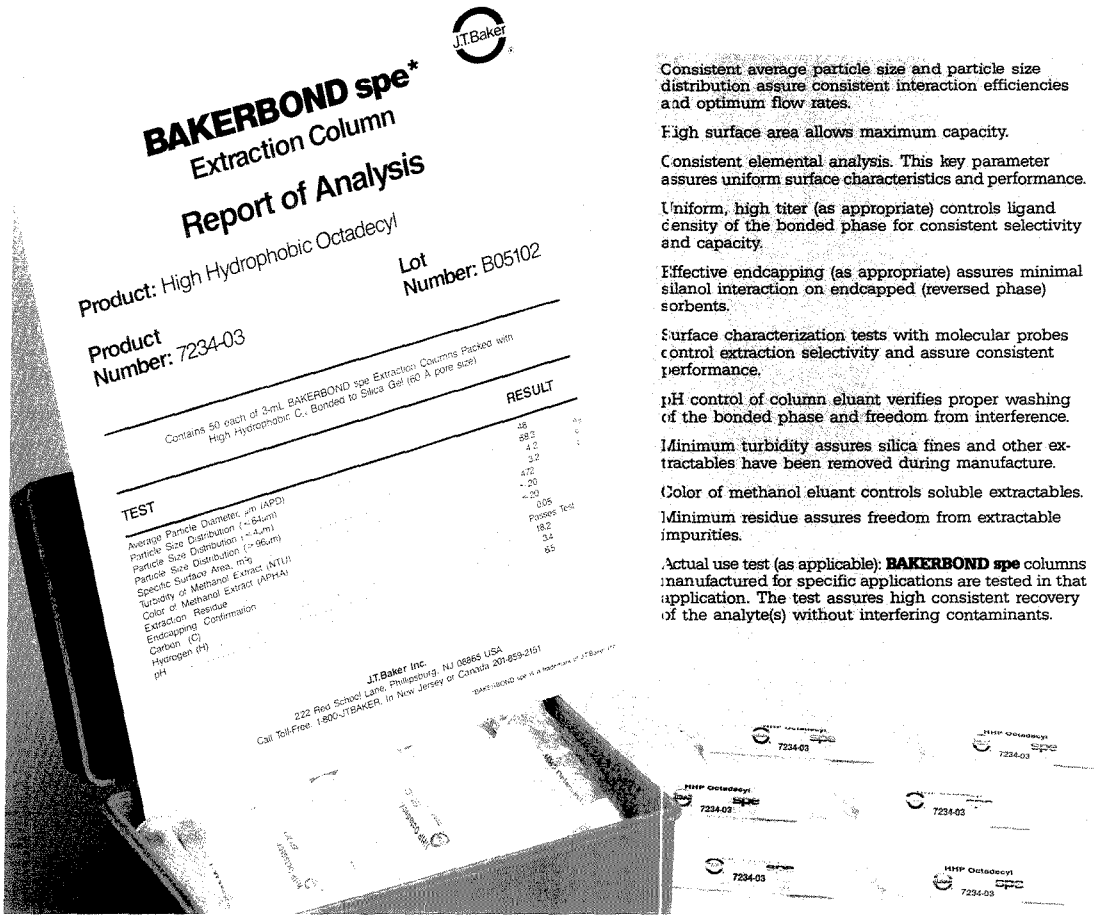

Consistent average particle size and particle size distribution assure consistent interaction efficiencies and optimum flow rates.

High surface area allows maximum capacity.

Consistent elemental analysis. This key parameter assures uniform surface characteristics and performance.

Uniform, high titer (as appropriate) controls ligand density of the bonded phase for consistent selectivity and capacity.

Effective endcapping (as appropriate) assures minimal silanol interaction on endcapped (reversed phase) sorbents.

Surface characterization tests with molecular probes control extraction selectivity and assure consistent performance.

pH control of column eluant verifies proper washing of the bonded phase and freedom from interference.

Minimum turbidity assures silica fines and other extractables have been removed during manufacture.

Color of methanol eluant controls soluble extractables.

Minimum residue assures freedom from extractable impurities.

Actual use test (as applicable): **BAKERBOND spe** columns manufactured for specific applications are tested in that application. The test assures high consistent recovery of the analyte(s) without interfering contaminants.

One of the major concerns with solid phase extraction has been reproducibility. Here's how J.T.Baker has solved it.

And a Report of Analysis to prove it.

Today's solid phase extraction columns from J.T.Baker are the state of the art.

To assure you accurate, reproducible solid phase sample preparation, J.T.Baker has developed some of the industry's most advanced technology and meaningful test result information:

State-of-the-art bonded phase (batch sizes up to 150 Kg) and **BAKERBOND spe*** column manufacturing techniques—to give you consistent sample preparation performance and reliable delivery.

Solid phase extraction products manufactured using Statistical Quality Control (SQC) and Statistical Process Control (SPC)—to assure you that key parameters are consistently held within narrow limits for minimum lot-to-lot variation.

Detailed quality characterization and a complete Report of Analysis in every box to prove it.

Experience a new level of solid phase extraction reproducibility. Call or write today for complete technical support and product information. 1-800-JTBAKER (1-800-582-2537). In NJ 201-859-2151.

J.T.Baker Inc.
J.T.Baker® 222 Red School Lane
Phillipsburg, NJ 08865

BAKERBOND spe* is a trademark of J.T.Baker Inc.

CIRCLE 20 ON READER SERVICE CARD

JULY 1, 1989
VOLUME 61
NUMBER 13

ANCHAM
The Audit Bureau
61(13) 755A–818A/1313–1472 (1989)
ISSN 0003-2700

ANALYTICAL CHEMISTRY (ISSN 0003-2700) is published semimonthly by the American Chemical Society at 1155 16th St., N.W., Washington, DC 20036. Editorial offices are located at the same ACS address (202-872-4600; TDD 202-872-8733). Second-class postage paid at Washington, DC, and additional mailing offices. Postmaster: Send address changes to ANALYTICAL CHEMISTRY Member & Subscriber Services, P.O. Box 3337, Columbus, OH 43210.

Claims for missing numbers will not be allowed if loss was due to failure of notice of change of address to be received in the time specified; if claim is dated (a) North America: more than 90 days beyond issue date, (b) all other foreign: more than one year beyond issue date, or if the reason given is "missing from files."

Advertising Management: Centcom, Ltd., 500 Post Rd. East, Westport, CT 06880 (203-226-7131)

1989 subscription rates include air delivery outside the U.S., Canada, and Mexico

	1 yr	2 yr
Members		
Domestic	$ 27	$ 45
Canada and Mexico	56	103
Europe	83	157
All Other Countries	120	231
Nonmembers		
Domestic	49	83
Canada and Mexico	78	141
Europe	155	280
All Other Countries	192	354

Three-year and other rates contact: Member & Subscriber Services, ACS, P.O. Box 3337, Columbus, OH 43210 (614-447-3776 or 800-333-9511).

Subscription orders by phone may be charged to Visa, MasterCard, Barclay card, Access, or American Express. Call toll free at (800-ACS-5558) from anywhere in the continental United States; from Washington, DC, call 872-8065. Mail orders for new and renewal subscriptions should be sent with payment to the Business Management Division, ACS, P.O. Box 57136, West End Station, Washington, DC 20037.

Subscription service inquiries and changes of address (Include both old and new addresses with ZIP code and *recent mailing label*) should be directed to the ACS Columbus address noted above. Please allow six weeks for change of address to become effective.

ACS membership information: Lorraine Bowlin (202-872-4567)

Single issues, current year, $7.00 except review issue and LabGuide, $12.00; **back issues and volumes and microform editions** available by single volume or back issue collection. For information or to order, call (800-ACS-5558) or write the Microform & Back Issues Office at the Washington address.

Nonmembers rates in Japan: Rates above do not apply to nonmember subscribers in Japan, who must enter subscription orders with Maruzen Company Ltd., 3–10 Nihonbashi 2-chome, Chuo-ku, Tokyo 103, Japan. Tel: (03) 272-7211.

Analytical CHEMISTRY®

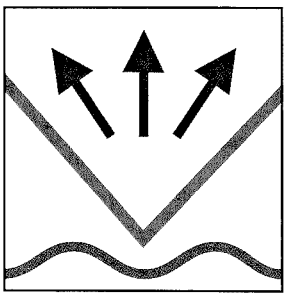

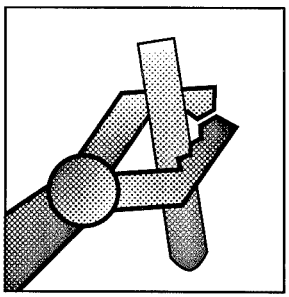

BRIEFS

Articles

* Corresponding author

Discover

FT-IR 800

The new Nicolet System 800 shapes the future of FT-Spectroscopy

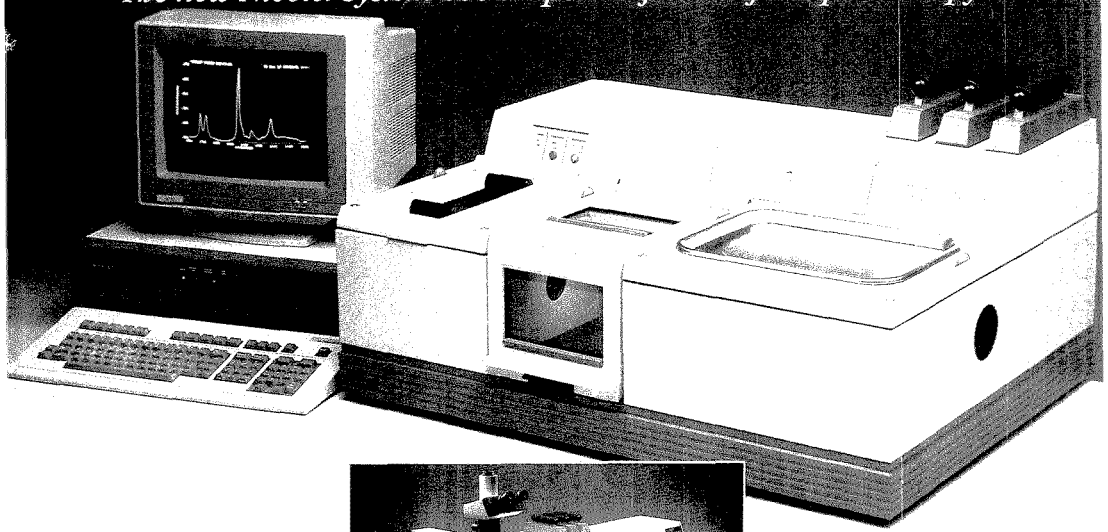

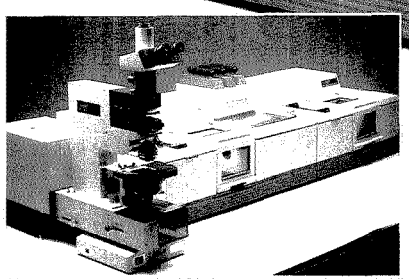

The System 800 represents the new generation in research tools. It is the synthesis of advances in optical, electronic and mechanical design. The System 800 combines an ultra-stable interferometer design with a unique dynamic alignment system, for superior data throughout the spectral range.

The System 800 provides the stability, signal-to-noise performance, and repeatability required for demanding applications. Whether your experiments involve long-term data acquisitions or rapid short-term dynamic spectroscopy applications, the 800 has the capabilities to solve your problems with confidence.

The System 800 incorporates the features demanded by leading research investigators throughout the world. Standard features include optical bench communications, optical bench configuration monitoring and status, rapid spectral range conversion, ultra-quiet electronics train, highest throughput optical design, dynamic alignment, fully expandable optical path, ultra high-output sources, and simplified experimental design for multiple modulation techniques.

The System 800 supports the full range of experiments including FT-Raman, Emission, Microspectroscopy, GC/FT-IR, SFC/FT-IR, and more. Multiple beam paths allow several different experiments or applications to be configured simultaneously.

Nicolet sets the standard for research performance. Let us show you the future of FT-Spectroscopy.

Nicolet

INSTRUMENTS OF DISCOVERY

Belgium: 02-762-2511	France: 1-30-81-3081	Japan: 06-863-1550	Switzerland: 056-834545
Canada: 416-625-8302	Germany: 069-837001	Netherlands: 03403-74754	United Kingdom: 0926-494111

Nicolet Analytical Instruments / 5225-1 Verona Rd. / Madison, WI 53711 / (608) 271-3333 / FAX: (608) 273-5046

To complement these direct Nicolet offices, Nicolet maintains a network of representatives in countries throughout the world.

CIRCLE 112 ON READER SERVICE CARD

Kinetic Determination of Primary and Secondary Amines Using a Fluoride-Selective Electrode and Based on Their Reaction with 1-Fluoro-2,4-dinitrobenzene 1358

Second-order rate constants are given, and a kinetic method is developed to determine primary and secondary amines in pharmaceuticals. The method, which can be used in colored and cloudy solutions, has a precision and accuracy of 2–3%.

Eleni Athanasiou-Malaki, Michael A. Koupparis*, and Themistocles P. Hadjiioannou, Laboratory of Analytical Chemistry, Department of Chemistry, University of Athens, 104 Solonos Street, Athens 10680, Greece

Extraction and Isolation of Phenoxy Acid Herbicides in Environmental Waters Using Two Adsorbents in One Minicartridge 1363

Simultaneous extraction and isolation of phenoxyacid herbicides from water is accomplished using a minicartridge filled with both a nonspecific adsorbent and a strong anion exchanger.

Antonio Di Corcia*, Marcello Marchetti, and Roberto Samperi, Dipartimento di Chimica, Università La Sapienza di Roma, Piazzale Aldo Moro 5, 00185 Roma, Italy

Theory of Optimization of the Experimental Conditions of Preparative Elution Chromatography: Optimization of the Column Efficiency 1368

The influence of column efficiency on the performance of preparative LC is discussed. The procedure for the optimization of column length, particle size, and flow velocity is also discussed.

Sadroddin Golshan-Shirazi and Georges Guiochon*, University of Tennessee, Department of Chemistry, Knoxville, TN 37996-1600 and Oak Ridge National Laboratory, Oak Ridge, TN 37831-6120

Direct Current Conductivity Detection in Ion Chromatography 1383

Monitoring the current resulting from a dc potential applied across two narrow-gauge hypodermic needles inserted inside a poly(tetrafluoroethylene) tube provides a low-volume, sensitive detector for IC. Cell volumes as low as 50 nL are easily obtained.

Dayong Qi, Tetsuo Okada, and Purnendu K. Dasgupta*, Department of Chemistry and Biochemistry, Texas Tech University, Lubbock, TX 79409-1061

Identification of Ions in Anion Chromatography by Stopped Flow Chronoamperometry 1387

A low-volume three-way valve and a conductivity detector are serially connected. Stopping the flow through the detector generates a chronoamperogram whose peak times and widths provide unique signatures of the eluting ions.

Tetsuo Okada, Purnendu K. Dasgupta*, and Dayong Qi, Department of Chemistry and Biochemistry, Texas Tech University, Lubbock, TX 79409-1061

Automated Determination of Manganese in Seawater by Electrolytic Concentration and Chemiluminescence Detection 1392

Mn(II) is electrochemically oxidized to Mn(IV) oxide and quantitatively electrodeposited on a glassy carbon electrode in the flow-through system. This concentration technique is coupled with an improved chemiluminescence method based on the oxidation of luminol with alkaline H_2O_2.

Eiichiro Nakayama*, Research Center for Instrumental Analysis, Faculty of Science, Kyoto University, Kyoto 606, Japan, **Kenji Isshiki and Yoshiki Sohrin,** Department of Chemistry, Faculty of Science, Kyoto University, Kyoto 606, Japan, and **Hajime Karatani,** Laboratory of Analytical Chemistry, Faculty of Textile Science, Kyoto Institute of Technology, Kyoto 606, Japan

Permselectivity and Ion-Exchange Properties of Eastman-AQ Polymers on Glassy Carbon Electrodes 1397

The permselective transport properties and ion-exchange binding of poly(ester sulfonic acid) films are explored, and their suitability for chemically modified electrode sensors is illustrated.

Joseph Wang* and Teresa Golden, Department of Chemistry, New Mexico State University, Las Cruces, NM 88003

Second Dissociation Constant and pH of *N*-(2-Hydroxyethyl)piperazine-*N'*-2-ethanesulfonic Acid from 0 to 50 °C 1400

HEPES is recommended as a pH buffer for physiological measurements. The pH values for the buffer system at ionic strengths similar to those in physiological fluids are determined at temperatures from 0 to 50 °C.

Daming Feng, W. F. Koch*, and Y. C. Wu, National Institute of Standards and Technology, Gaithersburg, MD 20899

Fluorescence Studies of Energy Transfer in Sodium Taurocholate and Sodium Dodecyl Sulfate Micellar Solutions 1405

When sodium taurocholate is used for solubilization, less energy transfer is observed between PAHs in aqueous solution, as compared with sodium dodecyl sulfate.

Kasem Nithipatikom and Linda B. McGown*, Department of Chemistry, P. M. Gross Chemical Laboratory, Duke University, Durham, NC 27706

Flow Injection Donnan Dialysis Preconcentration of Cations for Flame Atomic Absorption Spectrophotometry 1410

A cation preconcentration method provides 100-fold enhancement of the detection limit with a dialysis time of 5 min. Application of the approach to trace determination of lead in drinking water is demonstrated.

John A. Koropchak* and Lori Allen, Department of Chemistry and Biochemistry, Southern Illinois University, Carbondale, IL 62901-4409

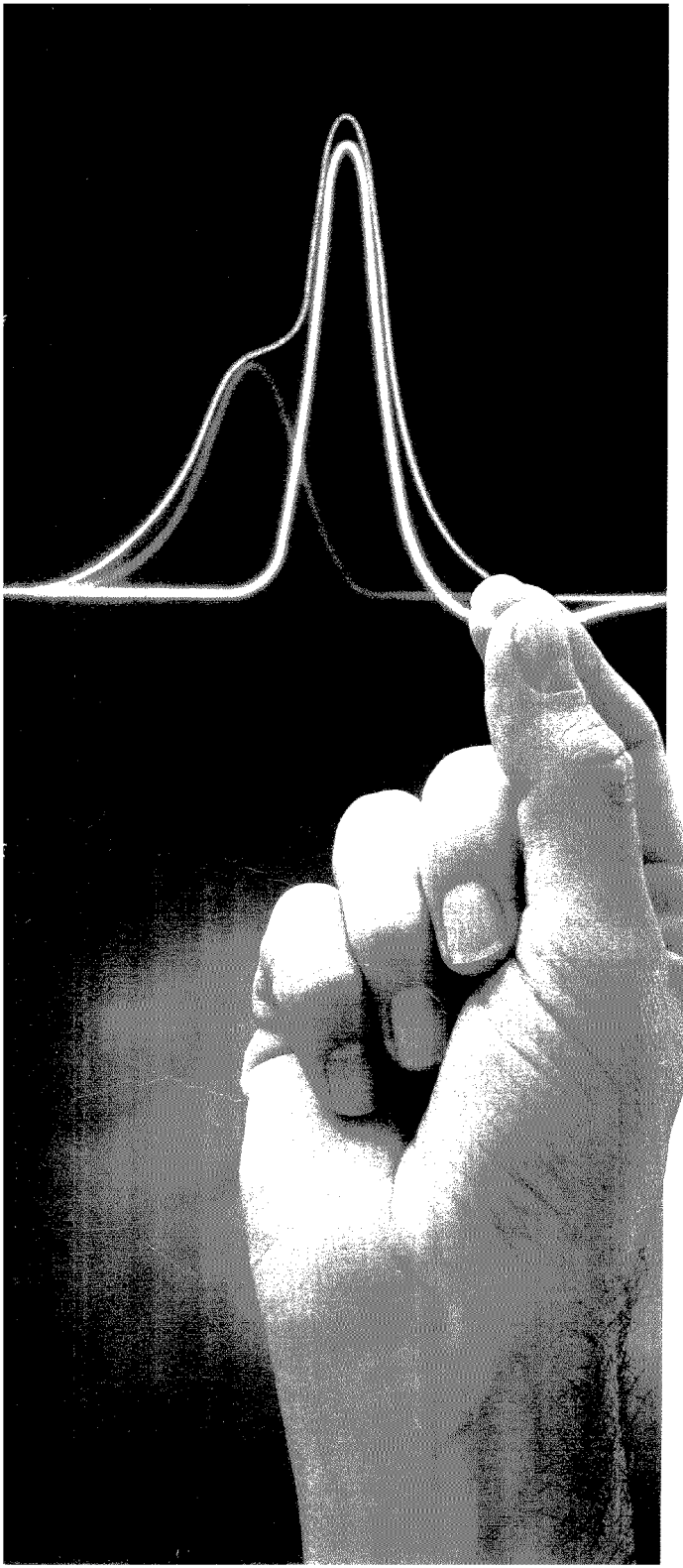

Now, advanced methods development is System Gold™ easy.

System Gold,™ the Personal™ Chromatograph, is the most advanced, easiest-to-learn, easiest-to-use HPLC.

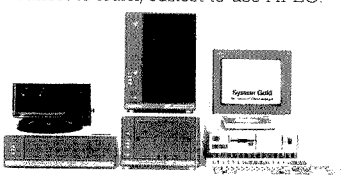

And now it offers the fully automated convenience of our new Model 168 Diode Array Detector Module and new Model 507 Autosampler.

You get rapid acquisition of complete UV/VIS spectra through diode array detection. And you get the programmable versatility of the 507 Autosampler.

All with a level of convenience and automation never before available with *any* HPLC.

And it's System Gold easy.

Find out for yourself how easy methods development can be with System Gold. Contact your local Beckman representative. Offices in major cities worldwide.

Call 800/742-2345 in the US. Or write Beckman Instruments, Inc., Altex Division, 2350 Camino Ramon, P.O. Box 5101, San Ramon, CA 94583.

BECKMAN

A SMITHKLINE BECKMAN COMPANY

Australia, Sydney **Austria,** Vienna **Canada,** Toronto **France,** Gagny **Germany,** Munich **Hong Kong,** Aberdeen **Italy,** Milano **Japan,** Tokyo **Mexico,** Mexico City **Netherlands,** Mijdrecht **Puerto Rico,** Carolina **Singapore. South Africa,** Johannesburg **Spain,** Madrid **Sweden,** Bromma **Switzerland,** Nyon **Taiwan,** Taipei **United Kingdom,** High Wycombe AX88-1043A

CIRCLE 22 FOR REPRESENTATIVE & LITERATURE.

CIRCLE 23 FOR LITERATURE ONLY.

Automated Slurry Sample Introduction for Analysis of a River Sediment by Graphite Furnace Atomic Absorption Spectrometry 1414

The heterogeneity of NIST SRM 2704 river sediment is studied for Pb, Mn, As, and Fe using samples in microgram amounts in the furnace. The results are in good agreement with certified values for the four elements.

M. S. Epstein, G. R. Carnrick, and Walter Slavin*, The Perkin-Elmer Corporation, Norwalk, CT 06859 and **N. J. Miller-Ihli,** U.S. Department of Agriculture, Nutrient Composition Laboratory, Beltsville, MD 20705

Measurement of Caustic and Caustic Brine Solutions by Spectroscopic Detection of the Hydroxide Ion in the Near-Infrared Region, 700–1150 nm 1419

The spectrum of the hydroxide ion is obtained using difference spectra, second-derivative techniques, and multivariate spectral reconstruction. Multivariate calibration yields results that are resistant to interference from large variations in brine concentration (0.01–5.0 M).

M. Kathleen Phelan, Clyde H. Barlow, Jeffrey J. Kelly, Thomas M. Jinguji, and James B. Callis*, Center for Process Analytical Chemistry, Department of Chemistry, BG-10, University of Washington, Seattle, WA 98195

Near-Infrared Laser Diode Intracavity Absorption Spectrometry 1425

A near-IR laser diode intracavity absorption spectrometer is developed using a commercial laser diode. Detection limits of 10^{-4}–10^{-5} AU are obtained with this single-beam instrument.

Ed Unger and Gabor Patonay*, Department of Chemistry, Georgia State University, Atlanta, GA 30303

Atomic Absorption Determination of Copper in Silicate Rocks by Continuous Precipitation Preconcentration 1427

A manifold is designed for the determination of Cu at the μg/g level. The ion is precipitated with rubeanic acid and then dissolved with potassium dichromate.

Ricardo E. Santelli, Mercedes Gallego, and Miguel Valcárcel*, Department of Analytical Chemistry, Faculty of Sciences, University of Córdoba, Córdoba-14004, Spain

Light Absorption and Mixed Micelle Composition as Factors in Determining Intensities of Room-Temperature Phosphorescence 1431

Experiments show that SO_3^{2-} forms a light-absorbing complex with Tl^+ that can attenuate UV excitation in micelle-stabilized RTP. This reaction offsets gains derived from increased Tl^+ concentrations achieved using mixed surfactants.

N. E. Nugara and A. D. King, Jr.*, Department of Chemistry, School of Chemical Sciences, University of Georgia, Athens, GA 30602

Aromatic Bases as Eluent Components for Conductivity and Indirect Ultraviolet Absorption Detection of Inorganic Cations in Nonsuppressed Ion Chromatography 1435

Alkali metal and earth cations are separated using substituted pyridines and aromatic amines in water as eluents. Detection limits in the low-ppb range are obtained using conductivity and UV absorption detectors.

Paul R. Haddad* and Roy C. Foley, Department of Analytical Chemistry, University of New South Wales, P.O. Box 1, Kensington, New South Wales 2033, Australia

Fast Atom Bombardment Induced Reduction of Aromatic Oximes 1442

Evidence is presented to support the observation that fast atom bombardment of oximes leads to reduction of imines. Aspects of the mechanism of reduction are revealed by time-dependent FAB studies.

M. Graca O. Santana-Marques and António J. V. Ferrer-Correia, Department of Chemistry, University of Aveiro, 3800 Aveiro, Portugal and **Michael L. Gross*,** Midwest Center for Mass Spectrometry, Department of Chemistry, University of Nebraska, Lincon, NE 68588

Ion Confinement in the Collision Cell of a Multiquadrupole Mass Spectrometer: Access to Chemical Equilibrium and Determination of Kinetic and Thermodynamic Parameters of an Ion–Molecule Reaction 1447

Equilibrium and rate constants of ion–molecule reactions are determined by confining ions in an rf-only quadrupole collision cell for a variable interaction time (up to 250 ms).

Claude Beaugrand, SN Nermag, 49 quai du Halage, 92500 Rueil-Malmaison, France and **Daniel Jaouen, Hélène Mestdagh, and Christian Rolando*,** Ecole Normale Supérieure, Département de Chimie, Laboratoire de l'Activation Moléculaire, UA 1110, 24 rue Lhomond, 7531 Paris Cedex 05, France

Sequence Analysis of Highly Sulfated, Heparin-Derived Oligosaccharides Using Fast Atom Bombardment Mass Spectrometry 1453

Negative ion FAB-MS analysis of a series of enzymatically prepared, highly sulfated, heparin-derived oligosaccharides using triethanolamine as the FAB matrix is presented.

Larry M. Mallis*, High Resolution Mass Spectrometry Facility, The University of Iowa, Iowa City, IA 52242 and **Hui M. Wang, Duraikkannu Loganathan, and Robert J. Linhardt,** Division of Medicinal and Natural Products Chemistry, College of Pharmacy, The University of Iowa, Iowa City, IA 52242

Our low-cost 250 LC Systems give you upward mobility

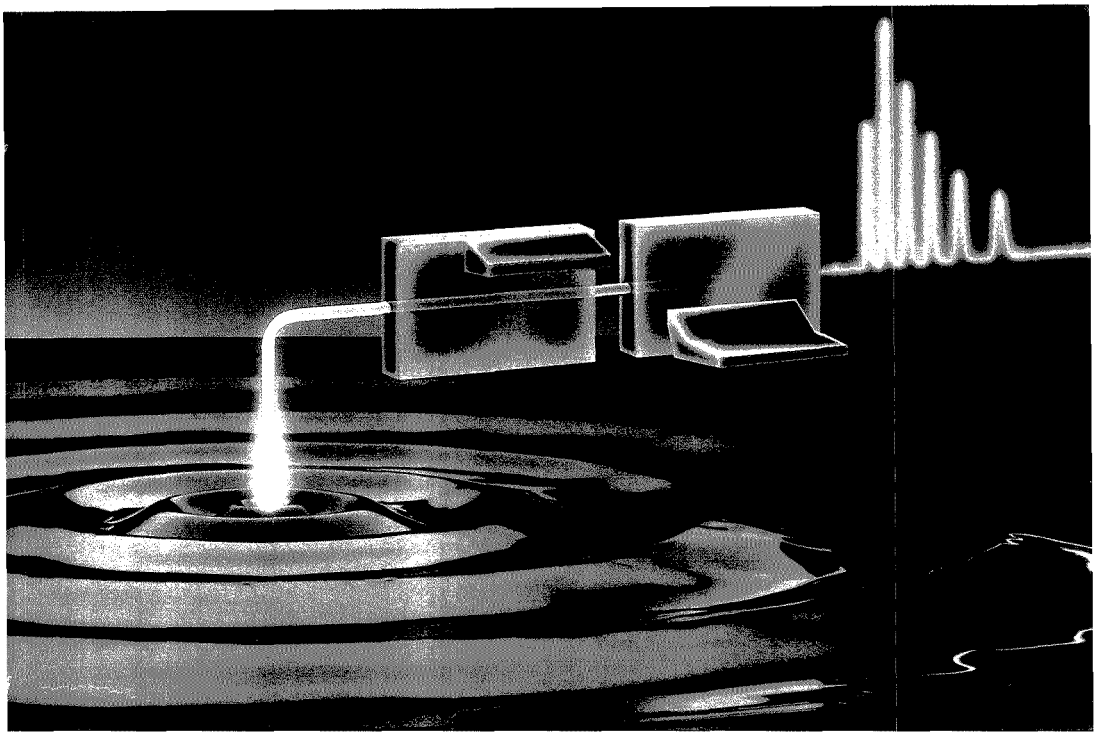

Perkin-Elmer 250 LC Systems grow with your laboratory. Modular design lets you upgrade to gradient/diode array capabilities at the lowest price. Move up to higher LC performance at your own pace.

BETTER PUMP CAPABILITY

Get started with a system incorporating our Model 250 Isocratic Pump. When the time's right, upgrade to the 250 Binary Pump for unsurpassed multisolvent gradient capability.

BETTER SENSITIVITY

Only 250 LC Systems put the highest diode array sensitivity within easy reach. With a simple field upgrade, you can convert our programmable, dual-wavelength LC-135 into an LC-235 with full spectral performance.

BETTER VERSATILITY

With 250 LC systems, you can choose from Perkin-Elmer's line of the most sensitive UV/VIS, diode array, and fluorescence detectors in the world. Including the extraordinary LC-480 AutoScan for high resolution diode array performance.

From low-cost, entry-level reliability to sophisticated, full spectral power, Perkin-Elmer 250 LC systems have it all. Find out how you can move up to LC at its best by contacting your Perkin-Elmer representative. Or call toll-free 1-800-762-4000.

Perkin-Elmer Corp., 761 Main Avenue,
Norwalk, CT 06859-0012 U.S.A.
Tel: (203) 762-1000. Telex 965-954
Bodenseewerk Perkin-Elmer & Co., GmbH,
Postfach 1120, 7770 Ueberlingen,
Federal Republic of Germany.
Tel: (07551)810
Perkin-Elmer Ltd., Maxwell Road,
Beaconsfield, Bucks HP9 1QA, England.
Tel: Beaconsfield (0494)676161

HPLC. Confidence in Analysis.

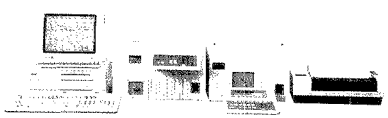

PERKIN ELMER

Correspondence

Technical Notes

Your LC Bench will never be the same!

Your lab can easily change from Thermospray to Electron Ionization with the flip of a switch.
No need to break vacuum.
No need to crowd your lab space (and budget) with other instruments that accomplish only half as much with twice the effort.

Vestec's commitment to Liquid Chromatography and Mass Spectrometry doesn't end here. We are providing a multitude of combinations and features for our systems that make them the most versatile chromatography detector available.

With all of this, the best feature is still Thermospray LC/MS from the original source... Vestec!

EI is just the beginning of a whole new set of features from Vestec, the recognized leader in LC/MS technology. At the heart of the Dedicated Model 201 is a ***new*** high performance **TS-EI** (Thermospray-Electron Ionization) **Combination Source**.

The System combines advanced Thermospray technology with Electron Ionization via a unique particle beam interface. This interface provides high solvent removal efficiency and enhanced sensitivity - even at low mass.

Ask us about the Vestec particle beam **LC-EI** interface for your existing mass spectrometer.

VESTEC
CORPORATION
The Dedicated LC/MS People

9299 Kirby Drive
Houston, Texas 77054
(713) 796-9677

CIRCLE 168 ON READER SERVICE CARD

Now any* Macintosh™ can be an HPLC data system!

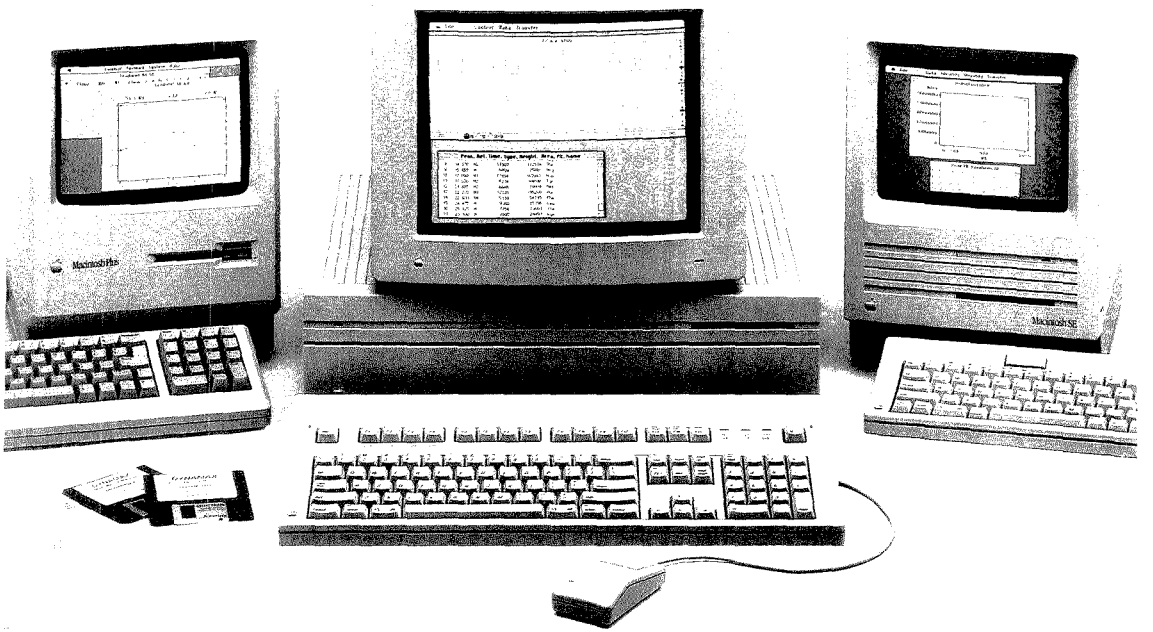

Rainin's new Dynamax* HPLC Method Manager for the Macintosh incorporates features that significantly expand its chromatographic utility...like total Mac II compatibility...and background operation under MultiFinder* so you can do word processing or run other applications simultaneously with data collection and analysis.

Dynamax Method Manager is incredibly easy to use. The Macintosh user interface eliminates complex menu trees. Needed functions are always available, just a mouse click away.

Rainin software and hardware let the Mac* acquire data and display the chromatogram on the high-resolution screen. The program locates peaks, identifies analytes, calculates amounts and concentrations, and, uniquely, displays all this information on-the-fly, while data is being collected. No waiting to see results!

After each analysis, the computer prints the chromatogram and report. Complete copies of raw data and method specifications, as well as reported values, can be saved automatically on any Macintosh-compatible storage device.

Dynamax HPLC Method Manager can recall chromatographic data again and again for reprocessing with different integration parameters. Fine tuning processing conditions is easy! Optimum conditions can be saved for later use in real-time analyses.

Automatic calculation of correlation coefficients, peak asymmetries, and efficiencies simplifies quality control of chromatographic methods. A new desk accessory, ChromPic*, converts any chromatogram to a PICT-file object for incorporation into graphic and word-processing documents. Report files are compatible with Microsoft Excel and other spreadsheet programs. Contact-closure inputs and outputs facilitate use with automated systems. The list goes on!

As a gradient controller, Dynamax HPLC Method Manager works with any Rainin or Gilson HPLC system. There are no hardware modifications to the Mac, just one convenient connection to the modem port.

If you're getting ready to purchase a complete HPLC system, or just an HPLC data system, let Rainin show you how easy HPLC can be with a Macintosh. Call **800-FOR-HPLC** for a free consultation. (In Massachusetts, call 617-935-3050). Or write:

RAININ
INSTRUMENT CO. INC

Mack Road, Woburn, MA 01801
617-935-3050
1715 64th Street, Emeryville, CA 94608
415-654-9142

*Macintosh-Plus, Macintosh-SE, or Macintosh II.

"Dynamax" and "ChromPic" are trademarks of Rainin Instrument Co., Inc.

"Macintosh", "Mac", and "MultiFinder" are trademarks of Apple Computer, Inc.

CIRCLE 138 ON READER SERVICE CARD

EDITORIAL

Publish or Perish

One of the most interesting museums in the world is the Plantin–Moretus Museum in Antwerp, Belgium, which is dedicated to the art and science of book printing. Christopher Plantin, originally from France, started a printing house in Antwerp and published his first book in 1555. In 34 years he managed to publish more than 1500 works—an average of nearly 50 a year. This number, which was phenomenal for that time, made Plantin the first great "industrial" printer. However, he was an industrial printer who knew how to publish perfectly, and he was always dedicated to publishing the most meritorious and prominent works.

His son-in-law Jan Moretus, who became his partner and successor, continued in the fine tradition of his mentor. Run by various members of the family, the firm continued for several centuries until 1866, when the last book left the old presses. In 1877 the Plantin House became a museum owned by the city of Antwerp, thereby preserving many treasures of the early history of printing.

A visitor to the museum today can appreciate the remarkable accomplishments of the early pioneers in book publishing. The printing of a book is the result of many operations, and the showcases in the museum bring together the different materials and instruments that were necessary at that time. Included are the manuscript of the author ready for press, the casting of the printing types, the wood blocks and copper plates of the illustrations, the punches and casting molds necessary for the compositor's sticks, and other tools for composition.

In each period of its history the book had a particular appearance, and the displays illustrate the characteristics and peculiarities of the book in its historical evolution from the time of Guttenberg (ca. 1450) until the end of the eighteenth century. The Plantin–Moretus Museum also contains libraries of about 30,000 volumes and about 500 manuscripts, many of which have extraordinary historical and artistic importance. About 150 paintings by Flemish masters, including 18 by P. P. Rubens, decorate the walls of the museum.

To mark the 400th anniversary this year of the death of Christopher Plantin, the museum has assembled an impressive exhibit of the early published works of science and medicine. For those who think of printing as a business, a visit to the museum will quickly reveal the wealth of culture in this important endeavor.

G. H. Morrison

VARIAN LC STAR SYSTEM WITH SINGLE POINT CONTROL OPENS WINDOWS TO ADVANCED CHROMATOGRAPHY.

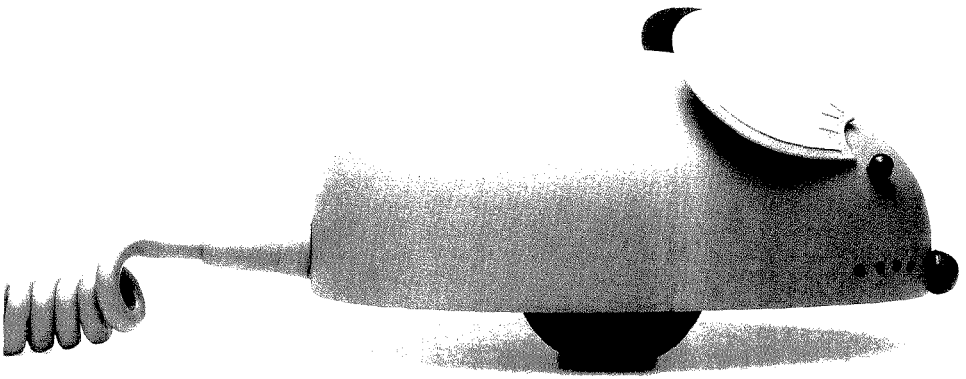

NO IFS, ANDS OR SQUEAKS.

Microsoft® Windows and the powerful IBM PS/2™ computer gives single point mouse control to the new Varian LC Star System.

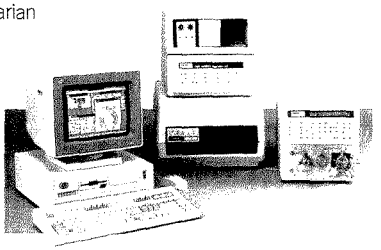

State-of-the-art software gives all the advantages of a centrally controlled system with extensive color graphics. It minimizes error, saves you time, and provides full data handling, including diode array spectral processing.

All of the Star System modules are independently intelligent. Even without the workstation, powerful capability is maintained within each individual component. If you have the need for rapid throughput, methods diversity and reliable automation, you'll be delighted by the real flexibility and versatility of this HPLC system.

The Varian LC Star System is designed for maximum reliability and easy maintenance. It is designed for continuous automation, including unattended sample preparation. It is designed to give you the best chromatographic results. And, best of all, it is designed by a single company to supply and support it. Varian.

For more information, call **800-231-8134**. In Canada, call **416-457-4130**.

Varian is your full-line company for analytical instrumentation
UV-Visible-NIR
LIMS
Data Systems
Atomic Absorption
NMR
Liquid Chromatography
Gas Chromatography

CIRCLE 170 ON READER SERVICE CARD

LC WITH A FUTURE

Eastern Analytical Symposium Announces Award Winners

Five scientists will be honored at this year's Eastern Analytical Symposium (EAS), to be held September 24–29 at the New York Hilton Hotel in New York City.

David Hercules, professor of chemistry at the University of Pittsburgh, will receive the EAS Award for Outstanding Achievements in the Fields of Analytical Chemistry. The award cites his contributions to the analytical chemistry of surfaces and solid-state MS. This research has employed a host of techniques, including X-ray photoelectron spectroscopy, Auger spectroscopy, secondary ion MS, ion-scattering spectroscopy, FT-IR spectroscopy, and laser microprobe MS.

Hercules earned his B.S. degree from Juniata College in 1954 and his Ph.D. from the Massachusetts Institute of Technology in 1957. He held academic positions at Lehigh University, Juniata, MIT, and the University of Georgia before joining the University of Pittsburgh faculty in 1976.

EAS's New York Section will award the Applied Spectroscopy Medal to **James Winefordner,** University of Florida professor of chemistry, for his research contributions in atomic and molecular emission, absorption, and fluorescence in hot gases such as flames; molecular fluorescence and phosphorescence of species in the condensed phase; and the development of spectroscopic instrumentation.

Winefordner received his B.S. and M.S. degrees and his Ph.D. from the University of Illinois in 1954, 1955, and 1958, respectively. Following another year at Illinois as a postdoctoral student, he joined the faculty at the University of Florida.

This year's EAS Award in Chromatography will be given to **Harold McNair,** professor of chemistry at the Virginia Polytechnic Institute and State University. His research has focused on the analysis of trace organics in water and soil; the development of automated chromatographic systems involving LC/LC, LC/GC, and LC/LC/GC; packed capillary LC and IC columns; and the manufacture and characterization of high-efficiency cross-linked GC and SFC columns.

McNair obtained his B.S. degree from the University of Arizona in 1955 and his M.S. degree and Ph.D. from Purdue University in 1957 and 1959, respectively. He spent a year at the Technical University Eindhoven in The Netherlands on a Fulbright fellowship. In the years that followed, McNair worked for Esso Research and Engineering, F&M Scientific, and Varian Aerograph before joining the faculty of VPI in 1968.

K. L. Cheng, professor of chemistry at the University of Missouri—Kansas City, will receive the Benedetti-Pichler Memorial Award in Microchemistry. He has pioneered the use of EDTA to mask and demask metal species, introduced the reagents PAN (pyridylazonapthaol) and Thio-Michler's ketone, provided a theory of double-layer capacitance, developed the analytical uses of photoelectron spectroscopy, and recently worked with positron annihilation spectroscopy for chemical analysis.

Cheng earned his B.S. degree from Northwestern College in China and obtained his M.S. degree and Ph.D. from the University of Illinois in 1949 and 1951, respectively. He then worked for Commercial Solvents Corporation, the University of Connecticut, Westinghouse, Kelsey-Hayes Company, and RCA laboratories. In 1966 Cheng joined the University of Missouri faculty.

The first EAS Award in Near-Infrared Spectroscopy will honor **Karl Norris,** generally recognized as the "father" of modern near-IR spectroscopy.

A 1942 graduate of the Pennsylvania State University, Norris has worked for Airplane and Marine Instrument Company, the University of Chicago, and the U.S. Department of Agriculture, where he was appointed chief of the Instrumentation Research Laboratory in 1977. Norris is now retired.

ANALYTICAL CHEMISTRY Monitored

As part of its continuing program to monitor the Society's publications, the Society Committee on Publications (SCOP) has formed an ad hoc task force to monitor ANALYTICAL CHEMISTRY. Monitoring task forces are charged with investigating the intellectual and editorial health of the publications and determining if they adequately fill the needs to which they are addressed.

Comments are invited and should be directed to the task force chair, Lockhart (Buck) Rogers (c/o Randall Wedin, Publications Division, American Chemical Society, 1155 16th St., NW, Washington, DC 20036). Other members of the task force who also may be contacted are Jeanette Grasselli, David Hercules, Mary Kaiser, Barry Karger, James McCloskey, Lawrence Pachla, W. D. Shults, Isiah Warner, R. Mark Wightman, Nicholas Winograd, Richard Zare, and Ned Heindel (SCOP representative).

Society for Analytical Chemists of Pittsburgh Starter Grants Awarded

The Society for Analytical Chemists of Pittsburgh has awarded $10,000 starter grants to Werner Kuhr, University of California at Riverside, and to Jennifer Brodbelt-Lustig, University of Texas at Austin. The grants are designed to encourage high-quality innovative research by young professors in the field.

Kuhr received his Ph.D. under the direction of R. Mark Wightman at Indiana University and carried out postdoctoral work at Iowa State University with Edward Yeung. He joined the Riverside faculty in 1988 and will use the grant to develop capillary zone electrophoresis to sample transient neurochemical events in the brain.

Brodbelt-Lustig earned her Ph.D. from Purdue University under the joint direction of R. Graham Cooks and Peter Kissinger. She is currently a postdoctoral student with Michael Bowers at the University of California, Santa Barbara, and will join the University of Texas staff in September. Brodbelt-Lustig's research will focus on ion–molecule reactions in MS.

NMR Finds Foul Fuels

Proton NMR spectra may provide a rapid method for predicting the thermal stability of hydrocarbon jet fuels. John Russell and Brent Bailey, researchers with the Southwest Research Institute in San Antonio, TX, are developing this thermal stability analysis to screen fuels for the National Aerospace Plane (NASP), the high-tech aircraft being developed by the United States for flight at Mach 7 to 10.

Fuel aboard the NASP is slated to double as a coolant, circulating through heat exchangers in the aircraft's leading edges and engines. As it carries heat away from the fuselage and engine, fuel temperatures could approach 500 °C. If the fuel decomposes prior to combustion, the resulting gums and soot could foul heat exchangers, plug filters, and clog fuel injectors.

According to Russell, fingerprint regions of the NMR spectrum can be matched to a fuel's deposit-forming tendencies at high temperatures. For instance, NMR peaks for aromatic hydrocarbons indicate a lower fuel stability.

The Sound of a Thirsty Tree

Drought-stressed trees emit an ultrasonic yelp that may attract bark- and wood-boring insects. Robert Haack of the U.S. Department of Agriculture Forest Service in East Lansing, MI, has characterized the duration and strength of these signals using sound transducers attached to trees. He is now generating these same sounds and testing insect response to the ultrasonic pulses.

The noise, first reported in 1983, occurs when water columns running up the tree snap apart. Because these columns are under tremendous tension, breaking the column generates a pulse with a frequency of > 20 kHz. The ultrasonic sound has been recorded in hardwoods, such as apple and red maple; conifers, including Scotch pine and eastern hemlock; and even in corn.

Haack, speaking at the Acoustical Society of America's meeting in Syracuse, NY, also pointed out that drought-stricken trees emit different volatile chemicals and have higher temperatures than normal. These factors may also aid insects looking for a drought-weakened tree.

Killer Bee Buzz

Also speaking at the Acoustical Society of America meeting, Howard Kerr and M. E. Buchanan of B-Tec, Inc., Maryville, TN, reported that sound signals can differentiate flying European bees from the more aggressive Africanized or "killer" bees.

Because of taxonomical differences, European honeybees emit an acoustic power peak in the 210–230-Hz range, whereas the Africanized bees produce a signature at 260–280 Hz. The researchers found the signal difference after collecting time-averaged signals from bees in flight and using Fourier analysis to create power spectral density plots, which revealed the acoustic variation.

B-Tec has applied for a patent based on the finding. The firm will use the sound difference to market a field instrument called "Buzz Buster" for screening Africanized bees.

Chip off the Old Prism

What may be the world's smallest optical prism has been unveiled by physicists Robert Gallawa of the National Institute of Standards and Technology laboratories in Boulder, CO, and Zongjian Sun, visiting scientist from Tongji University in Shanghai, China. Measuring less than 125 μm on a side, this microprism (shown next to a 125-μm optical fiber) is barely visible to the naked eye.

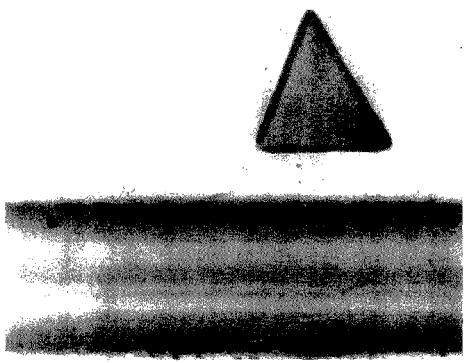

According to Gallawa, the prism was carved from optical glass in a "brute force approach" requiring approximately 16 h of constant grinding. Microprisms such as these could be used as measuring tools to determine the light propagation characteristics of fiber optics that relate to the material's ability to carry information. In addition, these prisms might someday find a role in miniaturized optical circuits.

"It was a demonstration that has served its purpose," Gallawa explained. "It is one of those things that is motivated by curiosity, and when finished you are amazed."

For Your Information

The International Union of Pure and Applied Chemistry (IUPAC) **Analytical Chemistry Division has formed a Committee on Environmental Analytical Chemistry.** The committee's agenda ranges from problems in particle sampling to redox processes and eutrophication. For more information, contact Jacques Buffle, Department of Inorganic, Analytical, and Applied Chemistry, Sciences II, 30 quai E. Ansermet, 1211 Genève 4, Switzerland.

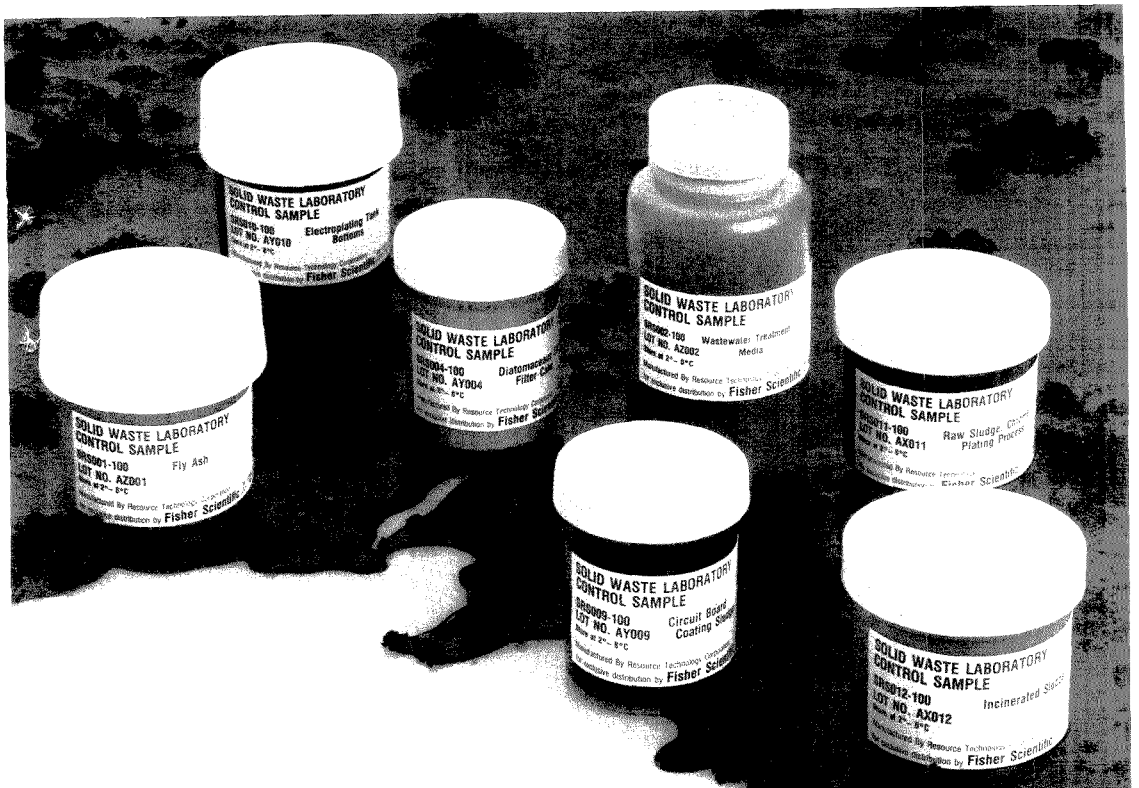

Get realistic about solid waste analysis

Satisfy SW846 QA/QC requirements with the first commercial reference samples *derived from real-world hazardous waste*

Valid results are critical in analyzing solid waste. Obtain *certified confidence* with Fisher Scientific's Solid Waste Reference Samples (SWRS). SWRS are produced from *actual* industrial waste streams—homogenized, analyzed and packaged. They are *not* spiked. Their matrices and analytes parallel the analytical samples you receive from clients.

Real-world SWRS let you evaluate how well your lab handles difficult analyses. You can compare your results to an interlaboratory reference value reliable at the 95% confidence level, assuring the accuracy of your QA/QC methods. For details on our new SWRS, contact your local Fisher Representative or circle the Reader Service number below.

Expect more from FisherChemical

FisherChemical

Fisher Scientific

Excellence in Serving Science...Since 1902

CIRCLE 50 ON READER SERVICE CARD

Waters Adds a New Dimension to Gas Chromatography

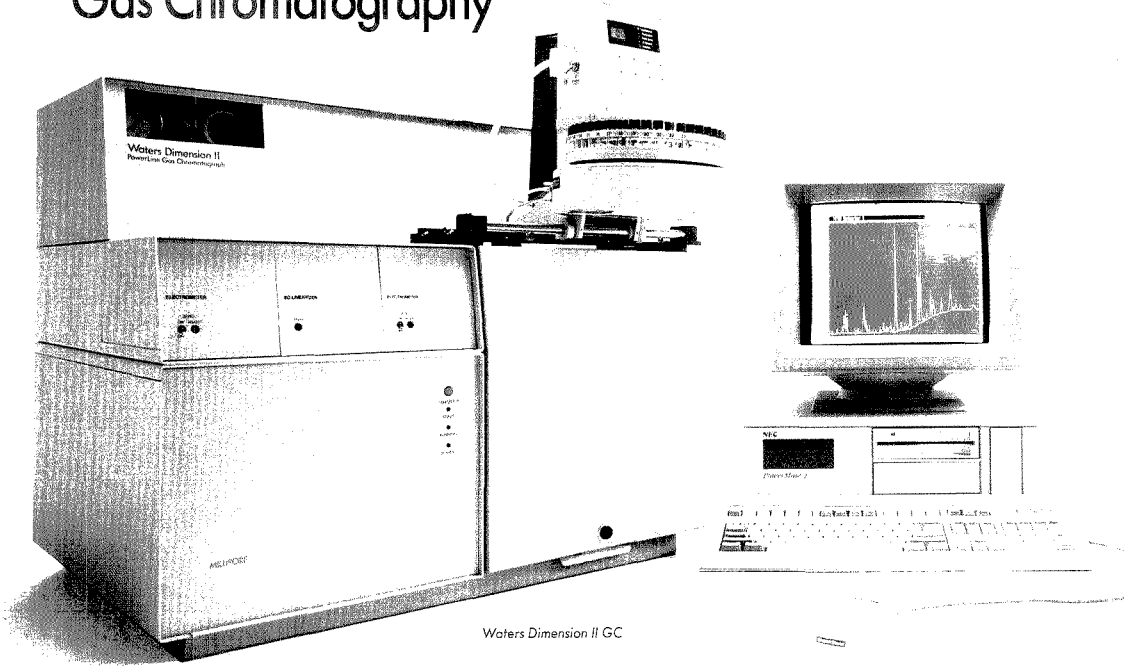

Waters Dimension II GC

Waters® Dimension GC Series Takes You Beyond Conventional Performance.

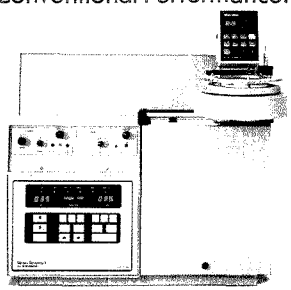

Waters Dimension I GC

Integrated diagnostics.
Built-in ability to monitor fuel, oxidant, and detector gases saves precious time.

Increased productivity.
Direct autosampler transfer between independently heated injectors increases throughput.

Mouse driven software.
Advanced multi-tasking Maxima™ software provides easy mouse driven operation and PowerLine™ system control of either LC or GC systems.

Convenient column accessibility.
A large dual column oven with independent side-by-side access lets you change columns swiftly.

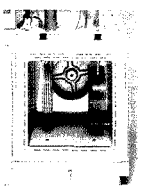

Detection versatility.
A complete line of high performance GC detectors provides unmatched versatility. Choose from flame ionization, flame photometric, Ni63 electron capture, electrolytic conductivity, photoionization, nitrogen/phosphorous, discharge ionization and thermal conductivity detection.

Unique sample cleanup.
Waters MilliLab™ Workstation couples automated sample cleanup and preparation with GC analytical power. Automate a wide variety of repetitive tasks while feeding autosampler carousels completely unattended.

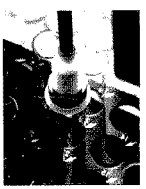

Only a Waters Dimension I or II GC System can give you all of these performance options, plus the industry's most reputable support program.

Call 1-800-456-WDGC for the Waters representative in your area.

Division of MILLIPORE

Raman Monitoring of Dynamic Electrochemical Events

Richard L. McCreery
Department of Chemistry
The Ohio State University
Columbus, OH 43210

Richard T. Packard
E. I. du Pont de Nemours and Co.
Deepwater, NJ 08023

Most electrochemical phenomena and techniques are based on electron transfer between a conductor and a redox system, usually dissolved in a solution. Electrosynthetic processes such as metals production, electroplating, electroanalysis, and electrochemical energy conversion account annually for more than $30 billion worth of products (~1% of the U.S. GNP) and contribute to a range of industries worth much more (*1*). All of these processes rely on the direct interconversion of electrical current and chemical energy in the form of a redox system.

For problems in analytical chemistry, the heterogeneous electron transfer phenomenon results in certain important consequences (*2*). First, electroanalytical measurements can be extremely sensitive, with measurable currents corresponding to minute amounts of analyte. For example, easily measured currents of 10^{-12} amp equal 10^{-17} mol/s of a one-electron redox system, and state-of-the-art techniques are approaching detection limits corresponding to single redox events. Even small currents can be measured with high precision and accuracy, resulting in electroanalytical techniques with similarly high quantitative accuracy.

A second consequence of particular relevance to this article is the continuously tunable driving force available for electron transfer, in the form of the electrode potential. Variations in potential correspond to changes in electron energy, and the free-energy change associated with a redox reaction can therefore be controlled. The electrode behaves like a tunable redox reagent that can be made, at will, as oxidizing as fluorine or as reducing as lithium. The ability to impose extreme redox potentials is the reason that aluminum, alkali metals, fluorine, chlorine, and so forth are produced electrochemically. Furthermore, changes in electrochemical driving force can be executed rapidly (i.e., electrode potential changes can be made on a submicrosecond time scale). An analogous approach is stopped-flow kinetics, except the time scale is longer (~ milliseconds) and one is constrained to redox potentials available with known chemical reagents.

Electrochemical initiation of a reaction in solution

Consider an electrode immersed in a solution containing the stable, reduced form of a redox couple, denoted Red. If the applied potential, E_{app}, is negative relative to the standard potential, $E°$, for the redox system, electrons are more stable in Red than in the electrode, and no current flows. If E_{app} is changed to a value that is positive relative to $E°$ (rapidly if desired), electrons will be more stable in the now positive electrode, and heterogeneous electron transfer will occur from Red to the electrode, thereby generating the oxidized form, Ox. If Ox is unstable in solution, it may undergo homogeneous reactions to form new products, some of which may themselves be electroactive.

Various electrochemical methods have long been used to monitor such electroinitiated reactions. This is usually done by monitoring the perturbation of the observed current caused by the homogeneous reaction (*3, 4*). An example of the ECE mechanism, in which a homogeneous chemical reaction occurs between two heterogeneous electron transfer reactions, is shown in Figure 1 and involves the oxidation of the neurotransmitter dopamine in HBr solution (*5–7*). The additional current resulting from the reaction in Equation 3 is directly related to the rate constant, k_c. Not only has the electrode reaction (Equation 1) provided a convenient means to produce the reactive orthoquinone, it has done so on a fast time scale, submilliseconds if necessary. Because the whole process occurs within the diffusion layer, extremely small amounts of dopamine are consumed (~30 ng for typical conditions and a 1-s experiment).

The excellent time resolution and tunable driving force inherent in electrochemical generation of reactive species have resulted in widespread application. However, electrochemical monitoring of the homogeneous reaction, usually via the current, has two drawbacks. First, current measurements are rather nonselective compared with analogous spectroscopic observations, leading to difficulties with complex reaction sequences. For some mecha-

INSTRUMENTATION

0003-2700/89/0361-775A/$01.50/0

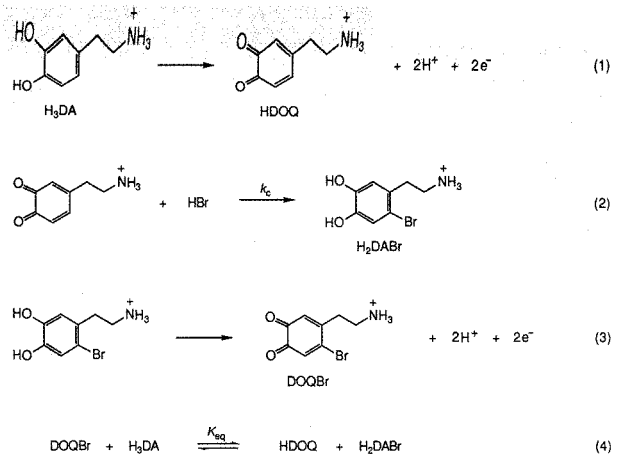

Figure 1. Reaction mechanism for the oxidation of dopamine, H_3DA, in 1 M HBr solution.

k_c is the pseudo first-order rate constant for HBr addition; K_{eq} is the equilibrium constant for the redox cross reaction in Equation 4. HDOQ = dopamine orthoquinone, H_2DABr = 6-bromodopamine, DOQBr = 6-bromodopamine orthoquinone.

nisms, the homogeneous reaction does not perturb the current at all, making measurements of current uninformative. A second problem is the paucity of structural information available from the current response. Although $E°$ is sensitive to structure in many cases, there is no systematic procedure to deduce structure from electrochemical currents or observed $E°$. Chemists who study homogeneous solutions are used to deducing structures from NMR spectroscopy, mass spectrometry, vibrational spectroscopy, and the like, but electrochemists cannot obtain this type of structural information if they are constrained solely to electrochemical measurements.

Spectroelectrochemistry

The desire for greater selectivity and molecular information led to the development of hybrids of spectroscopic and electrochemical techniques under the general label of spectroelectrochemistry (SEC) (*2, 8–12*). A common SEC experiment might involve reflection of a spectrophotometer beam off a planar electrode, thus permitting electrochemical reactant generation and spectroscopic monitoring. UV–vis absorption techniques have been developed extensively and are characterized by excellent quantitative accuracy and time resolution in both transmission and reflection modes. Although UV–vis techniques have been applied to many problems with valuable results, they are still constrained by the nature of the spectroscopic transition. Vibrational spectroscopy, magnetic resonance, or other techniques commonly used to probe homogeneous reactions provide structural information that UV–vis absorption does not. Furthermore, electronic absorption spectra of solution species have very broad linewidths, often making it difficult to monitor several species in a possibly complex reaction path.

Thus the driving force for developing vibrational spectroscopy of electrode reactions is the need for high-resolution, narrow-linewidth spectra to improve selectivity and provide structural information. Given that electrochemistry permits easy generation of a reactive species by a charge transfer reaction, vibrational spectroscopy is an informative means to monitor the fate of an electrogenerated material. Specifically, the spectroscopic probe must

- provide information about molecular structure,
- have sufficient resolution to permit selective monitoring of more than one species,
- have time resolution comparable to or better than the electrode process that generates the reactive species (spectral information must be obtained on a rapid time scale, to exploit the advantages of electrochemical generation), and
- possess sufficient sensitivity to detect and monitor the very small amounts of material in the electrochemical diffusion layer.

The majority of techniques commonly used for structure determination, such as NMR spectroscopy, MS, EXAFS, and so forth, lack either the sensitivity or the time resolution required for SEC applications. Recall that the amount of material generated in a typical diffusion layer is small, on the order of 10^{-10} mol/cm^2 for a 1-ms experiment. In the case of FT-IR reflectance, the required sensitivity is available with sufficient signal averaging, but it is difficult to mate the instrumental requirements of an FT instrument with the transient nature of electrochemical reactant generation.

Raman spectroscopy

Starting in the mid-1970s, Van Duyne reported the use of resonance Raman spectroscopy for SEC applications (*13–15*). Raman spectroscopy involves scattering of incident light from a laser beam ($h\nu_0$) reflected from the electrode. The vast majority of laser light is scattered without a change in frequency and carries little chemical information. Such Rayleigh scattering is responsible for the blue sky, because it is more efficient at shorter wavelengths. Raman scattered light has lost energy to the sample molecule through vibrational excitation and is shifted in energy from the input laser light by a vibrational quantum ($h\nu_1$). If the incident light wavelength is close to an electronic absorption band of the sample molecule, the scattering is more intense (by factors of 10–10^6) and the process is called resonance Raman scattering.

Being a vibrational spectroscopy, Raman produces high-resolution spectra with significant structural information. Because there are usually many Raman lines, comparisons to known spectra may allow structure identification in "fingerprint" mode. Changes in normal modes or bond strengths may be inferred from changes in the Raman spectrum accompanying a redox reaction. Raman peaks are narrow compared with UV–vis absorptions, so it may be possible to selectively monitor one component in a reaction sequence. For the case of resonance Raman, one species may have a much higher scattering cross section than others, thus enhancing its Raman spectrum. With suitable choice of input laser wavelength, the enhanced species may be monitored with high sensitivity and selectivity. Several aspects of resonance enhancement will be discussed later.

To exploit the significant advantages in selectivity and information content of Raman SEC over UV–vis SEC, the instrumentation must address a funda-

TASK MASTER.

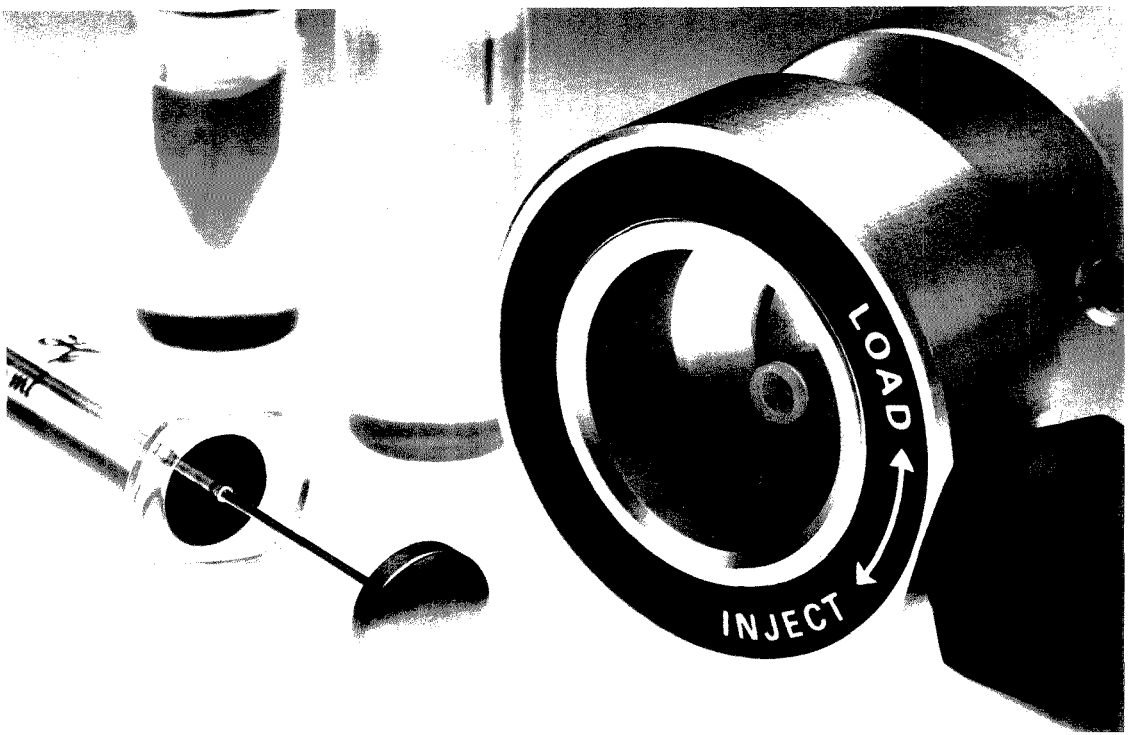

The Rheodyne 7125 LC sample injector is equipped with two operating modes to master every injection task.

In the "partial-fill" mode, the sample from a syringe fills a sample loop only partially. No sample is lost. The amount injected is the exact volume dispensed from the syringe.

You use this mode when you need to conserve sample or change sample volume frequently. You can inject from 1 μL to 2.5 mL with a precision of 1%.

In the "complete-fill" mode, sample from a syringe fills the loop completely–using excess sample. The amount injected is the exact volume of the loop.

You use this mode when you need the maximum volumetric precision of 0.1%, or you wish to load sample without having to read syringe calibrations carefully. You can inject from 5 μL to 5 mL using one of ten interchangeable sample loops.

Variations of the Model 7125 perform yet other tasks. Model 8125 minimizes sample dispersion with micro columns. And Model 9125 uses inert plastic flow passages to prevent the mobile phase from contacting metal.

For more information about these versatile injectors, phone your Rheodyne dealer. Or contact Rheodyne, Inc., P.O. Box 996, Cotati, California, 94931, U.S.A. Phone (707) 664-9050.

RHEODYNE
THE LC CONNECTION COMPANY

CIRCLE 142 ON READER SERVICE CARD

mental issue regarding sensitivity. Raman scattering is a weak effect, and cross sections are much lower than those common to UV–vis absorption. Consider the experiment depicted in Figure 2, in which a laser beam reflects off the electrode surface and the Raman scattering is collected normal to the electrode plane. Given the small amount of scatterer generated by a transient electrochemical experiment, instrument sensitivity is crucial to successful acquisition of spectra.

The usual case of a species generated at a diffusion-controlled rate by a potential step is depicted in Figure 3. Although the current exhibits a transient response with a $t^{-1/2}$ decay, the Raman scattering results from the integrated concentration of electrogenerated scatterers in the laser beam. For a stable species, this integral is proportional to $t^{1/2}$, yielding a parabolic shape of Raman intensity versus time (*13*, *16*, *17*). The predicted Raman signal is given by Equation 5

$$S = 4P_0\beta N^b(Dt)^{1/2}A_D\frac{\Omega TQ}{\pi^{3/2}a^2} \quad (5)$$

where S = Raman signal, counts s^{-1}
P_0 = incident laser power, photons s^{-1}
β = differential Raman scattering cross section, $cm^2\ sr^{-1}$ molecule^{-1} (often denoted $d\sigma/d\Omega$); sr indicates steradian, unit of solid angle
N^b = bulk number density of starting material (Red in the discussion so far), molecules cm^{-3}
D = diffusion coefficient of Red, $cm^2\ s^{-1}$
t = time from beginning of diffusion-controlled oxidation, s
Ω = collection efficiency of spectrometer and collection optics, sr
T = spectrometer and optics transmission, unitless
Q = detector quantum yield, counts photon^{-1}
A_D = electrode area sampled by the spectrometer, cm^2
a = laser beam radius at electrode, cm

Equation 5 assumes the laser spot on the electrode overfills the spectrometer and detector. The many variables in Equation 5 can be classified into four subgroups. First, the laser power P_0 is limited by the laser employed and the damage threshold of the electrode surface or the diffusion layer. Second, the cross section β varies greatly (at least a factor of 10^6) for different molecules and ultimately controls signal-to-noise

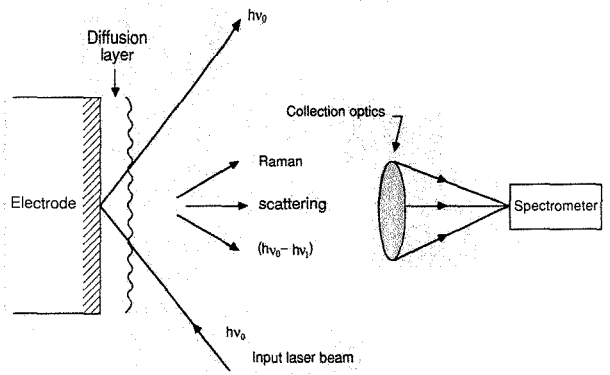

Figure 2. Geometry of typical Raman SEC experiment for monitoring solution species generated at a planar electrode.
Incident beam ($h\nu_0$) enters the cell and reflects off the electrode, and scattered light is collected normal to the electrode surface. The electrochemical diffusion layer, which is typically 1–100 μm thick, contains a solution scatterer.

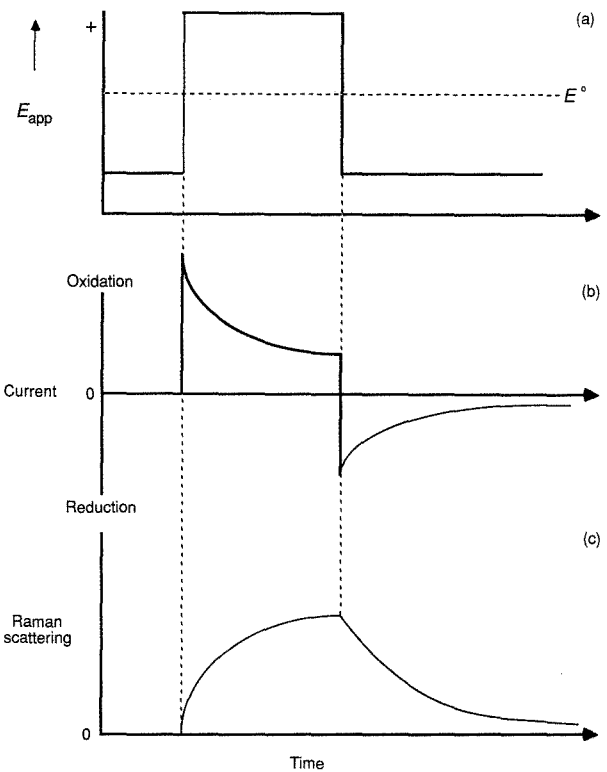

Figure 3. Electrochemical generation of a Raman scatterer by oxidation of a stable reduced material.
(a) Potential, (b) current, and (c) Raman scattering waveforms.

The Sartorians announce the end of an era.

Our PLUS Performance Package has put the calculator in its rightful place among scientific memorabilia. Alongside the abacus, the slide rule, and the ENIAC computer.

For, unlike other balances which merely give you the weight, ours also calculates the answer.

Now standard on many Sartorius balances, the PLUS Performance Package features a choice of three key pad overlays which activate 16 pre-programmed functions and calculations. They make check weighing, animal weighing, parts counting, formulations and other applications faster and easier than ever before. Our analytical balances will even perform molarity and normality calculations.

For more information or a free demonstration, call or write Sartorius Instruments, P.O. Box 770, McGaw Park, IL 60085, (312) 578-4297. Or contact your representative from Baxter Healthcare Corporation, Scientific Products Division, or any authorized dealer.

Unless you're just a sentimentalist.

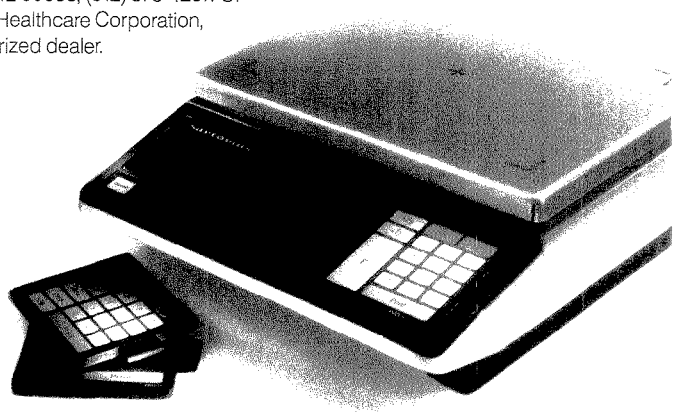

sartorius

perfect balance.

CIRCLE 150 ON READER SERVICE CARD

(S/N) ratio and sensitivity. Third, the product $N^b(Dt)^{1/2}A_D$ equals the number of electrogenerated molecules observed by the spectrometer. As the diffusion layer thickens with time, this quantity increases with $t^{1/2}$, yielding the parabolic response of Raman signal versus time. Fourth, the product $\Omega TQ/\pi^{3/2}a^2$ is an indication of the spectrometer's performance and permits comparison of different instruments.

Several conclusions relevant to the problem of detecting electrogenerated species can be drawn from Equation 5. First, a high β permits the observation of low concentrations or short-lived species. As β decreases, the experimental time scale or the concentration will have to increase to maintain the same signal. Second, improvements in the instrument (ΩTQ) will permit experiments on weaker scatters, shorter times, or lower concentrations. Third, the ability to monitor a larger A_D is important, particularly for SEC applications. Surface damage or thermal disturbance of the diffusion layer limits the acceptable power density, so a larger A_D yields a larger signal before the damage threshold is reached. Finally, spectral monitoring of normal Raman scatterers will be much more difficult than observing resonance Raman scatterers because of the 10–10^6-fold difference in β.

As with any spectroscopic method, the quality of the spectra and detection limits are determined by S/N ratio, not just signal. Noise sources include shot noise from both sample and background scattering, detector dark noise, and detector readout noise. In most cases, the background scatter from an electrochemical solution is large compared with detector shot or readout noise. In this limiting but often valid case, the S/N ratio is proportional to the square root of the signal given in Equation 5. If a multichannel detector having N channels is employed (as described below), a factor of $N^{1/2}$ is added to the S/N ratio expression. After reducing the S/N ratio equation to include only terms involving the spectrometer and detector, Equation 6 is obtained

$$S/N = K(A_D TQN)^{1/2} \qquad (6)$$

for the case of a photon shot noise limited experiment and a fixed total measurement time (*18*). K is a constant, derived from concentration, laser power, and other factors and is related to Raman scattering intensity. The $N^{1/2}$ enhancement in S/N ratio is predicted for multichannel Raman detectors and will be beneficial under certain conditions, as discussed below.

Instrumentation

Now that the variables of Raman SEC have been defined, the instrument necessary to obtain spectral information about electrogenerated species, as well as two data acquisition modes, can be described. First, it is usually desirable to obtain complete spectra after electrolysis begins (preferably time resolved) to produce a 3D data set of Raman intensity versus Raman shift and versus time. Such data will reveal vibrational spectral changes following electrochemical generation and will provide the most structural information. Once time-dependent spectral changes are observed, it is often desirable to conduct fixed-wavelength experiments in which a particular Raman peak intensity is monitored as a function of time.

The first Raman SEC experiments employed an instrument similar to that in Figure 4 (*14*, *16*). In addition to the considerations of designing a Raman spectrometer, the cell design and optics are crucial to assure that the region sampled by the spectrometer coincides optically with the electrode surface and diffusion layer. The first reported Raman SEC experiments were conducted at steady state, with a square wave potential perturbation (*14*, *19*). E_{app} was oscillated between values above and below $E°$, thus establishing a concentration of electrogenerated products. In this condition the Raman spectrometer could be scanned slowly relative to the potential perturbation frequency, producing a spectrum of intensity versus Raman shift.

As far as the spectrometer is concerned, the experiment is conventional, whereas in fact the advantages of electrochemical generation are being exploited to produce a possibly reactive sample. Because of the steady-state nature of sample production, the steady-state scatterer concentration will decrease for shorter lived species, thus degrading the S/N ratio. For this reason and because of certain instrumental factors, the initial experiments examined resonance-enhanced scatterers with relatively large cross sections. For stable electrogenerated products, this relatively simple, static acquisition mode and related procedures proved particularly valuable for identifying molecular structures, and excellent examples are available in the literature (*14*, *20*, *21*). A sample spectrum obtained in our lab with this acquisition mode appears in Figure 5.

To obtain time-resolved spectra following electrochemical generation, an important change in spectrometer design is required. Not only is scanning impractical on a short time scale (a few seconds or less), but transient signals are weak as a result of the $t^{1/2}$ factor of Equation 5, and high sensitivity is required. Consider the apparatus of Figure 4, after replacement of the photomultiplier tube (PMT) with a multichannel detector. The detector consists of many (500–1000) photosensitive elements, each monitoring a different wavelength at the focal plane (*22*). The most important benefit of such a change in spectrometer design is the operation of the spectrometer as a spectrograph rather than a scanning monochromator. Instead of scanning wavelength (and Raman shift) across the exit slit, the dispersed spectrum is focused onto a multichannel detector at the focal plane. An intensified pho-

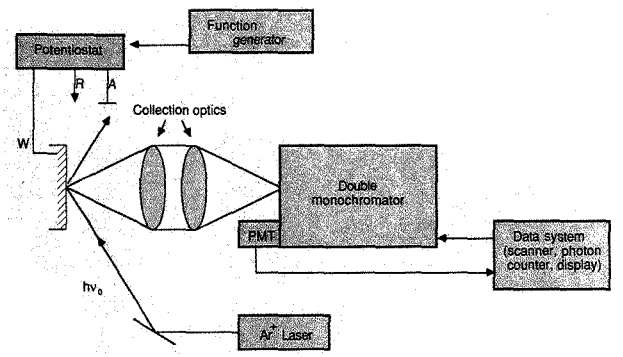

Figure 4. Block diagram of scanning Raman spectrometer.
PMT is a single-photon photomultiplier tube. Working, reference, and auxiliary electrodes (W, R, and A, respectively) are immersed in the solution of interest.

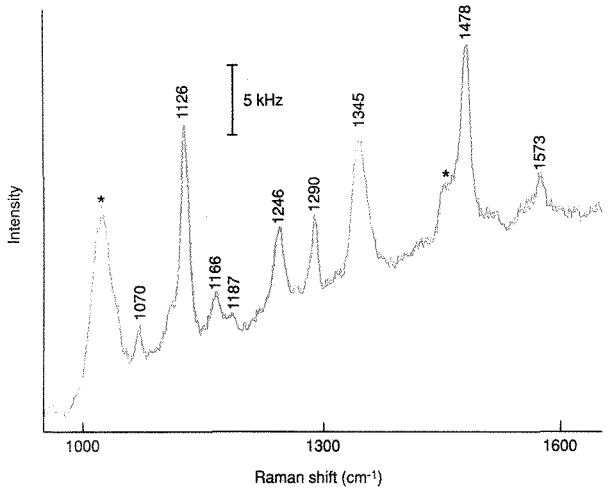

Figure 5. Resonance Raman spectrum of chlorpromazine cation radical ($CPZ^{+\cdot}$) generated electrochemically in steady-state mode from reduced CPZ.
Laser wavelength was 514.5 nm. CPZ is not resonance-enhanced and scatters too weakly to interfere with the $CPZ^{+\cdot}$ spectrum. * denotes solvent peaks. (Adapted from Reference 16.)

todiode array (IPDA) positioned at the focal plane can monitor 1000 wavelengths simultaneously, in principle producing a complete spectrum in as little as 10 ns. Each channel of the IPDA is physically a 25 μm × 2.5 mm rectangle and acts as a detector analogous to the PMT used for the scanning experiment. A range of wavelengths is monitored at all times, thus lengthening the time monitored for each wavelength and providing S/N ratio enhancement. The width of the spectrum typically monitored by our spectrometer is 600 cm^{-1}.

Although the PMTs normally employed for Raman spectroscopy operate in a single-photon counting mode, an IPDA is inherently an integrating detector. Each element of the IPDA stores charge proportional to the integral of the number of photons striking the element. At intervals of 10 ms or more, the stored charge from all pixels is read out, and the pixel is reset. With repetitive integration and readout, it is possible to generate a series of spectra, each of which represents Raman scattering during a 10-ms segment of time after electrogeneration begins. The sequence of events for the on-the-fly ac-

quisition of a series of Raman spectra is shown in Figure 6, and a series of spectra obtained in this manner is shown in Figure 7.

The 3D data set of Raman scattering versus Raman shift and time contains several types of information of significant value for diagnosing the fate of electrogenerated species. The most obvious is the sensitivity of the spectra to structural changes evolving with time. Because certain Raman peaks correspond to particular normal modes of the intermediates of interest, changes in peak intensities with time reflect concentration versus time behavior and provide implications about reaction mechanism. An informative example is the oxidation of dopamine (H_3DA) in the presence of HBr, shown in Figure 8. H_3DA is a relatively weak Raman scatterer, so the initial spectrum (Figure 8a) shows no features in the 1300–1800 cm^{-1} region. After the initial spectrum was acquired, the electrode potential was stepped to a value that oxidized H_3DA at a diffusion-controlled rate. Raman peaks at 1572 cm^{-1} and 1672 cm^{-1} appear rapidly and are assignable to the dopamine orthoquinone (HDOQ). If HDOQ were stable (e.g., in $HClO_4$), these peaks would grow with the $t^{1/2}$ dependence expected from Equation 5. However, it is obvious that the 1572 cm^{-1} band is weakening with time as a strong new band at 1540 cm^{-1} appears. At least two products are formed, one an intermediate and the other a more stable product. Less obvious but similar changes also occur in the 1600–1750 cm^{-1} range. These spectral changes have been assigned to particular species in the reaction mechanism, and the mechanism of Figure 1 has been confirmed (*17*).

The time-resolved spectra from the multichannel spectrometer provide valuable qualitative information about reactive systems, on a millisecond to several second time scale. In principle, one could construct quantitative intensity versus time transients for particular peaks from the 3D data set, thus permitting quantitative kinetic analysis. In practice, better S/N ratio and time resolution are possible with a single-channel detector (PMT in this case), because the integrative nature of the IPDA and readout requirement are avoided. In single-wavelength mode, one is sacrificing the structural information available from complete spectra such as those of Figure 8, but one is still exploiting the high resolution of Raman spectroscopy to monitor individual species. As an indication of the resolution and narrow linewidth of Raman features compared with UV–vis absorption spectra, consider the 1540 cm^{-1} and 1572 cm^{-1} peaks in Figure 8. These two features and the species to which they correspond are easily resolved on the Raman spectrum, yet the difference in Raman shift expressed in wavelength is only 1 nm. The UV–vis spectra of the two quinones are severely overlapped, and independent quantitative monitoring of them would be difficult.

The timing for single-wavelength transient Raman spectroelectrochemistry is shown in the bottom two traces in Figure 6. With the exception of the

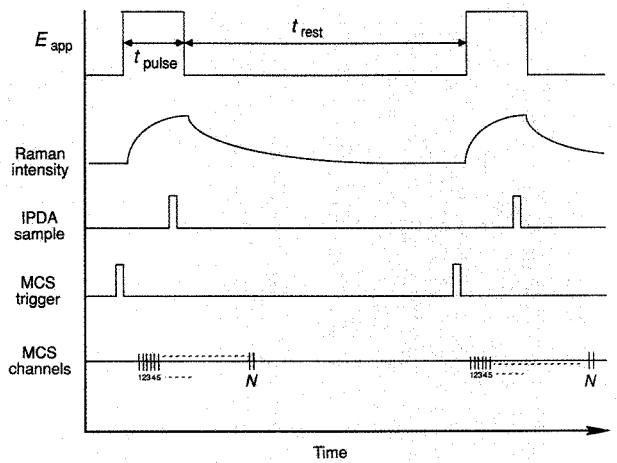

Figure 6. Relationship between E_{app}, Raman signal, and timing of detector electronics for time-resolved spectral acquisition and single-wavelength monitoring.
The third waveform from the top shows sampling by the intensified photodiode array (IPDA) detector, wherein each readout produces a spectrum over some wavelength interval. The fourth waveform is the multichannel scaler (MCS) trigger, and the fifth trace shows which MCS channels are active after the trigger.

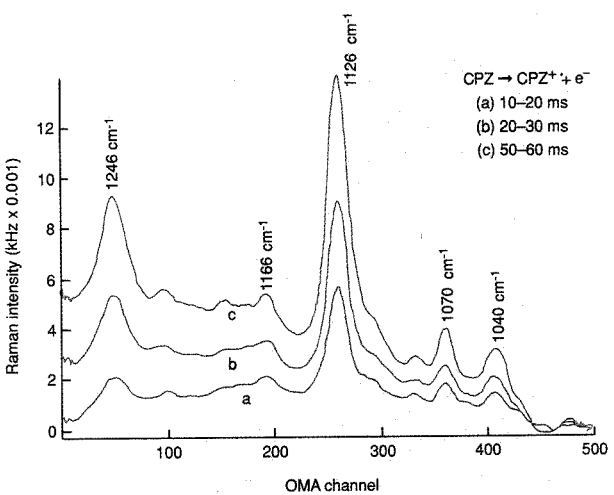

Figure 7. Time-resolved spectra obtained with a multichannel detector (third trace of Figure 6) during the oxidation of CPZ to $CPZ^{+\cdot}$.
Each spectrum represents a 10-ms period after the beginning of the potential step. OMA denotes the multichannel detector.

counting electronics and potential waveform, the spectrometer is the same as the scanning system of Figure 4. The spectrometer is set and held at the wavelength of interest (e.g., 1572 cm^{-1}) for the H_3DA oxidation. Photons detected by the PMT are counted, as they were for a scanning system, except the counts are stored in a multichannel scaler (MCS). The MCS consists of many (~1000) channels, each of which is assigned to a different time interval following a trigger. As a shown in Figure 6, photon counts arriving after the trigger are stored in MCS channels, according to arrival time. The width of a channel varies from a microsecond up to several seconds. If the potential step that initiates the electrochemical reaction is used as the trigger, the MCS will store the Raman intensity versus time at a given wavelength into the series of successive channels. Thus an intensity versus time transient is obtained at fixed wavelength, with time resolution equal to the MCS channel width. Several intensity versus time transients are shown in Figure 9 for the dopamine oxidation monitored at 1540 and 1572 cm^{-1}. The lines were calculated for the reactions of Figure 1; details of the approach appear elsewhere (*17*, *18*).

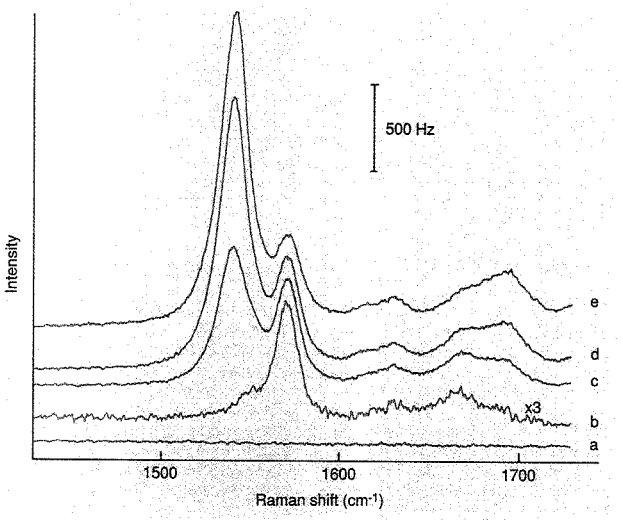

Figure 8. Time-resolved spectra of dopamine oxidation in 1 M HBr solution obtained with a multichannel spectrometer.

Times after initiation of oxidation are (a) 0 ms, (b) 0–50 ms, (c) 100–150 ms, (d) 200–250 ms, and (e) 400–450 ms. Integration period was 50 ms; successive spectra are displaced upward for clarity. (Adapted from Reference 17.)

The sensitivity constraints of normal Raman SEC are more fundamental than merely instrumental limitations. Although instruments, cross sections, and laser powers vary greatly, a crude estimate of signal strength may be calculated from Equation 5. For the case of electrogenerated benzoquinone, a Raman signal of ~10 kHz is predicted at 1s after a potential step. At $t = 1$ ms, this value is 300 Hz, or 3 photons in a 10-ms MCS channel. Even for ideal detectors and spectrometers ($T = 1$, Ω = large), the count rate might be increased by a factor of 10–100, but one would still be dealing with a few counts in each interval at short times. Signal averaging, digital filtering, and the like can be used to enhance S/N ratio, but eventually one is always limited by the weakness of Raman scattering. The performance of the instrument determines how closely this fundamental limit is approached.

As noted earlier, any increase in scattering cross section (β in Equation 5) results in improved S/N ratio or faster time resolution. Partly for this reason,

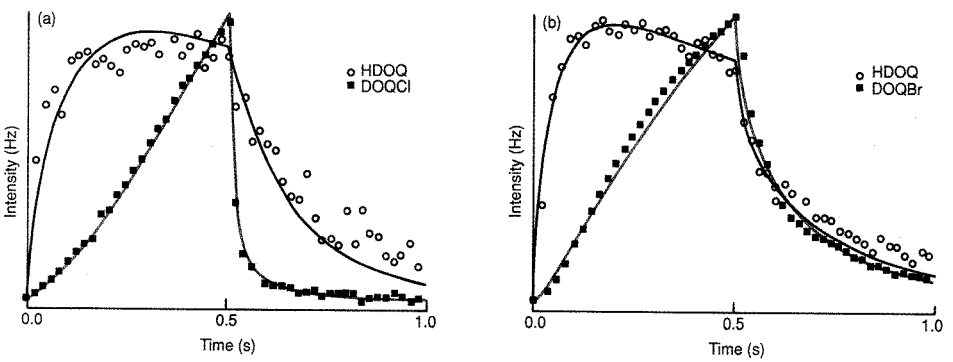

Figure 9. Raman intensity versus time curves for double potential step experiment on the H_3DA system.

Solid curves are simulated results. (a) 8.0 mM H_3DA in 0.8 M HCl, simulated $k_c = 4.0\ s^{-1}$, $K_{eq} = 20$ for reactions 1–4. (b) 8.0 mM H_3DA in 0.8 M HBr, simulated $k_c = 5.0\ s^{-1}$, $K_{eq} = 0.5$. Transients obtained with PMT detection at 5 cm^{-1} resolution. Incident laser power was 40 mW at 488 nm. Width of each MCS channel was 20 ms. HDOQ was monitored at 1572 cm^{-1} (circles), DOQCl at 1548 cm^{-1} (squares in a), and DOQBr at 1539 cm^{-1} (squares in b). (Adapted from Reference 17.)

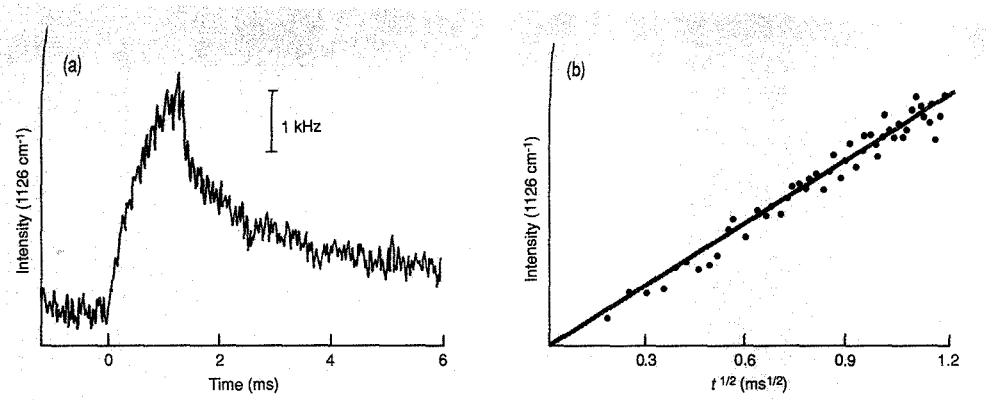

Figure 10. Transient intensity of the 1126 cm^{-1} band of $CPZ^{+\cdot}$ generated by potential pulses from 0.4 to 0.8 V versus SCE.
The transient was recorded by a 1024 multichannel scaler with a dwell time of 30 μs. Potential pulse duration was 1.5 ms before returning to 0.4 V and was repeated every 30 ms to allow signal averaging for a total of 50,000 runs. Curve a shows raw data, and curve b is a plot of intensity versus $t^{1/2}$ for the 1.5 ms duration of the potential pulse. (Adapted from Reference 16.)

resonance Raman SEC (RRSE) was developed before normal Raman SEC. Not only is β much higher (by factors of $10–10^6$), but the resonance enhancement permits improved selectivity, because only one or a few components of a mixture will exhibit strong resonance enhancement. RRSE was presented initially in the mid-1970s (*13*), and microsecond time resolution was demonstrated in the mid-1980s (*16*, *22*). As shown in Figure 10, a resonance-enhanced electrogenerated scatterer can be monitored quantitatively, and the expected $t^{1/2}$ dependence at short electrolysis times is down to tens of microseconds.

Unfortunately, strong resonance enhancement occurs only near an absorption band of the scatterer of interest, and the input laser power is necessarily attenuated as the beam passes through the diffusion layer. Because Equation 5 assumes constant laser power (P_0), any attenuation will lead to a negative deviation from a $t^{1/2}$ dependence (*17*). This effect is shown in Figure 11 for the case of electrogenerated chlorpromazine cation radical ($CPZ^{+\cdot}$) monitored with a 515-nm laser. It is obvious that attenuation is severe, at times greater than a few milliseconds, and quantitative deductions about kinetics or mechanisms would be invalid if attenuation were ignored. A nontrivial correction involving some mathematical complexity can be made to extend the useful time scale of RRSE from 50 μs to 5 s, but this correction must be applied with care for any but the simplest systems (*17*, *18*). Thus RRSE pays significant benefits in sensitivity, time resolution, and selectivity, but at the cost of mathematical complexity and loss of quantitative accuracy.

Electrode surface structure

The discussion presented thus far has dealt with solution species generated electrochemically, which may be stable or reactive. A more difficult but equally important problem is the spectroscopic observation of electrode surface structure and dynamics. Because heterogeneous events are the basis of all electrochemical phenomena, it is particularly important to probe the electrode/solution interface to determine its molecular structure, both statically and dynamically. To determine the relationship between interfacial structure and electrochemical behavior, it is essential for researchers to have informative structural probes.

As has already been noted, Raman spectroscopy can provide such information on a millisecond time scale for electrogenerated species in solution. Unfortunately, the sensitivity problem

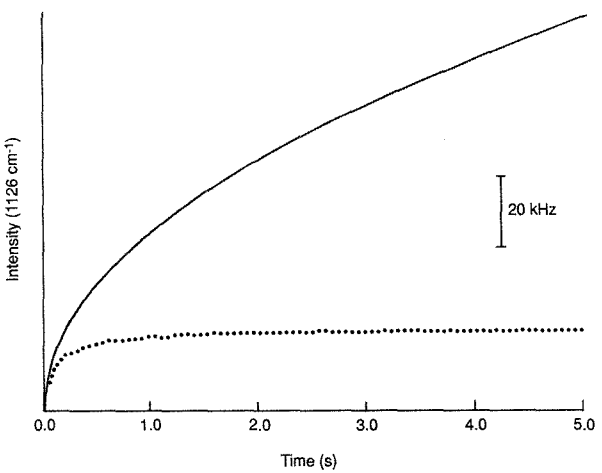

Figure 11. Transient Raman intensity of the 1126 cm^{-1} band of $CPZ^{+\cdot}$ generated by potential pulses from 0.2 to 0.85 V versus Ag/AgCl.
The solid line is the simulated result assuming no input light absorption by $CPZ^{+\cdot}$. Points are the experimental values. CPZ concentration was 5 mM in 1.0 M HCl in 43% (w/w) $MeOH/H_2O$. Input laser beam was 20 mW at 458 nm. Ten transients were averaged; spectral resolution was 7 cm^{-1}. (Adapted from Reference 17.)

becomes even more severe for thin layers (perhaps submonolayer) of species on the electrode surface. For the case of an adsorbed layer of analyte or the interfacial layers of the electrode material, Equation 5 can be modified to produce Equation 7 (*16, 23, 24*)

$$S_{surf} = \frac{P_0 \beta N_{surf} \Omega T Q A_D \cos \alpha}{\pi a^2} \quad (7)$$

where S_{surf} = Raman signal from surface species, counts s^{-1}
N_{surf} = surface number density, molecules cm^{-2}
α = incident beam angle, relative to surface normal

N_{surf} need not be restricted to a monolayer case; for multilayer film or finite laser penetration depth into the electrode material, N_{surf} will equal the total density of molecules sampled by the laser beam and spectrometer.

An important difference between the surface and solution experiments is apparent after comparing Equations 5 and 7. S_{surf} is not time-dependent, because the number of scattering molecules on the surface does not usually increase with diffusional time. All else being equal, a monolayer of a normal Raman scatterer will result in an S_{surf} roughly comparable to solution scatterer generated by a 1-ms potential step. Thus the surface signal is very small because so few molecules are sampled ($\sim 10^{-13}$ mol) and the Raman effect is so weak. For a normal scatterer with no enhancement mechanisms, a monolayer will produce a few counts per second of signal, and the experiment is very demanding. The consequence of this weak signal has been investigation of a variety of enhancement mechanisms and a comparative dearth of surface dynamic experiments.

The current state of the art in instrumentation has resulted in examples of unenhanced surface Raman spectra in an ultra-high-vacuum environment (*24*). However, the vast majority of surface Raman results have exploited surface enhancement (SERS), which primarily involves an increase in P_0 of Equation 7. Local electromagnetic effects on certain roughened electrode materials (e.g., Ag, Au, Cu) enhance the Raman signal by factors of up to 10^6 and make detection and spectral characterization of even submonolayers straightforward (*23–26*). (SERS was the subject of a recent A-page article [*27*] and will not be discussed extensively here.) Surface enhancement may also involve an increase in β through chemical interactions of the adsorbate and metal. SERS has proven to be a very valuable technique for examining Ag, Au, and Cu electrodes in vacuum,

solution, and so forth and has revealed significant new information about electrochemical interfaces.

Less explored but still valuable approaches include surface resonance Raman spectroscopy (SRRS), which exploits the high β of adsorbed RR molecules to enhance the signal, and surface enhanced RRS (SERRS), which combines resonance and surface enhancement (*13*, *28*). SERS, SRRS, and SERRS can exhibit strong signals that are easily measured, but SERS and SERRS have the added advantage of providing surface selectivity. Because both local field and cross section enhancements are short-range (<~100 Å), surface scattering will be much stronger than that from species in solution. In the absence of surface selectivity by the enhancement mechanism or instrument, it is important that the scatterer be present only on the electrode surface. The high sensitivity and surface selectivity of SERS have stimulated a large volume of important research, directed primarily toward elucidating the SERS enhancement mechanism and determining interfacial structure. Relatively few reports have appeared on applications of SERS to surface dynamics. There is no known fundamental reason that SERS should not be valuable for monitoring time-dependent surface structure, but such applications have not yet been pursued in significant numbers. The vast literature on SERS mechanisms and applications is beyond the scope of this discussion.

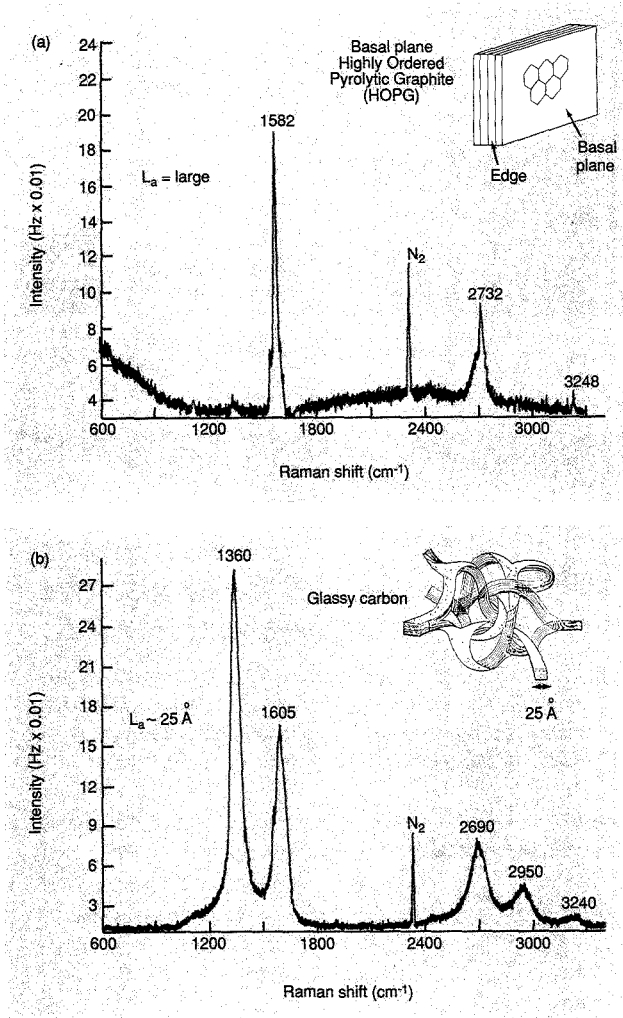

Figure 12. Raman spectra of carbon materials obtained with spectrometer of Figure 4, scanned in a conventional manner.

Laser (515 nm) was reflected off carbon surface as shown in Figure 2, but solution was absent. Spectrum a, HOPG (basal plane); spectrum b, glassy carbon.

As an example of Raman monitoring of surface structural dynamics, we will discuss some work from our lab on carbon electrodes (*29*, *30*). sp^2 hybridized carbon materials have large Raman cross sections, and their vibrational spectra provide useful information about microstructure. For example, the spectrum of highly ordered pyrolytic graphite (HOPG) differs greatly from glassy carbon (Figure 12), because the intensity of the 1360 cm^{-1} band is strongly dependent on microcrystallite size. As the size of the graphite layers increases, the 1360:1582 cm^{-1} intensity ratio decreases, providing a quantitative measure of average microcrystallite size. Thus the Raman spectrum is an excellent probe of the carbon microstructure in the first few carbon layers at the surface. If the microstructure changes as a result of surface treatment or reactions, the Raman spectrum should reveal the nature of such changes.

The effect of an electrochemical oxidation–reduction cycle on HOPG surfaces is shown in Figure 13 (*18*). After 2 min at 1.60 V followed by reduction at 0.00 V, the spectrum is unchanged from the original HOPG spectrum. Upon oxidation at higher potentials, two new peaks appear at 1360 and 1620 cm^{-1}. These peaks grow with time, at a more rapid rate at higher potentials. As has been discussed in detail elsewhere (*29*, *30*), the 1360 cm^{-1} band arises from the edges of graphitic carbon planes and indicates the fracturing of the hexagonal lattice during electrochemical oxidation. The 1620 cm^{-1} band has been observed in intercalation compounds of graphite and indicates delamination of the stacked hexagonal planes.

As shown in Figure 14, the intensities of the 1360 and 1620 cm^{-1} bands vary in different directions during intentional laser heating, verifying the conclusion that they arise from distinct structural features of the sample. Note that each spectrum in Figure 14 was obtained in 10 s, permitting time-dependent changes of the surface to be observed. With a conventional scan-

ning system requiring at least a few minutes to obtain a spectrum, much of the important information would have been missed. In this example, the fundamental conclusion available from Raman spectroscopy was the correlation between the heterogeneous electron transfer rate observed electrochemically and the edge plane density deduced from the Raman spectra. In addition, the Raman spectra of various types of carbon provided a basis for determining microstructural effects on electron transfer activity and for predicting electrochemical properties.

Future developments

Further progress in Raman SEC instrumentation is likely to involve radical rather than evolutionary steps. Possible areas for improvement include spectrometer design, increases in scattering for a given analyte, and operation at different laser wavelengths. Further evolution of spectrometer design will be slow because of the fundamental limitations on improvement of the common dispersive design. There is headroom for increased performance in detector quantum yield, number of channels, and $A_D\Omega$ product, but it does not appear that major improvements are forthcoming. In our opinion, it is hard to anticipate large performance gains with multichannel dispersive spectrometers applied to solution-phase experiments with moderate to high background. As shown by examples herein, such spectrometers can be useful in many areas of science but they may have reached their limit in instrumental performance for SEC applications.

A radical change in spectrometer design is the interferometer approach that has become known as FT-Raman (*31–33*). Interferometers have excellent wavelength accuracy and spectral coverage. Of fundamental importance is their potentially high $A_D\Omega$ product resulting from the absence of slits. In principle, FT instruments can sample a large area of an electrode or diffusion layer, allowing experiments at low radiation density. Because sample damage is the ultimate limit on laser power density, a high sampled area may be attractive. Unfortunately, FT instruments do not provide a S/N ratio advantage over scanning instruments when detection is shot noise limited, as is the case in the visible wavelength region. Thus current FT systems do not outperform dispersive instruments with regard to sensitivity and are not easily amenable to time-resolved experiments. Perhaps for these reasons, FT-Raman has not yet been applied to dynamic experiments with visible lasers. Given the fundamental advantage of the high $A_D\Omega$ product, however, the future use of FT-Raman in the visible wavelength region should not be ruled out. FT-Raman has been reported in the near-IR, as noted below.

We discussed earlier the use of resonance Raman and SERS to greatly increase the Raman scattering of sample molecules, to the point where monolayer or nanomolar detection limits are not difficult. These effects will be particularly valuable for examining the systems to which they apply. A promising possibility is the modification of SERS-active metals with overlayers of

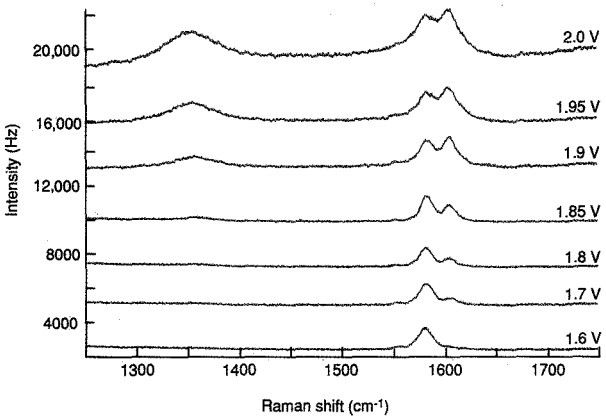

Figure 13. Raman spectra of HOPG oxidized in 0.1 M KNO_3 at various potentials and monitored with a multichannel spectrometer.
(Adapted from Reference 18.)

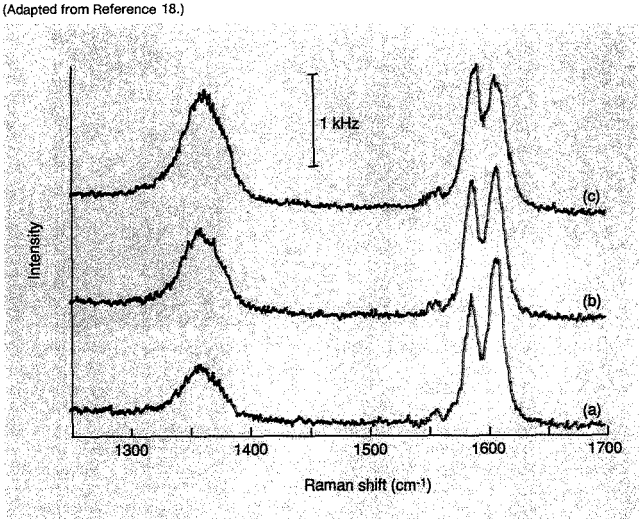

Figure 14. Time-resolved spectra of electrochemically pretreated HOPG undergoing changes caused by laser irradiation.
Note that the 1360 cm^{-1} peak increases and the 1620 cm^{-1} peak decreases with laser exposure. (Adapted from Reference 18.)

SERS-inactive metals, thus permitting the study of adsorption and other phenomena on surfaces not normally amenable to SERS (*34*). The outstanding detection limits of SERS and, in many cases, resonance Raman will continue to provide driving force for future applications, and the number of surfaces or solution systems is likely to broaden.

In addition to FT spectrometers and continued exploitation of scattering enhancement, future developments of Raman SEC may include the use of a wider range of lasers. Both pulsed and quasi-CW ultraviolet lasers have been used for SERS, leading to the first observation of the hyper-Raman effect on surfaces. Because both IR and normal Raman vibrations are active for hyper-Raman, more structural information is available (*35*). Even when nonlinear effects such as hyper-Raman are not involved, UV lasers should result in a significant enhancement in cross section because of the ν^4 factor. For example, the cross section of a normal Raman scatterer will increase by a factor of 21 when the laser wavelength is decreased from 515 to 240 nm. This factor may be much larger if resonance enhancement occurs in the UV, as will be the case for most aromatic molecules. Depending on background noise, the S/N ratio may increase linearly with cross section, thus permitting faster experiments or lower concentrations. Raman SEC in the UV is currently far from routine, but developments in laser technology should continue to reduce the difficulty of such experiments.

Another current development with possible future importance involves operation in the near-IR rather than the UV. Because of the same ν^4 factor, one loses significant sensitivity in the near-IR, but certain compensating aspects of the near-IR experiment make it useful. A wide range of solution or surface scatterers, or impurities in them, fluoresce weakly when irradiated with intense laser light. Even weak fluorescence can overwhelm still weaker Raman scattering, and the vibrational information is lost. Several laboratories have reported that near-IR Raman with 1064-nm excitation by a Nd:YAG laser exhibits little or no fluorescence (*31–33*), because electronic transitions required for fluorescence emission are rarely excited by 1064-nm photons. This feature has been exploited for SERS by combining a Nd:YAG laser with a modified FT-IR interferometer (*36*, *37*). The background fluorescence common with SERS in the visible was suppressed, and high-quality spectra were obtained. Unfortunately, the fluorescence rejection came at the cost of decreased sensitivity, not only because of the ν^4 factor but also because of the poor noise characteristics of near-IR detectors. With current technology, Raman with 1064-nm lasers is unlikely to approach the sensitivity available with visible excitation, but it will be applicable to strong scattering where fluorescence is a problem or there is some other reason to use 1064-nm light.

Recent developments may provide an alternative approach that permits near-IR laser operation while retaining the sensitivity of dispersive/multichannel spectrometers. Current charge-coupled device (CCD) array detectors have reasonable quantum efficiency at wavelengths up to 1100 nm, thus permitting laser excitation in the 600–850 nm range. For example, a diode laser operating at 783 nm (*38*), or a He–Ne laser at 632.8 nm (*39*) was used

with a CCD array to produce Raman spectra with good S/N ratios. Although the fluorescence rejection at 783 nm or 633 nm will not be as good as at 1064 nm, a large gain in sensitivity relative to 1064-nm excitation results from the characteristics of the detector. In general, detection limits degrade with increasing laser wavelength, and a sharp loss of S/N ratio occurs when shot noise limited detection is no longer possible. In contrast, fluorescence (and photolytic damage) becomes less likely with increasing wavelength. Thus the user faces a trade-off between sensitivity and fluorescence rejection, with the choice depending on the application.

The work described here was supported by the Chemical Analysis Section of the National Science Foundation.

References

(1) Alkire, R. C. *New Horizons in Electrochemical Science and Technology*; National Academy Press: Washington, DC, 1986; NMAB Publication 438–1.
(2) McCreery, R. L. *Prog. Anal. Spectrosc.* **1988,** *11,* 141.
(3) Bard, A. J.; Faulkner, L. R.; *Electrochemical Methods*; John Wiley and Sons: New York, 1980.
(4) Kissinger, P. T.; Heineman, W. R., Eds. *Laboratory Techniques in Electroanalytical Chemistry*; Marcel Dekker: New York, 1984.
(5) Hawley, M. D.; Tatawawadi, S. V.; Pierkarski, S.; Adams, R. N. *J. Am. Chem. Soc.* **1967,** *89,* 447.
(6) Hawley, M. D.; Feldberg, S. W. *J. Phys. Chem.* **1966,** *70,* 3459.
(7) Adams, R. N.; Hawley, M. D.; Feldberg, S. W. *J. Phys. Chem.* **1967,** *71,* 851.
(8) Heineman, W. R.; Hawkridge, F. M.; Blount, H. N. In *Electroanalytical Chemistry*; Bard, A. J., Ed.; Marcel Dekker: New York, 1983; Vol. 13.
(9) Kuwana, T.; Winograd, N. In *Electroanalytical Chemistry*; Bard, A. J., Ed.; Marcel Dekker: New York, 1974; Vol. 7.
(10) Heineman, W. R. *Anal Chem.* **1978,** *50,* 390 A.
(11) McCreery, R. L. In *Physical Methods of Chemistry, Vol. 2: Electrochemical Methods*; Bryant Rossiter, Ed.; John Wiley and Sons: New York, 1986; Chapter 7.
(12) *Spectroelectrochemistry, Theory and Practice*; Gale, R. J., Ed.; Plenum Press: New York, 1988.
(13) Jeanmaire, D. L.; Van Duyne, R. P. *J. Electroanal. Chem.* **1975,** *66,* 235.
(14) Jeanmaire, D. L.; Suchanski, M. R.; Van Duyne, R. P. *J. Am. Chem. Soc.* **1975,** *97,* 1699.
(15) Van Duyne, R. P.; Haushalter, J. P. *J. Phys. Chem.* **1984,** *88,* 2446.
(16) Schwab, S. D.; McCreery, R. L.; Gamble, F. T. *Anal. Chem.* **1986,** *58,* 2486.
(17) Packard, P. T.; McCreery, R. L. *J. Phys. Chem.* **1988,** *92,* 6345.
(18) Packard, R. T. Ph.D. Dissertation, The Ohio State University, 1988.
(19) Van Duyne, R. P. *J. Phys. (Paris),* Colloq. **1977,** *38,* C5-239–252.
(20) Suchanski, M. R.; Van Duyne, R. P. *J. Am. Chem. Soc.* **1976,** *98,* 250.
(21) Cotton, T. M.; Parks, K. D.; Van Duyne, R. P. *J. Am. Chem. Soc.* **1980,** *102,* 6399.
(22) Packard, R. T.; McCreery, R. L. *Anal. Chem.* **1987,** *59,* 2631.
(23) Van Duyne, R. P. In *Chemical and Biological Applications of Lasers*; Moore, L. B., Ed.; Academic: New York, 1979; Vol. 4, Chapter 4.
(24) Campion, A.; Brown, J.; Grizzle, W. M. *Surf. Sci.* **1982,** *115,* L153.
(25) "In-situ Characterization of Electrochemical Processes"; report of the National Materials Advisory Board, publication NMAB 438–3; National Academy Press: Washington, DC, 1987, Larry Faulkner, Chairman.
(26) Birke, R.; Lombardi, J. In *Spectroelectrochemistry, Theory and Practice*; Gale, R. J., Ed.; Plenum Press: New York, 1988.
(27) Garrell, R. *Anal. Chem.* **1989,** *61,* 401 A.
(28) Van Duyne, R. P. et al. *J. Am. Chem. Soc.* **1982,** *104,* 6528.
(29) Bowling, R.; Packard, R.; McCreery, R. L. *J. Electrochem. Soc.* **1988,** *135,* 1605.
(30) Bowling, R.; Packard, R.; McCreery, R. L. *J. Am. Chem. Soc.* **1989,** *111,* 1217.
(31) Chase, D. B. *J. Am. Chem. Soc.* **1986,** *108,* 7485.
(32) Chase, D. B. *Anal. Chem.* **1987,** *59,* 881 A.
(33) Lewis, E. N.; Kalasinsky, V. F.; Levin, I. W. *Anal. Chem.* **1988,** *60,* 2306.
(34) Desilvestro, J.; Corrigan, D. A.; Weaver, M. J. *J. Electrochem. Soc.* **1988,** *135,* 885.
(35) Golab, J. T.; Sprague, J. R.; Carron, K. T.; Schatz, G. C.; Van Duyne, R. P. *J. Chem. Phys.* **1988,** *88,* 7942.
(36) Chase, D. B.; Parkinson, D. A. *Appl. Spectrosc.* **1988,** *42,* 1186.
(37) Angel, S. M.; Katz, L. F.; Archibold, D. D.; Lin, L. T.; Honigs, D. E. *Appl. Spectrosc.* **1988,** *42,* 1327.
(38) Williamson, J. M.; Bowling, R.; McCreery, R. L. *Appl. Spectrosc.* **1989,** *43,* 372.
(39) Pemberton, J. E.; Sobocinski, R. L. *J. Am. Chem. Soc.* **1989,** *111,* 432.

Richard L. McCreery joined the faculty of The Ohio State University in 1974, where he is currently professor of chemistry. He received his B.S. degree in chemistry at the University of California, Riverside, and his Ph.D. in analytical chemistry at the University of Kansas, where he worked under the direction of Ralph N. Adams. McCreery's research interests include electroanalytical chemistry, electrocatalysis, and spectroscopic probes of electrochemical processes. Of particular interest is Raman spectroscopy applied to dynamic electrochemical events.

Richard T. Packard is a development chemist with E. I. du Pont de Nemours and Co. at Jackson Laboratory, Deepwater, NJ. He received his B.S. degree from Kansas Wesleyan University (Salina) in 1983 and a Ph.D. in analytical chemistry from The Ohio State University in 1988. His research interests include the application of novel sampling techniques to spectroscopic methods development and new detection strategies for process control.

MEETINGS

Conferences

■ **Annual Meeting of the American Electrophoresis Society.** July 6–11. Washington, DC. *Contact: Electrophoresis Society, Box 6182, Station B, Vanderbilt University, Nashville, TN 37235 (615-327-7070)*

■ **Meeting of the American Association for Clinical Chemistry.** July 23–27. Atlanta, GA. *Contact: AACC, 2029 K St., N.W., Washington, DC 20006*

■ **2nd International Conference on Chemical Kinetics.** July 23–27. Gaithersburg, MD. *Contact: John Herron, A147 Chemistry Bldg., National Institute of Standards and Technology, Gaithersburg, MD 20899 (301-975-2569)*

■ **5th Annual Waste Testing and Quality Assurance Symposium.** July 24–28. Washington, DC. *Contact: Gail Hansen, Office of Solid Waste (OS-331), U.S. EPA, 401 M St., S.W., Washington, DC 20460*

■ **12th International EPR Symposium.** July 30–Aug. 3. Denver, CO. *Contact: Gareth Eaton, Dept. of Chemistry, University of Denver, Denver, CO 80208 (303-871-2980)*

■ **31st Rocky Mountain Conference.** July 30–Aug. 4. Denver, CO. *Contact: Carol Gies, Rockwell International, General Lab., Bldg. 881, P.O. Box 464, Golden, CO 80401 (303-966-7380)*

■ **SAC '89—International Conference on Analytical Chemistry.** July 30–Aug. 5. Cambridge, U.K. *Contact: Royal Society of Chemistry, Analytical Division, Burlington House, London W1V 0BN, U.K.*

■ **38th Annual Denver X-ray Conference.** July 31–Aug. 4. Denver, CO. *Contact: Lynne Bonno, Dept. of Engineering, University of Denver, Denver, CO 80208 (303-871-3515)*

■ **32nd Congress of the International Union of Pure and Applied Chemistry.** Aug. 2–7. Stockholm, Sweden. *Contact: 32nd IUPAC Congress, c/o Stockholm Convention Bureau, P.O. Box 6911, S-102 39 Stockholm, Sweden*

■ **Symposium for Innovation in Measurement Science.** Aug. 6–11. Geneva, NY. *Contact: Instrument Society of America, 67 Alexander Dr., P.O. Box 12277, Research Triangle Park, NC 27709 (919-549-8411)*

■ **Meeting of the Electron Microscopy Society of America.** Aug. 6–11. San Antonio, TX. *Contact: EMSA, Box EMSA, Woods Hole, MA 02543*

■ **7th Danube Symposium on Chromatography.** Aug. 21–25. Leipzig, G.D.R. *Contact: Organization Committee, Karl Marx University of Leipzig, Dept. of Chemistry, Talstrasse 35, DDR-7010 Leipzig, G.D.R.*

■ **2nd International Symposium on Mass Spectrometry in the Health and Life Sciences.** Aug. 27–31. San Francisco, CA. *Contact: M. F. Schwartz, Dept. of Pharmaceutical Chemistry, University of California, San Francisco, CA 94143 (415-476-2582)*

■ **11th International Symposium on Microchemical Techniques.** Aug. 28–Sept. 1. Wiesbaden, F.R.G. *Contact: Gesellschaft Deutscher Chemiker, Abteilung Tagungen, Varrentrappstrasse 40–42, P.O. Box 90 04 40, D-6000 Frankfurt am Main 90, F.R.G.*

■ **12th International Congress on X-ray Optics and Microanalysis.** Aug. 28–Sept. 1. Cracow, Poland. *Contact: 12th ICXOM, Institute of Metallurgy, Academy of Mining and Metallurgy, al. Mickiewicza 30, Pl-30-059 Cracow, Poland*

■ **7th International Conference on Secondary Ion Mass Spectrometry.** Sept. 3–8. Monterey, CA. *Contact: SIMS VII, Charles Evans & Associates, 301 Chesapeake Dr., Redwood City, CA 94063 (415-369-4567)*

■ **Symposium on Biosensors.** Sept. 7–9. Chapel Hill, NC. *Contact: William E. Hatfield, Dept. of Chemistry, University of North Carolina, Chapel Hill, NC 27514 (919-966-2297)*

■ **3rd European Conference on the Spectroscopy of Biological Molecules.** Sept. 10–15. Bologna, Italy. *Contact: A. Bertoluzza, Dipartimento di Biochimica, Centro di Studio Interfacolta sulla Spettroscopia Raman, Via Selmi, 2, 40126 Bologna, Italy*

■ **198th National Meeting of the American Chemical Society.** Sept. 10–15. Miami Beach, FL. *Contact: Meetings Dept., American Chemical Society, 1155 16th St., N.W., Washington, DC 20036 (202-872-4396)*

■ **150th Anniversary Commemorative Meeting of the Royal Microscopical Society.** Sept. 11–12. London, U.K. *Contact: The Royal Microscopical Society, 37/38 St. Clements, Oxford OX4 1AJ, U.K.*

■ **2nd International Ion Chromatography Forum.** Sept. 17–19. Boston, MA. *Contact: Gerald Hawk or Janet Strimaitis, Century International Inc., P.O. Box 249, Franklin, MA 02038 (508-520-3539)*

■ **8th Symposium on Artificial Intelligence-Based Measurement and Control.** Sept. 17–19. Kyoto, Japan. *Contact: K. Kariya, Dept. of Electrical Engineering, Ritsumeikan University, 56-1, Tojiin-kita, Kita-ku, Kyoto 603, Japan*

■ **Annual Conference of the Canadian Society of Forensic Science.** Sept. 18–22. Edmonton, Alberta, Canada. *Contact: Canadian Society of Forensic Science, 2660 Southvale Crescent, Suite 215, Ottawa, Ontario, Canada K1B 4W6 (613-731-2096)*

■ **CANBIOCON '89.** Sept. 19–20. Ottawa, Ontario, Canada. *Contact: Rachel Boekman, 100 Alexis Nihon, Suite 875, Montreal, Quebec H4M 2P4, Canada*

■ **12th International Symposium on Polynuclear Aromatic Hydrocarbons.** Sept. 19–21. Gaithersburg, MD. *Contact: Willie May, A113 Chemistry Bldg., NIST, Gaithersburg, MD 20899 (301-975-3108)*

■ **5th Conference on Separation of Gases.** Sept. 19–21. Birmingham, U.K. *Contact: Royal Society of Chemistry, Burlington House, London W1V 0BN, U.K.*

■ **International Symposium on the Analysis of Nucleoside, Nucleotide, and Oligonucleotide Compounds.** Sept. 19–22. Antwerp, Belgium. *Contact: E. L. Esmans, University of Antwerp (R.U.C.A.), Laboratory for Organic Chemistry, Groenenborgerlaan 171, B-2020 Antwerp, Belgium*

■ **Symposium on Detection in High-Performance Liquid Chromatography and Flow-Injection Analysis.** Sept. 20–22. Cordoba, Spain. *Contact: Miguel Valcarcel, Quimica Analytica, Facultad de Ciencias, University of Cordoba, 14004 Cordoba, Spain*

■ **Eastern Analytical Symposium.** Sept. 24–29. New York, NY. *Contact: EAS, P.O. Box 633, Montchanin, DE 19710 (302-453-0785)*

■ **4th Conference on Sensors and Their Applications.** Sept. 25–27. Canterbury, U.K. *Contact: Meetings Office, Institute of Physics, 47 Belgrave Square, London SW1X 8QX, U.K.*

■ **103rd Annual AOAC International Meeting and Exposition.** Sept. 25–28. St. Louis, MO. *Contact: Margaret Ridgell, AOAC, 1111 North 19th St., Suite 210, Arlington, VA 22209*

■ **3rd International Symposium on Kinetics in Analytical Chemistry.** Sept. 25–28. Cavtat, Yugoslavia. *Contact: Gordana Milovanović, Dept. of Chemistry, University of Belgrade, KAC, P.O. Box 550, 11001 Belgrade, Yugoslavia*

■ **International GPC Symposium.** Oct. 1–4. Boston, MA. *Contact: Lorraine Carter, Waters Chromatography Division of Millipore, 34 Maple St., Milford, MA 01757 (508-478-2000)*

■ **International Conference on Separation Science and Technology.** Oct. 1–4. Hamilton, Ontario, Canada. *Contact: V. I. Lakshmanan, Ontario Research Foundation, Sheridan Park, Mississauga, Ontario L5K 1B3, Canada*

■ **3rd International Meeting on Chemical Sensors.** Oct. 1–5. Toronto, Canada. *Contact: M. Thompson or U. J. Krull, Dept. of Chemistry, University of Toronto, 80 St. George St., Toronto, Ontario, Canada M5S 1A1*

■ **16th Annual Meeting of the Federation of Analytical Chemistry and Spectroscopy Societies.** Oct. 1–6. Chicago, IL. *Contact: Paul Bourassa, Memphis Environmental Center, Suite 100, 2603 Corporate Ave. East, Memphis, TN 38132 (901-345-1788)*

■ **International Conference on New Trends in Liquid Scintillation Counting and Organic Scintillators.** Oct. 2–5. Gatlinburg, TN. *Contact: Harley Ross, Analytical Chemistry Division, ORNL, P.O. Box 2008, Oak Ridge, TN 37831-6375 or John Noakes or Jim Spaulding, Center for Applied Isotope Studies, University of Georgia, 120 Riverbend Rd., Athens, GA 30605*

■ **2nd International Symposium on Philosophy and History of Analytical Chemistry.** Oct. 6–7. Vienna, Austria. *Contact: R. Kellner, Institute for Anal. Chem., Technical University Vienna, A-1060 Vienna, Austria*

■ **Kinetics of Nonhomogeneous Processes—Nonlinear Dynamics.** Oct. 7–13. Banff, Alberta, Canada. *Contact: G. R. Freeman, Chemistry Dept., University of Alberta, Edmonton, Alberta, Canada (403-492-3468)*

■ **5th Annual Scientific Computing and Automation Conference and Exposition.** Oct. 11–13. Philadelphia, PA. *Contact: Don Weise, 301 Gibraltar Dr., P.O. Box 650, Morris Plains, NJ 07950-0650 (201-292-5100)*

■ **7th International Symposium on Laboratory Robotics.** Oct. 15–18. Boston, MA. *Contact: Christine O'Neil, Zymark Corp., Zymark Center, Hopkinton, MA 01748 (508-435-9501)*

■ **Annual Meeting of the Optical Society of America.** Oct. 15–20. Orlando, FL. *Contact: Optical Society of America, 1816 Jefferson Pl., N.W., Washington, DC 20036*

■ **CIS '89 Tokyo (International Symposium on Chromatography).** Oct. 17–20. Tokyo, Japan. *Contact: T. Hoshino, Secretary General, Pharmaceutical Institute, School of Medicine, Keio University, 35 Shinano-machi, Shinjuku-ku, Tokyo 160, Japan*

■ **Laboratory Strategies for Automation Forum.** Oct. 18–20. Boston, MA. *Contact: Gerald Hawk or Janet Strimaitis, Century International, Inc., P.O. Box 249, Franklin, MA 02038 (508-520-3539)*

■ **Pacific Conference on Chemistry and Spectroscopy.** Oct. 18–21. Pasadena, CA. *Contact: Peter Baine, California State University, Long Beach, CA (213-985-4908)*

■ **6th Symposium on Separation Science and Technology for Energy Applications.** Oct. 22–27. Knoxville, TN. *Contact: J. T. Bell, Oak Ridge National Laboratory, P.O. Box 2008, Oak Ridge, TN 37831*

■ **Diagnostic Genetics and Immunology V.** Oct. 22–27. Santa Barbara, CA. *Contact: Engineering Foundation, 345 East 47th St., New York, NY 10017 (212-705-7835)*

■ **European Conference on Applications of Surface and Interface Analysis (ECASIA 89).** Oct. 23–27. Antibes—Juan-les-Pins, France. *Contact: Société Française du Vide, 19, rue du Renard, 75004 Paris, France*

■ **International Chromatography Meeting.** Oct. 23–27. Mexico City, Mexico. *Contact: S. Ahuja, Ciba-Geigy Corp., Old Mill Road, Suffern, NY 10901*

■ **International Biotechnology Exposition.** Oct. 24–26. San Mateo, CA. *Contact: Linda Cartlidge, Cartlidge & Associates, 3097 Moorpark Ave., Suite 202, San Jose, CA 95128 (408-554-6644)*

■ **9th International Symposium on HPLC Separation of Proteins, Peptides, and Polynucleotides.** Nov. 6–8. Philadelphia, PA. *Contact: Janet Cunningham, Barr Enterprises, P.O. Box 279, Walkersville, MD 21793 (301-898-3772)*

■ **Fall Meeting of the Materials Research Society.** Nov. 27–Dec. 2. Boston, MA. *Contact: MRS, 9800 McKnight Rd., Suite 327, Pittsburgh, PA 15237*

■ **Symposium on Modern Methods of Elemental Analysis of Petroleum Products and Lubricants.** Dec. 11–13. New Orleans, LA. *Contact: Kishore Nadkarni, Exxon Chemical Co., Chemicals Analytical Laboratory, P.O. Box 536, Linden, NJ 07036 (201-474-6380)*

■ **International Chemical Congress of Pacific Basin Societies (Pacifichem '89).** Dec. 17–22. Honolulu, HI. *Contact: Pacifichem '89 Secretariat, American Chemical Society, 1155 16th St., N.W., Washington, DC 20036 (202-872-8069)*

Short Courses and Workshops

■ **Short Course on Quality Assurance for Analytical Laboratories.** July 11–12. Arlington, VA. *Contact: Carolyn Brown, AOAC, 1111 North 19th St., Suite 210-B, Arlington, VA 22209 (703-522-3032)*

■ **Advanced HPLC Workshop.** July 11–13. Blacksburg, VA. *Contact: Harold McNair, Chemistry Dept., Virginia Polytechnic Institute and State University, Blacksburg, VA 24061-0212 (703-231-6579)*

■ **Short Course on LC/MS, SFC/MS, and CZE/MS.** July 17–18. Ithaca, NY. *Contact: Jack Henion, Equine Drug Testing and Toxicology Program, New York State College of Veterinary Medicine, Cornell University, 925 Warren Dr., Ithaca, NY 14850 (607-255-6556)*

■ **Short Course on Applied Molecular Spectroscopy—Infrared.** July 24–28. Tempe, AZ. *Contact: Jacob Fuchs, Dept. of Chemistry, Arizona State University, Tempe, AZ 85287*

■ **Course on Environmental Applications of Gas Chromatography/Mass Spectrometry.** July 24–28. Bloomington, IN. *Contact: Executive Education Program, Indiana University, SPEA 410H, Bloomington, IN 47405 (812-855-0193)*

■ **Short Course on Modern Industrial Spectroscopy.** Aug. 7–18. Tempe, AZ. *Contact: Jacob Fuchs, Dept. of Chemistry, Arizona State University, Tempe, AZ 85287*

■ **Course on Principles of Chemical Sensors.** Sept. 25–28. Wildbad Kreuth, Bavaria, F.R.G. *Contact: M. Josowicz, Institut für Physik, Fakultät für Elektrotechnik Universität der Bundeswehr München, D-8014 Neubiberg, F.R.G.*

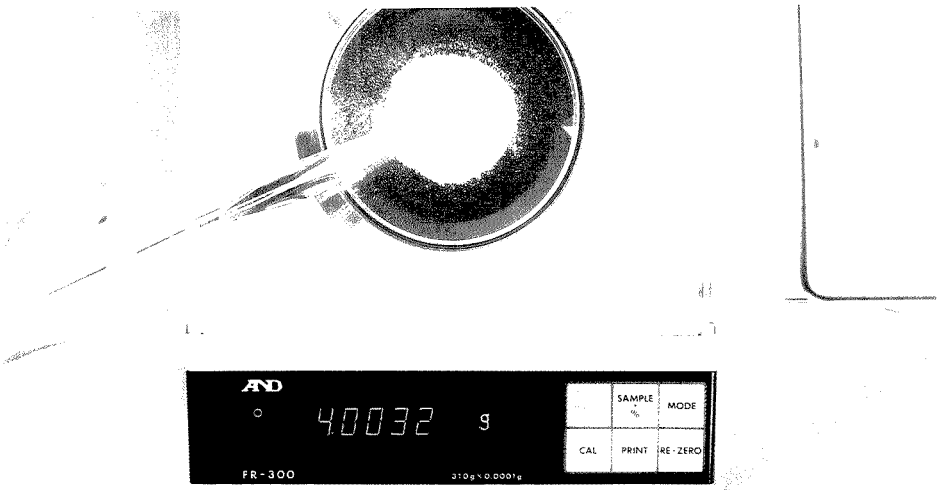

Ultra Wide Range! The FR Series Precision Multi-Function Analytical Balances

Another first from A&D — Analytical precision balances with multi weighing units, multi-functions and optional wireless remote control.

By using the latest electronic technology combined with easy-to-use multi-function features and extensive ergonomic design — the FR series will revolutionize the ways you can use an analytical balance. Multi weighing units; Comparator mode; Percentage add/subtract mode; Counting mode; Environmental conditions adjustment (including last-digit blanking during course weighing); Auto power ON; — and much, much more.

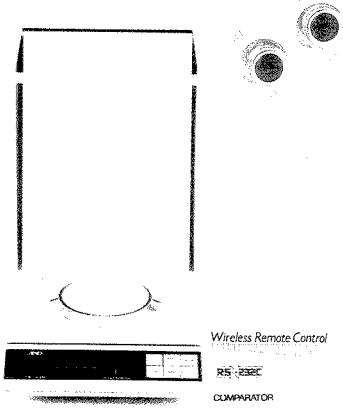

Start with an optional wireless remote control that simplifies and expands operation of every feature the balance has available — then, enjoy the rest of the full range of options available for the FR Series.

A&D ENGINEERING, INC.
1555 McCandless Drive, Milpitas, CA 95035
Fax: (408) 263-0119 Telex: 346940 AANDD SNJ

EAST COAST BRANCH OFFICE
2165-M West Park Court, Stone Mountain, GA 30087
(800) 426-4480 In Georgia (404) 498-9732
Fax: (404) 498 4877

CIRCLE 4 ON READER SERVICE CARD

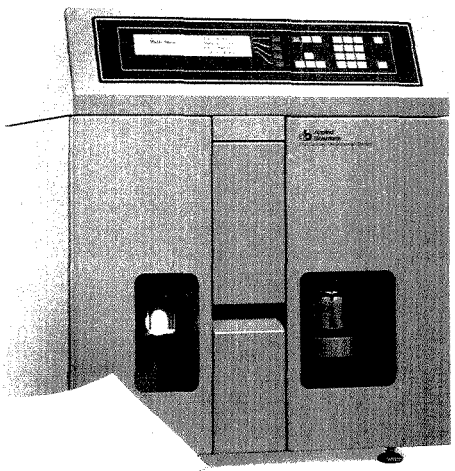

In the fast-moving field of capillary electrophoresis, only the Model 270A puts you in the lead.

Harness the power of capillary electrophoresis (CE) with high performance instrumentation. For meaningful quantitation and reliable analysis, CE's inherent selectivity and resolution must be complemented with accuracy and precision.

The Model 270A Analytical Capillary Electrophoresis System is the first fully integrated system designed to meet the stringent demands of quantitative CE. The system you need when every minute, every result, counts.

The human serum albumin digest was provided courtesy of Delta Biotechnology Ltd., Nottingham, U.K.

True quantitation begins with precision and accuracy in both sample injection and column temperature control. The Applied Biosystems Model 270A combines automation with a unique injector design, a thermostatted capillary compartment and proven detector technology to achieve unsurpassed reproducibility of peak areas and electrophoretic mobility.

Count on your first results within minutes after installing the Model 270A. Select a preprogrammed separation protocol, or create and store your own methods using the interactive display and keypad. The Model 270A is designed for both the novice and the seasoned user of analytical instrumentation.

Contact Applied Biosystems today, and join the leaders in advancing capillary electrophoresis from theory to application.

Applied Biosystems

U.S.A. 850 Lincoln Centre Drive, Foster City, CA 94404. Tel: (415) 570-6667, (800) 874-9868, in California (800) 831-3582. Telex: 470052 APBIO UI. Fax: (415) 572-2743.
Mississauga, Canada. Tel: (416) 821-8183. Fax: (416) 821-8246.
Warrington, U.K. Tel: 0925-825650. Telex: 629611 APBIO G. Fax: 0925-828196.
Weiterstadt, West Germany. Tel: 06151-87940. Telex: 4197318 Z ABI D. Fax: 06151-84899.
Paris, France. Tel: (1) 48 63 24 44. Telex: 230458 ABIF. Fax: (1) 48 63 22 82.
Milan, Italy. Tel: 02-835 4920. Fax: 02-832 1655.
Rotterdam, The Netherlands. Tel: (0) 10 452 35 11. Telex: 26249. Fax: (0) 10 452 91 57.
Burwood, Australia. Tel: (03) 288-7777. Fax: (03) 887-1469.
Tokyo, Japan. Tel: (03) 699-0700. Fax: (03) 699-0733.

Circle No. 1 for information. Circle No. 2 for sales call.

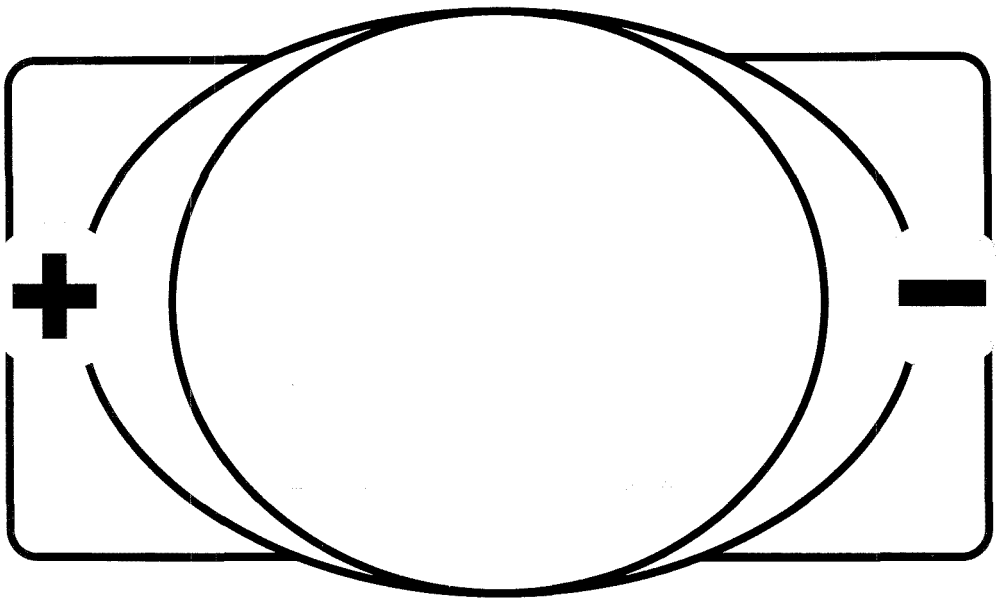

One of the most rapidly expanding areas of analytical chemistry is capillary electrophoresis (CE), a highly efficient technique that offers short analysis times and can be used to solve bioanalytical problems. In November 1987 Georges Guiochon of the University of Tennessee suggested to Barry Karger of Northeastern University that they hold a topical meeting on CE. Karger assembled an international scientific advisory committee consisting of himself; Frans Everaerts of the Eindhoven University of Technology, The Netherlands; Stellan Hjerten of the University of Uppsala, Sweden; James Jorgenson of the University of North Carolina; and Shigeru Terabe of Kyoto University, Japan. An organizing committee, chaired by Karger and Tom Gilbert of Northeastern University, was also formed.

Despite initial concern that CE was perhaps too young a field to support a full-fledged meeting, the First International Symposium on High-Performance Capillary Electrophoresis was held April 10–12 in Boston. More than 450 scientists attended the meeting, which featured 10 invited talks by the foremost researchers in the field as well as 50 contributed posters. An exhibition of CE instruments and related equipment drew big crowds during session breaks, and this was one indication of how the technology has grown during the past couple of years. When HPCE '89 was being organized, there were no commercially available instruments for CE. Today there are seven, from Applied Biosystems, Beckman Instruments, Bio-Rad Laboratories, Dionex, Microphoretic Systems, Shimadzu, and SpectroVision.

Basic concepts

The meeting began with an overview of the history of electrophoresis by Olof Vesterberg of the National Institute of Occupational Health in Solna, Sweden. Vesterberg, best known for his work on the use of carrier ampholytes in isoelectric focusing (IEF) of proteins, discussed the evolution of electrophoresis from the initial observations of Reuss in 1807 to the use of sophisticated electrophoretic techniques in the international project to map the human genome.

FOCUS

Presentations on the theoretical basis and limitations of CE were given by J. Calvin Giddings of the University of Utah, Jorgenson, Everaerts, Hjerten, and Glyn O. Roberts of Roberts Associates (Vienna, VA). Giddings noted that "we at the University of Utah believe that electrical forces can be used for just about anything: one day for electrophoresis, the next day for fusion," referring to the Pons–Fleischmann claim of electrochemical fusion (see NEWS and FOCUS in the June 1 issue of ANALYTICAL CHEMISTRY). He then described the theory underlying different ways of using electrical forces for separation, including CE, IEF, electrical field-flow fractionation, and continuous separation using split-flow thin cells.

Jorgenson discussed the theoretical limits of CE in terms of separation efficiency, resolution, peak capacity, and analysis time. Up to a point, he said, the length of the column doesn't matter, and short columns work just as well as long ones. But with very short columns, heating can cause serious problems. Following Jorgenson's fairly general talk, particular aspects of CE theory were examined. The effects of electroosmotic flow on CE separations, band broadening, and dispersion were discussed by Everaerts, Hjerten, and Roberts, respectively.

Selectivity

The focus of the session then shifted to ways of enhancing the selectivity of CE in presentations by Terabe, Karger, and Richard Mosher of the University of Arizona. Terabe is perhaps best known for his work with micellar electrokinetic capillary chromatography (MECC), which can be used to separate neutral compounds electrophoretical-

ly. By substituting either cyclodextrin derivatives or optically active ionic surfactants for the surfactants used in MECC, Terabe has separated chiral compounds, including a mixture of dansylated amino acids, electrophoretically.

Karger described some of his work on capillary gel electrophoresis of biopolymers. Using polyacrylamide gel-filled capillaries, Karger and co-workers at the Barnett Institute have generated CE columns with more than 5 million theoretical plates. Such columns can provide rapid separations with selectivity by size (shape) and charge, and they have been used to separate oligonucleotides into their respective "mers." The resolving power of the capillary columns compared with that of a conventional slab gel is demonstrated by the fact that a single band on the slab gel produces several peaks when run through a gel-filled capillary column. Such technology should prove extremely useful for DNA sequencing as well as evaluating the purity of material from DNA synthesizers, said Karger.

Mosher discussed the use of chiral buffers containing metal ions for separating mixtures of dansylated amino acids, proteins, and peptides. In free solution, the interaction of a metal ion with a peptide produces diastereomeric complexes with electrophoretic mobilities that differ from those of the free peptide. Mosher has found that resolution of dipeptides containing histidine can be enhanced by the addition of metal ions to the CE buffer; resolution increases as metal concentration increases. He believes that in the future this technique should prove valuable for chiral separations of larger peptides.

Detection

Sensitive detection strategies for CE were discussed by Richard Zare of Stanford University, Norman Dovichi of the University of Alberta, Ubbo Tjaden of the University of Leiden, Edward Yeung of Iowa State University, and Milos Novotny of Indiana University. Zare discussed the theory involved in CE detection, including the ever-present question of sensitivity versus resolution. The same problems encountered in capillary liquid chromatographic detection, including small column dimensions and narrow zone widths, are also present in CE, said Zare. Many of the same detectors, including those based on absorption, fluorescence, conductivity, electrochemical reactions, refractive index, radioisotope labeling, and MS, have been used for CE detection.

Dovichi discussed the use of laser-induced fluorescence (LIF) for detection of attomole amounts of amino acids. Using LIF and a sheath flow cuvette, Dovichi has attained subattomole detection limits for fluorescein–isothiocyanate derivatives of 14 amino acids; this corresponds to only 6000 molecules. The ultimate fluorescence detection limit for amino acid derivatives, said Dovichi, should approach a microattomole (tens of molecules).

Not all compounds that can be separated by CE are fluorescent, however, and derivatization is necessary to make them amenable to fluorescence detection methods. Pre- and postcolumn detection can be used, but these methods require additional labor and equipment. Tjaden described a method for performing on-line derivatization in which the buffer solution contains the derivatization reagent, and after injection of the sample, derivatization takes place in the capillary.

"Capillary gel electrophoresis should prove useful for DNA sequencing and for evaluating the purity of materials from DNA synthesizers."

Two other approaches to fluorescence detection were discussed by Yeung and Novotny. Yeung described a method for universal indirect detection of analytes at the 50-attomole level. Displacement of analytes by fluorescent buffer ions results in negative peaks upon elution. The sensitivity of the indirect measurement is independent of the many physical properties of the analyte and depends only on the signal-to-noise ratio of the background signal and the concentration of the visualizing agent.

Novotny described the development of several fluorogenic reagents for the detection of amino acids, tryptic protein digests, and hydrolytic degradation products of ribonucleic acid molecules at the femtomole level. He emphasized the importance of chemistry and precleanup to successful analysis by CE.

Applications

Applications of CE to problems in the biomedical/biotechnology field were presented by Ernst Gassmann of Ciba-Geigy (Switzerland), Andrew Ewing of Penn State University, Bill Hancock of

Genentech (S. San Francisco), Randall Nielsen of Eli Lilly (Indianapolis), Steve Fazio of Sandoz Research Institute (E. Hanover, NJ), Ferenc Kilar of Uppsala University, and Louis Yu of R. W. Johnson Pharmaceutical Research Institute (Raritan, NJ).

Ewing described the use of CE in a study of single functioning nerve cells. Cytoplasmic samples are extracted from single cells, and electrophoretic separations subsequently are performed using amperometric or mass spectrometric detection. The system permits detection of subattomole amounts of easily oxidized neurotransmitters in picoliter volumes.

Gassmann, Hancock, Fazio, Neilsen, Yu, and Kilar described methods for analyzing peptides synthesized using recombinant DNA technology, for which small variations in the primary or secondary structure of the peptide can produce a small change in the overall charge on the molecule. In the past, said Hancock, electrophoretic techniques such as SDS electrophoresis and IEF were used to separate protein variants and impurities, but compared with liquid chromatographic techniques, traditional slab gel electrophoretic techniques are difficult to quantitate. CE, however, combines the power of electrophoresis with the instrumental capabilities of chromatographic methods and can be applied to such protein pharmaceuticals as human growth hormone, tissue plasminogen activator, and γ-interferon. Because of their different separation mechanisms, CE and LC can be viewed as complementary techniques in the biotechnology laboratory.

HPCE/MS

The symposium wound up with two sessions on combining CE with mass spectrometric detection. Instrumentation and applications of this new technique were discussed by Richard Smith of Pacific Northwest Laboratory (Richland, WA), Jack Henion of Cornell University, Herbert Hill of Washington State University, Richard Caprioli of the University of Texas, and Arthur Moseley of the University of North Carolina at Chapel Hill.

Smith described his work in combining CE with MS using an electrospray ionization interface. Capillary zone electrophoresis (CZE) and capillary isotachophoresis have already been successfully interfaced, said Smith, and extension to IEF, MECC, and polyacrylamide gel-filled capillaries appears feasible. Detection limits of a few attomoles have been achieved, and proteins of up to 75,000 daltons can be separated and determined. The major difficulty appears to be loss of separation efficiency because of protein interactions with surfaces of the capillary, leading to higher detection limits for large biomolecules.

A system for CZE/MS/MS with atmospheric pressure ionization was described by Henion, who has used it to analyze synthetic peptide mixtures and tryptic digests and to determine sulfonated azo dyes isolated from wastewater samples. The mild conditions of atmospheric ionization allow accurate molecular weight determination, and tandem MS provides sequence information for each peptide. The detection limit of the system is in the low attomole-to-femtomole range.

Hill described results of initial investigations of the use of ion mobility spectrometry as a detection method for CE. Electrified spray ionization methods such as electrospray and corona spray are incorporated into the CZE/ion mobility detection system.

Finally, both Caprioli and Moseley described the combination of CZE with continuous-flow fast atom bombardment (CF-FAB) MS for analysis of peptide mixtures. In Caprioli's system, a fused-silica capillary column is connected to the CF-FAB probe via an interface that allows a total flow of ~5 μL/min into the mass spectrometer. Peptide solutions are loaded pneumatically onto the capillary, and the desired mass range is scanned with a magnetic mass spectrometer.

Moseley's system, developed with Jorgenson and Ken Tomer of the National Institute of Environmental Health Sciences (Research Triangle Park, NC), uses a set of coaxial 10-μm capillaries to independently deliver the microcolumn effluent and the FAB matrix directly to the FAB probe tip face. The system was designed to minimize band broadening and preclude any deleterious effects of the FAB matrix on the separation process. It has been used with both CE and capillary LC to obtain on-the-fly FAB/MS spectra of several analyte classes, including peptides, and can be used to obtain sequence information of subpicomole amounts of proteins.

The next CE meeting, to be chaired by Karger, is scheduled for January 29–31, 1990, in San Francisco. The organizers had originally planned the next meeting for February 1991 to give the field a chance to mature, but the impressive attendance at HPCE '89 prompted them to schedule an interim meeting. Given the anticipated growth of this technique and its increasing use in solving bioanalytical problems, HPCE '90 should be even better than HPCE '89. *Mary Warner*

NEW PRODUCTS

SFC. Series 600-D supercritical fluid chromatograph features computerized data collection, processing, and storage and a Microsoft Windows-based computer operating system. Data-handling capabilities include peak integration and pressure/density calculations. Lee Scientific 404

Concentrator. A290 automated concentration station accommodates up to 200 individual samples in either aqueous or organic solvents. The system, which uses centrifugal force, applied heat, and high vacuum, can be programmed to start at any time and to stop at a predetermined dryness level. Savant Instruments 405

Microscopy. STM-SU2 scanning tunneling microscope system features a stage designed to be mounted to an 8-in. vacuum port and an HP Model 340C+ graphic workstation. System capabilities include parallel image acquisition at multiple bias voltages and spatially localized I–V and dI/dV characterization. Park Scientific Instruments 406

GPC. Model 150CV integrated GPC system incorporates a differential refractive index detector that measures polymer concentration and a single capillary viscometer that measures intrinsic viscosity over a temperature range from ambient to 150 °C. Waters Chromatography Division of Millipore 407

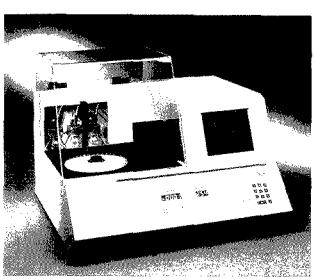

CES I capillary electrophoresis system includes a 40-place autosampler and fiber-optic-based detectors for UV–vis absorbance and fluorescence. The system is controlled via menu-driven software. Dionex 401

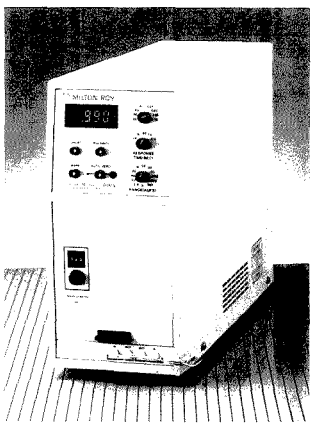

SpectroMonitor 3100X allows differential absorbance measurements to be made from 190 to 700 nm without a lamp change. The standard low-RI high-pressure fluid cell features a noise specification of $\pm 1 \times 10^{-5}$ AU at 200–300 nm. Milton Roy, LDC Division 403

MS. Leybold Inficon Auditor II mass spectrometer features a plug-in ion source, selectable temperature interface, jet separator with independent variable-temperature control, foreground/background operation, and automatic report generation. U.S. Analytical Instruments 408

Spectrofluorometer. Model HPSF-56 high-pressure stopped-flow spectrofluorometer can be operated between −60 °C and 100 °C and at pressures up to 2000 bar. The flow circuit and observation cell are contained within a high-pressure vessel. Hi-Tech Scientific 409

Sample preparation. BenchMate workstations can perform liquid-dispensing operations, including solvent and reagent additions, internal standard additions, and serial dilutions; membrane filtrations; solid-phase extractions; and HPLC injections. Zymark 410

Water. Mega-Pure MP-270 is a double-pass, reverse-osmosis water purification system that produces ultrapure water free of bacteria, pyrogens, and organics. The system, which delivers 70 L of water per hour, can be sanitized without disassembly. Corning Science Products 411

DNA synthesis. Generator DNA synthesizer features a syringe-based delivery system that ensures minimal reagent usage and provides for homogeneous mixed-base additions. The video screen displays reaction cycle status and sequence base position during operation. Du Pont 412

Titration. TR600 titration system, controlled by an IBM PS/2 personal computer, features a color monitor that displays real-time titration curves. Data can be imported into spreadsheet or database programs. Great Lakes Instruments 413

Software

Mathematics. MathCAD, which runs on Apple Macintosh computers, features comprehensive matrix arithmetic, trigonometric and inverse trig functions, integrals and derivatives, real and complex fast Fourier transforms, cubic splines, and user-defined and statistical functions. MathSoft 415

Scientific software. Lab Calc is designed to handle 2D data from hyphenated or other techniques and features interactive graphics for displaying contour, 3D perspective, stacked, overlaid, and scatter plots. Galactic Industries 416

Manufacturers' Literature

Newsletter. *Applied Fluorescence Technology*, Vol. I, No. 1, contains articles on fluoroprobes, voltage-sensitive dyes, cellulase substrates, and a fluorescent lipoprotein label. 16 pp. Polo-Lambda 418

For more information on listed items, circle the appropriate numbers on one of our Readers' Service Cards

Biomolecules. Bulletin describes biomolecule recovery with an electroelutor/concentrator. Methods for recovering nucleic acids and proteins from agarose and polyacrylamide gels and concentrating macromolecules in solution are discussed. 10 pp. Isco 419

Computers. "Glossary of Microcomputer Data Acquisition Terms" contains definitions for approximately 300 terms related to data conversion, signal conditioning, and microcomputer systems and software. 23 pp. Metra-Byte 420

LC. Brochure highlights the SIL-9A autosampler that performs sampling, injection, dilution, and dispensing functions. Application to precolumn derivatization is discussed. 10 pp. Shimadzu 421

IR. *FT-IR Spectral Lines*, Vol. 10, No. 1, includes articles on SFC/FT-IR analysis of nitrated diphenylamine and nitrated aniline propellant stabilizers and uses of FT-IR in the explosives industry. 34 pp. Nicolet 422

Oxygen analyzer. Brochure describes the Type A-Plus oxygen analyzer, which features a nondepleting coulometric oxygen sensor. Specifications, measuring ranges, and optional equipment are discussed. 4 pp. Delta F 423

Catalogs

Scientific products. Catalog includes electrodes, centrifuges, spectrophotometers, computer hardware and software, plasticware, storage cabinets, timers, and products for safety and hygiene. 160 pp. Whatman LabSales 431

Viscosity. Catalog lists glass capillary and automatic viscometers, constant-temperature baths, viscosity standards, distillation flasks, and accessories. 32 pp. Cannon Instrument Co. 426

Scientific products. Catalog features chromatography media, columns, and instruments as well as products for sample preparation, electrophoresis, and immunology. 200 pp. Bio-Rad 427

Chemicals. Catalog includes amino acids, biological stains, carbohydrates, chelants, environmental standards, inhibitors, inorganics, organics, and surfactants. 280 pp. Chem Service 428

LC. Catalog features fittings, detector and pump components, filtration devices, columns, data-handling products, and supplies for sampling and fraction collection. 60 pp. Perkin-Elmer 429

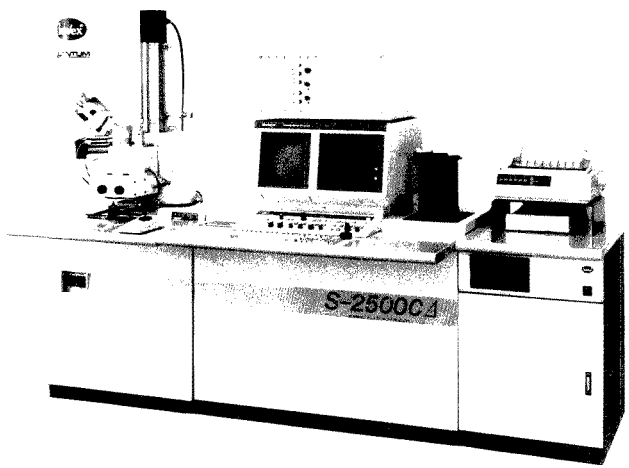

Model S-2500C Delta scanning electron microscope features built-in image processing and a conical lens that allows high tilt angles on large specimens at a short working distance. Hitachi 402

Editor: **William H. Glaze,** *University of California, Los Angeles*

Associate Editors: **J. H. Seinfeld,** *California Institute of Technology*•**P. C. Singer,** *Univ. of North Carolina*

Advisory Board: R. Atkinson, *Univ. of California, Riverside*•**J. M. Daisey,** *Lawrence Berkeley Lab*•**F. H. Frimmel,** *Technical Univ. of Munich, Germany*•**N. E. Gallopoulos,** *General Mtrs. Res. Labs*•**G. R. Helz,** *Univ. of Maryland*•**R. A. Hites,** *Indiana Univ.*•**J. Leckie,** *Stanford Univ.*•**D. Mackay,** *Univ. of Toronto, Canada*•**R. Mitchell,** *Harvard Univ.*•**W. J. Weber, Jr.,** *Univ. of Michigan*•**A. J. B. Zehnder,** *Agricultural Univ. of Wageningen, Netherlands*•**R. G. Zepp,** *U.S. EPA*

Leak-tight Valves & Fittings for Analytical Instrument Applications

The leak-tight technology of the SWAGELOK Companies is built into all the products you see here.

They work with each other to give you design flexibility. You can select sizes, shapes, materials and ratings to handle *your* service conditions.

They're all manufactured to the same standards of precision and quality control. You can count on consistent tolerances, compatible end connections, and reliable seals.

They're available locally from Authorized Sales and Service representatives. You can save money through efficient purchasing, controlled inventories, and on-time delivery.

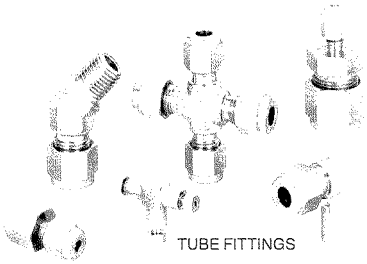

TUBE FITTINGS

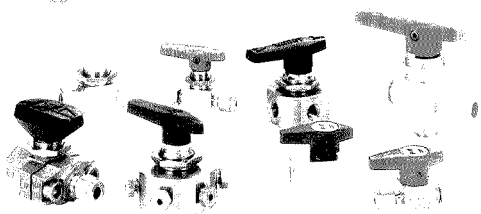

BALL & PLUG VALVES

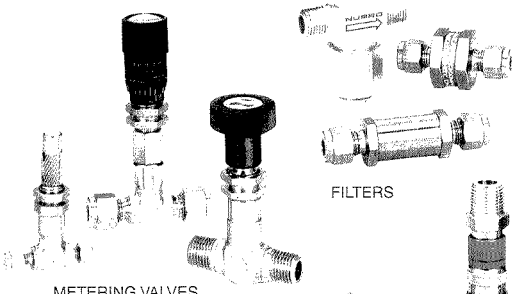

FILTERS

CHECK & RELIEF VALVES

METERING VALVES

QUICK-CONNECTS

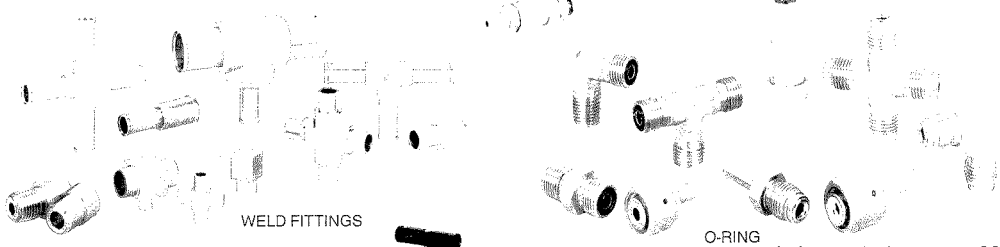

WELD FITTINGS

O-RING & METAL GASKET FACE SEAL FITTINGS

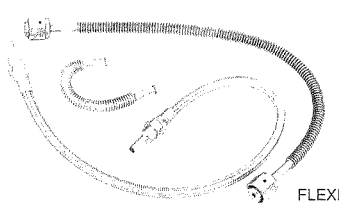

FLEXIBLE HOSE

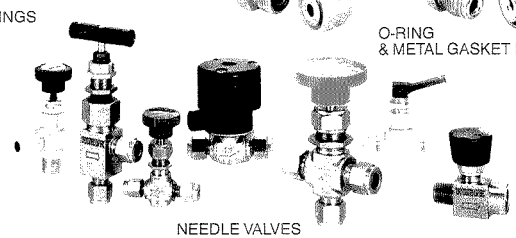

NEEDLE VALVES

SWAGELOK Co.
Solon, Ohio 44139
SWAGELOK Canada Ltd., Ontario

the SWAGELOK companies

CIRCLE 152 ON READER SERVICE CARD

Intelligent Robots—The Next Step in Laboratory Automation

T. L. Isenhour and S. E. Eckert
Department of Chemistry
Kansas State University
Manhattan, KS 66506

J. C. Marshall
Department of Chemistry
St. Olaf College
Northfield, MN 55057

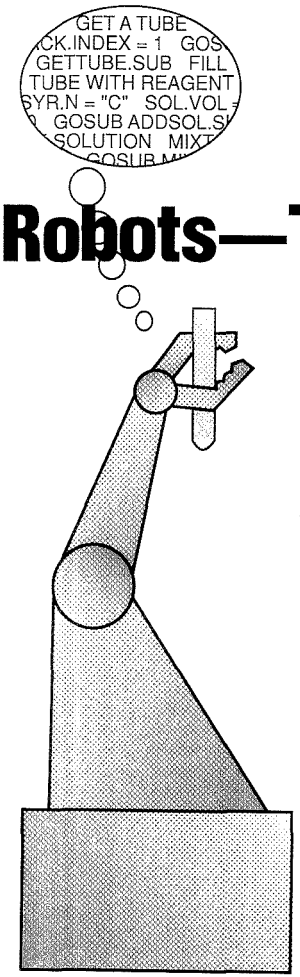

Laboratory robotics had its origins in devices constructed to perform specific and generally invariant mechanical tasks in the laboratory. Examples of laboratory automation are well known and include automatic titrators, sample collectors, and autoanalyzers. These devices will always have a place in the analytical laboratory, because they can be optimized for a specific repetitive task. But automated devices are limited and can perform only those specific tasks for which they were designed.

With the advent of inexpensive microelectronics and microcomputers, it is now possible to build flexible automated devices. These developments have led to programmable laboratory automation devices, which we now call robots. Programmable laboratory robots can be taught to perform a series of tasks within the domain of their mechanical capabilities. The use of such devices is having a major impact on how we perform routine laboratory procedures.

The programmable robot of today, like its early electromechanical counterpart, is usually dedicated to a single task. Detailed programming is required for even the simplest of tasks. No laboratory robot can yet carry out an order such as "Titrate three 25-mL aliquots of the sample with HCl," an instruction that we would expect a laboratory technician to perform without supervision. Programming a robot to perform even a common task (such as a titration) requires hundreds of steps and may take days or even weeks to perfect.

A/C INTERFACE

We believe that the next step in bringing the laboratory robot to its full potential will require control programs that use artificial intelligence. Expert systems, knowledge-based systems that can effectively represent and apply factual knowledge in specific areas of human expertise, seem ideally suited to the supervision of a robot. A laboratory robot under expert system supervision would be able to carry out the functions of a human expert in the analytical laboratory environment.

Another important step in laboratory automation will be achieved when standard chemical procedures, written in natural language, can be parsed into unit laboratory operations. Unit operations could then be selected and translated by an expert system to produce a set of primitive instructions for a laboratory robot. The combination of expert systems and robotics has the potential to perform an order such as "Titrate three 25-mL aliquots of the sample with HCl."

In this article we will summarize our recent work related to the development of the Analytical Director. The Analytical Director project seeks to combine laboratory robots with expert system control programs that have a knowledge base about analytical chemistry and the ability to use that knowledge.

The laws of robotics

The robot is revolutionizing laboratory work, particularly in high-volume industrial analytical labs. Increases in sample volume, reliability, and efficiency are well documented. However, there are several problems that anyone contemplating using laboratory robots should consider. In our work on the An-

0003-2700/89/0361-805A/$01.50/0

alytical Director project, we examined some of these problems by using a robot to perform the classical inorganic qualitative analysis scheme. This study resulted in some purposely overstated "laws" of laboratory robotics.

1. It will take a laboratory robot much longer to perform any nonroutine, complicated task than it would a skilled technician.

In our initial study of laboratory robotics we critically examined the difficulties in performing the classical qualitative analysis scheme with a Zymate laboratory robot (Zymark Corp., Hopkinton, MA). The time required for the analysis of two Group I samples was about 4 h. Because a manual implementation of this analysis requires much less time to perform, we studied ways to minimize the time required by a laboratory robot. In general, the ability of robot manipulators to perform complex multistep procedures in a cost-effective way will depend on the availability of effective general strategies for optimization.

Some of the problems that make optimization difficult are inherent in the design of the Zymate system used in this work. The Zymate robotic arm moves through a series of operator-defined absolute positions. Because the movement is from absolute position to absolute position, the controller does not "know" where the arm is between positions. Time is wasted in moving to "safe positions" to avoid collisions with other objects in the work space. Another factor in the Zymate design that must be considered is the servo motor control of the arm. The three servo motors operating the motions of the arm (in/out, up/down, and rotation) run at fixed speeds. The first two motions are fast, whereas the rotation is quite slow. Thus fixed stations on the table that are frequently used together should be as close as possible. As seen in Figure 1, this is difficult to do with a large number of stations.

Some steps in complicated procedures require a great deal of programming. Very often these are actions that technicians, as parallel processors, do easily and quickly. A good example is the complete dissolution of a precipitate. Typically, instructions to a human technician are: Check the test tube for the presence of a precipitate; if a precipitate is present, shake the tube to see if it will dissolve; if it does not dissolve, continue adding reagent and shaking until the precipitate is gone. (A technician may even decide to heat the tube for dissolution.) Many of these steps may be performed by a technician almost simultaneously; but for the robot, each step must be performed separately. It must pick up the tube, move to the detector, and check for any precipitate. If a precipitate is detected, the robot would then add the reagent, move the tube to the vortex mixer, stir the solution, and then place the tube in the centrifuge. After centrifugation, the robot must return to the precipitate detector and check for remaining solid. If present, the procedure must be repeated. If heating is an option, that must also be included in the program along with the criterion for performing that option. At any time during the procedure, a technician can stop when the precipitate is dissolved. For the robot, this procedure will terminate only at points where the check for a precipitate has been programmed. For different samples, this could be at different points.

Frequently, some modifications of the analysis procedure are necessary, because procedures that are designed for humans are not generally optimum for robot manipulation. For example, a modification was necessary to separate the mercurous cation in Group I. Although the procedure requires a complete separation of the lead and silver from the mercury, this is not absolutely necessary for a technician. After addition of NH_4OH to the residue (possibly containing AgCl, Hg_2Cl_2, and residual $PbCl_2$), the resulting solution should contain all the silver and any residue should contain all the mercury. A white residue could indicate incomplete separation of lead and/or silver; a technician could confirm this by noting the color of the precipitate, but the precipitate detector used in this work cannot distinguish between a white precipitate and a black one, so the best solution to this problem is to separate the cations completely. Residue is washed at each precipitation step, and more reagent is added when needed. These extra steps increased the time required for analysis significantly.

The decision must also be made whether to perform operations in series or in parallel. Humans usually operate in parallel, executing the same step on several samples at a time. In some cases, the robot also does best working in parallel. For example, the same reagent can be added to several samples at the same time; if the robot has to change hands to add the reagent, this is certainly the best strategy. However, if the reagent were to be added from a fixed solvent delivery station, the samples might best be processed one at a time, in a serial manner.

Parallel programming, whether of samples or of entire tests, increases efficiency in some cases, but loss of versatility makes it less efficient in other cases. For example, in the case of a group of cations, confirmation tests were left until the very end. Once all the cations were separated, the proper reagent was added to each tube. The solutions were mixed, centrifuged, and checked for the confirming precipitate, and the results stored as an array for further reference. Although this procedure was efficient in cases when a majority of the ions were present, it did not allow for the efficient handling of a sample that was, for example, pure water. Finding the optimum combination of parallel and serial operation is a difficult problem.

2. When a laboratory robot is left to function unattended for a long period of time, something disastrous will happen almost immediately after the last observer leaves.

The long-term reliability of any multistep procedure is likely to be low unless extreme care is taken to ensure almost perfect reliability for each step. If, for example, a procedure contains 100 steps and the reliability of each step is 99%, the probability of one or more failures in the procedure is more than 60%. Even if the reliability of each of the 100 steps is 99.99%, there is still about a 1% chance of failure. Furthermore, such failures not only could result in the loss of a single sample, but could create some condition in the robot's environment that would cause all subsequent procedures to fail until corrective action was taken. There are few sights more pathetic than a laboratory robot, its work space awash with spilled solvents and littered with broken containers, moving empty-handed yet faithfully about its appointed tasks.

3. A gross of supposedly identical containers to be used in a robotic procedure will come in 144 unique configurations.

In normal laboratory operations, small variations in the size and shape of containers is not a problem. In multistep continuous robotics procedures, however, nearly perfect uniformity of containers is required. During our preliminary investigation using the qualitative analysis scheme, the detection of precipitates proved troublesome. The photodiode sensor was capable of determining the presence of large amounts of precipitate but had much more difficulty in detecting small amounts of crystalline precipitate. This problem was primarily caused by the inconsistency of the thickness of the sample tubes, especially the thickness of the bottoms. It was therefore necessary to compare the value of the readings at several positions on each tube rather than only at the center and the bottom. The size problem is also

INTRODUCING A NEW LINE OF LABORATORY INSTRUMENTS FROM AN OLD NAME IN INSTRUMENTATION.

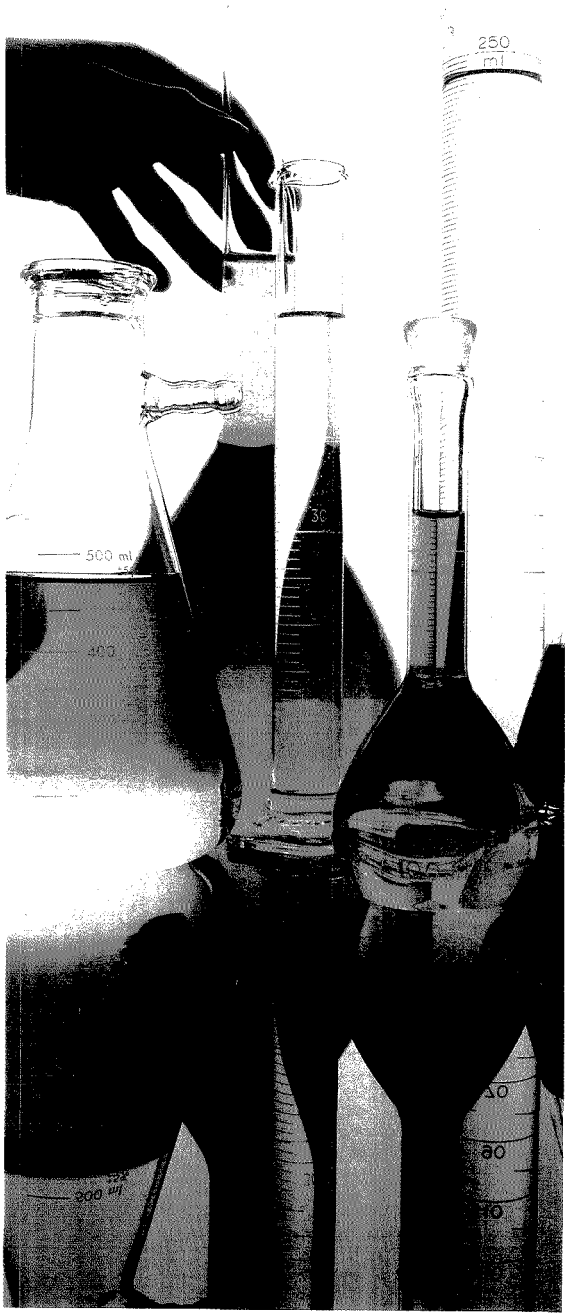

Now you have a new source for laboratory instrumentation...one that has built an 80-year reputation for producing high-quality, economical detection, testing and measurement equipment...BACHARACH. We're proud to announce we are now manufacturing the Coleman® line of analytical instruments, including the 3D HPLC™ and three spectroscopy-based products for laboratory use. Buy our lab equipment and you'll get not only a superior product for your investment, but also superior customer service...including in-house sales, repair and technical staff. Quality, economy and service...Bacharach Coleman Instruments.

The 3D HPLC System is the first of its kind to combine three of the most popular

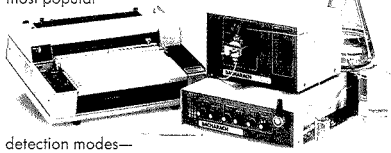

detection modes—
UV, fluorescence and conductivity—
into a single, compact unit. The System comes complete with pump, injector, cartridge column, recorder and patented TriDet trifunctional detector for under $7000.

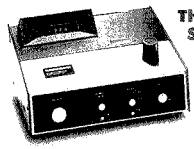

The Model 35 Spectrophotometer provides excellent photometric accuracy and is suitable for most quantitative measurements in the visible range.

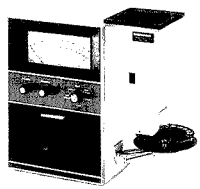

The Model 51Ca Flame Photometer delivers precise, fast, quantitative determination of sodium, potassium, lithium and calcium from a single sample.

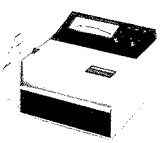

The Model MAS-50B Mercury Analyzer System utilizes the "Hatch and Ott Cold Vapor Technique" for high resolution and easy operation.

For more information, call your local lab equipment dealer or contact:

Bacharach Coleman Instruments
625 Alpha Drive, Pittsburgh, PA 15238
(412) 963-2000 Fax: (412) 963-2091

BACHARACH
Coleman® Instruments

CIRCLE 18 ON READER SERVICE CARD

manifested by containers not being picked up, solvent delivery errors, and capping station failures. Although most problems resulting from nonuniform container size can be solved by checks built into the control program, the amount of time required for these checks can substantially increase the time required to perform a procedure.

4. The item needed for the next step in the procedure is always on the other side of the robot's environment.

Space utilization in robotics procedures is very important. A typical fixed-base laboratory robot must arrange everything in a highly constricted work space. For example, the Zymate robot operates in a cylindrical work space constrained by a 60-cm reach and a 56-cm elevation, with the center of this cylinder occupied by the robot itself. In a laboratory of rectangular work spaces and rectangular instruments, the robot is an anomaly. Great care must be given to the placement and grouping of the apparatus in this limited space to ensure the minimum amount of wasted motion as the robot moves from station to station. Unfortunately, the most efficient arrangement of equipment is likely to vary with each procedure. As procedures become more and more complex, the space allocation problem becomes more and more difficult and in some instances impossible to solve without additional hardware. This problem has led to the development of track-mounted robots and dynamically allocated work spaces. An alternative strategy is to use multiple robots that can pass materials and samples back and forth. Kramer and Fuchs (*1*) have described what is perhaps the most novel implementation of robot-to-robot communication—a computer-controlled toy train.

Although the above laws have purposely overstated the difficulties inherent in laboratory robotics, the successful automation of any procedure requires careful development and extensive testing.

The Analytical Director project

The Analytical Director project is a major effort in our laboratory. The goal is to build a system to control laboratory robots that can design, test, and implement their own analytical procedures. A primary emphasis of this work is to use expert system techniques to store chemical information and to make decisions based on this information.

The initial step in the Analytical Director project was to design a flexible robot control language. Analytical Robot Telecommunications Software (ARTS) (*2*) was developed to give the research scientist flexible and adaptive control of laboratory robots and instruments and to allow direct control of the robot and its resources with an expert system. As a stand-alone program, ARTS is a complete laboratory control language that can interpret commands in either interactive or batch modes. ARTS can also be an extension of other software in either a master or a slave mode. As master, ARTS can call on other software to perform certain tasks; in the slave mode, it can act as a sensory extension of the calling software that is envisioned to be an expert system. The ARTS interpreter is written in the C programming language and uses Reverse Polish notation.

A set of commands that is specific to the ARTS environment is given in Table I. The most nonstandard command is the EVAL command, which allows a string (or string variable) received from an external source (or generated in ARTS) to be executed. The EVAL command provides adaptive programming capabilities. The LDEF command can be used to load a file containing system defaults. ARTS loads a default file when it is first executed but allows a different default file to be loaded at any time. The SDEF command saves the current defaults to a disk file. The ECHO command is used to turn on or off the echoing of routine commands on screen as they are being executed. The ASSIST command is a debugging tool for communication between ARTS and laboratory instruments; it can be used to echo the values sent on the communication lines to ensure that proper formats are being used. The QUIT command can be executed in batch or interactive mode to return to the operating system. Alternatively, the F5 key can be used in interactive mode to exit ARTS.

The F1 key is used to toggle the display of the mnemonic command menu on the upper portion of the screen. When the menu is present, a command can be highlighted by using the arrows, page up, page down, home, and end keys. Once highlighted, the command can be placed on the command line by pressing the F4 key. The F6 key can be used to produce a stream-oriented file. Values typed in or extracted from the mnemonic menu are directed to a specified file. The file is closed the second time the F6 key is pressed; the resulting file can then be executed as a routine.

Table I. Commands used in ARTS

Operating System Commands	
CD	Changes default drives and/or directory; can also be used to display current drive and directory
COPY	Copies a disk file to a different disk file
DEL	Deletes disk file(s)
DIR	Lists directory
EDIT	Invokes a user-specified editor
REN	Renames a disk file
Memory Management Commands	
DEF	Defines numeric variables
DEFS	Defines string variables
DISP	Displays all variables in memory
ERA	Erases variables from memory storage
Additional ARTS Commands and Function Keys	
EVAL	Executes a string or variable containing string
SDEF	Saves default values to a disk file
LDEF	Loads default values from a disk file
ECHO	Toggles echo of subroutine command lines
ASSIST	Displays activity on communication lines
QUIT	Returns control to operating system
F1	Displays mnemonic commands
F2	Activates DOS shell
F4	Accesses highlighted mnemonic command
F5	Leaves ARTS (same function as QUIT)
F6	Creates a stream-oriented file
F9	Accesses default values
F10	Interrupts active routines

The F9 key is used to gain access to a series of menus to set system and instrumental defaults. The F10 key is used to interrupt execution of a routine. Once the F10 key is pressed, a message is displayed on the screen, and the user can stop the execution of the routine, step one line at a time through the routine, enter a series of commands, or continue the execution of the current routine.

Instrument commands fall into four categories: those that send parameters to instruments, those that receive data from instruments, those that send parameters and receive data, and those that cause the instrument to perform an action. Table II contains some characteristic examples of these categories. Commands in the first category can be used to pass information, such as the grip tension for a robot hand or the parameters needed to collect a spectrum. The second category is used when instruments return data that can be used in conditional statements or, as in the examples, stored in variables for later use. The first example of this category shows how the weight of a sample is returned by a balance and stored as the first entry of array WEIGHT. The second of these examples stores the number of scans for a spectrum in the variable MEASUREMENTS. Combinations of the previous two commands are shown in the third category of commands. In the first example of this type, the time is returned from clock 4 and stored in the variable TIME, whereas in the second example, the absorbance value at 750 nm is stored in the variable ABSORBANCE. The last category of commands only requires that the command be sent to the instrument; the examples in this category show commands that control a syringe station, MLS, and collect a reference spectrum on a spectrophotometer, REFERENCE. Information about the number of parameters to be sent, the direction of data transfer, and the instrument to which the command is to be sent is required to communicate with any laboratory instrument. The variety of commands implemented by ARTS allows the user to exploit the full power of a microcomputer to control laboratory equipment.

ARTS is capable of controlling any type of programmable laboratory instrument or robot, although it was originally used to control a Zymate I robot. Control is implemented using RS 232 communication links between the microcomputer and the laboratory instruments. The methods of communicating with different instruments vary with the manufacturer; for this reason, a menu is used to define the communication protocol necessary for each instrument. Parameters such as baud rate and parity must be specified, stored in a file, and used to control communication with the instruments.

Table II. Instrument commands

Commands that send parameters
GRIP = 100
MEASURE 1, 0, 0, 0
Commands that receive data
WEIGHT (1) = WEIGH
MEASUREMENTS = NMEAS
Commands that send parameters and receive data
TIME = CLOCK (4)
ABSORBANCE = VALUE (750)
Commands that perform an action
MLS
REFERENCE

A robot is operated as just another instrument in the system. Some commercial laboratory robots use predefined positions in their normal operations; these positions are defined by using a teaching method supplied with the robot. During the teaching process, the robot is positioned at a point in its field of influence. The user supplies this position with an ASCII name, which is used to access it. These position names, along with other robot control commands, can be grouped into routines to perform tasks such as picking up a test tube. Line numbers are only used when needed for a GOTO statement. Routines can be combined to perform complete analyses.

To facilitate communication with instruments, a look-up table is used. The table allows the user to give a simple mnemonic definition to a complex sequence of commands that contain the number of parameters to be sent, the direction of data transfer, and the communication port to use for the instrument. In addition to simplifying commands, this method also allows the program to check for the proper number and type of parameters to be sent. The error checking of incorrect argument lists helps the user in debugging experimental procedures. As a convenience, a menu with a list of command mnemonics can be displayed at the top of the screen. Along with the command, the communication port is displayed to show to which instrument the command is directed.

The mnemonic definitions are stored in an ASCII file in the format:

MNEMONIC, COMMUNICATION PORT, NUMBER OF ARGUMENTS, ARGUMENTS

Each mnemonic definition takes one line of the file. The argument list is used to notify ARTS of the direction of communication (to or from the instrument) and the type of argument (string, floating point number, integer, array of strings, array of floating point numbers, or array of integers). If the argument is a valid string or number, it is sent to the instrument, as follows:

MLS, 1, 1, 301

In this example, the mnemonic MLS is used to send one parameter, 301, to a robot using communication port 1. If data are to be returned from an instrument, the argument consists of a "?" followed by a one-letter specifier (F—floating point, D—integer, S—string, AS—array of strings, AF—array of floats, or AD—array of integers) to determine the type of data returned from the instrument. The following entry

NMEAS, 2, 2, NMEAS, ?D

is used to send one argument, NMEAS, to a spectrophotometer and to receive data from the spectrophotometer using communication port 2. The data from the instrument are evaluated as integers. When the type consists of an array, the number of members immediately precedes AS, AD, or AF. For commands that need to have parameters evaluated during execution, a "*" precedes the type description. One such command is GRIP, for which the grip tension follows the mnemonic name. The file entry would be

GRIP, 1, 2, 100, *F

wherein two arguments are to be sent to the robot through communication port 1. The first argument is a 100 and is used by the robot to issue a grip command. The robot expects a second argument to be sent specifying the tension of the grip; this parameter is evaluated by ARTS as a floating point number. A final example of the four types of commands given in Table II consists of sending a command and a parameter and then receiving data from the instrument, as in:

VALUE, 2, 3, VALUE, *D, ?F

When the "VALUE(750)" is issued in the ARTS program, the string "VALUE" is sent to a spectrophotometer. The 750, representing the wavelength in nanometers, is evaluated as an integer and is transmitted. The transmission of these commands causes the

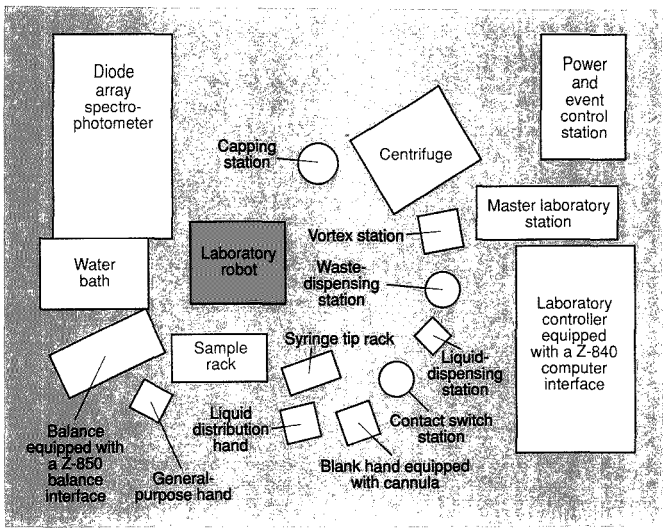

Figure 1. Layout of laboratory robot system.

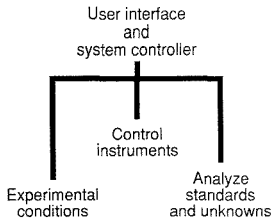

Figure 2. Hierarchy of the complexometric expert system.

spectrophotometer to return the absorbance at 750 nm to ARTS. The data received are evaluated as floating point numbers. The mnemonic definitions allow ARTS to communicate with laboratory instruments and to notify the user when an incorrect number of parameters has been entered.

The ability of ARTS to work in conjunction with external software increases the versatility of laboratory control. The researcher is no longer limited by the instrument control software, because external software can be incorporated into ARTS.

The artificial intelligence driven robotic system

The next step in the Analytical Director project is to introduce artificial intelligence supervision. We have demonstrated the automation of a complexometric titration using an expert system control program (*3*).

The layout for the laboratory robot system is shown in Figure 1, and the outline of the expert system is shown in Figure 2. The top-level program contains the user interface and controls the execution of the subsystems that determine the appropriate experimental conditions, control analytical instrumentation, and analyze standards and unknowns.

Communication between the user and the expert system is accomplished through menus and queries. The user can describe the sample to be analyzed, including potential interferences, by choosing the appropriate responses from the menus. Any additional information required to perform the titration is sought by the expert system in the knowledge base. Information determined by the expert system to be necessary, but not available from either user input or from the knowledge base, will generate queries to the user for such information. Information acquired in this fashion will automatically be added to the system knowledge base for future use.

An analysis problem is processed by first determining whether the same problem has been solved previously. If a solution exists, the experimental conditions are recalled and used. If the problem has not previously been encountered, a set of heuristic rules based on conditional stability constants is used to limit the set of possible solutions. From the constrained set of solutions, one possible solution is extracted. The system will then check a file of past experiments to determine if the chosen solution previously failed to produce adequate results. If so, an alternate solution is sought. Any unverified experimental conditions are tested against standard solutions prior to the titrations.

Thus it is feasible to design and carry out a rather complex analytical procedure using a laboratory robot under expert system supervision. The decisions made are based on chemical theory, data collected from actual experiments, and user input. The ability of the user to set experimental parameters allows the expert system to learn from instruction. Because the expert system keeps a record of past experiments, it is able to learn as the system is used.

This expert system was designed to perform direct complexometric titrations. With modifications, various other types of titrations—including stepwise, indirect, and replacement—could be incorporated. Knowledge collected by an expert system can easily be transferred to a different expert system, thus allowing almost instantaneous teaching. The system can also be used to teach humans by displaying experimental conditions to the user. Since all data collected by the system are archived, procedures that once were rarely used are now routine.

Temporal optimization of robots

The automation of complex procedures envisioned in the Analytical Director project requires consideration of both task scheduling and resource allocation. Most laboratory procedures can be broken down into a series of tasks. Each task requires certain resources, reagents, equipment, instruments, or personnel. The order in which the tasks are completed is important, because it will affect the overall completion time of the procedure. Scheduling, queuing, and network theories have been devised to maximize the efficiency of one or more procedures by sequencing tasks and allocating resources (*4–6*).

Programming robotic systems to run laboratory procedures efficiently is both tedious and time-consuming. Furthermore, robot systems are expensive. As a consequence, once an effective robot program is obtained, the programmer is often reluctant to modify it. For variable or one-of-a-kind procedures, the time required to program laboratory robotic systems will likely exceed the time required for the chemist to do the procedure manually. For this reason, current robot applications in the laboratory are usually limited to nonvarying procedures repetitiously applied to a large number of samples.

Variable robotic procedures would be feasible if efficient robot programs could be developed rapidly. The Temporal Optimizer of Robotic Task Sequences (TORTS) expert system has been developed as a programming aid for versatile and facile robot program development (*7, 8*). An advantage of the TORTS system is that a programmer can quickly evaluate a robotic program configuration on a computer without using the actual robotic system. For variable robotic programs that execute different procedures based on test results acquired at run time, each procedure may be optimized separately. The TORTS system was devised to maximize the productivity of a laboratory procedure, shorten the robotic program development time, and acquire knowledge of robotic systems. This expert system is a critical step in the development of the Analytical Director project (*9*).

The robotic system paradigm

The optimization of complex robotic procedures is a formidable problem. The TORTS system will generate robot task schedules for which no constraints are violated, and the start and finish times are predicted for each task. Many task schedules can thus be evaluated, because computer simulation is much faster than running and timing robotic procedures. The best task schedule can be defined as the one producing the shortest project completion time. Cases may arise for which other constraints must be met at the cost of longer completion times.

For this discussion, a useful definition of a task is the generalized subroutine, which in turn may be a collection of subroutines. A robot may be easily programmed to handle diverse laboratory procedures if a generalized set of subroutines is built. Table III contains a section of a robotic program written in the ARTS control language (*2*). Table IV is an example of a generalized subroutine to mix a solution in a tube for a specified amount of time. The generalized subroutines are customized for a specific need by setting global variables in the main program. The global variable, MIXTIME, in Table III and Table IV specifies the time the vortex mixer is to run.

If a robot control module could direct and queue robot commands to more than one module, tasks could be executed simultaneously. Most laboratory robotic control systems allow only one module to be controlled at a time; commands cannot be sent and queued at each module. Instead, the programmer is required to merge commands manually to execute tasks concurrently. TORTS allows multiple-task optimization in anticipation of robots that will allow true task concurrency.

The TORTS system requires the user to specify task and orientation times and, optionally, lock times and timing constraints. The task times will vary for different applications, may have to be measured for each different procedure, and are independent of sequencing. An optimum sequence should be obtainable, although the predicted times will depend on the accuracy of the programmer's estimates for task times. The orientation time is the time required for the robot to move from the completion of a task to the start of a subsequent task. Lock time specifies the time penalty for interrupting a process. An example is the time required to stop the centrifuge to add more tubes while centrifugation is in progress. Finally, tasks may have timing constraints; a minimum or maximum time must elapse before a successive task is initiated. Such constraints are crucial for kinetic studies.

Table III. Section of a robotic program written in ARTS

```
REM
REM *** GET A TUBE
REM
   RACK.INDEX = 1
   GOSUB GETTUBE.SUB
REM
REM *** FILL TUBE WITH REAGENT
REM
   SYR.N = "C"
   SOL.VOL = 3.0
   GOSUB ADDSOL.SUB
REM
REM *** MIX SOLUTION
REM
   MIXTIME = 120
   GOSUB MIX.SUB
REM
```

Table IV. Generalized subroutine

```
REM MIX. SUB
REM
REM *** ROUTINE TO PLACE A TUBE
   IN VORTEX, MIX, AND REMOVE
   TUBE
REM
   IF FREE (MIXTIME) THEN MIXTIME =
   15
REM
REM *** PLACE TUBE IN VORTEX
REM
   CLEAR.VORTEX
   OVER.VORTEX
   IN.VORTEX
REM
REM *** RELEASE THE TUBE
REM
   GRIP = 120
REM
   VORTEX.ON
   SLEEP (MIXTIME)
   VORTEX.OFF
REM
REM *** REMOVE TUBE FROM
   VORTEX
REM
   GRIP = 35
   OVER.VORTEX
   CLEAR.VORTEX
```

Optimization

The TORTS system uses a depth first search of the space of feasible solutions. The depth first search is directed by heuristics and expert strategies (*10, 11*). Figure 3 outlines the optimization procedure. Solutions are generated one at a time. Each improved solution lowers the upper bound on the predicted completion time. Each time an improved solution is found or the upper bound is exceeded, the system will backtrack and try an alternative feasible task. The optimization is completed when all feasible task sequences have been evaluated and the system backtracks to the top.

The TORTS system can expand a single sample procedure into a multiple-sample or duty cycles procedure. This step of the optimization occurs after an optimum task sequence is obtained for the single-sample procedure. Optimizing multiple-sample proce-

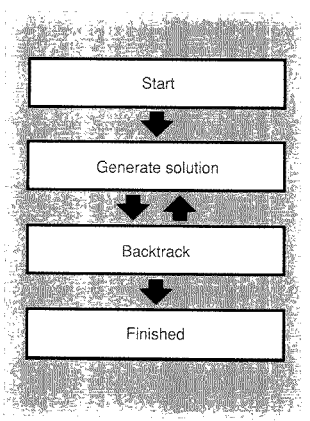

Figure 3. Flow chart for the exploration of the solution search space in TORTS.

dures allows the duty cycles to overlap, which further minimizes the total completion time.

Each task of a single procedure will form a parallel task for the additional duty cycles. All the tasks will be coded by a unique integer, but parallel tasks are identified by their Primitive Identifier (PI) as shown in Table V. Expanding a single procedure to multiple procedures also relaxes the constraint of the logical sequence of procedures. Consequently, the larger the number of duty cycles optimized, the greater the potential time savings.

The correct choice of the number of duty cycles to be optimized is important because the search space will increase exponentially with the number of duty cycles. The run time for the TORTS system will also increase because of the search of the entire solution space and the validation of the optimum task sequence. Another consideration is the turnaround time for each procedure. If a delay in the completion of a single procedure is not allowable, the optimum task sequence would be to run each procedure serially. For procedures that require many samples or duty cycles, efficient patterns of task sequences may be obtained from optimizations of a reduced number of duty cycles. The robot programmer needs to follow this pattern while programming the robot to perform the larger number of duty cycles.

An enzyme assay was chosen to evaluate the TORTS system because the timing of the spectrophotometric measurements is crucial to the analysis. The assay is the activity determination for liver alcohol dehydrogenase (*12*). The method is based on spectrophotometric measurement of the amount of nicotinamide adenine dinucleotide (NAD) undergoing reduction in 3 min at a pH of 9.6 in the presence of excess alcohol. The time estimates of the optimized task sequences are in good agreement with experimental results, as shown in Table V.

Table V. Predicted and experimental start times

Level	Task	PI	Times (s) Predicted	Times (s) Experimental
1	1	1	0.0	0.3 ± 0.0
2	2	2	4.9	5.1 ± 0.2
3	3	1	32.2	32.4 ± 0.2
4	4	2	37.1	37.5 ± 0.2
5	5	1	64.4	64.8 ± 0.2
6	6	2	69.3	69.5 ± 0.2
7	7	1	96.6	96.1 ± 0.2
8	8	2	101.5	100.6 ± 0.2
9	9	9	128.8	129.3 ± 0.2
10	10	10	270.4	271.2 ± 1.1
11	11	11	492.6	492.0 ± 1.3
12	12	12	623.6	623.1 ± 1.6
13	22	9	643.8	644.1 ± 1.8
14	13	13	786.8	787.0 ± 2.3
15	14	1	1016.3	1017.4 ± 2.3
16	15	2	1021.2	1022.0 ± 2.3
17	16	1	1048.5	1049.6 ± 2.2
18	17	2	1053.4	1054.5 ± 2.2
19	18	1	1080.7	1081.9 ± 2.3
20	19	2	1085.6	1086.5 ± 2.3
21	20	1	1112.9	1113.4 ± 2.2
22	21	2	1117.8	1117.9 ± 2.2
23	23	10	1151.7	1151.9 ± 2.2
24	24	11	1373.9	1375.2 ± 2.6
25	25	12	1504.9	1506.4 ± 2.5
26	26	13	1567.3	1565.6 ± 2.7
Project Completion Time			1795.6	1793.6 ± 3.1

Note. The experimental results were obtained from six runs.

Database considerations in expert systems

Integral to the Analytical Director project is the knowledge base of chemical information used by the system to design, store, and reason about analytical procedures. We have used object-oriented programming strategies that allow all data objects, quantitative and qualitative, to be represented as objects and to be manipulated directly. Expert system methods theoretically are capable of classifying such data objects on the basis of randomly organized rules that characterize them. This process may be conceptualized as traversing a logic tree. However, in complex problems, the rules used to span the information in the knowledge base must be efficiently organized or the rule structure will become unmanageable in size and logical complexity. Recent work (*13*) suggests that the ID3 (*14–16*) algorithm is useful for establishing efficient rules for knowledge-base interrogation.

The knowledge base used by an expert system can be most efficiently represented as a set of rules based on the minimal decision tree spanning the data. The root node of this tree is the attribute that minimizes the number of branches from the root. Each branch from the root node contains a different value of the root attribute. Each branch required from these second-level nodes may be branched further using attributes different from the previous attributes used to split the data. If more than one attribute is used to describe the data, the decision tree will not be unique. As the number of attributes used to describe the data increases, the number of possible decision trees also increases. In complex data sets, this proliferation demonstrates the critical importance of the most efficient structure for the decision tree.

The ID3 algorithm can be used to determine classification trees that minimize the number of tests needed to classify objects based on information theory and the entropy of classification. As a simple demonstration of this operation, IR data are given in Table VI for substituted benzenes. Although this is admittedly a very simple classification problem, it does not differ in principle from more complex classification problems. The ID3 algorithm creates the decision tree shown in Figure 4. Furthermore, the PROLOG implementation of this algorithm writes syntactically correct PROLOG rules that can be used to span the database.

Standard robotics method—the next step

Our work on the Analytical Director project has demonstrated expert system control of laboratory robots. The next desirable step would be the transition from the description of an analyti-

cal procedure to the actual performance of that procedure by an automated laboratory robot. This will require several developments that have not yet taken place. A formal model of the chemical analysis domain is required if a computer system is to design, plan, manage, and ultimately control the actions of a robot during the performance of a laboratory procedure.

Table VI. Data for benzene substitution used to generate decision tree

Compound name	Degree of substitution	IR absorption ranges (cm^{-1}) 650–699	700–749	750–799	800–849	850–899
toluene	mono	S	S	W	W	W
m-xylene	meta	S	W	S	W	W
o-xylene	ortho	W	S	S	W	W
p-xylene	para	W	W	S	W	W
1,2,3-trimethylbenzene	1,2,3-tri	W	S	S	W	W
1,2,4-trimethylbenzene	1,2,4-tri	W	W	W	S	M
1,3,5-trimethylbenzene	1,3,5-tri	S	W	W	S	W
1,2,3,4-tetramethylbenzene	1,2,3,4-tetra	W	W	S	S	W
1,2,3,5-tetramethylbenzene	1,2,3,5-tetra	W	S	W	W	S
1,2,4,5-tetramethylbenzene	1,2,4,5-tetra	W	W	W	W	M
pentamethylbenzene	penta	W	W	W	W	S

Note. Absorption is denoted by W (weak), M (medium), and S (strong).

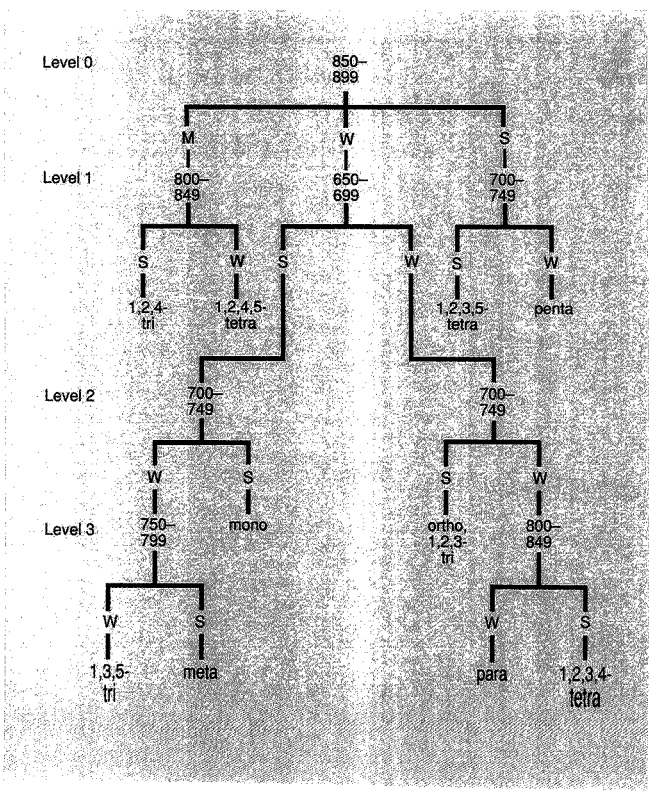

Figure 4. *Decision tree generated from data in Table VI.*

Such a formal model will include a state space representation of the robotic table layout and a set of primitive actions that perform operations in that state space. The ARTS programming language provides an adequate framework for accomplishing this robotics programming goal.

The more difficult problem is mapping chemical procedures into the robotic environment so as to accomplish the desired task. To date, little attention has been given to the formal representation of chemical procedures. One approach, a Symbolic Synoptic System for Analytical Chemistry (SSSAC) (*17*), appears to have attracted little attention. However, we are currently studying the use of natural language parsing to map chemical procedures directly into robotics procedures. Although the solution of the natural language parsing of laboratory procedures is not yet feasible in the general case, recent developments in natural language interpretation (*18*) indicate that chemical procedures written in a simple, prescribed syntax could be interpreted automatically.

The goal of this work is the standard robotics method. Standard reference materials have been used for many years to help individual laboratories test the reliability of their analytical procedures, but no scheme has been developed to guarantee that complex analytical procedures performed by a robot would give the same results in different laboratories. The standard robotics method that we envision would allow a method to be transferred from one laboratory to another and would ensure the same quality of results in each lab.

The success of the standard robotics method project will require that a standard set of primitive robot unit operations be defined for each laboratory environment. The text of a procedure, written in the prescribed syntax, could then be mapped onto the primitive robot operations. The operations so mapped would constitute the standard robotics method. Laboratories equipped with Analytical Director units could transfer procedures and not lose quality control because of technician inconsistency from laboratory to laboratory.

References

(1) Kramer, G. W.; Fuchs, P. L. In *Advances in Laboratory Automation—Robotics*; Strimaitis, J. R.; Hawk, G. L., Eds.; Zymark Corporation: Hopkinton, MA, 1988; Vol. 4.

(2) Schlieper, W. A.; Isenhour, T. L.; Marshall, J. C. *J. Chem. Inf. Comput. Sci.* **1987**, *27*(3), 137-43.

(3) Schlieper, W. A.; Isenhour, T. L.; Marshall, J. C. *Anal. Chem.* **1988**, *60*, 1142.

(4) French, S. *Sequencing and Scheduling:*

An Introduction to the Mathematics of the Job-Shop; John Wiley and Sons: New York, 1982.
(5) Cooper, R. B. *Introduction to Queuing Theory*; North Holland: New York, 1981.
(6) Phillips, D. T. *Fundamentals of Network Analysis*; Prentice-Hall: Englewood Cliffs, NJ, 1981.
(7) Harrington, P. B.; Isenhour, T. L. Presented at the Pittsburgh Conference, Atlantic City, NJ, March 1986; paper 1008.
(8) Harrington, P. B.; Isenhour, T. L. Presented at the Pittsburgh Conference, Atlantic City, NJ, March 1987; paper 1136.
(9) Isenhour, T. L. *J. Chem. Inf. Comput. Sci.* **1985**, *25*, 292.
(10) Nilsson, N. J. *Principles of Artificial Intelligence;* Tioga Publishing Company: Palo Alto, CA, 1980.
(11) Pearl, J. *Heuristics;* Addison-Wesley: Reading, MA, 1984.
(12) *Methods in Enzymology*; Colowick, S. P.; Kaplan, N. O., Eds.; Academic Press: New York, 1955; p. 495.
(13) Schlieper, W. A.; Isenhour, T. L.; Marshall, J. C. *J. Chem. Inf. Comput. Sci.*, in press.
(14) Quinlan, J. R. In *Machine Learning—An Artificial Intelligence Approach*; Michalski, R. S.; Carbonaell, J. G.; Mitchell, T. M., Eds.; Tioga Publishing Company: Palo Alto, CA, 1983.
(15) Thompson, B.; Thompson, W. *Byte* **1986**, *11*(12), 149.
(16) Derde, M. *Anal. Chem.* **1987**, *59*, 1868.
(17) Kateman, G. *Fresenius Z. Anal. Chem.* **1978**, *293*, 338.
(18) Rettig, M.; Bates, M. *A. I. Expert* **1988**, *3*(7), 41.

T. L. Isenhour (left) is dean of arts and sciences at Kansas State University. He received his B.S. degree in chemistry from the University of North Carolina in 1961 and his Ph.D. from Cornell University under the direction of George H. Morrison in 1965. He has been a member of the faculties of the University of Washington, the University of North Carolina, and Utah State University.

J. C. Marshall (center) has been a member of the faculty of St. Olaf College for 28 years. He received his B.S. degree in chemistry from Luther College (Decorah, IA) in 1956 and his Ph.D. from the University of Iowa under the direction of Alex Popov in 1960. He carried out postdoctoral work with I. M. Kolthoff from 1960 through 1961 and worked with Charles N. Reilly from 1969 through 1970. He has since worked in collaboration with T. L. Isenhour.

S. E. Eckert (right) is currently completing her Ph.D. in chemistry at Kansas State University under the direction of T. L. Isenhour. She received her B.S. degree in chemistry from Eastern Illinois University in 1977 and worked as an instrument chemist at Sterling Drugs and as an assistant analyst at Warner Lambert.

LABORATORY SERVICE CENTER

NMR ANALYSIS

MULTINUCLEAR LIQUID or
MULTIFIELD SOLID STATE
SPECTRAL DATA SERVICES, INC.
818 Pioneer
Champaign, IL 61820
(217) 352-7084

HELP WANTED ADS

ROP display at ROP rates. Rate based on number of insertions within contract year. Cannot be combined for frequency.

Unit	1-Ti	6-Ti	12-Ti
1″ (25 mm)	$180	$160	$150
	24-Ti	48-Ti	72-Ti
	$140	$130	$125

CALL OR WRITE JANE GATENBY

ANALYTICAL CHEMISTRY
500 Post Road East
P.O. Box 231
Westport, CT 06880
203-226-7131
FAX: 203-454-9939

FREE DATA, FAST

To quickly amass data on all of the products you need, consult the Lab Data Service section on our *Analytical Chemistry* reader reply card insert.

USE LABORATORY SERVICE CENTER

Laboratory Service Center (Equipment, Materials, Services, Instruments for Leasing), Maximum space — 4 inches per advertisement. Column width, 2-3/16″; two column width, 4-9/16″. Artwork accepted. No combination of directory rates with ROP advertising. Rates based on number of inches used within **12** months from first date of first insertion. Per inch: 1″ — **$155; 12″ — $153; 24″ — $150; 36″ — $145; 48″ — $140.**

CALL OR WRITE JANE GATENBY

ANALYTICAL CHEMISTRY
500 Post Road East
P.O. Box 231
Westport, CT 06880
203-226-7131/FAX: 203-454-9939

NEED AN ARTICLE FROM AN EARLIER ISSUE?

GET IT FROM CAS DOCUMENT DELIVERY SERVICE®

Does your research depend on locating an article published in this journal a few years back? The CAS Document Delivery Service can provide copies of articles from *all ACS journals from initial publication to the present.*

You'll also find CAS DDS an excellent source for documents related to chemistry and allied disciplines drawn from *the more than 10,000 scientific and technical publications received at Chemical Abstracts Service each year.*

Order articles, patents, and reports back to 1975 (1970 for Soviet material). Most orders are on their way within 24 hours. Call for more information. Ask about our FREE 1989 Directory of Publications.

Chemical Abstracts Service®
2540 Olentangy River Road
P.O. Box 3012
Columbus, OH 43210

Phone: (toll-free) 800-848-6538, ext. 3670
or 614-447-3670

Chemical Abstracts Service is a division of the American Chemical Society.

INDEX TO ADVERTISERS IN THIS ISSUE

Directory section, see page 816A.

** See ad in ACS Laboratory Guide.*

*** Company so marked has advertisement in Foreign Regional edition only.*

Advertising Management for the American Chemical Society Publications

CENTCOM, LTD

President
Thomas N. J. Koerwer

Executive Vice President *Senior Vice President*
James A. Byrne **Benjamin W. Jones**

Clay S. Holden, *Vice President*
Robert L. Voepel, *Vice President*
Joseph P. Stenza, *Production Director*

500 Post Road East
P.O. Box 231
Westport, Connecticut 06880
(Area Code 203) 226-7131
Telex No. 643310
FAX No. 203-454-9939

ADVERTISING SALES MANAGER
Bruce E. Poorman

ADVERTISING PRODUCTION MANAGER
Jane F. Gatenby

SALES REPRESENTATIVES

Philadelphia, PA . . . Patricia O'Donnell, CENTCOM, LTD., GSB Building, Suite 405, 1 Belmont Avenue, Bala Cynwyd, Pa. 19004. Telephone: 215-667-9666, FAX: 215-667-9353

New York, NY . . . John F. Raftery, CENTCOM, LTD., 60 East 42nd St., New York, N.Y. 10165. Telephone: 212-972-9660

Westport, CT . . . Edward M. Black, CENTCOM, LTD., 500 Post Road East, P.O. Box 231, Westport, Ct. 06880. Telephone: 203-226-7131, Telex 643310, FAX: 203-454-9939

Cleveland, OH . . . Bruce E. Poorman, John C. Guyot, CENTCOM, LTD., 325 Front St., Suite 2, Berea, Ohio 44017. Telephone: 216-234-1333, FAX: 216-234-3425

Chicago, IL . . . Michael J. Pak, CENTCOM, LTD., 540 Frontage Rd., Northfield, Ill. 60093. Telephone: 312-441-6383, FAX: 312-441-6382

Houston, TX . . . Michael J. Pak, CENTCOM, LTD., Telephone: 312-441-6383

San Francisco, CA . . . Paul M. Butts, CENTCOM, LTD., Suite 1070, 2672 Bayshore Frontage Road, Mountain View, CA 94043. Telephone: 415-969-4604

Los Angeles, CA . . . Clay S. Holden, CENTCOM, LTD., Newton Pacific Center, 3142 Pacific Coast Highway, Suite 200, Torrance, CA 90505. Telephone: 213-325-1903

Boston, MA . . . Edward M. Black, CENTCOM, LTD., Telephone: 203-226-7131

Atlanta, GA . . . Edward M. Black, CENTCOM, LTD., Telephone: 203-226-7131

Denver, CO . . . Paul M. Butts, CENTCOM, LTD., Telephone: 415-969-4604

United Kingdom

Reading, England . . . Malcolm Thiele, Technomedia Ltd., Wood Cottage, Shurlock Row, Reading RG10 OQE, Berkshire, England. Telephone: 073-434-3302, Telex #848800, FAX: 073-434-3848

Lancashire, England . . . Technomedia Ltd., c/o Meconomics Ltd., Meconomics House, 31 Old Street, Ashton Under Lyne, Lancashire, England. Telephone: 061-308-3025

Continental Europe . . . Andre Jamar, International Communications, Inc., Rue Mallar 1, 4800 Verviers, Belgium. Telephone: (087) 22-53-85, Telex #49263, FAX: (087) 23-03-29

Tokyo, Japan . . . Sumio Oka, International Media Representatives Ltd., 2-29 Toranomon, 1-Chome Minato-ku Tokyo 105 Japan. Telephone: 502-0656, Telex #22633, FAX: 591-2530

New! Hands-on! A four-and-a-half day intensive laboratory and lecture course . . .

MASS SPECTROMETRY

Principles and Practice

Monday - Friday, September 11-15, 1989
Monday - Friday, December 11-15, 1989
Michigan State University, East Lansing

An integrated approach combining lectures, demonstrations, and hands-on experiments

Who Should Attend

Industrial, government, and academic researchers and technicians—any technically oriented person wishing to gain both theoretical and practical knowledge of the mass spectrometry technique. Some familiarity with nomenclature of organic chemistry would be helpful.

Key Topics

- Operating principles of MS instrumentation
- Vacuum systems
- Inlet system, including GLC
- Ionization techniques, including EI, CI, and FAB
- Data systems
- Fragmentation patterns for a variety of compound types
- Strategy for data interpretation
- Troubleshooting

What You'll Learn from this Course

- How to interpret mass spectral data
- The types of compounds for which MS can be used
- The complexity and care with which the mass spectrometer must be operated
- How to tune a mass spectrometer, troubleshoot it, introduce samples, collect data by scanning, and process data with a data system
- How to use a variety of GC/MS instruments, including a Hewlett-Packard mass selective detector (MSD)

The Instructors

J.T. Watson (Course Director), Professor, Biochemistry and Chemistry, Michigan State University, is an expert in quantitative techniques and methodology of GC/MS.

Plus J.F. Holland, C.C. Sweeley, C.G. Enke, M. Micke, J. Allison, D.A. Gage, and M. Davenport.

Course Site

The course will be held at the Mass Spectrometry Facility, Michigan State University, East Lansing, Michigan.

Register today for this intensive, hands-on course!

For a FREE brochure describing this course, return the coupon below, or call COLLECT (202) 872-4508, ext. 9110.

Yes! Please send me a free brochure describing Mass Spectrometry: Principles and Practice to be held September 11 - 15, 1989, and December 11 - 15, 1989, at Michigan State University in East Lansing, Michigan.

Name _____

Title _____

Organization _____

Address _____

City, State, Zip _____

American Chemical Society
Department of Continuing Education
Meeting Code MAS89090
1155 Sixteenth Street, N.W.
Washington, DC 20036

Analytical CHEMISTRY

EDITOR: **GEORGE H. MORRISON**

ASSOCIATE EDITORS: **Klaus Biemann, Georges Guiochon, Walter C. Herlihy, Robert A. Osteryoung, Edward S. Yeung**

Editorial Headquarters
1155 Sixteenth St., N.W.
Washington, DC 20036
Phone: 202-872-4570
Telefax: 202-872-6325

Managing Editor: Sharon G. Boots

Associate Editors: Louise Voress, Mary Warner

Assistant Editors: Grace K. Lee, Alan R. Newman

Editorial Assistant: Felicia Wach

Director, Operational Support: C. Michael Phillippe

Production Manager: Leroy L. Corcoran

Art Director: Alan Kahan

Designer: Amy Meyer Phifer

Production Editor: Elizabeth E. Wood

Circulation: Claud Robinson

Editorial Assistant, LabGuide: Joanne Mullican

Journals Dept., Columbus, Ohio

Associate Head: Marianne Brogan

Journals Editing Manager: Joseph E. Yurvati

Associate Editor: Rodney L. Temos

Staff Editor: Sharon K. Hatfield

Published by the
AMERICAN CHEMICAL SOCIETY
1155 16th Street, N.W.
Washington, DC 20036

Publications Division

Director: Robert H. Marks

Journals: Charles R. Bertsch

Special Publications: Randall E. Wedin

Manuscript requirements are published in the January 1, 1989 issue, page 91. Manuscripts for publication (4 copies) should be submitted to ANALYTICAL CHEMISTRY at the ACS Washington address.

AUTHOR INDEX

Analytical Potential of Protein A for Affinity Chromatography of Polyclonal and Monoclonal Antibodies

Bruce Jon Compton,* MaryAnn Lewis, Frances Whigham, Jennifer Shores Gerald,[1] and George E. Countryman

Fermentation Development Laboratories, Bristol-Myers Company Industrial Division, P.O. Box 4755, Syracuse, New York 13221-4755

Protein A based rapid affinity chromatography for quantitation of various immunoglobulins of class G (IgG) is described. Three-minute analysis using either citrate or phosphate buffers and detection with 220- or 280-nm ultraviolet absorption was found to be optimum for quantitation of IgG from 0.25 to 250 μg of IgG on-column with a percent relative standard deviation (% RSD) of 2–3% RSD. The method has a detection limit estimated to be 100 ng of IgG on-column. It has been used to analyze a variety of IgG-containing samples from such diverse sources as hybridoma selection, media cultivation, and purification studies. Gradient elution studies and the relationship of IgG elution to IgG isoelectric point (pI) are also described.

INTRODUCTION

It is well-known that many products derived from monoclonal antibody (mAb) hybridomal technology are in the process development and scale-up stage of commercialization. Clearly, rapid, accurate, automated analysis of samples related to mAb development efforts is needed.

One mAb immunoglobulin class frequently developed is class G (IgG). Determinations of these large molecular weight proteins (MW approximately 150 000) are normally accomplished by using immunoassay techniques in conjunction with latex coagulation, or radio-, fluoro-, or enzyme-linked development methods (*1*). These methods are well suited and widely used in hybridomal selection since they are highly sensitive (ng/mL concentration range), but they are, in general, difficult to automate and often lack sufficient accuracy for process optimization studies. Additional methods involve a variety of electrophoretic, immunodiffusion, and immunonephalometric methods (2). These methods are 1–2 orders of magnitude less sensitive than the various immuno-linked methods previously mentioned. In general, they are also ill-suited for rapid automated analysis. For instance, radial immunodiffusion (RID) assays are widely used for following hybridomal production and mAb purifications, but they may take up to 3 days to execute.

Our approach to implementation of large-scale routine mAb analysis has been the use of affinity chromatography based on high-performance liquid chromatographic (HPLC) equipment. Automated HPLC systems are well developed commercially and as such are regarded as reliable for routine usage. A classic means of studying and isolating antibodies, particularly those of the IgG class, has been the use of protein A from various *Staphylococcus* species or more recently as a recombinant product (*3–5*). Studies on the interactions of protein A with IgG classes and subclasses have progressed to a state where much is known and understood regarding the stoichiometry and physiochemical interactions (*6–9*) of protein A and IgG's. Additionally, protein A or the more recently commercially available protein G can be used with sufficient selectivity to allow IgG class and subclass separations (*10–12*).

One interesting aspect of the literature on protein A as seen in numerous reviews (*3–5*) is the general omission of studies on the use of protein A for rapid, reproducible quantitation of IgG's; in other words, the analytical chemistry potential of protein A binding to IgG has not, with a few exceptions (*13, 14*), been extensively examined or appreciated.

We report here on the use of protein A for rapid (less than 3 min), automated IgG analysis of various polyclonal and monoclonal IgG's. Some fundamental studies on rapid affinity chromatography recently have been published (*15–17*), but our intent is to illustrate the use of commercial instrumentation and materials for rapid, reliable automated IgG analysis for production-related samples. For instance, over 20 000 IgG-related samples have been analyzed by us with this method over the last year by using one instrument and little analyst intervention. A correlation of IgG elution time to the isoelectric point (pI) of IgG is also demonstrated.

EXPERIMENTAL SECTION

Apparatus and Materials. Protein A bound to a rigid macroreticular polymer support was commercially obtained (Affi-Prep protein A, Bio-Rad, Richmond, CA). One 25-mL bottle was adequate to pack 20 4.6 mm i.d. × 5 cm HPLC stainless steel blanks (Type LTS 5 cm, No. 820-05, Keystone Scientific, State College, PA). Column packing was accomplished by pipetting the slurry directly into the column, running eluent through the column for a few minutes, and then adding more packing to fill any column voids.

Various mobile phases such as citrate, borate, 2-amino-2(hydroxymethyl)-1,3-propanediol (Tris), and orthophosphate buffers were studied as mentioned and prepared with either sodium or chloride counterions from concentrated HCl or 19 N NaOH. Most studies and routine analyses were conducted with 25 mM sodium citrate (pH 7.6 ± 0.1) as loading buffer, and elution was done using 25 mM citric acid (pH 2.4 ± 0.1) and 280-nm detection. High-sensitivity analysis was done using a 25 mM sodium phosphate (pH 7.6 ± 0.1) loading buffer and 100 mM sodium phosphate (pH 2.4 ± 0.1) elution buffer with 220-nm detection. In general, the loading buffer (high pH) was made by using the elution buffer (low pH) and adjusting its pH to 7.6 ± 0.1 with 19 N sodium hydroxide.

All chemicals were of reagent grade and were from Sigma Chemical Co. (St. Louis, MO) or Aldrich Chemical Co. (Milwaukee, WI) except Dulbecco's phosphate buffered saline (DPBS), which was from Gibco (Grand Island, NY), and water was deionized. Monoclonal antibodies produced by Bristol-Myers Industrial Division (Syracuse, NY) or Oncogen (Seattle, WA), polyclonal murine IgG (Zymed Laboratories, Inc., South San Francisco, CA), and polyclonal bovine IgG (Sigma) were diluted with DPBS and used as obtained.

The HPLC analysis system consisted of a low-pressure proportioning valve gradient system, diode array spectrophotometric detector, and microprocessor controller and data system (Model 1090M with PV5 option, Hewlett-Packard, Palo Alto, CA) and was used without modification.

Procedure. Measurement of IgG Concentration. Samples were collected and centrifuged to remove cells, and aliquots of supernatants were stored frozen. IgG's can precipitate at high concentrations (>5 mg/mL), especially in unbuffered or ill-suited buffer solutions. At low concentrations, many proteins adsorb

* Author to whom correspondence should be addressed.
[1] On leave from Johns Hopkins Medical School, Baltimore, MD.

0003-2700/89/0361-1314$01.50/0

to plastic and glass surfaces. Low-concentration IgG standards were often stabilized with bovine serum albumin (10 mg/mL) solutions of DPBS.

Once rapidly thawed in tap water, samples were centrifuged to clarity and analyzed immediately or stored refrigerated at 4 °C for not more than 48 h.

Routine analysis of samples containing 10–1000 μg/mL IgG involves equilibration of the protein A affinity chromatography system with 90% sodium citrate buffer–10% citric acid buffer (flow rate 3 mL/min, column temperature 25 °C), followed by blank runs with DPBS to determine if the system base line was appropriate at 280-nm detection. Elution involved a step gradient at 1 min to 10% sodium citrate buffer and 90% citric acid elution buffer. This mixture of loading and elution buffer results in actual pH values of 6.0 and 2.8, respectively. A 250-μL aliquot of IgG standard was injected in triplicate, and peak areas were determined by standard chromatographic integration methods. For standards at a concentration of 100 μg/mL, the RSD of the peak areas should be less than 2%. Samples were analyzed by using a 250-μL injection on-column. Sample preparation involved adjusting sample to pH 6.5 or greater as elaborated on later. Additionally, ascites fluid was diluted with DPBS such that IgG levels were below 1000 μg/mL. Unbound material is eluted from the column prior to elution of IgG. Bound IgG eluted slightly after the elution buffer breakthrough and was quantitated by using the same method as that for the standard.

For high-sensitivity analysis of samples below 10 μg/mL concentration, a 25 mM sodium phosphate (pH 7.6 ± 0.1) loading buffer and 100 mM sodium phosphate (pH 2.4 ± 0.1) elution buffer and 220-nm detection were used.

RESULTS AND DISCUSSION

The concept of executing affinity chromatography using protein A is uncomplicated. Protein A binds at or above physiological pH (pH 7.2) to the Fc region of IgG molecules (*3–5*) in a pseudoimmunological response. The mode of binding probably involves hydrophobic interactions since many protein A loading systems use salt concentrations, often as high as 3 M sodium chloride, along with buffers such as Tris, borate, or phosphate (*7–11*) to maintain appropriate pH. Elution traditionally occurs at low pH (<4.0) and low citrate or phosphate salt concentration.

The major experimental parameter studied was loading and elution buffer because base-line perturbations from ill-suited buffers are the main impediment to using affinity chromatography for quantitation. The other parameters of column configuration, loading and elution buffer flow rate, sample pH, and the nature of the stationary phase were briefly investigated as described.

Conceptually, the ideal buffer would not interfere with IgG to protein A binding, be transparent in the UV detection range (220 or 280 nm), and have a diprotic nature with pK_a 2.5 and 8.5. Unfortunately, no such buffer has been found, and traditional buffer systems such as 100 mM Tris (ph 8.5)–citric acid (pH 2.6) can lead to large base-line perturbations that are sufficient to interfere with IgG analysis below 100 μg/mL concentration. Linear elution gradients using pH changes and chaotropic agents, which can be used for isotype separations (*7–9*), do not generate such large base-line perturbations but cause excessive IgG band broadening, limiting the method's sensitivity. Thus, rapid step gradients are better suited for routine sensitive IgG analysis.

Three buffer systems we investigated most thoroughly are based on combinations of citrate, phosphate, and Tris. They are all compatible with 280-nm detection, while the phosphate system can also be used with 215-nm detection. Some representative chromatograms of mAb BM1 (murine IgG_{2a}) obtained with various combinations of the three buffer systems are shown in Figure 1. It is apparent from these examples that the phosphate and Tris buffers cause peak artifacts (peak fronting and splitting) while the Tris system additionally causes base-line perturbations that interfere with peak

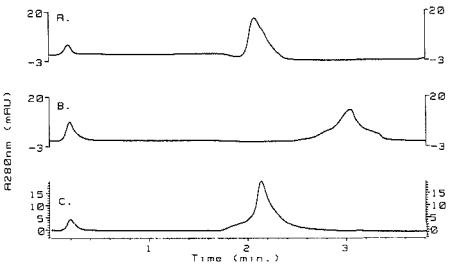

Figure 1. Comparison of elution of 21 μg of mAb murine IgG_{2a} BM1 with 25 mM (A) sodium citrate (pH 7.6)–citric acid (pH 2.6), (B) sodium phosphate (pH 7.6)–sodium phosphate (pH 2.6), and (C) Tris HCl (pH 7.5)–Tris HCl (pH 2.6) loading–elution buffer combinations and 280-nm detection. Peak shape may be a reflection of the pH elution profiles shown in Figure 2 for the various buffer combinations.

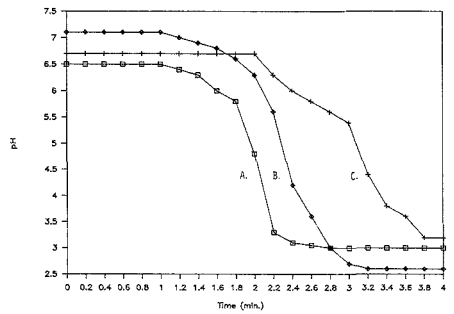

Figure 2. Eluent pH during a step gradient from 90–10% to 10–90% 25 mM (pH 7.6 to 2.6) sodium citrate–citric acid (A), Tris HCl (B), and sodium phosphate (C). These profiles are a reflection of the differences in buffer pK_a and mixing in the pumping system of the chromatograph.

quantitation. We surmise that the variations in BM1 peak shape with these various eluents arise from the differences in pH profile as shown in Figure 2. Split peaking may be related to the heterogeneous nature of the system since both protein A and IgG's have multiple binding sites for each other, all IgG's exhibit microheterogeneity with regard to isoelectrotypes, and often mAbs contain mixed light chains. As such, mAbs exhibit variable physiochemical and immunochemical properties as manifested here with regard to binding to protein A.

The citrate system gives little base-line perturbation and symmetrical peak elution. This triprotic acid has pK_a's in the range 2.6–7.5, which result in a linear pH drop upon stepping from pH 6.5 to 3.0, as seen in Figure 2. Further development work on the sodium citrate–citric acid system, where 10–250 mM loading–elution buffer concentrations were investigated, indicated 25 mM sodium citrate–citric acid as the best buffer system for routine analysis work since this concentration maintains relatively sharp elution band integrity and generates little base-line interference. Additionally, a 25 mM sodium phosphate–100 mM sodium phosphate system is used for analyses requiring high sensitivity since it is compatible with detection at 220 nm. This buffer system gives split peaks at low IgG amounts (<10 μg on-column), which require operator intervention for interpretation since it is not always obvious if split peaking arises from eluent effects or column channeling.

We have also attempted to use a 25 mM universal buffer combination (phosphate, borate, citrate, Tris (ref 18)) that reportedly does not interfere with detection above 240 nm. This approach allows fractionation of polyclonal murine IgG, bovine IgG, and mAb BM1, but leads to large base-line per-

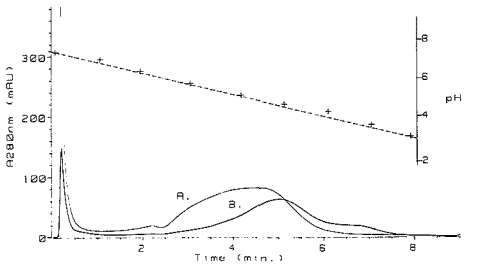

Figure 3. Elution of 500 μg of polyclonal (A) bovine IgG (Sigma) and (B) murine IgG (Zymed) using a 25 mM universal buffer mixture (see text for reference) with an 8-min linear gradient (pH 7.2 to 2.9) and 280-nm detection. Fractionation of the sample indicates IgG's elute from protein A at different eluent pH's, as also shown above. Bovine IgG is known to have less affinity for protein A than does murine IgG, as evident here from the large breakthrough peak and skewing of the bovine peak to earlier elution times.

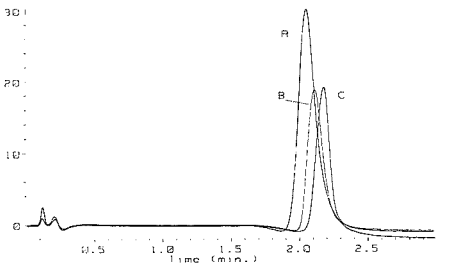

Figure 4. Elution of 25 μg of mAb (A) BM1 (pI 9.2, murine IgG_{2a}), (B) BM2 (pI, 9.5, human IgG_1), and (C) BM3 (pI 9.7, human IgG_1) using the standard 25 mM sodium citrate loading and citric acid elution buffers and 280-nm detection. Differences in retention time of peak modes are reproducible and, as shown in Figure 5, correlate with mAb pI.

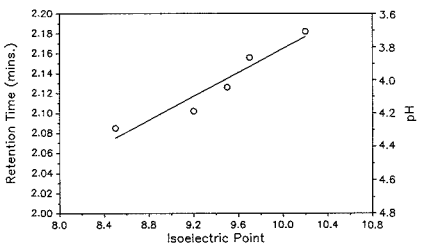

Figure 5. Plot of mAb pI and peak retention time or eluent pH obtained with the standard citrate buffer system. Antibody species and isotype are murine IgG_3, murine IgG_{2a}, human IgG_1, human IgG_1, and human–murine chimer IgG_1, respectively, from left to right. This unexpected correlation of pI to eluent pH for band elution has many ramifications with regard to protein A usage in mAb analysis and purification.

turbations similar to those caused by Tris when used in a step gradient mode. This universal buffer combination, used as shown in Figure 3, is still under investigation.

It is noteworthy that various precautions were taken to implement the high-sensitivity analysis described here. The same buffer type was used for loading and unloading and was usually made by starting with a stock solution of the acid form and titrating this from pH 2.4 to 7.6 with 19 N NaOH. Eluents were also made with low buffer concentrations (25 or 100 mM). Finally, both loading and elution buffer channels were run simultaneously at all times as 90–10% mixtures to minimize artifacts arising from stationary solutions in the pump channels.

Other column configurations besides 4.6 mm × 5 cm were investigated. Columns with lower volume lacked sufficient excess capacity of stationary phase to allow reproducible long-term use of one column. According to Biorad, the manufacturer of the stationary phase, a 4.6 mm × 5 cm column containing approximately 1 g of stationary phase has a capacity of approximately 5–9 mg of IgG (depending on specific IgG type and isotype) and thus an approximately 20–40-fold excess capacity for the upper sample concentration range of interest (1 mg/mL). This excess capacity has allowed us to use an individual column for thousands of analyses provided the column is washed with methanol after approximately every 200 injections.

With regard to sample pH, it is generally accepted that if an IgG has an ability to bind to protein A, it will bind at or above physiological pH (pH 7.2). The linear pH gradient elution profile shown in Figure 3 indicates that for polyclonal IgG, various IgGs elute at different pHs, and consequently sample pH for loading must be evaluated on a case-by-case basis with regard to individual mAbs. We show in Figure 4 that various mAbs elute with differing peak mode retention times. These mAbs differ by their isoelectric points (pI), and a direct correlation of pI to pH of elution is seen for various human, chimeric, and murine mAbs as shown in Figure 5. This correlation is interesting because it indicates that the method described here can be used to estimate IgG pI, a measurement that is often difficult to make by using isoelectric focusing electrophoresis (IEF) for IgG's with pI's above 9. It also indicates that if protein A is used for mAb selection there is a tendency to select for IgG's that have high pI's, which may have ramifications with regard to mAb solubility and stability.

Some other examples of the method's pI selectivity are seen in analysis of polyclonal IgG's from various sources. In studies of polyclonal murine IgG and mAb BM1 a coincidence of retention is seen because the polyclonal IgG sample was purified by its supplier, Zymed Laboratories, using protein A affinity chromatography. This can be contrasted with the elution of a polyclonal bovine IgG sample where a large IgG breakthrough peak and little coincidence with mAb BM1 have been seen. The polyclonal bovine IgG sample was supplied and purified by Sigma Chemical Co. using ion-exchange and size-exclusion column methods and, as such, is more representative of IgG's present in the animal. The large IgG breakthrough peak arises because not all IgG isotypes from different species bind to protein A (*3–5*). Generally, bovine IgG has poor affinity for protein A, and estimates of bovine IgG from protein A affinity underestimate bovine IgG levels determined by RID analysis by 50%. It is not known if the general ability of immunoglobulin isotypes and classes to bind to protein A is strictly correlated to pI, but this may be the case, since we have found using isoelectric focusing studies that early eluting IgG from large-scale columns contains low-pI (<7) material.

The parameter of flow rate was investigated early in the development of the method, and it was found that 3 mL/min was the maximum flow rate that could be used with the stationary phase without having excessive back-pressure. Flow rates greater than 3 mL/min were not investigated, and lower flow rates increased analysis time.

The stationary phase choice was based on availability (at the time these studies were started, only Biorad and Repligen (Immobilized rProtein A, IPA-300, Cambridge, MA) offered bulk material) and stability of the stationary phase support. The Biorad material is a macroreticulated polymer with high mechanical stability, allowing its use at high linear flow velocities. Repligen material is a soft gel.

Linearity studies of BM1 and other mAb's indicate linearity of the citrate buffer system (280-nm detection) to 1 mg/mL for a 250-μL injection. For instance, a typical linear regression

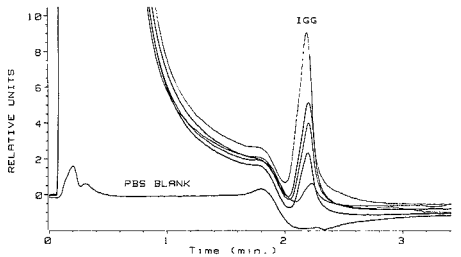

Figure 6. Overlapping rapid affinity chromatograms obtained with the standard citrate buffer system and 280-nm detection of various conditioned media samples from large-scale mAb production. The samples represent a time course from day 0 to harvest and a DPBS blank. This method is subsequently used to monitor concentration, purification, and formulation of the IgG.

analysis for nine standards injected in triplicate in the 1–1000 μg/mL concentration range will yield $R^2 = 0.9963$ and $y = 3.35x + 20.1$ with a standard error of 71.69 and 0.0772 for the y estimate and x coefficient, respectively. The detection limit is estimated to be 1 μg on-column for typical conditioned media samples. The analytical range of interest for process samples falls within the 10–1000 μg/mL concentration range. It should be noted that a cultivation medium that contains 5% fetal calf serum typically gives rise to IgG blanks of 1–5 μg/mL, which limits the method's sensitivity. For routine analysis the method has an estimated precision of 0.5–2% RSD above 10 μg/mL. Sensitivity of the method can be increased by increasing the injection volume to 1 mL, since the capacity of the stationary phase used here, as stated previously, is approximately 5–9 mg of IgG per column.

Method validation has been achieved through crossover with RID and spiked recovery studies. The RID studies showed general trends for sample levels to be comparable, but RID lacks the sensitivity required (IgG concentrations of 1–300 μg/mL) for direct analysis of conditioned media samples. As such, samples for RID analysis require 10–30-fold concentration, a sample preparation step that is difficult to execute accurately.

For the spiked recovery studies sample blanks consisting of synthetic media supplemented with 2% fetal calf serum were spiked with IgG to give six concentrations from 0 to 500 μg of IgG/mL, and IgG was quantitated in triplicate in these samples. Linear regression analysis of the mean of the results gave $R^2 = 0.9999$, with $y = 0.9968x + 2.66$ and a standard error of the y estimate and slope of 1.755 and 0.00392, respectively. The slight positive bias (2.66 μg/mL) of the results represents measurable (protein A bindable) bovine IgG in the blank.

An example of the use of the method for following the production of IgG in vitro is shown in Figure 6, where overlapping chromatograms of a DPBS blank and time course samples from initial to harvest are shown.

The characteristics of the phosphate buffer system (220-nm detection) are similar to that of the citrate system, except it is an order of magnitude more sensitive, with a detection limit of less than 100 ng of IgG on-column. The main limitation of the phosphate buffer system is, as previously shown in Figure 1, that IgG elution band shape is often split, making peak integration difficult. Actual application of the phosphate system involves the use of 25 mM sodium phosphate (pH 7.6) binding and 100 mM sodium phosphate (pH 2.6) elution buffer. The higher concentration of elution buffer compresses the IgG elution band such that it is better defined than that shown for the 25 mM sodium phosphate in the figure.

The main general limitations of the method are that not all IgG classes bind to protein A, and occasional anomalous results are found during routine analysis. The first limitation may be overcome with the use of protein G, which has recently been commercialized as an immobilized recombinant product for IgG purification. The second limitation of anomalous results manifests itself with a positive bias in IgG values. This has been traced to the occurrence in some samples of IgG precipitates that elute from the column only in the presence of some solubilizing agent such as bovine serum albumin. For instance, on occasion a column has been observed to give high results for a number of samples known to contain low IgG concentrations, but when an IgG standard or buffer blank is injected, no anomalous results are seen. However, injection of a bovine serum albumin sample causes elution of precipitated IgG, indicating that the column is fouled and should be repacked.

One final note addressed earlier was that column life can be extended if the column is washed periodically (after every 200 samples) with methanol. It has been observed that the stationary phase rapidly loses IgG binding capacity if, for instance, the column was used and then allowed to remain overnight without a wash. Loss of protein A from the stationary phase is thought to be through protease activity originating from the samples or from microbial growth in the eluent.

ACKNOWLEDGMENT

Helpful discussions with Thomas G. Heckler, Edward C. Walsh, and John. J. Usher of Bristol-Myers Fermentation Development and Genetic Engineering Groups, Syracuse, NY, and with Dale Yelton and Mark Byrnes of Oncogen, Seattle, WA, are gratefully acknowledged.

LITERATURE CITED

(1) Hamilton, R. G.; Hussain, R.; Ottesen, E. A.; Adkinson, F., Jr. *J. Immunol. Methods* **1981**, *44*, 101.
(2) Markowitz, H.; Jiang, N.-S. *Fundamentals of Clinical Chemistry*; Tietz, N. W., Ed.; W. B. Saunders Co.: Philadelphia, PA, 1976; pp 274–297.
(3) Langone, J. J. *Adv. Immunol.* **1982**, *22*, 157.
(4) Langone, J. J. *J. Immunol. Methods* **1982**, *55*, 277.
(5) Lindmark, R.; Thorén-Tolling, K.; Sjöquist, J. *J. Immunol. Methods* **1983**, *62*, 1.
(6) Hjelm, H.; Sjödahl, J.; Sjöquist, J. *Eur. J. Biochem.* **1975**, *57*, 395.
(7) Sjödahl, J. *Eur. J. Biochem.* **1977**, *78*, 471.
(8) Hanson, D. C.; Phillips, M. L.; Schumaker, V. N. *J. Immunol.* **1984**, *132*, 1396.
(9) Moks, T.; Abrahmsén, L.; Nilsson, B.; Hellman, U.; Sjöquist, J.; Uhlén, M. *Eur. J. Biochem.* **1986**, *156*, 637.
(10) Mackenzie, M. R.; Warner, N. L.; Mitchell, G. F. *J. Immunol.* **1978**, *120*, 1493.
(11) Chalon, M. P.; Milne, R. W.; Vaerman, J.-P. *Scand. J. Immunol.* **1979**, *9*, 359.
(12) Ey, P. L.; Prowse, S. J.; Jenkin, C. R. *Immunochemistry* **1978**, *15*, 429.
(13) Hammen, R. F.; Pang, D.; Remington, K.; Thompson, H.; Judd, R. C.; Szuba, J. *Biochromatography* **1988**, *3*, 54.
(14) Crowley, S. C.; Walters, R. R. *J. Chromatogr.* **1983**, *266*, 157.
(15) Hage, D. S.; Walters, R. R. *J. Chromatogr.* **1987**, *386*, 37.
(16) Hollis, D. F.; Ralston, S.; Suen, E.; Cooke, N.; Shorr, R. G. L. *J. Liquid Chromatogr.* **1987**, *10*, 2349.
(17) Walters, R. R. *J. Chromatogr.* **1982**, *249*, 19.
(18) Davies, M. T. *Analyst* **1959**, *84*, 248.

RECEIVED for review October 25, 1988. Accepted March 1, 1989.

Anal. Chem. 1989, 61, 1318–1321

Determination of the Dissociation Temperature of Organic Micelles by Microcapillary Hydrodynamic Chromatography

Jaap Bos,* Robert Tijssen, and M. Emile van Kreveld

Koninklijke/Shell-Laboratorium, Amsterdam (Shell Research B. V.), Badhuisweg 3, 1031 CM Amsterdam, The Netherlands

Microcapillary hydrodynamic chromatography has been used to study the temperature behavior of micelles of a poly(styrene–isoprene) block polymer in the nonpolar solvent *n*-decane. A deactivation scheme for the fused silica column, necessary for working with nonpolar solvents, is given. Results for the dissociation range of the micelle are compared with those of the light-scattering technique used by Mandema et al. on a comparable polymer. In the transition range (for this polymer–solvent system, 20–30 °C) we have observed both the micellar and the molecular form of the polymer. Information on the micelle size was obtained. In our study we have found no evidence for the existence of very large structures in the transition region as reported by Mandema.

INTRODUCTION

Hydrogenated poly(styrene–isoprene) two-block polymers in nonpolar solvents such as *n*-decane show a nonlinear relationship between inherent viscosity and temperature. The inherent viscosity is defined as

$$\eta_{inh} = (1/C) \ln (\eta/\eta_0) \quad (1)$$

where η_0 is the (dynamic) viscosity of the solvent, η is that of the polymer solution, and C is the polymer concentration. A typical case of nonlinear behavior for the polymer/solvent combination mentioned above can be found in the work of Mandema et al. (*1*), who reported that high values of η_{inh} at low temperatures suddenly drop to lower values at increased temperature.

The common interpretation is that at low temperatures micellar aggregates exist with the polar polystyrene part of the molecules in the core, *n*-decane being a nonsolvent for polystyrene. At higher temperatures these micelles dissociate into a normal molecular solution.

Using light-scattering techniques, Mandema showed the existence of the larger aggregates at lower temperatures. However, with these techniques it is impossible to establish exactly at what temperature the micelles start to dissociate or when the dissociation is complete. Also, in the transition range, after an initial decrease of the scattering intensity, corresponding to the presence of a smaller particle, the scattering increased again to high values in a small temperature interval. The latter phenomenon was interpreted as pointing to the existence of large conglomerates with dimensions of the order of the optical wavelength, i.e. much larger than the micelle at lower temperature. We have studied the same type of polymer/solvent system by using microcapillary hydrodynamic chromatography (HDC). HDC is a separation technique that makes it possible to observe, in principle, both the micellar and the molecular species during dissociation.

EXPERIMENTAL SECTION

General Procedure. The instrumental setup for the experiments is similar to the one we used in our earlier publications on HDC (*2*, *3*). The only difference is that the injector and the major part of the column are immersed in a thermostated bath. An M6000 pump (Waters Associates, Milford, MA) was used to deliver the mobile phase, except during deactivation experiments where caustic and acid aqueous phases were delivered by a 114 M solvent system (Beckman, Berkeley, CA). The (high-temperature/high-pressure) injector was an M-4-C6W Vespel type (Valco, Schenkon, Switzerland) equipped with an external 180-μL loop. Between the pump and the injector, a 20-m-long, 0.25-mm-i.d. stainless steel tubing was placed in the thermostated bath to equilibrate the mobile phase to the required temperature. Eluting species were monitored by ultraviolet absorption at 215 nm with a Uvidex 100-VI detector (Jasco, Tokyo, Japan). The detector cell was equipped with the adjustable knives slit described in ref 3. The detector signal, after 8-Hz analog to digital conversion, was stored in an HP 3357 lab automation system; interactive graphics manipulations and calculations were performed on an HP 300 computer system. Samples were injected as a block of 4-s duration after 2 min of equilibrium time in the sample loop. The length of the restriction capillary was chosen such that in all experiments at different temperatures the elution time of toluene was between 21 and 25 min. Retention times were determined as the first statistical moment of the eluting peaks.

Materials. Fused silica capillaries were supplied by SGE (North Melbourne, Australia). The restriction capillaries were of 100-μm i.d. The measuring capillary, bought as a nominally 5-μm-i.d. column, had an internal diameter of exactly 3.70 μm, as determined by the pressure drop–residence time method described in ref 3. The total length of the measuring capillary was 300 cm, with a flow cell created by burning off the polyimide coating at a position 28 cm before the column end. Of the chromatographic column length of 272 cm, a length of 15 cm next to the detector (at ambient temperature) was not thermostated.

Solvents. All the solvents were used without further purification. Tetrahydrofuran (THF) (HPLC grade No. 9441), dimethylformamide (DMF) (Baker-analyzed No. 7032), and toluene (Baker-analyzed No. 8077) were obtained from Baker (Deventer, Holland). *n*-Decane (Purum No. 30550) was supplied by Fluka (Buchs, Switzerland); *N*-(trimethylsilyl)imidazole (No. 270403) was purchased from Chrompack (Middelburg, Holland).

Polymers. To concur as closely as possible with the experiments of Mandema et al. (polymer designation S-2 in ref 1), we used the same type of hydrogenated poly(styrene–isoprene), which differed only in minor aspects from the S-2 polymer, as shown in Table I. Despite these differences the two polymers showed the same nonlinear relationship between inherent viscosity and temperature, as is shown in Figure 4 of ref 1, with the start of the nonlinear part, and so possibly the onset of the micelle dissociation, at 80 °C. In our experiments the polymer was dissolved (without stirring) in *n*-decane at 150 °C during 2 h. To prevent degradation of the polymer, the decane had been deaerated by bubbling a helium stream through it.

Table I

	S-2 polymer used by Mandema	polymer used in our work
wt-av mol wt	80 000	92 000
polydispersity	1.16	1.05
polystyrene content, % (w/w)	38.0	35.8

0003-2700/89/0361-1318$01.50/0

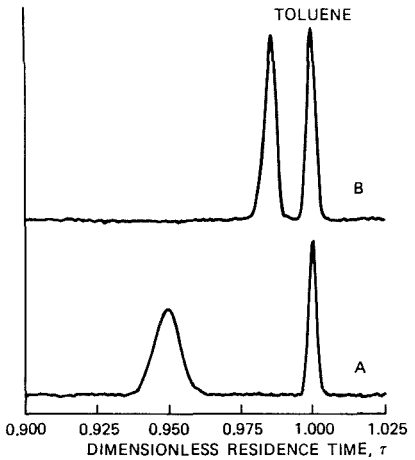

Figure 1. Hydrodynamic chromatography of the styrene–isoprene polymer in two different mobile phases at room temperature: (A) in *n*-decane, elution as the micellar aggregate; (B) in THF, elution as the molecular species. In both cases the injection concentration was 2 g/L polymer and 0.5 g/L toluene in the mobile phase. For column dimensions see Experimental Section.

THEORY

In HDC the relative retention time τ, defined as the ratio of the residence time for a particle or a macromolecule to the holdup time for small molecules, can be described by the relation (*3*)

$$\tau = (1 + 2\lambda - C\lambda^2)^{-1} \qquad (2)$$

where λ is the aspect ratio (particle size/column diameter = $2r/2R$). For macromolecular species the size can be described by $2\bar{r}$ where $\bar{r}$ represents the effective radius (*3*, *4*). C is a constant related to the relative (slip) velocity of the particles with respect to the surrounding liquid with a value that depends on the particles' geometry ($C = 2.698$ for free draining random macromolecular coils in a good solvent and $C = 4.89$ for solid spherical particles). The value of C for micelles is not known but is expected to be between the two extreme values mentioned.

However, for not too low values of τ (say $\tau \geq 0.945$) the exact value of C is not very important since the difference in λ values calculated from the two extreme values above amounts to less than 4%. So measurement of τ in this region will give a virtually model-free estimate of λ. From this and the known diameter of the HDC column, the size of the eluting species is obtained.

RESULTS AND DISCUSSION

In a good solvent such as THF in which both the polystyrene and polyisoprene parts of the molecule are soluble, the polymer is supposed to elute as the molecular species, while in the nonpolar solvent decane the polymer is expected, at room temperature, to elute as the larger micellar aggregate. The experimental results as shown in Figure 1 confirm that this is actually the case. In both chromatograms solutions of 2 g/L polymer in the mobile phase were injected. The injection solution also contained 0.5 g/L toluene, which was used as the holdup time indicator. In THF the polymer elutes at a relative retention time $\tau = 0.9855$, indicating an effective radius $\bar{r} = 13.8$ nm. In decane the polymer elutes earlier, viz. at $\tau = 0.9496$, indicating a larger species with $\bar{r} = 52.8$ nm, clearly the micelle. The values of the effective radii reported above and in the further part of the paper were calculated by using $C = 2.698$ (random coil value) for the molecular species, while for the micelle the value $C = 4.89$ (solid spheres) has been used.

Increasing the temperature of the decane experiment should in principle reveal the dissociation of the micelle by a shift in the relative retention toward the higher value for the molecular species, as we found in the THF experiment.

However, a complication arises due to the polarity of the fused silica column surface. This surface contains polar silanol groups, which can interact with eluting polar species. In polar solvents such as THF these silanol groups are sufficiently deactivated, but they play an important role with nonpolar mobile phases. In decane, as long as the polymer is present as a micelle with the nonpolar polyisoprene chains on the outside, there is no interaction with the column wall. However, as the micelle starts to dissociate, the more polar polystyrene part of the molecule will come into contact with the column wall and interact strongly with the silanol groups. So, upon increasing the temperature in the decane experiments, we find, up to 75 °C, a micelle peak that disappears completely at higher temperatures.

Only at temperatures of 140 °C or higher does the polymer elute as the molecular species, but it does so with the typical tailing profile that shows that it has been subject to an adsorptive process. This is in line with results of gel permeation experiments on related polymers (*5*) in weak mobile phases where also only elution of the micelle was observed, but the free polymer molecules were retained on the column packing material.

While it is virtually impossible to completely deactivate the tremendously large surface area of a gel permeation column packing material, we succeeded in deactivating our fused silica column by silylation. We found, however, that after direct silylation (*N*-(trimethylsilyl)imidazole in DMF at 150 °C) the column still showed a small degree of adsorption, probably due to epoxide-type oxygen that is known to be present on the silica surface. To convert these epoxide groups, which are difficult to silylate, to the more reactive silanol group we used as a first step the procedure of Tock et al. (*6*). For a complete deactivation of the column we used the following treatment:

(1) At room temperature we converted the epoxide groups by successively pumping through the following aqueous mobile phases: 1 M potassium hydroxide (2 h), water (10 min), and 0.03 M hydrochloric acid (2 h), followed by water (1 h).

(2) For the silylation we changed the mobile phase to DMF, increased the column temperature to 150 °C, and deactivated the column by repeated injection of a 1/1 (v/v) solution of the strong silylation agent *N*-(trimethylsilyl)imidazole in DMF.

(3) The column temperature was lowered to 60 °C, the DMF was replaced by THF, and the column temperature was lowered to ambient. Column internal diameter determination after this treatment showed no difference from the 3.70 μm found earlier for the untreated column.

(4) The THF was replaced by the *n*-decane mobile phase.

After this treatment the polymer could be detected at all temperatures between ambient and 140 °C, whether as the micelle or the molecular species or as both species if present. An example of the transition range is given in Figure 2. In this experiment the mobile phase contained 1 g/L polymer to provide a background micelle concentration. Polymer injections of 2 g/L in this mobile phase showed the micelle being present from ambient temperature up to 80 °C. Between 80 and 95 °C there is a gradual decrease in the concentration of the micelle, with material eluting at the retention time of the molecular species and also with some material eluting in between these peak positions. This effect can be interpreted as being due to polymer that exists partly as

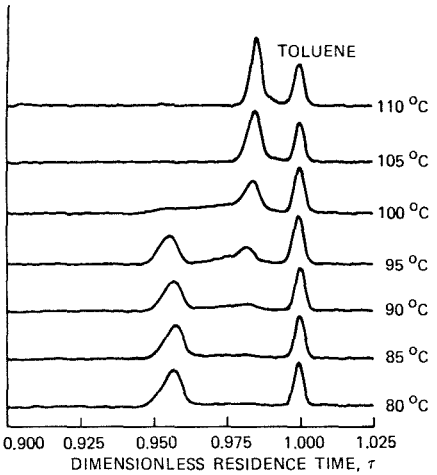

Figure 2. Temperature range of the micelle dissociation: mobile phase, *n*-decane containing 1 g/L polymer; injection concentration, 2 g/L polymer and 0.5 g/L toluene in the mobile phase.

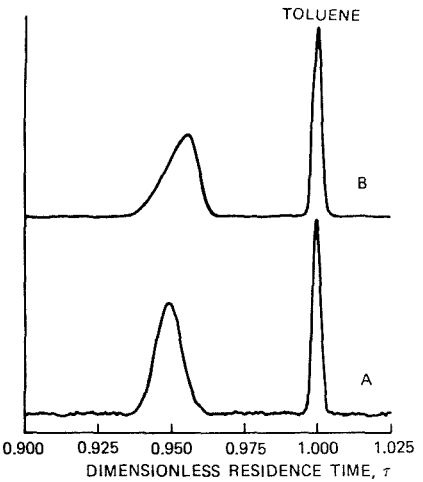

Figure 3. Peak distortion at higher polymer concentration at room temperature. In both cases the mobile phase was *n*-decane containing 1 g/L polymer. Injection concentrations in the mobile phase: (A) 2 g/L polymer and 0.5 g/L toluene; (B) 10 g/L polymer and 5 g/L toluene. (Attenuation of chromatogram B is 5 times higher than that of A.)

micelle, partly as molecular species during the time of the chromatographic process. At 105 °C no material is eluting at the micelle retention time, and at this point the peak area of the molecular species equals, within the experimental error, that of the micelle peak at lower temperatures (a 4-fold determination at low temperature gives a value for the peak area and its standard deviation of 7.15 ± 0.25 mVs; at 105 °C these values are 7.00 ± 0.15 mVs). This indicates that the conversion from micelles into the molecular species is complete, assuming the two forms to have the same ultraviolet absorption response. From 110 °C up to 140 °C no change in retention time of the molecular species was found, which at $\tau = 0.9856$ yielded the same molecular size as in the good solvent THF at room temperature.

Although the transition interval found above is in agreement with the viscometric experiments, we must bear in mind that so far we have used a lower polymer concentration than that used by Mandema et al. In their experiments the concentration was 7 g/L, while in our experiments, due to the dilution by chromatographic dispersion as the injection pulse is transported through the column, the concentration will, on the average, be lower than 3 g/L. Experiments with a background concentration of 7 g/L were, however, impossible due to the high viscosity of the mobile phase, which leads to a very poor injection quality. We therefore kept the mobile phase concentration at 1 g/L but increased the injection concentration from 2 g/L to 10 g/L (with 5 g/L toluene). As shown in Figure 3, this high concentration gives a badly distorted peak shape from which reliable size information can no longer be obtained. Qualitatively, however, the micelle transition can be studied, as is shown in Figure 4. Again, as in Figure 2, the transition is complete at about 110 °C. Due to the high chromatographic efficiency of the microcapillary column, the top concentration in the polymer elution profile is still as high as 7 g/L. So, even at this concentration the polymer appears to be incapable of forming a stable micelle above 110 °C.

We have shown that microcapillary HDC is a powerful tool for studying the dissociation behavior of organic micelles. Both the micelle and the molecular species can be detected in the same experiment. Compared to viscometric and light-scattering studies, HDC also has the advantage that the exact temperature can be determined at which micelle formation is no longer possible. Since, in contrast to gel permeation chromatography, HDC has no need of calibration standards, direct information on the micelle size can be obtained. As the precision of the τ value determination is high (a 10-fold determination for the micelle gives a standard deviation of 3×10^{-4} τ units), the sole uncertainty in the micellar size we report is in the unknown C factor of eq 2. For the extreme values of C we find sizes of 51.0 (C = 2.698, random coil model) and 52.8 nm (C = 4.89, solid sphere model), so a difference exists of less than 4%.

In our experiments we have found no evidence for the existence of very large particles in the transition range as reported by Mandema et al. (*1*).

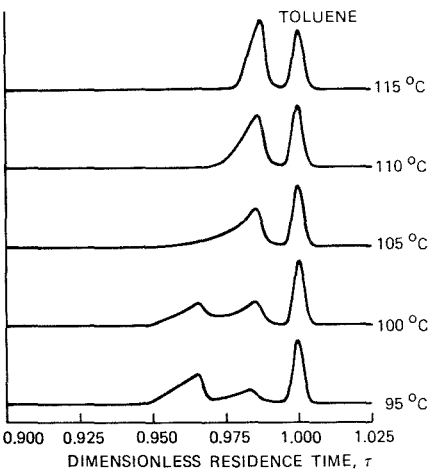

Figure 4. Temperature range of the micelle dissociation at higher polymer concentrations: mobile phase, *n*-decane containing 1 g/L polymer; injection concentration, 10 g/L polymer and 5 g/L toluene in the mobile phase.

LITERATURE CITED

(1) Mandema, W.; Zeldenrust, H.; Emeis, C. A. *Makromol. Chem.* **1979**, *180*, 1521–1538.
(2) Tijssen, R.; Bleumer, J. P. A.; van Kreveld, M. E. *J. Chromatogr.* **1983**, *260*, 297–304.
(3) Tijssen, R.; Bos, J.; van Kreveld, M. E. *Anal. Chem.* **1986**, *58*, 3036–3044.
(4) van Kreveld, M. E.; van den Hoed, N. *J. Chromatogr.* **1973**, *83*, 111.
(5) Price, C.; Hudd, A. L.; Booth, C.; Wright, B. *Polymer* **1982**, *23*, 650–653.
(6) Tock, P. P. H.; Stegeman, G.; Peereboom, R.; Poppe, H.; Kraak, J. C.; Unger, K. K. *Chromatographia* **1987**, *24*, 617–624.

RECEIVED for review November 17, 1988. Accepted March 10, 1989.

Size Exclusion Chromatography of Poly(ethylene terephthalate) Using Hexafluoro-2-propanol as the Mobile Phase

Sadao Mori

Department of Industrial Chemistry, Faculty of Engineering, Mie University, Tsu, Mie 514, Japan

A method for obtaining a calibration curve (CC) in hexafluoro-2-propanol (HFIP) using a characterized poly(methyl methacrylate) (PMMA) as a secondary standard was proposed. Polystyrene (PS) standards were used as a primary standard and a PS CC in tetrahydrofuran (THF) was converted to a PMMA CC in THF by use of a conversion equation. An integral molecular weight distribution curve of cumulative weight percent vs log molecular weight (M) for the PMMA secondary standard was constructed by using a PMMA chromatogram in THF and a PMMA CC. An integral distribution curve of cumulative weight percent vs retention volume (V_R) for PMMA in HFIP was obtained from a PMMA chromatogram in HFIP. Finally, a CC of log M of PMMA vs V_R in HFIP was obtained by using these two integral curves. PMMA equivalent number average molecular weights of poly(ethylene terephthalate) (PET) samples characterized by the end-group titration method were determined and the ratios of two averages were obtained. The ratio is designated as a correction factor, f, and an average value was 0.57. Therefore, corrected (true) molecular weight average of PET can be obtained from PMMA equivalent molecular weight by multiplying f.

INTRODUCTION

Solvents most commonly used for size exclusion chromatography (SEC) of synthetic polymers are tetrahydrofuran (THF), chloroform, and toluene, which are good solvents for polystyrene (PS) and other common polymers. The construction of a calibration curve of an SEC column system using these solvents as the mobile phase is easy for handling, because they can dissolve PS standards which are exclusively used for the calibration purpose. Polyacrylonitrile (PAN), for example, does not dissolve in these solvents and dimethylformamide (DMF) had to be used for SEC of PAN (*1*). However, DMF is a poor solvent for PS and other standard polymers such as poly(ethylene oxide) have been used for calibration standards.

Poly(ethylene terephthalate) (PET) is one of the unmanageable polymers for SEC with respect to solvents and calibration standards. *m*-Cresol has been used as the mobile phase for PET at 125 °C (*2*). However, *m*-cresol is viscous and requires a high column temperature, which leads to polymer degradation. Several solvent systems for the SEC of PET in which degradation was eliminated or kept to a minimum have been reported. A mixture of nitrobenzene and tetrachloroethane has been used for SEC of PET at room temperature (*3*) and degradation of PET was not observed for several months. The mobile phase was 0.5% nitrobenzene in tetrachloroethane. A sample (0.2 g) of PET was dissolved in 0.8 mL of nitrobenzene by heating at 180 °C and the solution was then diluted with 60 mL of hot tetrachloroethane. A mixture of phenol and tetrachloroethane (3:2, w/w) was also used for the SEC of PET (*4*). However, difficulties have been encountered in dissolving PET in these solvents at times. Hexafluoro-2-propanol (HFIP), pentafluorophenol, and their mixtures were used as the mobile phase in an SEC-LALLS system for PET (*5*).

The solvent HFIP has been found to be a superior solvent capable of dissolving PET at room temperature (*6*). HFIP has been commercially available and can be obtained in Japan. There are two major drawbacks in the use of HFIP as an SEC solvent. One is the expensive price of HFIP as a SEC solvent. The other is the insolubility of PS standards, which prevents the construction of a PS calibration curve in an SEC HFIP system. To overcome the high cost, semimicro-SEC using a mixture of HFIP and chloroform (1:1) has been proposed (*7*). However, the flow rate reliability in conjunction with a conventional pumping system for semimicro-HPLC was not sufficient in general for the determination of molecular weights of polymers. For calibration of a SEC system, Provder et al. proposed a general method for obtaining a calibration curve in a SEC trifluoroethanol (TFE) system for polyamide analysis (*8*). If HFIP alone can be used as a SEC solvent, then the availability of an SEC HFIP system can be expanded to polymers that can be dissolved in HFIP only.

In this paper methods to remove these two drawbacks have been proposed. Recycling use of the effluent from the column outlet by redistillation was employed to reduce the cost of the SEC measurement accompanied by the use of HFIP. A method to generate a calibration curve for a column system was similar to Provder's method (*8*), but the hydrodynamic volume concept and the Mark–Houwink constants were not employed here. PS standards were used as primary calibration standards and poly(methyl methacrylate) (PMMA) of known molecular weight averages was a secondary standard. A PMMA calibration curve in THF was constructed by using a PS calibration curve and a conversion equation (*9*). Integral molecular weight distribution curves in both THF and HFIP for the PMMA secondary standard were obtained from their respective SEC chromatograms and a PMMA calibration

0003-2700/89/0361-1321$01.50/0

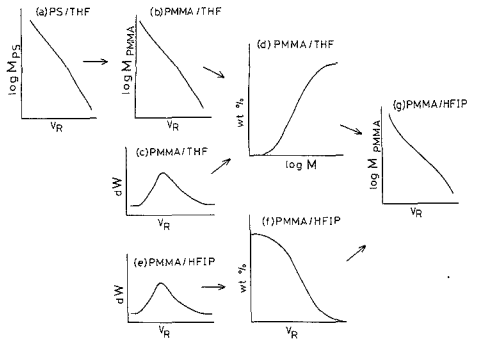

Figure 1. Illustrative process for the calibration of columns in HFIP using PS as primary standards and PMMA as a secondary standard: (a) a PS calibration curve in THF, (b) a PMMA calibration curve in THF, (c) an SEC chromatogram of the PMMA secondary standard in THF, (d) an integral molecular weight distribution of the PMMA standard, (e) an SEC chromatogram of PMMA in HFIP, (f) relationship of weight percent vs V_R of PMMA in HFIP, (g) a PMMA calibration curve in HFIP.

curve in HFIP was constructed from these two distribution curves.

EXPERIMENTAL SECTION

Apparatus and Materials. SEC measurements were performed on a Jasco TRIROTAR-V high-performance liquid chromatograph (Japan Spectroscopic Co., Ltd., Hachioji, Tokyo 192, Japan) with a Model SE-51 differential refractometer (Showa Denko Co., Ltd., Minato-ku, Tokyo 105, Japan) and a Model VL-614 loop injector. Two Shodex KF80M high-performance SEC columns (each 30 cm × 8 mm i.d.) (Showa Denko Co.) packed with PS gels for polymer separation were used and were thermostated at 35 °C in an air oven. These columns were equilibrated with tetrahydrofuran (THF) and had the number of theoretical plates (N) of 12 000 plates/30 cm by injecting 0.05 mL of a 0.1% benzene solution at a flow rate of 1 mL/min. After the required data were obtained from the THF mobile phase, the solvent in the columns was changed to HFIP at a flow rate of 0.3 mL/min. After enough HFIP solvent passed through the column to replace THF, the flow rate was increased to 0.5 mL/min and the columns were conditioned overnight by flowing HFIP at the same flow rate. The value of N was 11 000 plates/30 cm by injecting 0.05 mL of a 0.1% acetone solution at a flow rate of 0.5 mL/min.

PS standards were purchased from Pressure Chemical Co., Pittsburgh, PA, and a PMMA secondary standard was purchased from ArRo Laboratories, Inc., Joilet, IL. The molecular weight averages of these polymers were determined by the manufacturers. PET samples were obtained from Toray Co., Ltd., and their number average molecular weights ($\bar{M}_n$) were determined by the company by the end-group titration method. Sample concentrations were 0.1% (w/v) in THF for PS standards, 0.2% (w/v) in THF and in HFIP for a PMMA secondary standard, and 0.2% in HFIP for PET. The injection volume of the sample solutions was 0.1 mL and a 0.1-mL loop was used to inject these sample solutions.

HFIP was provided courtesy of Central Glass Co., Ltd., Chiyoda-ku, Tokyo 101, Japan. The solvent was reused several times by redistilling the waste solvent with a simple distilliation vessel composed of a round flask, a Liebig type condenser, and a mantelheater.

Calibration Procedure. A schematic illustration for calibration procedure is shown in Figure 1. (1) At first, a calibration curve of log molecular weight (M) vs retention volume (V_R) is constructed by using PS standards in the mobile phase of THF (Figure 1a). (2) The PS calibration curve in THF is converted to a PMMA calibration curve in THF by using the conversion equation (9) (Figure 1b)

$$\log M_{PMMA} = 0.2938 + 0.918 \log M_{PS} \quad (1)$$

(3) An SEC chromatogram of the PMMA sample in THF is measured (Figure 1c) and an integral molecular weight distribution of cumulative weight percent vs log M for the PMMA secondary standard (Figure 1d) is calculated by using the calibration curve (Figure 1b) and the SEC chromatogram (Figure 1c). (4) The mobile phase is changed to HFIP. The solvent, THF, in the columns is replaced by HFIP at a flow rate of 0.3 mL/min. (5) An SEC chromatogram of the PMMA secondary standard in HFIP is measured (Figure 1e) and an integral distribution of cumulative weight percent vs V_R for the PMMA secondary standard in HFIP is calculated (Figure 1f). (6) From two integral distributions, one is that of cumulative weight percent vs log M of PMMA in THF and the other is that of cumulative weight percent vs V_R of PMMA in HFIP, a calibration curve of log M of PMMA vs V_R in HFIP is constructed (Figure 1g).

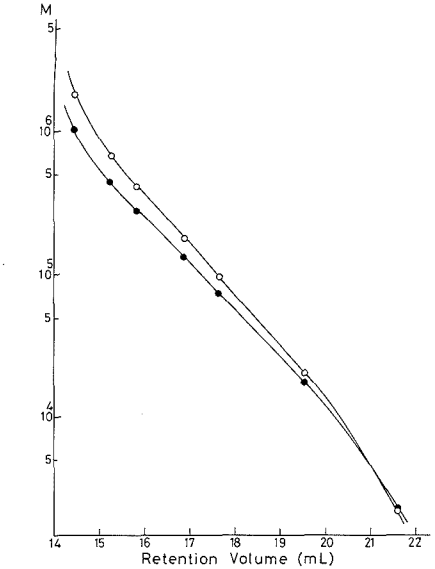

Figure 2. Calibration curves of log M vs V_R for PS (O) and PMMA (●) in THF.

The relationship of cumulative weight percent vs log M for PMMA shown in Figure 1d is assumed to be invariate for the PMMA secondary standard used and independent of the different mobile phases and their flow rates. Therefore, once the integral molecular weight distribution for the PMMA secondary standard is constructed, the repeat of steps 1–4 is not necessary as far as the same PMMA secondary standard is used for the calibration of the SEC system. Only steps 5 and 6 are required.

Calculation of molecular weight averages was performed in the usual manner: the SEC chromatogram was sliced into equal parts, the height of each sliced point was measured, and each height was multiplied or divided by molecular weight at each point.

RESULTS AND DISCUSSION

Calibration of Columns. Calibration curves obtained by steps 1 and 2 are shown in Figure 2. When a conversion equation for a secondary standard is known, a calibration curve of the secondary standard is easily obtained by using PS standards as primary standards. The conversion equation for PMMA in the literature (9) was

$$M_{PMMA} = 1.967 M_{PS}^{0.918} \quad (2)$$

By conversion of both sides of eq 2 to a common logarithmic scale, eq 1 was obtained. If a conversion equation for a secondary standard of known molecular weight averages has not been determined, then the equation can be generated according to the method in the literature (9). One of the advantages of the method described here is it is not necessary

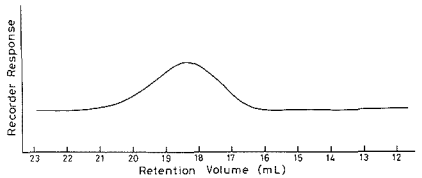

Figure 3. SEC chromatogram of the PMMA secondary standard in THF: concentration, 0.2%; injection volume, 0.1 mL; detector, RI; attenuation, ×2.

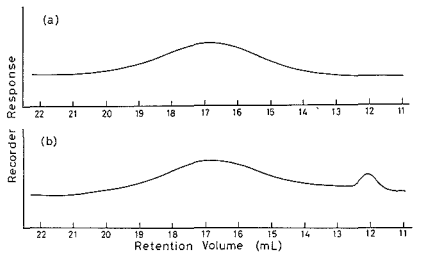

Figure 4. SEC chromatograms of the PMMA secondary standard in HFIP: concentration, 0.2%; injection volume, 0.1 mL; detector, RI; attenuation, ×4; (a) injection 10 days after the sample preparation, (b) injected day after the sample preparation.

to use the so-called hydrodynamic volume concept. Equation 1 is not based on the concept.

An SEC chromatogram of the PMMA secondary standard in THF is shown in Figure 3. Molecular weight averages of the sample were calculated by using the PMMA calibration curve in Figure 2. The values were $\bar{M}_w = 5.87 \times 10^4$ and $\bar{M}_n = 3.39 \times 10^4$, which were nearly equivalent to the manufacturer's data as $\bar{M}_w = 6.08 \times 10^4$ (obtained by light scattering) and $\bar{M}_n = 3.32 \times 10^4$ (obtained by membrane osmometry). An integral molecular weight distribution of the PMMA secondary standard was obtained by using the chromatogram in Figure 3 and the PMMA calibration curve in Figure 2.

The next step was the change of the mobile phase from THF to HFIP. The solvent THF in the column was replaced with HFIP at a flow rate of 0.3 mL/min. For replacing solvent in a column to other type of solvent, it is required to deliver new solvent into a column as slow as possible for the protection of the decrease in column efficiency. As HFIP is more viscous than THF, a decrease of a flow rate to 0.5 mL/min was required to keep the column inlet pressure as low as possible.

The SEC chromatogram of the PMMA secondary standard in HFIP was then measured and an example is shown in Figure 4. The SEC chromatogram of PMMA sometimes showed a small peak at the exclusion limit of the column system (Figure 4b) and this peak was not observed when the PMMA solution prepared more than 10 days before was injected (Figure 4a). Figure 4b was obtained when a sample solution prepared just 1 day before was injected. This small peak is probably the aggregation of PMMA molecules and it disappeared by heating or by ultrasonic treatment as well as leaving the sample solution more than 10 days after preparation at room temperature. The integral molecular weight distributions calculated from the chromatogram having a small peak at the exclusion limit did not give an accurate result due to the peak as well as due to base-line drifts or fluctuations.

The integral distribution of the cumulative weight percent vs V_R for the PMMA secondary standard in HFIP was calculated by step 5. A PMMA calibration curve in HFIP was constructed by step 6 and is shown in Figure 5. Pairs of two data points, log M_{PMMA} and V_R, were obtained at the same

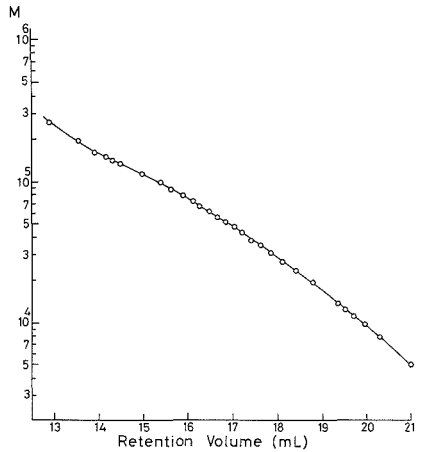

Figure 5. PMMA calibration curve of log M of PMMA vs retention volume in HFIP.

cumulative weight percent of two ordinates of two distribution curves (Figure 1d,f by sampling at every 5% from 5 wt % to 95 wt % and at every 1% from 0 wt % to 4 wt % and 96 wt % to 100 wt % of the ordinate. Pairs of each two data points were plotted.

The slope of the PMMA calibration curve in an SEC THF system (Figure 2) is steeper than that in an SEC HFIP system (Figure 5). In other words, at the same retention volume, a molecule in an SEC HFIP system has lower molecular weight than that in an SEC THF system. Ideally it should be the same molecular weight, because retention volumes of benzene and acetone in THF and HFIP were almost the same. It can be said that the sum of the interstitial volume V_0 and the pore volume V_i was unchanged by changing the solvent in the column from THF to HFIP. From the comparison of two calibration curves, it is obvious that the value of V_0 in an SEC HFIP system became smaller and that of V_i larger. Compared to an SEC THF system, therefore, it may be assumed that the difference of the slopes of two calibration curves has arisen from one of four reasons.

In an SEC HFIP system, (1) polystyrene gel swelled to some extent and the pore size of the gel became small without changing the inner volume of the pore; (2) the elution of PMMA molecules was accelerated by the ion-exclusion effect; (3) aggregation of PMMA molecules in HFIP was considered by the observation of two chromatograms in THF (Figure 3) and in HFIP (Figure 4); (4) the hydrodynamic volume of a PMMA molecule in HFIP was larger than that of the same molecular weight in THF.

Among these four assumptions, the last one is the most probable. Exponents and coefficients in a Mark–Houwink equation for PMMA in TFE and in THF were as follows (*8*):

$$[\eta] = KM^a \tag{3}$$

at $M < 31\,000$, $a = 0.461$, $K = 1.81 \times 10^{-3}$ in TFE and $a = 0.406$, $K = 2.1 \times 10^{-3}$ in THF; at $M > 31\,000$, $a = 0.791$, $K = 5.95 \times 10^{-5}$ in TFE and $a = 0.697$, $K = 1.04 \times 10^{-4}$ in THF. If the values of a and K for PMMA in HFIP are assumed to be similar to those in TFE, then hydrodynamic volume of a PMMA molecule in HFIP is higher than that of the same molecular weight in THF and the ratio of hydrodynamic volumes of a PMMA molecule in HFIP and THF becomes higher at higher molecular weight than lower one. The plots of hydrodynamic volume $[\eta]M$ vs V_R in HFIP (by using the

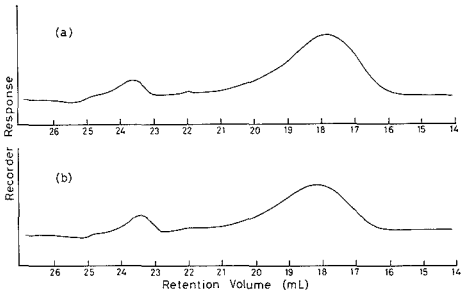

Figure 6. SEC chromatograms of PET samples: (a) $\bar{M}_n$ = 13 000, (b) $\bar{M}_n$ = 8300; detector attenuation, ×4.

values of a and K in TFE) and in THF were similar, indicating our assumption is positive. The values of K and a for PMMA in HFIP may be obtained by a separate experiment and are discussed elsewhere. However, there was still a small divergence between both plots in the high molecular weight region and the early elution of PMMA in HFIP due to the ion-exclusion effect cannot be ignored, even though the small addition of sodium trifluoroacetate in HFIP did not make any change in the shape of chromatogram for PMMA.

Determination of PET. SEC chromatograms of several PET samples were determined and examples are shown in Figure 6. PET in HFIP was very stable, though HFIP is slightly acidic, and there was no change in chromatograms or in the values of calculated molecular weight averages after leaving the PET solution for 3 months. A broad peak after retention volume 23 mL was due to the solvent HFIP and it appeared every time even when only HFIP was injected.

PMMA equivalent molecular weight averages of PET samples were calculated by using a PMMA calibration curve (Figure 5). The term correction factor f is designated as

$$f = \frac{\bar{M}_n \text{ obtained by the end-group titration method}}{\text{PMMA equivalent } \bar{M}_n} \quad (4)$$

Therefore, PMMA equivalent molecular weight averages are converted to real PET molecular weight averages by multiplying f to PMMA equivalent molecular weight averages. PMMA equivalent molecular weight averages, number average molecular weights obtained by the end-group titration method, and correction factors f of PET samples are listed in Table I.

For the correction factor f concept to be valid, it is necessary to make sure that the PET is a linear homopolymer with no short or long chain branches. Among several side reactions during the condensation–polymerization of PET, incorporation of diethylene glycol terephthalate units is well-known and the percentages of diethylene glycol in PET were ranging between 0.6% and 3.6% (*10*). Copolymerization with diethylene glycol of this amount may not influence the validity of the correction factor method. Two or more types of diacid and/or diol have frequently been incorporated into a given polyester to optimize its properties (*11*). Besides this incorporation, the author has never seen any reports on short or long chain branches in PET in the literature. Comparative experiment of $\bar{M}_n$ values for several other PET samples by end group titration with the SEC correction factor method is needed to say that the correction factor method is valid. However, since the correction factor f only varies from 0.54 to 0.58 over a range of molecular weight tested, it can be concluded that the correction factor method proposed here appears quite valid.

The higher molecular weight part of an SEC chromatogram affects the value of weight average molecular weight and the lower molecular weight part affects number average molecular weight. The absence of the data for the PMMA calibration curve after retention volume 21 mL affects the accuracy and the precision of the value of $\bar{M}_n$. The calibration curve between 21 mL and 22.9 mL, which was equivalent to retention volume of acetone, was obtained by intrapolation. The accuracy of number average PMMA equivalent molecular weights may decrease by this reason and therefore, one or two more characterized PMMA standards of different molecular weight range should be incorporated to span the entire retention volume range of interest. As benzene molecules adsorbed on the column when HFIP was the mobile phase, acetone was used as the probe for the estimation of column efficiency. Retention volume of benzene when THF was the mobile phase was 23.6 mL and that of acetone was 23.0 mL, respectively. Acetone can be used as a probe when THF is the mobile phase, but the response of an RI detector for acetone was worse than that for a benzene probe.

Table I. Molecular Weight Averages of PET Samples and Correction Factor f

	molecular weight average					
	PMMA equivalent		other method[a]	correction	corrected mol wt av[b]	
sample	$\bar{M}_w$	$\bar{M}_n$	$\bar{M}_n$	factor f	$\bar{M}_w$	$\bar{M}_n$
1	37 600	22 500	13 000	0.58	21 430	12 820
2	25 800	14 900	8 300	0.56	14 700	8 490
3	13 300	8 640	5 000	0.58	7 580	4 920
4	9 320	4 450	2 400	0.54	5 310	2 530
av				0.57		

[a] Obtained by the end-group titration method. [b] Average f × PMMA equivalent molecular weight.

Flow rate fluctuation also affects the accuracy and the precision of the values of molecular weight. However, the pumping system employed here was very reliable and the precision of flow rate was below 0.04%. For example, flow rate was measured on seven consecutive days by filling the effluent from the column into a measuring flask of 10 mL and reading the time required to fill it with the solvent. The range of the flow rate was 0.5012 and 0.5019 mL/min, average was 0.5015 mL/min, and average deviation was 0.0002 mL/min. The flow rate after 1 month was almost unchanged. Therefore, the effect of flow rate fluctuation on the value of molecular weight averages is concluded to be negligible in our work.

After the mobile phase was changed in the SEC columns from THF to HFIP, the value of N was slightly decreased as described in the Experimental Section. Lifetime of the columns after the solvent change was more than one year. According to the manufacturer's information, the change of solvent in the columns from THF to HFIP is possible without any damage in the column efficiency, but the reverse change back to THF should be avoided.

HFIP is a very expensive solvent; the price is $560 (¥70 000) per 1 kg. Specific gravity of HFIP is 1.59 and the price per 1 L is therefore $890 (¥111 300). The volume of HFIP required to measure one chromatogram is at least 26 mL, costing $23 (¥2900). It usually requires more volume because of loss of HFIP during the experiment. Recycling of the solvent reduces the cost. Therefore, the effluent from the columns was collected and distilled for reuse. The initial volume of HFIP was 2 L and after 144 measurements, the volume of HFIP was 1 L. Therefore, the consumption of HFIP per one measurement was 6.9 mL and the cost was reduced to $5.80 (¥733). Distillation was repeated 10 times.

ACKNOWLEDGMENT

The author is grateful to Akihiro Nishimuar for his technical assistance.

LITERATURE CITED

(1) Mori, Sadao *Anal. Chem.* **1983**, *55*, 2414–2416.
(2) Overton, J. R.; Rash, J.; Moor, L. D., Jr. Sixth International GPC Seminar Proceedings, Miami Beach, FL, 1968, 422–432.
(3) Paschke, E. E.; Bidlingmeyer, B. A.; Bergmann, J. G. *J. Polym. Sci., Polym. Chem. Ed.* **1977**, *15*, 983–989.
(4) Uglea, C. V.; Aizicovici, A.; Mihaescu, S. *Eur. Polym. J.* **1985**, *21*, 677–679.
(5) Berkowitz, Steven *J. Appl. Polym. Sci.* **1984**, *29*, 4353–4361.
(6) Drott, E. E. *Liquid Chromatography of Polymers and Related Materials*; Cazes, Jack, Ed.; Chromatographic Science Series Vol. 8, Marcel Dekker: New York, 1976; pp 41–50.
(7) Hibi, Kiyokatsu; Wada, Akio; Mori, Sadao *Chromatographia* **1986**, *11*, 635–641.
(8) Provder, Theodore; Woodbrey, James C.; Clark, James H. *Sep. Sci.* **1971**, *6*, 101–136.
(9) Mori, Sadao *Anal. Chem.* **1981**, *53*, 1813–1818.
(10) Janssen, R.; Ruysschaert, H.; Vroom, R. *Makromol. Chem.* **1964**, *35*, 153–158.
(11) Russell, G. A.; Henrichs, P. M.; Hewitt, J. M.; Grashof, H. R.; Sandhu, M. A. *Macromolecules* **1981**, *14*, 1764–1770.

RECEIVED for review December 7, 1988. Accepted March 13, 1989.

Gas Chromatographic Determination of Water Using 2,2-Dimethoxypropane and a Solid Acid Catalyst

Kevin D. Dix, Pamela A. Sakkinen, and James S. Fritz*

Ames Laboratory—U.S. Department of Energy and Department of Chemistry, Iowa State University, Ames, Iowa 50011

The amount of water in various organic and inorganic substances is determined by reaction with 2,2-dimethoxypropane (DMP), followed by measurement of a product of the reaction (acetone) by capillary column gas chromatography. The reaction of water with DMP requires only 5 min when Nafion is used as a solid acid catalyst. Various experimental parameters are investigated to optimize the analytical procedure. The percentage of water in a variety of analytical samples was determined successfully.

INTRODUCTION

The determination of small amounts of water in various organic and inorganic compounds is of great practical importance. The Karl Fischer method (*1*) is perhaps the most widely used procedure for the determination of water. Although this method works well in many cases, the commercial reagents are rather costly, the visual titration end point is difficult to discern, and there are numerous interferences.

Although water can be determined directly by gas chromatography using a thermal conductivity detector (TCD) (*2*), surprisingly few laboratories seem to use this approach. Furthermore, a packed column rather than a capillary GC column must be used because of the large cell volume of the traditional TCD.

A few authors have used the acid-catalyzed hydrolysis of 2,2-dimethoxypropane (DMP), the dimethyl ketal of acetone, as a way to determine water.

$$CH_3C(OCH_3)_2CH_3 + H_2O \xrightarrow{H^+} CH_3COCH_3 + 2CH_3OH$$

Critchfield and Bishop (*3*) determined water by reaction with DMP in the presence of methanesulfonic acid and measured the acetone formed by infrared spectroscopy at 5.75 μm. Hager and Baker (*4*) made a cursory investigation of the use of DMP for the indirect GC determination of water. Martin and Knevel (*5*) proposed a quantitative method for water by reaction with DMP and measurement of the change in height of the GC peaks of DMP and acetone. The method required accurate weighing of both DMP and acetone, as well as the sample itself, and the sensitivity of the method was somewhat limited. Blanco et al. (*6*) used a somewhat similar method for determining water in nitroglycerin–nitrocellulose pastes by GC.

In the present method the sample is combined with a solution containing DMP and an internal standard. A small amount of Nafion (*7*) is added to catalyze the reaction of water with the DMP. Then an aliquot is injected into a gas chromatograph equipped with a capillary column and a flame ionization detector. The amount of water is calculated from the ratio of the peak areas (or peak heights) of the acetone and internal standard. The method is both sensitive and convenient; it has been applied successfully to a wide variety of analytical samples.

EXPERIMENTAL SECTION

Glassware and Apparatus. The reactions were carried out in 5-mL glass microreaction vessels fitted with Teflon-lined septa (Supelco Glass Co., Bellefonte, PA).

Reagents and Chemicals. The 2,2-dimethoxypropane was obtained either from Aldrich Chemical (Milwaukee, WI) or from Eastman Kodak Chemical (Rochester, NY). Nafion 1100 EW resin (60–100 mesh) was purchased from C. G. Processing, Inc., (Rockland, NY) and was dried at 100 °C for 3 h under vacuum before use. Amberlyst-15 resin was obtained from Rohm and Haas (Philadelphia, PA) and dried as above. All other reagents were of reagent grade or better and were "blanked" before use. Distilled water was further purified with the Barnstead Nanopure II system before use.

Gas Chromatography. A Hewlett-Packard 5790A gas chromatograph equipped with a flame ionization detector (FID) was used in the split mode. The split ratio was 80–100:1 and was held constant during a series of experiments. The injection liner was packed with a small amount of 80–100-mesh silanized glass beads to prevent contamination of the column with nonvolatile components. The beads were changed periodically, and the injector was held at 150 °C. Two different carrier gas flow rates were used in this study. Initially, a flow of 2.5 mL/min of zero grade He was used with an oven profile of 5.2 min at 40 °C. Later, it was found that a flow rate of 5.0 mL/min and an oven profile of 2.2 min at 40 °C provided adequate resolution and decreased the analysis time. In each case, the oven temperature was stepped to 220 °C after the initial hold at 40 °C. This rapid increase in temperature served to remove any later-eluting peaks in less than 5 min. The column was a 30 m × 0.53 mm J+W DB-5 Megabore with a film thickness of 1.5 μm. The detector was an FID held at 250 °C.

Reactant Solution. A reactant solution was prepared in a dry 100-mL volumetric flask from a 5-mL aliquot of DMP and

0003-2700/89/0361-1325$01.50/0

a 1-mL aliquot of 3-methylpentane, the internal standard, and diluted to the mark with pure solvent. This solution permitted a simple one-step addition of the necessary chemicals. Both ethyl acetate and dimethylformamide were used as the solvent with no problems.

Standardization. Internal standardization was used (*8*). This method allows for small differences in the injected volume. First, the reactant solution was chromatographed to determine the amount of initial acetone present. Then 10 μL of acetone was added, and the solution was chromatographed again. By subtraction of the initial acetone, a response factor can be calculated. Since this factor varies only very slightly during a day, it is only necessary to do this periodically.

Procedure. The required amount of Nafion resin was weighed into the reaction vessel, which was then capped. Then 1 mL of the reactant solution was added to the vessel via syringe to minimize uptake of water from the atmosphere. The vessel was shaken for a specific length of time and a 1-μL aliquot injected into the gas chromtograph. The area of the acetone peak represents the water blank of the system. Next, a specific amount of liquid sample was introduced via syringe, or solid was added to the reaction vessel. The mixture was shaken again for a specific length of time, and a 1-μL aliquot was introduced into the gas chromatograph.

A ratio of peak areas of acetone to internal standard is calculated. This ratio, minus the blank, yields a relative response to acetone generated from the reaction of water in the sample. From the response factor previously determined for acetone, a value for the absolute amount of acetone is found. This value is easily converted to the amount of water by considering the stoichiometry of the reaction and the molecular weights of acetone and water:

$$W_W = \text{weight of water}$$

$$W_A = \text{weight of acetone}$$

$$W_W = W_A \times \frac{\text{1 mol of water}}{\text{1 mol of acetone}} \times \frac{\text{MW of water}}{\text{MW of acetone}}$$

RESULTS

Time of Reaction. The reaction vessel containing 1 mL of reactant solution, 2 mL of ethyl acetate, and 12 mg of Nafion was shaken, and aliquots were taken at various time periods for gas chromtographic analysis. The acetone peak attains its maximum height after 5 min, and its height remains constant between 5 and 45 min of reaction time. From these results, 5 min was selected as the optimum reaction time for the determination of water.

A similar experiment was performed using 12 mg of Amberlyst-15 cation-exchange resin instead of Nafion as the acid catalyst. The curve requires approximately 25 min to reach the plateau region. This experiment shows Nafion to be a superior catalyst.

Amount of Nafion Resin. Using the reaction conditions above, we varied the amount of Nafion catalyst. It was determined that at least 6 mg of Nafion was needed to reach the maximum height of the acetone peak within 5 min. For all remaining determinations of water at least 10 mg of Nafion was added as the catalyst.

Calibration Curves. In the reaction system used it is necessary to know the range over which water can be determined and whether the formation of acetone is linear over this range. A nonlinear response indicates the possibility of a side reaction or the loss of acetone by other means. A 2-mL portion of dried ethyl acetate was added to 1 mL of the reactant solution and 12 mg of Nafion as before, and the amount of water in this blank was determined from the area of the acetone peak. Then a small amount of water was added via a 0.5-μL syringe, and the amount of water now present was determined chromatographically. This procedure was repeated until there was no further increase in the amount of acetone generated from the reaction. Figure 1 shows the relative response of acetone as a function of the amount of water added. The response is linear up to about 0.275% water (v/v). At this point all of the DMP is consumed and the formation of acetone ceases. This point agrees with the point that can be calculated from the amount of DMP that was initially added. The correlation coefficient for the linear portion is 0.9995. Extrapolation of this line to zero relative response and subtracting the blank yield the amount of water in the 2-mL sample of ethyl acetate. This value, 0.047% (v/v), agrees closely with 0.045% found by using the internal standardization method.

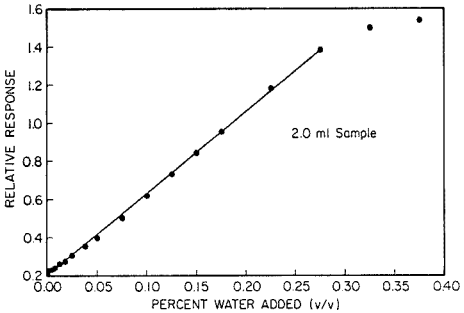

Figure 1. Relative response of acetone for the addition of increasing amounts of water in a 2.0-mL sample of ethyl acetate. Other conditions are given in the text.

A similar series of experiments were performed with samples containing higher percentages of water. This is done by simply reducing the size of the sample. Only a 0.20-mL sample of ethyl acetate was used, and the water additions were similar to those before. A straight-line response is obtained for up to 2.75% water in the sample. The correlation coefficient for this line is 0.9991. Although the experiment was not performed, it seems that virtually any amount of water, even up to 100%, can be determined just be reducing the sample size.

Since methanol is also produced in this reaction, its peak area can also be plotted. The correlation coefficient for such a plot from these data is 0.9963. Similarly, the decrease in the DMP peak was monitored with a correlation coefficient of 0.9973.

Reproducibility. The reproducibility of the indirect GC method was estimated by independently determining the amount of water in six 2-mL samples of tetrahydrofuran. The mean of the six samples was 0.0523% water with a standard deviation of 0.0015%. This corresponds to a relative standard deviation of 2.8%. The relative standard deviation of the blank alone was 1.2% for the six runs.

Limit of Detection. The limit of detection of water by the indirect GC procedure is apt to depend more on external factors than on the measurement method itself. Thus the detection limit depends to a major extent (a) on the ability to dry and keep dry Nafion, reactant solution, and glassware and (b) on avoiding adding water during transport or weighing. It is this "extra" water that makes up the blank. There are larger variances associated with a larger blank, and these inevitably result in a higher limit of detection.

By careful handling and by drying the components of the reactant solution over calcium hydride and drying the Nafion at 110 °C, we were able to determine as low as 0.001% water in various samples.

Determination of Water in Various Samples. Water in several organic liquids was determined both by the gas chromatographic method and by the well-known Karl Fischer (KF) method (see Table I). The KF solution was standardized just before use, and the titrations were performed in triplicate. The end point in the Karl Fischer titration is often difficult to determine visually, and in some cases precipitation

Table I. Comparison of Water Determination by Indirect GC and by Karl Fischer Titration

compound	% water (w/w)	
	GC method	KF titration
ethyl acetate	0.059	0.056
tetrahydrofuran	0.0355	0.0361
dimethylformamide	0.0075	0.0074
methylene chloride	0.0121	0.0142
dioxane	0.489	0.479

Table II. Determination of Water in Liquid and Solid Samples

compound	sample size, mL	% water (w/w)	water spikes, mg	
			added	found
	Liquid Samples			
methylene chloride	2.00	0.0121	0.50	0.51
toluene	2.00	0.0186	0.50	0.49
ethyl acetate	2.00	0.2309	0.50	0.58
1,1,2-trichlorotrifluoroethane	2.00	0.0030	0.50	0.48
"dry" ethyl acetate	2.00	0.0064	0.50	0.43
methyl ethyl ketone	2.00	0.4078	0.50	0.58
carbon disulfide	2.00	0.0029	0.40	0.37
anisole	2.00	0.0127	0.40	0.41
tetrahydrofuran	2.00	0.0800	0.50	0.50
1-propanol	0.05	3.0707	0.50	0.53
	Solid Samples			
oxalic acid dihydrate (28.6% H_2O)	10	30.1	0.40	0.39
phenol	50	0.701	0.40	0.39

occurred, which made the end point even more difficult to locate. Despite these difficulties, good agreement was obtained between the percentages of water determined by the two methods.

Several liquid and solid samples were analyzed for water by the GC method. Then a measured amount of additional water was added to each sample, and the total amount of water present was determined by the GC method. Table II gives results for the percentages of water in the original samples, the amounts of water added, and the amounts of added water found by the GC method. The excellent recoveries of added water demonstrate that the new GC method gives dependably accurate results for a wide variety of samples.

Samples containing even a small amount of ascorbic acid cannot be titrated by the Karl Fischer method. However, no difficulty is encountered when the indirect GC method is used. This was demonstrated in two ways. First, a 2-mL sample of dimethylformamide was analyzed for water by the GC method before and after addition of 20.0 mg of ascorbic acid. Second, the amount of water in 20.0 mg of ascorbic acid was determined by the regular GC method. In both cases the amount of water in the ascorbic acid was 0.026% (w/w).

DISCUSSION

It might be expected that samples containing high-boiling or nonvolatile components could not be analyzed for water by a GC method because of irreversible adsorption on the chromatographic column. However, our experiments indicate that this is not the case with the present method. Use of a capillary column means that a smaller sample is injected than in previous methods in which a packed GC column was employed. Insertion of glass wool and silanized glass beads seems to adsorb the nonvolatile sample components while allowing acetone to pass quantitatively onto the column. A rapid temperature increase at the end of a chromatographic run serves to remove any high-boiling compounds that might be retained by the column.

The absolute amount of water that can be determined in this procedure could obviously be increased by adding a larger amount of DMP to the sample. However, this could increase the blank and reduce the accuracy in samples containing a low percentage of water. It is also likely that other acetals or ketals could be used in place of DMP for the determination of water.

Registry No. DMP, 77-76-9; H_2O, 7732-18-5; Nafion, 39464-59-0; dimethylformamide, 68-12-2; dioxane, 123-91-1; methylene chloride, 75-09-2; toluene, 108-88-3; ethyl acetate, 141-78-6; 1,1,2-trichlorotrifluoroethane, 76-13-1; methyl ethyl ketone, 78-93-3; carbon disulfide, 75-15-0; anisole, 100-66-3; tetrahydrofuran, 109-99-9; 1-propanol, 71-23-8; oxalic acid dihydrate, 6153-56-6; phenol, 108-95-2.

LITERATURE CITED

(1) Scholz, E. *Karl Fischer Titration*; Springer-Verlag: Berlin, 1984.
(2) Mitchell, J., Jr.; Smith, D. M. *Aquametry*; Wiley-Interscience: New York, 1977.
(3) Critchfield, F. E.; Bishop, E. T. *Anal. Chem.* **1961**, *33*, 1034.
(4) Hager, M.; Baker, G. *Proc. Mont. Acad. Sci.* **1962**, *22*, 3.
(5) Martin, J. H.; Knevel, A. M. *J. Pharm. Sci.* **1965** *54*, 1464.
(6) Blanco, J. A.; Rucci, A. O.; Revuelto, S. C.; Dubini, A. A.; Gonzalez, R. A. *Propellants Explos.* **1979**, *4*, 27.
(7) *Polymeric Reagents and Catalysts*; Ford, W. T., Ed.; ACS Symposium Series 308; American Chemical Society: Washington, DC, 1986; p 42.
(8) Debbrecht, F. J. *Modern Practice of Gas Chromatography*, 2nd ed.; Grob, R. L., Ed.; Wiley: New York, 1985.

RECEIVED for review October 4, 1988. Revised March 15, 1989. Accepted March 28, 1989. Ames Laboratory is operated for the U.S. Department of Energy under Contract No. W-7405-ENG-81. This work was supported by the Director of Energy Research, Office of Basic Energy Sciences, and by a research fellowship from Phillips Petroleum Co., Bartlesville, OK. Portions of this paper were presented at the 30th Rocky Mountain Conference, Denver, CO, August 1988.

Anal. Chem. 1989, 61, 1328-1332

Computer-Assisted Prediction of Gas Chromatographic Retention Indices of Pyrazines

David T. Stanton and Peter C. Jurs*

152 Davey Laboratory, Penn State University, University Park, Pennsylvania 16802

The gas–liquid chromatographic retention indices for 107 substituted pyrazines on OV-101 and Carbowax-20M are successfully modeled with the aid of a computer and the ADAPT software system. Structural descriptors are calculated and multiple linear regression analysis methods are used to generate model equations relating structural features to observed retention characteristics. Separate equations are found to be necessary in order to accurately predict the retention indices for the same set of compounds on the two different stationary phases. Comparisons are made between models generated for the two stationary phases, and descriptors that may encode differences in solute interactions with stationary phases of differing polarity are discussed.

INTRODUCTION

Alkoxy- and alkylthiopyrazines are known for their characteristic flavoring properties. These compounds have been found in roasted nuts and beans and a variety of other cooked vegetables (*1*). They have been reported to possess a variety of odors such as that of bell pepper (*2*) and licorice-woody odor (*3*). In studies of these materials, identification of a compound is often accomplished on the basis of gas chromatographic peak comparisons with an authentic standard of the suspected material. However, it is not always possible to obtain samples of the pure standard materials for such comparisons. It is then desirable to develop methods for the prediction of retention characteristics of the unknown based on the structural features and chromatographic properties of other representative compounds on hand. Mihara and Enomoto have reported such a structure–property relationship for a set of substituted pyrazines in which retention index increments corresponding to various ring substituents were determined for a small series of substituents and the parent (unsubstituted) pyrazine (*4*). Retention index values for new compounds were then calculated by summing the necessary increment values for the substituents present. The method was later expanded to include additional substituents and to add a term that encoded the relative position of one substituent to others on the ring (*5*). In a related approach, Masuda and Mihara described the use of modified molecular connectivity indices (*6*) to predict gas chromatographic retention indices for a series of substituted pyrazines. These methods yield good results providing that the experimentally determined index increments for all the substituents for the unknowns involved are available. A primary disadvantage of such approaches is that retention indices cannot be predicted for compounds containing substituents other than those available in the table of index increments. In addition, little insight concerning the physical processes involved in the separation can be gained through the examination of the independent variables in the resulting equations.

The goal of the present work is to employ computer-assisted methods to develop model equations relating structural features of substituted pyrazines to their observed retention indices and to learn how differences in the models may describe polarity differences between two stationary phases. The predictive models are generated through multiple linear regression analysis of calculated structural descriptors which encode topological, geometrical, electronic, and physical properties of the solute molecules in question. Such models are termed quantitative structure–retention relationships (QSRR). The derivation of such relationships and the definitions of several typical descriptors have been described by Kaliszan (*7*) and have been employed in studies related to that reported here (*8*, *9*). An advantage of the QSRR approach is that the equations generated allow for the prediction of retention indices for compounds which are structurally similar to those used to develop the model but which were not specifically represented in the training set. Another advantage is that differences in models developed for the same compounds on stationary phases of differing polarity may provide insight as to which structural features of the molecules may be responsible for polar interactions with stationary phases. Also, use of a computer allows for the rapid and facile input of the structures of the compounds being studied, calculation and subsequent analysis of descriptors, and the generation and validation of the model regression equations.

EXPERIMENTAL SECTION

The procedure used in the current study is outlined in the flow diagram shown in Figure 1. All computations were performed by using the Penn State University Chemistry Department's PRIME 750 computer running the ADAPT software system (*10*, *11*).

The Data Set. The compounds involved in this study have the general structure I.

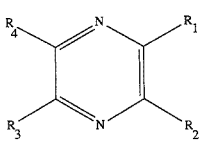

I

R_1 : H, alkyl, alkoxy, alkylthio, aryloxy, arylthio, acetyl, chloro.

R_2 : H, alkyl, chloro.

R_3 : H, alkyl.

R_4 : H, alkyl.

The retention data for the compounds chromatographed on the OV-101 and Carbowax-20M stationary phases were taken from Mihara and Masuda (*5*) and are listed in Table I. Of the 114 pyrazines included in their study, two were not included in the present study. Of the remaining 112 compounds, two had not been analyzed on both columns. Both of these were retained but were only included in the modeling process for the stationary phase on which they had been analyzed. This yielded a final data set of 111 compounds for each stationary phase.

Structure Entry. The hydrogen-suppressed structural diagrams of all the compounds were entered into the computer by sketching them on a graphics terminal, followed by storage in connection tables. Bond lengths and angles were corrected to

0003-2700/89/0361-1328$01.50/0

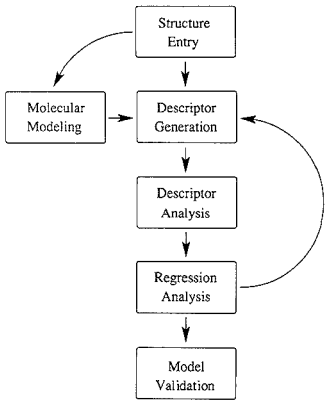

Figure 1. Procedure flow diagram for development of retention index prediction models.

standard values, and the structures were placed in energy-minimized conformations using molecular mechanics calculations.

Descriptor Generation. A total of 85 separate molecular structure descriptors were calculated for the entire set of 112 pyrazines. These descriptors can be separated into four categories: topological, geometric, physical, and electronic. The topological descriptors included path counts and molecular connectivity indices. Geometric descriptors included shadow areas (*12*), length to breadth ratios, van der Waals volumes, surface area, and principal moments of inertia. Calculated physical property descriptors included molecular polarizability and molar refractivity. The electronic descriptors included the most positive and most negative σ charges in the molecule and the submolecular polarity parameter (Δ) described by Kaliszan (*7*).

Once the descriptors were generated, the process of objective descriptor (feature) selection was initiated. The descriptors were examined, and those exhibiting high pairwise correlations to other descriptors and those values that were identical for the majority of the data set or were predominantly zero were discarded. This was done because such descriptors encode little discriminating information. In the case of high pairwise correlations, those descriptors that were easy to calculate or that possessed direct physical meaning, were retained. The remaining 45 descriptors were then examined by using a vector space analysis method to select a subset of 30 to 35 descriptors that are the most orthogonal to each other. The process of orthogonalization is accomplished by selecting as the initial basis vector a descriptor that is highly correlated to the dependent variable. The next descriptor chosen is one that yields the largest projection angle to the initial basis vector, forming a plane in the vector space. The next descriptor is chosen that has the largest projection angle to the plane formed by the first two, and so on, until a subset of the desired size has been selected. This reduction prior to regression analysis was necessary to minimize information overlap between descriptors and to reduce the possibility of chance correlations (*13*). A limiting ratio of five objects (compounds) to each descriptor is typical. Since the feature selection procedure, for the most part, ignores the dependent variable, in this case the retention index, the same final subset of descriptors was available for regression analysis for each stationary phase.

Regression Analysis. Variable selection was performed by using the method of multiple regression by progressive deletion (*14*). Linear models are formed by a stepwise addition of terms where inclusion of terms is based on F statistic values. A deletion process is then employed where each variable in the model is held out in turn and a model is generated by using the remaining pool of descriptors. Then each combination of two, three, and so on, descriptors are held out, followed by model generation. This combination of steps has the effect of uncovering potentially superior equations that may have been otherwise obscured by the existence of a descriptor which is highly correlated to the dependent variable. A final set of selected equations were then tested for stability and validity through a variety of statistical methods.

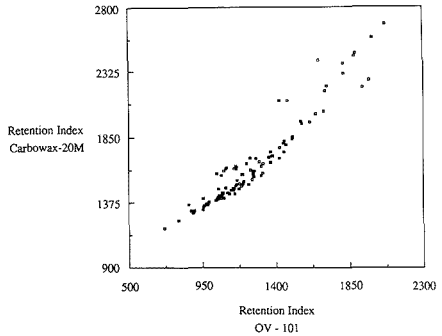

Figure 2. Plot of the correlation of retention indices for pyrazines on OV-101 and Carbowax-20M.

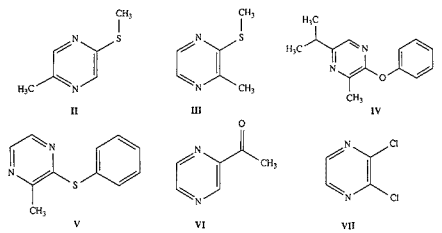

Figure 3. Structural diagrams of the six compounds identified as outliers.

RESULTS AND DISCUSSION

The retention indices for the two stationary phases were compared, yielding a correlation coefficient (R) of 0.951. A plot of the comparison of observed retention on Carbowax-20M versus observed retention on OV-101 is given in Figure 2. Results of initial experiments identified six of the 112 compounds as outliers. The structures of the six compounds are shown in Figure 3. The criterion for identifying a compound as an outlier was that compound being flagged by three or more of six standard statistical tests used to detect outliers in regression analysis. These tests were (1) residual, (2) standardized residual, (3) Studentized residual, (4) leverage, (5) DFFITS, and (6) Cook's distance (*15*). The residual is the difference between the actual value and the value predicted by the regression equation. The standardized residual is the residual divided by the standard deviation of the regression equation. The Studentized residual is the residual of a prediction divided by its own standard deviation. Leverage allows for the determination of the influence of a point in determining the regression equation. DFFITS describes the difference in the fit of the equation caused by removal of a given observation, and Cook's distance describes the change in a model coefficient by the removal of a given point. Since it was undesirable to assign too much weight to any one of these tests, the criterion of any combination of three of the tests to indicate a given compound as an outlier was used. For each stationary phase, four compounds were identified as outliers, with two of the six compounds being outliers common to both phases. No specific reason could be determined to explain why these six compounds act as outliers. They are not structurally unique, and the final conformational energies, as calculated by using the molecular mechanics programs, were found to be reasonable as compared to the rest of the data set. The outliers were dropped from consideration in sub-

Table I. Experimentally Determined Retention Indices for Pyrazines on OV-101 and Carbowax-20M[a]

name	OV-101	CW-20M	name	OV-101	CW-20M
pyrazine	710	1179	3-methyl-2-methoxy-5-(2-methylpentyl)pyrazine	1444	1737
methylpyrazine	801	1235	ethoxypyrazine	959	1348
2,3-dimethylpyrazine	897	1309	2-ethoxy-3-methylpyrazine	1029	1385
2,5-dimethylpyrazine	889	1290	2-ethoxy-5-methylpyrazine	1047	1418
2,6-dimethylpyrazine	889	1300	2-ethoxy-3-ethylpyrazine	1101	1439
trimethylpyrazine	981	1365	2-ethoxy-3-isopropylpyrazine	1143	1431
tetramethylpyrazine	1067	1439	2-ethoxy-5-isopropyl-3-methylpyrazine	1230	1500
ethylpyrazine	894	1300	2-ethoxy-5-isobutyl-3-methylpyrazine	1314	1584
2-ethyl-5-methylpyrazine	980	1357	5-*sec*-butyl-2-ethoxy-3-methylpyrazine	1306	1566
2-ethyl-6-methylpyrazine	977	1353	2-ethoxy-3-methyl-5-(2-methylbutyl)pyrazine	1415	1693
2,5-dimethyl-3-ethylpyrazine	1059	1400	2-ethoxy-3-methyl-5-(2-methylpentyl)pyrazine[c]	0	1771
2,6-dimethyl-6-ethylpyrazine	1064	1415	(methylthio)pyrazine	1076	1600
2,3-dimethyl-5-ethylpyrazine	1066	1421	3-methyl-2-(methylthio)pyrazine	1151	1616
2,3-diethylpyrazine	1065	1417	5-methyl-2-(methylthio)pyrazine[d]	1163	0
2,3-diethyl-5-methylpyrazine	1137	1459	3-ethyl-2-(methylthio)pyrazine	1237	1695
propylpyrazine	986	1374	3-isopropyl-2-(methylthio)pyrazine	1273	1692
2-methyl-3-propylpyrazine	1072	1438	5-isopropyl-3-methyl-2-(methylthio)pyrazine	1362	1737
2,3-dimethyl-5-propylpyrazine	1154	1500	5-*sec*-butyl-3-methyl-2-(methylthio)pyrazine	1441	1800
2,5-dimethyl-3-propylpyrazine	1142	1474	5-isobutyl-3-methyl-2-(methylthio)pyrazine	1446	1816
2,6-dimethyl-3-propylpyrazine	1151	1493	3-methyl-5-(2-methylbutyl)-2-(methylthio)pyrazine	1552	1941
isopropylpyrazine	949	1316	3-methyl-5-(2-methylpentyl)-2-(methylthio)pyrazine	1638	2008
2,3-dimethyl-5-isopropylpyrazine	1112	1431	(ethylthio)pyrazine	1148	1635
butylpyrazine	1088	1474	2-ethylthio-3-methylpyrazine	1215	1655
2-butyl-3-methylpyrazine	1121	1459	2-ethylthio-5-isopropyl-3-methylpyrazine	1418	1769
3-butyl-2,5-dimethylpyrazine	1184	1487	5-*sec*-butyl-2-ethylthio-3-methylpyrazine	1494	1832
3-butyl-2,6-dimethylpyrazine	1196	1514	2-ethylthio-5-isobutyl-3-methylpyrazine	1496	1843
5-butyl-2,3-dimethylpyrazine	1254	1600	2-ethylthio-3-methyl-5-(2-methylbutyl)pyrazine	1602	1951
isobutylpyrazine	1043	1406	2-ethylthio-3-methyl-5-(2-methylpentyl)pyrazine	1686	2026
2,3-dimethyl-5-isobutylpyrazine	1200	1525	phenoxypyrazine	1415	2104
2-isobutyl-3,5,6-trimethylpyrazine	1263	1556	2-methyl-3-phenoxypyrazine	1465	2103
sec-butylpyrazine	1040	1394	5-isopropyl-3-methyl-2-phenoxypyrazine	1620	2114
5-*sec*-butyl-2,3-dimethylpyrazine	1194	1500	5-*sec*-butyl-3-methyl-2-phenoxypyrazine	1694	2173
pentylpyrazine	1192	1575	5-isobutyl-3-methyl-2-phenoxypyrazine	1706	2209
2,3-dimethyl-5-pentylpyrazine	1352	1700	3-methyl-5-(2-methylbutyl)-2-phenoxypyrazine	1807	2301
isopentylpyrazine	1157	1530	(phenylthio)pyrazine	1606	2400
2,3-dimethyl-5-isopentylpyrazine	1317	1655	3-methyl-2-(phenylthio)pyrazine	1658	2399
(2-methylbutyl)pyrazine[b]	1151	1527	5-isopropyl-3-methyl-2-(phenylthio)pyrazine	1806	2375
2,3-dimethyl-5-(2-methylbutyl)pyrazine	1306	1636	5-*sec*-butyl-3-methyl-2-(phenylthio)pyrazine	1874	2430
2-(2-methylbutyl)-3,5,6-trimethylpyrazine	1363	1661	5-isobutyl-3-methyl-2-(phenylthio)pyrazine	1882	2452
(2-methylpentyl)pyrazine	1240	1606	3-methyl-5-(2-methylbutyl)-2-(phenylthio)pyrazine	1985	2569
(2-ethylpropyl)pyrazine[b]	1121	1449	3-methyl-5-(2-methylpentyl)-2-(phenylthio)pyrazine	2064	2669
(1-methylbutyl)pyrazine	1133	1471	acetylpyrazine	993	1571
2,3-dimethyl-5-(2-methylpentyl)pyrazine	1377	1710	2-acetyl-3-methylpyrazine	1061	1567
hexylpyrazine	1293	1668	2-acetyl-5-methylpyrazine	1093	1625
octylpyrazine	1495	1845	2-acetyl-6-methylpyrazine	1088	1618
2-methyl-3-octylpyrazine	1546	1956	2-acetyl-3-ethylpyrazine	1138	1617
2-methyl-5-(2-methylbutyl)-3-octylpyrazine	1923	2200	2-acetyl-3,5-dimethylpyrazine	1153	1629
2-methyl-6-(2-methylbutyl)-3-octylpyrazine	1962	2254	chloropyrazine	861	1351
methoxypyrazine	877	1306	2,3-dichloropyrazine	1032	1581
2-methoxy-3-methylpyrazine	954	1339	2-chloro-3-methylpyrazine	951	1399
2-methoxy-5-methylpyrazine	969	1358	2-chloro-3-ethylpyrazine	1044	1467
3-ethyl-2-methoxypyrazine	1037	1400	2-chloro-3-isobutylpyrazine	1187	1575
3-isopropyl-2-methoxypyrazine	1078	1400	2-chloro-5-isopropyl-3-methylpyrazine	1173	1505
5-isopropyl-3-methyl-2-methoxypyrazine	1170	1467	5-*sec*-butyl-2-chloro-3-methylpyrazine	1256	1577
5-*sec*-butyl-3-methyl-2-methoxypyrazine	1250	1536	2-chloro-5-isobutyl-3-methylpyrazine	1264	1600
5-isobutyl-3-methyl-2-methoxypyrazine	1257	1556	2-chloro-3-methyl-5-(2-methylbutyl)pyrazine	1371	1710
3-methyl-2-methoxy-5-(2-methylbutyl)-pyrazine	1362	1664	2-chloro-3-methyl-5-(2-methylpentyl)pyrazine	1456	1789

[a] Taken from ref 5. [b] Compounds not included in current study. [c] No reported retention index on OV-101. [d] No reported retention index on Carbowax-20M.

sequent work leaving a data set of 107 compounds for each stationary phase.

The models generated were of the general form

$$\mathrm{RI}\ \{\mathrm{sp}\} = b_0 + \sum_{i}^{n} b_i x_i$$

The equations generated give the retention index for a given stationary phase as the intercept (b_0) plus the sum of the product of the ith regression coefficient (b_i) and the ith independent variable or descriptor (x_i), where n is the number of independent variables in the model. Development of the models proceeded by treating each stationary phase separately.

Since the same final descriptor pool was available to the regression analysis procedure, it was of interest to see which of the descriptors were condsidered important in predicting the retention index values for each column type. The regression analysis procedure produced several reasonable equations. The choice of which equation to consider further was made by using three criteria: multiple correlation coefficient (R), standard error (s), and the number of descriptors in the model. An ideal model is one that has a high R value, a low standard error, and the fewest independent variables. The best models found for each stationary phase are given below. The definition of each descriptor is given in Table II.

Table II. Definitions of the Descriptors Used in the Retention Index Prediction Models

descriptor code	definition
ALLP-2	number of paths in the molecule between the upper and lower limits (0–45) divided by the number of atoms in the molecule
EDEN-1	most negative approximated σ electron density
FRAG-12	number of single bonds in the molecule
MOMI-1	first moment of inertia
MOMI-6	ratio of the second and third moments of inertia
MPOL	molecular polarizability
MPOS	most positive partial atomic charge in molecule
WTPT-1	molecular ID (sum of atomic IDs for the molecule[a])
WTPT-3	sum of atomic IDs for all heteroatoms in molecule
WTPT-4	sum of atomic IDs for oxygen atoms in molecule

[a] The atomic ID is the sum of all path weights for a given atom (*16*).

Table III. Correlation Matrix for the Descriptors in the Retention Index Prediction Model

a. OV-101

FRAG-12	1.000					
EDEN-1	0.045	1.000				
MOMI-6	0.769	0.164	1.000			
WTPT-1	0.673	−0.038	0.596	1.000		
WTPT-3	0.111	−0.703	−0.029	0.304	1.000	
WTPT-4	0.019	−0.802	−0.087	0.091	0.522	1.000

b. Carbowax-20M

FRAG-12	1.000					
ALLP-2	0.582	1.000				
MOMI-1	0.856	0.767	1.000			
MPOL	0.893	0.865	0.926	1.000		
WTPT-1	0.679	0.895	0.802	0.871	1.000	
MPOS	−0.041	0.066	−0.055	−0.078	0.026	1.000

The coefficient of multiple determination (R^2) indicates the amount of variance in the data set accounted for by the model. The standard error of the regression coefficient is given in each case, and n indicates the number of molecules involved in the regression analysis procedure.

OV-101:

$$\mathrm{RI} = [40.77 \pm 0.55(\mathrm{WTPT\text{-}1})] - [31.68 \pm 3.10(\mathrm{WTPT\text{-}4})] + [56.63 \pm 2.46(\mathrm{WTPT\text{-}3})] + [602.2 \pm 66.35(\mathrm{EDEN\text{-}1})] + [7.22 \pm 0.84(\mathrm{MOMI\text{-}6})] - [9.74 \pm 1.53(\mathrm{FRAG\text{-}12})] + 16.08$$

$$R^2 = 0.994 \qquad n = 107 \qquad s = 22.92$$

Carbowax-20M:

$$\mathrm{RI} = [32.58 \pm 1.43(\mathrm{WTPT\text{-}1})] - [86.23 \pm 4.57(\mathrm{ALLP\text{-}2})] - [213.5 \pm 6.9(\mathrm{FRAG\text{-}12})] + [145.7 \pm 5.8(\mathrm{MPOL\text{-}1})] + [311.4 \pm 23.0(\mathrm{MPOS})] + [(6.50 \times 10^{-2}) \pm (9.30 \times 10^{-3})(\mathrm{MOMI\text{-}1})] - 53.08$$

$$R^2 = 0.986 \qquad n = 107 \qquad s = 36.33$$

The correlation matrix for the OV-101 model and the Carbowax-20M model is given in parts a and b of Table III, respectively. The descriptors were chosen by the regression calculation in the order indicated in the models above and were based on the statistical significance of the descriptor and its utility in predicting the dependent variable.

Examination of the models shows that although the sets of descriptors availabile in regression analysis were identical for both stationary phases, some different individual descriptors were found to be important in the prediction of the retention indices. There exists some similarity in what types of descriptors (i.e. topological, geometric, or electronic) were important. Even though the compounds in the dataset contained a diverse collection of substituents, only one of the descriptors (WTPT-4) encodes information specific to one type of substituent. The remainder are broader in scope. Both models contain at least three topological descriptors. These encode information on the complexity and bonding within the molecules. The other descriptors present in the models are encoding geometric and electronic properties of the molecules, which presumably relate to the polar interactions between the solutes and the stationary phase. Predictions of retention indices for a diverse set of structures on more polar stationary phases have historically been difficult. This is evident in the somewhat poorer statistics found for the Carbowax-20M model. Even though the Carbowax-20M model contains more of the electronic/geometric types of descriptors than the OV-101 model, the descriptors used do not appear to encode enough information concerning the various polar interactions taking place during the separation. It is apparent that additional work should be done in order to find descriptors that can improve predictions on such polar phases.

An experiment was done where the experimentally determined retention index for the compounds on OV-101 were used as descriptors for prediction of retention on the more polar Carbowax-20M phase. It was postulated that any nonpolar interactions encoded in the retention indices for compounds on OV-101 could be the same as those for compounds on Carbowax-20M, and any additional structural descriptors indicated as significant by the regression analysis would therefore encode only the polar interactions. Although highly correlated, when other descriptors were available, the retention index on OV-101 is not significant in predicting retention on Carbowax-20M, and it is possible that the indices for the two phases are related in some nonlinear fashion. Similarly, when descriptors for one model were used for generating models for the other phase, the models obtained were generally poorer, indicating that the descriptors are encoding significantly different types of interactions, reinforcing the notion of modeling each type of stationary phase separately.

The next step was to test the quality of the models. Several methods exist for this purpose. First, the interrelation of descriptors used in each of the two models was examined. As shown in parts a and b of Table III, a few of the descriptors are fairly highly correlated. However, they are all below the cutoff value used in this study. A test for multicollinearities was then performed by holding each descriptor out in turn and using the remaining descriptors in the model equation as independent variables in a regression analysis attempting to predict the descriptors held out. Some fairly high multicollinearities were found, so an additional test was done to determine if these high multicollinearities affect the quality of the model equation. This was done by calculating the principal components for the data space, one for each descriptor present in the model. Principal components regression analysis was used to generate a new model equation, which was then compared to the original equation. This comparison showed the same standard error and coefficient of variance for both the original and principal components model. Also, all six principal components were retained in the regression analysis. These results indicate that any multicollinearities present in the original model do not adversely affect the quality of the equation.

The final test of the models is to determine their ability to predict the retention indices of compounds not used to generate the predictive equations. Due to the diverse nature of the data set, the method of internal validation was chosen. The descriptors used in the generation of the predictive equations were taken from the models generated for the whole

dataset. Next, 27 compounds were held out as a prediction set, while the remaining 80 compounds comprised the learning set. The prediction set compounds were chosen so as to give a subset that was statistically similar to the learning set. The learning sets for each stationary phase were then used to generate new model equations. These new equations were found to be similar to the original models. The new OV-101 model yielded an R^2 value of 0.994 and a standard error of 21.44, while the new model for the Carbowax-20M data set gave an R^2 value of 0.986 and a standard error of regression of 33.72. The new models were then used to predict the retention indices for the prediction set compounds. For the OV-101 dataset, the residual mean square (rms) error for the predictions was 32.42 (2.46%) with a correlation for predicted to experimental values of 0.996. The Carbowax-20M equation fared slightly worse with a rms error of 51.59 (2.90%) and a correlation between predicted and experimental retention indices of 0.993.

CONCLUSIONS

The computer-assisted prediction of the retention indices for a diverse set of substituted pyrazines, based on structurally derived descriptors, has been successfully demonstrated. The ability to input, manipulate, and store structures and calculated descriptors by using systems such as ADAPT increases the facility and speed with which such a study can be accomplished. Examination of the models produced shows that the descriptors encode information related to the types of interactions that take place between the solute molecules and stationary phase during the separation process. It has also shown that different descriptors become important in such predictive models as the polarity of the stationary phase is changed, and therefore each phase should be modeled separately. The predictive ability of models generated in this fashion has been shown to be accurate within a few percent of the mean retention index value, indicating that such models could be used in lieu of authentic standards for the partial identification of chromatographic peaks. The results also suggest the need for further investigation into the problem of improving predictions of retention indices for such diverse sets of compounds on the more polar phases.

ACKNOWLEDGMENT

We are grateful to G. P. Sutton for his guidance in the area of regression analysis.

LITERATURE CITED

(1) Barlin, G. B. *The Pyrazines*; Wiley-Interscience: New York, 1982.
(2) Parliment, T. H.; Epstein, M. F. *J. Agric. Food Chem.* **1973**, *21*, 714–716.
(3) Masuda, H.; Misaku, Y.; Shibamoto, T. *J. Agric. Food Chem.* **1981**, *29*, 944–947.
(4) Mihara, S.; Enomoto, N. *J. Chromatogr.* **1986**, *324*, 428–430.
(5) Mihara, S.; Masuda, H. *J. Chromatogr.* **1987**, *402*, 309–317.
(6) Masuda, H.; Mihara, S. *J. Chromatogr.* **1986**, *366*, 373–377.
(7) Kaliszan, R. *Quantitative Structure-Chromatographic Retention Relationships*; Wiley-Interscience: New York, 1987.
(8) Rohrbaugh, R. H.; Jurs, P. C. *Anal. Chem.* **1986**, *58*, 1210–1212.
(9) Hasan, M. N.; Jurs, P. C. *Anal. Chem.* **1988**, *60*, 978–982.
(10) Stuper, A. J.; Brugger, W. E.; Jurs, P. C. *Computer Assisted Studies of Chemical Structure and Biological Function*; Wiley-Interscience: New York, 1979.
(11) Jurs, P. C.; Chou, J. T.; Yuan, M. In *Computer-Assisted Drug Design*; Olson, E. C., Christoffersen, R. E., Eds.; American Chemical Society: Washington, DC, 1979; pp 103–129.
(12) Rohrbaugh, R. H.; Jurs, P. C. *Anal. Chim. Acta* **1987**, *199*, 99–109.
(13) Topliss, J. G.; Edwards, R. P. *J. Med. Chem.* **1979**, *22*, 1238–1244.
(14) Small, G. W.; Jurs, P. C. *Anal. Chem.* **1983**, *55*, 1121–1127.
(15) Belsley, D. A.; Kuh, E.; Welsch, R. E. *Regression Diagnostics*; Wiley: New York, 1980.
(16) Randic, M. *J. Chem. Inf. Comput. Sci.* **1984**, *24*, 164–175.

RECEIVED for review January 23, 1989. Accepted April 3, 1989. This work was supported by the National Science Foundation under Grant CHE85 03542. The PRIME-750 computer was purchased with partial financial support of the National Science Foundation.

Measurement of Natural Trace Dissolved Hydrocarbons by in Situ Column Extraction: An Intercomparison of Two Adsorption Resins

Mark B. Yunker,* Fiona A. McLaughlin, Robie W. Macdonald, and Walter J. Cretney

Ocean Chemistry Division, Institute of Ocean Sciences, P.O. Box 6000, Sidney, British Columbia V8L 4B2, Canada

Brian R. Fowler

Seakem Oceanography Limited, 2045 Mills Road, Sidney, British Columbia V8L 3S1, Canada

Trevor A. Smyth

C. B. Research International Corporation, P.O. Box 2010, Sidney, British Columbia V8L 3S3, Canada

Chromosorb T and XAD-2 resins are compared for the in situ extraction of alkane and polycyclic aromatic hydrocarbons (PAHs) from fresh- and seawater. In column efficiency experiments, Chromosorb T yielded higher recoveries than XAD-2 for *n*-alkanes at 3 and 0.6 ng/L concentrations per component. Chromosorb T columns gave good recoveries for PAHs of three and more rings (0.4 ng/L per component) and XAD-2 for PAHs of four and more rings (0.06 ng/L per component). Lower molecular weight PAHs were recovered poorly by Chromosorb T and contaminated by XAD-2. Principal component analysis (PCA) discriminated well between Chromosorb T and XAD-2 dissolved hydrocarbon in situ samples and their respective blanks. The PCA models could also distinguish between the groups of samples collected with each resin. Between-resin difference was more important than sampling location for hydrocarbon composition; this difference in resin adsorption characteristics shows up dramatically in the mean sample and blank plots for the hydrocarbons. The majority of blank-corrected XAD-2 alkane concentrations were below the limit of detection. In contrast, the majority of the alkanes below triacontane were quantifiable for the samples on Chromosorb T. PAHs in the phenanthrene to chrysene range gave comparable results for the two resins. The Chromosorb T in situ methodology provides the first dissolved hydrocarbon measurements that are unquestionably above the measured mean blank. With this technique individual alkanes and PAHs at pg/L concentrations in natural waters can be quantified.

INTRODUCTION

One of the most challenging tasks in analytical chemistry is the unambiguous determination of trace constituents in natural waters. For hydrocarbons, the classical technique has been the collection and extraction of bulk water samples. However, the level of contamination that may result from such bulk collections can overwhelm the natural concentrations of hydrocarbons to the extent that "many of the analytical values to be found in the older literature merely immortalize the extent of shipboard contamination" (*1*).

A more effective sampling method for dissolved trace constituents is the in situ pumping method (*1–4*). Large volumes of water are pumped through an adsorption column by a noncontaminating pumping system. The sampling apparatus can be passed through the surface microlayer before starting, and sample manipulations on the concentrated sample can take place under clean-room conditions either onboard ship or in a shore-based laboratory. The technique is limited only by the capacity of the prefilter, the backpressure of the adsorption column, and the battery supply for the pump.

To use the in situ pumping method, one must select an appropriate adsorption resin with known extraction efficiency for hydrocarbons and know the minimum volume of water required to produce a sample statistically greater than the mean blank. Polystyrene–divinylbenzene copolymer resin (XAD-2) has been widely used for the extraction of hydrocarbons from water (*4*, *5*), and the long-term stability of hydrocarbon samples on this resin has been demonstrated (*4*). However, XAD-2 does not perform well at seawater pH, and it is extremely difficult to clean and keep clean (*1*). Many aromatic impurities have been identified in the XAD-2 resin (*6*, *7*); after contact with water the cleaned resin continues to release aromatic hydrocarbons, which may then be extracted with ether (*6*). These impurities raise the detection limits and can invalidate quantitation of these compounds in water, even after thorough cleaning of the resin.

Chromosorb T porous poly(tetrafluoroethylene) (TFE) Teflon has been recommended (*8*) for the adsorption of PAHs from water. Slauenwhite et al. (*1*) found no measurable hydrocarbon blanks with it (using thin-layer chromatography with flame ionization detection) and therefore chose Chromosorb T over XAD-2 and C_{18} bonded silica gel as the preferred packing for hydrocarbons. In view of the above, we judged Chromosorb T resin to have better potential for sampling dissolved trace hydrocarbons than its leading rival, the more widely used XAD-2 resin. Gómez-Belinchón et al. (*9*) have recently reported an intercomparison study of XAD-2 with polyurethane foam and liquid–liquid extraction for the extraction of hydrocarbons from seawater.

This work is part of the hydrocarbon method development and technique validation performed prior to carrying out a large sampling program in the Canadian Beaufort Sea and Mackenzie Estuary during 1987. When we began, little was known about the natural levels of dissolved hydrocarbons we were likely to encounter. Erickson and Fowler (*10*) found wintertime dissolved hydrocarbon concentrations in the Mackenzie Delta to be less than detectable either by routine in situ sampling on XAD-2 resin (volumes up to 100 L) or by conventional water sampling and batch extraction with 20-L samples. Accordingly, we set our preliminary target sample volumes at 200 L of water by in situ pumping.

EXPERIMENTAL SECTION

General Procedures. Analytical procedures were carried out in a class-100 clean room dedicated to hydrocarbon analyses with access restricted to trained analytical staff wearing one-piece clean

0003-2700/89/0361-1333$01.50/0

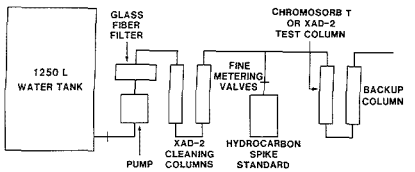

Figure 1. Schematic of the experimental system for the resin column efficiency tests.

room suits. Solvents (BDH Omnisolv) were redistilled through burle packed columns. Hydrocarbon-free water was prepared from glass-distilled water refluxed overnight with alkaline potassium permanganate, redistilled, and extracted with dichloromethane. Sodium hydroxide (10 M, Baker Analysed) was extracted with 7:3 dichloromethane/hexane (6 × 100 mL). Saturated sodium chloride solution (BDH assured) was solvent extracted before dilution to a 3% solution. Glassware was soaked in 2% RBS detergent (Pierce Chemical), baked overnight (a 350 °C forced-air oven was used for all baking), and rinsed with dichloromethane before use. Sodium sulfate (BDH assured) and silica gel (BDH, 60–120 mesh) were baked overnight. Teflon fittings and film were soaked in 2% RBS and Soxhlet extracted overnight with dichloromethane. Glass fiber filter papers (Whatman, 142 mm), both GF/D and GF/F (nominal pore size 2.7 and 0.7 μm, respectively), were baked overnight and stored in baked aluminum foil pouches.

In Situ Water Sampler Columns. Chromosorb T Teflon TFE resin (Manville Corp., approximately 30–45 mesh, special order) was sieved to 30–45 mesh size (375–500 μm). The resin was slurried in acetone and packed, with tapping, into Teflon columns (Seastar Instruments, 37 cm long, 2.5 cm o.d., 1.9 cm i.d.) while a flow (30–50 mL/min) of acetone was maintained. Each column contained 55 g of resin retained at each end by FEP (fluorinated ethylene polypropylene) Teflon mesh (Micromesh, 297 μm) secured between two Teflon collars. For Norman Wells (Mackenzie River) Chromosorb T resin samples, the 0.5-in. (1.25 cm) pipe thread Teflon end plugs for the water sampler columns (supplied by the manufacturer) were replaced with Swagelok stainless steel 0.5-in. (1.25 cm) pipe thread to 0.375-in. (0.95 cm) tube male connectors and corresponding end caps. This modification provided a more positive seal at low temperatures and reduced the risk of contamination during connection of the columns to the sampler. The XAD-2 resin columns (20–60 mesh) and their cleaning have been described by Green and Le Pape (*4*). Identical Teflon columns were used for both resins.

Water sample columns were cleaned in batches of four or eight by using freshly distilled solvent produced by a 5-L Soxhlet still. Methanol was pumped (Micropump, Teflon gears) at 75 mL/min per column for 24 h, dichloromethane for a further 24 h, and methanol for a final rinse until there was no dichloromethane in the effluent. Columns were sealed as described above and stored with the contents under methanol until use.

Column Efficiency Tests. A 1250-L aluminum tank (1.14 m diameter, 1.22 m deep) and lid were cleaned by recirculating RBS detergent solution for several hours and thoroughly flushing with filtered (Filtrite polyester cartridge) tap water for 24 h. The tank was filled with filtered tap water, which was used as a clean water supply. The experimental system is shown schematically in Figure 1. All components in contact with the feed water were thoroughly cleaned sequentially with acetone, dichloromethane, methanol, and water prior to assembly.

The tank supplied 1000 L of water, which was continuously spiked with dissolved hydrocarbon standards to produce concentrations of approximately 1–2 and 0.1–0.2 ng/L of individual *n*-alkane and PAH components, respectively, delivered to each extraction column. Water from the tank was pumped (Micropump, graphite gears, variable speed) through a glass fiber filter (Gelman AE) in an all-Teflon housing and then through two XAD-2 cleanup columns in series. A standard, containing even *n*-alkanes and selected PAHs dissolved in acetonitrile, was dispensed continuously from a nitrogen-pressurized (0.5–0.7 atm) reservoir using two fine metering valves (Nupro, SS-SS2) in series. The spike was added at 16–20 μL/min to the clean feed water, which was delivered at 150 mL/min to the test and backup extraction columns. The volume of standard delivered was recorded hourly with flow rates being adjusted as necessary. The feed water was flushed through for 1 h before installing the columns. Column experiments were conducted in duplicate with approximately 500 L of water pumped through each column.

Sampling. Hydrocarbons in water were extracted in situ with Seastar water samplers (2). The sampler is a microprocessor-controlled battery-powered pump in a pressure case which draws water at a preset flow rate through a filter unit and extraction column and measures the volume pumped. A flow rate of 150 mL/min was used. Before each field trip, the Teflon filter holders and connecting tubing were cleaned with 2% RBS detergent, distilled water, acetone, and dichloromethane. Filters were loaded before each deployment by using clean tweezers with GF/F on the bottom (outlet end) and GF/D on top. The Teflon column was then attached to the sampler, and all tubing connections were tightened. During operation, water passed sequentially through the GF/D and GF/F filters, the resin column, and the pump.

Samples from the Fraser River and Captain Passage, Saltspring Island, were collected from the CSS *Vector*. Four in situ water samplers and in situ pumps were bolted to a submersible frame to obtain simultaneous samples of the dissolved, particulate, and colloidal phases for hydrocarbon analysis (*11*). The in situ pumps sampled through a common port (upstream end of the frame) with a 500-μm stainless steel screen prefilter. Teflon tubing connected the sampling port to the sampler filter pack inlets. Just before sampling (frame-mounted deployments only) these inlet hoses were filled with methanol to prevent air locks. The samplers were started with a 10-min delay and lowered over the side to the desired depth. This delay allowed the samplers to be submerged *before* pumping, thus minimizing contact between the sample and the surface microlayer. To terminate sampling, the frame was raised until the inlet port was just under the surface and the in situ samplers were turned off.

For deployments in Patricia Bay, Saanich Inlet, each sampler was lowered individually over the side of a barge tied to the dock. A 1.0-min delay was used, and after 5 min at the selected depth each sampler was raised to just under the surface to verify that it was still operating (the samplers are designed to shut off after 4 min if the flow is too low). In a few cases the pumps had to be restarted.

For through-ice deployments in the Mackenzie River, a hot-water hole melter was used. Teflon lines and the filter pack on the in situ sampler were protected from freezing before deployment. A 0.1-min delay was used and operation of the samplers verified after 5 min as above.

After sampling, the columns were detached and capped. Filter papers were folded one-quarter round and stored in labeled baked aluminum foil pouches. All samples were stored frozen until extraction.

Analytical Procedures. *Column Elution Procedure.* The elution apparatus, with an empty stub column in place of the extraction column, was rinsed with methanol and dichloromethane (150 mL each) and methanol again (100 mL). Fittings were installed with care to avoid contamination. For column blanks, methanol was displaced from unused columns with 100 mL of hydrocarbon-free water.

For a single-column extraction, a 1.00-mL aliquot of the working internal standard was added directly to a dichloromethane-wetted 1-L separatory funnel. The working internal standard contained known amounts of the 13 perdeuterated hydrocarbons described below. The column was eluted upward into the separatory funnel with methanol (150 mL) and then dichloromethane (250 mL) at a flow rate of 2–5 mL/min. Hydrocarbon-free water (200 mL) was added and the separatory funnel shaken vigorously for 1 min. If phase separation was poor, hydrocarbon-free water saturated with sodium chloride (50 mL) was added; this step was seldom required. The dichloromethane layer was drawn off into a 500-mL flask and the aqueous methanol extracted twice more with dichloromethane (50 mL). The combined dichloromethane extracts were back-washed twice with 3% hydrocarbon-free aqueous sodium chloride (50 mL) and dried over sodium sulfate (5 g). The extract was transferred in portions to a 250-mL Kuderna-Danish concentrator, 1 mL of carbon tetrachloride was added, and solvent volume was reduced to approximately 0.5 mL in a water bath at

50–55 °C. The extract was quantitatively transferred with dichloromethane (2 mL) to a silica gel filter column (60 × 5 mm, 1 g of 5% water deactivated silica gel) and eluted with dichloromethane (10 mL).

In subsequent Beaufort Sea field studies (*12*), dual (parallel) Chromosorb T column deployments were used for sampling due to the high resistance to flow of the Teflon resin (see part 2 of Results and Discussion). The column blanks used with those samples are included as part of this comparison.

The double-column extraction required a change in procedure to guard against loss of internal standard from the larger 2-L separatory funnel. Hydrocarbon-free water (50 mL) was added to the 2-L separatory funnel, both columns were eluted simultaneously into it with methanol (150 mL each) and then dichloromethane (250 mL each), and the internal standard (1.00 mL) was added, followed by hydrocarbon-free water (350 mL). The remainder of the extraction procedure was identical with the single-column procedure, except that amounts of material and sizes of glassware were doubled.

Analysis. Samples were analyzed by using a Finnigan 9600/3300E GC/MS with an Incos 2300 data system running SuperIncos software, revision 5.5. A 1-m uncoated fused silica retention gap was installed in conjunction with a 30-m DB-5, 0.25-μm film capillary column (J & W Scientific) inserted directly into the ion source. The mass spectrometer was tuned and mass calibrated daily with perfluorotributylamine (FC43). MS scans were acquired from 41 to 500 amu in 1.00 s with a 0.01-s settling time and with storage to disk of mass peaks greater than 50 counts.

Samples (0.5–1.0 μL) were introduced by using a 1-min splitless Grob injection at room temperature. At 2 min the oven was heated ballistically to 80 °C, and at 4 min the MS source and detector were turned on. At 4.5 min the oven temperature was programmed at 6 °C/min to 300 °C. Data were acquired from the beginning of the temperature program for 38.3 min (2300 scans).

A GC calibration standard containing 47 hydrocarbons, 13 perdeuterated internal standards, and a fragmentation standard (decafluorotriphenylphosphine, DFTPP) was run daily to determine retention times, response factors (relative and absolute), and system performance. The MS fragmentation performance was determined periodically with DFTPP and met the accepted ion abundance criteria for this compound (*13*).

The *n*-alkanes from C_{11} to C_{36} plus seven isoprenoids were quantified relative to [$^2H_{50}$]tetracosane. [$^2H_{26}$]Dodecane and [$^2H_{74}$]hexatriacontane were used to monitor volatility losses and high-temperature GC behavior, respectively, and were also quantified relative to [$^2H_{50}$]tetracosane. The 21 PAHs measured from naphthalene to benzo[*ghi*]perylene were quantified relative to [$^2H_8$]naphthalene, 1-methyl[$^2H_{10}$]naphthalene, [$^2H_8$]-acenaphthylene, [$^2H_{10}$]acenaphthene, [$^2H_{10}$]anthracene, [$^2H_{10}$]-pyrene, [$^2H_{12}$]chrysene, [$^2H_{12}$]benzo[*k*]fluoranthene, [$^2H_{12}$]-benzo[*a*]pyrene, and [$^2H_{14}$]dibenz[*a,h*]anthracene with the appropriate deuterated standard being used for each class of PAH. In all cases, target compounds were located and quantified with automated procedures using relative retention times and mass chromatogram peak maxima for characteristic ions. Where possible, the relative responses of the PAH to the perdeuterated standards were calibrated with the National Bureau of Standards (NBS) SRM-1647 mixture of PAH in acetonitrile.

Principal Components Analysis. Unsupervised principal components analysis (PCA) was used to examine the interrelationship among samples in the various data sets (*14*, *15*). Since a hydrocarbon data set can exhibit large differences in absolute magnitude between, for example, the alkanes and PAHs in a given sample, data were initially log-transformed, as recommended by Kvalheim (*15*). This minimizes the influence of large differences in the absolute size of GC peaks and makes the distribution of each variable more normal. To eliminate zero values in the data sets, half of the minimum peak area (50 counts) was substituted into the calibration routine and adjusted for the peak area and relative response of the appropriate deuterated standard. Incos procedures require that mass peaks of greater than the specified storage limit of 50 counts be present in a minimum of two adjacent scans before a peak is detected, and hence the actual instrument detection limit is 100 area counts.

The PCA program used the nonlinear iterative partial least-squares (NIPALS) algorithm (*14*, *16*, *17*) and allowed us to examine both scores and loadings. The scores and loadings represent, respectively, the contributions of each sample and each variable to each principal component. The log-transformed variables were mean centered (by subtracting the mean from each variable on a variable by variable basis) before PCA analysis. Mean centering was chosen to avoid closure (*17*), which could arise from the normalization technique recommended by Kvalheim (*15*).

RESULTS AND DISCUSSION

Hydrocarbons in natural water are distributed among the dissolved, colloidal, and particulate phases: Assignment to phase is operationally defined by the sampling techniques used (*18*, *19*). Companion papers (*11*) will discuss the intercomparison of hydrocarbon sampling techniques for particulates and make an assessment of the importance of each phase to the overall hydrocarbon budget. Here, we define dissolved hydrocarbon phase as the fraction that passes through stacked GF/D and GF/F glass fiber filters (nominal pore size 2.7 and 0.7 μm, respectively) and is adsorbed onto the resin column. The measurements reported here provide no information on colloidal hydrocarbons, which pass through both filter and resin column.

The performance of the Chromosorb T and XAD-2 resins was compared in three ways: (1) column efficiency obtained by using 350–500 L of water spiked with dissolved hydrocarbons at anticipated "natural" levels, (2) hydrocarbon blank levels from resin columns (both in part 1), and (3) comparison of resin columns attached to in situ samplers deployed simultaneously (part 2).

1. Comparison of Resin Sorption Efficiencies and Blank Characteristics. Resin Column Efficiency Tests. Many tests on spike recovery and column efficiency have been performed previously with XAD-2 resin. None have utilized more than a few aliphatic and aromatic hydrocarbons nor have they approximated the hydrocarbon concentrations found in natural water samples. From winter studies in the Mackenzie River (*10*) we expected dissolved hydrocarbon concentrations to be a maximum of approximately 1–2 ng/L per alkane and 0.1–0.2 ng/L per individual PAH component. By contrast, for example, Osterroht (*20*) performed recovery tests in seawater using pristane, *n*-hexadecane, and phenanthrene at concentrations greater than or equal to 1 μg/L, and James et al. (*21*) used perdeuterated *p*-xylene, naphthalene, hexadecane, and phenanthrene spiked into drinking water at 100 ng/L. For Chromosorb T, the only hydrocarbon spike recovery tests we are aware of utilized phenanthrene at concentrations of 500 μg/L (*1*).

To simulate natural hydrocarbon concentrations in our column efficiency tests (3–4 orders of magnitude below those previously attempted), prefiltered water from a reservoir tank was pumped through two XAD-2 precolumns to remove dissolved hydrocarbons, spiked with even *n*-alkanes and selected PAHs, and then pumped through the Chromosorb T or XAD-2 test column (Figure 1). Two Chromosorb T and two XAD-2 columns were evaluated (Table I). The measured concentrations of the even *n*-alkane spikes were blank corrected for each column by using an average of the two adjacent odd *n*-alkanes. For PAH, column blanks from the same time period as that of the tank tests were used for blank correction; for Chromosorb T only naphthalene required correction.

Table I gives the effective aqueous concentration of the hydrocarbon spike for each component and the percent recovered from each column after elution. For *n*-alkanes, Chromosorb T gave comparable recoveries that were in general higher than the XAD-2 recoveries (also comparable) for most of the alkanes. The general fall-off in recovery for triacontane and above is likely linked to the extremely low solubility of these *n*-alkanes.

Chromosorb T showed poor recovery of PAHs with molecular weight less than that of phenanthrene. Recoveries were

Table I. Results of the Column Efficiency Determination

	Chromosorb T				XAD-2			
	402-L extracted vol		355-L extracted vol		495-L extracted vol		480-L extracted vol	
compound	effective concn,[a] ng/L	spike recov, %	effective concn,[a] ng/L	spike recov, %	effective concn,[a] ng/L	spike recov, %	effective concn,[a] ng/L	spike recov, %
dodecane	2.6	67	2.7	59	0.62	73	0.64	140
tetradecane	2.5	55	2.6	49	0.53	25	0.54	89
hexadecane	2.6	47	2.7	57	0.51	26	0.52	56
octadecane	2.7	60	2.8	70	0.57	<3	0.58	79
eicosane	2.7	72	2.9	83	0.57	40	0.58	29
docosane	2.8	76	2.9	82	0.57	52	0.58	21
tetracosane	3.0	71	3.2	89	0.63	49	0.65	27
hexacosane	4.4	79	4.6	98	0.89	48	0.92	29
octacosane	2.7	40	2.9	65	0.57	36	0.58	33
triacontane	2.4	24	2.5	55	0.51	44	0.52	22
dotriacontane	3.2	13	3.3	43	0.65	10	0.67	16
tetratriacontane	2.9	10	3.0	36	0.59	14	0.60	9
hexatriacontane	3.0	4	3.2	30	0.63	3	0.65	51
total *n*-alkanes (*n*-C_{12}–*n*-C_{36})	37.6		39.2		7.80		8.04	
naphthalene	0.88	3	0.92	1	0.08	25000	0.08	87000
2-methylnaphthalene	–	–	–	–	0.05	380	0.05	260
acenaphthylene	0.75	<4	0.78	1	–	–	–	–
acenaphthene	0.82	2	0.86	2	–	–	–	–
fluorene	0.19	9	0.20	10	0.08	116	0.08	<230
phenanthrene	0.20	81	0.21	46	0.06	1500	0.06	390
anthracene	0.13	55	0.13	36	0.05	220	0.05	440
fluoranthene	0.40	89	0.41	63	0.05	130	0.05	190
pyrene	0.39	88	0.40	60	0.07	130	0.07	91
benz[*a*]anthracene	0.20	92	0.21	75	0.05	56	0.06	81
chrysene	0.18	150	0.19	112	0.05	130	0.06	100
benzo[*k*]fluoranthene	0.40	110	0.42	75	–	–	–	–
benzo[*a*]pyrene	0.21	24	0.22	71	0.06	100	0.06	0
total PAH	4.73		4.95		0.60		0.61	

[a] The effective concentration is the spike quantity divided by the extracted volume. A dash indicates that the compound was not added in the spike.

generally good for PAHs of three and more rings. XAD-2 appeared to be contaminated for PAHs with molecular weight less than that of fluoranthene and to give good recoveries for PAHs of four and more rings. For subnanogram per liter concentrations, neither appears to be usable for studies of the lower molecular weight PAHs but both can give good recoveries for the higher PAHs.

Elution and Column Blanks. In the discussion below, we refer to two types of blanks. Elution procedural blanks were measured by using the entire column elution apparatus, solvents, etc. with an empty stub column used in place of the resin column. Column blanks were measured by eluting resin columns after cleaning. Glass fiber prefilters were not used for either blank.

Assembly of the Blank Set and PCA Testing. Initially, dissolved hydrocarbon samples and a selected number of the elution and column blanks were analyzed by GC/MS without using a silica column sample cleanup step. Most of the dissolved hydrocarbon samples gave a high background on GC that could be attributed to humic acid. Reliable GC/MS quantitation of the target PAH (on the molecular ion) and, to a lesser extent, the alkanes (on m/z 57) was still possible for these samples because the humic acid interfered primarily with the lower mass ions. However, the accumulation of nonvolatile or thermally unstable components in the injector or on the column rapidly degraded GC performance and necessitated a cleanup step. From these initial analyses, we assessed Chromosorb T resin to be the most suitable for Beaufort Sea sampling. Unfortunately, we had to suspend further evaluation for the duration of the field season. Blanks and samples were stored refrigerated with 1 mL of carbon tetrachloride "keeper" in each vial.

After 7 months of storage, blanks and samples were cleaned on a silica gel filter column and reanalyzed by GC/MS. Column blanks (in particular for Chromosorb T) had suffered almost total evaporative loss of the lower molecular weight hydrocarbons. The XAD-2 column blanks showed this loss in only one or two cases. The dissolved hydrocarbon samples were almost entirely unaffected.

With these losses we did not have enough post-silica gel filter column blanks to allow reliable blank correction of the dissolved hydrocarbon samples. Accordingly, perdeuterated dodecane remaining in a blank (or sample) was adopted as the primary criterion of an acceptable GC/MS analysis, and a data subset was assembled from all of the available elution and column blanks that would allow PCA testing of the effects of (1) Chromosorb T and XAD-2 resins and (2) silica gel filter column treatment on blank levels. In a few cases, where the levels of the deuterated dodecane were low or zero, adequate amounts of perdeuterated naphthalene were present and the run was accepted. Only a few blanks showed detectable amounts of any PAH above the methylnaphthalenes (there were no patterns for these PAHs); hence all of the values for PAHs above methylnaphthylene were removed from the test data set. The absence of these PAHs in the blanks was confirmed by selective ion monitoring.

Potential volatility losses from some blanks and spurious contamination of a few of the earlier blanks by undecane and dodecane necessitated the removal of these two alkanes from the data set. Levels of hexatriacontane, pristane, phytane, and the two methylnaphthalenes were above the detection limit for less than half of the blanks, and these variables were also excluded.

The PCA test data subset thus included the normal alkanes from tridecane to pentatriacontane and naphthalene. "Zero values" in the data set made up 10% of the total. For one

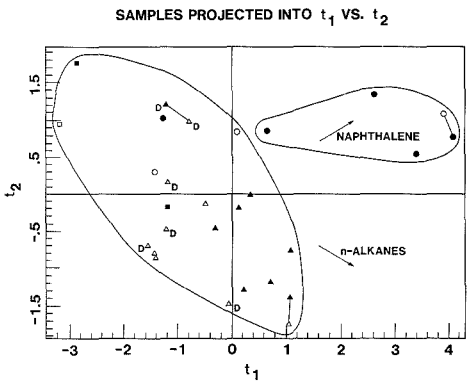

Figure 2. Scores plot for the first two principal components for the elution and column blank data set. The *n*-alkanes from C_{13} to C_{35} and naphthalene were used as variables. The symbols indicate Chromosorb T (pre- (▲) and post-silica gel (△) and XAD-2 (pre- (●) and post-silica gel (○) columns, elution blanks (pre- (■) and post-silica gel (□) and double-column blanks (D). Pairs of points joined by a line highlight the same column blank analyzed before and after the silica column.

blank, tetracosane was obscured by a coeluting impurity and the mean of the two adjacent even *n*-alkanes was substituted.

The scores plot, which reflects the contribution of each blank to the first two principal components (PCs), is shown in Figure 2. For this PCA model, the first three PCs accounted for 52.0, 14.9, and 12.9% of the variance; the third PC could not discriminate among the types of blanks. Naphthalene made the strongest contribution in the loadings of the first PC. The alkane contribution to this PC was relatively constant (45 ± 7%, $n = 23$) relative to naphthalene. Naphthalene also made the strongest contribution to the second PC with the alkane contribution being more variable as well as smaller (11 ± 26%, $n = 23$) relative to naphthalene and having a negative minimum at heptacosane. Thus in Figure 2, the contribution of naphthalene to a blank increases in the direction of the upper right quadrant and the contribution of the alkanes in general increases in the direction of the lower right quadrant (indicated by arrows).

Blank Test Results. The PCA model readily splits the blanks into two subgroups (encircled in Figure 2). The points in the upper right quadrant (except for the one closest to the vertical axis) are XAD-2 blanks from the beginning of the study from columns that were used as received just prior to the Fraser River–Saanich Inlet sampling. All of these XAD-2 columns had high levels of naphthalene (and the methylnaphthalenes); the majority showed elevated levels (relative to Chromosorb T, see part 2) of the alkanes from nonacosane to pentatriacontane. The subgroup extending from the lower center to the upper left encompasses all the available Chromosorb T column blanks, the three XAD-2 blanks from columns recleaned in the clean room, and three elution blanks. Data from one additional elution blank were not included in the PCA model because all the variables except those for tetra-, penta-, and hexatriacontane and naphthalene were below instrument detection.

Most of the trends in the blank data reflect the evolution of column cleaning procedures over the course of the study. The first batch of XAD-2 columns was used as received from the manufacturer (ACS grade solvents were used in the Soxhlet still, solvent was continuously recirculated from the Soxhlet reservoir through the columns, and the cleaning was performed outside a clean room). The Chromosorb T columns used for the Fraser River–Saanich Inlet work were cleaned in the clean room by using glass distilled solvents (BDH Omnisolv) with the solvent continuously recirculated through the columns. The high levels of naphthalene in the first XAD-2 columns can thus be attributed to the cleaning procedures. Subsequent (Norman Wells and following, ref 12, 22) Chromosorb T and XAD-2 columns were cleaned in the clean room with glass distilled solvents. Initial cleaning was performed overnight with solvent continuously recirculated through the columns, but an additional final cleaning was done throughout a working day with each freshly distilled 3-L batch of solvent being flushed through the columns and back into the distillation flask.

In Figure 2, the earliest blanks in the Chromosorb T subgroup are generally located in the lower center area of the scores plot and the latest and cleanest blanks (subjected to the most rigorous column cleaning) in the upper left area. This general trend of column blanks toward getting cleaner as the study progressed also extended to XAD-2 (see part 2), but the cleanest of all the column blanks was from a Chromosorb T column. The two cleanest blanks, in the upper left of the plot, were both elution blanks, one with and one without the silica gel filter column.

Double-column Chromosorb T column blanks (see part 2) are indicated by the letter D beside the points in Figure 2. The hydrocarbon levels in these double-column blanks were lower than in most of the single-column blanks since they were eluted later in the study. The blank levels were not significantly influenced by doubling the number of columns.

PCA Testing with Naphthalene Excluded. In this first PCA model (Figure 2), the separation between the first batch of XAD-2 blanks (the upper right of the scores plot) and the rest of the XAD-2 and Chromosorb T blanks appears to be strongly influenced by naphthalene. The high levels of naphthalene (and methylnaphthalenes) in the XAD-2 blanks and samples are likely a result of the divinylbenzene copolymer used to make the resin (see also ref 6, 7). To remove this specific influence of the resin type on the hydrocarbon blank, the PCA analysis of the blank data set was repeated without naphthalene (i.e., only the *n*-alkanes from tridecane to pentatriacontane were used). For this PCA model, "zero values" in the data set were 10% of the total and the first three principal components accounted for 53.0, 15.6, and 10.7% of the variance. The loadings for the first PC were very similar to those in the previous model and showed a fairly constant *n*-alkane contribution of 85 ± 13% ($n = 23$) relative to (and including) triacontane, the *n*-alkane with the highest loading. The loadings of the second PC were very similar to those of the third PC of the first model. A scores plot based on the first two PCs indicated that the second PC was very poor for discriminating between the different types of blanks. The third PC, however, was very similar to the second PC of the first model. It also had an inverted bell-shaped loadings plot with tridecane and pentatriacontane showing strong positive loadings and heptacosane showing a negative minimum. The *n*-alkane loadings were 9 ± 47% ($n = 23$) relative to and including the highest loading, pentatriacontane.

The scores plot for the first and third principal components is shown in Figure 3. The results for this model are similar to those of the model shown in Figure 2. The first XAD-2 blank set can still be distinguished in the upper right quadrant, and the remainder of the blanks fall along a line from the lower center to the upper left quadrant (both encircled). Individual blanks have shifted slightly in this new model, but the specific trends toward cleaner blanks over time (including the double columns) and the replication of blanks pre- and post-silica gel remain unchanged. In this model, the *n*-alkane concentration of a blank increases to the right (see arrow in Figure 3).

Table II. Summary of in Situ Sampler Deployments

location	lat/long	date	depth, m	salinity	number of samples	
					Chromosorb T	XAD-2
Pattullo Bridge Fraser River	49 11.9 N 122 54.5 W	2/2/87	7	0.04	2	2
Steveston Island Fraser River	49 06.6 N 123 08.5 W	3/2/87	5	4.1–19.0	–	2
Captain Passage Saltspring Island	48 49.5 N 123 26.2 W	5–6/2/87	7	29.5–29.7	1	2
Patricia Bay Saanich Inlet	48 39.2 N 123 27.1 W	10–12/2/87	5	29[a]	4	4
Norman Wells Mackenzie River, NWT	65 16.7 N[c] 126 50.3 W	1–4/4/87	1[b]	0[a]	2	3
	65 16.8 N[d] 126 52.5 W	4–7/4/87	1[b]	0[a]	3	3

[a] Not measured; based on expected values derived from other programs. [b] Samples were deployed at approximately 0.5–1 m below the bottom of the ice. [c] Upstream of refinery. [d] Downstream of refinery.

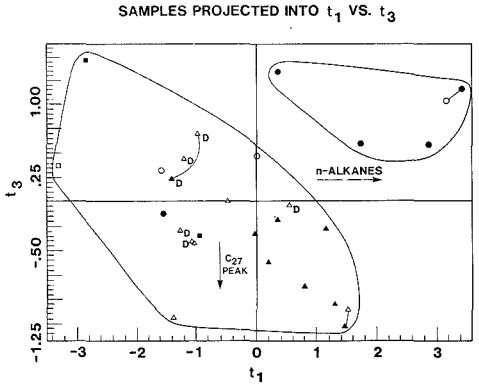

Figure 3. Scores plot for the first and third principal components for the elution and column blank data set. Only the *n*-alkanes from C_{13} to C_{35} were used as variables. Symbols are as in Figure 2.

Overall, hydrocarbon blanks are improved by the refinements in the column cleaning procedures; this trend is not affected by contaminants generated by the resin. Use of double columns or a silica gel cleanup step is overshadowed by the progression to cleaner blanks with time.

For the subsequent stages of the data analysis, column blanks were selected from the time period appropriate to the samples. When both pre- and post-silica gel blanks were available, the blank with the best analytical quality was chosen.

2. Field Investigations. In Situ Sampling. Chromosorb T and XAD-2 columns were used to collect dissolved hydrocarbon samples from areas in British Columbia and the Canadian Northwest Territories that would include the range of Beaufort Sea temperature and salinity conditions (Table II). This collection included sampling in freshwater (Fraser and Mackenzie Rivers), estuarine (Fraser River at Steveston Island), and marine (Saltspring Island and Saanich Inlet) environments that were likely to have different anthropogenic inputs.

Samples were collected first from the Fraser River near the Pattullo Bridge (in the center of the industrialized New Westminster city area of Greater Vancouver Regional District). Samples were collected next near Steveston Island, at the mouth of the Fraser River, where the salinity varies widely with tidal cycle. Finally, samples were collected from the marine area of Captain Passage just outside Ganges Harbour (which has a small marina).

A smaller number of Chromosorb T samples were available for testing than XAD-2 samples due to in situ sampler failures during the cruise (Table II). Two further sets of sampler deployments were made off the Institute of Ocean Sciences dock at Patricia Bay, Saanich Inlet. In the Northwest Territories, samples were collected from the Mackenzie River at two locations 1.75 km apart (upstream and downstream of the oil refinery at Norman Wells).

Chromosorb T columns operate with a higher back-pressure than XAD-2 columns because the soft Teflon resin tends to compress into the outlet end of the column and thus restrict water flow. This caused problems during sampling because the in situ water samplers were designed to shut off after 4–5 min of flow below a set threshold (2). The problem was exacerbated by cold (−1.7 to 0 °C depending on salinity), high-viscosity water encountered in the Beaufort Sea; a large number of in situ sampler failures resulted during the first ice trip (concurrent with Norman Wells sampling, ref 12). For subsequent sampling (*12, 22*) we used parallel Chromosorb T columns with matching back-pressure (see part 1 and Experimental Section).

Our two validity criteria for a suite of dissolved hydrocarbon measurements were that (1) it was distinguishable from the resin column blanks and (2) it included no measurements from samples contaminated during sampling. For the first criterion, the quantified samples and blanks (with concentrations in nanograms relative to the internal standards) were compared by PCA and graphing before blank and volume correction. Data were split into two sets: samples from the Fraser River, Captain Passage, and Saanich Inlet and samples from Norman Wells. The same elution blanks were included in both data sets to allow comparison between the sets.

Comparison of Resin Column Samples and Blanks. *PCA of the Fraser River–Saanich Inlet Data Set.* Hydrocarbon concentrations for all in situ samples in this data set were from results of post-silica gel column analyses. The pre-silica gel PAH values were substituted to correct for evaporative losses in one case and for high mass mass-spectrometer run problems in another. Usually the pre- and post-silica gel PAH analyses showed excellent agreement; therefore this substitution should not bias the results. All column blanks were chosen from the pre-silica gel set; because the post-silica gel column blanks suffered considerable volatility losses, this is the more conservative blank correction.

The scores plot for the first two PCs for the dissolved hydrocarbon samples and elution and column blanks for the Fraser River–Saanich Inlet data is shown in Figure 4. The PCA test data set included *n*-alkanes from tridecane to pentatriacontane, pristane and phytane plus naphthalene and both methyl derivatives, acenaphthene, fluorene, phenan-

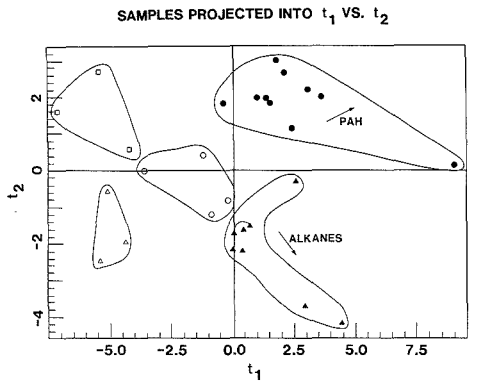

Figure 4. Scores plot for the first two principal components for the Chromosorb T (▲) and XAD-2 (●) dissolved hydrocarbon samples, Chromosorb T (△) and XAD-2 (○) column blanks, and the elution blanks (□) from the Fraser River–Saanich Inlet data set. The pair of points joined by a line are analytical replicates of the same sample.

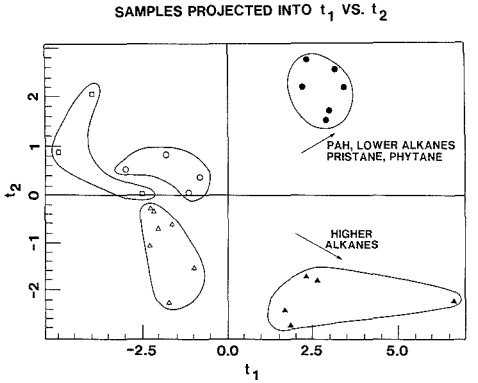

Figure 5. Scores plot for the first two principal components for the Chromosorb T (▲) and XAD-2 (●) dissolved hydrocarbon samples, Chromosorb T (△) and XAD-2 (○) column blanks, and the elution blanks (□) for the Norman Wells data set.

threne, fluoranthene, and pyrene. All other variables contained too many not-detected values for valid testing. "Zero values" in the data set totaled 12.3% with half of the not-detected values arising from PAH blanks.

The first PC accounted for 59.0% of the variance and the second for 19.2%. The PAH made the strongest contribution to the first PC with a mean of 93 ± 7% (n = 8) relative to (and including) phenanthrene, the PAH with the highest loading. The n-alkane contribution to the first PC was lower and more variable with a mean of 39 ± 8% (n = 23) relative to phenanthrene. Pristane and phytane loaded more similarly to the PAH than the alkanes with loadings relative to phenanthrene of 76% and 63%, respectively. The PAH also made the strongest positive contribution to the second PC, with naphthalene, the methylnaphthalenes, and acenaphthene contributing 91 ± 10% (n = 4) relative to (and including) naphthalene (the variable with the largest loading). The other four PAHs contributed 33 ± 11% (n = 4) relative to naphthalene. The n-alkanes, pristane, and phytane all loaded negatively with a mean of 43 ± 24% (n = 25) and a negative minimum of 90% at heptacosane with both percentages expressed as an absolute value relative to the positive naphthalene loading. Thus, as marked in Figure 4, the PAH contribution increases in the direction of the upper right quadrant and the contribution of n-alkanes, pristane, and phytane increases toward the lower right of center.

PCA of the Norman Wells Data Set. Hydrocarbon concentrations for all in situ samples in this data set were taken from results of post-silica gel column analyses. For one sample, the pre-silica gel values for the PAH and tri- and tetradecane were substituted to correct for evaporative losses; for another, calculated values for pristane and phytane were added by using heptadecane/pristane and octadecane/phytane ratios from similar dissolved hydrocarbon samples. Column blanks were chosen from both pre- and post-silica gel results with the continued presence of perdeuterated dodecane being used as the primary selection criterion. One XAD-2 column blank was added to increase the blank correcting ability for the n-alkanes. This blank did not contain either perdeuterated dodecane or naphthalene and was not used in the blank PCA data set (part 1).

The scores plot for the first two PCs is shown in Figure 5. The PCA data set includes n-alkanes from tridecane to hexatriacontane, pristane and phytane, naphthalene and both methyl derivatives, fluorene, and phenanthrene. All other variables contained too many not-detected values for valid testing. "Zero values" in the data set made up 17% of the total with 41% of the not-detected values being PAH blanks.

The first PC accounted for 56.8% of the variance and the second for 19.9%. Pristane made the strongest contribution to the first PC. Penta-, hexa-, and heptadecane and phytane contributed 66 ± 4% (n = 4) relative to pristane, and all other n-alkanes contributed a fairly constant 29 ± 7% (n = 21). The naphthalenes loaded at 57 ± 2% (n = 3), and fluorene and phenanthrene at 38 ± 4% (relative to pristane). Heptacosane and octacosane had the strongest (negative) loading to the second PC. The alkanes formed the basis for an inverted bell-shaped loadings plot with tridecane to octadecane and phytane having small positive loadings and hepta- and octacosane showing a negative minimum. The n-alkane and phytane loadings were 43 ± 45% (n = 25) relative to (and including) heptadecane. Pristane and the PAH all showed positive loadings, 71 ± 17% (n = 6). Thus the contributions of pristane, phytane, PAH, and lower n-alkanes to octadecane increase toward the upper right quadrant of the scores plot (arrows in Figure 5). The higher molecular weight alkanes increase toward the lower right quadrant.

Comparison of the Two Resins. The PCA models (Figures 4 and 5) distinguish easily between the Chromosorb T and XAD-2 dissolved hydrocarbon samples and their respective blanks (see outlined regions); we have successfully sampled dissolved hydrocarbons and can identify features beyond variation in the blank. The PCA models also cleanly separate the Chromosorb T and XAD-2 samples, graphically demonstrating that the two resins have different hydrocarbon adsorption characteristics. For the Fraser River–Saanich Inlet data set (Figure 4), these differences make a stronger contribution to the hydrocarbon composition than differences in sampling location (Table II). The elution blanks, which are cleaner than most of the column blanks, project separately and provide a basis to compare Figures 4 and 5.

Differences between the two resins are shown further in Figures 6 and 7. These plots and the respective PCA use the same sample data and variables; mean sample and mean blank concentrations in nanograms are plotted on a variable by variable basis for each resin. The figures provide graphic representation of the data for each variable before blank or volume corrections.

The sample means in Figure 6 are plotted for every variable with three Fraser River sample outliers excluded (identified with footnote a in Table III) and for the n-alkanes from

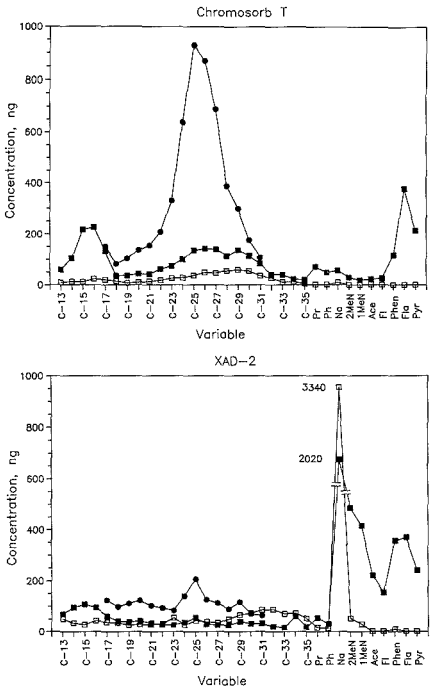

Figure 6. Plot of the mean sample concentration (■) and the mean blank concentration (□) for every variable with sample outliers removed (samples marked by footnote a in Table III) for the Fraser River–Saanich Inlet data set. The *n*-alkanes from heptadecane to untriacontane (●) are plotted with outliers included in the means. Concentrations are in nanograms before blank or volume correction of samples, and the same variables used for the PCA in Figure 4 are plotted. Variable abbreviations indicate the *n*-alkanes from tridecane (C-13) to pentatriacontane (C-35), pristane (Pr), phytane (Ph), naphthalene and 2- and 1-methyl derivatives (Na, 2MeN, 1MeN), acenaphthene (Ace), fluorene (Fl), phenanthrene (Phen), fluoranthene (Fla), and pyrene (Pyr).

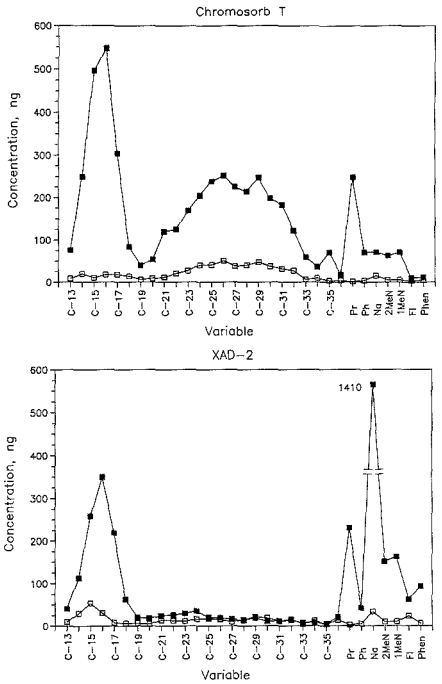

Figure 7. Plot of the mean sample concentration (■) and the mean blank concentration (□) for each variable for the Norman Wells data set. Concentrations are in nanograms before blank or volume correction of samples, and the same variables used for the PCA in Figure 5 are plotted. Variable abbreviations are as in Figure 6; note that the *n*-alkanes extend to hexatriacontane.

heptadecane to untricontane with the outliers included in the means. With the exception of the very high PAH levels in the XAD-2 outlier, the outliers had very little impact on variable means outside this range.

The differences in the adsorption characteristics of the two resins are dramatic (Figures 6 and 7). For both data sets the *n*-alkanes between nonadecane and untriacontane are clearly distinguishable from the blanks for Chromosorb T but indistinguishable for XAD-2. In Figure 6 the outliers reinforce this distinction for Chromosorb T but have a much smaller impact on XAD-2 results. The Chromosorb T outliers were primarily enhanced in the alkanes, the XAD-2 outlier in the PAH. The lower alkanes are distinguishable from the blanks for both resins, but sample levels are lower for XAD-2. Mean alkane blanks are comparable for both resins for the Fraser River–Saanich Inlet data and slightly higher for Chromosorb T than XAD-2 for Norman Wells.

For the Fraser River–Saanich Inlet data set (Figure 6) the high levels of naphthalene in the XAD-2 resin blank can be attributed to the cleaning procedures (part 1). However, the subsequent Norman Wells XAD-2 naphthalene blanks (Figure 7) were only slightly larger than the Chromosorb T naphthalene blanks, thus illustrating that cleaning procedures could not account for differences observed between the resins. The separation between samples and blanks and the blank levels were comparable for both resins for the higher PAHs.

The results shown in Figures 6 and 7 provide additional insight into the PCA separations of Figures 4 and 5. In both cases the separations between the Chromosorb T and XAD-2 samples are due to differences in both naphthalene and alkane concentrations; alkanes are always higher for Chromosorb T, and naphthalene is always higher for XAD-2. For the Fraser River–Saanich Inlet data set the separations between the Chromosorb T and XAD-2 blanks are due primarily to the higher XAD-2 naphthalene concentrations, for Norman Wells the differences between the blanks are much less pronounced and relate primarily to relative proportions of alkanes. The results presented in Figures 6 and 7 are not due to differences in sample volume (Table III). For both data sets the mean volumes sampled for each resin are statistically equivalent ($\alpha(2) = 0.05$).

Results of Blank Correction. The mean Chromosorb T or XAD-2 column blank was used to correct the measured resin column hydrocarbon data before conversion to concentration units. If a blank-corrected concentration (before volume correction) was an amount less than 3 times the standard deviation of the mean blank, it was regarded as not detected; if the amount was less than 10 standard deviations, it was regarded as detected but not quantified (*23*). The results of blank correction on the data are summarized in Table IV for the Fraser River–Saanich Inlet data set and in Table V for the Norman Wells data set.

Hydrocarbon concentrations, the sample volume, and the percent recovery of perdeuterated dodecane and hexatriacontane (C_{12}-d_{26} and C_{36}-d_{74}) are given in Table III for each

Table III. Hydrocarbon Concentration Summary for the Dissolved Hydrocarbon Samples

location	resin	sample	vol, L	C_{12}-d_{26}, %	C_{36}-d_{74}, %	concentration, ng/L				PAH sum[d]	H/C sum	OEP C_{25}
						C_{13}–C_{19}[c]	C_{20}–C_{29}	C_{30}–C_{36}	C_{13}–C_{36}[c]			
Pattullo Bridge	Chromosorb T	1	40.3	13.8	107	5.08	23.2	0.03	28.3	13.1	41.4	1.66
Fraser River		2[a]	34.5	25.9	96.2	22.9	375	7.54	406	16.0	422	1.10
	XAD-2	1	47.2	3.0	96.0	0.00	0.00	0.00	0.00	55.4	55.4	
		2[a]	44.3	6.7	130	76.3	190	21.3	287	3290	3580	1.31
Steveston Island	XAD-2	1	70.0	3.8	46.4	4.33	2.00	0.00	6.33	69.9	76.3	
Fraser River		2	75.9	69.9	50.1	1.15	1.12	0.00	2.27	56.2	58.5	
Captain Passage	Chromosorb T	1[a]	139.0	5.4	98.2	13.3	127	6.83	147	9.88	157	1.10
Saltspring Island	XAD-2	1	148.1	3.0	97.5	0.00	0.00	0.00	0.00	6.75	6.75	
		2	157.2	26.2	95.1	1.43	0.30	0.00	1.73	6.67	8.40	
Patricia Bay	Chromosorb T	1	154.4	0.0	63.1	5.42	4.64	3.53	13.6	10.3	23.9	0.943
Saanich Inlet		2	174.0	31.9	97.7	7.20	2.32	0.00	9.52	5.05	14.6	0.977
		3A[b]	207.9	25.3	83.2	3.99	1.52	0.00	5.51	4.10	9.62	
		3B[b]	207.9	0.5	63.9	5.35	2.27	0.12	7.74	4.02	11.8	1.01
		4	182.4	35.1	59.0	3.75	4.63	0.69	9.07	4.28	13.4	0.84
	XAD-2	1	201.5	25.9	102	0.71	0.00	1.44	2.15	9.75	11.9	
		2	218.7	13.5	66.9	5.00	0.00	0.00	5.00	11.8	16.8	
		3	202.3	66.6	89.6	3.33	0.00	0.00	3.33	6.48	9.80	
		4	82.2	0.7	94.6	1.02	0.00	0.00	1.02	6.88	7.90	
Norman Wells	Chromosorb T	1	56.9	11.7	104	2.13	14.0	11.2	27.3	0.00	27.3	
Northwest	upstream	2	256.1	6.3	96.9	0.33	3.96	1.60	5.90	0.00	5.90	1.11
Territories	downstream	1	169.4	6.6	82.1	1.79	4.89	0.18	6.85	0.25	7.10	
		2	223.5	67.7	77.4	2.02	3.65	1.33	7.00	0.02	7.02	1.05
		3	110.8	6.9	115	79.8	35.9	11.8	128	6.67	134	1.00
	XAD-2	1	244.1	27.3	60.7	4.62	0.13	0.00	4.74	4.10	8.84	
	upstream	2	235.8	0.0	117	4.37	0.29	0.00	4.66	15.4	20.1	
		3	200.1	18.6	94.4	3.94	0.14	0.00	4.08	3.72	7.79	
	downstream	1	217.3	10.5	63.5	7.46	0.19	0.00	7.66	9.91	17.6	
		2	176.7	23.7	112	3.54	0.23	0.48	4.25	5.79	10.0	
		3	211.6	14.4	102	5.64	0.61	0.00	6.26	12.3	18.5	

[a] Indicates an outlier that may have been contaminated in sampling. [b] Results of replicate GC/MS analyses of the same sample. [c] Includes pristane and phytane. [d] Includes naphthalene and its monomethyl derivatives and the PAHs listed in Table VI.

Table IV. Results of the Blank Correction of the Fraser River–Saanich Inlet Data

variable	number of measured concentrations							
	Chromosorb T				XAD-2			
	total no.	below detctn	below quantatn	above quantatn	total no.	below detctn	below quantatn	above quantatn
n-C_{13}–n-C_{19}, pristane, phytane	72	4	16	52	90	60	18	12
n-C_{20}–n-C_{29}	80	8	34	38	100	86	4	10
n-C_{30}–n-C_{36}	56	36	12	8	70	65	5	0
naphthalene and 1- and 2-Me deriv	24	15[a]	1	8	30	19	3	8
higher PAHs[b]	72	26[a]	–[c]	46	90	17[a]	–[c]	73

[a] Most of these values were below the minimum area cutoff of the GC/MS. [b] Higher PAHs are listed in Table VI. [c] A standard deviation was not available for the blank.

Table V. Results of the Blank Correction for the Norman Wells Data Set

variable	number of measured concentrations							
	Chromosorb T				XAD-2			
	total no.	below detctn	below quantatn	above quantatn	total no.	below detctn	below quantatn	above quantatn
n-C_{13}–n-C_{19}, pristane, phytane	45	13	16	16	54	11	26	17
n-C_{20}–n-C_{29}	50	2	36	12	60	42	16	2
n-C_{30}–n-C_{36}	35	6	20	9	42	40	2	0
naphthalene and 1- and 2-Me deriv	15	11	1	3	18	0	–[c]	18
higher PAHs[b]	45	43[a]	–[c]	2	54	31[a]	–[c]	23

[a] Most of these values were below the minimum area cutoff of the GC/MS. [b] Higher PAHs referred to are the same as those in Table VI. [c] A standard deviation was not available for the blank.

dissolved hydrocarbon sample. To calculate odd–even predominance we used the formula of Scalan and Smith (*24*) for the five n-alkanes centered at pentacosane. This rather low central carbon was selected due to the large number of undetected n-alkanes above heptacosane. The numbers 3A and 3B refer to replicate GC/MS determinations.

Alkanes. The vast majority of XAD-2 alkane concentrations were below detection due to the poor adsorption ability

of the resin (Figures 6 and 7). Virtually all the Fraser River–Saanich Inlet alkane values above the limit of quantitation (Table IV) were from one very high sample from the first day on the Fraser River at the Pattullo Bridge (footnote a in Table III). For Norman Wells (Table V), most XAD-2 alkane concentrations were below detection even though the blanks for this data set were cleaner than many of the Chromosorb T column blanks (Figure 7, Figure 2, closed and open circles encircled in upper left quadrant). Two-thirds of the alkanes from the lower molecular weight ranges (tridecane to docosane) were detectable on XAD-2, but virtually all the higher molecular weight parameters were below detection. The results shown in Tables IV and V illustrate the power of PCA (*17*): PCA could discriminate between the XAD-2 blanks and dissolved hydrocarbon samples (Figures 4 and 5); standard deviation of the mean blank (*23*) showed little discrimination.

In contrast, as can be expected from Figures 6 and 7, the majority of the alkane values from the lower and middle molecular weight ranges were quantifiable for the Chromosorb T columns (Table IV and V). For the Fraser River–Saanich Inlet data set, two of the samples, one from the Pattullo Bridge and the one from Captain Passage, Saltspring Island, exceeded the limit of quantitation for all *n*-alkanes between tridecane and triacontane and could also be described as outliers (footnote a in Table III). Even with these two samples removed, 90% of the Chromosorb T concentrations exceeded the detection limit for the alkanes from tridecane to triacontane. The largest number of quantifiable Chromosorb T values were from the tridecane to nonadecane range (which should have the highest water solubility) and the lowest number from the range above triacontane (the lowest water solubility).

For the Norman Wells Chromosorb T samples (Table V), only 16% of the alkanes were below detection for the entire alkane data set, and the majority of these were for the low molecular weight range of one column sample. The XAD-2 resin is clearly inferior to Chromosorb T for the quantitation of alkane hydrocarbons.

PAH. Many values were below detection for naphthalene and its methyl derivatives for both resins for the Fraser River–Saanich Inlet Data set (Table IV). These compounds were detectable on XAD-2 only when the concentrations exceeded the high blank levels (Figure 6).

For Norman Wells Chromosorb T samples (Table V), the naphthalenes (parent and methyl derivatives) were above the limit of quantitation for the one high downstream sample and essentially undetectable for all other samples. For XAD-2, all the naphthalenes were above the limit of quantitation. This result reflects the low levels of naphthalenes in this set of XAD-2 blanks (Figure 7), but the values are still suspect due to the ability of the resin to autogenerate these aromatic hydrocarbons (*6*, *7*).

The field results reinforce the data presented in Table I. Chromosorb T adsorbs poorly for the lower PAHs; XAD-2 results are often confounded by high blanks (Figure 6). While it is possible to obtain very low levels of naphthalenes in XAD-2 blanks (Figure 7), the resin is contraindicated for studies of naphthalene in natural waters.

Comparable data for the two resins are obtained only for the higher PAHs (above acenaphthylene). For the Fraser River–Saanich Inlet data set those results are presented in Table VI and Figure 6. The one XAD-2 outlier (Table III) was removed from Table VI due to the very high PAH levels. The PAH blanks were not measurable for most of the higher PAHs for both resins, and blank correction with standard deviation testing (*23*) was only possible for phenanthrene for XAD-2. Where blanks were measured they were usually insignificant. The Chromosorb T columns (Table VI) had less

Table VI. Blank Corrected PAH Concentrations for the Fraser River–Saanich Inlet Data Set

location	resin	sample	concentration, ng/L: acenaphthylene	acenaphthene[b]	fluorene[b]	phenanthrene	anthracene	fluoranthene	pyrene	benz[*a*]anthracene	chrysene
Pattullo Bridge	Chromosorb T	1				1.9	0.35	6.4	3.8		0.69
Fraser River		2			1.7	6.3	0.19	3.4	2.0		
	XAD-2	1	2.3	4.6	5.8	11[a]		2.9	2.0		
Steveston Island	XAD-2	1	1.7	5.7	5.4	7.9[a]	1.3	3.7	2.4		
Fraser River		2	1.6	5.3	4.7	7.7[a]	0.59	5.6	4.2		0.49
Captain Passage	Chromosorb T	1			1.2	4.6		2.1	1.3		
Saltspring Island	XAD-2	1	0.23	0.33	0.43	2.0[a]	0.22	2.1	1.3		0.21
		2	0.38	0.56	0.64	1.3[a]	0.07	1.8	1.5	0.09	0.37
Patricia Bay	Chromosorb T	1		0.74	0.79	0.76	0.11	2.7	1.6	0.11	0.24
Saanich Inlet		2			0.07	1.4		2.2	1.1		0.30
		3A[c]				0.69		1.8	1.1		0.48
		3B[c]				0.40	0.10	1.9	1.0	0.12	0.31
		4	0.02	0.01	0.03	0.18	0.05	2.4	1.4	0.09	0.15
	XAD-2	1	0.78	1.3		1.7[a]	0.15	2.5	1.4	0.49	0.71
		2	0.83	1.1	0.55	1.6[a]	1.6	3.4	2.2		
		3	0.19	1.3	0.40	0.90[a]		2.2	1.2		0.34
		4		0.70		1.3[a]		2.9	2.0		

[a] Indicates a concentration above the limit of quantitation. [b] Indicates that the measurement could be blank corrected but not tested against the detection limit since a standard deviation was not available for the blank. In all other cases there was no measurable blank, and measurements are not blank corrected. [c] Replicate GC/MS analysis of the same sample.

acenaphthylene, acenaphthene, and fluorene but agreed well with XAD-2 for phenanthrene and above, particularly for the higher volume samples.

The PAH levels were much lower in the Mackenzie River than in southern British Columbia. As only two of the higher PAH concentrations were above detection for the Chromosorb T columns, there is no basis for comparison of the PAH for this data set. Fewer than half of the higher PAH concentrations were above detection for XAD-2.

CONCLUSIONS

Dissolved hydrocarbon measurements have been made of individual alkanes and PAHs at pg/L concentrations in natural waters by using Chromosorb T resin. Many of the alkane measurements reported here were just below the limit of quantitation; an increase in the volume of water sampled can lead to improvements in quantitation for the alkanes below triacontane (22).

In column spike experiments and simultaneous in situ sampling, Chromosorb T resin has proven superior to XAD-2 for the quantitation of alkane hydrocarbons. The two resins are comparable for the study of three-ring and higher PAHs. We have also shown that PCA is an elegant method for studying resin column sample and blank hydrocarbon composition.

Since we sampled the Fraser and Mackenzie Rivers each at their minimum flow, we expected dissolved hydrocarbon levels (from both industrial and natural inputs) to be at their highest. In addition, the Mackenzie River was ice-covered with a very low suspended particulate load, which should reduce both evaporative losses and scavenging of dissolved hydrocarbons. If outliers are removed from consideration (Table III), the total dissolved alkane concentrations in southern British Columbia waters and the Mackenzie River are very similar. These hydrocarbon concentrations may serve as an estimate of the upper limit of true dissolved hydrocarbon concentrations in natural waters.

ACKNOWLEDGMENT

We thank Peter Wangersky of Dalhousie University, Halifax, NS, and Blair Humphrey of Seakem Oceanography Ltd., Sidney, BC, for their help during the planning phases of this study. We also thank Hillary Adams of the Institute of Ocean Sciences and Dave Herbert, Dave Hope, Romey Cole, and Georgina Brooks of Seakem Oceanography for their assistance with the extraction and analysis of samples and the column spike recovery tests. Dave Veltkamp of the University of Washington, Seattle, is also thanked for his instruction and helpful advice in the use of principal components analysis. Dale McCullough and Glen Miskulin of the Institute of Ocean Sciences assisted with the design and construction of sampling equipment, and the officers and crew of the CSS *Vector* helped during the sampling.

Registry No. Dodecane, 112-40-3; tetradecane, 629-59-4; hexadecane, 544-76-3; eicosane, 112-95-8; docosane, 629-97-0; tetracosane, 646-31-1; hexacosane, 630-01-3; octadecane, 593-45-3; triacontane, 638-68-6; dotriacontane, 544-85-4; tetratriacontane, 14167-59-0; hexatriacontane, 630-06-8; naphthalene, 91-20-3; 2-methylnaphthalene, 91-57-6; acenaphthylene, 208-96-8; acenaphthene, 83-32-9; fluorene, 86-73-7; phenanthrene, 85-01-8; anthracene, 120-12-7; fluoranthene, 206-44-0; pyrene, 129-00-0; benz[*a*]anthracene, 56-55-3; chrysene, 218-01-9; benzo[*k*]-fluoranthene, 207-08-9; benzo[*a*]pyrene, 50-32-8; Chromosorb T, 9002-84-0; Amberlite XAD-2, 9060-05-3; water, 7732-18-5.

LITERATURE CITED

(1) Slauenwhite, D. E.; Johnson, B. D.; Wangersky, P. J. Column Design and Testing for the Johnson-Wangersky In Situ Pump Sampler. *Rep. Nat. Res. Counc. Can., Mar. Anal. Chem. Stand. Program* **1985**, No. 26325.
(2) Green, D. R. An Advanced Water Sampling System for In Situ Concentration of Trace Compounds from Water. In *Proceedings of Marine Data Systems International Symposium*; New Orleans, LA, April 30–May 2, 1986; Marine Technology Society: 1986.
(3) Green, D. R.; Stull, J. K.; Heesen, T. C. *Mar. Pollut. Bull.* **1986**, *17*, 324–329.
(4) Green, D. R.; Le Pape, D. *Anal. Chem.* **1987**, *59*, 699–703.
(5) Harris, J. C.; Cohen, M. J.; Grosser, Z. A.; Haynes, M. J. "Evaluation of Solid Sorbents for Water Sampling." EPA-600/2-80-193; 1980.
(6) Care, R.; Morrison, J. D.; Smith, J. F. *Water Res.* **1982**, *16*, 663–665.
(7) Hunt, G.; Pangaro, N. *Anal. Chem.* **1982**, *54*, 369–372.
(8) Josefson, C. M.; Johnston, J. B.; Trubey, R. *Anal. Chem.* **1984**, *56*, 764–768.
(9) Gómez-Belinchón, J. I.; Grimalt, J. O.; Albaigés, J. *Environ. Sci. Technol.* **1988**, *22*, 677–685.
(10) Erickson, P.; Fowler, B. The Flux of Suspended Particulates, Petroleum Related Hydrocarbons, Trace Metals and Nutrients from the Mackenzie River During the Winter Season: A Pilot Study of the East Channel. Indian and Northern Affairs Canada Environmental Studies Report No. 48, Ottawa, Canada, 1987.
(11) McLaughlin, F. A.; Yunker, M. B.; Macdonald, R. W.; Whitehouse, B. G.; Fowler, B. R.; Smyth, T. A.; Cretney, W. J. NOGAP B.6: Hydrocarbon sampling intercomparisons conducted in the Fraser River and Saanich Inlet, BC and at Norman Wells, NWT. Can. Data Report Hydrogr. Ocean Sci. 60, in preparation.
(12) Yunker, M. B.; McLaughlin, F. A.; Fowler, B. R.; Smyth, T. A.; Cretney, W. J.; Macdonald, R. W.; McCullough, D. NOGAP B.6: Methods of hydrocarbon sample collection and analysis. Can. Data Report Hydrogr. Ocean. Sci. 60, in preparation.
(13) Eichelberger, J. W.; Harris, L. E.; Budde, W. L. *Anal. Chem.* **1975**, *47*, 995–1000.
(14) Geladi, P.; Kowalski, B. R. *Anal. Chim. Acta* **1986**, *185*, 1–17.
(15) Kvalheim, O. M. *Anal. Chim. Acta* **1985**, *177*, 71–79.
(16) Wold, S. *Technometrics* **1978**, *20*, 397–406.
(17) Wold, S.; Albano, C.; Dunn, W. J.; Edlund, U.; Esbensen, K.; Geladi, P.; Hellberg, S.; Johansson, E.; Lindberg, W.; Sjöström, M. In *Chemometrics, Mathematics and Statistics in Chemistry*; Kowalski, B. R., Ed. D. Reidel: Boston, 1984; pp 17–95.
(18) Parrish, C. C. *Mar. Chem.* **1988**, *23*, 17–40.
(19) Whitehouse, B. G.; Parrish, C. C.; Wangersky, P. J. The Analysis of Organic Compounds in Seawater, 1978–1983. *Rep. 9—Nat. Res. Counc. Can., Mar. Anal. Chem. Stand. Program* **1984**, No. 23609.
(20) Osterroht, C. *J. Chromatogr.* **1974**, *101*, 289–298.
(21) James, H. A.; Steel, C. P.; Wilson, I. *J. Chromatogr.* **1981**, *208*, 89–95.
(22) Yunker, M. B.; Fowler, B. F. NOGAP B.6: Hydrocarbons in the Mackenzie River Delta and Beaufort Sea coastal zone. Can. Contractor Report Hydrogr. Ocean Sci., in preparation.
(23) Keith, L. H.; Crummett, W.; Deegan, J.; Libby, R. A.; Taylor, J. K.; Wentler, G. *Anal. Chem.* **1983**, *55*, 2210–2218.
(24) Scalan, R. S.; Smith, J. E. *Geochim. Cosmochim. Acta* **1970**, *34*, 611–620.

RECEIVED for review September 29, 1988. Accepted March 15, 1989. This study was part of Project NOGAP B.6 Beaufort Sea Oceanography, directed by the Department of Indian and Northern Affairs Canada. Principal components software was provided by the Chemometrics Clinic, Seattle, WA, under the terms of Contract 06SB FP941-6-2751. A large portion of the extractions and analyses was performed by Seakem Oceanography Ltd. and CBR International Corp. of Sidney, BC, under Contracts 09SB FP941-7-7137 and 06SB FP941-6-2324. Additional funding by the Environmental Protection Service and Indian and Northern Affairs Canada was provided to carry out the sampling at Norman Wells, NWT, under the terms of Contract 01SG KE501-6-0105.

Anal. Chem. 1989, 61, 1344–1347

Fluorescence-Detected Circular Dichroism for On-Column Detection in Capillary Electrophoresis

Patrice L. Christensen and Edward S. Yeung*

Ames Laboratory—USDOE and Department of Chemistry, Iowa State University, Ames, Iowa 50011

Fluorescence-detected circular dichroism (FDCD) is a selective and information-rich detection method that has obvious applications for biological analytes that are chiral and exhibit fluorescence. This technique is suitably applied for on-column detection in capillary electrophoresis (CE), and advantages over a previous FDCD–HPLC system are discussed. Operation is simplified, analysis is faster, selectivity is increased, and detection limits are improved. The absolute limit of detection ($S/N = 3$) for riboflavin by FDCD–CE is 0.2 fmol or 0.07 pg. This is an improvement of more than 3 orders of magnitude for FDCD. The FDCD–CE system allows optical activity measurements in picoliter volumes. FDCD, indirect fluorescence, and direct fluorescence analysis can all be carried out with the detector system described here.

Many of the current challenges facing analytical chemists arise from the rapidly advancing and expanding fields related to biology and medicine. The need for improved analytical separation and detection methods, especially those suitable for complex biochemical systems, is increasing. In the area of separations, the move has been toward smaller diameter chromatographic columns. Capillary chromatography and capillary electrophoresis (CE) are now offering highly efficient and versatile separations.

On the detection side, a number of well-known methods have been modified for increased sensitivity and applied to these separation techniques. Some methods such as conductivity (*1*, *2*) and indirect fluorescence (*3*, *4*) are essentially universal. The best reported detection limits, given as quantity injected, for these techniques are approximately 500 fmol (*2*) and 50 amol (*4*), respectively. However, in complex biological samples a detection method with additional selectivity can be advantageous. Since many biomolecules are inherently chiral, it seems reasonable to look toward methods that take advantage of the specificity due to optical activity. Fluorescence-detected circular dichroism (FDCD) (*5*) is one such method.

In addition to high selectivity, the inherent chirality information of FDCD is an advantage over many commonly used detection methods. Chiral molecules exhibit circular dichroism (CD) that varies in relation to molecular conformation. Since FDCD measurements can be directly related to standard CD measurements (*6*), they can provide the analyst with important structural information. This type of information can be useful for monitoring the progress of a reaction or comparing the effects of different solvents on conformation.

Optical rotation is another method that gives this type of structural information for chiral molecules. A laser-based micropolarimeter (*7*) has been introduced as an optical activity detector (OAD) for liquid chromatography (LC) and demonstrated in the analysis of a variety of samples (*8–13*). One system employing high-frequency modulation (*14*) can measure rotations as small as 1×10^{-6} deg, which corresponds to detectability of approximately 1 ng or 10^{-7} M for favorable analytes. Modifications to the polarimeter have enabled its coupling to microbore LC (*15*), but further miniaturization is not likely to produce a polarimetric detector suitable for capillary columns smaller than 200-μm i.d. Further improvements in the OAD and application to very small volumes are hindered by the signal dependence on path length. Thus, it does not readily lend itself to on-column detection, and other methods capable of measuring optical activity need to be explored for capillary systems.

The potential information content of FDCD is further increased by the ease with which total fluorescence (FL) can be measured simultaneously. In this way, it may be possible to actually identify a compound on the basis of its unique FDCD/FL signal ratio, as was shown in an analogous manner for PTH amino acids (*16*) by use of optical rotation and UV absorbance (OA/UV) measurements. Likewise, determination of enantiomeric purity, which is especially important in the pharmaceutical industry, may be possible with the FDCD/FL measurement, as has been shown for OA/UV and OA/RI (refractive index) methods (*17*, *11*).

Because of the ease of miniaturization and high sensitivity, direct fluorescence analysis is especially suited to detection in CE. Sub-attomole detection limits have recently been reported for direct fluorescence of derivatized amino acids in capillary electrophoresis. Kuhr and Yeung report a detection limit of 0.5 amol for dansyl alanine (*4*), and Cheng and Dovichi report 0.009 amol as the detection limit for a better-matched chromophore, the FITC derivative of alanine (*18*). FDCD is a variation of FL and is therefore also readily interfaced to CE.

The previous FDCD–HPLC system (*5*) employed a postcolumn flow cell with a 1.2-cm observation path length and 14-μL total volume. Although the method showed an improved riboflavin limit of detection (LOD) by FDCD (170 pg), it also showed significant artifact signals. This was demonstrated by the substantial FDCD signal obtained for an optically inactive sample component, 4-methylumbelliferone. The artifact is attributed to an imbalance in the modulation of the incident light. Although such artifacts do not necessarily reduce the detection power of FDCD, they do reduce the selectivity of the technique and complicate quantitation. Reducing or eliminating these artifacts is of current interest.

Capillary electrophoresis, first introduced as high-performance zone electrophoresis (HPZE) (*1*) and capillary zone electrophoresis (CZE) (*19*, *20*), has rapidly come to the forefront in analytical chemistry as a very promising technique for the separation of charged species. This is substantiated by a recent review (*21*). Capillary internal diameters typically range from 5 to 100 μm, and detection volumes can be few to tens of picoliters. The current surge of activity in molecular biology and biotechnology and the potential applications of CE involving analytically interesting biomolecules make a strong argument for coupling the separation with FDCD detection. Our goal in this study is to demonstrate the successful application of on-column FDCD in CE and to show improved limits of detection and better discrimination of artifact signals.

EXPERIMENTAL SECTION

Electrophoresis Apparatus. The electrophoresis system used in this work is very similar to that described previously (*4*). A high-voltage power supply (Spellman, Plainview, NY; Model

0003-2700/89/0361-1344$01.50/0

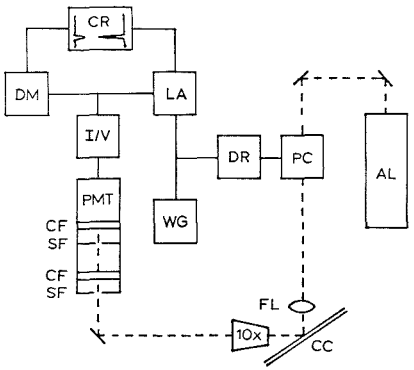

Figure 1. Schematic diagram of FDCD and FL detection system for capillary electrophoresis: AL, argon laser; PC, Pockels cell; DR driver; WG, waveform generator; LA, lock-in amplifier; DM, digital multimeter; CR, dual-pen chart recorder; FL, focusing lens; CC, capillary column; 10×, microscope objective; SF, spatial filters; CF, color filters; PMT, photomultiplier tube; I/V, current-to-voltage converter. Solid lines indicate electrical connections, and dashed lines show the optical path.

UHR50PN50) provides the electromotive force across the capillary. The anodic, high-voltage lead is isolated in a Plexiglass box with a safety interlock, and the cathodic end is at ground potential.

Capillary Columns. A variety of fused silica capillaries (10–25-μm i.d., 150-μm o.d., 50–80 cm in length; Polymicro Technologies, Phoenix, AZ), both untreated and silylated, were used in this work. The silylation procedure employed here was a modification of a method originally described for the silylation of glass plates (*22, 23*). The columns were first rinsed with acetone to remove impurities and then filled with a 0.2% solution of γ-(methacryloxy)propyltrimethoxysilane (Sigma, St. Louis, MO) in a 1:1 (v/v) ethanol/water solvent mixture. After they were heated to 60 °C for 45 min, the capillaries were rinsed with methanol, filled with buffer solution, and equilibrated in the electrophoresis system.

FDCD Detection System. A schematic diagram of the detection system, which has similarities to the earlier system (*5*), is shown in Figure 1. An argon ion laser (Control Laser Corp., Orlando, CA; Model 554A) operating at 488 nm is the excitation source. The linearly polarized laser light is converted into alternating left and right circularly polarized light (LCPL, RCPL) by a Pockels cell electrooptic modulator (Lasermetrics Inc., Teaneck, NJ; Model 3030) as described elsewhere (*24*).

The modulated light is focused onto the detection region of the capillary by a short focal length lens, and collection of fluorescence is at 90° to the incident beam with a 10× microscope objective. An enlarged image of fluorescence from within the capillary is focused on the photomultiplier tube (PMT) (Hamamatsu, Middlesex, NJ; Model R928). Two sets of spatial filters and color filters (Corning Glass, Corning, NY; Model 3-70) are mounted in a blackened tube before the PMT to selectively pass fluorescence while rejecting scattered laser light and room light. Earlier work in indirect fluorescence detection with capillary electrophoresis (*3, 4*) had the column mounted for Brewster's angle of incidence to minimize scattering. However, in FDCD it is necessary to preserve the circular polarization purity inside the column, and the Brewster's angle arrangement is not suitable. Therefore, the column is mounted for normal incidence in these experiments. When properly focused, all light rays will enter perpendicular to the cylindrical cell, thereby preserving the circular polarization. The angle between the column and the collection optics can be adjusted (*25*) to minimize the amount of scatter collected while retaining normal incidence at the capillary.

The fluorescence signal from the PMT is converted to a voltage and sent to the lock-in amplifier (EG&G PARC, Princeton, NJ; Model HR-8) and a digital multimeter (Keithley Instruments, Cleveland, OH; Model 160B) simultaneously. The demodulated FDCD signal is obtained from the lock-in amplifier using a 1-s time constant, and the digital multimeter displays the average total fluorescence signal. Both of these signals are displayed on the dual-pen chart recorder (Measurement Technology, Inc., Denver, CO; Model CR452).

Reagents. All chemicals were of certified grade unless specified differently. Sodium bicarbonate (Fisher Scientific, Fair Lawn, NJ) buffers were prepared in deionized water (Millipore Corp., Bedford, MA; Milli-Q System) and pH-adjusted with sodium hydroxide solution. Standard samples of (−)-riboflavin (Aldrich Chemical, Milwaukee, WI; 98%) and disodium fluorescein (Eastman Kodak, Rochester, NY) were dissolved in the electrophoretic buffer solutions employed. Fluorescein was also included in some of the buffer systems. Because these experiments were carried out in basic solution (pH 8.5–10.5), buffers were purged with nitrogen before use and the pH was checked or adjusted on a daily basis. All quantitative data were obtained with freshly prepared buffer and sample solutions.

Operating Procedures. In the studies reported here, the argon laser is under servo control for power stability and provides between 150 and 300 mW at the capillary. Unless otherwise specified, LCPL and RCPL are modulated at 1 kHz. The modulation electronics are optimized for balance and efficiency (typically 90%) before making any fluorescence measurements. Optimal positioning of the capillary requires fine two-dimensional adjustment and is characterized by good beam quality in the transmitted beam. Initially the electrophoresis buffer contains a low concentration of disodium fluorescein (10^{-5} to 10^{-6} M) to aid in alignment of collection optics. The total background fluorescence signal for these buffers is kept in the 2–5-μA range by adjustment of the PMT voltage (200–700 V).

The major buffer component is sodium bicarbonate at approximately 1×10^{-3} M. All injections are by electromigration, typically 1 s at +30 kV, and the voltage is held constant at +30 kV throughout each run. Estimation of injection volume is based on column diameter, elution time, and injection time and is 0.6 nL for a 20-μm capillary. Simultaneous FDCD and FL electropherograms are obtained for all samples injected. Calculations are based on peak heights, and peak-to-peak noise is measured from the recorded electropherograms.

RESULTS AND DISCUSSION

Feasibility. It is first necessary to show that FDCD is feasible as a detection method in open tubular capillaries of typical CE dimensions. With this as our aim we chose to use a simple electrophoretic separation and did not necessarily optimize the CE system for highly efficient separations. Because the balance between incident intensity for LCPL and RCPL ($I_{0,L}$ and $I_{0,R}$) and the stability in the modulation are very critical for CD measurements (*5*), routine stability measurements are made to assess system performance. The fluorescence signal produced as fluorescein flows through the capillary provides the data for this measurement. Stability is calculated as $^1/_2(I_F/N)$, where I_F is the total fluorescence signal from the phototube, and N is the noise on the lock-in base line.

A stability of 5000 is routinely obtained in this system. Greater stability (1×10^4) was seen for larger diameter columns under gravity flow or compressed-gas-pressure flow, and stabilities as high as 1×10^5 have been measured for the incident light and for the laser light transmitted through the capillary. The stability measured for fluorescence is typically 10 times worse than that of the incident light. It is also expected that stability will decrease as the capillary dimensions become smaller due to increased restraints on alignment and mechanical rigidity. In addition, complications such as heating the analyte or bleaching out its fluorescence will become more severe and limit stability as the laser is focused into smaller volumes. Considering these factors, a stability of 5000 is still quite reasonable, and FDCD signals for 5×10^{-5} M riboflavin can easily be obtained.

In some ways, FDCD seems better suited to CE separations than to high-performance liquid chromatography (HPLC). Optimization of modulation and detection requires that the

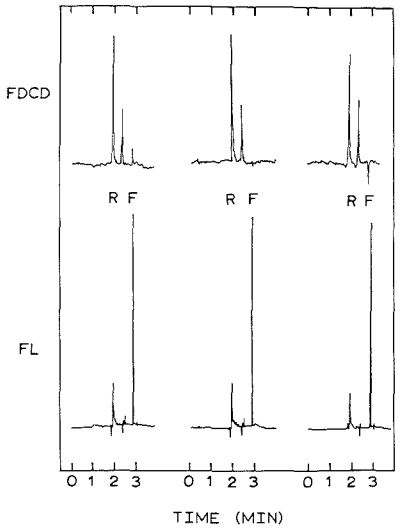

Figure 2. Control of suppression for non-CD artifact. A series of simultaneous FDCD and FL electropherograms is presented, showing changes in suppression of a non-CD artifact. Conditions: sample, 4 × 10^{-5} M riboflavin (R), 6 × 10^{-6} M fluorescein (F); buffer, 2 × 10^{-3} M bicarbonate, 2 × 10^{-6} M fluorescein, pH 9.3; column, 20 μm i.d. × 50 cm, untreated.

analyst be able to change the composition of eluting buffer rapidly and with relative ease. It is also important that this procedure not alter the optical alignment or any other experimental parameters that can affect the balance between $I_{0,L}$ and $I_{0,R}$. In the HPLC system (*5*) it was necessary to connect a second eluent pump to the detection cell in order to introduce an optically inactive fluorophore for the purpose of balancing I_0. In CE, it is very simple to change the eluting buffer. The injection end of the capillary is simply inserted into another vial containing the new buffer, just as when a sample is injected. The reequilibration of the column and fluorescence signal following a buffer change is rapid in comparison to that required in HPLC, and switching buffers does not disturb the precise alignment or alter modulation. In addition, the methods developed here for assessment of stability and for continuous monitoring of direct fluorescence make FDCD more attractive because they do not require any changes in the optical system.

Discrimination of Artifacts. Actual verification that stability is sufficient can only be seen in the FDCD results. Figure 2 shows the FDCD and FL electropherograms for a sample containing riboflavin and fluorescein. The lower traces correspond to direct fluorescence while the upper traces show the FDCD signal. Under these separation conditions, riboflavin elutes first. A second optically active peak eluting after riboflavin is apparent in these traces and has been attributed to a photodecomposition product of riboflavin, as it is not present in freshly prepared solutions but begins to appear after a few hours of exposure to light at pH 9.3. Fluorescein is the latest eluting peak in these experiments. Figure 2 shows that good separation efficiencies are obtained. The 1-s injection time and 120-s elution time for riboflavin limit the number of available theoretical plates to 57 600 [$N = 4(t_R/W_{1/2})^2$]. We measured a plate count of 80 000 for riboflavin and more for fluorescein in Figure 2. This is in good agreement with predictions since the injected plug is probably not square.

Because fluorescein is not optically active, it cannot produce a true FDCD signal. However, as seen previously (*5*) and as evident in the first trace in Figure 2, there is some FDCD signal associated with the elution of the optically inactive species. A ratio of merit (discrimination or suppression ratio) can be calculated directly from these simultaneous measurements for comparison of artifact suppression. We define this ratio, r, as

$$r = \frac{\mathrm{fdcd(oi)/fl(oi)}}{\mathrm{fdcd(oa)/fl(oa)}}$$

where fdcd is the fluorescence-detected circular dichroism signal, fl is the direct fluorescence signal, and (oi) and (oa) indicate optically inactive and optically active samples, respectively. As long as both FDCD and FL signals are obtained simultaneously, r values for a given optically active analyte can be validly compared, even if other experimental parameters vary.

In Figure 2 the concentration of fluorescein is selected to produce a FL signal much larger than the riboflavin FL signal in order to emphasize the degree to which the non-CD artifact is suppressed. This series of electropherograms is obtained by varying the relative amounts of incident LCPL and RCPL by adjusting the bias voltage on the Pockels cell driver. This shows how very small changes in modulation can dramatically affect the suppression of artifacts while the riboflavin FDCD signal changes very little. Similar results can be seen if the lock-in amplifier phase is adjusted. In the FDCD–HPLC system (*5*), the r value for riboflavin is calculated to be +0.55. The r values for the three traces in Figure 2 (left to right) are +0.03, −0.007, and −0.03. This demonstrates the ability to substantially reduce and essentially eliminate these artifacts with careful adjustment in the FDCD–CE system.

We had originally hoped that by placing fluorescein in the buffer solution, the stability could be continuously monitored and adjustments made to maintain good suppression. However, we discovered that it was just as simple to inject a plug of fluorescein only when it was necessary to see the fluorescent image, to measure stability, or to set the driver bias for balance of I_0. Removal of fluorescein from the buffer also led to improved S/N by eliminating background fluorescence signal.

It is apparent that very precise and stable alignment is necessary to achieve good suppression. In fact the modulation seemed to wander frequently without any operator intervention, and artifacts that had been suppressed began to reappear after many minutes. These changes may be caused by electronic instability in the driver, temperature changes in the electronic components or in the Pockels cell crystal itself, or microscale mechanical movement of optical components, especially the capillary.

This points to areas of improvement for the FDCD–CE technique. The Pockels cell requires relatively high modulated voltages and is also temperature-sensitive. A photoelastic modulator (PEM) device can also produce alternating LCPL and RCPL (*26*) and is expected to have higher long-term stability than a Pockels cell. In addition, mounting of the capillary at the detector region can be more rigid to reduce mechanical vibration.

Another example of artifact suppression for a mixture of riboflavin and fluorescein is shown in Figure 3. In this case, the ratio of fluorescein to bicarbonate in the buffer solution has been increased 10-fold. This causes greater displacement of fluorescein in the buffer when riboflavin elutes. Riboflavin is a much weaker fluorophore than fluorescein, and this results in a negative FL peak for riboflavin, similar to the indirect fluorescence peaks (*3, 4*). Interestingly, the FDCD trace is unaffected because ΔI_F is derived only from the riboflavin molecules, and the background fluorescence shows no optical activity. This further supports the selectivity of the FDCD method.

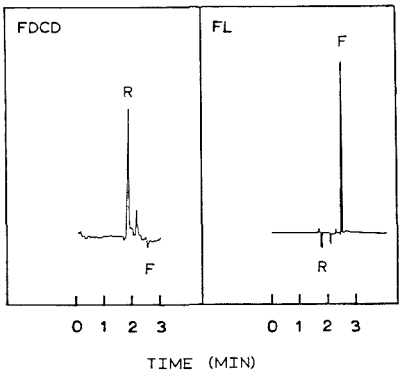

Figure 3. Simultaneous FDCD and FL electropherogram showing negative FL signal for riboflavin due to displacement of fluorescein in buffer solution. Conditions: sample, 1×10^{-4} M riboflavin (R), 5×10^{-5} M fluorescein (F); buffer, 1×10^{-3} M bicarbonate, 1×10^{-5} M fluorescein, pH 9.3; column, 20 μm i.d. × 50 cm, untreated.

Limit of Detection. Although the artifact signals here are usually small, all FDCD signals are corrected for any artifact prior to other calculations. The corrected FDCD signal, fdcd′, is given by

$$\text{fdcd}'(\text{oa}) = \text{fdcd}(\text{oa}) - \frac{\text{fdcd}(\text{oi})}{\text{fl}(\text{oi})} \times \text{fl}(\text{oa})$$

where all terms are defined above.

The best FDCD LOD ($S/N = 3$) achieved for riboflavin is 0.2 fmol (0.07 pg), as calculated from the corrected FDCD signal of 45.5 units (90 μV) and the FDCD base-line noise of 0.3 unit (0.6 μV). The concentration LOD is 1×10^{-6} M injected. This result is obtained for a 0.2-nL injection of a solution containing 5×10^{-5} M riboflavin and 7×10^{-6} M fluorescein in a 10-μm-i.d. silylated column. The electrophoretic buffer, 2×10^{-3} M bicarbonate at pH 9.3, contains no fluorescein. This detection limit shows more than a 2000-fold improvement over that obtained with the FDCD–HPLC system (*5*). Also important for consideration is the dynamic range of the system. We found that in general the analyte concentration has to be lower than that of the running buffer by a factor of 10 to preserve the separation efficiency. This then provides a dynamic range of 200 in the present experiment. Naturally, higher buffer strength can be used (which in general is better for CE) to extend the dynamic range. Since the buffer is nonfluorescing, the detection limit should not change, in contrast to the case of indirect fluorescence detection (*3*, *4*).

Several differences in the two systems are worth noting. The wavelength used in the earlier system was 325 nm and is more favorable than 488 nm for riboflavin CD. Also, the previous system used a 150-kHz modulation frequency and a 10-s time constant, compared to 1-kHz modulation and a 1-s time constant used here. We found it difficult to achieve the same high degree of artifact discrimination at the higher frequencies, which may indicate that the Pockels cell driver becomes less stable as frequency increases. Despite the disadvantages associated with these factors, the reduced column diameter and detection volume in CE and the use of an imaging system with better stray light rejection allow improvement in the FDCD detection limit.

Future Directions. The ability to measure optical activity in such a small sample has obvious applications in biological fields, where sample quantities are often very limited. The technique can be applied to a wide varity of analytes including derivatized amino acids, peptides, and proteins. The very rapid separation (<2 min) of several NDA amino acids by CE (*27*) has recently been demonstrated. Even though all amino acids could not be separated with this method, simultaneous FDCD/FL detection of these amino acid derivatives using a helium cadmium (442 nm) laser may allow identification for implementation in protein sequencing, where the increased speed of analysis would be of great advantage. McCormick (*28*) shows highly efficient separations of proteins and peptides in modified capillaries. By use of the UV lines of an argon ion laser, the natural fluorescence of tryptophan (and tyrosine) should allow FDCD analysis for these types of separations. The application of such an FDCD–CE system for the analysis of protein components from a single cell is also of interest. Even when chiral species are separated in CE (*29*), FDCD will allow identification of the order of elution of the enantiomers.

To our knowledge, this work demonstrates the measurement of an optical activity signal for the smallest volume and smallest absolute quantity of any chiral species. Fluorescence-detected circular dichroism will never be as sensitive as direct fluorescence because the signal is derived from $\Delta\epsilon$ rather than ϵ, the molar absorptivity, and $\Delta\epsilon$ is typically orders of magnitude smaller than ϵ. Thus, FDCD trades some sensitivity for the increase in selectivity. The fact that fluorescence, indirect fluorescence, and FDCD analyses can all be done with the same apparatus and applied to minute volumes typical of capillary electrophoresis and capillary chromatography should lead to increased use of these techniques, both in combination and separately.

ACKNOWLEDGMENT

We thank T. Garner for his assistance in the setup of the CE system and silylation of columns.

LITERATURE CITED

(1) Mikkers, F. E. P.; Everaerts, F. M.; Verheggen, Th. P. E. M. *J. Chromatogr.* **1979**, *169*, 11–20.
(2) Huang, X.; Pang, T. J.; Gordon, M. J.; Zare, R. N. *Anal. Chem.* **1987**, *59*, 2747–2749.
(3) Kuhr, W. G.; Yeung, E. S. *Anal. Chem.* **1988**, *60*, 1832–1834.
(4) Kuhr, W. G.; Yeung, E. S. *Anal. Chem.* **1988**, *60*, 2642–2646.
(5) Synovec, R. E.; Yeung, E. S. *J. Chromatogr.* **1986**, *368*, 85–93.
(6) Lobenstine, E. W.; Turner, D. H. *J. Am. Chem. Soc.* **1980**, *102*, 7786–7787.
(7) Yeung, E. S.; Steenhoek, L. E.; Woodruff, S. D.; Kuo, J. C. *Anal. Chem.* **1980**, *52*, 1399–1402.
(8) Kuo, J. C.; Yeung, E. S. *J. Chromatogr.* **1981**, *223*, 321–329.
(9) Kuo, J. C.; Yeung, E. S. *J. Chromatogr.* **1982**, *229*, 293–300.
(10) Kuo, J. C.; Yeung, E. S. *J. Chromatogr.* **1982**, *253*, 199–204.
(11) Reitsma, B. H.; Yeung, E. S. *J. Chromatogr.* **1986**, *362*, 353–362.
(12) Reitsma, B. H.; Yeung, E. S. *Anal. Chem.* **1987**, *59*, 1059–1061.
(13) Reitsma, B. H.; Yeung, E. S. *J. Chromatogr.* **1987**, *405*, 295–303.
(14) Bobbitt, D. R.; Yeung, E. S. *Appl. Spectrosc.* **1986**, *40*, 407–410.
(15) Bobbitt, D. R.; Yeung, E. S. *Anal. Chem.* **1984**, *56*, 1577–1581.
(16) Chan, K. C.; Yeung, E. S. *J. Chromatogr.* **1988**, *457*, 421–426.
(17) Boehme, W.; Wagner, G.; Oehme, U.; Priesnitz, U. *Anal. Chem.* **1982**, *54*, 709–711.
(18) Cheng, Y. F.; Dovichi, N. J. *Science* **1988**, *242*, 562–564.
(19) Jorgenson, J. W.; Lukacs, K. D. *Anal. Chem.* **1981**, *53*, 1298–1302.
(20) Jorgenson, J. W.; Lukacs, K. D. *Science* **1983**, *222*, 266–272.
(21) Gordon, M. J.; Huang, X.; Pentoney, S. L., Jr.; Zare, R. N. *Science* **1988**, *242*, 224–228.
(22) Neuhoff, V. *Electrophoresis* **1984**, *5*, 251.
(23) Radola, B. J. *Electrophoresis* **1980**, *1*, 43–56.
(24) Christensen, P. L.; Yeung, E. S. *Talanta* **1989**, *36*, 179–184.
(25) Folestad, S.; Johnson, L.; Josefsson, B.; Galle, B. *Anal. Chem.* **1982**, *54*, 925–929.
(26) Kemp, J. C. *J. Opt. Soc. Am. A* **1969**, *59*, 950–954.
(27) Nickerson, B.; Jorgenson, J. W. *HRC CC, J. High Resolut. Chromatogr. Chromatogr. Commun.* **1988**, *11*, 533–534.
(28) McCormick, R. M. *Anal. Chem.* **1988**, *60*, 2322–2328.
(29) Gozel, P.; Gassmann, E.; Michelsen, H.; Zare, R. N. *Anal. Chem.* **1987**, *59*, 44–49.

RECEIVED for review December 2, 1988. Accepted March 28, 1989. The Ames Laboratory is operated by Iowa State University for the U.S. Department of Energy under Contract No. W-7405-Eng-82. This work was supported by the Director of Energy Research, Office of Basic Energy Sciences, Division of Chemical Sciences.

Anal. Chem. 1989, 61, 1348–1353

Stationary Phase Solvation in Capillary Supercritical Fluid Chromatography

Clement R. Yonker* and Richard D. Smith

Chemical Methods and Separations Group, Chemical Sciences Department, Pacific Northwest Laboratory (Operated by Battelle Memorial Institute), Richland, Washington 99352

Mass spectrometric tracer pulse chromatography was used to study stationary phase solvation in capillary supercritical fluid chromatography. A 5% phenyl poly(methylsiloxane) (SE-54) stationary phase was studied by using various binary fluid mixtures of 2-propanol in supercritical CO_2. Sorption isotherms were determined as a function of density (pressure), temperature, and concentration of the binary modifier in the fluid. Results demonstrate that the amount of 2-propanol sorbed in the bonded polymer decreased with increasing fluid density (i.e., pressure). Heats of sorption of 2-propanol for transfer from the fluid phase into the stationary phase were determined.

INTRODUCTION

The interaction of supercritical fluids with a coated liquid stationary phase has been known since 1966, when it was described by Sie et al. in their pioneering studies of solute retention at near-critical and supercritical conditions with CO_2 (*1*). Such effects are important in determining chromatographic retention and are crucial to understanding the details of the separation process in supercritical fluid chromatography (SFC). The solvation of the polymer poly(methyl methacrylate) by CO_2 at selected temperatures as a function of pressure has been reported by Wissinger and Paulaitis (*2*). Novotny and co-workers (*3*) have reported on the swelling of nonextractable polymer films in capillary SFC using supercritical butane and CO_2. The physicochemical effects of swelling on retention and chromatographic performance were discussed.

Recently, Lochmüller and Mink (*4*) have described the adsorption isotherms for ethyl acetate, which was used as a modifier in supercritical CO_2 on a packed column containing unmodified silica. Selim and Strubinger (*5*) have reported the partition behavior of supercritical *n*-pentane in SE-54 (phenyl poly(methylsiloxane)) and SE-30 (poly(methylsiloxane)) in capillary SFC using the mass spectrometric tracer pulse chromatography technique. In spite of these initial reports there is still a fundamental gap in the understanding of stationary phase solvation by a supercritical fluid and the role of solvation on the retention mechanism in both capillary and packed column SFC.

Mass spectrometric tracer pulse chromatography (MSTPC) is a simple, rapid technique for determining phase equilibria at high temperatures and pressures. As described initially by Peterson et al. (*6*), tracer pulse chromatography does not require any deductions from the shapes of diffuse concentration boundaries (*7*) or from asymmetric peaks (*8*, *9*). In tracer pulse chromatography the adsorption isotherm of a single component in the mobile phase is obtained from the net retention volume of the tracer component at several pressures. The only special requirement is the use of mass spectrometric detection of the isotopic tracer. MSTPC has been used by Parcher and co-workers (*10–15*) to study the adsorption isotherms of selected components from the gas phase adsorbed onto solid surfaces, sampling adsorbents and liquid phases. Parcher et al. (*15*) were able to study gas–solid chromatography as a function of surface coverage by various volatile modifiers to determine the effect of the modifier on solute retention as a function of the modifier isotherm.

In this article we report results obtained by using MSTPC applied to capillary SFC with binary fluid solutions of 2-propanol/CO_2. This system was chosen due to the common use of 2-propanol as a fluid modifier for SFC and the fact that the solvent properties of the binary fluid have been extensively studied by the solvatochromic technique. Sorption isotherms for 2-propanol were determined as a function of density (pressure), temperature, and concentration of 2-propanol in CO_2. Heats of sorption were determined for 2-propanol at constant density. These results can lead to a better understanding of the retention process in SFC and a more fundamental comprehension of solvation of the bonded stationary phase when supercritical fluid solutions are used as the mobile phase.

THEORY

Tracer pulse chromatography is a technique that involves the measurement of the retention time of a group of tracer molecules and not the concentration pulse perturbing the system from the introduction of the tracer sample. Some of the inherent assumptions involved in MSTPC are as follows:

(a) The pressure of the isotopic tracer is very low compared to that of the modifier along the column.

(b) The pressure drop along the capillary column is small.

(c) The chromatographic system is at local equilibrium; that is, the partitioning process is both rapid and reversible.

(d) The partition coefficient of the isotope tracer and the nonlabeled modifier are identical.

Therefore, the net retention volume (V_n) of the tracer component can be used to determine the concentration of the solute (i) in the stationary phase ($\bar{C}_i$) as a function of solute concentration in the mobile phase (C_i) and the volume of the stationary phase (V_s) (*6*, *16*):

$$V_n = \bar{C}_i V_s / C_i \tag{1}$$

From chromatographic retention theory

$$N_i^{sp} = \bar{C}_i V_s \tag{2a}$$

and

$$C_i = N_i^{mp} / V_m \tag{2b}$$

where N_i^{sp} is the moles of solute (i) in the stationary phase, N_i^{mp} is the moles of solute (i) in the mobile phase, and V_m is the volume of the mobile phase. For a highly compressible solvent system, such as a supercritical fluid, one can relate the compressibility (Z) to the physical state of the system:

$$Z = PV_m / N_{mp} RT \tag{3}$$

where P is the pressure of the fluid, N_{mp} is the total number

*Author to whom correspondence should be addressed.

0003-2700/89/0361-1348$01.50/0

of moles of fluid solution in the column, R is the gas constant, and T is the system temperature. For an ideal gas $Z = 1$; using a supercritical fluid solution Z must be determined. The compressibility can be calculated from an appropriate equation of state that describes the physicochemical phase behavior of the solution. For this work, a two-parameter cubic equation of state was used to calculate Z as a function of pressure, temperature, and mole fraction for the binary supercritical fluid. The Peng–Robinson equation of state (P-R EOS) was chosen because of its greater accuracy near the critical point of the fluid, using relatively simple mixing rules (*17*). Substituting eq 3 into eq 2b and rearranging, one obtains

$$C_i = N_i^{mp}P/N_{mp}ZRT = Y_iP/ZRT \quad (4)$$

where Y_i is the mole fraction of the solute molecule to be studied in the mobile phase. Upon further substitution of eq 2a and 4 into eq 1 and solving for N_i^{sp}, one finds that the moles of solute in the stationary phase are related to

$$N_i^{sp} = V_nY_iP/ZRT \quad (5)$$

which is similar to the equation reported by Parcher (*12*) except in the case of supercritical fluids, $Z \neq 1$. The independent parameters of P, Y_i, and T can be varied to determine their effect on N_i^{sp} or N_i^{sp}/W_L (where W_L is the weight of the polymeric stationary phase present in the capillary column). Therefore, from simple chromatographic experiments using an isotopically labeled solute (in this case, C_3D_7OD) in MSTPC, one can determine the amount of solute reversibly partitioned into the stationary phase by varying the system pressure or temperature.

EXPERIMENTAL SECTION

SFC/MS System. The SFC/mass spectrometry (MS) system has been described in detail (*18*). The interface between the capillary column restrictor and the MS ion source involved a high flow rate interface (HFR) and is described elsewhere (*19*). The capillary column effluent expands into an independently pumped chamber before the standard chemical ionization source. This allows one to work with high flow rates in the chromatographic system using splitless injections.

Materials and Column. The 2-propanol used in the binary fluid mixtures was obtained from Burdick and Jackson (Muskenburg, MI) and was used without further purification. SFC grade CO_2 was obtained from Scott Specialty Gases (Plumsteadville, PA). The binary fluid mixtures of 2-propanol/CO_2 were mixed directly in the high-pressure syringe pump. This procedure involved first adding a known volumn of 2-propanol into the pump, to which was then added a known weight of CO_2 from a lecture bottle (filled from a CO_2 cylinder). The binary solution is then quickly mixed in the pump, and the concentration (mole fraction) of 2-propanol calculated. Deuterated 2-propanol (C_3D_7OD) was obtained from Cambridge Isotope Laboratories (Woburn, WA) and was mixed with *n*-hexane for injection. The concentration of the deuterated 2-propanol was approximately 5.0×10^{-3} M, of which 0.2 μL was injected on the column. This amount of deuterated 2-propanol injected was much less than that of the natural 2-propanol in the mobile phase.

The capillary column used was prepared in our laboratory and was 30 m long, having a 100 μm i.d. The column was coated by using a pentane solution of the SE-54 stationary phase and was cross-linked twice with azo-*tert*-butane (Alfa Products, Danvers, MA), which prevents extraction by the supercritical fluid mobile phase. The stationary phase had a calculated film thickness of approximately 0.10 μm.

Distribution Isotherms. The MSTPC technique used in this study is based upon mass spectrometric detection of the peak due to the isotopically labeled pulse of solvent modifier as it elutes from the capillary column. Adsorption data can be determined from simple chromatographic experiments that measure the retention time of the tracer pulse. As the amount of partitioning of the solvent modifier into the stationary phase increases, then retention also increases. The sorption data for 2-propanol in the bound SE-54 polymeric stationary phase were determined at temperatures and pressures above the critical temperature and critical pressure for the binary mixtures of 2-propanol/CO_2 (*20*). The MSTPC experiments involved the injection of argon (to determine the true volume of the capillary column for a nonretained component) followed immediately by an injection of the deuterated 2-propanol in *n*-hexane. The mass spectrometer was operated in the electron-impact mode and used single ion monitoring to determine the retention time of argon and of C_3D_7OD in the presence of 2-propanol. From the net retention time of the deuterated 2-propanol and the geometric volume of the capillary column, the net retention volume for the isotope was calculated. Using eq 5, knowing the pressure, temperature, and mole fraction of modifier and calculating the compressibility of the binary fluid solution, one can calculate the number of moles of 2-propanol sorbed into the bonded polymeric stationary phase.

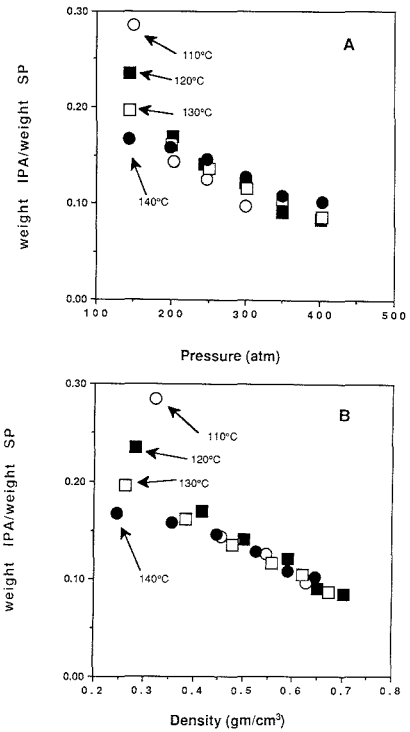

Figure 1. Weight of IPA (2-propanol) absorbed per weight of stationary phase in the capillary column versus pressure (A) and versus density (B) for a constant mole fraction of 0.0258 2-propanol in CO_2 at (○) 110, (■) 120, (□) 130, and (●) 140 °C.

RESULTS AND DISCUSSION

Tracer pulse chromatography, particularly MSTPC, is a technique from which important physicochemical information about the role of fluid pressure, temperature, and modifier composition in stationary phase solvation in SFC can be obtained. The results for the sorption of 2-propanol either onto or into the bonded polymeric stationary phase for a select mole fraction of modifier in CO_2 as a function of pressure and density at various temperatures are shown in parts a and b of Figure 1, respectively. At each temperature studied, the amount of 2-propanol found in the stationary phase decreases as the pressure increases. The amount of 2-propanol associated with the bonded stationary phase also decreases with increasing temperature at constant pressure and constant mole fraction of binary modifier. As density increases for the four

Table I. Weight Percent of 2-Propanol Partitioned into the Stationary Phase as a Function of Density (Pressure) for a Constant Mole Fraction of 0.0258

temp, °C	density, g/cm³	pressure, atm	wt % of 2-propanol[a]
110	0.323	150	22.2
	0.457	203	12.6
	0.546	248	11.2
	0.626	300	8.9
120	0.282	144	19.0
	0.416	201	14.5
	0.503	245	12.4
	0.589	300	10.8
	0.651	350	8.4
	0.704	402	7.8
130	0.263	144	16.4
	0.385	200	13.9
	0.480	251	11.9
	0.557	301	10.4
	0.619	350	9.5
	0.674	403	8.0
140	0.245	143	14.3
	0.358	199	13.7
	0.446	248	12.7
	0.525	300	11.4
	0.589	350	9.8
	0.645	403	9.3

[a] wt % of 2-propanol at 0.0258 mol fraction is 3.5 wt %.

different temperatures, the amounts of 2-propanol sorbed into the stationary phase converge (within experimental error) as seen in Figure 1b.

The interesting question of whether the 2-propanol is adsorbed onto the surface of the bound polymer or whether it is absorbed into the polymer can be ascertained from the simple calculation of the surface area of the capillary column and the number of moles of 2-propanol needed to form a monolayer on this surface. The surface area of 2-propanol was calculated from the molar volume of the molecule. In all cases studied for this report, the amount of 2-propanol sorbed with the SE-54 stationary phase was at least 2 orders of magnitude greater than that needed for monolayer coverage. Therefore, one could conclude that 2-propanol was partitioning into the bound polymeric phase, solvating the polymer rather than adsorbing onto the surface. These data are consistent with data reported with pure polymers (2) and other chromatographic systems where the swelling factors are quite appreciable (*1*, *3*). The data shown in Figure 1 are also consistent with that reported by Selim and Strubinger for supercritical pentane on SE-30 and SE-54 as a function of pressure (*5*, *21*).

The decrease in the amount of 2-propanol partitioned into the stationary phase with pressure can be explained by examining the change in weight percent of the binary modifier in the bound polymer as compared to the bulk weight percent of 2-propanol in the mobile phase. A 0.0258 mol fraction of 2-propanol in CO_2 corresponds to 3.5 wt % of 2-propanol in CO_2. The weight percent of 2-propanol sorbed into the stationary phase is easier to calculate than the mole fraction value because of the unknown molecular weight of the polymer after cross-linking. The estimated weight of 2-propanol in the stationary phase could be high because of the unknown weight of CO_2 also sorbed into the polymer. An additional source of uncertainty is related to the absolute amount of polymeric phase in the capillary, which we believe contributes <10% error to these measurements, but the overall trends will remain constant. The data presented in Tables I–IV show the weight percent of 2-propanol [weight of 2-propanol/(weight of 2-propanol + weight of stationary phase)] partitioned into the stationary phase as pressure increases.

Table II. Weight Percent of 2-Propanol Partitioned into the Stationary Phase as a Function of Density (Pressure) for a Constant Mole Fraction of 0.0371

temp, °C	density, g/cm³	pressure, atm	wt % of 2-propanol[a]
140	0.35	193	18.6
	0.40	219	18.1
	0.50	279	14.3
	0.60	355	14.0
150	0.35	203	17.2
	0.40	231	17.0
	0.50	297	9.5
	0.60	317	13.6
160	0.35	215	16.9
	0.40	245	16.4
	0.50	382	11.0
	0.60	410	13.6

[a] wt % of 2-propanol at 0.0371 mol fraction is 5.0 wt %.

Table III. Weight Percent of 2-Propanol Partitioned into the Stationary Phase as a Function of Density (Pressure) for a Constant Mole Fraction of 0.0509

temp, °C	density, g/cm³	pressure, atm	wt % of 2-propanol[a]
110	0.35	153	34.1
	0.40	171	29.9
	0.50	213	27.5
	0.60	270	24.3
120	0.35	165	30.1
	0.40	186	26.8
	0.50	232	22.7
	0.60	296	23.8
130	0.35	177	26.8
	0.40	200	24.2
	0.50	252	20.7
	0.60	322	20.2

[a] wt % of 2-propanol at 0.0509 mol fraction is 6.8 wt %.

Table IV. Weight Percent of 2-Propanol Partitioned into the Stationary Phase as a Function of Density (Pressure) for a Constant Mole Fraction of 0.0642

temp, °C	density, g/cm³	pressure, atm	wt % of 2-propanol[a]
110	0.35	149	41.4
	0.40	166	36.9
	0.50	207	28.7
	0.60	265	25.4
120	0.35	162	35.9
	0.40	180	31.8
	0.50	227	27.0
	0.60	291	26.0
130	0.35	174	33.4
	0.40	196	29.7
	0.50	246	25.2
	0.60	318	21.7
140	0.35	183	31.0
	0.40	209	27.3
	0.50	267	23.8
	0.60	345	23.9

[a] wt % of 2-propanol at 0.0642 mol fraction is 8.6 wt %.

In this study the stationary phase contained the greater amount of partitioned 2-propanol at the lower densities; as density increases the amount of 2-propanol decreases. This behavior likely reflects the greater solvating power of the mobile phase (compared to that of the stationary phase) as density increases. Similar results were observed in spectroscopic experiments studying the local composition of the binary modifier in the cybotactic region of a probe molecule in a supercritical fluid as a function of density (pressure) (22).

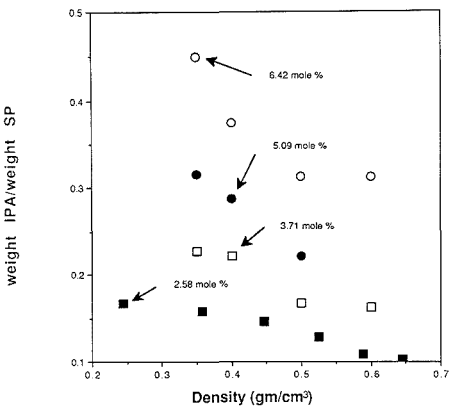

Figure 2. Weight of IPA (2-propanol) absorbed per weight of stationary phase in the capillary column versus density for a constant temperature of 140 °C at (■) 0.0258, (□) 0.0371, (●) 0.0509, and (○) 0.0642 mol fraction of 2-propanol/CO_2.

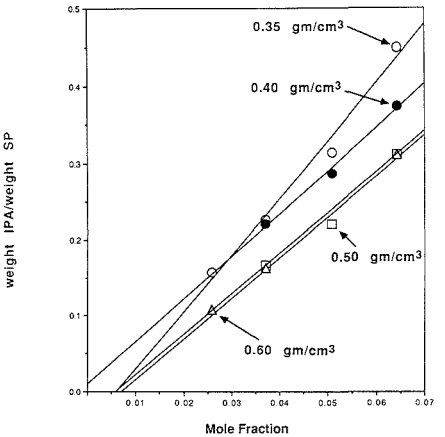

Figure 3. Weight of IPA (2-propanol) absorbed per weight of stationary phase in the capillary column versus mole fraction of 2-propanol/CO_2 at a constant temperature of 140 °C at (○) 0.35, (●) 0.40, (□) 0.50, and (△) 0.60 gm/cm³ densities of the binary fluid.

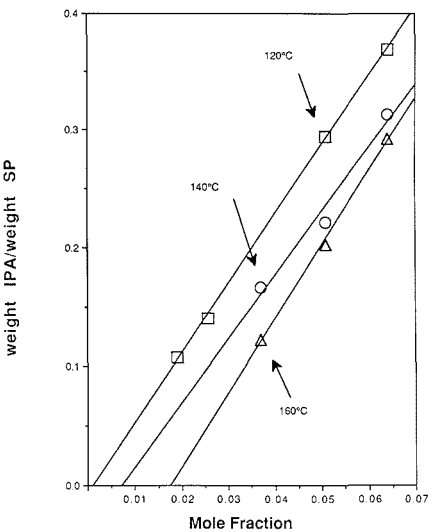

Figure 4. Weight of IPA (2-propanol) absorbed per weight of stationary phase in the capillary column versus mole fraction of 2-propanol/CO_2 at a constant binary fluid density of 0.50 gm/cm³ at (□) 120, (○) 140, and (△) 160 °C.

The local composition about a solute molecule was found to be substantially enriched at lower pressures. The concentration of the organic binary modifier decreased and approached the bulk composition of the binary fluid as density increased, reflecting the increasing solvent strength of the mobile phase as density increases.

The temperature effect shown in Figure 1 is quite substantial at the lower densities and pressures. The increase in temperature could contribute enough thermal energy to the system to begin overcoming the attractive interactions between 2-propanol and the stationary phase. This could contribute to the decreased amount of 2-propanol absorbed into the stationary phase as temperature increases.

The data shown in Figure 2 illustrate the effect of modifier concentration on the amount of 2-propanol absorbed into the stationary phase at constant temperature (140 °C) as a function of mobile phase density. As one would expect, Figure 2 demonstrates that at constant temperature and density the amount of 2-propanol partitioning into the stationary phase decreases as the bulk modifier concentration decreases. Figure 2 also shows a decrease in 2-propanol partitioning into the bound polymeric phase as density increases, which is consistent with Figure 1b.

A replotting of the data in Figure 2 as a function of modifier mole fraction at constant temperature (140 °C) for the various densities is displayed in Figure 3. The 140 °C isotherm data show that as the bulk modifier mole fraction approaches zero, the amount of 2-propanol absorbed into the stationary phase also approaches zero (within the experimental error) for the fluid densities studied. This result is not unexpected, and the linear relationship between binary mole fraction and the amount of 2-propanol absorbed into the stationary phase demonstrates that the bound polymer is still being solvated by 2-propanol as the mole fraction increases.

Figure 4 is a plot of the amount of 2-propanol absorbed into the stationary phase versus mole fraction of 2-propanol at a constant density of 0.50 gm/cm³ for the various temperatures of 120, 140, and 160 °C. For the temperatures of 120 and 140 °C a zero intercept (within experimental error) is obtained at zero binary mole fraction. At 160 °C the data are not readily interpreted, which may be due to a stationary phase transition occurring between 140 and 160 °C as the glass transition temperature for the polymer changes upon solvation by the binary fluid (2). The possible change in the physical state of the bound polymer upon solvation could contribute to the observed deviation in the y intercept as the mole fraction approaches zero. More experimental work at high temperatures with different stationary phases for binary supercritical fluids is needed to resolve this question.

The absorption enthalpy for the partitioning of the binary modifier 2-propanol, between the fluid and stationary phases, can be determined from the MSTPC experiment. From the MSTPC experiments the retention factor, k', can be obtained for the deuterated 2-propanol at constant density of the binary fluid solution. Van't Hoff plots of the natural logarithm of the retention factor for the deuterated 2-propanol versus reciprocal temperature can be made, from which the enthalpy of partitioning (ΔH) for 2-propanol can be obtained (*23*, *24*). Figure 5 shows a plot of ΔH (kcal/mol) against mole fraction

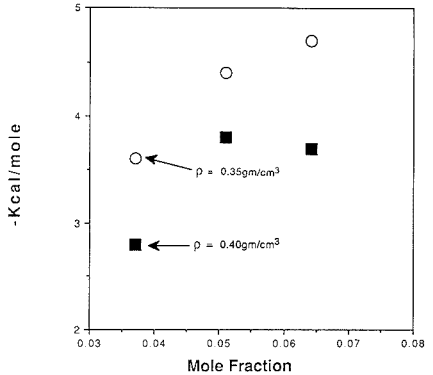

Figure 5. Partition enthalpy (-kcal/mol) versus mole fraction of the binary modifier for the densities of (O) 0.35 and (■) 0.40 gm/cm³.

Table V. Correlation Coefficients for Linear Least-Squares Fit to ln k' versus Reciprocal Temperature for Various Mole Fractions at Constant Density

	correlation coefficients for the following mole fractions		
	0.0371	0.0509	0.0642
ρ = 0.35	0.983	0.992	0.991
ρ = 0.40	0.991	0.989	0.982

of the binary modifier in the fluid. The correlation coefficients from the linear least-squares fit to the experimental data of ln k' versus T^{-1} are shown in Table V. The heats of absorption determined for 2-propanol at a density of 0.35 gm/cm³ range from −3.5 to −4.7 kcal/mol and at a density of 0.40 gm/cm³ from −2.8 to −3.8 kcal/mol. The isosteric heats of adsorption for propane, *n*-butane, and acetone on graphitized carbon black were −5.6, −7.7, and −7.5 kcal/mol, respectively (*15*). The heats of absorption for 2-propanol reported here are reasonable for a system undergoing a process where the mobile phase is partitioned into the bound polymer, rather than the adsorption of 2-propanol onto the surface of the polymer (*23*).

The heat of vaporization for 2-propanol is 9.5 kcal/mol at its boiling point, 82.2 °C (*25*). If 2-propanol was adsorbing in multilayers on the bound polymer surface, then one might expect the heat of adsorption for 2-propanol to approach the heat of vaporization. In the system studied, the heat of absorption for 2-propanol reflects the intermolecular interactions between the bound polymer and 2-propanol, rather than 2-propanol with itself. At higher mole fractions of 2-propanol in the binary fluid solution, the ΔH values for 2-propanol seem to approach a limiting value. This likely reflects the extent of intermolecular interactions between 2-propanol and the stationary phase. As the amount of 2-propanol absorbed into the stationary phase increases, a limit is reached where the extent of intermolecular interactions between the bound polymer and 2-propanol no longer changes with increasing mole fraction of 2-propanol.

CONCLUSIONS

The MSTPC technique can be used to determine absorption isotherms for pure and binary supercritical fluid solutions. The absorption isotherms determined for binary fluid mixtures of 2-propanol in CO_2 showed that at increasing density (pressure) the amount of 2-propanol partitioning into the bound polymeric stationary phase decreased. In the limit of increasing density, the concentration of 2-propanol sorbed in the stationary phase apparently approaches that of 2-propanol in the bulk mobile phase. At lower mobile phase densities 2-propanol partitioned more extensively into the stationary phase. Enthalpies of absorption were also determined from retention factors for deuterated 2-propanol from the MSTPC experiments. These enthalpies are indicative of a partitioning process as compared to the heats of adsorption reported for carbon black.

The present results raise several interesting questions related to the partitioning of solvent modifiers into SFC stationary phases. It has previously been demonstrated that these cross-linked stationary phases can be "swelled" by mobile phases consisting of CO_2 or alkanes (*1*, *3*). The mechanism of such swelling is not well understood, but studies of other polymers by McHugh and co-workers (*26*) suggest that at least two separate processes occur: a kinetically slow process (in which the polymers "conditioned") requiring hours or longer and a second kinetically fast process amenable to the present chromatographic experiments. The present experiments provide no direct information on kinetically slow changes in the stationary phase. The existence of such a slow kinetic process (perhaps due to the extent of cross-linking of the stationary phase) is indicated by the fact that replacement of the CO_2/IPA mobile phase by pure CO_2 results in a gradual decrease in IPA detected by the mass spectrometer, which can be followed over several hours. It is likely that this component of IPA in the stationary phase is also both pressure and temperature dependent and may have an effect on the fraction of IPA that can exchange rapidly with isotopically labeled IPA (as required for the MSTPC approach).

This study clearly shows that the use of solvent modifiers in capillary SFC can affect the chromatographic partitioning by means other than just changes in mobile phase solvating power. The decreased partitioning of IPA into the stationary phase at higher temperatures and higher densities may be qualitatively explained by the greater solvating power of the mobile phase under these conditions. Similar trends are generally observed in studies of partition coefficients for solutes of low volatility. As pressure is increased, density and solvating power increase dramatically while that of the stationary phase remains uncertain. Under such conditions one would expect (at constant density and temperature) that the amount of modifier (solute) in the stationary phase would increase linearly with modifier concentration, consistent with experimental results. Further experimental work remains to define the extent of stationary phase solvation, the dependence upon pressure, and precise mechanism and its role in swelling of the stationary phase in capillary SFC.

ACKNOWLEDGMENT

This work was supported by the Director, Office of Energy Research, Office of Basic Energy Sciences, Chemical Sciences Division of the U.S. Department of Energy, under Contract DE-AC06-76RLO 1830.

LITERATURE CITED

(1) Sie, S. T.; Van Beersum, W.; Rijnders, G. W. A. *Sep. Sci.* **1986**, *1*, 459–490.
(2) Wissinger, R. G.; Paulaitis, M. E. *J. Polym. Sci. Phys. Ed.* **1987**, *25*, 2497–2505.
(3) Springston, S. R.; David, P.; Steger, J.; Novotny, M. *Anal. Chem.* **1986**, *58*, 997–1002.
(4) Lochmüller, C. H.; Mink, L. P. *J. Chromatogr.* **1987**, *409*, 55–60.
(5) Selim, M. I.; Strubinger, J. R. *Fresenius' Z. Anal. Chem.* **1988**, *330*, 246–249.
(6) Peterson, D. L.; Helfferich, F.; Carr, R. J. *AIChE J.* **1986**, *12*, 903–905.
(7) Glueckauf, E. *Nature* **1945**, *156*, 748–749.
(8) Cremer, E.; Huber, J. F. K. *Angew. Chem.* **1961**, *73*, 461–465.
(9) Conder, J. R.; Young, C. L. *Physicochemical Measurements by Gas Chromatography*; Wiley: New York, 1979; Chapter 9.
(10) Parcher, J. F.; Selim, M. I. *Anal. Chem.* **1979**, *51*, 2154–2156.
(11) Parcher, J. F.; Lin, P. J. *Anal. Chem.* **1981**, *53*, 1889–1894.
(12) Parcher, J. F. *J. Chromatogr.* **1982**, *251*, 281–288.
(13) Hyver, K. J.; Parcher, J. F. *Anal. Chem.* **1984**, *56*, 274–278.
(14) Parcher, J. F.; Johnson, D. M. *J. Chromatogr. Sci.* **1985**, *23*, 459–464.

(15) Parcher, J. F.; Lin, P. J.; Johnson, D. M. *Anal. Chem.* **1986**, *58*, 2207–2212.
(16) Peterson, D. L.; Helfferich, F. *J. Phys. Chem.* **1965**, *69*, 1283–1293.
(17) Peng, D. Y.; Robinson, D. B. *Ind. Eng. Chem. Fundam.* **1976**, *15*, 59–64.
(18) Smith, R. D.; Kalinoski, H. T.; Udseth, H. R. *Mass Spectrom. Rev.* **1987**, *6*, 445–496.
(19) Smith, R. D.; Udseth, H. R. *Anal. Chem.* **1987**, *59*, 13–22.
(20) Radosz, M. *J. Chem. Eng. Data* **1986**, *31*, 43–45.
(21) Selim, M. I.; Strubinger, J. R. *J. Chromatogr. Sci.* **1988**, *26*, 579–583.
(22) Yonker, C. R.; Smith, R. D. *J. Phys. Chem.* **1988**, *92*, 2374–2378.
(23) Yonker, C. R.; Smith, R. D. *J. Chromatogr.* **1986**, *351*, 211–218.
(24) Martire, D. E. *J. Liq. Chromatogr.* **1987**, *10*, 1569–1588.
(25) Reid, R. C.; Prausnitz, J. M.; Sherwood, T. K. *The Properties of Gases and Liquids*, 3rd Ed.; McGraw-Hill: New York, 1977; Appendix A.
(26) Liau, I. S.; McHugh, M. A. *Supercritical Fluid Technology*; Penninger, J. M. L., Radosz, M., McHugh, M. A., Krukonis, V. J., Eds.; Elsevier: Amsterdam, 1985; pp 415–434.

RECEIVED for review January 25, 1989. Accepted March 29, 1989.

Investigations of Stationary Phase Modification by the Mobile Phase Surfactant in Micellar Liquid Chromatography

Michael F. Borgerding[1] and Willie L. Hinze*

Department of Chemistry, Wake Forest University, P.O. Box 7486, Winston-Salem, North Carolina 27109

Larry D. Stafford, George W. Fulp, Jr., and William C. Hamlin, Jr.

R. J. Reynolds Tobacco Company, Bowman Gray Technical Center, Winston-Salem, North Carolina 27102

The extent of stationary phase modification possible in micellar liquid chromatography (MLC) is studied by examining the adsorption characteristics of two nonionic surfactants, polyoxyethylene(10 or 23)dodecanol [Brij-22 or Brij-35], and one anionic surfactant, sodium dodecyl sulfate (SDS), on a Resolve C-18 column packing material. Adsorption isotherms are determined by measuring the increase in percent carbon content after equilibration with various amounts of each surfactant. Results obtained, in each case, suggest that surfactant modification of the stationary phase continues well above the critical micelle concentration, in contrast to some previous reports. Nitrogen surface area and pore volume measurements and nitrogen adsorption isotherm hysteresis loop data provide a qualitative understanding of the stationary phase modification produced. All surfactants are found to adsorb as a thick film, with the general structure and pore shapes of the original material retained. Taken together, these data lead to the conclusion that a reported advantage of gradient MLC, i.e., the ability to perform gradient separations without reequilibration of the column, may not apply to all MLC systems. Studies have also been completed in which Resolve C-18 packing material is equilibrated with alcohol-modified SDS surfactant solutions. It is found that approximately twice the amount of the surfactant is sorbed from a methanol modified surfactant solution as compared to a 1-pentanol modified solution. Concomitant nitrogen surface area and pore volume changes are observed. Comparison of these data with chromatographic parameters obtained by using similar alcohol-modified surfactant mobile phases suggests surfactant modification of the stationary phase is largely responsible for reduced efficiency in MLC.

INTRODUCTION

The addition of surfactants as a mobile phase component in high-performance liquid chromatography (HPLC) began as early as the mid-1960's (*1*). When surfactants are added at a concentration below the critical micelle concentration (cmc), i.e. the concentration at which the surfactant monomer dynamically aggregates to form micelles, the technique has been termed ion-pair, soap, and/or paired-ion chromatography, among others. In this mode surfactant molecules act as hydrophobic counterions, producing increased retention of charged analytes. It is clear that in many of the systems studied, surfactant adsorbs into the chromatographic stationary phase, although the contribution to the retention mechanism thus produced continues to be a topic of discussion and experiment (*2*). Dynamic modifications of silica oxide, titanium boride, zirconium oxide, activated carbon, and bonded C18 stationary phases have been observed with charged surfactants and combinations of nonionic and charged surfactants (*3–12*). The extent of dynamic modification in some cases approaches a mass loading equivalent to the original bonded stationary phase, with surface concentrations as great as 8 μmol/m^2 reported.

The use of surfactants in the mobile phase at a concentration exceeding the cmc, termed micellar liquid chromatography (MLC) was first introduced by Armstrong and Henry in 1980 (*13*). In MLC, a micellar pseudophase replaces the typical organic solvent component in the reversed-phase liquid chromatography (RPLC) mobile phase. Although the role of the surfactant in the mobile phase in MLC has been extensively studied (*14–18*), interaction of the surfactant with the chromatographic stationary phase has been investigated to a much lesser extent (*19*, *20*).

In our previous work with nonionic polyoxyethylene(23)-dodecanol (Brij-35) surfactant was observed to adsorb onto the stationary phase at some mobile phase concentrations in amounts approximating that of the bonded hydrocarbon (*21*, *22*). The effects of the surfactant-modified stationary phase were evaluated by comparing the chromatographic behavior of a test mixture as separated by a reference acetonitrile–water mobile phase before and after separations which employed the aqueous Brij-35 surfactant mobile phase. Surfactant modification produced distinct changes in chromatographic selectivity and efficiency with the test solutes studied. Adsorption of the surfactant was found to impart a more polar character to the stationary phase and to produce much reduced chromatographic efficiency, the latter a consistently observed limitation of MLC when no other organic modifier is present in the mobile phase. From this work, we concluded

[1] Present address: R. J. Reynolds Tobacco Company, USA, Bowman Gray Technical Center, Winston-Salem, NC 27109.

0003-2700/89/0361-1353$01.50/0

that reduced efficiency in nonionic MLC is caused in large measure by an increase in the effective film thickness and order of the stationary phase, which is associated with surfactant sorption (*21*). A similar conclusion was reached based on diffusion studies (*23*).

On the basis of alcohol additive studies, other groups had previously attributed the poor chromatographic efficiency observed with micellar mobile phases either to poor wetting of the stationary phase (*24*) or to the diminished rate constants for solute exit from the micellar aggregate in the mobile phase and from the surfactant-modified stationary phase (*25*). It has been demonstrated by use of sodium dodecyl sulfate (SDS) that chromatographic efficiency in MLC can be improved by the addition of several percent alcohol to the mobile phase (*24*, *25*). One of the goals of this work, therefore, was to reexamine those previously published observations in the context of stationary phase modification by characterizing the relationship between organic modifier content of the MLC mobile phase, the amount of surfactant sorbed, and the chromatographic efficiency.

The adsorption characteristics of different surfactants on a RPLC packing material when the surfactants are present above the cmc is another focus in this work. Previously, it has been reported that the ultimate degree of surfactant sorption onto the column packing material in MLC is dictated by the cmc of the particular surfactant in use (*26*, *27*). When the concentration of surfactant is increased above the cmc, the concentration of micelles in solution increases, but the concentration of free monomer remains "essentially" constant and equivalent to the cmc. This property of micellar solutions has been cited as the fundamental reason column reequilibration is not needed in gradient MLC, the premise being that surfactant sorption is only dependent on the concentration of free monomer, hence constant above the cmc. Although earlier reports have implied that this premise is true for all surfactants (*26*, *27*), our previous work indicated that nonionic Brij-35 continues to adsorb on reversed-phase packing at concentrations well above the cmc (*21*). This is not surprising in view of work by Sasaki et al. (*28*) which showed that the free monomer concentration with nonionic surfactants continues to increase above the cmc. Similarly, Berthod et al. have reported continued adsorption, with as much as 20% of the total sorption occurring at surfactant concentrations greater than twice the cmc (*19*, *20*). In fact, reports in the micellar literature indicate that the monomer concentration and amphiphile ion activity of many ionic surfactants do not remain constant as the surfactant concentration is increased above the cmc (*29*, *30*). Thus, the potential advantages of gradient elution MLC may be limited to only a few fortuitous surfactant/stationary phase combinations in which surfactant modification of the stationary phase ceases upon reaching the cmc.

To better understand the extent of stationary phase modification possible in MLC, the adsorption behavior of two nonionic surfactants, Brij-35 and polyoxyethylene(10)dodecanol or Brij-22, and one ionic surfactant, SDS, have been investigated in this work. Instead of using the often employed chromatographic breakthrough method (*5*, *27*), the increase in percent carbon content of the column packing material was monitored before and after surfactant adsorption. Use of this static mode to prepare the modified stationary phase permitted additional evaluation using nitrogen porosimetry. When taken together, a clearer picture of the surfactant-modified stationary phase in MLC begins to emerge from these data.

EXPERIMENTAL SECTION

Apparatus. A Perkin-Elmer 240C elemental analyzer (Perkin-Elmer, Norwalk, CT) equipped with an autosampler, data station, and AD-6 autobalance was used for the determination of percent carbon. All surface area and pore volume measurements were made with a Digisorb 2600 (Micromeritics, Norcross, GA). The chromatographic system employed consisted of Waters components, i.e., automated Model 680 controller, Model 510 pumps, UK-6 injector, and a Model 481 LC spectrophotometric detector, equipped with a 14-μL cell.

Reagents. A 30% (w/v) aqueous solution of Brij-35 [polyoxyethylene(23)dodecanol], obtained from Fisher Scientific Co. (Raleigh, NC), Brij-22 [polyoxyethylene(10)dodecanol], Sigma Chemical Co. (St. Louis, MO), and SDS [sodium dodecyl sulfate], Bio-RAD Laboratories (Richmond, CA), electrophoresis grade; methanol, Burdich and Jackson; 200 proof anhydrous, USP grade ethanol, U.S. Industrial Chemicals Co.; and all other alcohols, Fisher Scientific, were used as received. The column packing material used in this work was Resolve C18 which was purchased by special agreement from Waters Associates (Milford, MA).

Procedures. *Measurement of Surfactant Isotherms.* Surfactant adsorption isotherms were constructed by measuring the carbon content of Resolve C18 packing material after exposure to various amounts of surfactant. For Brij-35, the initial solution concentrations studied included 0.006, 0.1, 0.25, 0.5, 1, 2, 4, 6, 10, and 20% (w/v), corresponding to the range 0.5 to ca. 1700 times the cmc. For Brij-22, 0.2, 0.5, 2, 3, 4, 5, 6, and 10% (w/v) solutions were used, which represents 33 to ca. 1700 times the cmc. For SDS, the initial solution concentrations used were 0.006, 0.02, 0.1, 0.25, 0.5, 1, 6, and 15.8% (w/v) or 0.03 to ca. 70 times the cmc. Following literature convention, in some of the plots (i.e. Figures 1, 2, and 4), the equilibrium surfactant concentration rather than the initial surfactant concentration is utilized. The equilibrium surfactant concentration refers to the actual concentration of surfactant remaining in the solution after accounting for the amount of surfactant sorbed on the Resolve C-18 packing.

To prepare the samples, Resolve C18 was equilibrated with aqueous (or aqueous alcohol) surfactant solutions at a ratio of 25 mL of solution per 1 g of Resolve C18. During the total surfactant exposure period of 24 h, all samples were agitated for ca. 3 h on a wrist-action shaker.

After exposure, each sample was vacuum filtered onto a 0.45-μm Nylon 66 membrane filter, transferred to a sample vial, and dried in a vacuum oven at 60 °C for a minimum of 48 h. After drying, the carbon content of each sample was determined according to standard procedures and the adsorbed surfactant calculated as

$$A_s = \frac{(C_f - C_0)}{(P_s - C_0)} 1000 \qquad (1)$$

where A_s is the amount (mg) of surfactant sorbed per gram of material analyzed, C_f is the percent carbon found, C_0 is the initial carbon content (10.5%) of the Resolve C18 material, and P_s is the carbon weight percent of the surfactant. In addition to correcting for the initial carbon content of the packing material, eq 1 corrects for the fact that the carbon content is determined on an unknown mixture of surfactant and Resolve packing material, of which the surfactant may comprise a significant weight percent (e.g. as much as 15%). The amount (mg) of surfactant sorbed per gram of Resolve C18, A_p, was calculated from eq 2.

$$A_p = \frac{A_s}{1 - (A_s/1000)} \qquad (2)$$

Determination of Surface Areas and Pore Distributions Using Nitrogen Porosimetry. Surface area and pore volume distribution measurements were made on all samples by using the Digisorb 2600, with sample preparation as described above. Standard adsorption and desorption procedures were performed under computer control to develop the nitrogen adsorption isotherm at 77 K. Surface areas, S_{BET}, were calculated by using the BET equation from adsorption isotherm data between relative pressures of 0.05 and 0.21. Pore volume distributions and the cumulative pore volume, V_{cum}, were calculated from the adsorption isotherm for pore diameters between 20 and 600 Å, assuming cylindrically shaped pores, using the method of Barrett et al. (*31*).

Evaluation of Alcohol Modifier Effects. Solutions of 0.285 M SDS containing 5% (v/v) methanol, ethanol, 1-propanol, 1-butanol, or 1-pentanol as organic modifier were agitated on a wrist-action shaker for 1 h. Resolve C18 packing material was

Table I. Effects of Various Alcohol Modifiers on Stationary Phase Modification and Chromatographic Performance

0.285 M SDS alcohol modifier	SDS sorbed (mg/g of Resolve C18)	BET surface area (m^2/g of Resolve C18)	cumulative pore volume, cm^3/g	stationary phase volume, cm^3/g	stationary phase surfactant volume reduction, %	chromatographic parameters[a]		
						k'	N	B/A
none	146	59	0.135	0.35	0	7.1	1530	2.8
5% MeOH	132	63	0.146	0.34	7	6.9	2080	2.0
5% EtOH	128	68	0.153	0.33	13	6.5	2600	1.8
5% 1-PrOH	104	80	0.176	0.31	28	5.7	3100	1.2
5% 1-BuOH	101	88	0.198	0.28	44	5.1	3400	1.2
5% 1-PeOH	83	97	0.213	0.27	54	4.7	3600	1.1
Resolve C18	0	121	0.279	0.20		7.4[b]	6010[b]	1.1[b]

[a] See experimental for details. [b] Column performance with benzene as test solute using a conventional 50:50 (v/v) methanol:water hydroorganic mobile phase.

equilibrated with these aqueous SDS–alcohol modified solutions (25 mL/g of packing material) with sample preparation, measurement of adsorbed surfactant, and other physical properties carried out as described above.

Chromatographic investigations of each aqueous SDS alcohol modified mobile phase were also completed (*32*). In all cases, the mobile phase flow rate was 1.0 mL/min. The capacity factor of the test solute, benzene (monitored at 254 nm), was calculated in the usual fashion by using nitrate ion as the void marker. The number of theoretical plates was calculated by using the method of Foley and Dorsey (*33*); i.e.

$$N = \frac{41.7(t_r/W_{0.1})^2}{(B/A) + 1.25} \quad (3)$$

where $W_{0.1}$ is the peak width at 10% height and B/A is the asymmetry factor (determined at 10% peak height). The column employed was an Advanced Separation Technologies, Inc., spherical 5 μm C-18, 100 × 4.6 mm.

RESULTS AND DISCUSSION

Evaluation of Alcohol Modifier Effects. The effects of various alcohol additives on stationary phase parameters and chromatographic efficiency using SDS in MLC are summarized in Table I. Exposure of the packing material to an aqueous 0.285 M [8.2% (w/v)] SDS mobile phase results in ca. 150 mg of sorbed surfactant per gram of Resolve C18, essentially doubling the effective stationary phase weight. The addition of relatively small amounts (5%, v/v) of alcohol modifiers to the SDS solution consistently reduces the amount of sorbed surfactant, with a clear trend evident between the amount of surfactant sorbed and the molecular weight of the alcohol. While the addition of 5% (v/v) methanol reduces the amount of SDS sorbed by ca. 10%, the addition of 5% (v/v) 1-pentanol reduces the sorbed surfactant by ca. 50%. Similar trends are observed for S_{BET} and V_{cum} (Table I), both of which increase as the amount of sorbed surfactant decreases. Finally, the stationary phase volume, i.e., the difference between V_{cum} for the unbonded Resolve silica and V_{cum} for the bonded C18 with or without adsorbed surfactant, also increases with the amount of sorbed surfactant, as expected. In addition, others have reported that the presence of organic additives (MeOH, 1-PrOH, THF, acetonitrile, 1-pentanol) decreases the amount of surfactant sorbed on ODS, LC-7, or silica gel materials (*11, 12, 20, 34*) and that the amount of ionic surfactant desorbed from such packings is directly proportional to the additive concentration present in the surfactant mobile phase (*11, 20*).

Reduced chromatographic efficiency is to be expected given the magnitude of surfactant adsorption observed in MLC. The diminished efficiency observed with such surfactant-modified C18 phases is akin to the reduced efficiency reported upon increasing the carbon loading of an octadecyl silica stationary phase (*35*). Hennion et al. have shown that an increase in the carbon loading of an ODS stationary phase (from ca. 15% to 25%) caused a deterioration in the efficiency. This was attributed to an increase in the thickness of the hydrocarbonaceous layer in the pores of the packing which increased the resistance to solute diffusion (*35*). The nature of a surfactant-modified C18 stationary phase is analogous to this situation in that the effective film thickness is increased and solute diffusion is decreased which leads to diminished chromatographic efficiency.

The addition of alcohols to the mobile phase reduces the amount of sorbed surfactant, which in the limit, should cause the chromatographic efficiency to reapproach that of the unmodified C18 stationary phase. The chromatographic parameters, N, and B/A in Table I confirm this premise. In the adsorption experiments, it was found that the contribution of the adsorbed surfactant to the stationary phase volume decreases ca. 10% to 50% upon addition of methanol through 1-pentanol to the surfactant mobile phase. Correspondingly, the chromatographic efficiency, N, approximately doubles for the same series of SDS mobile phases.

These data when considered in light of recent reports provide some insight into the origins of the diminished efficiency typically associated with MLC. Equation 4 shows the various factors contributing to the plate height, H, in liquid chromatography

$$H = \frac{1}{(1/C_e d_P) + (1/(C_m d_P^2 u/D_m))} + \frac{C_d D_m}{u} + \frac{C_{sm} d_P^2 u}{D_m} + \frac{C_s d_f^2 u}{D_s} \quad (4)$$

where C_e, C_m, C_d, C_{sm}, and C_s are the respective plate height coefficients due to Eddy diffusion, mobile phase mass transfer, longitudinal diffusion, stagnant mobile phase mass transfer, and stationary phase mass transfer with the variables including the particle diameter, d_p, mobile phase velocity, u, solute diffusion coefficients in the mobile phase (D_m) and stationary phase layer (D_s), and stationary phase film thickness, d_f (*36*). Several reports indicate that mobile phase mass transfer effects are only relatively minor contributors to the poor efficiency observed in MLC (*20–23, 32*). The predominant term influencing band broadening in MLC appears to be stationary phase mass transfer (*20, 21, 23, 25*). As in the example with the increased carbon loading of the ODS phase, in MLC, the surfactant-modified C18 stationary phase is quite different from the original C18 phase in that the carbon load and film thickness are increased (*20, 21, 23*) while the fluidity of surfactant-modified C18 ligands and the solute diffusion coefficient in the modified stationary phase layer are decreased (*20, 21*). Thus, mass transfer characteristics and chromatographic efficiency in MLC appear to be dictated mainly by the amount and fluidity of surfactant sorbed on the stationary

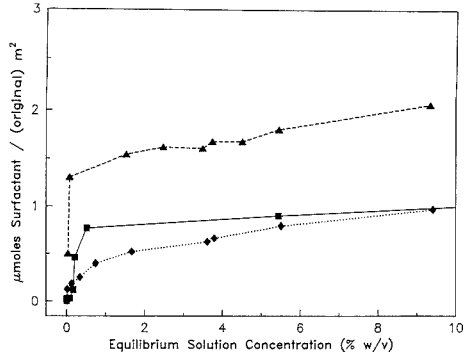

Figure 1. Adsorption isotherms for two nonionic surfactants, (◆) Brij-35 and (▲) Brij-22, and one anionic surfactant, (■) SDS, on Resolve C-18 column packing material. The dual data points (nonionic curves only) at equilibrium solution concentrations slightly below 4% (w/v) are samples in which the amount of surfactant solution was doubled during preparation to test for equilibrium conditions.

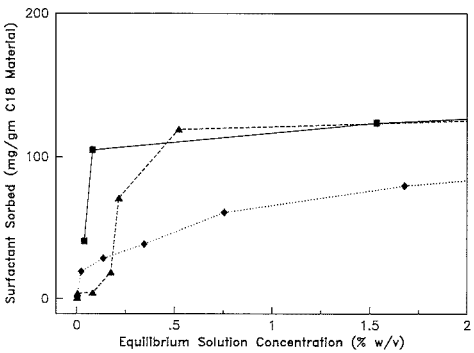

Figure 2. Expanded scale version of Figure 1. Note the slight "knee" with (▲) SDS as compared to (◆) Brij-35 and (■) Brij-22. Virtually all data points are beyond the surfactant cmc values.

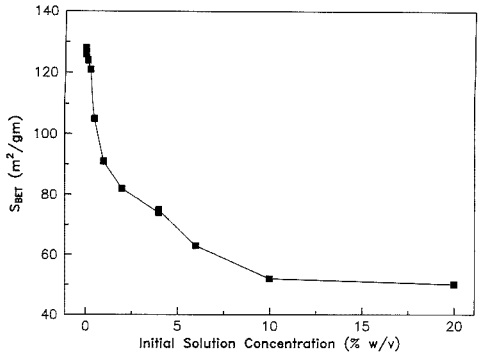

Figure 3. Plot showing the effect of initial solution concentration on Resolve C-18 BET surface area. The curve is, in essence, a reflection of the Brij-35 adsorption isotherm.

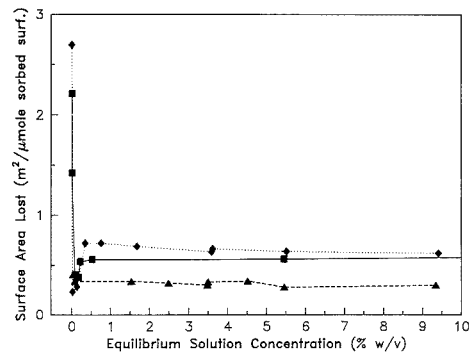

Figure 4. Plot showing the Resolve C-18 BET surface area lost as a function of equilibrium solution concentration (% w/v). The minimum in the curves at very low concentration corresponds roughly to the critical micelle concentrations for the surfactants: (◆) Brij-35, (▲) Brij-22, and (■) SDS.

phase. This in turn, is dependent upon the type and amount of the organic modifier in the mobile phase, the type and concentration of the surfactant employed, and the chemical characteristics of the bonded stationary phase.

Determination of Surfactant Adsorption Isotherms on Resolve C18. The adsorption isotherms for Brij-35, Brij-22, and SDS on Resolve C18 packing material at 25 °C are presented in Figures 1 and 2. It is not easily discerned from the figures that a small percentage of the total surfactant adsorption (only ca. 3% or less) occurs below the cmc. In fact, greater than 58% of the total SDS adsorption occurs at initial solution concentrations ranging from 2 to 70 times the cmc. Similarly, for Brij-35 and Brij-22, more than 50% of the total surfactant adsorption occurs at initial solution concentrations which exceed ca. 50 times the cmc. Clearly the concept that surfactant sorption ceases at the cmc is not true for the systems studied in this work. Adsorption continues well beyond the cmc with similar amounts of each surfactant sorbed at equilibrium saturation, i.e., 169 mg of SDS/g, 152 mg of Brij-35/g, and 165 mg of Brij-22/g.

Although the adsorption of surfactant takes place over a larger concentration range compared to some previous reports, the total amount of surfactant sorbed is comparable to earlier work. From Figure 1, ca. 2 μmol/m^2 of Brij-22, 1 μmol/m^2 Brij-35, and 1 μmol/m^2 SDS are sorbed at equilibrium. For comparison, Dorsey and co-workers have reported 1.8 μmol/m^2 for SDS adsorbed on an Ultrasphere ODS column packing material (*27*) and Berthod et al. have reported 0.5–5.0 μmol/m^2 for SDS and CTAB (cetyltrimethylammonium bromide) with a range of packing materials including C18 bonded materials and unbonded silica (*19*, *20*). The adsorption isotherms for the nonionic surfactants resemble L2 types according to the Giles classification (*37*), and the SDS isotherm resembles an L4 type (Figure 2).

Taken together, these data imply that the reported advantage of gradient MLC and the premise upon which it is based should be reexamined. Given that the concentration of free monomer is not constant above the cmc for at least one surfactant class and considering the extent of adsorption observed above the cmc in this work with both an anionic and nonionic surfactants, the previous reports may be limited in scope.

Additional Characterization of the Surfactant Modified Stationary Phase. Consistent with accepted conventions, the data in Figure 1 are presented as μmol/m^2 of surface area of the parent material (ca. 130 m^2/g). When the surface areas of the individual surfactant-modified samples are measured, however, the surface area is found to decrease consistently as more surfactant is adsorbed (Figure 3). S_{BET} decreases ca. 60% for Brij-35, with similar reductions observed for SDS and Brij-22. If adsorption isotherm data and surface area data are evaluated in terms of surface area lost per amount of surfactant adsorbed, then an interesting pattern

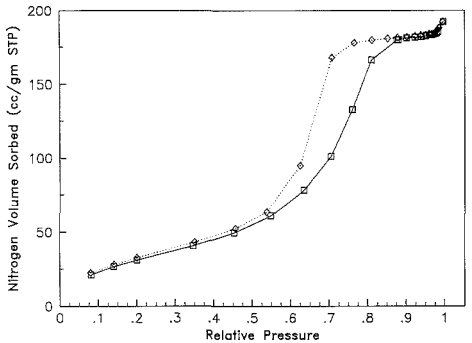

Figure 5. Hysteresis loop associated with the nitrogen adsorption and desorption isotherms at 77 K for untreated Resolve C-18 packing material.

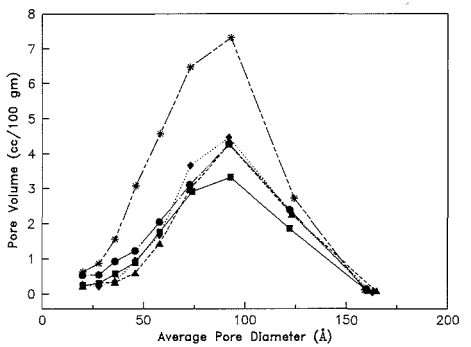

Figure 6. Plot showing the effect of surfactant sorption on Resolve C-18 pore volume as a function of average pore diameter: (*) untreated Resolve C-18, (●) equilibrated with 5% 1-propanol (v/v)/8.4% SDS (w/v), (▲) equilibrated with 6% (w/v) Brij-22, (◆) equilibrated with 6% (w/v) Brij-35, and (■) equilibrated with 6% (w/v) SDS. Note the similarity between the two SDS curves.

is found (Figure 4). Maximum surface areas lost per micromole of surfactant sorbed occur at very low surfactant concentrations, passing through a minimum at approximately the cmc for each surfactant and then becoming essentially constant at all higher concentrations. The "plateau region" values are ca. 0.5 $m^2/\mu mol$ for Brij-35 and SDS, and ca. 0.25 $m^2/\mu mol$ for Brij-22. For the nonionic surfactants, the ratio of these values is proportional to their partial molar volumes, i.e., 1.08 M^{-1} for Brij-35 and 0.60 M^{-1} for Brij-22. The partial molar volume of SDS (0.25 M^{-1}) is much less than that of the nonionic surfactants, yet a similar amount of packing material surface area is lost per micromole of SDS and Brij-35. This implies that the dominant factors in the surfactant/stationary phase interactions are quite different for the nonionic and ionic surfactants, as expected.

In 1958, de Boer described the pore shapes within different materials based on nitrogen sorption isotherms (*38*). In his work, five types of hysteresis loops associated with nitrogen adsorption and desorption were distinguished and pore shapes were classified as belonging to one of 15 groups. According to de Boer's scheme, the hysteresis loop of Resolve C18 material (Figure 5) shows a combination of type A and type E character with shape groups II (capillaries with wide, spheroidally shaped parts) and XV (capillaries linked together to form tubes) being responsible for the shape of the hysteresis loop. The loop in Figure 5, which is strikingly similar to silica hysteresis loops reported in de Boer's work and elsewhere (*39*), is in fact typical of the structure formed by compressing small spheres together.

Examination of the hysteresis loop for surfactant modified Resolve C18 material provides additional information about the extent of stationary phase modification. On the basis of the data in Figure 3, there is a 60% reduction in surface available to the nitrogen molecules at 77 K, prompting the question as to whether the pore shapes in the surfactant-modified stationary phase are distorted or absent due to filling with surfactant. Since the hysteresis loops for nonionic, anionic, and alcohol-modified anionic surfactant solutions exhibited no observable differences, the general pore shapes of the parent C18 material would appear to be retained in the surfactant-modified material, indicating the surfactant produces a thick film on the interior walls, rather than completely filling the pores. This conclusion is also supported by Figure 6, in which the pore volume is plotted as a function of average pore diameter for the Resolve C18 reference material, and for Resolve C18 equilibrated with solutions of 6% Brij-35, 6% Brij-22, 6% SDS, and 8.4% SDS with 1-propanol modifier. The curve shapes are similar in all cases, with maximal contribution to the pore volume from pores with an average diameter of ca. 100 Å. The surfactant-modified phases exhibit decreased pore volumes, but retention of the general curve shape suggests interior coating of the capillary walls and not complete filling of the pores. The curves from materials exposed to 6% SDS and 8.4% SDS with 1-propanol modifier are virtually superimposable, which is additional confirmation of the alcohol modifier effect discussed above, i.e. alcohol modifiers reduce the amount of surfactant sorbed at equilibrium.

CONCLUSION

The ability of surfactants to modify the stationary phase in MLC and the role of the surfactant-modified stationary phase in the MLC separation process have been both misunderstood and often ignored by practitioners of the technique. In this work, both nonionic and anionic surfactants were found to adsorb on Resolve C18 packing material at initial solution concentrations well above the critical micelle concentration, consistent with our previous observations with Brij-35. On the basis of these results, the previously reported advantages of gradient MLC do not appear to be generally appliable to all MLC systems. Further work is needed with other packing materials and surfactants to clarify which adsorption extreme predominates, i.e. adsorption which ceases at the cmc or adsorption which proceeds well beyond the cmc.

Physical measurements that characterize the surfactant-modified packing material indicate surfactant is adsorbed onto the material as a thick film, with pore structure and pore shapes of the original material retained. Consistent with our earlier work, results from this study indicate the general reduction of chromatographic efficiency observed with MLC is primarily caused by poor mass transfer characteristics of the surfactant-modified stationary phase. The addition of alcohol to ionic micellar mobile phases is found to reduce the amount of adsorbed surfactant, yielding improved chromatographic efficiency.

ACKNOWLEDGMENT

The authors wish to thank F. H. Quina (University Sao Paulo, Brazil), D. W. Armstrong (University of Missouri), and A. Berthod (University Claude Bernard, France) for their helpful comments and suggestions with regard to this work.

LITERATURE CITED

(1) *Ion-Pair Chromatography*; Hearn, M. T. W., Ed.; Marcel Dekker, Inc.: New York, 1985.

(2) Melander, W. R.; Horvath, C., ref 1, Chapter 2.
(3) Ghaemi, Y.; Wall, R. A. J. Chromatogr. 1979, 174, 51–59.
(4) Ghaemi, Y.; Wall, R. A. J. Chromatogr. 1980, 198, 397–405.
(5) Knox, J. H.; Hartwick, R. A. J. Chromatogr. 1981, 204, 3–21.
(6) Wall, R. A. J. Chromatogr. 1980, 194, 353–363.
(7) Terweij-Groen, C. P.; Heemstra, S.; Kraak, J. C. J. Chromatogr. 1978, 161, 69–82.
(8) Sorel, R. H. A.; Hulshoff, A.; Wiersema, S. J. Liq. Chromatogr. 1981, 4, 1961–1985.
(9) Dusart, O.; Mazet, M.; Khadirian, R. D.; Hassani, M. A. J. Chim. Phys. 1985, 82, 983–991.
(10) Girard, I.; Gonnet, C. J. Liq. Chromatogr. 1985, 8, 2035–2046.
(11) Mullins, F. G. P.; Kirkbright, G. F. Analyst 1986, 111, 1273–1279.
(12) Gao, Y.; Du, J.; Gu, T. J. Chem. Soc., Faraday Trans. 1 1987, 83, 2671–2679.
(13) Armstrong, D. W.; Henry, S. J. Liq. Chromatogr. 1980, 3, 657–662.
(14) Armstrong, D. W.; Nome, F. Anal. Chem. 1981, 53, 1662–1666.
(15) Armstrong, D. W. Sep. Purif. Methods 1985, 14, 213–304.
(16) Arunyanart, M.; Cline Love, L. J. Anal. Chem. 1984, 56, 1557–1561.
(17) Pramauro, E.; Saini, G.; Pelizzetti, E. Anal. Chim. Acta 1984, 166, 233–241.
(18) Pelizzetti, E.; Pramauro, E. J. Phys. Chem. 1984, 88, 990–996.
(19) Berthod, A.; Girard, I.; Gonnet, C. Anal. Chem. 1986, 58, 1356–1358, 1362–1367.
(20) Berthod, A.; Roussel, A. J. Chromatogr. 1988 449, 349–360.
(21) Borgerding, M. F.; Hinze, W. L. Anal. Chem. 1985, 57, 2183–2190.
(22) Borgerding, M. F.; Hinze, W. L. Abstracts of Papers; 191st Meeting of the American Chemical Society, New York, NY; American Chemical Society: Washington, DC, 1986; Abstr. No. 102.
(23) Armstrong, D. W.; Ward, T. J.; Berthod, A. Anal. Chem. 1986, 58, 579–582.
(24) Dorsey, J. G.; DeEchegaray, M. T.; Landy, J. S. Anal. Chem. 1983, 55, 924–928.
(25) Yarmchuk, P.; Weinberger, R.; Hirsch, R.; Cline-Love, L. J. J. Chromatogr. 1984, 283, 47–54.
(26) Landy, J. S.; Dorsey, J. G. J. Chromatogr. Sci. 1984, 22, 68–70.
(27) Dorsey, J. G.; Khaledi, M. G.; Landy, J. S.; Lin, J. J. Chromatogr. 1984, 316, 183–191.
(28) Sasaki, T.; Yasuoka, M.; Suzuki, H. Bull. Chem. Soc. Jpn. 1977, 50, 2538–2541.
(29) Gunnarsson, G.; Jonsson, B.; Wennerstrom, H. J. Phys. Chem. 1980, 84, 3114–3121.
(30) Lindman, B.; Puyal, M. C.; Kamenka, N.; Rymden, R.; Stilbs, P. J. Phys. Chem. 1984, 88, 5048–5057.
(31) Barrett, E. P.; Joyner, L. G.; Halenda, P. P. J. Am. Chem. Soc. 1951, 73, 373–380.
(32) Hinze, W. L.; Fu, Z. S.; Williams, R. W.; Sadek, F. S.; Berthod, A., submitted for publication in Anal. Chem.
(33) Foley, J. P.; Dorsey, J. G. Anal. Chem. 1983, 55, 730–737.
(34) Del Rey, M. E.; Vera-Avila, L. E. J. Liq. Chromatogr. 1987, 10, 2911–2929.
(35) Hennion, M. C.; Picard, C.; Caude, M. J. Chromatogr. 1978, 166, 21–35.
(36) Snyder, L. R.; Kirkland, J. J. Introduction to Modern Liquid Chromatography, 2nd ed.; John Wiley & Sons, Inc.: New York, 1979; pp 298–301.
(37) Giles, C. H.; MacEwan, T. H.; Hakhwa, S. N.; Smith, D. J. Chem. Soc. 1960, 3973–3993.
(38) deBoer, J. H. In The Structure and Properties of Porous Materials; Everett, D. H., Stone, F. S., Eds.; Butterworths Scientific Publications: London, 1958.
(39) Gregg, S. R.; Sing, K. S. W. Adsorption, Surface Area, and Porosity; Academic Press: New York, 1967.

RECEIVED for review June 20, 1988. Accepted March 29, 1989.

Kinetic Determination of Primary and Secondary Amines Using a Fluoride-Selective Electrode and Based on Their Reaction with 1-Fluoro-2,4-dinitrobenzene

Eleni Athanasiou-Malaki, Michael A. Koupparis,* and Themistocles P. Hadjiioannou

Laboratory of Analytical Chemistry, Department of Chemistry, University of Athens, 104 Solonos Street, Athens 10680, Greece

A kinetic–potentiometric method is described for the determination of 24 primary and secondary amines, based on monitoring their reaction with 1-fluoro-2,4-dinitrobenzene by using a fluoride-selective electrode at pH 9.0 and 25 °C. Initial-slope and fixed-time (60–180 s) methods were used to construct calibration graphs, in most cases in the range 1×10^{-4} to 1×10^{-3} M. Various amine drugs (octamylamine, amphetamine, gentamycin, tobramycin, and propranolol) were determined in commercial formulations with a precision and accuracy of 2–3%, and the results were comparable with those obtained by the official methods. Common excipients do not interfere, and the method can be used in colored and cloudy sample solutions. A detailed kinetic study of the above reactions was also carried out, and the second-order overall rate constants are given. The fluoride-selective electrode is proven to be a valuable tool in monitoring organic reactions that liberate fluoride for kinetic studies and kinetic analysis.

1-Fluoro-2,4-dinitrobenzene (FDNB) has been proposed as a label in the determination of the amino acid sequence of proteins (*1*), for active site labeling of enzymes, and for studying protein tertiary structures (*2*). Besides its use in structural analysis, FDNB has been employed for the spectrophotometric determination of amino acids and primary and secondary amines (*3–9*), amino acid nitrogen in plasma and urine (*10, 11*), isoniazid (*12*), various aminoglycoside antibiotics (*13*), phenols (*14*), and the enzyme amidase (*15*). It has also been used in the gravimetric determination of morphine (a phenolic alkaloid) (*16*) and other phenols (*17*), as a derivative reagent in gas–liquid chromatography (GLC) for phenols (*18*) and amines (*19*), in high-performance liquid chromatography (HPLC) for amines and aminoglycosides (*20–22*), and in thin-layer chromatography (TLC) and mass spectrometry for amines (*23*).

The above spectrophotometric methods have inherent disadvantages in that a long time is required for the completion of the reaction and that heating is required to speed up the reaction. Additional steps are also required for the hydrolysis of the excess FDNB and the extraction of the DNB–amino product for measurement, and the methods cannot be applied to determinations in colored or turbid samples. All these drawbacks can be eliminated, with a slight decrease of sensitivity, by using a kinetic–potentiometric method based on monitoring the FDNB–amines reaction with a fluoride-selective electrode. The combination of the selectivity, sensitivity, and simplicity of kinetic methods of analysis with the inherent advantages of ion-selective electrodes, i.e., high selectivity, sensitivity, and freedom from optical interferences, produces an excellent and versatile technique (*24*). The fluoride-selective electrode, extensively used in direct potentiometry of fluoride, has recently been used in the kinetic–potentiometric determination of peroxidase,

0003-2700/89/0361-1358$01.50/0

Table I. Kinetic Parameters of the Reaction of Amines with FDNB[a]

amine	pK_a ($-NH_3^+$)	K^{st} (±SD), M^{-1} s^{-1} × 10^2	K (±SD), M^{-1} s^{-1} × 10^2	reactn order (resp to amine) (±SD)
		A. Monoamines		
n-butylamine	10.64	4.42 ± 0.08	163 ± 3	0.94 ± 0.07
octamylamine		14.4 ± 0.2		0.91 ± 0.08
aniline	4.63	4.42 ± 0.02	4.42 ± 0.02	1.08 ± 0.07
sulfanilic acid	0.64	0.220 ± 0.005	0.220 ± 0.005	0.90 ± 0.06
p-ethoxyaniline	5.24	19.4 ± 0.4	19.4 ± 0.4	1.02 ± 0.05
amphetamine	9.83	16.9 ± 0.2	108 ± 1	0.91 ± 0.08
		B. Polyamines		
propylenediamine	9.72, 6.61	12.20 ± 0.08		1.018 ± 0.007
o-phenylenediamine	4.47	1.52 ± 0.03	1.52 ± 0.03	1.06 ± 0.09
p-phenylenediamine		83 ± 3	83 ± 3	0.91 ± 0.04
2,5-toluenediamine		77 ± 3	77 ± 3	1.03 ± 0.06
N-(1-naphthyl)ethylenediamine		286 ± 6		0.91 ± 0.04
piperazine	9.73, 5.33	31.9 ± 0.5		0.94 ± 0.08
triethylenetetramine	9.80, 9.26, 6.76, 3.55	11.7 ± 0.1		0.92 ± 0.01
gentamycin	8.2	35.2 ± 0.5		1.04 ± 0.09
tobramycin		26.7 ± 0.7		1.04 ± 0.07
		C. Hydroxyamines		
hydroxylamine	5.96	3.65 ± 0.04	3.65 ± 0.04	0.99 ± 0.01
2-methylaminoethanol	9.77	8.5 ± 0.2	51 ± 1	0.93 ± 0.04
2-ethylaminoethanol	10.21	0.62 ± 0.01	8.9 ± 0.1	0.94 ± 0.03
1-aminopropanol	9.62	2.28 ± 0.04	10.9 ± 0.2	0.94 ± 0.07
diethanolamine	8.88	7.2 ± 0.2	12.5 ± 0.3	0.98 ± 0.02
p-aminophenol	5.48	32.8 ± 0.4		1.05 ± 0.09
p-aminosalicylic acid	2.02	0.219 ± 0.004		1.00 ± 0.08
propranolol	9.45	25.3 ± 0.7	100 ± 2	1.03 ± 0.07
ephedrine	9.63	0.198 ± 0.005	1.02 ± 0.02	0.99 ± 0.03

[a] Conditions: pH = 9.0; 25 °C; [FDNB] = 1.78×10^{-3} M, $n = 5$.

glucose, and cholesterol in serum (*25*) and of peroxidase in colored and turbid extracts of plants, where the official titrimetric and other available spectrophotometric methods are unsuitable (*26*).

The reaction between FDNB and various amines and amino acids has been extensively studied by spectrophotometry in organic and aqueous–organic solvents (*27–36*). The reaction is a two-stage process involving nucleophilic addition followed by the loss of the fluoride ion. Although in some solvents this second step is slow and is subject to base catalysis (*28*), it is relatively rapid in polar solvents containing the hydroxy group (*31*). Kinetic studies in aqueous solutions showed an increased reaction rate, and the reactions were found to be accelerated by micellar catalysis, which was used to speed up spectrophotometric determinations (*37*). Hydroxide ions also react with FDNB (*21*, *31*), but the pH dependence of the rates of the reactions between FDNB and amino compounds is entirely accounted for by the effect of pH on the degree of ionization of the amino group, and there is no evidence for base catalysis (*38*).

In this paper the fluoride-selective electrode is used for the kinetic study of the FDNB reaction with primary and secondary amines in aqueous weak basic solutions. On the basis of this study a kinetic–potentiometric method for the determination of amines is developed and is evaluated for the assay of drug formulations.

EXPERIMENTAL SECTION

Apparatus. The system for potentiometric rate measurements consists of a combination fluoride electrode (Orion Model 96-09) and a conventional analog electrometer (Corning Model 12 research pH meter) with 0.1-mV resolution connected to a multispeed variable-span recorder. All measurements were carried out in a thermostated (±0.2 °C) plastic double-wall reaction cell with continuous magnetic stirring.

Reagents. All reagents were of analytical reagent grade, and deionized, distilled water was used throughout. Working standard solutions of the amines, shown in Table I, in the range 1×10^{-5} to 5×10^{-2} M were prepared daily from 0.1000 M stock standard solutions made from analytical reagent or USP grade substances (analyzed by the official methods) in water. FDNB working solution, 5.00% (w/v) (0.269 M) in acetone, was prepared by dissolving 1.25 g of FDNB (Sigma) in 25.0 mL of acetone. This solution was stored in a sealed amber glass vial in the refrigerator that was opened only when used. It was stable for at least 1 month. This reagent should be carefully handled, as it is vesicatory. Mixed borate buffer solution, 0.0300 M, pH 9.0, was made to contain 3.00×10^{-5} M NaF and 5.00×10^{-3} M *trans*-1,2-diaminocyclohexane-*N*,*N*,*N*′,*N*′-tetraacetic acid (DCTA). Fluoride working standard solutions were prepared from a stock 1.000 M NaF solution with appropriate dilution. All fluoride solutions were stored in polyethylene bottles.

Measurement Procedure. Pipet 10.00 mL of a working standard or sample solution of the analyte and 5.00 mL of the pH 9.0 mixed borate buffer into the thermostated (25.0 °C) reaction cell. Start the stirrer, and after the potential has stabilized, initiate the reaction by the injection of 100 μL of FDNB working solution with a Hamilton microsyringe and record the reaction curve for about 2–3 min. A blank (H_2O) should be included for each set of measurements. Estimate graphically the initial slope $(\Delta E/\Delta t)_0$ (mV s^{-1}) of each reaction curve, for the kinetic study and the analytical determinations with the initial-slope procedure, or the potential change ΔE (mV) for a time interval of 60–180 s depending on the reaction rate, for the analytical determinations with the fixed-time procedure. Using the standard solutions of each analyte, construct a calibration graph of $(\Delta E/\Delta t)_0$ vs concentration (initial-slope method) or $(10^{\Delta E/S} - 1)$ vs concentration (fixed-time method). ΔE values for the blank should be subtracted from every ΔE measured for the standards or the samples. The slope of the electrode response (S) (required in the kinetic study and the fixed-time analytical procedure) is periodically determined by successive additions of 100 μL of 1.50×10^{-3} and 1.50×10^{-2} M NaF standard solutions in 10.00 mL of H_2O mixed with 5.00 mL of buffer and by measuring the potential with the electrometer.

Sample Preparation. The sample solutions should be approximately neutralized, if required, by using NaOH or HCl solutions and one drop of phenolphthalein indicator. For the assays of drug formulations the official USP procedures for sampling and treatment were followed. A suitable portion of the homogenized sample is dissolved or diluted with water so that

the concentration of the obtained sample solution lies within the range covered by the corresponding calibration curve. Sample dissolution was assisted by using a Vortex mixer, and measurements were performed in the clear supernatant.

Reference Methods. The official or established methods used for comparison in the assay of drug formulations (Table IV) were as follows: nonaqueous titration with perchloric acid in dioxane and methyl red indicator, after extraction, for octamylamine; UV spectrophotometry after isolation with column chromatography for amphetamine; microbiological assay for gentamycin and tobramycin; UV spectrophotometry after extraction with hexane from alkaline solution for propranolol.

RESULTS AND DISCUSSION

Selection of Experimental Conditions. It is well-known that the rate of the FDNB reaction with amines is affected drastically by the pH of the reaction solution, which controls the degree of the protonation of the amino group (*38*). Hence, most of the spectrophotometric methods based on this reaction are performed in alkaline solutions with NaOH or borax (*3, 5, 7, 10–12*). A borate buffer of pH 9.0 was chosen as optimum for the proposed kinetic method as a compromise between a moderate measurable reaction rate, low interference from the hydroxide ions to the electrode response, and low hydrolysis rate of the FDNB. From experiments of the electrode response at various pH values in the range 6–12 a potentiometric selectivity coefficient $K^{pot}_{F^-,OH^-} = 0.040 \pm 0.004$ was found (mixed solution method, $[F^-] = 1 \times 10^{-3}$ M). A final borate concentration of 0.0100 M in the reaction mixture was chosen as optimum as a compromise between maintaining low ionic strength and sufficient buffer capacity. A preliminary approximate neutralization of very acidic or alkaline sample solutions is necessary to ensure precise control over pH.

The electrode characteristics were studied in the chosen buffer. Nernstian response (slope of 59 mV) with a lower linear concentration limit (LLCL) of 1×10^{-5} M was found during the first 2 years of the electrode operative life. The slope decreased slowly to 49 mV in the third year. The dynamic response time measured for a concentration change of 5×10^{-5} M, at an initial concentration of 1×10^{-5} M (25 °C), was 24 s. The time constant (T) corresponding to this response time, as it was calculated by the approximate exponential equation of E/t curves for stepwise concentration changes (*24*), was found to be 8 s. The $\Delta E/\Delta t$ slopes calculated from the E–t recordings are valid and useful for kinetic information if a fluoride concentration equal to the LLCL is present before the start of the reaction and the initial slopes are measured after a time of $4.6T$ (i.e. 37 s) (*24*).

The DCTA was added to the mixed buffer to mask the possible interferences of Fe^{3+} and Al^{3+} present from the sample container. The kinetic study and the analytical determinations were performed at 25 °C. At higher temperatures the rate of both the main reaction and the FDNB hydrolysis is accelerated. Acetone was used as the reagent solvent because it shows negligible solvolysis, it is dissolved rapidly in the aqueous buffered sample solution, and the small amount of this solvent used (100 μL) has no practical effect on the electrode response.

Kinetic Study of Amine – FDNB Reactions. The reaction of amines with FDNB is a well-known example of a nucleophilic aromatic substitution reaction, with the formation of an intermediate complex, and can be depicted by the following scheme (*39*):

$$RNH_2 + (NO_2)_2C_6H_3F \underset{k_{-1}}{\overset{k_1}{\rightleftharpoons}} (NO_2)_2\bar{C}_6H_3(F)^+NH_2R \xrightarrow{k_2} (NO_2)_2C_6H_3NHR + H^+ + F^- \quad (1)$$

Assuming a steady state, the rate of fluoride formation is described by the equation

$$d[F^-]/dt = \frac{k_1k_2}{k_{-1} + k_2}[RNH_2]_t[FDNB]_t = K[RNH_2]_t[FDNB]_t \quad (2)$$

where K is the overall second-order rate constant. By differentiation of the Nernst equation for the fluoride electrode with respect to time, we have

$$dE/dt = S'(1/[F^-])(d[F^-]/dt) \quad (3)$$

where S' is the slope of the E vs ln C calibration graph. Equation 3 is valid in the linear part of the electrode response graph, i.e., for $[F^-] > 1 \times 10^{-5}$ M.

Combining eq 2 and 3, at the start of the reaction where the initial slope is measured (with the precautions discussed previously), we have

$$(\Delta E/\Delta t)_0 = S'(1/[F^-]_0)K[RNH_2]_0[FDNB]_0 \quad (4)$$

As the pH seriously affects the concentration of the reactive nonprotonated amino group (*38*), the stoichiometric concentration C_{0,RNH_2} of the amine can be used in eq 4, with substitution of the reaction rate constant K by the experimental (pH 9) stoichiometric reaction rate K^{st}.

$$(\Delta E/\Delta t)_0 = S'(1/[F^-]_0)K^{st}C_{0,RNH_2}[FDNB]_0 \quad (5)$$

The value of K for monoamines can be easily calculated from K^{st} by using the equation $K = K^{st}/\alpha_i$, where α_i is the fraction of the free amino group at pH 9.0, provided that the amino group is the only group that reacts with FDNB.

As FDNB is also subject, to a small extent, to hydrolysis at pH 9.0 (with a rate constant of 0.121 M^{-1} s^{-1} at 25 °C) (*31*), the initial rate $(\Delta E/\Delta t)_0$ for the FDNB–amine reaction must be corrected accordingly. A blank of $(\Delta E/\Delta t)_{0,hydrl}$ can be easily measured or taken as equal to the intercept of the $(\Delta E/\Delta t)_0$ vs C_{RNH_2} plot.

From experiments in which the FDNB concentration was varied in the range $(1.8–7.2) \times 10^{-4}$ M with constant amine concentration (aniline, 6.7×10^{-4} M), the reaction order for FDNB was found to be 1.02 ± 0.03, which agrees with previous spectrophotometric results (*37, 38*). From experiments with various concentrations of the amines tested and a constant concentration of FDNB, the reaction order with respect to the amine and K^{st} (and thus K) can be obtained.

Figure 1 shows typical E–t curves of the FDNB–gentamycin reaction, used for the calculation of the kinetic parameters. Table I shows the results of this kinetic study at 25 °C for all the amines studied, grouped in three categories, i.e., monoamines, polyamines, and hydroxyamines. The reaction is seen to be first order with respect to all the amines. Values of K^{st} are given for all the amines tested, but K values were calculated only for those amines with a single amino group and no other reactive functional group (i.e., phenolic or other amino group).

Literature kinetic data for the reactions of FDNB with amines are based on spectrophotometric data (monitoring the intermediate complex and the final product) under pseudo-first-order conditions. From the amines studied in this work, bibliographical data were found only for aniline. The reported values for the second-order rate constant (M^{-1} s^{-1}), 0.0550 (*37*), 0.030 (*31*), and 0.0400 (*35*), are in good agreement with that found by the described potentiometric method (0.0442 ± 0.0002).

Comparing the rate constants of the aniline derivatives, one can observe that the reactivity of the amines increases with the basicity of the amino group. Thus, sulfanilate (*p*-anilinesulfonate) and *p*-aminosalicylate have the lowest reactivity, followed by aniline and *p*-ethoxyaniline. *p*-Aminophenol has the highest reactivity, which is due to, besides its increased basicity, the reactive phenolic group at the para position. It seems that the reactivity of the phenolic group

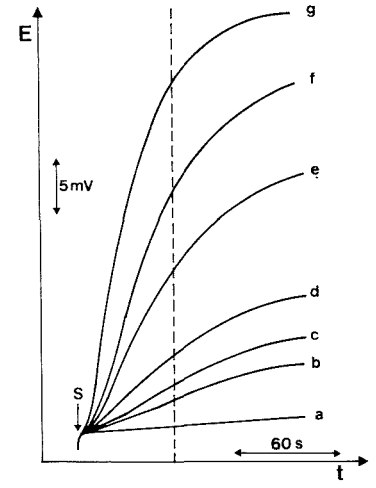

Figure 1. Typical reaction curves of the FDNB–gentamycin reaction for calibration graphs. Concentration of gentamycin: (a) blank, (b) 4.0×10^{-5}, (c) 6.0×10^{-5}, (d) 1.0×10^{-4}, (e) 3.0×10^{-4}, (f) 6.0×1.0^{-4}, and (g) 1.0×10^{-3} M. Dashed line shows the ΔE measurement in the fixed-time method.

of *p*-aminosalicylate is affected stereochemically by the vicinity of the carbonyl group.

The reactivity of the three aryl diamines increases from *o*-phenylenediamine, for which it is low because of the vicinity of the two amino groups, to 2,5-toluenediamine and further to *p*-phenylenediamine. The reactivity of the primary alkyl monoamines also follows their basicity (hydroxylamine, aminopropanol, amphetamine, and butylamine).

The hydrolysis of FDNB was also studied by using the potentiometric procedure. The values of K_h (first-order reaction rate constant for hydrolysis) found were 6 (±1) × 10^{-6} s^{-1} (35 °C), 2.6 (±0.5) × 10^{-5} s^{-1} (45 °C), and 7.6 (±1.6) × 10^{-5} s^{-1} (55 °C). For the reaction with hydroxide ions, second-order rate constants K_{OH^-} (M^{-1} s^{-1}) of 0.05 ± 0.01 (35 °C), 0.24 ± 0.08 (45 °C), and 0.8 ± 0.3 (55 °C) were found. By the use of mixed experimental hydrolysis constants from different temperatures, the E_a of the hydrolysis of FDNB was found to be 27.5 ± 0.9 kcal mol^{-1}. Barends et al. (*21*) reported values of 5 × 10^{-6} s^{-1} for K_h and 0.12 M^{-1} s^{-1} for K_{OH^-} at 40 °C using HPLC, whereas Bunton and Robinson (*31*) reported a K_{OH^-} of 0.12 M^{-1} s^{-1} at 25 °C obtained by spectrophotometry at high (0.01 M) hydroxide concentrations.

Analytical Applications. As shown by eq 5, the initial slope of the reaction curve is linearly related to the amine concentration, since the reaction is first order with respect to amine (Table I). As shown in Figure 1, two kinetic methods can be used for such graphs, the initial-slope or the fixed-time method (*24*). Table II shows typical examples of the experimental data for the calibration graphs for determination of gentamycin using the two methods. Excellent linearity and good precision were obtained with both methods.

For the determination of the various amines with the fixed-time method, a Δt value of 60, 120, or 180 s was selected, depending on the relative rate of the individual reaction. It is clear from the shape of the reaction curves that the so-called reciprocal time method cannot be used in these kinetic determinations. Data obtained for the amines tested are shown in Table III for the initial-slope method, summarizing the useful analytical ranges, the slopes of the calibration graphs along with their standard deviation and correlation coefficient,

Table II. Experimental Data for the Construction of Calibration Graphs for the Determination of Gentamycin with Initial-Slope and Fixed-Time Procedures[a]

concn, 10^5 M	initial-slope method		fixed-time method		
	$(\Delta E/\Delta t)_0$, mV s^{-1}	% RSD (n = 3)	$\Delta E'$, mV	% RSD, (n = 3)	$10^{\Delta E'/S} - 1$
4.00	0.0697		−2.60		0.129
6.00	0.0951		−4.20		0.217
10.00	0.153	3.1	−7.50	2.9	0.419
30.0	0.319		−16.60		1.171
60.0	0.578		−26.80		2.500
100.0	0.943		−36.00		4.391

Equations of Calibration Curves

initial-slope: $(\Delta E/\Delta t)_0 = 0.046\ (\pm 0.007) + 895\ (\pm 13)C$, $r = 0.9995$

fixed-time: $10^{\Delta E'/S} - 1 = -0.07\ (\pm 0.04) + 4399\ (\pm 79)C$, $r = 0.9993$

[a] $S = -49.3$ mV/log C, $\Delta t = 60$ s.

Table III. Analytical Characteristics of the Determination of Amines in Aqueous Solutions Using the Initial-Slope Method

amine	lin range tested, 10^4 M	slope (±SD), mV s^{-1} M^{-1}	r	% RSD (n = 3)
n-butylamine	1–80	113 ± 2	0.9994	4.2
octamylamine	1–8	365 ± 5	0.9998	3.1
aniline	1–10	113 ± 3	0.999	2.7
sulfanilic acid	50–500	5.62 ± 0.13	0.9997	1.5
p-ethoxyaniline	0.5–5	495 ± 11	0.9994	2.1
amphetamine	1–10	429 ± 6	0.9996	1.7
propylenediamine	1–10	312 ± 2	0.99995	1.1
o-phenylenediamine	1–30	39.0 ± 0.8	0.999	2.2
p-phenylenediamine	0.1–1	2132 ± 93	0.998	4.0
2,5-toluenediamine	0.1–1	1969 ± 91	0.998	3.5
N-(1-naphthyl)-ethylenediamine	0.1–1	7324 ± 151	0.999	2.8
piperazine	1–5	816 ± 14	0.9997	1.8
triethylenetetramine	1–10	299 ± 3	0.9995	2.7
gentamycin	0.4–10	895 ± 13	0.9995	3.1
tobramycin	0.5–10	679 ± 18	0.9990	2.1
hydroxylamine	1–10	93.3 ± 0.9	0.9998	1.4
2-methylaminoethanol	1–10	217 ± 5	0.999	2.2
2-ethylaminoethanol	10–100	15.8 ± 0.3	0.9997	1.3
1-aminopropanol	1–10	58.3 ± 0.9	0.999	2.1
diethanolamine	3–10	183 ± 4	0.9993	0.8
p-aminophenol	0.3–3	839 ± 10	0.999	2.3
p-aminosalicylic acid	10–500	5.60 ± 0.09	0.999	2.1
propranolol	1–10	644 ± 18	0.9991	1.8
ephedrine	10–100	5.06 ± 0.13	0.999	1.7

and the precision (obtained by triplicate measurements of a medium standard). As it is shown, the proposed kinetic determination of amines with the initial-slope method has a wide range of sensitivity, depending on the reaction rate of each amine. The most sensitive determination is that of *N*-(1-naphthyl)ethylenediamine, while the least sensitive is that of ephedrine. Slow reaction rates can be considerably accelerated by using micellar catalysis (*37*, *40*), thus increasing the sensitivity of the determination. The precision of the measurements was good for kinetic–potentiometric determinations,

Table IV. Comparison of Results Obtained by the Proposed Kinetic–Potentiometric and Established Methods in the Assay of Drug Formulations

formulation	nominal content[a]	content found (±SD, n = 3)[a] present method	content found (±SD, n = 3)[a] reference method	t-test[g]
		Octamylamine, HCl		
Octinum D[b]				
drops	50	51 ± 1	51 ± 1	0.000
tablets	50	52 ± 1	51 ± 2	0.774
		Amphetamine		
Dexedrine[c]				
tablets	5	5.08 ± 0.09	5.13 ± 0.08	0.719
		Gentamycin		
Garamycin[d]				
injections	10	11.2 ± 0.3	10.8 ± 0.5	1.188
injections	40	42 ± 1	41 ± 1	1.225
		Tobramycin		
Nebcin[e]				
injections	40	41.2 ± 0.8	42.1 ± 0.9	1.294
injections	80	80 ± 1	81 ± 2	0.774
		Propranolol, HCl		
Inderal[f]				
tablets	40	40.8 ± 0.8	41.2 ± 0.7	0.652

[a] Drops and injections measured in milligrams per milliliter and tablets measured in milligrams. [b] Knoll. [c] Smith Kline and French. [d] Schering Corp. [e] Eli Lilly. [f] ICI. [g] t-test (theoretical, 95%) = 4.303.

with the percent relative standard deviation (% RSD) varying from 0.8 to 4.2 (n = 3). The linearity of the calibration graphs was also good with correlation coefficients in the range 0.998–0.99995. The fixed-time method also provides analytical determinations with good sensitivity, linearity, and precision. Depending on the reaction rate of each amine, an increase of the sensitivity can be achieved by increasing the value of Δt. The total measurement time for both kinetic methods ranged from 2 to 3 min depending on the reaction rate.

The proposed potentiometric method was applied to the determination of various amines with pharmaceutical interest in commercial formulations. More specifically the following drugs were determined: (a) octamylamine (*N*-isopentyl-1,5-dimethylhexylamine), an anticholinergic and antispasmodic drug, administered as its hydrochloride salt in the form of drops, injections, and tablets; (b) amphetamine (α-methylbenzeneethanamine), a central nervous system stimulant drug, administered as its sulfate salt in the form of capsules, tablets, and elixirs; (c) gentamycin, an antibacterial of the aminoglycoside group, administered as its sulfate salt in injections, ear and eye drops, and eye ointment; (d) tobramycin, an antibacterial of the aminoglycoside group also, administered as its sulfate salt in the form of injections and powders for solutions; and (e) propranolol (1-(isopropylamino)-3-(1-naphthoxy)-2-propanol), an antiarrhythmic and β-adrenergic blocker drug, administered as its hydrochloride salt in the form of tablets, capsules, and injections. The results of the analysis of some commercial formulations of the above drugs and comparisons with official or established methods are shown in Table IV. It can be seen that good precision (2–3% RSD, n = 3) and good agreement with the reference methods were obtained.

A recovery study performed on synthetic solutions of propranolol with various excipients used in tablet formulation gave a mean recovery of 99.7% (range (98.4–102.5%) (Table V), showing the absence of any interference of these excipients. The selectivity of the proposed method is also proved from the results shown in Table IV, where the various excipients

Table V. Recovery of Propranolol (1.00×10^{-3} M) from Synthetic Mixtures with Various Excipients (100 mg/mL)

excipient	% recovery
NaCl	101.0
Carbobol 4000[a]	98.9
magnesium stearate	97.1
talc	98.4
lactose	102.5
mannitol	98.7
galactose	100.7
sorbitol	98.3
sugar	102.1
mean	99.7

[a] Carboxypolymethylene.

of the analyzed formulations had no effect on the determination. FDNB reacts only with primary and secondary amines, phenols, mercaptans, hydrazines, and hydrazides, so a selective determination of an amine drug, in the presence of other drugs or excipients having other functional groups, is possible with the proposed method. It must be emphasized that most of the sample solutions obtained in the above assays were colored or cloudy, a case in which the superiority of the ion-selective potentiometry is obvious.

The proposed kinetic–potentiometric determination for the two aminoglycosides, gentamycin and tobramycin, is of particular interest, since it is simple and fast and can be used in conjunction with the time-consuming official microbiological assay (a direct spectrophotometric method is not feasible because of the absence of any spectrophotometric characteristics of these two compounds). The reaction of FDNB has already been used in the spectrophotometric determination of these aminoglycosides (based on the absorbance measurement of the reaction product after the stopping of the reaction after 20 or 30 min) (*13*), and for derivative formation for HPLC (*21*).

Besides the amino compounds shown in Table I, the reaction rate of which with FDNB was measurable and thus a kinetic determination feasible, a number of other compounds, members of the groups tertiary amines, amides, sulfonamides, ureas, and thioureas, and also ammonia and tris(hydroxymethyl)aminomethane, were found unreactive, allowing a selective determination of a primary or secondary amine in the presence of these compounds.

Conclusions. This work shows the usefulness of ion-selective electrodes in kinetic studies of reactions, where an ion monitored by the electrode is produced or consumed. Furthermore, it proves their usefulness in kinetic analysis by providing very simple, rapid, and selective analytical methods. The application of the proposed method in the pharmaceutical routine control shows the advantages of ion-selective electrodes in the analysis of colored and cloudy sample solutions.

ACKNOWLEDGMENT

We are very grateful to N. Psaroudakis for his assistance during the course of this study.

LITERATURE CITED

(1) Sanger, F. *Biochem. J.* **1945**, *39*, 507–515.
(2) Singer, S. J. *Adv. Protein Chem.* **1967**, *22*, 1–54.
(3) McIntire, F. C.; Clements, L. M.; Sprouli, M. *Anal. Chem.* **1953**, *25*, 1757–1758.
(4) Lowry, H. O.; Graham, H. T.; Harris, F. B.; Priebat, K. M.; Marks, R. A.; Bregman, V. R. *J. Pharmacol. Exp. Ther.* **1954**, *112*, 116–126.
(5) Rosenthal, S. M.; Tabor, C. W. *J. Pharmacol. Exp. Ther.* **1956**, *116*, 131–138.
(6) Kolbenzen, M. J.; Eckert, J. N. E.; Brefschneider, B. F. *Anal. Chem.* **1962**, *34*, 583–584.
(7) Dubin, D. T. *J. Biol. Chem.* **1960**, *235*, 783–786.
(8) Couch, R. *J. Assoc. Off. Anal. Chem.* **1975**, *58*, 599–601.
(9) Weber, J. D. *J. Pharm. Sci.* **1976**, *65*, 105–108.
(10) Goodwin, J. F. *Clin. Chim. Acta* **1968**, *21*, 231–240.

(11) Goodwin, J. F. *Clin. Chem.* **1968**, *14*, 1080–1090.
(12) Poole, N. F.; Meyer, A. E. *Proc. Soc. Exp. Biol. Med.* **1958**, *98*, 375–377.
(13) Ryan, J. A. *J. Pharm. Sci.* **1984**, *73*, 1301–1302.
(14) Lehmann, P. A. *Anal. Chim. Acta* **1971**, *54*, 321–336.
(15) Chen, P. R.; Dauterman, W. C. *Anal. Biochem.* **1970**, *38*, 224–228.
(16) Garratt, D. C.; Johnson, C. A.; Lloyd, C. J. *J. Pharm. Pharmacol.* **1957**, *9*, 914–928.
(17) Zahn, H.; Wurz, A. *Z. Anal. Chem.* **1951**, *134*, 183–187.
(18) Cohen, J. C.; Norcup, J.; Ruzicka, J. H. A.; Wheals, B. B. *J. Chromatog.* **1969**, *44*, 251–255.
(19) Timbrell, J. A.; Wright, J. M.; Smith, C. M. *J. Chromatog.* **1977**, *138*, 165–172.
(20) Lawrence, J. F.; Frei, R. W. *Chemical Derivatization in Liquid Chromatography*; Elsevier; Amsterdam, 1976.
(21) Barends, D. M.; Blauw, J. S.; Mijnsbergen, C. W.; Govers, C. J. L. R.; Hulshoff, A. *J. Chromatogr.* **1985**, *322*, 321–331.
(22) Sadee, W.; Beelen, G. C. M. *Drug Level Monitoring*; J. Wiley and Sons: New York, 1980; p 251.
(23) Zeman, A. Wirotama, J. P. G. *Z. Anal. Chem.* **1969**, *247*, 155–158.
(24) Efstathiou, C. E.; Koupparis, M. A.; Hadjiioannou, T. P. *Ion-Sel. Electrode Rev.* **1985**, *7*, 203–259.
(25) Siddiqi, I. W. *Clin. Chem.* **1982**, *28*, 1962–1967.
(26) Skaltsa, H. D.; Koupparis, M. A.; Philianos, S. M. *J. Assoc. Off. Anal. Chem.* **1986**, *69*, 1006–1008.
(27) Bunnett, J. F.; Garbisch, E. W.; Pruitt, K. M. *J. Am. Chem. Soc.* **1957**, *79*, 385–391.
(28) Bunnett, J. F.; Randall, J. *J. Am. Chem. Soc.* **1958**, *80*, 6020–6030.
(29) Bunnett, J. F.; Garst, R. H. *J. Am. Chem. Soc.* **1965**, *87*, 3875–3878.
(30) Ross, S. D. *Tetrahedron* **1969**, *25*, 4427–4436.
(31) Bunton, C. A.; Robinson, L. *J. Org. Chem.* **1970**, *35*, 733–736.
(32) Kavalek, J.; Haasova, J.; Sterba, V. *Collect. Czech. Chem. Commun.* **1972**, *37*, 3333–3338.
(33) Kavalek, J.; Kubias, J.; Sterba, V. *Collect. Czech. Chem. Commun.* **1972**, *37*, 4041–4045.
(34) Kavalek, J.; Sterba, V. *Collect. Czech. Chem. Commun.* **1972**, *38*, 884–891.
(35) de Rossi, R. H.; Pierini, A. B.; Rossi, R. A. *J. Org. Chem.* **1978**, *43*, 2982–2986.
(36) Forlani, L. *J. Chem. Res., Synop.* **1984**, 260–261.
(37) Wong, M. P.; Connors, K. A. *J. Pharm. Sci.* **1983**, *72*, 146–150.
(38) Bunnett, J. F.; Hermann, D. H. *Biochemistry* **1970**, *9*, 816–822.
(39) Connors, K. A. *Reaction Mechanisms in Organic Analytical Chemistry*; Wiley: New York, 1972; p 274.
(40) Athanasiou-Malaki, E.; Koupparis, M. A. *Anal. Chim. Acta*. in press.

RECEIVED for review July 28, 1988. Accepted March 14, 1989.

Extraction and Isolation of Phenoxy Acid Herbicides in Environmental Waters Using Two Adsorbents in One Minicartridge

Antonio Di Corcia,* Marcello Marchetti, and Roberto Samperi

Dipartimento di Chimica, Università La Sapienza di Roma, Piazzale Aldo Moro 5, 00185 Roma, Italy

Selective solid-phase extraction from environmental waters of nine popular acidic herbicides was accomplished by using one miniaturized cartridge containing in the top side 50 mg of a nonspecific adsorbent, that is graphitized carbon black (Carbopack B), and in the lower side 70 mg of a silica-based strong anion exchanger (SAX). After sample percolation, the SAX material was activated by passing through the trap sodium acetate, 1 mol/L. A 3-mL solvent mixture of CH_2Cl_2/CH_3OH (80:20, by volume) basified with 1 mmol/L NaOH was then allowed to flow through the cartridge, and phenoxy acids were removed from the Carbopack surface and selectively readsorbed on the exchanger surface. After washing, the nine herbicides were desorbed from the SAX surface with 0.6 mL of water/methanol (50:50, by volume) containing trifluoroacetic acid and potassium chloride. A 100-μL portion of this solution was directly injected into the HPLC column, operating in the ion suppression–reversed-phase mode. As ion suppressor, the substitution of the commonly used acetic acid with trifluoroacetic acid allowed sensitive detection at 230 nm. Recovery of the nine acidic herbicides ranged between 94% and 100%, irrespective of the sample type considered. By this extraction method, basic, neutral, and weakly acidic compounds do not interfere with the analysis. Interestingly, this cartridge is suitable for field sampling, as Carbopack is able to adsorb phenoxy acids from water at whatever pH value. The limits of detection of the nine herbicides were well below 0.1 μg/L. The effectiveness in terms of recovery and selectivity of the two-adsorbent tandem system was compared with that of a C-18 disposable cartridge.

* To whom correspondence should be addressed.

In the last decade, as an alternative to liquid partitioning, the method of combined extraction and preconcentration of organic compounds in water by adsorption on proper solid materials followed by desorption with a small quantity of an organic solvent has been employed extensively for trace determination of contaminants in environmental waters (*1–8*). The recent availability of sorbents in small, inexpensive cartridges has contributed to the dramatic expansion of the use of solid-phase extraction (SPE), as evidenced by some selected publications (*9–13*). Besides solving well-known problems associated with the classical solvent extraction–solvent removal method, the SPE technique is particularly attractive as it lends itself to coupling with chromatographic systems for on-line applications (*14*). Another impressive feature of the SPE technique is that small sorbent traps can be deployed in the field by using newly available submersible instrumentation (*15, 16*) In this way, combined sampling, extraction, and preconcentration are done at the sampling site, thus eliminating most contamination and handling problems connected to the sample collection. In addition, immediate isolation of organics from the aqueous matrix by an adsorbing material can preserve analytes from bacterial attack occurring between the time of sample collection and analysis (*17, 18*). The small-volume column could be sealed and shipped to the laboratory for elution and chromatographic analysis.

Phenoxy acid herbicides have become widely used because of their relative cheapness and effectiveness in controlling the presence of unwanted broad-leaf weeds in crops. For the extraction of this class of herbicides from water, various procedures involving the SPE technique by an anion exchanger (*19*) and C-18 bonded silica (*20–22*) have been proposed. None of these methods, however, seems to be sufficiently sensitive to detect phenoxy acids at concentrations lower than 1 μg/L. Moreover, compared to the three-step

0003-2700/89/0361-1363$01.50/0

liquid extraction procedure, i.e. solvent extraction, back-extraction with basified water, and reextraction with an organic solvent (*23*), the proposed SPE methods are certainly less tedious, but also less selective.

When one is analyzing largely contaminated water samples and selective detection cannot be used, a rapid and simple procedure for cleanup of the extract prior to chromatographic analysis is desirable as, at least, it can provide added evidence for peak identity. Very recently, we succeeded in developing a selective high-performance liquid chromatography (HPLC) assay for eight triazine herbicides in water and vegetables by coupling a graphitized carbon black (Carbopack) cartridge (extraction column) to another one filled with a strong cation exchanger (isolation column) (*24*).

The object of this work was that of developing a sensitive and specific HPLC assay for monitoring phenoxy acid herbicides in environmental aqueous samples. The extraction and purification of the sample were performed by one single miniaturized cartridge containing in the upper part Carbopack and in the lower part a silica-based strong anion exchanger (SAX). Concentration factors higher than 500 were achieved by suitably sizing the trap. Direct injection of a large fraction of the final sample extract into the HPLC column operating in the reversed -phase mode was possible, as the eluotropic strength of the solvent system for elution of phenoxy acids from the trap was lower than that of the mobile phase for HPLC. Possible interferences by other acidic pollutants, such as phenols, were considered.

EXPERIMENTAL SECTION

Reagents and Chemicals. Authentic phenoxy acids and one benzoic acid derivative were purchased from Eurobase (Milan, Italy). The purity grade was equal or more than 99%. They are as follows: 2-methoxy-3,6-dichlorobenzoic acid (Dicamba); 2,4-dichlorophenoxyacetic acid (2,4-D); 4-chloro-2-methylphenoxyacetic acid (MCPA); 2-(2,4-dichlorophenoxy)propionic acid (2,4-DP); 2,4,5-trichlorophenoxyacetic acid (2,4,5-T); 2-(4-chloro-2-methylphenoxy)propionic acid (MCPP); 4-(2,4-dichlorophenoxy)butyric acid (2,4-DB); 4-(4-chloro-2-methylphenoxy)butyric acid (MCPB); 2-(2,4,5-trichlorophenoxy)propionic acid (2,4,5-TP). A standard solution was prepared by dissolving 1 g of each herbicide in 1 L of methanol. This solution was further diluted to obtain a working standard solution of 10 mg/L.

For HPLC, distilled water was further purified by passing it through a Norganic cartridge (Millipore, Bedford, MA). Methanol of HPLC grade was from Carlo Erba, Milan, Italy. Trifluoroacetic acid was supplied by Fluka AG, Buchs, Switzerland. All other chemicals were of analytical reagent grade (Carlo Erba).

Apparatus. Both Carbopack B and the silica-based anion exchanger had a particle size between 37 and 74 μm. As supplied, chloride was the counterion of the exchanger. They were packed in polypropylene tubes, 6 × 0.5 cm i.d. Polyethylene frits, 20-μm pore size, were located above and below each sorbent bed. All the materials cited above were kindly supplied by Supelco, Bellefonte, PA. The extraction/purification cartridge was prepared by introducing first 70 mg of the SAX material and then 50 mg of Carbopack B, with one frit interposed between the two sorbent beds. Before water samples were processed, no prewashing of the cartridge was necessary. The trap was fitted into a side-arm filtering flask, and liquids were forced to pass through the cartridge by vacuum done by a water pump.

Procedure. Aqueous samples were fortified with the nine herbicides by adding known volumes of the working standard solution. Water samples were then introduced in a polypropylene sample reservoir that was connected to the trap through an adapter. Suspended sediments contained in river and seawater samples, which can obstruct the cartridge, were removed by interposing between the reservoir and the cartridge a 6 cm × 1 cm i.d. plastic tube containing only two polyethylene frits (20-μm pore size). Samples were percolated through the cartridge at a flow rate of 9–10 mL/min, which was the maximum flow rate attainable with the apparatus used. After the sample was passed through the two-adsorbent trap, vacuum was reduced to give a flow rate of about 2 mL/min, as measured for water. An 8-mL aliquot of 1 mol/L sodium acetate in water was percolated through the cartridge to displace inorganic anions from the ion-exchange sites of the SAX material and convert it to the acetate form. The salt excess was eliminated by 2 mL of distilled water, which was in turn removed from the trap by 0.5 mL of acetonitrile. Then, the vacuum was further decreased, and phenoxy acids and Dicamba trapped by the Carbopack column were removed from it to the SAX surface by passing slowly through the trap 3 mL of methylene chloride/methanol (80:20, by volume) basified with sodium hydroxyde, 1 mmol/L, at a flow rate of about 1 mL/min. This solvent mixture was freshly prepared every 3 days, since it lost gradually its extraction efficiency on aging. Residual amounts of neutral and basic organic compounds remaining in the cartridge were drained with 0.5 mL of acetonitrile. Thereafter, the analytes of interest were eluted from the SAX column by passing through the cartridge at a flow rate of about 0.3 mL/min water/methanol (50:50, by volume) containing trifluoroacetic acid (0.5%, by volume) and KCl (0.16 mol/L) and collecting the first 600 μL of this solution. A 100-μL aliquot of this was injected into the HPLC column.

Table I. Recovery of Herbicides at Increasing Drinking Water Volumes Sampled[a]

	% recovery[b]		
	100 mL	200 mL	400 mL
Dicamba	98.4	96.6	98.6
2,4-D	97.3	99.0	98.7
MCPA	98.2	97.9	98.5
2,4-DP	98.0	97.3	98.7
MCPP	96.7	96.8	96.2
2,4,5-T	94.5	94.9	96.5
2,4-DB	99.3	100.3	98.9
MCPB	96.7	96.3	97.2
2,4,5-TP	94.7	95.3	96.0

[a] Water was spiked with 0.5 μg/L of each compound. [b] Mean values were calculated from three determinations.

HPLC Apparatus. A Model 5000 liquid chromatograph (Varian, Walnut Creek, CA) equipped with a Rheodyne Model 7125 injector having a 100-μL loop and with a Model 2050 UV detector (Varian) was used. A 25 cm × 4.6 mm i.d. column filled with 5-μm LC-18 reversed-phase packing (Supelco) was used. The mobile phase was a premixed water/methanol (41:59, by volume) solution containing 0.08% (v/v) trifluoroacetic acid. The flow rate was 1.5 mL/min. The herbicides considered were monitored with the detector set at 230 nm.

The concentrations of the herbicides in water were calculated by measuring the peak height of each herbicide and comparing them with those obtained with a standard solution. The latter was prepared by adding an appropriate volume of the herbicide working standard solution to 600 μL of the same aqueous solution used for elution of the herbicides from the trap.

RESULTS AND DISCUSSION

Recovery Studies. For the herbicides considered, the extraction efficiency of the Carbopack/SAX cartridge at increasing volumes of a drinking water specimen (pH 7.1) was evaluated. Water samples were spiked with the nine analytes at an individual concentration of 0.5 μg/L. No pH adjustment of the sample was done prior to extraction. Data are reported in Table I. Under the conditions mentioned above, the acidic herbicides considered were present in water virtually as anions. To first view, it is surprising that the small cartridge has the ability to trap such very water soluble analytes from relatively large sample volumes. Carbopack B was responsible for this effect, as, when in the chloride form, the low-capacity anion exchanger material located below the Carbopack particles has almost no affinity for organic anions. In two previous papers (*25*, *26*) it was reported that some anomalous effects displayed by Carbopack particles immersed in water could be explained by assuming that some carbon–oxygen complexes naturally contaminating its graphitic surface framework are rearranged

Table II. Recovery of Herbicides at Increasing River and Seawater Volumes Sampled[a]

	% recovery[b]					
	river water, mL			seawater, mL		
	50	200	400	50	200	400
Dicamba	98.5	31.6 (96.8)[c]	7.9 (97.4)	98.7	48.9 (97.8)	22.7 (98.1)
2,4-D	97.6	96.8	96.1	96.6	97.9	98.6
MCPA	98.4	98.0	98.9	98.1	98.5	99.0
2,4-DP	98.2	97.5	99.0	97.7	98.5	97.5
MCPP	96.6	96.4	95.7	96.4	95.2	96.1
2,4,5-T	94.7	94.9	95.6	95.0	94.6	96.5
2,4-DB	98.9	98.1	98.2	98.8	98.5	99.1
MCPB	97.3	97.3	97.0	96.5	97.3	96.1
2,4,5-TP	94.8	95.1	94.3	94.3	95.8	96.7

[a] Water was spiked with 2 μg/L of each compound. [b] Mean values were calculated from three determinations. [c] In parentheses are reported recovery values of Dicamba after sample acidification.

to form chemical groups bearing a positive charge. This surface modification enables Carbopack to strongly but reversibly adsorb organic anions; this is likely due to the added contributions of electrostatic and van der Waals forces. By taking advantage of this feature, workers have successfully employed Carbopack for the extraction of very polar phenols (7) and for the class separation of conjugated estrogens (27).

The effect that the matrix can have on the breakthrough volumes of the phenyl acetic derivative (Dicamba) and phenoxy acids was assessed by assaying increasing volumes of water samples from two different sources, that is river and seawaters. Likewise with solvent extraction methods, when the sorbent trap technique is used with nonspecific materials, such as chemically bonded silica (20–22), ion suppression by suitable pH adjustment is usually an unavoidable preliminary step in order to retain ionogenic substances. Obviously, this precludes field sampling of water by the use of extraction columns. On purpose, the addition of the herbicides considered at the individual concentration of 2 μg/L was the only modification we made on the environmental samples. As measured, the apparent pH values of the river and seawater specimens were respectively 8.1 and 7.8. Both the river and seawater samples, the latter being collected very close to the outlet of the river considered (Tevere), contained a lot of unknown acidic organic compounds, as evidenced by a large initial front appearing on chromatographing the relative sample extracts. In spite of this, recovery data (Table II) of the eight phenoxy acids were very comparable to those obtained for drinking water extraction. Evidently, no significant adverse saturation effect took place on the Carbopack surface, within the range of water volumes considered. On the contrary, a dramatic loss of the phenylacetic derivative, that is Dicamba, occurred by sampling water volumes larger than 100 mL. Among the acidic herbicides considered, Dicamba was observed to have by far the highest mobility on the Carbopack column. Competition for the relatively few, positively charged active centers of the Carbopack surface mentioned above by the other organic anions naturally contaminating the two environmental aqueous samples considered was supposedly responsible for the loss of Dicamba. This hypothesis was substantiated by the fact that no significant loss of Dicamba was further observed by acidifying the water samples (pH 2). In such ambient, the phenyl acetic derivative is virtually un-ionized, and as such, its adsorption takes place on the predominant, normal adsorption sites of the Carbopack surface, which are far from saturation. Anyway, an accurate determination of Dicamba at concentrations lower than 1 μg/L could be still performed without sample manipulation by submitting to the extraction procedure only 50 mL of a surface water specimen.

Finally, another interesting feature of the combined use of a nonspecific adsorbent and an ion exchanger is that selective, quantitative extraction of ionogenic organic compounds can still be accomplished from high-ionic-strength aqueous samples, such as seawater, where an ion exchanger alone fails.

Table III. Accuracy and Precision of the Method with High and Low Herbicide Contents in 200-mL Groundwater Samples

	% recovery ± SD[a]	
	0.1 μg/L	50 μg/L
Dicamba	98.8 ± 5.7	98.3 ± 2.0
2,4-D	98.2 ± 2.6	98.9 ± 1.6
MCPA	99.3 ± 2.4	97.9 ± 1.3
2,4-DP	98.7 ± 2.1	98.8 ± 1.4
MCPP	96.3 ± 2.7	96.7 ± 1.6
2,4,5-T	95.4 ± 2.9	96.1 ± 2.1
2,4-DB	99.0 ± 1.8	98.0 ± 1.1
MCPB	96.6 ± 2.9	97.4 ± 1.5
2,4,5-TP	94.9 ± 3.2	95.6 ± 2.3

[a] Standard deviation calculated from six determinations.

Precision. The recovery and the within-run precision of this method at low and high concentrations of the nine herbicides considered were assessed. A sample of groundwater was divided into two portions that were supplemented with the analytes respectively at the levels of 0.1 and 50 μg/L. Each portion was divided into six 200-mL aliquots, which were analyzed by this procedure. Quantitative results are reported in Table III. As can be seen, the recovery efficiency was independent of the herbicide concentration, thus demonstrating the absence of any adverse effect of both irreversible adsorption by the materials composing the extraction apparatus and saturation of the two adsorbents.

Method Comparison. In terms of recovery and selectivity, the effectiveness of the extraction procedure by the two-adsorbent tandem assembly was compared with those obtained by using a 1-g C-18 disposable extraction column (Baker Chemical Co., Phillipsburg, NJ) (20, 22) and a homemade cartridge containing 50 mg of a high-capacity resin-based strong anion exchanger, such as Amberlite CG-400-II (Fluka). This material was converted to the hydroxide form prior to use. For these experiments, 50-mL aliquots of a Tevere River water sample were supplemented with the nine herbicides at the individual concentration of 2 μg/L. The extraction of the analytes with the C-18 cartridge was performed from both unacidified and acidified (pH 2) water samples. According to the method of Hoke et al. (20), the herbicides were eluted from the C-18 cartridge with two 1-mL portions of methanol that were suitably diluted with water prior to HPLC quantification. Removal of the analytes from the anion exchanger material was performed first by washing it with 1 mL of acidified water (pH 1) and then desorbing the analytes with 1 mL of water/methanol (50:50, by volume) acidified with HCl,

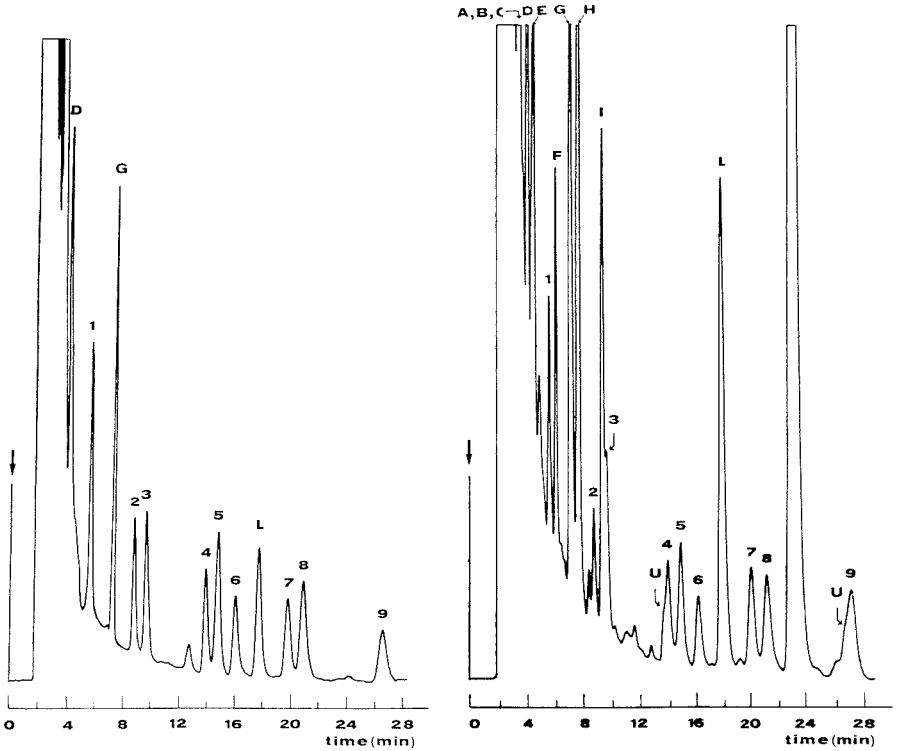

Figure 1. Chromatograms obtained on sampling 50 mL of river water (Tevere, June 1988) spiked with 2 μg/L concentrations of the nine herbicides considered and 4 μg/L concentrations of the 11 priority pollutant phenols by this extraction procedure (A) and the 1-g, C-18 extraction column (B): 1, Dicamba; 2, 2,4-D; 3, MCPA; 4, 2,4-DP; 5, MCPP; 6, 2,4,5-T; 7, 2,4-DB; 8, MCPB; 9, 2,4,5-TP; A, phenol; B, *p*-nitrophenol; C, *o*-chlorophenol; D, 2,4-dinitrophenol; E, *o*-nitrophenol; F, 2,4-dimethylphenol; G, 4,6-dinitro-*o*-cresol; H, 4-chloro-*m*-cresol; I, 2,4-dichlorophenol; J, 2,4,6-trichlorophenol; U, unknown compounds contaminating the water specimen. Pentachlorophenol was eluted with a retention time greater than 50 min.

0.1 mol/L. Recovery data are reported in Table IV. A large loss of Dicamba and incomplete recovery of phenoxy acids were obtained by using the resin-based exchanger material. Moreover, the breakthrough volumes of the herbicides considered on the exchanger column were strictly dependent upon the ionic strength of the water sample percolating through it, as observed by adding moderate amounts of an inorganic salt to the aqueous sample considered. A good extraction efficiency for the nine herbicides from acidified water was obtained with the C-18 cartridge, but this material was ineffective for use in field extraction of ionogenic compounds since the herbicides considered passed almost unretained along it when the preliminary acidification step of the water sample was omitted.

As designed, the Carbopack/SAX cartridge is able to trap selectively only compounds acidic in nature. Among these, we considered the 11 priority pollutant phenols as compounds that may interfere with the analysis of the herbicides considered. In terms of selectivity, the performance of the two-adsorbent tandem assembly was assessed and compared with that of the 1-g, C-18 extraction cartridge by sampling surface water spiked with both the nine acidic herbicides and the 11 phenols. Figure 1 shows typical chromatograms obtained by the two extraction procedures. As can be seen, the selective extraction procedure developed by us was able to eliminate not only two unknown neutral compounds present in the environmental water sample that interfere with the analysis of 2,4-DP and 2,4,5,-TP during extraction of water with the C-18 cartridge, but also a weak acidic compound, such as 2,4-dichlorophenol, that interferes with the analysis of MCPA. This phenol derivative, together with phenol, *o*-chlorophenol, 2,4-dimethylphenol, and 4-chloro-*m*-cresol, was completely washed out from the trap under consideration likely because, although adsorbed on the Carbopack surface, these compounds are not sufficiently acidic to be retained by the SAX material in the acetate form.

Table IV. Recovery of Herbicides from 200-mL Groundwater Samples by the Proposed Method Compared with That from Two Other Extraction Methods

	% recovery[a]			
	C-18			
	pH 2	pH 7.9	anion exchanger	this method
Dicamba	94.2	<10	23.0	97.3
2,4-D	96.1	<10	78.3	98.4
MCPA	96.4	<10	77.7	97.6
2,4-DP	97.7	<10	76.8	96.4
MCPP	94.4	<10	82.0	97.3
2,4,5-T	93.5	<10	81.4	95.4
2,4-DB	96.0	<10	82.3	98.9
MCPB	95.8	<10	81.5	96.5
2,4,5-T	93.1	<10	77.3	95.2

[a] Mean values were calculated from two determinations.

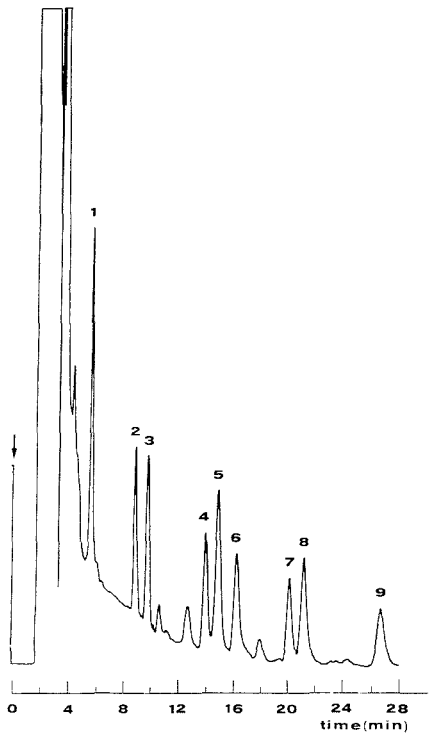

Figure 2. Chromatogram obtained on sampling 100 mL of drinking water spiked with 0.3 μg/L concentrations of each herbicide. Peak numbering is the same as in Figure 1.

Limits of Detection. Reversed-phase HPLC of phenoxy acids has usually been performed by adding acetic acid to the mobile phase as an ion suppressor (*20–22, 28*). Under this condition, UV detection at 230 nm, where phenoxy acids have the absorption maximum, is precluded because of the absorption of acetic acid itself at this wavelength. This obstacle was overcome by replacing acetic acid with a much more acidic organic compound, such as trifluoroacetic acid. By this modification, sharp peaks for phenoxy acids with a low base line at 230 nm were obtained because, compared to acetic acid, trifluoroacetic acid is a very weak UV-absorbing species, and a very small amount of it sufficed to suppress ionization of the acidic herbicides.

Under the chromatographic conditions selected, the limits of detection (signal-to-noise ratio = 3) ranged from 0.3 to 1.2 ng, respectively, for Dicamba and 2,4,5-TP, which are the first and last compounds, respectively, to be eluted from the HPLC column. It follows that by sampling only 100 mL of a drinking water sample this method can determine phenoxy acids and Dicamba at concentrations much lower than 0.1 μg/L and consequently can satisfy fully the expected new EEC regulations. Figure 2 shows a typical chromatogram obtained on sampling a drinking water sample fortified with the nine herbicides considered.

Sample Storage. As discussed earlier, no sample pretreatment is necessary on extracting phenoxy acids from water with the Carbopack/SAX cartridge. Therefore, this trap can be suitable for use in field extraction of phenoxy acids. On the other hand, as already observed for benzidine extracted with Carbopack from a largely contaminated surface water sample (*29*), it is possible that some chemical alteration of the sample catalyzed by the Carbopack surface takes place between the time of the extraction and that of the solvent desorption. For the nine herbicides studied, the effect of storage was evaluated by extracting 200 mL of a Tevere River sample spiked with 2 μg/L of each herbicide. After the water had been passed through it, the cartridge was stored for 25 days at ambient temperature. Thereafter, the herbicides were desorbed and determined by the proposed procedure. The recoveries of the nine herbicides considered ranged between 94.7 for 2,4,5-T and 98.7 for 2,4-D. Hence, no significant adverse effect occurred during storage.

Registry No. 2,4-D, 94-75-7; MCPA, 94-74-6; 2,4-DP, 120-36-5; MCPP, 7085-19-0; 2,4,5-T, 93-76-5; 2,4-DB, 94-82-6; MCPB, 94-81-5; 2,4,5-TP, 93-72-1; H_2O, 7732-18-5; dicamba, 1918-00-9.

LITERATURE CITED

(1) Takeda, A.; Fritz, S. J.; *J. Chromatog.* **1978**, *152*, 329–340.
(2) Picer, N.; Picer, M. *J. Chromatogr.* **1980**, *193*, 357–369.
(3) Bacaloni, A.; Goretti, G.; Lagana, A.; Petronio, B. M.; Rotatori, M. *Anal. Chem.* **1980**, *52*, 2033–2036.
(4) Mangani, F.; Crescentini, G.; Bruner, F. *Anal. Chem.* **1981**, *53*, 1627–1632.
(5) Josefson, C. M.; Johnston, J. B.; Trubey, R. *Anal. Chem.* **1984**, *56*, 764–768.
(6) Rice, M. R.; Gold, H. S. *Anal. Chem.* **1984**, *56*, 1436–1440.
(7) Borra, C.; Di Corcia, A.; Marchetti, M.; Samperi, R. *Anal. Chem.* **1986**, *58*, 2048–2052.
(8) Di Corcia, A.; Marchetti, M.; Samperi, R. *J. Chromatogr.* **1987**, *405*, 357–363.
(9) Rostad, C. E.; Percira, W. E.; Ratcliff, S. M. *Anal. Chem.* **1984**, *56*, 2856–2860.
(10) Ozretich, R. J.; Schroeder, W. P. *Anal. Chem.* **1986**, *58*, 2041–2048.
(11) Robinson, J. L.; John, J.; Safa, A. I.; Kirkes, K. A.; Griffith, P. E. *J. Chromatogr.* **1987**, *402*, 201–210.
(12) Bellar, T. A.; Budde, W. L. *Anal. Chem.* **1988**, *60*, 2076–2083.
(13) Junk, G. A.; Richard, J. J. *Anal. Chem.* **1988**, *60*, 451–454.
(14) Nielen, M. W. F.; Brinkman, U. A. Th.; Frei, R. W. *Anal. Chem.* **1985**, *57*, 806–810.
(15) Green, D. R.; Stull, J. K.; Heesen, T. C. *Mar. Pollut. Bull.* **1986**, *17*, 324–329.
(16) Schatzberg, P.; Adema, C. M.; Thomas, W. M.; Mangum, S. R. *Oceans '86 Conference Record*; Marine Technology Society: Washington, DC, 1986; pp 1155–1159.
(17) Mallet, V. N.; Brun, G. L.; MacDonald, A. N.; Berkane, K. *J. Chromatogr.* **1978**, *160*, 81–88.
(18) Green, D. R.; Le Pape, D. *Anal. Chem.* **1987**, *59*, 699–703.
(19) Renberg, L. *Anal. Chem.* **1974**, *46*, 459–461.
(20) Hoke, S. H.; Brueggemann, E. E.; Baxter, L. J.; Trybus, T. *J. Chromatogr.* **1986**, *357*, 429–432.
(21) Sherma, J. *J. Liq. Chromatogr.* **1986**, *9*, 3433–3438.
(22) Wells, M. J. M.; Michael, J. L. *Anal. Chem.* **1987**, *59*, 1739–1742.
(23) Bierl, R.; Kaa, W.; Thomas, W. *Fresenius' Z. Anal. Chem.* **1984**, *319*, 172–179.
(24) Battista, M.; Di Corcia, A.; Marchetti, M. *Anal. Chem.* **1989**, *61*, 935–939.
(25) Di Corcia, A.; Samperi, R.; Sebastiani, E.; Severini, C. *Anal. Chem.* **1980**, *52*, 1345–1350.
(26) Campanella, L.; Di Corcia, A.; Samperi, R.; Gambacorta, A. *Mater. Chem.* **1982**, *7*, 429–438.
(27) Andreolini, F.; Borra, C.; Caccamo, F.; Di Corcia, A.; Samperi, R. *Anal. Chem.* **1987**, *59*, 1720–1725.
(28) Hamann, R.; Kettrup, A. *Chemosfere* **1987**, *16*, 527–536.
(29) Di Corcia, A.; Liberatori, A.; Marchetti, M.; Samperi, R. *Organic Micropollutants in the Aquatic Environment*; Proceedings of the workshop, Berlin, October 1986; pp 103–116.

RECEIVED for review December 20, 1988. Accepted March 13, 1989.

Anal. Chem. 1989, 61, 1368–1382

Theory of Optimization of the Experimental Conditions of Preparative Elution Chromatography: Optimization of the Column Efficiency

Sadroddin Golshan-Shirazi and Georges Guiochon*

University of Tennessee, Department of Chemistry, Knoxville, Tennessee 37996-1600, and Oak Ridge National Laboratory, Oak Ridge, Tennessee 37831-6120

The effect of column efficiency on the recovery yield and the production rate of the second component of a binary mixture purified by preparative liquid chromatography at a certain required degree of purity is discussed. Equations relating these functions to the characteristics of the separation problem studied are derived by combining the analytical solution of the ideal model to the band broadening effects due to the finite column efficiency. The optimization of the parameters that control the column efficiency (the column length, L, the particle size diameter, d_p, and the mobile phase velocity, u) is described. It is shown that there is an optimum value for the ratio of d_p^2/L, for which the production rate is maximum. This optimum value depends on the selectivity of the chromatographic system used, on the maximum pressure under which the equipment and column can be safely operated, on the relative composition of the feed, on the required degree of purity, on the parameters of the competitive equilibrium isotherms of the mixture components, and on the parameter of the plate height equation accounting for the resistances to radial mass transfer inside the phases and between them (the classical "C" term). The production rate increases monotonically with increasing maximum pressure under which the equipment and the column can be operated. It increases as the square of $(1 - (1/\alpha))$, which is nearly as the square of $(\alpha - 1)$, at low values of the phase system selectivity. The optimum value of the sample size is independent of the column efficiency.

INTRODUCTION

In a recent paper we have developed the theoretical framework for a theory of optimization of preparative chromatography based on the use of the ideal model (*1*). This model provides powerful insights into the interactions between some of the most critical parameters controlling the performance of a preparative liquid chromatograph. Since this model assumes a column of infinite efficiency, however, there is one issue for which it is unable to suggest any relevant answer, the influence of the column efficiency on the production rate and the recovery yield. Optimization of the design parameters that determine the column efficiency (column length, particle size, and quality of the packing material) is of major importance, however, because making very efficient columns is costly, so we do not want to use columns more efficient than necessary. The most efficient columns are made of small average particle size, narrow size distribution packing materials. Operation of these columns at the proper (relatively high) mobile phase velocity requires the use of high inlet pressures, which in turn demands sophisticated, high-performance pumps, thick wall, heavy column tubings, and fittings made of high tensile strength alloys.

The complete optimization of the experimental conditions of preparative liquid chromatography would require the derivation of procedures permitting the calculation of the design and operation characteristics of the chromatograph which permits the minimum production cost for a compound with certain specifications, using a feed of known composition. It is not possible at this stage, for an academic research group, to incorporate such esoteric parameters as labor costs, headquarters overhead, and amortization in an optimization study. The estimate of these parameters is often specific to a company, or even to a plant. We shall discuss here the conditions permitting the achievement of the highest possible production rate with columns of a given diameter. It is implicitly assumed that the production rate is proportional to the square of the column diameter. As long as the column efficiency is independent of the column diameter and the combined effects of the heat of sorption/desorption and radial heat transfers on column performance seem negligible, there is no reason to doubt this basic assumption.

In the search for the maximum production rate we shall take a few constraints into account. First, the products collected must satisfy some purity requirements. Usually, the products of the chromatographic separation must be between 95% and 99% pure. Sometimes, however, specifications as low as 90% or exceeding 99.9% are found. Second, the recovery yield must often, but not always, exceed a certain threshold, sometimes as high as 98%, other times lower than 60%. In other cases, only the maximum production rate is of interest; intermediate fractions can be recycled or wasted. Finally, the column must be operated with an inlet pressure that should not be too high. There is much ambiguity here, and it is rarely possible to define an accurate threshold. The maximum pressure allowed depends to some extent on the column diameter. It is easy to find 1 mm i.d. metal tubings which can stand pressures well exceeding 1000 atm. It is very expensive to make a 60 cm diameter column that can be operated at 100 atm inlet pressure.

Most previous studies published on the optimization of column efficiency in preparative liquid chromatography are based on the variation of the bandwidth of the main component zone with increasing sample size. Although it has been known for many years that the band broadening observed at large column loadings is due to thermodynamical reasons and is nearly independent of the kinetics of mass transfer between phases, it has often been wrongly concluded that, since the apparent column efficiency decreases with increasing sample size, efficient columns are not useful in preparative chromatography (*2*). This is contradictory with previous experimental results obtained in gas chromatography (*3*) and in liquid chromatography (*4*), which indicate that the best results are obtained with the most efficient columns (smallest values of the A and C coefficients). This is because the real column

*Author to whom correspondence should be addressed at the University of Tennessee.

0003-2700/89/0361-1368$01.50/0

efficiency is a measure of the kinetics of mass transfer between phases and determines the sharpness of the band profiles, whereas the general profiles of high concentration bands depend also on the thermodynamics of phase equilibria. An efficient column can be used at a much higher flow velocity than a poor column and still provide the same efficiency, as measured by the number of theoretical plates for a small sample. It will thus permit the achievement of a larger production rate. We show in the present paper why and to which degree the column efficiency influences the performance of a preparative chromatograph.

Similarly, attempts at optimizing the column efficiency that are based on the use of the resolution equation classical in analytical (i.e., linear) chromatography and on relationships between apparent column efficiency and sample size (*5*) are doomed to failure as they neglect the two fundamental aspects of nonlinear chromatography, the interaction between the band profiles of the various components of the feed during their migration in the column (*6*) and the occurrence of shocks or shock layers between these bands (*7*). The thickness of the shock layer between the bands of the two components of a binary mixture, for example, depends on the column efficiency, which, accordingly, controls also the production rate and the recovery yield. For this very reason, the otherwise excellent work by Knox and Pyper (*8*), which explicitly neglects the interaction between the two components and assumes for them two independent, single-component, Langmuir equilibrium isotherms, cannot give satisfactory results, although the authors considered exact resolution of the two elution band at column exit (*9*). But the bands have interfered and considerably interacted during their entire migration along the column.

In a previous paper (*1*), we have discussed the use of the ideal model of chromatography for the optimization of the experimental conditions of a preparative separation. We have derived analytical expressions for the optimum sample size, the cutting times, the recovery yield, and the production rate. One of the most important results of that work was the demonstration that the optimum sample size is independent of the column efficiency. The maximum production rate achieved, on the contrary, depends markedly on this efficiency, but our former work (based on the ideal model, i.e., on the assumption of a column of infinite efficiency) does not permit the derivation of a predictive relationship which could be used for optimization purposes. It is obvious that, with the infinitely efficient column of the ideal model, the separation should be performed at the highest flow velocity acceptable. In practice, however, the column efficiency is finite and depends on the mobile phase velocity. At high flow rates, the column efficiency is low and the border lines between incompletely resolved bands become blurred. The recovery yield falters.

The purpose of this paper is the derivation of analytical expressions relating the production rate, the recovery yield, and the cutting times to the column efficiency and the optimization of the relevant design and operation parameters of an industrial preparative chromatograph.

THEORY

In this paper we combine the results of several previous studies, (i) the analytical solution of the ideal model of chromatography in the case of a binary mixture, when the equilibrium isotherm for the two components are competitive Langmuir isotherms (*10*), (ii) the optimization of the sample size for maximum production rate of one of the two components of a binary mixture with or without certain constraints of purity and recovery yield (*1*), and (iii) the relationship between apparent column efficiency and sample size in the case of the semiideal model of chromatography (*11*).

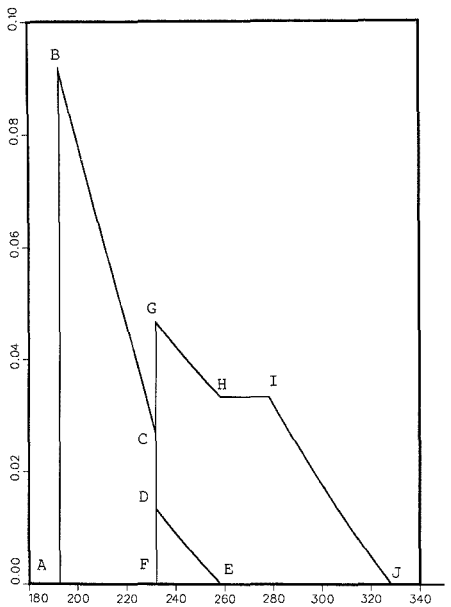

Figure 1. Solution of the ideal model of chromatography for a large injected plug of a binary mixture: feed composition, 1/1; phase selectivity, 1.20; AB, front shock, shock separating a solution of the first component from the pure mobile phase; BC, diffuse rear profile of the pure first component (first zone of the chromatogram); CD, rear shock of the first component; DE, diffuse rear profile of the first component in the mixed band (second zone of the chromatogram); FG, front shock of the second component, separating the solution of pure first component from a mixed band of the two components); GH, diffuse, rear profile of the second component in the mixed band; HI, plateau of the pure second component (third zone of the chromatogram); IJ, diffuse rear profile of the pure second component (end of the third zone of the chromatogram). The elution times of AB, FDCG, EH, I, and J are given in Table IA. The equations for the arcs BC, DE, GH, and IJ are given in Table IB. The concentrations in C, D, G, and H are given in Table IC.

The definitions of throughput, cycle time, production rate, recovery yield, and purity are the same as those used in the previous work (*1*).

I. Summary of Previous Results. The equations giving the characteristic features (retention times and height of the concentration shock between the two components, elution profiles of the two components) of the system of two interfering bands corresponding to the injection of a large sample of a binary mixture, whose components are incompletely resolved, are summarized in our previous paper (*1*). These equations are reported again here, on a different, more condensed tabular form (see Figure 1 and Table I).

The equations derived previously (*1*), relating the cutting times, the recovery yield, and the production rate to the characteristics of the separation problem investigated (parameters of the equilibrium isotherms of the compounds, composition of the feed, required degree of purity of the collected fraction) are summarized in Tables II (definitions) and III (results). These equations have been derived within the framework of the ideal model of chromatography. They assume a column of infinite efficiency. We want to emphasize here that the loading factor for the mixed zone, L_f (Table IIa eq II-2c), is not related simply to the feed composition: it is not equal to the sum of the loading factors for the two components.

Table I. Characteristics of the Analytical Solution of the Ideal Model for a Binary Mixture[a]

A. Retention Times

End of the Band of the Second Component (J):

$$t_j = t_p + t_{R,2}^0 = t_p + (1 + k'_{0,2})t_0 \quad \text{(I-1)}$$

End of the Plateau of the Second Component (I):

$$t_I = t_E + \frac{\gamma(\gamma - 1)}{\alpha^2}(t_{R,2}^0 - t_0) \quad \text{(I-2)}$$

End of the Band of the First Component (E):

$$t_E = t_p + t_0 + \frac{\gamma}{\alpha}(t_{R,1}^0 - t_0) \quad \text{(I-3)}$$

Retention Time of the Second Component (FG):

$$t_F = t_p + t_0 + \gamma(t_{R,2}^0 - t_0)\,(1 - L_f^{1/2})^2 \quad \text{(I-4)}$$

Retention Time of the First Component (A):

t_A cannot be calculated analytically, but either by solving numerically a first-order differential equation or by calculating the lower boundary of the integral of the profile BC (eq I-5) so the mass of the first component is conserved

B. Arcs of the Profiles

First Component, First Arc (BC):

$$t = t_p + t_0 + (t_{R,1}^0 - t_0)\left[\frac{1}{(1 + b_1C_1)^2} - L_{f,2}\frac{\alpha - 1}{\alpha}\frac{1}{[(\alpha - 1)/\alpha + b_1C_1]^2}\right] \quad \text{(I-5)}$$

First Component, Second Arc (DE):

$$C_1 = \frac{1}{b_1 + b_2/\alpha r_1}\left[\left(\frac{\gamma}{\alpha}\frac{t_{R,1}^0 - t_0}{t - t_p - t_0}\right)^{1/2} - 1\right] \quad \text{(I-6)}$$

Second Component, First Arc (GH):

$$C_2 = \frac{1}{b_2 + \alpha b_1 r_1}\left[\left(\gamma\frac{t_{R,2}^0 - t_0}{t - t_p - t_0}\right)^{1/2} - 1\right] \quad \text{(I-7)}$$

Second Component, Second Arc (IJ):

$$C_2 = \frac{1}{b_2}\left[\left(\frac{t_{R,2}^0 - t_0}{t - t_p - t_0}\right)^{1/2} - 1\right] \quad \text{(I-8)}$$

C. Concentrations

Concentration of the Plateau of Second Component (HI):

$$C_H = \frac{\alpha - 1}{b_2 + \alpha b_1 r_1} \quad \text{(I-9)}$$

Concentration of the Second Component at the Shock (G):

$$C_G = \frac{1}{b_2 + \alpha b_1 r_1}\frac{L_f^{1/2}}{1 - L_f^{1/2}} \quad \text{(I-10)}$$

Concentration of the First Component on the Shock Rear Side (D):

$$C_D = \frac{r_1}{b_2 + \alpha b_1 r_1}\frac{1 - \alpha + \alpha L_f^{1/2}}{1 - L_f^{1/2}} \quad \text{(I-11)}$$

Concentration of the First Component on the Shock Front Side (C):

$$C_{1,C} = \frac{((1 - \alpha)/\alpha) + L_f^{1/2}}{b_1(1 - L_f^{1/2})} \quad \text{(I-12)}$$

[a] See Figure 1 (location of points A, F, E, I, J).

Table II. Definitions and General Equations

A

Equilibrium Isotherms for the Two Components:

$$Q_1 = \frac{a_1C_1}{1 + b_1C_1 + b_2C_2} \quad \text{(II-1a)}$$

$$Q_2 = \frac{a_2C_2}{1 + b_1C_1 + b_2C_2} \quad \text{(II-1b)}$$

Loading Factor:

The ratio of the amount of a component injected in the column to the column saturation capacity for this compound.

$$L_{f,2} = \frac{C_2^0 b_2 t_p}{t_{R,2}^0 - t_0} = \frac{n_2 b_2}{F_v(t_{R,2}^0 - t_0)} = \frac{n_2 b_2}{\epsilon S L K_2'^0} \quad \text{(II-2a)}$$

$$L_{f,1} = L_{f,2}\frac{b_1C_1^0\alpha}{b_2C_2^0} \quad \text{(II-2b)}$$

$$L_f = \left(1 + \frac{b_1 r_1}{b_2}\right)L_{f,2} \quad \text{(II-2c)}$$

r_1 is the positive root of the following equation:

$$\alpha b_1 C_2^0 r^2 - (\alpha - 1 + \alpha b_1 C_1^0 - b_2 C_2^0)r - b_2 C_1^0 = 0 \quad \text{(II-3)}$$

$$\gamma = \frac{\alpha b_1 r_1 + b_2}{b_1 r_1 + b_2} \text{ and } \alpha = \frac{a_2}{a_1} \quad \text{(II-4)}$$

B

Production Rate for Component i:

$$P_i = \frac{n_i - A_i}{t_c} \quad \text{(II-5)}$$

Recovery Yield for Component i:

$$R_i = \frac{n_i - A_i}{n_i} \quad \text{(II-6)}$$

Purity of the Fraction of Component i Collected:

$$\mathrm{Pu}_i = \frac{n_i - A_i}{n_i - A_i + B_i} \quad \text{(II-7)}$$

with:

$$A_2 = F_v\int_{t_F}^{t_{c,2}} C_2\,dt \quad \text{(II-8a)}$$

$$A_1 = F_v\int_{t_{c,1}}^{t_E} C_1\,dt \quad \text{(II-8b)}$$

$$B_2 = F_v\int_{t_{c,2}}^{t_E} C_1\,dt \quad \text{(II-9a)}$$

$$B_1 = F_v\int_{t_F}^{t_{c,1}} C_2\,dt \quad \text{(II-9b)}$$

where $t_{c,1}$ and $t_{c,2}$ are the cutting times for the first and second component, respectively, i.e., the times when the fraction collector of the first component is closed ($t_{c,1}$) and when the fraction collector for the second component is open ($t_{c,2}$, see Figure 1).

II. Principle of the Introduction of the Column Efficiency in the Solution of the Ideal Model. We want to modify the solution derived from the ideal model to account for the finite efficiency of the column. Obviously, this cannot be done in a rigorous way. We cannot derive an analytical solution of the semi-ideal model of chromatography, which takes into account the finite column efficiency. We know how to calculate numerical solutions for this model (*6, 12*), however, and it has been shown that the profiles obtained are in excellent agreement with the experimental results (*13, 14*). The use of numerical solutions for the investigation of the optimization of the column design and operation parameters is

Table III. Yield (R_2), Production Rate (P_2), and Cutting Time ($t_{c,2}$) for the Purification[a] of the Second Component of a Binary Mixture (Optimum Conditions under the Ideal Model of Chromatography)

Yield at Maximum Production Rate:

$$R_2 = \frac{1}{L_{t,2}(1 + b_1r_1/b_2)}\left[1 - \left(\frac{t_{c,2} - t_p - t_0}{\gamma(t_{R,2}{}^0 - t_0)}\right)^{1/2}\right]^2 \quad \text{(III-1)}$$

Maximum Production Rate:

$$P_2 = \frac{\epsilon S L k_2{}'^0}{(b_2 + b_1r_1)t_c}\left[1 - \left(\frac{t_{c,2} - t_p - t_0}{\gamma(t_{R,2}{}^0 - t_0)}\right)^{1/2}\right]^2 \quad \text{(III-2)}$$

Optimum Cutting Time:

$$t_{c,2} = t_p + t_0 + \gamma(t_{R,2}{}^0 - t_0)\left[\frac{1/\alpha - x}{1 - x}\right]^2 \quad \text{(III-3)}$$

with:

$$x = \left(\frac{1 - Pu_2}{Pu_2\alpha r_1}\right)^{1/2} \quad \text{(III-4)}$$

and Pu_2 is the required purity of the fraction collected.
Optimum Loading Factor:

$$L_{t,2} = \frac{1}{(1 + b_1r_1/b_2)}\left[\frac{1 - 1/\alpha}{1 - x}\right]^2 \quad \text{(III-5)}$$

[a] Required degree of purity, Pu_2, see eq III-4.

long, complicated, and difficult, as it is a multiparameter optimization that has to be carried out numerically without the help of a theoretical model (*15*).

Since we have an exact analytical solution of the ideal model, we are going to derive an approximate solution of the semiideal model, extending previous results by Knox and Pyper (*8*) and by us (*11*, *16*). Then, we shall compare the results predicted by this approximation to those of numerical calculations carried out in a number of different cases, to estimate the degree of accuracy of this approach. Since the results of this comparison are satisfactory (see below), the approximate equation, whose use is much simpler than that of the numerical program, will be available for the solution of practical problems and will serve as a basis for an optimization of the column characteristics.

When we consider a column that has a finite efficiency and inject a finite size sample, there are two independent contributions to the bandwidth, thermodynamic and kinetic contributions. The former arises from the nonlinear behavior of the equilibrium isotherm of the components of the mixture between the two phases of the chromatographic system. It is properly accounted for by the ideal model (*10*). The latter is due to the finite kinetics of radial mass transfer in the chromatographic column. It is responsible for the column efficiency and is neglected in the ideal model (infinite column efficiency). In a first approximation, these two contributions can be treated as independent from each other (*8*). We may assume that the kinetics of mass transfer, either through the mobile phase (whether flowing between packing particles or stagnant inside the pores of these particles) or between the mobile and the stationary phases, does not vary with increasing concentration of the sample components in the eluate. We know that the column efficiency is controlled by diffusion in most cases and that the diffusion coefficients of dilute solutions vary only slightly with their concentration in the range used in preparative liquid chromatography (0–5%), except for high polymers, so we may expect this assumption to hold in most practical cases.

III. Procedure for Relating Column Efficiency and Production Rate. Because of the finite column efficiency, the concentration shocks predicted by the ideal model do not take place. They are replaced by the formation of very steep fronts, called shock layers (*7*). Accordingly, the top of the second shock layer of the first component (point C, Figure 1) is eluted slightly before its bottom (point D), while, for the second component, point F elutes slightly before point G. The thickness of the shock layers, i.e., the times between the elution of C and D or of F and G, is proportional to the column HETP. Furthermore, the second part of the first component profile (arc DE, Figure 1) and the rear of the second component profile (arcs GHIJ, Figure 1) are diffuse and tail somewhat longer than predicted by the ideal model. The extent of this tailing depends on column efficiency and, in turn, influences the position of the cutting times for the collection of the purified fractions. For both components, the lower the column efficiency, the smaller the production rate for a given degree of purity and the lower the recovery yield. The effects of the column efficiency on the production rate of the two components have different origins, however, and must be treated differently. For component 1, the origin of the decrease in production rate is in the thickness of the shock layer of the second component. For component 2, it is in the diffusive tailing of component 1. This paper is concerned only with the second phenomenon.

Compared to the production rate predicted by the ideal model, the production rate of the second component by a real column, having a finite efficiency, is reduced because the elution of the first component takes longer. Accordingly, the cutting time has to be delayed to permit collection of a fraction at the required degree of purity. Thus, a fraction of the eluate containing the second component at a high concentration (of the order of C_H) is rejected. The extent of this fraction, i.e., the recovery yield loss, depends on the importance of the tailing of the rear profile of the first component and hence on the column efficiency.

In order to estimate by how much we have to delay the fraction cutting, we must remember that the thermodynamic drive which shapes the elution profile as described by Figure 1 and the equations in Table I is concentration dependent. The intensity of the nonlinear effects (due to the nonlinear behavior of the isotherms and to the dependence of the amount of one component sorbed on the concentrations of both in the mobile phase) is predominant in the part of the chromatogram where the concentrations of one or the other solute is large. On the contrary, the influence of the apparent diffusion (axial diffusion and resistances to radial mass transfer) predominates where these concentrations are small.

During the migration of the band along the column, the second component tends to displace the first one. This is the effect responsible for the second concentration shock, which takes place between the two components. The concentration of the first component in the second zone of the chromatogram (arc DE, Figure 1) is determined by the entire concentration profile of the second component (are FGHIJ, Figure 1), but essentially by the part HIJ which is also the one most sensitive to the diffusion effects. Because the concentration of the second component in the section HI of the chromatogram is nearly constant (it is truly constant only for an ideal column), the influence of the second component on the diffusive tailing of the rear of the profile of the first component will be such that the rear tails of the two profiles are very similar. As a first approximation we may assume that they are identical, that is that the delay in the cutting time is equal to the distance between the time J and the end of the real profile of the second component.

In theory, the end of the real profile of an overloaded band is asymptotic to a Gaussian profile and does never end. In practice, we take as end of the profile the time defined by the base-line width calculated after the procedure suggested by Knox and Pyper (*8*) and discussed below.

IV. Production Rate of the Second Component and Column Efficiency. Because of the finite column efficiency, the elution of the first component of the mixture lasts somewhat longer than that predicted by the ideal model (Figure 1). In order to collect a fraction of the second component having the same requested degree of purity, Pu_2, we must open the valve to the fraction collector a little later. The collection time, $t_{c,2}$, becomes

$$t_{c,2} = t_p + t_0 + \gamma(t_{R,2}^\circ - t_0)\left[\frac{1/\alpha - x}{1 - x}\right]^2 + \delta \quad (1)$$

where the first three terms represent the optimum cutting time for maximum production derived from the ideal model (see eq III-3, Table III) and δ represents the additional bandwidth due to the kinetic contribution. To calculate it, we shall use the same procedure suggested by Knox and Pyper (*8*), which we have previously employed to investigate the dependence of the apparent column efficiency on the sample size for a pure compound (*11*). The results obtained in this earlier work were in excellent agreement with experimental determinations (*16*).

In order to obtain an estimate of the increase in the cutting time, δ, we assume, as we have explained above, that the profile of the first component tail (arc DE modified by the apparent diffusion due to the finite column efficiency) is essentially controlled by the profile of the second component (arcs GHIJ, modified by apparent diffusion). This means that the cutting time is delayed by the same amount as the rear of the second profile. As we have shown previously (*10*), the rear of the band (arc IJ) is undistinguishable from the profile of a band of pure component 2 with a loading factor, $L_{f,2p}$, representing the amount of component 2 eluted under the part IJ of the profile (Figure 1). Thus, δ is equal to the difference between the real and the thermodynamic bandwidth of a sample of the pure second component equal to $L_{f,2p}$.

Since the thermodynamic and the kinetic contributions to band broadening are assumed to be independent, the width of the real band profile is given by (*8*)

$$W^2_T = W^2_{th} + W^2_{kin} \quad (2)$$

where W_T, W_{th}, and W_{kin} stand for the total or apparent base-line bandwidth and the thermodynamic and the kinetic contributions to the bandwidth, respectively. The ideal model gives the thermodynamic bandwidth (*11*)

$$W_{2,th} = (t_{R,2}^\circ - t_0)(2L_f^{1/2} - L_f) \quad (3)$$

The base-line width of the band obtained with a sample of extremely small size is equal to the kinetic band width contribution

$$W_{2,kin} = 4t_{R,2}^\circ / N_0^{1/2} \quad (4)$$

Combination between eq 2 to 4 gives

$$\delta = W_{2,T} - W_{2,th} = (t_{R,2}^\circ - t_0)w_{2,th}\left(\left(1 + 16\frac{(1 + k'_{0,2})^2}{k'^2_{0,2}N_0 w_{2,th}^2}\right)^{1/2} - 1\right) \quad (5)$$

where $w_{2,th}$ stands for

$$w_{2,th} = \frac{W_{2,th}}{t_{R,2}^\circ - t_0} = 2L_{f,2p}^{1/2} - L_{f,2p} \quad (6a)$$

and $L_{f,2p}$ is given by (*10*)

$$L_{f,2p} = \frac{(1 - 1/\alpha)^2}{(1 + b_1 r_1/b_2)^2} \quad (6b)$$

The cutting time is given by a combination of eq 1, 5, and 6. Combining this new value of the cutting time with eq III-1 and III-2 gives the value of the recovery yield in real (i.e., nonideal, nonlinear) chromatography

$$R_2 = \frac{1}{L_{f,2}(1 + b_1 r_1/b_2)}\left\{1 - \left[\left(\frac{1/\alpha - 1}{1 - x}\right)^2 + \frac{\phi}{\gamma}\right]^{1/2}\right\}^2 \quad (7)$$

where ϕ stands for the ratio $\delta/(t_{R,2}^\circ - t_0)$, and the value of the maximum production rate

$$P_2 = \frac{\epsilon S u}{b_2 + b_1 r_1}\left\{1 - \left[\left(\frac{1/\alpha - 1}{1 - x}\right)^2 + \frac{\phi}{\gamma}\right]^{1/2}\right\}^2 \quad (8)$$

x being derived from the required purity of the collected fraction (eq III-4, Table III). Deriving the optimum conditions for maximum production rate requires finding the values of the parameters that maximize P_2.

V. Optimization Procedure. The optimum loading factor for maximum production is given by eq III-5 (Table III). Using numerical solutions of the semiideal model, we have shown previously (*1*) that the optimum sample size for maximum production rate decreases only marginally when the column efficiency becomes finite, even if it is very small. In practice, the optimum sample size can be considered as independent of the column efficiency. Accordingly, it will remain constant when the flow rate is increased. Of course, the value of the maximum production rate decreases steadily with decreasing column efficiency for columns operated at the same velocity. For a given column, since the efficiency and the cycle time are functions of the flow velocity, the production rate will go through a maximum for a certain value of the flow velocity and the efficiency (see below).

Equation 8 depends on the mobile phase flow velocity both by explicit means and through ϕ and the dependence of the column efficiency on the velocity. For this purpose we have adopted the relationship developed by Knox (*17*), whose validity has been demonstrated by a generation of theoretical and experimental results

$$h = \frac{L}{d_p N_0} = \frac{B}{\nu} + A\nu^{1/3} + C\nu \quad (9)$$

where h and ν are the reduced plate height and mobile phase velocity, respectively (dimensionless numbers). As theory indicates, common sense predicts, and experimental results confirm, the column efficiency has a relatively small influence on the elution profiles of the two components when the sample size is large. Thus, if we start from a mobile phase flow velocity of the order of that corresponding to the maximum column efficiency, the production will first increase rapidly with increasing flow velocity, because the cycle time decreases rapidly. At very large values of the velocity, the column efficiency becomes poor, the amount of the collected fraction of purified component decreases, and both recovery yield and production rate drop. The optimum flow velocity is reached when the two effects compensate each other exactly. This corresponds usually to high values of the reduced velocity.

The linear velocity of the mobile phase is related to the characteristics of the column and to the pressure drop applied between the column inlet and outlet by the classical equation (*18*)

$$u = \frac{k_0 \Delta P d_p^2}{\eta L} \quad (10)$$

where ΔP is the pressure drop, k_0 the specific column permeability (ca. 1×10^{-3}), and η the mobile phase viscosity.

If we assume the mobile phase velocity to be large and the plate height equation (eq 9) to be reduced to $h = Cv$, the column efficiency obtained for a given value of the pressure drop is given by

$$N_0 = \frac{\eta D_m}{k_0 \Delta P C}\left[\frac{L}{d_p^2}\right]^2 \tag{11}$$

Combining eq 5, 8, 10, and 11 permits the derivation of the relationship between the production rate, a function of the mobile phase velocity, through the cycle time and the column efficiency, and the characteristics of the column, length, particle size, pressure drop

$$P_2 = \frac{\epsilon S k_0 \Delta P (d_p^2/L)}{\eta(b_2 + b_1 r_1)}\left[1 - \left\{\left(\frac{1/\alpha - 1}{1 - x}\right)^2 + \frac{w_{2,th}}{\gamma}\left(\left[1 + 16\frac{(1 + k'_{0,2})^2 k_0 \Delta P C (d_p^2/L)^2}{\eta k'^2_{0,2} w^2_{2,th} D_m}\right]^{1/2} - 1\right)\right\}^{1/2}\right]^2 \tag{12}$$

Equation 12 depends explicitly on the pressure drop and on the coefficient of the third term (C) of the plate height equation. This is an approximate equation, valid only at high values of the flow velocity, and especially for columns packed with large size particles, when the plate equation can be reduced to its third term. In many cases, especially with fine particles (below 10 μm), it is not possible to operate the column at values of the reduced velocity for which the second contribution in the rhs of eq 9 is negligible. Then a more complicated equation can be derived, by combining eq 5, 6, 8, and 9. A numerical solution of the system of these equations is much easier to calculate.

VI. Optimization of the Column Design. It is remarkable that the production rate depends on the maximum allowed pressure drop and on the ratio d_p^2/L, but not separately on the particle size and the column length. Between columns having different lengths and packed with packing materials differing only by their size, the choice appears to depend mainly on the economics of column packing. However, the freedom of choice between different designs is more limited than could appear at first glance, because of the square dependence of the column length on the particle size at constant d_p^2/L. For example, at the optimum value of the ratio d_p^2/L, it is possible to combine many different values of column lengths and particle sizes, but if a "reasonable" set of experimental conditions is a 30 cm long column packed with 10-μm particles and we want to use coarse (50 μm) particles, we may have to operate a gigantic column (7.5 m long), and if we need to employ fine particles (e.g., 3 μm), we may end up with a thin disk of a column (1 in. long). In the next section we discuss the dependence of the optimum value of d_p^2/L on the other experimental conditions.

VII. Optimization of the Mobile Phase Flow Velocity. Differentiation of eq 12 with respect to d_p^2/L is possible and leads to a very complex equation. From eq 12, it is obvious, however, that at the low values of d_p^2/L allowed, the production rate increases in proportion to this ratio. There exists, however, a finite value of d_p^2/L for which the production rate is zero (the big square root in eq 12 is equal to 1). Thus, there is an optimum ratio d_p^2/L for which the production rate is maximum.

For a more detailed discussion of the optimization of the mobile phase velocity, taking into account the complete HETP equation (eq 9), we have preferred a graphic presentation (see next section), where plots of the production rate versus d_p^2/L are given.

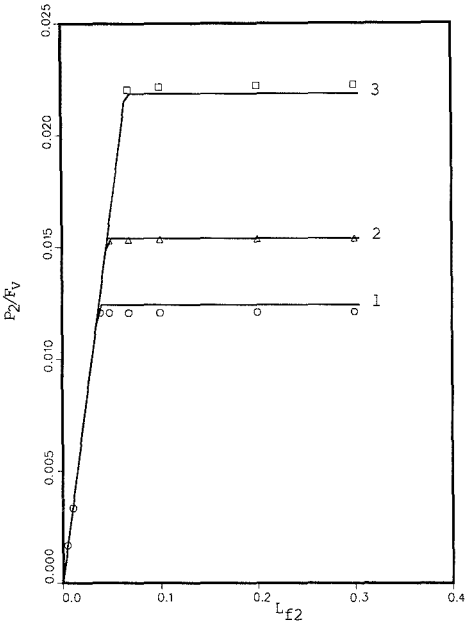

Figure 2. Influence of the sample size on the production rate of a preparative chromatographic column. Plot of the production rate per unit mobile phase flow rate (P_2/F_V) versus the loading factor, $L_{f,2}$. The solid lines are plots derived from eq 5, 6, and 8. The points are determined from elution profiles of the two components obtained by calculating the numerical solutions of the semiideal model in the corresponding conditions. $C_1^\circ = 0.5$ M; $C_2^\circ = 4.5$ M. $t_p = 1$ s. Column: $L = 25$ cm; particle size, 10 μm; efficiency, 5000 theoretical plates. Isotherms: relative retention, $\alpha = 1.2$; $b_1 = 2.5$; $b_2 = 3.0$. Column capacity factor: $k_1'^\circ = 6.0$. Feed composition solute 1/solute 2, 1/9. Purity requirements: 1, 99.5%; 2, 99%; 3, 98%.

RESULTS AND DISCUSSION

I. Influence of the Sample Size (i.e., Loading Factor). Figure 2 shows the variation of the production rate of the second component as a function of the column loading factor for this compound, at different required degrees of purity. The solid lines on this figure are derived from eq 5, 6, and 8, while the points represent individual results determined from elution profiles for the two components calculated numerically, as solutions of the semiideal model (*6*, *12*). The results of the approximate solution derived here from the exact analytical solution of the ideal model and the results of numerical calculations performed with the semiideal model of chromatography are nearly identical. The procedure described in the present paper is more general and simpler, since a pocket calculator is all the help that is needed to carry out the arithmetic and very simple algebraic calculations required. It should be preferred.

As previously reported, the production rate increases linearly with increasing loading factor, until a plateau is reached (*1*). The beginning of this plateau corresponds to a collection time equal to the retention time of the second component of the binary mixture (i.e., to the retention time of the second shock layer). The plateau is reached very abruptly, even when the column efficiency is moderate. Increasing the sample size beyond the linear range of the plot P_2 versus the loading factor results in a decrease of the recovery yield and an increase of

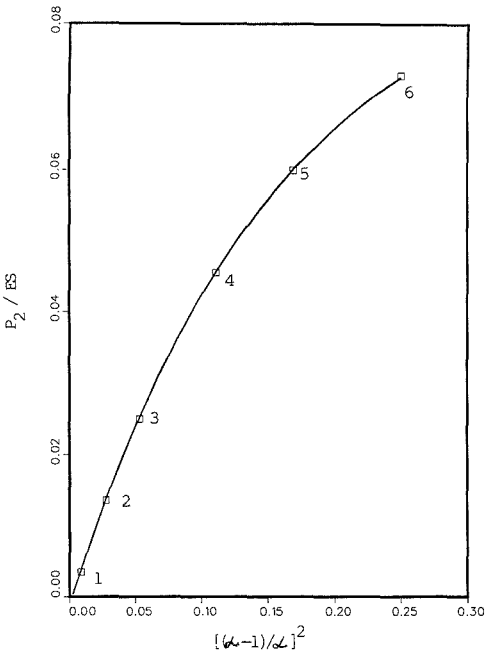

Figure 3. Influence of the selectivity of the phase system on the maximum production rate. Plot of the production rate per unit cross-section area of the column ($P_2/\epsilon S$) versus the ratio $((\alpha - 1)/\alpha)^2$. The points are determined from elution profiles of the two components obtained by calculating the numerical solutions of the semiideal model in the corresponding conditions. The solid lines are derived from eq 5, 6, 8, and 9. Column: L = 20 cm; efficiency, 1370 theoretical plates; reduced velocity, 100. Isotherm coefficients and feed composition as for Figure 2. Purity required: 99%. Values of α: 1, 1.10; 2, 1.20; 3, 1.30; 4, 1.50; 5, 1.70; 6, 2.0.

the amount of material recycled or wasted but no increase in the production rate. It is certainly not economical to exceed this loading. We consider as optimum the experimental conditions corresponding to the onset of the plateau.

We observe that the optimum loading factor is still given by eq III-5 (Table III), and the corresponding sample size by eq II-2a (Table II), although this equation has been derived within the framework of the ideal model, in the case of an infinitely efficient column. As noted previously, the optimum loading factor is nearly independent of the column efficiency (*1*). On the other hand, the required purity of the collected fraction has a very strong influence on the optimum sample size and on the production rate, especially when the concentration of the second component in the feed is large.

II. Influence of the Selectivity of the Phase System. Equation 8 predicts a very rapid increase of the production rate with increasing selectivity of the stationary phase. Figure 3 shows a plot of the production rate versus the ratio $((\alpha - 1)/\alpha)^2$. As for Figure 2, the solid line is a plot derived from eq 5, 6, and 8 while the points correspond to results derived from elution profiles predicted by the numerical solution of the semiideal model for the same binary mixture. There is again an excellent agreement between the results of the two calculations, although the column efficiency used in this case is rather low (1370 theoretical plates). This confirms the validity of the assumptions made in the derivation of eq 8, regarding the influence of the column efficiency on the cutting time and on the production rate.

The production rate increases almost linearly with increasing value of that ratio until values of α equal to approximately 1.3 are reached. Beyond that, the production rate increases less rapidly. It should be emphasized, however, that separations involving compounds having a relative retention exceeding 1.3 are not very difficult.

It should be noted here that the analytical solution of the ideal model on which the previous (*1*) and the present discussions are based assume that the equilibrium isotherms of the two components of the binary mixture investigated are Langmuirian. Thus, these isotherms are "well behaved". They cannot "intersect" each other, for example, except in a vertical plane passing through the vertical (concentration axis), but deviate progressively from each other. Although this type of situation appears to be by far the most frequent, there are other, less frequent, cases where the elution order of the components of a binary mixture is different at high and at low concentrations (*19*). In such cases, the selectivity of the phase system, i.e., the ratio a_2/a_1 of the coefficients of the Langmuir isotherms, is insufficient to characterize the difficulty of the separation and predict the production rate in preparative liquid chromatography.

III. Influence of the Composition of the Feed. Figure 4a shows plots of the production rate per unit cross-section area of the column versus the composition of the feed material (ratio of the concentrations of the two components of the feed, C_2°/C_1°), for different values of the column efficiency. Figure 4b shows the same data, but with the production reported to the unit flow rate. The production rate of the second component decreases with decreasing concentration of the second component, which is expected. The dependence of the production rate on the feed composition (see eq 8) is not simple, however. P_2 depends implicitly on C_1°/C_2° through both the root r_1 of eq II-3 (practically r_1 is equal to C_1°/C_2°) and x (see eq III-4). Figure 4a shows that, for a given column, the production rate increases with decreasing efficiency. This is because a decrease in column efficiency has to be caused by an increase in the mobile phase flow velocity which in the same time decreases the cycle time and increases the production rate. As we show in a further section, there is for each column an optimum flow velocity giving maximum production rate. Figure 4b shows that the production per unit volume of mobile phase used increases slightly with increasing column efficiency.

The solid lines in Figure 4 are calculated by using eq 5, 6, and 8, while the points are derived from elution profiles calculated from numerical solutions of the semiideal model. Although the column efficiency is only 1370 theoretical plates on line 1, Figure 4a, there is an excellent agreement between the two sets of solutions. This is an important proof of the validity of our assumption, since the range of relative concentrations span on this figure is nearly 2 orders of magnitude (from 1/9 to 9/1). This shows that the combination of eq 5, 6, and 8 used to calculate the production rate of the second component is valid, regardless of the composition of the feed.

IV. Influence of the Column Efficiency. The discussion of the effect of the column efficiency is made more complex by the different ways in which we can vary this parameter. We can compare columns packed with particles of different size and operated at the same reduced velocity or columns packed with the same material but with different methods and operated at the same reduced velocity or the same column operated at different reduced velocities. The conclusions drawn from the comparison will differ. From what we have explained above, a meaningful comparison should be based on the production rate obtained at the optimum flow velocity.

Furthermore, we must point out that there is a difference between a highly efficient column and a column delivering highly efficient chromatograms. The latter is a highly efficient

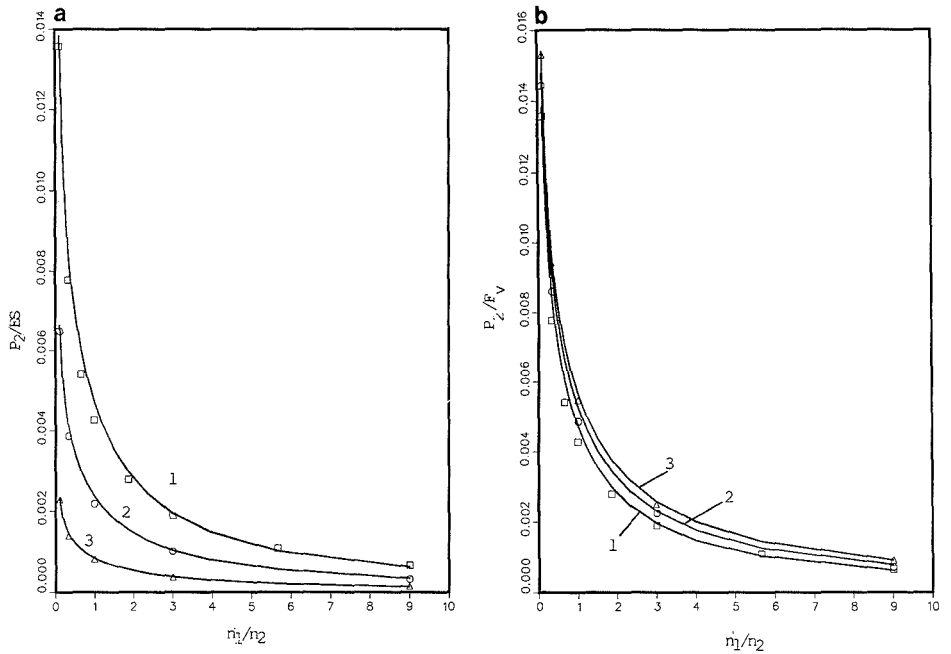

Figure 4. Influence of the feed composition on the maximum production rate. (a) Plot of the production rate per unit cross-section area of the column ($P_2/\epsilon S$) versus the feed composition (ratio C_1°/C_2° or n_1/n_2). The points are determined from elution profiles of the two components obtained by calculating the numerical solutions of the semiideal model in the corresponding conditions. The solid lines are derived from eq 5, 6, 8, and 9. Same experimental conditions as for Figure 3, except variable feed composition and $\alpha = 1.20$. Column efficiency: 1, 1370 theoretical plates, $\nu = 100$; 2, 2500 plates, $\nu = 45$; 3, 5000 plates, $\nu = 15$. (b) Same as Figure 4a, except plot of the production rate per unit volume flow rate of mobile phase.

column operated at or near its maximum efficiency. But a highly efficient column will give bands exhibiting a very low efficiency if it is operated at a very high flow velocity. The essential advantage of highly efficient columns for preparative chromatography is in the very possibility of this trade-off, where efficiency is sacrificed for high flow velocity and very short cycle times. Equation 9 shows that with $B = 2$, $A = 1$, and $C = 0.1$, the plate number of a 30 cm long column packed with 10-μm particles is 12 100 for $\nu = 4$, 2050 for $\nu = 100$, and 960 for $\nu = 250$. Nonetheless, the more efficient column at low flow velocity tends to remain more efficient at high velocities. This topic has been abundantly discussed in the literature on analytical high performance liquid chromatography and needs not be reviewed here. Suffice to say for our purpose that the kinetic of mass transfer in a highly efficient column are fast and that this advantage is conserved whether the column is operated at low or high flow velocity.

Parts a and b of Figure 5 show plots of the production rate (derived from eq 5, 6, and 8) versus the column efficiency, for different values of the required purity, at constant mobile phase velocity. Since the velocity is constant, the only possibility of changing the column efficiency when d_p^2/L is optimum is by changing the packing quality (i.e., A, B, and C in the plate height equation), as shown by eq 10. Parts a and b of Figure 5 illustrate the fact that the column efficiency is an important parameter to consider. In some cases it has a significant influence on the maximum production rate, especially when the selectivity is low and the proportion of the second component in the feed is small (compare parts a and b of Figure 5). These conditions correspond to the extraction of a minor component diluted in a compound having closely related properties, a difficult proposition, which requires an efficient column. In other cases, however (e.g., when α is large), the efficiency has almost no influence on the production rate, at least above some very low threshold (a few hundred theoretical plates). *Even then, highly efficient columns (i.e., columns with small coefficients A and C in eq 9) can be used to great advantage to increase the production rate, provided the high efficiency be traded for very fast elution, by operating at a high mobile phase velocity.* The utmost care should be given to the proper selection of high-quality packing materials, with narrow size distribution and to the development of a suitable packing technology, so values of A of the order of unity can be achieved reproducibly.

However, the selection of the optimum column efficiency is not straightforward, because there is a high price to pay for column efficiency: expensive, narrow size distribution, fine particle material must be selected. The pressure drop of the column becomes high, requiring a pump that can deliver large flow rates under high pressures and thick wall columns made of high resilience metal. Furthermore, the efficiency of any given column depends on the velocity at which it is operated. Increasing the mobile phase flow velocity results in a proportional decrease of the cycle time. It also results in a decrease of the column efficiency. As long as the production per cycle decreases less rapidly than the cycle time, the production rate will increase with increasing flow velocity. Thus, Figure 4a shows three plots of the production rate of a given column versus the relative concentration of the first component of a binary mixture, at three different mobile phase flow velocities. The production rate increases with increasing velocity, i.e., with decreasing efficiency (see Figure 4a). Thus,

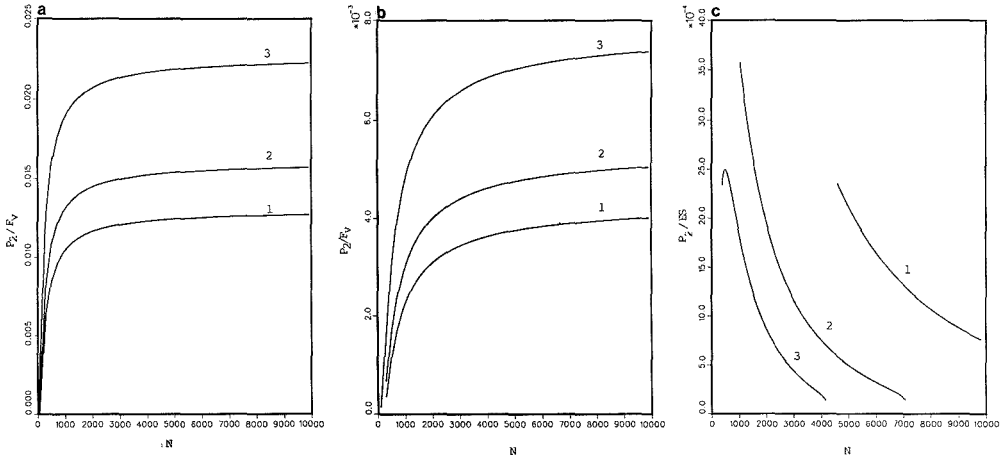

Figure 5. Influence of the column efficiency on the maximum production rate. (a) Plot of the production rate per unit mobile phase flow rate (P_2/F_v) versus the column efficiency. Same experimental conditions as for Figure 2, except variable column efficiency, feed composition 1/9, and $\alpha = 1.20$. Required degree of purity: 1, 99.5%; 2, 99%; 3, 98%. (b) Same as Figure 5a, except $\alpha = 1.10$. (c) Plot of the production rate per unit column cross-section area ($P_2/\epsilon S$) versus the plate number for three different columns, for which the mobile phase velocity varies. All columns, $d_p = 10$ μm. Key: 1, $L = 40$ cm; 2, $L = 17$ cm; 3, $L = 10$ cm. The curves end at the velocity corresponding to $\Delta P = 200$ atm.

highly efficient columns (those that are characterized by small values of both A and C) are interesting in preparative liquid chromatography, not because they give a high number of theoretical plates, but because they can be operated at very high velocities, while still giving a reasonable efficiency. Optimization procedures that concentrate on the variation of the apparent column efficiency with the sample size to conclude that poorly efficient columns are better because "their efficiency remains constant over a larger sample size range" miss the point and remain advertisement ploys (see ref 2, Figure 1.9 and 1.10 and comments thereof).

Finally, Figure 5c compares the performance (plots of production rate versus the column efficiency) of three different columns. The plots are limited at the velocity corresponding to an inlet pressure of 200 atm, considered (arbitrarily) as a practical maximum. The second column, which would be considered as intermediate by an analyst (column 2), performs the best under preparative conditions because its dimensions are such that the ratio d_p^2/L for this column is equal to the optimum for the pressure of 200 atm. Under this pressure, the best column (column 3) cannot be operated at a velocity high enough to achieve the maximum production rate it is capable of giving. With an instrument that could operate at a higher pressure, it would outperform the second column.

In practice, the column efficiency depends on three major parameters, that is when a proper packing technology is available and the column efficiency is proportional to the column length and to the reverse of the average diameter of the packing particles. These parameters are the average particle size, the column length, and the mobile phase flow velocity (or the pressure drop applied to the column). The influence of these parameters is now discussed.

V. Influence of the Maximum Allowed Pressure Drop. Figure 6a shows a plot of the production rate versus the pressure applied to the column inlet for columns having the same value of the ratio d_p^2/L. Line 1 on this figure is derived from eq 12, a simplified equation which assumes that the plate height is given by the third term of the HETP equation ($h \simeq C\nu$). Lines 2 and 3 are calculated by combining eq 5, 6, 8, and 9, the latter being the conventional plate height equation. Lines 2 and 3 correspond to two columns having different lengths and packed with particles of different sizes, but with the same value for the ratio d_p^2/L. When the column inlet pressure is increased, the cycle time decreases and the production rate increases, at first nearly in proportion to the pressure drop (see eq 12). At high flow velocities, however, the efficiency becomes low, the recovery yield drops, and the production rate decreases with increasing pressure drop. Accordingly, there is an optimum column inlet pressure. This optimum value increases slowly with increasing selectivity of the phase system. For the relatively difficult separation selected for Figure 6a ($\alpha = 1.10$) the maximum production rate is achieved for a pressure between 300 and 350 atm. The selection of the optimum pressure, however, must take costs into account, and a value exceeding 200 atm seems improbable. The shapes of the curves on Figure 6a reflect the same underlying phenomenon as those on Figure 5c: there is for each column an optimum velocity for which the maximum production is achieved; since the inlet pressure and the column efficiency are a function of the velocity, there seems to be an optimum inlet pressure and an optimum efficiency for each column.

Equation 12 permits the easy calculation of the production rate corresponding to any value of the column inlet pressure and any value of the ratio d_p^2/L, which characterizes a column. Figure 6b shows plots of the production rate versus d_p^2/L at three different values of the inlet pressure, 200, 500, and 1000 atm, respectively. In each case a maximum is observed showing the existence of an optimum value of the ratio d_p^2/L corresponding to each value of the pressure drop. If we plot the value of the maximum production rate versus the inlet pressure, we obtain the curve on Figure 6c. It is seen that the production rate increases steadily with increasing pressure at which the equipment can operate, provided the optimum column is used (the corresponding value of d_p^2/L is given on the figure; see next section). This is consistent with previous observation that the most efficient columns give also the highest production rate (*4*).

It is important to observe that the conclusions of this work recommend the use of values of the inlet pressure that are rather high by present day standards in preparative liquid chromatography. This points to the probable trend over the next few years, toward the use of rather fine particle packing materials and high-pressure equipment, in order to increase

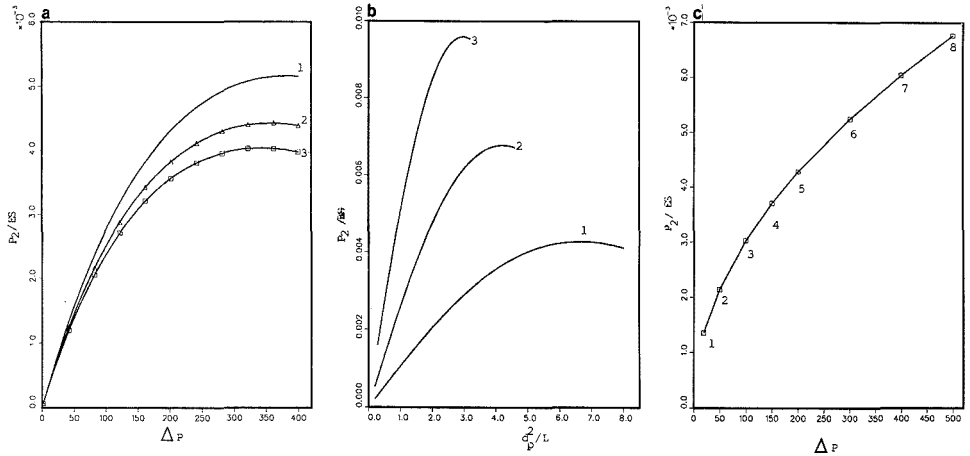

Figure 6. Influence of the column inlet pressure on the production rate. (a) Plot of the production rate per unit column cross-section area ($P_2/\epsilon S$) versus the column inlet pressure: feed composition, 1/9; phase selectivity, $\alpha = 1.10$. Line 1 is derived from eq 12. Line 2 is calculated by using eq 5, 6, 8, and 9, for a 20 cm long column packed with 10-μm particles. Line 3 is calculated as line 2, except for a 80 cm long column, packed with 20-μm particles (same ratio d_p^2/L as for line 2). (b) Plot of the production rate versus the ratio d_p^2/L for three different values of the inlet pressure: 1, $P = 200$ atm; 2, $P = 500$ atm; 3, $P = 1000$ atm. (c) Plot of the maximum production rate which can be achieved with a certain value of the inlet pressure versus the inlet pressure. Corresponding value of the ratio d_p^2/L (in 10^{-8} cm): 1, 21.1 ($P = 20$); 2, 13.1 ($P = 50$); 3, 9.3 ($P = 100$); 4, 7.65 ($P = 150$); 5, 6.65 ($P = 200$); 6, 5.4 ($P = 300$); 7, 4.75 ($P = 400$); 8, 4.25 ($P = 500$).

the production rate of a preparative chromatograph. Lower specifications are understandable only if the decrease in amortization cost of the instrument offsets the cost increase due to the lower production capacity.

Finally, Figure 6a shows that the production rate is nearly independent of the column length and the particle size separately, but depends essentially on the value of the ratio d_p^2/L. The production rate predicted by eq 12 depends only on d_p^2/L, but this equation has been derived with the assumption of a very high flow velocity. In fact it is less accurate for small particles than for large ones, for which it is possible to operate the column under such experimental conditions that the third term of the plate height equation (eq 9) is dominant. If eq 9 is used in combination with eq 5, 6, and 8 to predict the production rate, a slight influence of the column length and the particle size at constant ratio d_p^2/L is observed. The influence of these parameters on the production rate is discussed in the next three sections.

The following calculations have been carried out with the assumption that the maximum pressure allowed is 200 atm, the viscosity of the mobile phase is 1 cP, the specific permeability, k_0, is 1×10^{-3}, and the diffusion coefficient of the components of the mixture studied is 1×10^{-5} cm^2/s.

VI. Optimum Value of d_p^2/L. Equation 12 shows the importance of the ratio d_p^2/L for optimization purposes. The smaller this ratio, the longer the column and the finer the particles used to pack it. Small values of this ratio are thus associated with efficient columns. The natural unit for this ratio is 10^{-8} cm, i.e., we shall express d_p in micrometers and L in centimeters (see Table IV).

Figure 7 shows a plot of the production rate (calculated from eq 12) versus the ratio d_p^2/L of the column used, at constant inlet pressure, for different values of the selectivity ratio, α. For very low values of this ratio, the maximum production rate increases almost linearly with increasing values of d_p^2/L. When the ratio becomes larger, a saturation effect takes place and the production rate tends toward a limit. Table IV lists, for different values of α, the optimum values of the ratio d_p^2/L, the corresponding value of the maximum production rate, the corresponding column efficiency, and the efficiency that would be required under analytical conditions (i.e., in linear chromatography) to achieve a resolution unity between the two bands.

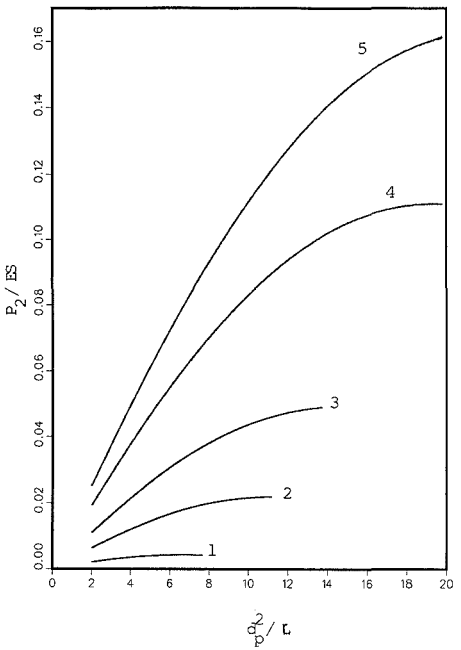

Figure 7. Influence of the ratio d_p^2/L on the maximum production rate, for different values of the phase selectivity. Plot of the production rate per unit column cross-section area ($P_2/\epsilon S$) versus the ratio d_p^2/L. P_2 is derived from eq 12, with $C = 0.1$. Isotherm coefficients and feed composition as for Figure 2. Values of α: 1, 1.10; 2, 1.20; 3, 1.30; 4, 1.50; 5, 1.70.

Table IV. Optimum Value of d_p^2/L, Column Efficiency, and Production Rate[a]

α	d_p^2/L (d_p, μm; L, cm)	production rate, μmol/(cm^2 s)	N_0 (eq 11)	N_a (res)[b]	u,[c] cm/s
1.10	6.54	4.29	1170	2635 (0.72)	1.38
1.20	11.5	21.9	380	784 (0.70)	2.3
1.30	14	49.1	250	409 (0.78)	2.80
1.50	17	109	175	196 (0.94)	3.4
1.70	21.8	163	105	128 (0.9)	4.36

[a] Calculated by using a simplified plate height equation: $h = C\nu$, with the following values of the parameters: inlet pressure, 200 atm; specific permeability, 10^{-3}; solute diffusion coefficients, 1×10^{-5} cm^2/s; mobile phase viscosity, 1 cP; coefficient of the plate height equation, $C = 0.1$; composition of the feed, 1/9; required degree of purity, 99%; parameters of isotherm, $b_1 = 2.5$; $b_2 = \alpha b_1$; $k'_{0,1} = 6$. [b] Efficiency required in linear chromatography to achieve a resolution unity between two bands of equal size, with the same relative retention, and analytical resolution achieved between these bands with an efficiency equal to N_0. [c] Equation 10.

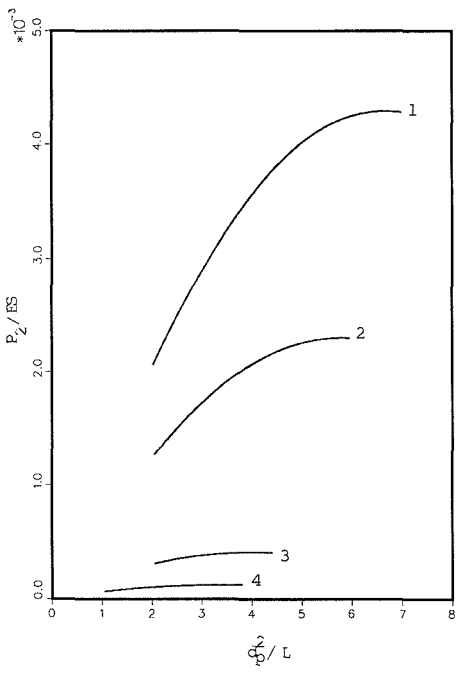

Figure 8. Influence of the ratio d_p^2/L on the maximum production rate, for different feed composition. Plot of the production rate per unit column cross-section area ($P_2/\epsilon S$) versus the ratio d_p^2/L. P_2 is derived from eq 12, with $C = 0.1$. Same experimental conditions as for Figure 7, except $\alpha = 1.1$ and feed composition. Feed composition: 1, 1/9; 2, 1/3; 3, 3/1; 4, 9/1.

The results agree with those derived from a previous empirical study using the semiideal model and a simplex optimization procedure (*15*). The optimum values of the column design parameters correspond to a column that would not give a resolution considered as adequate in quantitative analytical chromatography: the resolution obtained is around unity for easy separations (large α), well below unity for difficult ones (α close to 1). The lower the concentration of the second component, the larger this resolution. This does not mean, however, that the column is not capable of giving a much higher resolution. Far to the contrary, the selection of the optimum conditions corresponding to a certain problem involves the choice of a very high flow velocity, i.e., a compromise in which most of the actual column efficiency is traded for a very fast elution.

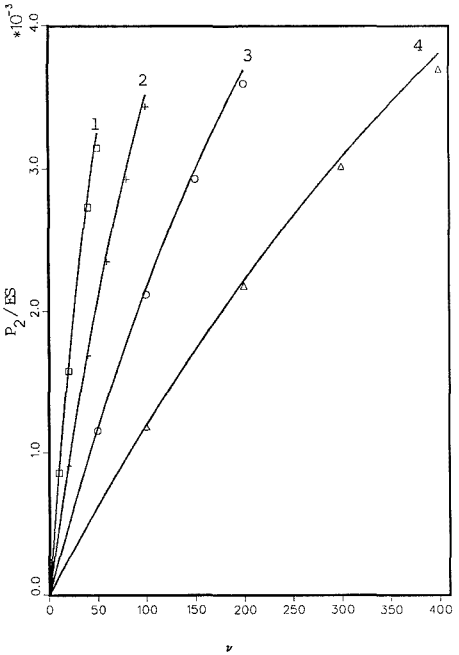

Figure 9. Influence of the ratio d_p^2/L on the maximum production rate. Plot of the production rate per unit column cross-section area ($P_2/\epsilon S$) versus the reduced mobile phase velocity. The points are determined from elution profiles of the two components obtained by calculating the numerical solutions of the semiideal model in the corresponding conditions. The solid lines are derived from eq 5, 6, 8, and 9. Plate equation, eq 9, with $A = 1$, $B = 2$, $C = 0.10$. Isotherm coefficients and feed composition as for Figure 2, except $\alpha = 1.10$ and 1, $d_p = 5$ μm, $L = 5$ cm; 2, $d_p = 10$ μm, $L = 20$ cm; 3, $d_p = 20$ μm, $L = 80$ cm; 4, $d_p = 40$ μm, $L = 320$ cm. The curves end for the velocity corresponding to $\Delta P = 200$ atm.

Figure 8 shows a plot of the production rate (calculated from eq 12) versus the ratio d_p^2/L for a constant value of α (1.10) and different values of the feed composition. The curves have all the same shape, exhibiting a maximum in the production rate for some optimum value of the ratio d_p^2/L. It is important to note, however, that this optimum value of d_p^2/L decreases with decreasing concentration of the second component in the feed. In other words, extracting at the same degree of purity a minor component from a matrix will require a more efficient column than purifying a rather concentrated technical product or a major component (assuming that in both cases we are dealing with the second eluted component of a binary mixture).

In order to confirm the generality of the conclusion that the maximum production rate depends on the ratio d_p^2/L and is almost independent of the column length and the particle size, we have performed the following calculation. Using eq 5, 6, and 8 and a complete plate height equation (eq 9), we have derived the production rate for the second component as a function of the mobile phase flow velocity assuming a feed of constant composition (1/9) on a given chromatographic system ($\alpha = 1.10$). The results are plotted in Figure 9.

Table V. Optimum Particle Size and Production Rate[a]

L, cm	$d_{p,opt}$, μm	N_0	ν	d_p^2/L, 10^{-8} cm	production rate,[b] μmol/(cm² s)	yield, %
5	5.4	900	63	5.83	3.31	53.0
20	11.0	990	133	6.05	3.63	56.1
80	22.4	1030	280	6.27	3.86	57.5
320	45.4	1060	585	6.44	4.01	58.1

[a] Calculated from eq 5, 6, 8, and 9, for different values of the column length, with the following parameters: $A = 1$, $B = 2$, $C = 0.1$ (eq 9). $\alpha = 1.10$, feed composition, 1/9. [b] Equation 12 gives $d_p^2/L = 6.54$, $N_0 = 1170$, and $P_2 = 4.29$ μmol/(cm² s).

Columns of different lengths, packed with particles of different sizes, but with the same value of the ratio d_p^2/L are considered. As for several previous figures, the solid lines are derived from eq 5, 6, 8, and 9 (with $A = 1$, $B = 2$). In order to compare the results of our simplified theory to those derived from the exact numerical calculations, the points on this figure represent the production rate derived from chromatograms generated with the semiideal model (*6*, *12*). The figure shows that the maximum production rate is nearly independent of the combination of column length and particle size used to achieve a certain value of d_p^2/L. The end of each curve corresponds to the highest value allowed for the inlet pressure, 200 atm. The abscissa of the ends of the four curves (i.e., the velocities) differ markedly (from $\nu = 50$ to $\nu = 400$), because of the differences in the particle sizes and lengths of the columns, but the maximum production rates are nearly identical. Accordingly, the simplified eq 12 can be used to derive an approximate optimum of the column design factor, d_p^2/L.

The reason for this agreement is that the optimum conditions correspond to a very high flow velocity, at which the plate height equation can be reduced to its third term, the one that accounts for the contribution of the resistances to radial mass transfer. With the most efficient columns, packed with fine particles, the second term of the plate height equation contributes significantly to the HETP, but its influence on the optimization of the column design remains moderate as long as the column is well packed (see below).

Once the column design factor, d_p^2/L, has been optimized, it is possible to select either the column length or the particle size and adjust the other parameter, or to search for a more satisfactory compromise between them. The mobile phase velocity is given by eq 10.

VII. Optimum Particle Size for Columns of Given Length. We have shown (see section above, Figures 7 and 8 and Table IV), that there is an optimum value for the ratio d_p^2/L, for each separation problem. For example, in the case selected for Table IV (feed composition, 1/9) and for $\alpha = 1.1$, this optimum ratio is 6.54. This corresponds for example to a 20 cm long column packed with 11.5-μm particles. We can select the column length, however, and optimize the particle size; hence the mobile phase velocity and the production rate for a certain value of the pressure drop.

For example, Table V gives the optimum experimental conditions for maximum production rate for four columns of different lengths, between 5 and 320 cm. These conditions have been calculated by using eq 5, 6, 8, and 9. The conditions derived from eq 12 are also given. This table shows that the optimum value of d_p^2/L is nearly constant and close to the value predicted by eq 12. The extent of the separate influence of the column length and particle size is obvious, although it is not very important. The optimum values of the particle size, the column efficiency, the limit resolution between the two components at infinite dilution, and the production rate increase slowly with increasing column length. The prediction of eq 12 is seen to be in good agreement with these results.

Table VI. Optimum Column Length and Production Rate[a]

d_p, μm	L_{opt}, cm	N_0	ν	d_p^2/L, 10^{-8} cm	production rate,[b] μmol/(cm² s)	yield, %
5	4.5	960	55	5.56	3.28	55.1
10	17.0	1020	118	5.9	3.6	56.5
20	65.5	1070	244	6.1	3.83	58.5
40	250.5	1060	511	6.39	3.99	58.3

[a] Calculated from eq 5, 6, 8, and 9, for different values of the particle size, with the following parameters: $A = 1$, $B = 2$, $C = 0.1$ (eq 9); $\alpha = 1.10$, feed composition 1/9. [b] Equation 12 gives $d_p^2/L = 6.54$, $N_0 = 1170$, and $P_2 = 4.29$ μmol/(cm² s).

Table VII. Optimum Column Length and Production Rate[a]

d_p, μm	L_{opt}, cm	N_0	ν	d_p^2/L, 10^{-8} cm	production rate,[b] μmol/(cm² s)	yield, %
5	2.5	340	100	10.0	18.1	56.5
10	9.5	350	210	10.42	19.4	57.5
20	36.4	355	439	10.98	20.3	57.5
40	145	370	882	11	20.9	59

[a] Same as Table VI, except $\alpha = 1.20$. [b] Equation 12 gives $d_p^2/L = 11.5$, $N_0 = 380$, and $P_2 = 21.9$ μmol/(cm² s).

Table VIII. Optimum Column Length and Production Rate[a]

d_p, μm	L_{opt}, cm	N_0	ν	d_p^2/L, 10^{-8} cm	production rate,[b] μmol/(cm² s)	yield, %
5	1.25	100	200	20.0	144	57.4
10	5	110	400	20.1	150	60.5
20	20	110	800	20.1	154	61.1
40	78	110	1650	20.5	157	61.1

[a] Same as Table VI, except, $\alpha = 1.70$. [b] Equation 12 gives $d_p^2/L = 21.8$, $N_0 = 105$, and $P_2 = 163$ μmol/(cm² s).

VIII. Optimum Column Length for Columns Packed with Particles of Given Size. If we have to pack the column with a certain packing material available in only one particle size grade, we can optimize the column length, following a similar procedure, from the approximate figures given in Table IV (using eq 12) or using the general equations 5, 6, 8, and 9. Table VI summarizes the optimum conditions for four columns packed with particles of different sizes, from 5 to 40 μm in diameter. The production rate is derived from eq 5, 6, 8, and 9 and the recovery yield from eq 7.

As we see in this table, the value of the ratio d_p^2/L is nearly constant and close to the value predicted by the use of a simplified plate height equation and eq 12. Similar data are shown in Tables VII ($\alpha = 1.20$) and VIII ($\alpha = 1.70$). The trends in each table are the same as that in Table VI; the value of the product d_p^2/L is nearly constant but increases very slowly with increasing particle size, as does the production rate. Comparison between the data in Tables VI to VIII shows that when the separation becomes less and less difficult, the optimum column length and the required efficiency for packing material with a certain particle size decrease, while the mobile phase velocity and the production rate increase.

Figure 10 shows a plot of the production rate for the second component of a pair, versus the reduced mobile phase velocity for columns of different lengths, all packed with 10-μm particles. The selectivity of the chromatographic system is such that $\alpha = 1.20$. Each curve ends up at the velocity which requires an inlet pressure equal to 200 atm. The optimum value of d_p^2/L is 11.5 (Table IV), corresponding to an optimum column length of 9 cm with these particles (see Table VII).

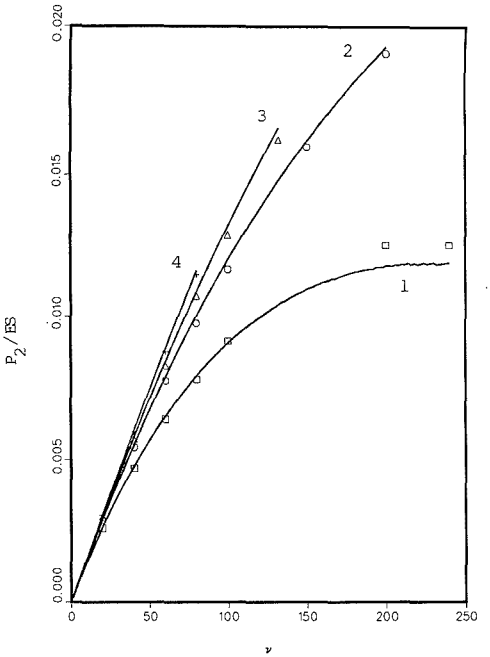

Figure 10. Influence of the column length on the production rate. Plot of the production rate per unit column cross section area ($P_2/\epsilon S$) versus the reduced mobile phase velocity. Points derived from numerical solutions of the semiideal model. Solid lines calculated from eq 5, 8, and 9. Same data as Figure 9, except α = 1.20, d_p = 10 μm. Column length: 1, 5 cm; 2, 10 cm; 3, 15 cm; 4, 25 cm.

The curves on the figure are derived from eq 5, 6, 8, and 9, while the points are derived from numerical solutions of the semiideal model. The results of both calculations are in excellent agreement and Figure 10 shows the optimum column length to be approximately 10 cm, in agreement with the prediction of the models.

In conclusion, the optimum column design is determined by the maximum pressure available, at which the preparative chromatograph can be used. This determines an optimum value for the ratio d_p^2/L, from which d_p and L can be determined, with some flexibility regarding the choice of one or the other. Long columns may be used with coarse particles and large sample sizes, with a rather long cycle time, or conversely, fine particles may be preferred, with a short column, small sample sizes injected at a higher frequency. But the only practical way to increase the production rate with a given feed and phase system is by raising the inlet pressure.

IX. Influence of the Coefficients of the HETP Equation. The first coefficient of the HETP equation accounts for the influence of axial dispersion. Since we have shown that preparative HPLC columns must be run at high flow velocities, its influence is negligible and does not deserve much attention.

The second coefficient accounts for the lack of homogeneity of the packing. It has been repeatedly reported by practitioners that present packing technology permits the preparation of columns with efficiencies comparable to that of analytical columns (*20*). The second coefficient of the HETP equation is usually between 1 and 2 (*21*). With such a narrow range of variation, there is little possibility for a serious influence on the production rate. We have carried out calculations similar to those whose results are reported in Table VI, but using a value of A = 2 instead of 1 in the plate height equation (eq 9). The results are reported in Table IX. The optimum column length is somewhat longer, the optimum values of the reduced velocity and ratio d_p^2/L somewhat lower than those reported in Table VI. The production rate is also lower but by less than 20%. The influence of the packing quality of the column is more important with fine particles than with coarse ones, because the former are operated at much lower reduced velocities than the latter; hence the relative importance of the second term of eq 9 is larger.

Table IX. Optimum Column Length and Production Rate[a]

d_p, μm	L_{opt}, cm	N_0	ν	d_p^2/L, 10^{-8} cm	production rate,[b] μmol/(cm^2 s)	yield, %
5	5.4	920	46	4.63	2.66	53.7
10	19.0	960	105	5.23	3.1	55.1
20	70.0	1000	228	5.72	3.46	56.5
40	265	1040	483	6.03	3.73	57.6

[a] Same as Table VI, except A = 2. [b] Equation 12 gives d_p^2/L = 6.54, N_0 = 1170, and P_2 = 4.29 μmol/(cm^2 s).

Table X. Optimum Column Length and Production Rate[a]

d_p, μm	L_{opt}, cm	N_0	ν	d_p^2/L, 10^{-8} cm	production rate,[b] μmol/(cm^2 s)	yield, %
5	3	880	100	8.33	4.65	52.2
10	10.7	950	210	9.34	5.49	55
20	39	1000	440	10.25	6.18	56.2
40	145	1020	882	11	6.71	56.6

[a] Same as Table VI, except C = 0.03. [b] Equation 12 gives d_p^2/L = 12.0, N_0 = 1140, and P_2 = 7.83 μmol/(cm^2 s).

The third coefficient accounts for the resistance to mass transfer inside the particles. It is a lump coefficient, for which different interpretations have been given (*22*, *23*) and which is usually difficult to measure accurately because the corresponding contribution becomes significant only at high values of the reduced velocities (*24*). Typical values reported in the literature range between 0.02 and 0.2. All the previous results reported above have been derived by using the same value of 0.1 for C as was used by Knox and Pyper (*8*). Results derived with C = 0.03 are reported in Table X. As expected, since the columns are operated at large flow velocity, decreasing the value of C results in (i) a larger optimum flow velocity, (ii) a larger optimum value of d_p^2/L, (iii) a shorter optimum column length at constant particle size, (iv) a larger value of the maximum production rate, and (v) larger deviations between the predictions of the combination of eq 5, 6, 8, and 9 and those derived from the simplified HETP equation (eq 12), especially for small particle sizes.

IX. Influence of the Feed Composition on the Production Rate. Table XI summarizes the optimum values of the ratio d_p^2/L for the separation of mixtures of various compositions of two components, on a phase system on which the selectivity is 1.20. We have also calculated the optimum length of columns packed with 10-μm particles, the limit efficiency of these columns at the optimum flow velocity (for a very dilute sample), the production rate, and the recovery yield. The larger the concentration of the second component, the easier and the faster the separation is performed. When the concentration of the second component is raised from 10% to 90%, the column required is twice as short, the flow velocity is faster, so the limit efficiency of the column is three times lower, and the production rate of the second component is 30 times larger. Also, since the relative contribution of the third term of the HETP equation is smaller at low flow velocity, the error made by neglecting the first two terms is larger

Table XI. Optimum Column Length and Production Rate[a]

feed compos	L_{opt}, cm	N_0	ν	d_p^2/L, 10^{-8} cm	production rate,[b] μmol/(cm² s)	yield, %
1/9	9.5	350	210	10.42	19.4	57.5
1/3	10.9	460	183	9.17	10.9	58.1
1/1	12.6	600	158	7.93	5.51	57.2
3/1	14.6	780	137	6.85	2.07	51.9
9/1	17.2	1050	116	5.81	0.63	47.7

[a] Same as Table VI, except, α = 1.20, particle size 10 μm and feed composition variable. [b] Equation 12 (with $h = 0.1\nu$) gives:

feed composit	d_p^2/L, (10^{-8} cm)	N_0	P_2, μmol/(cm² s)
1/9	11.5	380	21.9
1/3	10.1	490	12.4
1/1	8.9	630	6.38
3/1	7.4	910	2.44
9/1	6.5	1200	0.75

at small concentrations of the second component.

Figure 11 shows a plot of the production rate versus the reduced velocity at constant system selectivity (α = 1.20), but for different values of the relative composition of the mixture. As before, the solid lines are derived from eq 5, 8, and 9, while the points result from numerical calculations made by using the semiideal model. There is an excellent agreement between the solid lines and the corresponding points. This figure illustrates to which extent the production rate depends on the composition of the feed. It is in agreement with results described earlier in this paper.

X. Influence of the Isotherm Parameters. The influence of the phase selectivity, $\alpha = a_1/a_2$, has been discussed in a previous section. We are concerned here by the other coefficients of the isotherm, the absolute value of a_2, which determines the retention time of the second component and, hence, the cycle time and the coefficients b_1 and b_2, which characterize the curvature of the isotherm at the origin and the column saturation capacity (equal to a_1/b_1 and a_2/b_2 for the first and second components, respectively).

As can be seen from eq 8 or 12, decreasing the values of the second coefficients, i.e., increasing the column saturation capacity, results in an increase of the production rate. Equation 12 also shows that the production rate decreases with increasing value of the ratio $(1 + k'_{0,2})/k'_{0,2}$. Therefore it is attractive to use experimental conditions under which the absolute retention of the two components, i.e., the limit capacity factor of the second component $k'_{0,2}$ at infinite dilution, is relatively large. Calculations show, however, that beyond a value of $k'_{0,2}$ close to 3, the increase of the production rate is marginal.

XI. Comparison with the Results Derived by Pyper and Knox. In a classical paper (*8*), Knox and Pyper have derived an equation for the optimization of experimental conditions in liquid chromatography. They used an equilibrium model with a correction for the finite column efficiency which is similar to the one used here, but they ignored the interactions between the two components of the mixture and carried out the calculations on the assumption that the fractions prepared must be pure and that the recovery yield must be unity; hence the bands of the two compounds are exactly resolved at column inlet. An interesting conclusion of their work, in agreement with the present results, is the existence of an optimum value for the ratio d_p^2/L.

As we have shown, however, accepting the production of a partly purified fraction, with a small residual amount of the other component of the mixture (ca 1%), permits a considerable increase in the production rate (*1*). This is also illustrated by Figure 2. Most of the difference between the conclusions of this work and those derived by Knox and Pyper stems out from their assumption that the migration of the two component bands proceeds independently. As a result the displacement of the first component by the second one is ignored as is neglected the tag-along effect of the second component. The optimum value of the ratio d_p^2/L and the maximum production rate predicted by Knox and Pyper are much smaller than those resulting from eq 12 or from the combination of eq 5, 6, 8, and 9.

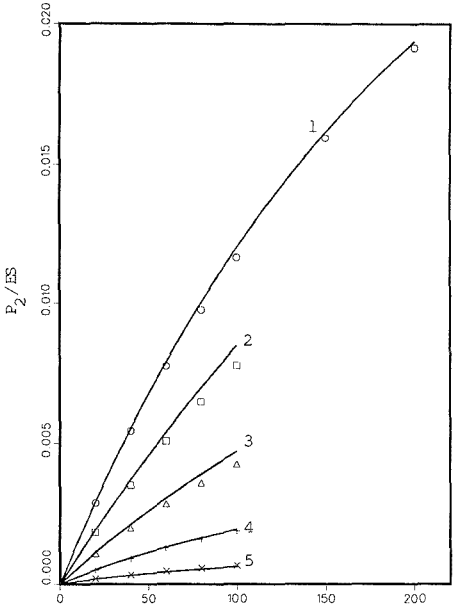

Figure 11. Influence of the feed composition on the production rate. Plot of the production rate per unit column cross-section area ($P_2/\epsilon S$) versus the reduced mobile phase velocity. Same as for Figure 10, except α = 1.20, column length and feed composition as follows: 1, L = 10 cm, feed composition 1/9; 2, L = 10 cm, feed 1/3; 3, L = 10 cm, feed 1/1; 4, L = 10 cm, feed 3/1; 5, L = 20 cm, feed 9/1.

For example, under the same set of experimental conditions as for Table XI, with the same definition of the cycle time and with the same simplified plate height equation (i.e., $h = 0.1\nu$), the optimum value of d_p^2/L derived from the results of Knox and Pyper is 4.61×10^{-8} cm and the optimum production rate is 1.19 μmol/(cm² s), values that are independent of the feed composition. On the other hand, we predict a strong dependence of the production rate on the composition of the mixture. Our equations give optimum values of d_p^2/L which are between 6.5 and 11.5×10^{-8} cm and a production rate between 0.75 and 21.9 μmol/(cm² s), for compositions between 9/1 and 1/9, respectively. The difference is extremely large, especially at large concentration of the second component, because the displacement effect of the second component on the first one has been neglected in their approach. Our method permits the determination of optimum conditions for the production of fractions at any degree of purity or with a recovery yield exceeding the value corresponding to the maximum production rate, if needed.

GLOSSARY

A	second parameter of the HETP equation (eq 9)
A_i	amount of component i found in the part of zone 2 which is rejected

a_i coefficient in the Langmuir isotherm (eq II-1a and II-1b)
B first parameter of the HETP equation (eq 9)
B_i amount of component i which is collected with the other component and reduces its purity
b_i coefficient in the Langmuir isotherm (eq II-1a and II-1b)
C third parameter of the HETP equation (eq 9)
C_i concentration of component i in the mobile phase
$C_1°$, $C_2°$ concentrations of the two components in the sample pulse
d_p average particle size of the packing material
F_v volume flow rate of mobile phase
h reduced plate height of the column at infinite dilution
k_0 specific column permeability
$k_2'°$ column capacity factor at infinite dilution for the second component
L column length
L_f loading factor corresponding to the mixed zone (eq II-2c)
$L_{f,i}$ loading factor for the component i, ratio between the sample size and the column saturation capacity for this compound
$L_{f,2p}$ equivalent loading factor for the second band tail, defined by eq 6b
N_0 number of theoretical plates of the column at infinite dilution
n_1, n_2 amounts of the two components in the sample pulse
P_2 production rate of component 2
Pu_2 purity of component 2
Q_i amount of component i adsorbed at equilibrium with the concentrations C_1 and C_2 of the first and second components in the mobile phase
R_2 recovery yield for component 2
r_1 positive root of eq II-3
S column cross-section area
t_A retention time of the shock of the first component
t_E end of the first component elution profile
t_F retention time of the maximum concentration of the elution band of the second component
t_I end of the elution of the plateau of the second component
t_J end of the chromatogram
$t_{R,i}°$ retention time of component i at infinite dilution (i.e., limit at zero sample size)
t_c cycle time
$t_{c,2}$ second cutting time, when the fraction containing the purified component 2 begins to be collected
t_0 retention time of an unretained compound (dead time)
t_p width of the injected band (in time unit)
u average linear velocity of the mobile phase
x parameter related to the required degree of purity (eq III-4)
W_T overall bandwidth
W_{kin} contribution of the kinetics of radial mass transfer and of the axial diffusion to the bandwidth
W_{th} contribution of thermodynamics (i.e., nonlinear equilibrium isotherm) to the bandwidth
w_{th} $W_{th}/(t_{R,2}° - t_0)$
α selectivity, i.e. ratio $k_2'°/k_1'° = a_2/a_1$
γ ratio $(\alpha b_1 r_1 + b_2)/(b_1 r_1 + b_2)$, used to simplify the writing of equations
ΔP pressure drop of the mobile phase in the column
δ additional bandwidth due to the kinetic contribution
ϵ volume void fraction of the column
ϕ $\delta/(t_{R,2}° - t_0)$
η viscosity of the mobile phase
ν reduced mobile phase velocity

LITERATURE CITED

(1) Golshan-Shirazi, S.; Guiochon, G. *Anal. Chem.* **1989**, *61*, 1276.
(2) Bidlingmeyer, B. A.; McDonald, P. D. In *Preparative Liquid Chromatography*; Bidlingmeyer, B. A., Ed.; Elsevier: Amsterdam, 1987; p 1.
(3) Roz, B.; Bonmati, R.; Hagenbach, G.; Valentin, P.; Guiochon, G. *J. Chromatogr. Sci.* **1976**, *14*, 367.
(4) Newburger, J.; Liebes, L.; Colin, H.; Guiochon, G. *Sep. Sci.* **1987**, *22*, 1933.
(5) Eble, J. E.; Grob, R. L.; Antle, P. E.; Snyder, L. R. *J. Chromatogr.* **1987**, *405*, 1.
(6) Guiochon, G.; Ghodbane, S. *J. Phys. Chem.* **1988**, *92*, 3682.
(7) Lin, B.; Golshan-Shirazi, S.; Ma, Z.; Guiochon, G. *Anal. Chem.* **1988**, *60*, 2647.
(8) Knox, J. H.; Pyper, M. *J. Chromatogr.* **1986**, *363*, 1.
(9) Katti, A.; Guiochon, G. *Anal.* Chem. **1989**, *61*, 982.
(10) Golshan-Shirazi, S.; Guiochon, G. *J. Phys. Chem.*, in press.
(11) Golshan-Shirazi, S.; Guiochon, G. *Anal. Chem.* **1988**, *60*, 2364.
(12) Guiochon, G.; Golshan-Shirazi, S.; Jaulmes, A. *Anal. Chem.* **1988**, *60*, 1856.
(13) Golshan-Shirazi, S.; Ghodbane, S.; Guiochon, G. *Anal. Chem.* **1988**, *60*, 2630.
(14) Golshan-Shirazi, S.; Guiochon, G. *Anal. Chem.* **1988**, *60*, 2634.
(15) Ghodbane, S.; Guiochon, G. *Chromatographia* **1989**, *26*, 53.
(16) Golshan-Shirazi, S.; Guiochon, G. *Anal. Chem.* **1989**, *61*, 462.
(17) Knox, J. H. *J. Chromatogr. Sci.* **1977**, *15*, 352.
(18) Martin, M.; Eon, C.; Guiochon, G. *J. Chromatogr.* **1974**, *99*, 357.
(19) Huang, J. X.; Guiochon, G. *J. Colloid Interface Sci.* **1989**, 128, 577.
(20) Guiochon, G.; Katti, A. *Chromatographia* **1987**, *24*, 165.
(21) Colin, H. *Sep. Sci. Technol.* **1987**, *22*, 1834.
(22) Huber, J. F. K. *Ber. Bunsen-Ges. Phys. Chem.* **1973**, *77*, 179.
(23) Horvath, C.; Lin, H. J. *J. Chromatogr.* **1978**, *149*, 43.
(24) Colin, H.; Czaychowska, T.; Miedziak, I.; Guiochon, G. *J. Chromatogr.* **1978**, *167*, 41.

RECEIVED for review December 28, 1988. Accepted March 13, 1989.

Direct Current Conductivity Detection in Ion Chromatography

Dayong Qi,[1] Tetsuo Okada,[2] and Purnendu K. Dasgupta*

Department of Chemistry and Biochemistry, Texas Tech University, Lubbock, Texas 79409-1061

Monitoring the current due to a dc potential applied across two narrow gauge hypodermic needles inserted inside a poly(tetrafluoroethylene) tube provides an inexpensive, low-volume, sensitive detector for ion chromatography (IC). With low background conductance IC systems, detection limits comparable to commercial detectors are attained. Effective cell volumes as low as 50 nL are easily obtained. An applied voltage of 6 V is routinely used without major noise problems from excessive gas evolution or base-line drifts due to electrode polarization. The flow direction, relative to the electric field, affects the response; this effect is dependent on the nature of the electrolyte flowing through the cell. The fundamental behavior of these systems is discussed along with reproducibility and calibration characteristics. Relative noise levels are reported for several other cell geometries.

Ionic solutes are unique in their effect on the electrical conductivity of a solution. A conductivity detector was therefore the one of choice in the pioneering work (*1*) on ion chromatography (IC) and remains to date the most widely used in both suppressed and single column IC (SCIC).

Classically, solution electrical conductivity is measured with an alternating potential (tens to thousands of hertz) and many commercial detectors based on this principle are in wide use. In the more recently introduced bipolar pulse technique (*2*), square-wave bipolar pulses are applied; the conductance is measured without significant capacitance effects by selective periodic sampling of the current. Applications of the bipolar pulse (BP) technique have been described (*3–5*); commercial detectors are available. For measuring low resistance, a four-electrode method is often considered the best approach. Solution electrical conductivity may also be measured this way (*6*) and the design has been incorporated in commercial detectors.

Like many other flow-through detectors used in liquid chromatography (LC), the flow-through conductivity detector has evolved from its static counterpart used with a quiescent fluid. Application of a dc potential with a static solution is problematic due to polarization and, at high enough potentials, the liberation of gases. It has been axiomatic that "... if the measurement of the electrical properties of ionic solutions is to be used effectively in a LC detecting system, AC potentials must be applied to any electrode configuration employed" (*7*). The obstacles to dc measurement of conductance are, however, largely absent in flow-through cells of the simplest geometry, e.g., liquid flowing at high velocity through two tubular electrodes. Continuous flow reduces concentration polarization and at small enough currents, liberated electrolytic products are dissolved and swept away before bubbles are formed and significantly alter the effective electrode surface area.

An amperometric detector placed after the suppressor in an IC system reportedly detects not only electrochemically active analytes but also inactive ions such as sulfate; the detection limits are said to be better than those obtained by conductimetry (*8, 9*). With a highly resistive background as in suppressed IC, the "set" electrode potential is likely not actually attained; the amperometric detector in this case may be behaving as a dc conductance monitor. A Czech study has also reported dc conductometry with wire electrodes (up to 30 V) in a tubular cell (*10*). The mechanism of this detection has not been explored. Approximate calculations suggest that the double-layer charging current is far too small to account for the observed response. Although the absolute potential of each electrode is not known, at the relatively high applied voltage used, both the cathode and anode must be at sufficiently high potentials for the respective reductive and oxidative breakdown of water. Further, the potentials are high enough to be located in the steeply rising portion of the $i-V$ response curve such that the resistance of the intervening solution merely serves to control the difference in electrode potential by governing the iR drop in the bulk solution (W. R. Heineman, University of Cincinnati, personal communication, 1987).

This paper reports the design and utilization of a flow-through two-electrode detector with an applied dc potential. The phrase "dc conductance" is used herein to describe the proportionality between observed current and applied voltage and is not synonymous with the ionic conductance of the solution measured by conventional ac methods.

EXPERIMENTAL SECTION

The experimental cell (Figure 1a) consists of two 27-gauge Pt hypodermic needles (point style no. 4, P/N 21127, Hamilton Co., Reno, NV) forcibly inserted into a small (~15 mm) segment of a 300 μm i.d., 1.5 mm o.d., PTFE tubing. Unless otherwise mentioned, the pointed ends faced each other in the manner shown. The pointed end has a curved profile and the interelectrode distance is not constant. The interelectrode distance cited is the distance between the entrance electrode tip and the nearest point on the exit electrode, as measured with a reticle-equipped microscope. Unless otherwise stated, this distance was 600 μm, resulting in a measurement volume of ~50 nL and a cell constant of ~11 cm^{-1}. A battery of alkaline C cells supplied 1.5–10.7 V; unless otherwise stated, the applied voltage was 6 V. The resulting current was measured with a current amplifier (Model 427, Keithley Instruments, Cleveland, OH) or a simple operational amplifier circuit (Figure 1b, parts cost under $30).

A prototype Model 4000i (Dionex Corp., Sunnyvale, CA) ion chromatograph with a 50-μL loop was used for all experiments. In many cases, a nonchromatographic (flow-injection) mode was used. The dc conductance cell was serially connected after the Dionex conductivity detector (CDM-I, a BP detector) with a short segment of narrow bore tubing. For suppressor experiments, an Anion Micro Membrane Suppressor (AMMS, Dionex) was used.

Water used was distilled and deionized and protected from the intrusion of CO_2. All reagents were of analytical reagent grade.

RESULTS AND DISCUSSION

Cell Dimensions and Applied Voltage. For applied voltages above ~3 V, the $i-V$ relationship was linear (correlation coefficient, $r > 0.999$) either for the background current (water carrier) or for the peak currents above the background elicited by injections of dilute HCl or H_2SO_4. Below 3 V, the current was less than that predicted from the linear $i-V$ relationship. The linearly extrapolated voltage intercept is ~2

[1] Permanent address: Research Center for Eco-Environmental Sciences, Academia Sinica, P.O. Box 934, Beijing, People's Republic of China.

[2] Permanent address: Faculty of Liberal Arts, Shizuoka University, 836 Ohya, Shizuoka 422, Japan.

0003-2700/89/0361-1383$01.50/0

Table I. Current Flowing through NaCl and HCl Solutions as a Function of Electrode Polarity and Flow Rate[a]

flow rate, mL/min	NaCl[b]			HCl[c]			ratio, HCl/NaCl	
	inlet positive	outlet positive	ratio[d]	inlet positive	outlet positive	ratio[d]	inlet positive	outlet positive
1.0	0.372	0.385	0.966	0.596	0.553	1.078	1.60	1.44
0.5	0.382	0.391	0.977	0.580	0.542	1.070	1.52	1.39
0.2	0.396	0.397	0.997	0.550	0.516	1.066	1.39	1.30
0.1	0.408	0.405	1.007	0.530	0.507	1.045	1.30	1.25

[a] In μA, 6 V dc applied. [b] 50 μM. [c] 25 μM. [d] Ratio of preceding two columns, inlet positive/outlet positive.

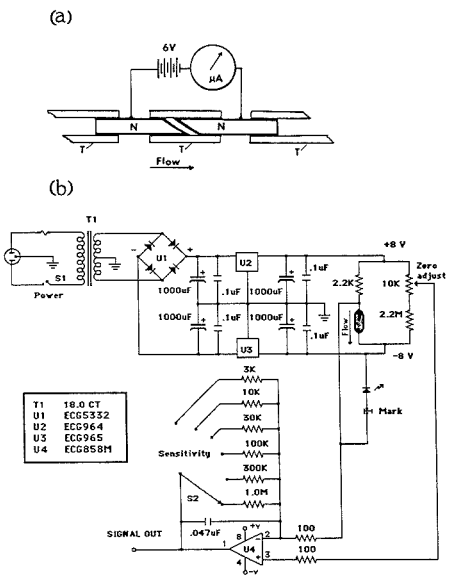

Figure 1. Basic experimental setup: (a) details of needle cell, 27-gauge needles (N) inserted in 0.3 mm i.d. PTFE tubes (T); (b) circuitry of simple operational amplifier based detector.

V, attesting to the electrolytic nature of the current.

With blunt needles, the observed current was inversely related to the interelectrode distance (0.5–4.5 mm, $r > 0.999$, intercept ~0). With cells made from different size (23, 25, 26, and 27 gauge) blunt end stainless steel needles, all with 1-mm interelectrode separation, the observed current was directly proportional to the terminal electrode area $r > 0.998$, intercept ~0).

All observations above were true regardless of the polarity of the applied voltage.

Polarity of Applied Voltage and Flow Rate. In the present system, the electric field may be parallel or opposed to the flow direction. The polarity consistently and reproducibly affects the results. In suppressed anion chromatography, analytes emerge as the corresponding acids atop a neutral to slightly acidic background. Both background current and analyte response in such a system were found to be higher with the inlet electrode positive. For example, for injections of 50 μM HCl, H_2SO_4, or n-$C_6H_{13}SO_3H$ into a water carrier (1 mL/min, interelectrode separations 1.8–3.5 mm), the peak height ratio (inlet positive/outlet positive) ranged from 1.01 to 1.37. In all cases the effect of polarity decreased with decreasing electrode separation.

The inlet electrode negative polarity resulted in a higher current also for continuous flow of acid solutions through the cell. Results of such experiments are shown in Table I for NaCl and HCl solutions (different concentrations chosen to obtain approximately the same current) as a function of electrode polarity and flow rate. The electrode polarity effect decreases with decreasing flow rate for both electrolytes and the inlet positive/outlet positive ratio approaches unity. The observed ratio of >1 for NaCl at the lowest flow rate is likely due to the conductance of the electrolytic products, NaOH and HCl, which are more conductive than NaCl. The increase in current due to electrolytically generated H^+, the highest mobility carrier, is likely favored with the inlet electrode positive, such that this anodically generated ion can be convected to the cathode. Even in this case this effect is likely small; a current of 0.4 μA can at most anodically generate 2.5 μM H^+ at a flow rate of 0.1 mL/min. Note that the flow velocity (1 mL/min ≃ 25 cm/s for 0.3 mm i.d.) is much higher than the electrical mobility (~3.6 mm/s at 100 V/cm for H^+) in these experiments. Interestingly, the inlet positive/outlet positive current ratio is greater than unity for HCl but less than unity for NaCl and even less for NaOH solutions (0.928 at 1 mL/min).

The above observation is understandable in the following framework: (a) the geometry of the cell leads to a smaller diffusion layer (DL) at the exit, compared to the entrance, electrode; (b) the DL is smaller at higher flow velocities, (c) the disruption of the DL is less with decreasing electrode separation, at small separations the radial sheath layers in the vicinity of the electrodes stagnate, and (d) the primary electrode processes are electrolytic breakdown of water and/or the reduction of H^+/oxidation of OH^-. With a strong acid, the cathodic process is reduction of H^+ and the anodic process is oxidation of water. With a strong base, the cathodic process is reduction of water and the anodic process is oxidation of OH^-. With a neutral solution, electrolytic breakdown of water occurs at both electrodes; H^+ and OH^- are respectively generated. With strong acids or bases, the current thus increases if convective transport of H^+/OH^- to the negative/positive electrodes are respectively promoted. With neutral salts, the polarity effect is much lower and similar in trend for $NaClO_4$, Na_2SO_4, $NaIO_3$, etc., i.e., regardless of the relative cation/anion mobility. The polarity effect with salts probably originates from the differences in transport of electrogenerated H^+ or OH^- to the inlet electrode. If the electrogenerated ion transported against the flow field is H^+ (inlet electrode negative) rather than OH^- (inlet electrode positive), higher currents result due to the greater mobility of H^+.

Comparison with Conventionally Measured Conductance. The last two columns of Table I compare the current ratios for HCl and NaCl. The true conductance ratio for this case is 1.69 (calculated for 25 °C, essentially this value is measured by the BP detector); this ratio is approached at high flow rates. Similarly, current ratios measured for dilute HCl and H_2SO_4 slightly but consistently differed from the BP conductance ratio. In IC, analytes are quantitated in reference to a calibration plot; the measurement of true ionic conductance is not essential. The responses of the serially connected BP and dc detectors were measured for 1–1500 μM Cl^- and SO_4^{2-} under actual chromatographic conditions (Dionex AS4A column, 20 mM NaOH at 1 mL/min). At concentrations ≤100 μM both detectors exhibited good linearity for both analytes

(r: Cl^- > 0.9999, BP and dc; SO_4^{2-} > 0.9992 BP, >0.9995 dc), near-zero intercepts and comparable precision (standard error: Cl^- 0.49 μM BP, 0.35 μM dc; SO_4^{2-} 1.40 μM BP, 1.08 μM dc). The calibration slope ratios were different for the two analytes (Cl^- 8.650 $\mu S \cdot cm^{-1}/\mu A$; SO_4^{2-} 9.247 $\mu S \cdot cm^{-1}/\mu A$). At high concentrations, both detectors showed negative deviations in response from the above linear relationship. The onset and the extent of response nonlinearity were strikingly similar for both detectors, however; across the entire 1–1500 μM concentration range the two detectors showed excellent correlation with each other (r > 0.9999) for either analyte. In terms of calibration behavior, the dc and BP measurements are therefore essentially indistinguishable.

The close correlation of the dc response with the BP conductance suggests that the dc response is controlled by the true conductance of the solution. As indicated in the introduction, the difference in electrode potential, ΔE, is related to the applied voltage (E_{app}) and the cell resistance (R_{cell}) and current (i) as

$$\Delta E = E_{app} - iR_{cell} \quad (1)$$

If the cell current is kinetically limited at the electrodes, a relationship of the form

$$i = Ae^{k(\Delta E - E^\circ)/RT} \quad (2)$$

should be applicable where E° is the standard potential for the breakdown of the solvent, A is a constant, and k is a rate constant. Equations 1 and 2 can be combined to

$$iR_{cell} = E_{app} - \frac{Rt}{k} \ln \frac{i}{A} - E^\circ \quad (3)$$

If k is not in fact a constant but related inversely to ln i, the experimental observations, i.e., the linear relationships between i and E_{app} at constant R_{cell}, and i and $1/R_{cell}$ at constant E_{app}, are expected.

As long as this basic model allows some participation of the dissolved ionic species in the electrode processes and allows for convective transport, all reported observations are explicable.

Reproducibility and Temperature Effects. Short-term reproducibilities in the flow-injection mode (water carrier, ~15 μM H_2SO_4 sample) for the two detectors were comparable (relative standard deviation 0.93% BP, 0.64% dc; n = 21). Reproducibility over five consecutive days showed an relative standard deviation of 3.1% for the dc response, compared to 2.9% for the BP detector without temperature compensation; much of the variability is likely thermal in origin. A limited temperature effect study (25, 30, 35 °C; 2 m × 1 mm i.d. thermostated stainless steel coil connected prior to the sequential detector systems) showed both the BP conductance (temperature compensation disabled) and the dc current to increase ~1.5%/°C for 15 μM H_2SO_4 flowing at 1 mL/min.

Initially, we used stainless steel electrodes. Although short-term performance was reproducible, the response increased slowly (~11% over 3 weeks) in continued use. This may be due to an increase in electrode area from anodic corrosion. If daily calibration is performed or internal standards are used, stainless steel electrodes would be acceptable. Whether steel or Pt electrodes are used, the initial response requires several minutes to decrease to a stable reproducible value after potential is first applied or electrode polarity is reversed. This is likely due to the time required for the electrode surfaces to attain stable steady-state conditions (e.g., formation of surface oxide layer). However, this equilibration (ca. 15 min) is substantially quicker than the stabilization of the entire IC system upon startup and represents no serious handicap of the dc detector for chromatography.

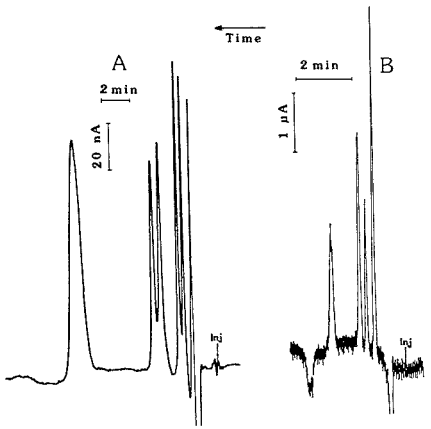

Figure 2. Low and high background conductance dc detection: (A) suppressed IC, background current 400 nA, from right to left, 4 μM IO_3^-, 6 μM Cl^-, 10 μM NO_2^-, 10 μM Br^-, 10 μM NO_3^-, 20 μM SO_4^{2-}; Dionex AS4A column, 10 mM NaOH at 1 mL/min; (B) SCIC, background current 65 μA, from right to left, 60 μM Cl^-, 25 μM Br^-, 33 μM NO_3^-, and 20 μM SO_4^{2-}; Wescan 269-013 column, 5 mM KHP, 3 mL/min.

Noise Levels and Limits of Detection. Performance as a Chromatographic Detector. For a given cell design, flow rate, and applied voltage, the observed noise levels are related to the steady-state background current and increase more than linearly with increasing background current. The chromatograms in Figure 2 illustrate this: Chromatogram A (suppressed hydroxide eluent IC system) has a low background current (~0.4 μA) and permits excellent detectabilities. Detection limit for chloride, for example, is estimated to be ~0.1 μM on a S/N = 3 criterion. The signal-to-noise (S/N) ratio in this chromatogram was equal to or marginally better than the results obtained by the serially connected BP detector. Chromatogram A was obtained with the Keithley current amplifier. The homebuilt detector shown in Figure 1b resulted in a 3-fold worse S/N ratio, still yielding adequate detectability for many applications at an attractive cost/performance ratio and produced a 1.5-fold better S/N ratio than an ac bridge type commercial detector (Model 213, Wescan Instruments, Santa Clara, CA). This inexpensive dc detector can be used successfully in gradient IC as well; Figure 3 shows a direct comparison with the BP detector.

The detection system for chromatograms A and B (Figure 2) was the same; in B, a nonsuppressed configuration was utilized with a 5 mM potassium acid phthalate eluent, highly conductive even by SCIC standards, resulting in a background current of ~65 μA. Due to excessive noise levels, detection limits are poor. The sharp noise spikes in this chromatogram suggest gas evolution, confirmed by microscopic observation of the cell during operation. Not only is the absolute noise level much higher in B, so also is the relative noise level (RNL, noise amplitude/background current). The dc detection approach is thus likely to be limited to low background conductance systems. While chromatogram B probably represents an extreme situation (S/N can be improved by reducing the cell current through applying a lower voltage and higher interelectrode spacing), the prospects of dc detection for such systems are limited.

Noise and Cell Geometry. Even at low background currents, detailed inspection of the noise characteristics suggests that the noise originates from gaseous microbubbles adhering to electrode surfaces. Although this could not be

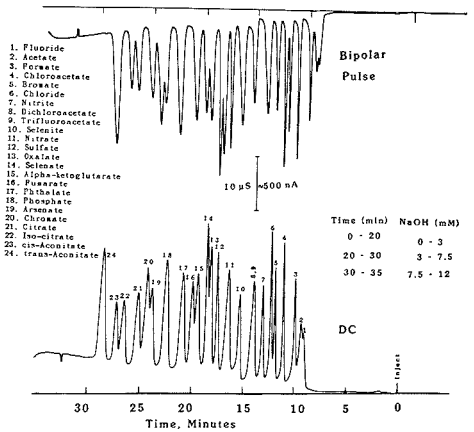

Figure 3. Comparison of gradient chromatograms obtained with sequential bipolar pulse and dc detector (shown in Figure 1b): analyte concentrations (in ppm) (1) 1.5, (3) 5.0, (6) 1.2, (7) 5.0, (12) 4.0, (24) 12.0, (2, 4, 5, 8–11, 13, 14) 10.0, (15–23) 20.0; Dionex AS4A column, 0.5 mL/min.

visually confirmed, ancillary observations support this conclusion. Flow velocity in the cell is critical; the noise is always lower at higher flow rates. For a dilute aqueous solution flowing at 3 mL/min through a 0.3 mm diameter conduit (velocity $\simeq$ 70 cm/s), the Reynolds number is $\sim$210, not enough for incipient turbulence. Any departure from laminar flow in such a system is caused by the disruption of the flow pattern by the electrode placement.

In considering noise levels obtained with various cell geometries and dimensions, the RNL is the appropriate comparison parameter. For a given eluent, the background current changes only if the cell constant or applied voltage is changed; these affect the analyte response in a proportionate manner. For our basic cell geometry, the optimum interelectrode separation is 0.5–1.5 mm for 27-gauge needles. For very short separations, the sheath layer stagnates, formation of gas bubbles at the electrode surfaces is promoted, and the RNL increases dramatically. With optimum separation, the turbulence generated at the exit electrode likely creates a backwash flow that affects the inlet electrode surface. At long separation distances, increased stagnation of the entrance electrode surface probably occurs. For a 27-gauge needle cell with an electrode separation of 1 mm and 10 mM NaOH as eluent (suppressed system, 1 mL/min, all RNL's cited below pertain to these conditions), the RNL is (2–3) $\times$ 10^{-4}.

RNL's were determined for the cell geometries shown in Figure 4. Because the overall dimensions of these cells are significantly larger than the 27-gauge needle cell, the results cannot be directly compared. If the same geometries could be attained in smaller dimensions, presumably the RNL would decrease due to an increase in linear velocity. The RNL's for these cell designs are reported in Table II.

Aside from the designs in Figure 4, a Z configuration, as in optical detectors, should be worthy of investigation. As long as the flow path is small enough in diameter, flow characteristics at the surface of both solid electrodes in a Z cell should deter adherence of gas bubbles.

Finally, the optimum cell geometry is dependent on the detection technique. For example, the Dionex CDM-I cell (containing stainless steel electrodes of circular cross section in a tubular flow path) produces an order of magnitude worse S/N in the dc mode compared to the BP mode. In contrast, the 27-gauge needle cell produces a slightly better S/N in the dc mode than when connected to the CDM-I electronics.

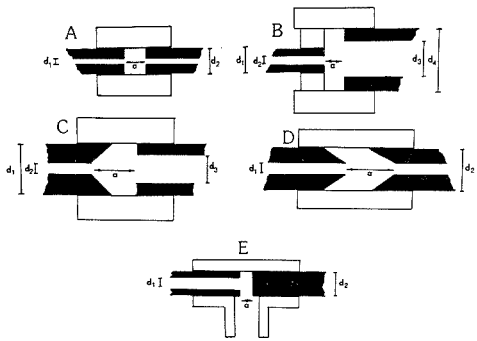

Figure 4. Cell designs used for relative noise evaluation. Tapered tubes are cut as close to 45° as possible. See Table II for dimensions.

Table II. Different Cell Geometries and Relative Noise Levels

geometry[a]	dimensions, mm	relative noise
A	$d_1 = 0.25$, $d_2 = 1.5$, $a = 0.5$	1.4×10^{-2}
	$d_1 = 0.5$, $d_2 = 1.5$, $a = 0.7$	9.8×10^{-3}
	$a = 1.5$	8.4×10^{-4}
	$d_1 = 0.75$, $d_2 = 1.5$, $a = 0.7$	3.6×10^{-3}
	$a = 1.5$	7.5×10^{-4}
B	$d_1 = 0.8$, $d_2 = 0.5$, $d_3 = 1.0$, $d_4 = 1.5$, $a = 0.5$	3.5×10^{-3}
	$a = 1.0$	1.4×10^{-3}
	$a = 1.5$	4.5×10^{-3}
	$a = 2.0$	5.1×10^{-3}
	$a = 2.0$[b]	6.7×10^{-3}
	$a = 2.6$	6.5×10^{-3}
C	$d_1 = 1.5$, $d_2 = 0.25$, $d_3 = 1.0$, $a = 0.3$	1.8×10^{-3}
D	$d_1 = 0.25$, $d_2 = 1.5$, $a = 0.8$	1.5×10^{-2}
	$a = 1.6$	6.8×10^{-4}
	$a = 2.6$	2.1×10^{-3}
	$a = 1.6$[c]	1.3×10^{-3}
E	$d_1 = 0.5$, $d_2 = 1.3$, $a = 0.5$	3.4×10^{-3}
	$a = 0.8$	1.8×10^{-3}

[a] See Figure 4, flow is left to right except as noted. [b] 17.3 V applied. [c] Flow is from right to left.

CONCLUSIONS

Application of a dc potential and monitoring of the resulting current provide a sensitive detector for low background conductance IC systems. Detectors can be made very inexpensively with cell volumes small enough to be directly used with microbore or packed capillary columns. Although studies on the effects of cell geometry have not suggested a single optimum design, sufficient insight has been gained toward future fabrication of better dc detectors. One important use of the dc detection scheme is stopped-flow measurements. Different ionic mobilities of various analyte ions generate different chronoamperometric profiles; this is useful for qualitative identification of ions eluting from an IC system (*11*).

ACKNOWLEDGMENT

We thank W. R. Heineman, John K. Foley, and an anonymous reviewer for valuable suggestions. The loan of the chromatographic equipment and the gift of the chromatographic columns from Dionex Corporation are gratefully acknowledged. Retention information provided by C. A. Pohl and J. R. Stillian was highly useful for conducting gradient chromatography experiments. D. T. Gjerde is thanked for the gift of the SCIC column.

LITERATURE CITED

(1) Small, H.; Stevens, T. S.; Bauman, W. C. *Anal. Chem.* **1975**, *47*, 1801–1809.
(2) Johnson, D. E., Enke, C. G. *Anal. Chem.* **1970**, *42*, 329–335.
(3) Caserta, K. J.; Holler, F. J.; Crouch, S. R.; Enke, C. G. *Anal. Chem.* **1978**, *50*, 1534–1541.
(4) Powley, C. R.; Geiger, R. F., Jr.; Neiman, T. A. *Anal. Chem.* **1980**, *52*, 705–709.
(5) Keller, J. M. *Anal. Chem.* **1981**, *53*, 344–345.
(6) Holler, F. J.; Enke, C. G. In *Laboratory Techniques in Electroanalytical Chemistry*; Kissinger, P. T., Heineman, W. R., Eds.; Marcel Dekker: New York, 1984.
(7) Scott, R. P. W. *Liquid Chromatography Detectors*, 2nd ed.; Elsevier: New York, 1986; pp 60–61.
(8) Tarter, J. G. *Anal. Chem.* **1984**, *56*, 1264–1268.
(9) Tarter, J. G. *J. Liq. Chromatogr.* **1984**, *7*, 1559–1566.
(10) Kourilova, D.; Slais, K.; Krejci, M. *Collect. Czech. Chem. Commun.* **1983**, *48*, 1129–1137.
(11) Okada, T.; Dasgupta, P. K.; Qi, D. *Anal. Chem.*, following paper in this issue.

RECEIVED for review October 26, 1989. Accepted March 21, 1989. This work was supported by the U.S. Department of Energy through Grant No. DE-FG05-84ER-13281. This report has not been subject to review by the DOE and no endorsement should be inferred.

Identification of Ions in Anion Chromatography by Stopped Flow Chronoamperometry

Tetsuo Okada,[1] Purnendu K. Dasgupta,* and Dayong Qi[2]

Department of Chemistry and Biochemistry, Texas Tech University, Lubbock, Texas 79409-1061

A low-volume three-way valve and a dc conductivity detector (see preceding paper) are connected serially after the bipolar-pulse conductivity detector of a suppressed hydroxide eluent anion chromatograph. Flow normally occurs through both detectors; upon valve activation, flow through the dc detector stops abruptly, trapping any desired portion of an eluite band while chromatography continues normally. Cessation of flow through the dc detector generates a "chronoamperogram", characteristic of the anion present in the measurement cell (the associated cation is H^+). The chronoamperogram consists of a current peak and a decay region and is reproducible as long as experimental parameters (applied voltage, electrode geometry and separation, prior flow rate and current level at which flow is stopped) are held constant. The entire chronoamperogram or the peak time, t_p, and/or the time for the current to decay to half its initial value, $\Delta t_{1/2}$, can be used for ion identification. For a large number of common anions, t_p is inversely proportional to the limiting equivalent conductance, λ. The values for t_p and $\Delta t_{1/2}$ for a large number of anions are presented. Current–time behavior in the decay region shows a linear i–$t^{1/2}$ relationship and the slope/intercept ratio of such a plot has been found to be linearly related to $\lambda^{1/2}$. In these respects, the system behaves as an ion mobility spectrometer for pure solutions of a single electrolyte.

Ion chromatography (IC) (*1*) is presently the most powerful and versatile technique for anion analysis. Conductometric detection is the most widely used in IC; it is uniquely selective for ionic analytes. In a preceding paper (*2*), we have outlined the utility of a dc conductivity detection approach.

Eluites from an IC system are typically identified by their retention times. False identification, especially in environmental samples containing unexpected analytes, is possible; coelution problems also exist. With the relatively low capacity columns used, the retention time can also be a function of the analyte concentration. Identification of the eluite by its optical absorption is possible only in few cases. Specific detectors, such as atomic spectrometers, have been utilized successfully in applicable cases but cannot be universally used (*3*). When identification is achieved only through specificity, wide applicability is necessarily sacrificed. The power of mass spectrometric detection methods lies in its ability of both nonselective and selective operation; IC–MS is presently only at an exploratory stage.

An analyte identification technique for IC should be applicable to all ionic analytes, perform meaningful identification at low levels without stopping chromatography, and be affordable. In exploratory experiments with dc conductivity measurements, we discovered that stopping the flow with the eluite trapped in the measurement cell results in a reproducible chronoamperometric profile, characteristic of the eluite. This paper describes the exploitation of such behavior for identification purposes.

EXPERIMENTAL SECTION

Major equipment has been described (*2*). The experimental arrangement is depicted in Figure 1. The common port of an electrically actuated inert three-way valve (type LFYA 1203032H, 12 V, 2 W, 15 μL volume, ~25 ms actuation time, The Lee Co., Westbrook, CT) was connected to the exit of the bipolar pulse conductance detection (BPCD) cell of the ion chromatograph with a short (~3 cm) segment of 300 μm i.d. PTFE tubing. The normally connected port of the valve led to the dc detector via a short segment of 300 μm i.d. PTFE tubing (*2*). The normally off port of the valve led to waste via a length of restriction tubing to provide approximately equal flow resistance in either valve position, to prevent a base-line shift of the BPCD at sensitive settings upon valve actuation. Normally, the flow proceeds through the BPCD, the valve, the dc detector, and to waste; when valve V is actuated, the flow is directed to waste through the dashed port of V and the flow through the dc detector stops. This arrangement is particularly useful because it permits chromatography to continue while isolating a desired fraction of the eluite. This can be beneficial also for other applications as in stopped-flow acquisition of the optical spectrum of an eluite fraction (*4*) or in electrochemical studies requiring measurements under both quiescent and flow conditions (*5*). In any case, an arrangement that requires shutting off the chromatographic pump is impractical.

Valve actuation was performed at any selected output level of the dc detector (hereinafter referred to as the switching threshold), either manually or automatically, using a voltage comparator-

[1] Permanent address: Faculty of Liberal Arts, Shizuoka University, 836 Ohya, Shizuoka 422, Japan.
[2] Permanent address: Research Center for Eco-Environmental Sciences, Academia Sinica, P.O. Box 934, Beijing, People's Republic of China.

0003-2700/89/0361-1387$01.50/0

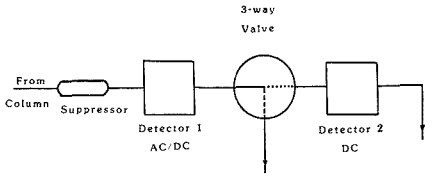

Figure 1. Flow schematic of experimental system. Normally flow proceeds through both detectors, when the valve is activated the flow through the dc detector stops.

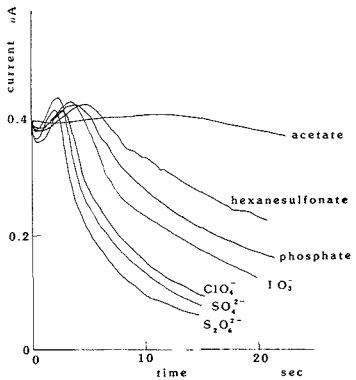

Figure 2. Stopped-flow chronoamperograms of some common anions: electrode separation 0.6 mm, prior flow rate 1 mL/min.

controlled relay. Unless otherwise stated, a switching threshold of 0.4 μA was used. With the typical dc measurement cell (6 V applied) and dilute H_2SO_4 as an electrolyte, this current level corresponds to a specific conductance of ~5.5 μS/cm (BPCD).

Unless otherwise stated, 27-gauge platinum needles with the tapered ends facing each other were used as electrodes in the dc detector, the inlet electrode was positive, and the cell current was amplified with a Keithley Model 427 current amplifier (*2*).

A cell with several voltage probes within the measurement volume was also constructed. Flat ends of 27-gauge platinum needles were inserted into a 0.0075 in. (~0.2 mm) i.d. PVC tube (Elkay Products, Shrewsbury, MA), with the ends 1–1.5 mm apart. Two or four 100 μm diameter gold wires (Johnson-Matthey/Aesar Inc., Seabrook, NH) were deployed in the intervening space perpendicular to the flow direction, the insertion being facilitated by a 30-gauge hypodermic needle temporarily put through the tube wall. The potentials of the two terminal electrodes (the negative electrode being the common ground) and the intervening gold wire probes, as well as the current flowing through the cell, were continuously measured with a multichannel, FET-input analog to digital (A/D) converter and the data stored on a microcomputer. The potential difference between the anode and its nearest gold probe, that between the two central gold probes, and that between the cathode and its nearest gold probe were divided by the instantaneous current to obtain the resistance values of the "anode compartment", "bulk solution", and the "cathode compartment", respectively. Because uniform placement of probes could not be ensured, comparison of the absolute resistance values for each compartment is not especially meaningful.

Experiments typically involved the injection of Na or K salts into a stream of dilute NaOH or water (13–15 MΩ·cm) with or without a serially connected membrane suppressor (AMMS, Dionex Corp.) which exchanged all cations for H^+.

RESULTS AND DISCUSSION

Anatomy of the Stopped-Flow Chronoamperometric Profile. Figure 2 shows chronoamperograms of a number of anions. The valve was activated at time zero. The profiles are characterized by a brief period over which the current decreases (not distinctly demarcated in some cases) followed by an increase in current leading to a maximum (broad and ill-defined for some ions) and finally a decay region.

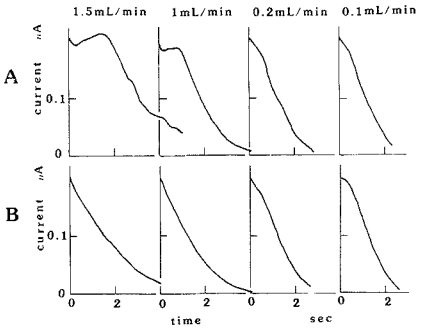

Figure 3. Stopped-flow chronoamperometric profiles for an acid electrolyte (H_2SO_4) as a function of prior flow rate (indicated in mL/min): (A) inlet electrode positive; (B) exit electrode positive.

If a similar experiment is carried out with a conventional conductance detector, the conductivity remains unchanged upon stopping the flow, regardless of the electrolyte. If a potential step is applied to a quiescent solution, a monotonic decay of current with a linear i–$t^{-1/2}$ relationship (hereinafter referred to as Cottrell-type behavior (*6*)) is expected. Although the Cottrell equation does not take into account ionic, migration-limited mass transfer, we do observe Cottrell-type behavior when a dc potential is suddenly applied to a stationary solution of a dilute acid (e.g., H_2SO_4) resident in our measurement cell; monotonic decay occurs without any peak formation. Thus, the chronoamperogram generated after the cessation of flow is, quixotically, dependent on the flow history.

Stopped-flow chronoamperograms for H_2SO_4 are shown in Figure 3A (inlet electrode positive) as a function of the prior flow rate: current maximum is only observable at high flow rates. Further, the current maximum becomes more distinct with an increase in the flow rate and its temporal location is shifted to longer times. The time for the peak maximum, t_p, for a series of experiments with H_2SO_4, was 1.0, 1.9, 2.8, and 3.8 for prior flow rates of 1.0, 1.5, 2.0, and 3.0 mL/min, respectively, all other parameters being constant. These t_p values show good linear correlation with the flow rate (r = 0.99).

Interestingly, if stopped-flow chronoamperograms are obtained with reversed electrode polarity (i.e., exit electrode positive) with a dilute acid electrolyte in the cell, no current maximum is observed, at any flow rate (Figure 3B). Exactly the opposite behavior is observed with dilute alkali (NaOH) in the measurement cell, distinct current maxima are produced only when the exit electrode is positive, again with a prior flow rate above some minimum value. With a neutral salt (i.e., Na_2SO_4), distinct current maxima are produced regardless of electrode polarity or prior flow rate.

It is useful at this point to compare the temporal change of electrical resistance in different regions within the measurement volume. The case for dilute (~10 μM) H_2SO_4 as electrolyte is presented in Figure 4. In A, dc potential is continuously applied with a prior flow rate of 3 mL/min and the inlet electrode is positive. B is the same as A, except the exit electrode is positive. In C, the dc potential is applied at t = 0 to a stationary solution. The individual electrical resistance of the loosely defined regions, "cathode compartment", "bulk solution", and "anode compartment" are shown. It is immediately obvious that case A, where a current maximum is observed, shows a different temporal development than for cases B and C. Whereas the individual resistance of each of the three regions shows a monotonic increase with time for

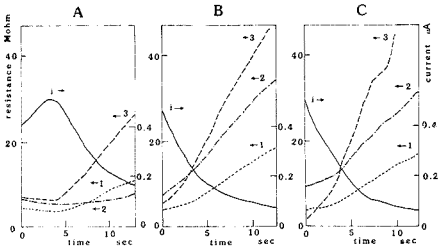

Figure 4. Temporal profile of electrical resistance in three regions of the measurement cell: (1) "anode compartment", (2) "bulk solution", and (3) "cathode compartment" for a dilute acid electrolyte (H_2SO_4); (A) inlet electrode positive, (B) outlet electrode positive, (C) quiet solution. Current profiles are shown as well. Prior flow rate for A and B were 3 mL/min.

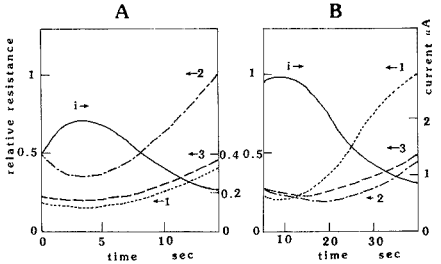

Figure 5. Temporal profile of electrical resistance in three cell regions, electrolyte: (A) dilute NaOH (B) dilute Na_2SO_4; exit electrode positive and prior flow rate 1 mL/min for both cases.

cases B and C (most markedly for the cathode compartment), the resistance initially remains constant, even decreases somewhat, for case A. It is also clear that the relative contribution of the cathode compartment to the total resistance during the initial period is the smallest for case A. The flow geometry is likely to enhance convective mass transport to the exit electrode (cathode for case A (2)). We thus hypothesize that immediately following the commencement of the experiment, the cathode diffusion layer dimensions are smaller for case A than for B and C. Since the "cathode compartment" probe region likely extends significantly beyond the diffusion layer, its resistance is the smallest for A. Possibly due to the efficient convective mass transport to the cathode prior to the cessation of flow, the cathode region for A develops an excess counterion concentration, relative to B and C, soon after flow stops. The continued transport of H^+ to the cathode itself thus becomes controlled by the counterion migration in the opposite direction. Meanwhile, H^+ is electrogenerated at the anode but is no longer directly convectively transported to the cathode. The migration of the counterion from the cathode region and the bulk solution to the bulk solution and the anode region, respectively, and the migration of the anodic electrogenerated H^+ to the anode region and the bulk solution govern the temporal development of the resistance profiles of the anode region and the bulk solution.

Formation of the Current Maximum. Cell Back Pressure and Remnant Flow Direction. The scenario above cannot alone account for current maxima, however; at best, the formation of a current plateau is suggested. For the current to rise above the level attained during steady state flow, a new influx of electrolyte must occur to replenish the steady state diffusion layer. One possibility for peak formation is that some fresh electrolyte enters the cell even after nominal flow cessation as the pressure of the compressed fluid dissipates. The effect of the exit pressure on the cell was therefore determined. Increasing the pressure consistently increased t_p and the peak current, i_p. Adding sufficient restriction tubing to the cell to increase the back pressure by 60 psi increased i_p from 0.44 to 0.63 μA and t_p from <3 to >13 s for sulfate. Thus, the effect of prior flow rate may partly be due to increasing exit pressure with flow rate. These results also led us to explore the effect of the remnant flow direction (i.e., that after the nominal cessation of flow). In the experiments described thus far, the remnant flow direction is the same as the original flow direction. With two three-way valves and sufficient restriction to the dc detector exit, a flow configuration was devised in which the remnant flow direction was opposite to the original. Under these conditions current maxima formed only when the original inlet electrode was negative (dilute H_2SO_4 electrolyte); i.e., in both configurations current maxima occur only when the exit for the remnant flow is the cathode. Fresh influx of H^+ stimulates the cathode process.

Alkali and Neutral Salts in the Measurement Cell. With an alkali in the measurement cell, the temporal profile of resistance in the three probe regions for the outlet electrode positive case (Figure 5A) is analogous to the inlet electrode positive case with an acidic electrolyte. With a quiet solution or with the inlet electrode positive with dilute NaOH in the measurement cell, the resistance increases monotonically (not shown) for all three probe regions. Figure 5B shows the case for a neutral salt, Na_2SO_4, with the exit electrode positive. The situation with the neutral salt is different from that of the acid and the base. The temporal resistance profiles are similar regardless of electrode polarity and existence of prior flow; further, the current maxima here are produced primarily by a drop in resistance of the "bulk solution". The "bulk solution" resistance probably decreases in this case due to the migration of electrogenerated H^+ and OH^-, which have substantially higher mobility than the ionic constituents of the salt, to the center of the cell. The current begins to decrease when the H^+ and OH^- begin to react with each other, causing a net loss of charge carriers and increased electrical resistance.

Ionic Mobility and Peak Time. While several previous studies dealing with electrochemistry in flow-through tubular electrodes under both constant and pulsed flow conditions are in the literature (*7–19*), the absence of any supporting electrolyte and the resulting constraints on charge transport, as well as the hydrodynamic shock upon abrupt cessation of flow, make the present system unique. Further, available theoretical models largely rely on the mass transfer equations as developed by Levich (*17*); these tacitly assume that the dimensions of the diffusion layer are insignificant compared to the tube radius (*7*). The validity of this assumption is doubtful in the present case. Although some efforts have been made to model the effects of axial (*7*, *16*) and cylindrical (*7*) diffusion, no experimental verifications have thus far been made. Inasmuch as convective transport, electromigratory transport, and irreversible electrode processes are all involved, formulation of exact equations governing the response behavior of the present system upon flow-cessation has thus far eluded us. However, if the cathodic process is the controlling event (with acidic solutions in the cell) and the continued reduction of H^+ at the cathode after the nominal cessation of flow is governed by the migration of the counterion away from the cathode, it may be expected that the decay region of the chronoamperogram will begin sooner with faster counterions. Thus, the peak time, t_p, should be inversely related to ionic mobility.

In Figure 6, t_p values for 38 anions are plotted against the reciprocal of their equivalent conductance at infinite dilution at 25 °C (λ, linearly related to the ionic mobility). The closed symbols indicate those ions for which we can unambiguously

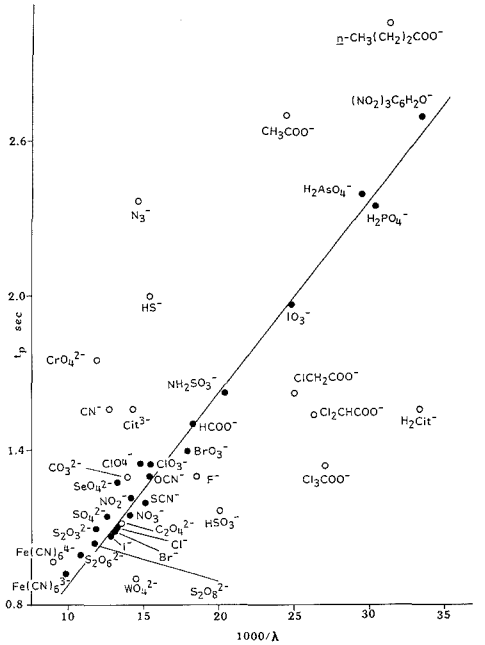

Figure 6. Values of peak time t_p vs reciprocal of equivalent conductance (λ): closed symbols, ionic form unambiguously assignable, regression line shown based only on these. All obtained under 6 V, interelectrode distance 0.9 mm, and switching threshold 0.4 μA.

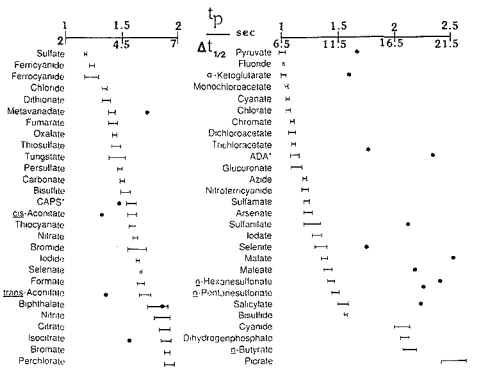

Figure 7. Time for current to fall to half of switching threshold for 56 ions; 95% confidence limits are indicated. Experimental conditions are as in Figure 6. The points show the t_p values for the ions of unknown λ and thus not in Figure 6. Key: CAPS, 3-(cyclohexylamino)-1-propanesulfonate; ADA, *N*-(2-acetamido)-2-iminodiacetate.

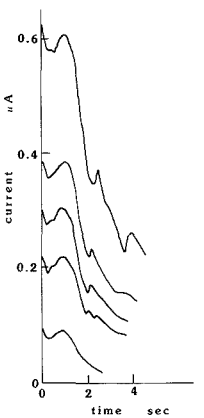

Figure 8. Stopped flow chronoamperogram for sulfate, as a function of the switching threshold. Prior flow rate 1 mL/min, electrode separation 2.2 mm.

assign the dominant form present as the indicated ion. For the concentration of the electrolyte present in the measurement cell, acids with $pK \leq 4$ should be completely dissociated. The best-fit line ($r = 0.994$) through these 22 points is indicated. All other cases are indicated as open symbols. Of these, for CO_3^{2-}, CN^-, HS^-, N_3^-, CH_3COO^-, $CH_3(CH_2)_2COO^-$, and $C_6H_5COO^-$, uncharged neutral acids are likely to be present and their dissociation (and migration of the resulting ions) during chronoamperometry is likely to increase the t_p values. Predictably, they are located above the regression line. In a similar vein, partially protonated forms of WO_4^{2-}, $Fe(CN)_6^{4-}$, $C_2O_4^{2-}$, citrate (shown both as the mono- and the trianion), and CrO_4^{2-} are likely to exist in significant concentrations because of the relevant pK values and we cannot unambiguously compute the $1/\lambda$ values. There is no ambiguity with the dominant ionic form of HSO_3^- present; however, this ion is oxidized so easily in dilute solution (to sulfate, which has a much higher λ), the t_p determination probably does not represent the pure species. The behavior of F^- and chloroacetates remains anomalous: none of these have $pK > 4$ and display much lower t_p values than expected. If significant formation of HF_2^- ($\lambda = 75$) can occur and the chloroacetates are readily electrochemically cleaved to yield the much faster chloride ion, these values can be rationalized.

The 22 anions shown as closed symbols range in λ from 30 to 101 and in t_p from 0.92 to 2.70 s; the λt_p product has the mean value of 85.3 with a standard deviation of 5.3. The constancy of the λt_p values becomes even more noticeable if singly charged and multiply charged ions are separated in two groups; the two groups are different by statistical significance tests and yield the λt_p values (mean ± standard deviation) of 82.8 ± 3.8 ($n = 16$) and 91.8 ± 1.9 ($n = 6$) for singly charged and multiply charged ions, respectively. The data in Figure 6 were obtained over a 6-week period without any efforts to thermostat the measurement cell or the liquid reservoirs. Considering that ionic mobility shows a typical variation of 2%/°C with temperature, we believe that the results presented in Figure 6 are remarkable. The t_p values for additional anions, of unknown λ, are indicated in Figure 7.

The Current Decay Region. For a diffusion-controlled, irreversible electrode process at a planar electrode, the i–t relationship may be given, for small values of t, by

$$i = nFAk_fC[1 - 2k_ft^{1/2}/(\Pi^{1/2}/D^{1/2})] \quad (1)$$

where k_f is a potential dependent rate constant and C and D are the bulk concentration and diffusion coefficient of the species undergoing electrochemical conversion, respectively (*6*). For a system obeying eq 1, an i vs $t^{1/2}$ plot is linear; the intercept and the slope should be $nFAk_fC$ and $-2k_f^2nFAC/(\Pi^{1/2}D^{1/2})$, respectively. The slope/intercept ratio, R, $-2k_f/(\Pi^{1/2}D^{1/2})$, is predicted to be independent of the bulk concentration. In our principal system of interest, suppressed anion chromatography, the electrolyte present in the measurement cell is always in the form of an acid and the reduction of H^+ at the cathode is believed to be the controlling process. At constant applied voltage between the two electrodes, the actual potential experienced by the cathode, and

Table I. Summary of i–t Behavior (Decay Region) for Six Ions

test anion	corr coeff[a]	slope,[b] $\mu A \cdot s^{-1/2}$	intercept,[b] μA	slope/intercept ratio, R	$\lambda^{1/2}$[c]
$S_2O_6^{2-}$	1.000	−0.238	0.431	−0.552	9.64
SO_4^{2-}	0.994	−0.266	0.530	−0.502	8.94
Cl^-	0.999	−0.228	0.458	−0.498	8.74
ClO_4^-	1.000	−0.183	0.392	−0.467	8.24
IO_3^-	0.994	−0.115	0.342	−0.336	6.36
$H_2PO_4^-$	0.997	−0.102	0.337	−0.303	5.74

[a] Linear regression coefficient for the i–$t^{1/2}$ plot, electrode separation is 0.9 mm for all cases. [b] For the i–$t^{1/2}$ plot. [c] λ is the limiting equivalent conductance at 25 °C.

thus k_f, is assumed to be constant as a first approximation.

In our system, choice of the switching threshold controls the concentration of the electrolyte trapped in the measurement cell and is thus directly related to the bulk concentration. Over a 4-fold range of the switching threshold (0.2–0.8 μA) i–$t^{1/2}$ behaviors of Cl^-, SO_4^{2-}, and hexanesulfonate were studied, each at seven to nine different thresholds. In each case, the i–$t^{1/2}$ plots for the decay period (i.e., the period after the current maximum) were linear. While individual slopes and intercepts varied considerably as a function of the threshold, the ratio R was virtually constant (relative standard deviation 2.1, 2.3, and 4.4% for Cl^-, SO_4^{2-}, and hexanesulfonate respectively). Note that even the decay region did not exhibit Cottrell-type behavior.

While detailed data are not presented for any given ion, the magnitude of the ratio R was found to increase with increasing applied voltage, decreasing prior flow rate, and decreasing electrode separation.

The applicability of eq 1 to the present system is questionable, however. Such equations implicitly assume presence of supporting electrolytes; further, the rate constant k_f is unknown and must be relatively small for the approximation represented by eq 1 to be applicable to a time scale of several seconds. Equation 1 predicts that the slope/intercept ratio should be inversely related to the square root of the diffusion coefficient (of H^+, if the cathode process is the governing one). In a system where mass transport is governed by ionic migration rather than by diffusion, it may be expected that the diffusion term may be replaced by a term related to ionic mobility. Table I presents the summary of the i–t behavior (decay region) for six ions. In each case, the i–$t^{1/2}$ plot exhibits good linearity. Most interestingly, the data in the last two columns show that the ratio R is linearly related to the square root of the anion mobility by the equation

$$R = -0.0646\lambda^{1/2} + 0.0707 \quad (2)$$

with a correlation coefficient >0.999. Further, considering the typical value of λ, the intercept in eq 2 is negligible as the general model of eq 1 would suggest.

Parameters Useful for Ion Identification. Under constant operating conditions, the entire chronoamperogram for an ion is highly reproducible. In consecutive runs, the profile is generally reproducible to within the width of the trace. Obviously, a simple way to check and confirm the identity of a particular chromatographic peak is to obtain its stopped-flow chronoamperogram and then inject a standard solution of the ion it is suspected to be. The chronoamperograms thus obtained can then be compared.

For most purposes, less exacting comparisons suffice; it is not necessary to construct i–$t^{1/2}$ plots or compute the slope/intercept ratios. Under constant operating conditions, any or all of the following parameters, temporal location and magnitude of the peak current (t_p and i_p) and the width of the peak, can be successfully used for identification. Smaller

Table II. Effect of Electrode Spacing on Peak Width ($\Delta t_{1/2}$)

electrode spacing, mm	$\Delta t_{1/2}$, s			
	chloride	sulfate	hexanesulfonate	acetate
0.55	1.69 ± 0.04	1.54 ± 0.05	3.98 ± 0.14	7.93 ± 0.17
0.90	2.13 ± 0.04	1.94 ± 0.05	5.36 ± 0.11	10.37 ± 0.10
1.20	3.58 ± 0.11	3.49 ± 0.12	10.19 ± 0.77	29.80 ± 2.04
2.00	8.75 ± 0.18	8.77 ± 0.16	29.9 ± 1.33	

t_p values do not necessarily produce higher i_p values (compare for example, sulfate and dithionate in Figure 2). As a measure of the peak width, we use the time necessary for the current to decay to half that of the starting value, termed $\Delta t_{1/2}$. This quantity is easily and precisely measured by a voltage activated timer such as that described in ref 21. The values of $\Delta t_{1/2}$ for 56 anions under specified operating conditions are presented in Figure 7; the width indicates the 95% confidence limit.

Parameters Affecting the Chronoamperogram. Increasing the applied voltage results in decreased t_p values. While the data reported here largely pertain to sharp ends of needle electrodes pointing toward each other, current maxima and characteristic chronoamperograms are also obtained with flat ends comprising the measurement cell. The latter permits more reproducible positioning and is therefore preferred for future work. Increasing the electrode separation increases t_p and $\Delta t_{1/2}$. Because the peak becomes broader and eventually can no longer be discerned, accurate measurement of t_p becomes difficult with large electrode separations. Representative values for $\Delta t_{1/2}$ as a function of electrode spacing are presented in Table II. Interestingly, while the ability to discriminate between hexanesulfonate and OAc^- is enhanced by increased electrode separation, the reverse is true for distinguishing Cl^- and SO_4^{2-}.

By far the most pronounced effect on improving resolution of t_p values is afforded by increasing the flow rate or the exit pressure on the cell. This was discovered fairly late in this work, and the bulk of the data (e.g., Tables I and II) were obtained at a modest flow rate (1 mL/min) and very little back pressure.

The effect of changing the switching threshold, which governs the concentration of the electrolyte trapped in the cell, is shown in Figure 8. All quantitative parameters are affected, but qualitatively, the chronoamperogram changes little. We have found, for all strong acid anions tested, $\Delta t_{1/2}$ to be linearly related to the switching threshold.

Distinction of Eluting Analytes. Using t_p and/or $\Delta t_{1/2}$ values we have been able to distinguish, for example, fluoride/iodate/acetate or sulfate/oxalate in real chromatographic experiments where these ions frequently coelute. We have also been able to unequivocally identify equimolar coeluting binary mixtures (IO_3^-/F^-, F^-/OAc^-, OAc^-/IO_3^-, SO_4^{2-}/Ox^{2-}) as *not* corresponding to either of the ions by themselves. Quantitative deconvolution of binary mixtures appears to be possible in favorable cases; the applicability to more complex mixtures does not seem feasible at this stage.

CONCLUSIONS

A simple inexpensive system, readily connected to a suppressed anion chromatograph, can be used to obtain stopped-flow dc chronoamperograms. Either the whole chronoamperometric profile or selected parameters derived therefrom can be used for the identification of anions eluting from the system or the occurrence of coelution can be tested for. The need for further quantitative understanding of the fundamental phenomena involved in this exploratory work is evident, but so is the potential utility of this approach. Ion

mobility spectrometry in the gas phase is well-known (22); in a way, the present system represents a step toward an ion mobility spectrometer for ions in aqueous solution.

LITERATURE CITED

(1) Small, H.; Stevens, T. S.; Bauman, W. C. *Anal. Chem.* **1975**, *47*, 1801–1809.
(2) Qi, D.; Okada, T.; Dasgupta, P. K. *Anal. Chem.*, preceding paper in this issue.
(3) Dasgupta, P. K. In *Ion Chromatography*; Tarter, J. G., Ed.; Marcel Dekker: New York, 1987.
(4) Sepaniak, M. J.; Kettler, C. N. In *Detectors for Liquid Chromatography*; Yeung, E. S., Ed.; Wiley: New York, 1986; p 177.
(5) Pratt, K. W. *Anal. Chem.* **1984**, *56*, 1967–1970.
(6) MacDonald, D. D. *Transient Techniques in Electrochemistry*; Plenum: New York, 1977; p 77.
(7) Flanagan, J. B.; Marcoux, L. *J. Phys. Chem.* **1974**, *78*, 718–723.
(8) Blaedel, W. J.; Olson, C. L.; Sharma, L. R. *Anal. Chem.* **1963**, *35*, 2100–2103.
(9) Blaedel, W. J.; Klatt, L. N. *Anal. Chem.* **1966**, *38*, 879–883.
(10) Klatt, L. N.; Blaedel, W. J. *Anal. Chem.* **1967**, *39*, 1065–1072.
(11) Klatt, L. N.; Blaedel, W. J. *Anal. Chem.* **1968**, *40*, 512–517.
(12) Osterling, T. O.; Olson, C. L. *Anal. Chem.* **1967**, *39*, 1546–1549.
(13) Blaedel, W. J.; Iverson, D. G. *Anal. Chem.* **1977**, *49*, 1563–1566.
(14) Blaedel, W. J.; Yim, Z. *Anal. Chem.* **1978**, *50*, 1722–1724.
(15) Blaedel, W. J.; Yim, Z. *Anal. Chem.* **1980**, *52*, 564–566.
(16) Razumney, G.; Wroblowa, H. S.; Schrenk, J. *J. Electroanal. Chem.* **1976**, *69*, 299–315.
(17) Levich, V. G. *Physicochemical Hydrodynamics*; Prentice-Hall: Englewood Cliffs, NJ, 1969; p 112.
(18) Meschi, P. L.; Johnson, D. C. *Anal. Chem.* **1980**, *52*, 1304–1308.
(19) Meschi, P. L.; Johnson, D. C. *Anal. Chim. Acta* **1981**, *124*, 303–314.
(20) *Lange's Handbook of Chemistry*, 12th ed.; Dean, J. A., Ed.; McGraw-Hill: New York, 1979; pp 6–34.
(21) Dasgupta, P. K.; Loree, E. L. *Anal. Chem.* **1986**, *58*, 507–509.
(22) Rokushika, S.; Hatano, H.; Hill, H. H., Jr. *Anal. Chem.* **1987**, *59*, 8–12, and references therein.

RECEIVED for review October 26, 1988. Accepted March 21, 1989. This work was supported by the U.S. Department of Energy through Grant No. DE-FG 05-84ER-13281. However, this manuscript has not been subjected to official review by the DOE and no endorsement should be inferred.

Automated Determination of Manganese in Seawater by Electrolytic Concentration and Chemiluminescence Detection

Eiichiro Nakayama*

Research Center for Instrumental Analysis, Faculty of Science, Kyoto University, Kyoto 606, Japan

Kenji Isshiki[1] and Yoshiki Sohrin[2]

Department of Chemistry, Faculty of Science, Kyoto University, Kyoto 606, Japan

Hajime Karatani

Laboratory of Analytical Chemistry, Faculty of Textile Science, Kyoto Institute of Technology, Kyoto 606, Japan

A new automated analytical method for determining manganese in seawater has been developed. The principle of the method is based on the combination of selective electrolytic preconcentration using a glassy carbon electrode and improved chemiluminescence (CL) detection in a flowthrough system. In this method, Mn(II) in a sample solution is oxidized to manganese(IV) oxide, which is electrodeposited onto the glassy carbon fiber electrode, followed by elution with acidic hydrogen peroxide solution. The resulting eluent is mixed with an alkaline luminol solution after removing the contaminating metal ions by column extraction based on extraction chromatography, and then the mixture is introduced into the CL cell. The manganese concentration is obtained from the CL intensity. The method was applied to seawater samples collected in seas adjacent to Japan.

Manganese is a geochemically active element in the ocean. The dissolved manganese is easily precipitated by oxidation to manganese(IV) oxide, which acts as a powerful scavenger for trace elements. The solidified manganese in sediments is reduced to Mn(II) and is regenerated into the water column under mild reducing conditions, for example in the oxygen minimum zone and the near-shore anoxic sediments (*1*). In recent years, it has also been found that a copious amount of manganese is injected into the deep waters by hydrothermal emanations through the active oceanic crusts (*2*). Therefore, it is very important to clarify the distribution of manganese in seawater to understand marine geochemistry. Furthermore, manganese is thought to be a promising element as a chemical tracer for probing the hydrothermal activities if it can be analyzed easily and quickly onboard ship.

In this paper, we describe a new automated analytical method for determining manganese in seawater combining electrolytic concentration and chemiluminescence (CL) detection. Although the use of CL for determining dissolved trace amounts of manganese has been long-established and is known to be highly sensitive (*3*), it has not been applied in a practical manner for analyzing natural waters. The reason is that it is not selective; other metals such as iron and cobalt interfere with the determination of manganese. Therefore, a selective separation of manganese is required to utilize the CL detection as a practical method. It was reported that cathodic stripping voltammetry, in which trace elements are oxidized anodically for preliminary accumulation on the indicator electrode, is relatively selective for manganese and lead (*4–6*). Since we have already developed an electrochemical technique for the determination of iodine species in natural waters by anodic electrolysis using a flow-through column electrode (*7*), a similar concentration method was tested for

[1] Present address: Kochi Women's University, 5-15, Eikokuji-cho Kochi 780, Japan.
[2] Present address: The Institute for Chemical Research, Kyoto University, Uji, Kyoto 611, Japan.

0003-2700/89/0361-1392$01.50/0

Mn(II) in seawater. It was found that Mn(II) is electrochemically oxidized to manganese(IV) oxide, which is quantitatively electrodeposited on the glassy carbon electrode in the flowthrough system. This concentration technique was coupled with an improved CL method based on the oxidation of luminol with alkaline hydrogen peroxide. As a result, a selective and highly sensitive method for determining manganese in seawater has been developed. Measurements made in seas adjacent to Japan showed that this method was efficient for shipboard analysis.

EXPERIMENTAL SECTION

Apparatus. The electrolytic concentration and CL systems are as follows. The electrolytic cell is the same as that previously reported (*7, 8*); its working electrode was a glassy carbon fiber (11 μm, Tokai Carbon Co., Ltd.) packed in a Vycor glass tube (Corning Co., Ltd.). An Ag/AgCl electrode in 1 M potassium chloride solution was used as a reference electrode (normal silver chloride electrode (NSE)), and a spiral platinum electrode was used as a counter electrode. The cell was controlled with a potentiostat that can be changed over to two arbitrary potentials. Two peristaltic pumps were used to send sample and cleaning solution, and counter electrolyte of the concentration cell, respectively. Three couples of solenoid valves were used to change the flow of solutions. An eight-way valve with a clear polyacrylamide sample box was set up at the entrance of sample solutions for the automatic sampling. The CL system (Model-CL-100, Kimoto Electric Co., Ltd.) was composed of a two-channel peristaltic pump for sending a carrier solution (eluent) and a reagent solution, a CL cell that has a flow cell and a photomultiplier tube (PMT) built in, a high-voltage power supply, and an electrometer. The flow cell was a clear 1.2-mm-i.d. Teflon tubing coiled on a vortex groove 28 mm in diameter notched on an aluminum block, which was fixed to a quartz screen facing the PMT. The cell was heated to 50 °C to accelerate the CL reaction. The PMT (Hamamatsu Photonics, R268) was cooled to 5 °C with an electronic cooler to reduce the dark current, and a voltage of −750 V was generally applied to it. Both the electrolytic concentration and CL systems were connected with a Kelex-100 (commercial name of 7-dodecenyl-8-quinolinol, Ashland Chemical Co.) column (*9*), which removes interfering metals in the carrier solution (eluent), and a 5-m reaction coil of Teflon tubing (1-mm i.d.) to gain reaction time and to mix the reagent and the carrier solutions sufficiently.

All of the Teflon tubing and connectors were washed with a hot mixture of nitric acid, perchloric acid, and sulfuric acid. The other parts in the flowthrough line were used after being soaked in 4 M nitric acid for a week.

The containers of reagent and carrier solutions and the reaction coil were put in a water bath regulated at 27 °C (room temperature of the laboratories on board and in the university was always maintained below 25 °C) to stabilize the CL reaction and to prevent the generation of air bubbles in the flow system.

The systems were controlled with interlocking five-step timers.

A Nippon Jarrel-Ash AA-8200 atomic absorption spectrometer equipped with a FLA-100 graphite furnace atomizer was used for metal measurements in the preliminary study.

Reagents. Luminol (Nakarai Chemicals) was used after double recrystallization from 0.6 M hydrochloric acid. Triethylenetetramine (TETA, Wako Pure Chemical Industries) was recrystallized twice from methanol and hydrochloric acid. Hydrochloric acid, nitric acid, and aqueous ammonia of reagent grade were further purified by rapid isopiestic distillation. Hydrogen peroxide (Wako Pure Chemical Industries, for the atomic absorption analysis), potassium carbonate (Merck, Supurapur), and acetic acid (Merck, Supurapur) were used without further purification.

All solutions were made up with Millipore Milli-Q water. Solutions of ammonium salts were prepared by mixing the purified aqueous ammonia and acids.

Artificial seawater was prepared according to Lyman and Fleming's formula (*10*) and was purified by pumping through the Kelex-100 column and the electrolysis column after passing through a 0.4-μm Nuclepore filter. With this treatment, almost all of the contaminating metal ions such as Cu(II), Fe(III), Co(II), Ni(II), Pb(II), Cd(II), and Zn(II) including Mn(II) originating from the reagents were thoroughly removed.

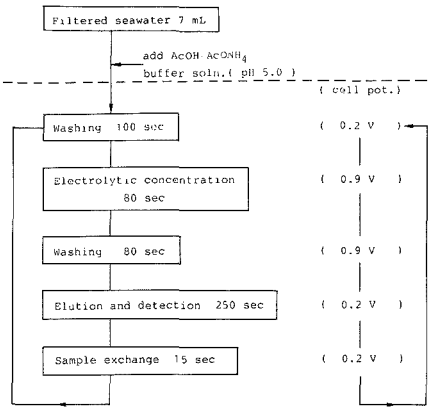

Figure 1. Flow chart of the analytical procedure for the automatic determination of manganese in seawater.

The carrier solution (eluent) was 0.1 M acetic acid containing 10 mM hydrogen peroxide and 25 mM aqueous ammonia (pH 3.7 acetic acid–ammonium acetate buffer solution). The reagent solution was 0.25 M potassium carbonate containing 0.25 mM luminol and an adequate amount of TETA. The cleaning solution was pure water. A stock solution of 100 ng of Mn(II)/mL was made from the 1000 ppm Mn(II) standard solution (Wako). Working standards were prepared by diluting the stock solution with purified artificial seawater. Standard solutions (1000 ppm) of Co, Pb, Ni, Cu, Fe, Cr, Cd, Sb, Mo, Se, and Ti (Wako) were used.

The counter electrolyte was 0.5 M potassium sulfate purified by passing through the Kelex-100 column.

Procedure. The analytical procedure is shown by the flow chart in Figure 1. Filtered and/or unfiltered seawater was adjusted at ca. pH 5 with 2 M acetic acid–ammonium acetate buffer solution (1 mL per 100 mL of sample solution). The polyethylene containers filled with the samples were set in the sample box. At the first stage, the residual sample in the system was exchanged with a new one. Then the potential applied to the preconcentration cell was changed from 0.2 to 0.9 V vs NSE. The sample solution was passed through the cell for 80 s at a flow rate of 5 mL/min. In this stage almost all of the other heavy metals were separated, together with major sea salts. After electrolysis, the cell was rinsed with the cleaning solution. The cell potential was again reduced to 0.2 V vs NSE to elute manganese from the electrode with the eluent. After the sample and cleaning solution pump was stopped, the eluent was passed through the cell for 3 min at a flow rate of 1 mL/min. After passing through the Kelex-100 column (in this stage codeposited metals were thoroughly removed), the resulting eluent was mixed with the reagent solution pumped at a flow rate of 1 mL/min, and the mixture was introduced into the CL cell through the mixing coil. The manganese was determined by the measurement of the CL intensity obtained 4.3 min after mixing of the eluent with the reagent solution.

In the preliminary study, artificial seawaters containing certain amounts of Mn(II) and other metal ions simultaneously were used instead of seawater. The eluent was 10 mL of 50 mM acetic acid (pH 3.1) containing 10 mM hydrogen peroxide and was trapped in a 30-mL Pyrex glass vial before and/or after passing through the Kelex-100 column.

RESULTS AND DISCUSSION

Electrolytic Concentration of Mn(II) and Effects of Other Metal Ions. Co(II), Pb(II), and Ni(II) are elements that deposit as insoluble oxides on the electrode similarly to Mn(II), when they are electrochemically oxidized ($Mn^{2+} + 2H_2O \rightarrow MnO_2 + 4H^+ + 2e^-$). Figure 2 shows the relationship between pH and the electrodeposition percentage of metals

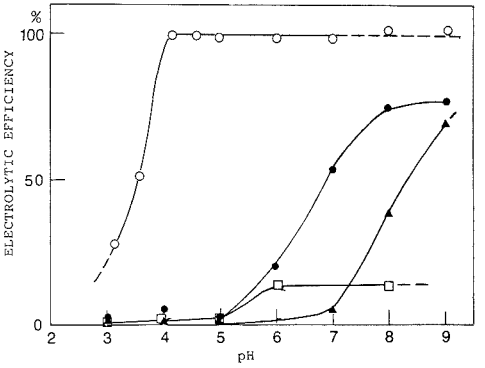

Figure 2. Relationship between pH and electrolytic efficiency of metal ions in artificial seawater: ○, 10 μg/L Mn(II); ●, 50 μg/L Pb(II); □, 100 μg/L Co(II); ▲, 200 μg/L Ni(II); potential, 0.9 V (--- 0.7 V) vs Ag/AgCl.

Table I. Percentage of Metal Ions Adsorbed onto the Glassy Carbon Electrode and Percentage Remaining in the Eluent after Passing through the Kelex-100 Column[a]

metals	ions adsorbed, %	ions remaining, %
Mn(II)	101 ± 4[b]	99 ± 4
Fe(III)	45 ± 5	<0.1
Cu(II)	8 ± 1	<0.05
Cr(III)	0.6 ± 0.2	0.5 ± 0.2
Zn(II)	<0.01	<0.01
Cd(II)	<0.01	<0.01

[a] Conditions: artificial seawater of pH 5.1, 20 mL; cell potential, 0.9 V (adsorption) and 0.2 V (elution) vs NSE; Mn(II), 10 μg/L; the other metals, 100 μg/L; eluent, 10 mL of 50 mM acetic acid containing 10 mM hydrogen peroxide. [b] Electrodeposition.

on the electrode. Mn(II) was quantitatively electrodeposited above pH 4.2 at a cell potential of 0.9 V vs NSE (0.7 V vs NSE above pH 7.0), while fairly large amounts of Pb(II), Co(II), and Ni(II) were also codeposited at higher pHs.

At pH 8.0, the natural pH of seawater, considerable amounts of Pb(II), Co(II), and Ni(II) were codeposited at any potentials required for complete electrolysis of Mn(II), whereas at pH 5.0 the other metals were hardly electrodeposited at all. At pH 5, the cell potentials suitable for quantitative electrolysis of Mn(II) were between 0.85 and 1.0 V vs NSE.

Also, the adsorption behavior of Fe(III), Cu(II), Cr(III), Cd(II), and Zn(II) onto the glassy carbon electrode was investigated. Appreciable amounts of Fe(III) and Cu(II) and a small amount of Cr(III) were adsorbed onto the electrode even from the sample solution at pH 5.1 and were eluted with the eluent as shown in Table I. Cd(II) and Zn(II) were hardly adsorbed at all. In order to remove the other metal ions in the eluent, the Kelex-100 column was tested, since we have previously found that extraction of Mn(II) with this column begins at pH 5.5 whereas Cu(II) and Fe(III) are completely recovered even at pH 2. As indicated in Table I, Fe(III) and Cu(II) were thoroughly removed by passing the eluent through this column. From our previous result, Al(III), Bi(III), Ga(III), and Ti(IV) are also expected to be removed by this column (*9*), although they were not tested in this work. Mn(II) is not captured under this condition, as seen in Table I. Additionally, Kelex-100 column extraction is useful for removing interfering metals such as iron that are included in the glassy carbon itself and are occasionally eluted.

Consequently, Mn(II) can be selectively concentrated from seawater samples at ca. pH 5 in distinction from the other metal ions by the electrolytic oxidation at a potential ca. 0.9 V vs NSE and by passing through the Kelex-100 column. Although a solitary exception is Cr(III), the total amount of Cr(III) adsorbed is considered to be extremely low because its concentration in seawater is very low (*11*, *12*). The recovery of manganese was constant at sample solution flow rates of 1–10 mL/min.

The elution of manganese was achieved with only 3 mL of the eluent by backward flow and by rapid reduction with acidic hydrogen peroxide.

The electrolytic efficiency of Mn(II) was almost 100% in the concentration range investigated (0.05–100 μg/L).

One of the drawbacks of column electrolysis using a carbon electrode for natural waters is that dissolved organic matter (DOC) included in the sample solutions is adsorbed onto the electrode, resulting in the degradation of the reproducibility of results. When a natural seawater sample, collected from offshore Shirahama in Wakayama in Japan and containing more than 3 mg/L DOC, was used, the reproducibility of results was reduced over a long period of use. This can be resolved by rinsing the electrolysis cell with a 1:1 mixture of 20% methanol and 4 M aqueous ammonia, as stated previously (*13*).

In the Mn(II)-catalyzed CL, Mn(II) produces a hydroxyl radical, HO·, by decomposing hydrogen peroxide in the alkaline solution (Fenton-type reaction) (*14*). The resulting hydroxyl radical oxidizes luminol to 3-aminophthalate dianion immediately. The 3-aminophthalate dianion just after the oxidation is in the excited state and emits light when going to the ground state. The produced amount of the 3-aminophthalate in the excited state is proportional to the concentration of Mn(II) under a certain condition. Thus, the concentration of Mn(II) can be determined by measuring the CL intensity.

Purity of Reagents. Since the CL reaction of luminol is catalyzed by trace amounts of various metal ions, the purity of reagents used is a very serious problem. Potassium carbonate of reagent grade gave high background CL even after double recrystallization, while that of Supurapur grade was suitable to reduce the background CL to a sufficiently low level. Luminol of reagent grade also gave high background CL without double recrystallization. The mineral acids and aqueous ammonia prepared by isopiestic distillation and the acetic acid of Supurapur grade gave hardly any increase of the CL intensity at all. TETA was recrystallized twice because it was not guaranteed reagent. When the background CL was large because of the contaminating metal ions, it was observed that a negative peak appeared in proportion to the extent of the background CL before the positive CL peak of manganese. The negative peak dulled the CL peak of manganese, resulting in a decrease of the analytical sensitivity.

Optimal Concentration of CL Species. The effect of the concentrations of the CL species luminol, hydrogen peroxide, and potassium carbonate was tested in a batch system. The maximum CL intensity was obtained at the following concentrations: luminol in the reagent solution, 0.25 mM; potassium carbonate in the reagent solution, 0.24 M; hydrogen peroxide in the carrier solution, 10 mM. Although aqueous ammonia was tested as an alkaline reagent instead of potassium carbonate, it promoted the decomposition of luminol and was unsuitable for the automated analysis.

Effect of the Length of the Reaction Coil. As shown in Figure 3, the CL intensity increased rapidly for 3 min after the mixing of reagent and carrier solutions in the batch system. Hence, the effect of the length of the reaction coil was investigated in the flow system. The results of the test for 2–10 m of Teflon tubing (1-mm i.d.) indicate that the background CL intensity decreased with increasing the length of the re-

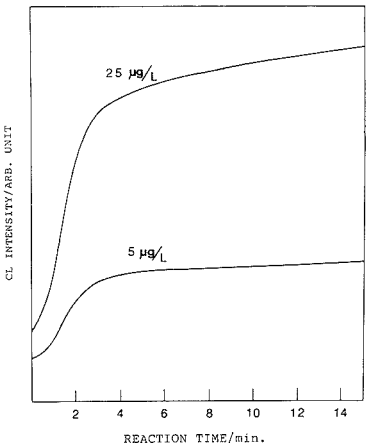

Figure 3. Relationship between CL intensity and reaction time for 5 and 25 μg/L Mn(II).

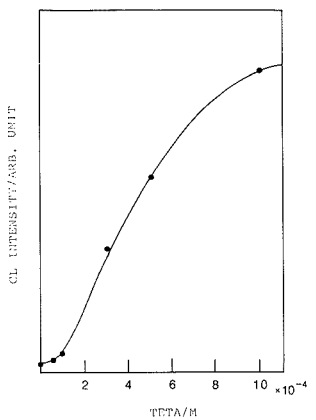

Figure 4. Effect of triethylenetetramine concentration on the CL intensity of Mn(II): reagent solution, 0.24 M K_2CO_3, 0.25 mM luminol, 0–10^{-3} M triethylenetetramine; carrier solution, 0.5 μg of Mn(II)/L, 10 mM H_2O_2, 0.1 M acetic acid, 25 mM NH_4OH.

action coil because of sufficient mixing of both the solutions. However, the CL catalyzed by manganese decreased with increasing the length of the coil due to the diffusion of the solution in the tubing line. Therefore, a reaction coil of 5 m was most suitable for low background CL and sensitive determination of manganese. All the investigations below were conducted by using the flow system.

Effect of Chelating Reagents. The chelating reagent often affects the catalytic activity of metal ions for the decomposition of hydrogen peroxide (*15*). As shown in Figure 4, the CL was noticeably enhanced by the addition of TETA into the reagent solution. Wang reported that catalytic activity of Fe(III) for the decomposition of hydrogen peroxide is increased by chelating with TETA because the reactivity of cis positions of Fe(III)–TETA is remarkably higher than that of the reaction sites of Fe(III) aqueous ion (*15*). It is thought that a similar effect should occur in the Mn(II)–hydrogen peroxide system. Although the CL intensity increased with increasing the TETA concentration, it reached an upper limit, i.e. CL intensity saturation phenomenon, at the lower manganese concentration in proportion to the TETA concentration. Therefore, the suitable TETA concentration was (2–3) × 10^{-4} M for the analysis of seawater of which manganese concentration ranges from 20 to 1000 ng/L.

Table II. Detection Limits of Metals Obtained with the CL Method Using the Luminol–Hydrogen Peroxide System and the Interference of Metals for This Method in the Absence and Presence of TETA[a]

metals	detectn lim[b], μg/L	metal concn, μg/L, with Mn concn, ng/L, given in parentheses: without TETA	with TETA[c]
Co(II)	0.006	2 (200 ± 10)	100 (20 ± 2)
		0.1 (<DL[d])	10 (<DL)
Cr(III)	0.01	100 (<DL)	100 (8 ± 1)
			10 (<DL)
Fe(III)	0.2	100 (<DL)	100 (<DL)
Mn(II)	0.5		
Ni(II)	0.6	100 (<DL)	100 (<DL)
Sb(V)	50	100 (<DL)	100 (<DL)
Cu(II)	60	100 (<DL)	100 (<DL)
Pb(II)	1000	100 (<DL)	100 (<DL)

[a] Interference is indicated as metal concentration (μg/L), which gives the CL intensity corresponding to that of the manganese concentration (ng/L) shown in parentheses. Conditions: artifical seawater of pH 5.1, 30 mL for the case without TETA and 7 mL for the case with TETA. [b] Literature data (ref 16). [c] 2.5 × 10^{-4} M. [d] Detection limit.

Coexisting salts and acids in the eluent affected the CL intensity slightly. Among the salts and acids tested, the mixture of acetic acid and ammonium acetate (0.1 M acetic acid plus 25 mM aqueous ammonia) gave most highly sensitive and reproducible result.

From the above-stated results, the most suitable composition of the reagent solution is 0.24 M potassium carbonate, 0.25 mM luminol, and 2.5 × 10^{-4} M TETA. The most suitable composition of the carrier solution is 10 mM hydrogen peroxide, 0.1 M acetic acid, and 25 mM aqueous ammonia.

Interference of the Other Metal Ions. As stated above, almost all portions of the other metal ions are separated in the stage of electrolysis and Kelex column extraction. It is, however, conceivable that a small remaining portion of them could interfere with the determination of manganese in the CL detection. Table II shows the detection limit of metal ions in the CL determination using the luminol–hydrogen peroxide system and the extent of interference of these metals for this method in both the absence and presence of TETA. Since the data for the detection limits are cited from various reports (*16*), the experimental conditions are not always the same. Therefore, these values are merely criteria for the extent of interference. In the absence of TETA, the detection limit of Mn(II) in this method using 30 mL of sample solution was 20 ng/L (S/N = 2). Cr(III), Fe(III), Ni(II), Sb(V), Cu(II), and Pb(II) gave no interference larger than the detection limit of Mn(II) in the concentration range up to 100 μg/L, whereas Co(II) gave no interference up to 0.1 μg/L and gave interference corresponding to 200 ng of Mn(II)/L at 2 μg of Co(II)/L. In the presence of 2.5 × 10^{-4} M TETA, the detection limit of Mn(II) in this method using 7 mL of sample solution was 5 ng/L (S/N = 2). Co(II) also gave interference corresponding to 20 ng of Mn(II)/L at 100 μg/L but not at 10 μg of Co(II)/L, while Cr(III) gave slight interference at 100 μg/L. Mo(VI), Se(VI), Zn(II), Cd(II), and Ti(IV), which are not considered to be involved in the CL reaction of luminol, gave no interference up to 1 mg/L.

Calibration. The relative standard deviation was 0.54% for 10 replicate measurements of an artificial seawater sample containing 100 ng/L Mn(II) and ca. 20% for 5 ng/L Mn(II). The calibration curve was linear in the concentration range

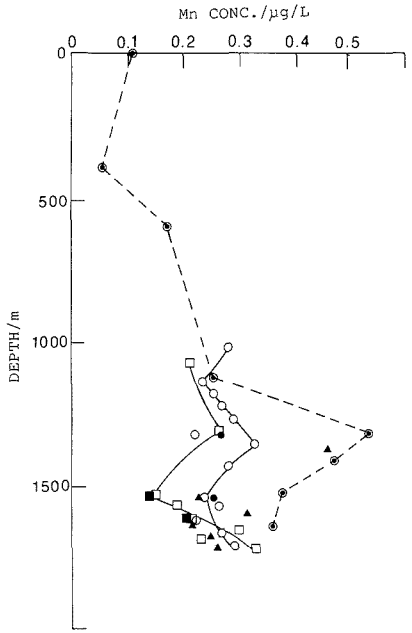

Figure 5. Vertical distribution of manganese in the water column at the Okinawa Trough. Solid line, determined by this method (unfiltered sample): □, CB6-12 (■, collected with clean sampler); ▲, CB6-14; ○, CB6-17 (●, collected with clean sampler). Dashed line, determined by 8-quinolinol extraction-ICP AES detection method (unfiltered sample): CB6-3 (collected with clean sampler).

of 50–500 ng of Mn(II)/L, but was somewhat curved in the lower and higher concentration ranges.

In addition, the CL signal was constant at flow rates of the sample solution between 2 and 8 mL/min in the case of a 100 ng/L Mn(II) solution.

Seawater Analyses. This method was applied to shipboard analysis of seawater samples collected during the cruise of R.V. *Hakuho-Maru* (University of Tokyo), KH-87-2 (May 7–21, 1987), at the Okinawa Trough, where hydrothermal activity was observed. It was also applied to the samples of R.V. *Tansei-Maru* (University of Tokyo), KT-88-2 (February 15–17, 1988), at the Sagami Bay, where a large seepage flux of methane was found to be expelled by the force of subduction-induced compaction (*17*). The distribution of manganese in the Okinawa Trough (Figure 5) reflected the hydrothermal activity, exhibiting a plume of highly concentrated manganese at a depth of around 1300 m. The dashed line indicates the results obtained by the 8-quinolinol concentration–inductively coupled plasma atomic emission spectroscopy (ICP AES) detection method (*18*) in the same sea area, though the sampling station is slightly different. The good agreement of the results shows that this method is valid

Table III. Manganese Concentration in the Sagami Bay (35° 00.075′ N, 139° 13.906′ E)

			Mn, μg/L	
sample no.	name	depth, m	filtered	unfiltered
6	towing	1220	0.45	0.50
7	1000	1012	0.41	0.43
8	750	761	0.28	0.31
9	500	508	0.19	0.23
10	150	155	0.21	0.25
1	0	2.4	0.095	0.097
3	200	203	0.078	0.114

for shipboard analysis. Table III shows one of the results of the Sagami Bay analysis. The concentrations of manganese in the unfiltered samples are somewhat higher than those in the filtered samples. This indicates that a part of particulate manganese, which may be active manganese(IV) oxide, is adsorbed onto the glassy carbon electrode. The concentrations of manganese obtained from unfiltered samples (total adsorbed manganese, TAM) are considered to correspond to those of total dissolvable manganese (TDM) (*1*). It will be clarified whether or not TAM is the same as TDM in a forthcoming report.

ACKNOWLEDGMENT

This research is dedicated to Hitoshi Sakai of Ocean Research Institute, University of Tokyo, who suggested the theme of this study to the authors.

Registry No. Mn, 7439-96-5; water, 7732-18-5; luminol, 521-31-3.

LITERATURE CITED

(1) Landing, W. M.; Bruland, K. W. *Earth Planet Sci. Lett.* **1980**, *49*, 45–56.
(2) Klinkhammer, G.; Bender, M.; Weiss, R. F. *Nature* **1978**, *269*, 319–320.
(3) Kalinichenk, I. E. *Ukr. Khim. Zh.* **1969**, *35*, 755–757.
(4) Huber, C. O.; Lemmert, L. *Anal. Chem.* **1966**, *38*, 128–129.
(5) Hrabankova, E.; Masin, V.; Dolezal, J. *J. Electroanal. Chem. Interfacial Electrochem.* **1969**, *22*, 195–201.
(6) Hrabankova, E.; Kolezal, J.; Beran, P. *J. Electroanal. Chem. Interfacial Electrochem.* **1969**, *22*, 203–206.
(7) Nakayama, E.; Kimoto, T.; Okazaki, S. *Anal. Chem.* **1985**, *57*, 1057–1060.
(8) Nakata, R.; Okazaki, S.; Hori, T.; Fujinaga, T. *Anal. Chim. Acta* **1983**, *149*, 67–75.
(9) Isshiki, K.; Tsuji, F.; Kuwamoto, T.; Nakayama, E. *Anal. Chem.* **1987**, *59*, 2491–2495.
(10) Lyman, J.; Fleming, R. H. *J. Mar. Res.* **1940**, *3*, 134–146.
(11) Nakayama, E.; Kuwamoto, T.; Tokoro, H.; Fujinaga, T. *Anal. Chim. Acta* **1981**, *131*, 247–254.
(12) Cranston, R. E.; Murray, J. M. *Anal. Chim. Acta* **1978**, *99*, 275–281.
(13) Nakayama, E.; Isshiki, K.; Sohrin, Y. *Mar. Chem.*, in press.
(14) Walling, C. *Acc. Chem. Res.* **1975**, *8*, 125–131.
(15) Wang, J. H.; *J. Am. Chem. Soc.* **1955**, *77*, 4715–4719.
(16) Fernandeg-Gutierrez, A.; Munoz De La Pena, A. *Molecular Luminescence Spectroscopy*; Schulman, S. G., Ed.; John Wiley & Sons, Inc.: New York, 1985; pp 372–546.
(17) Sakai, H.; Gamo, T.; Endow, K.; Ishibashi, J.; Ishida, T.; Yanagisawa, F.; Kusakabe, M.; Akagi, T.; Igarashi, G.; Ohta, S. *Geochem. J.* **1987**, *21*, 227–236.
(18) Ishibashi, J.; Gamo, T.; Sakai, H.; Nojiri, Y.; Igarashi, G.; Shitashima, K.; Tsubota, H., submitted for publication in *Geochem. J.*

RECEIVED for review May 10, 1988. Revised September 28, 1988. Accepted March 14, 1989. This research was supported by a grant from Nissan Science Foundation.

Permselectivity and Ion-Exchange Properties of Eastman-AQ Polymers on Glassy Carbon Electrodes

Joseph Wang* and Teresa Golden

Department of Chemistry, New Mexico State University, Las Cruces, New Mexico 88003

Eastman-AQ55D is a new poly(ester sulfonic acid) cation exchanger available in a commercial dissolved form. Films of this polymer were coated onto glassy carbon surfaces, and the resulting electrodes exhibit attractive permselectivity, ion-exchange, and antifouling properties. Substantial improvement in the selectivity is observed as a result of excluding anionic species from the surface. The charge-selective behavior is demonstrated in the presence of a variety of compounds of neurological significance. A rapid response to dynamic changes in the concentration of cationic and neutral species is observed. The polymer strongly binds multiply charged counterions. Cyclic voltammetry is used to determine the quantity of incorporated ions as a function of time, concentration, and other variables. The oxidation of hydrogen peroxide is catalyzed when $Ru(bpy)_3^{2+}$ is incorporated in the coating. The film can also protect the substrate electrode from foulants present in the contacting solution. These features, as well as the low cost, simple coating procedure, strong adherence to surfaces, and versatility, make the Eastman-AQ55D polymer well-suited for a variety of electroanalytical applications.

Substantial research efforts are being devoted to the development of voltammetric sensors based on chemical modification of electrodes (*1–4*). Polymer-modified electrodes, in particular, hold great promise for increasing the selectivity, sensitivity, and reproducibility of voltammetric measurements (*5–12*). Such improvements can be attained through enhanced electron-transfer kinetics, permselective transport, or preferential uptake. The attractive features of Nafion, cellulose acetate, polyaniline, polypyrrole, or poly(vinylpyridine) have been particularly useful for voltammetric sensing. Practical applications of these and other polymer-modified electrodes, including in vivo monitoring of primary catecholamine neurotransmitters, enhanced monitoring of chromatographic effluents, or reliable stripping analysis of biological samples for trace metals, have been described. New polymers with attractive permselective, collection, or catalytic properties are desirable for further development of chemically modified electrode sensors.

We describe here the ion-exchange properties and permeability characteristics of a new commercially available polymer, Eastman-AQ55D. This poly(ester sulfonic acid) cation exchanger is available in a commercial dissolved form (*13, 14*). It can be cast into films on electrode surfaces by evaporation of the solvent. The resulting coatings exhibit good adhesion to many substrates. Glassy carbon electrodes, coated with Eastman-AQ films, are shown in this study to exhibit attractive permselective, ion-exchange, and antifouling properties. In particular the polymer effectively excludes anions from the supporting surface while it strongly binds counterionic species (in a manner analogous to that of commonly used Nafion films). With its low cost, strong adherence to the surface, and rapid response, the Eastman-AQ polymer appears to open many new opportunities for future sensor developments.

EXPERIMENTAL SECTION

Apparatus. An EG&G PAR Model 264A voltammetric analyzer, in conjunction with an EG&G PAR Model 0073 X-Y recorder, was used for cyclic voltammetry and differential pulse voltammetry. A Bioanalytical Systems (BAS) Model VC-2 electrochemical cell was employed. The glassy carbon electrode (BAS MF2012, 2.5-mm diameter), reference electrode (BAS RE-1, Ag/AgCl (3 M NaCl)), and the platinum wire auxiliary electrode joined the cell through holes in its cover. All potentials reported are referenced to this reference electrode. The flow injection system was described previously (*5*). A glassy carbon thin-layer detector (Model TL-5, BAS) and a 20-μL sample loop were used in flow measurements.

Reagents. Deionized water was used to prepare all solutions. A solution of the Eastman-AQ55D polymer (28% dispersion) was obtained from Eastman Kodak Co. and was used as received. Dopamine hydrochloride, 3,4-dihydroxyphenylacetic acid (DOPAC), catechol, epinephrine, 4-methylcatechol, L-DOPA, norepinephrine hydrochloride, uric acid, caffeic acid, methyl viologen (MV^{2+}), bovine albumin, $Ru(bpy)_3Cl_2$ (bpy = 2,2′-bipyridine) (Sigma), $Ru(NH_3)_6Cl_3$, hydrogen peroxide (Aldrich), ascorbic acid (AA) (Baker), and (ferrocenylmethyl)trimethylammonium (FA^+) iodide (Pfaltz and Bauer) were used as received. Solutions of pH 7.4 phosphate buffer at 0.01 and 0.05 M ionic strength were used in batch and flow experiments, respectively.

Procedure. Prior to its coating, the electrode was hand-polished with alumina slurries of 1 and 0.05 μm. Residual polishing material was removed from the surface by sonication in a water bath for 5 min after each polishing process. The surface was modified by coating the disk and its surrounding with measured volumes of the diluted (1:20 (v/v) Eastman AQ:acetone) polymer solution (10 and 50 μL were used for batch and flow measurements, respectively). The film was allowed to dry in air for 5 min. Ion-exchange/cyclic voltammetric experiments were performed by equilibration with quiescent solutions of electroactive cations in 0.01 M phosphate buffer (pH 7.4). The amount (Γ) of ionic species incorporated into the film was estimated by measuring the area of the cyclic voltammetric peaks. Amperometric (flow) measurements were made by applying the desired working potential and allowing the background current to decay to a steady-state value. All experiments were carried out at room temperature.

RESULTS AND DISCUSSION

Permselective Transport. Figure 1 shows cyclic voltammograms for a series of cationic, nonionic, and anionic biologically important compounds at modified (solid line) and bare (dotted line) glassy carbon electrodes (at pH 7.4). As can be seen, the negatively charged film effectively excludes the anionic species (ascorbic and uric acids or DOPAC) from the surface. In contrast, the large permeability of the cationic neurotransmitters dopamine, epinephrine, and norepinephrine results in large peaks, similar to those obtained with a naked surface. Some shifts in peak potentials are also observed. Changes in the pH (in the interior of the coating) may account for these shifts. The neutral species catechol and 4-methylcatechol exhibit a similar behavior. Analogous differential pulse measurements, at lower concentrations, yielded similar observations with effective exclusion of oppositely charged species and a facile transport of co-ionic and neutral ones. Similar background currents were observed in blank (differential pulse and cyclic) voltammograms at the coated

0003-2700/89/0361-1397$01.50/0

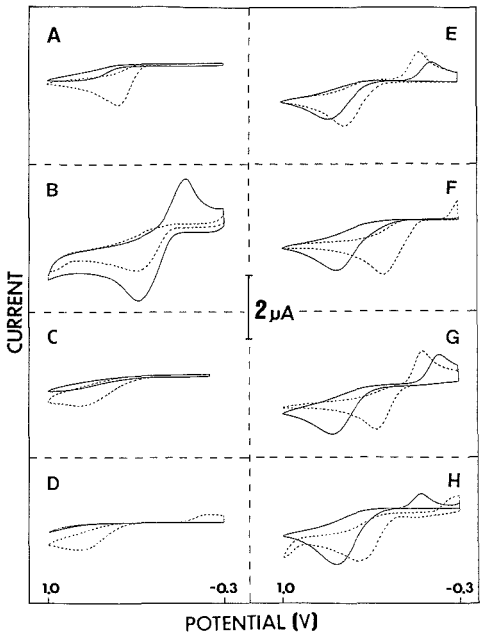

Figure 1. Cyclic voltammograms for 1×10^{-3} M uric acid (A), dopamine (B), ascorbic acid (C), DOPAC (D), catechol (E), epinephrine (F), 4-methylcatechol (G), and norepinephrine (H) at bare and coated glassy carbon electrodes (dotted and solid lines, respectively). Conditions: scan rate, 50 mV/s; electrolyte, 0.01 M phosphate buffer (pH 7.4).

and bare electrodes. The selective retardation of anionic species is of great significance for the development of neurochemical sensors (particularly as primary neurotransmitters are protonated at the physiological pH while DOPAC and ascorbic acid exist as anions). For example, differential pulse measurements of 5×10^{-5} M dopamine were not affected by adding a large excess (2×10^{-4} M) of its major metabolite DOPAC; in comparison, a large overlapping response was observed at the unmodified electrode. The charge of DOPAC ($pK_a = 4.22$) strongly influences its transport characteristics. At pH 2, for example, the modified electrode exhibited only a slightly (10%) diminished DOPAC response, compared to that at the bare electrode.

The permeability features of the polyester ionomer were tested also under hydrodynamic conditions, utilizing flow injection analysis (FIA). Such FIA data for 10 biologically significant compounds are presented in Table I. The ratio between the peak current of each compound over that of catechol ($i_{p,x}/i_{p,cat.}$) is presented. Note that anionic species yield small response peaks under forced-convection conditions. Nevertheless, these signals are significantly smaller relative to those of cationic and neutral ones. For example, $i_{p,x}/i_{p,cat.}$ values of 0.04, 0.12, 0.18, and 0.18 are observed for caffeic acid, DOPAC, ascorbic acid, and uric acid, respectively. Analogous observations (i.e., incomplete rejection of anionic species) were reported for Nafion-coated flow detectors (*15*, *16*). The $i_{p,x}/i_{p,cat.}$ value for the zwitterionic L-DOPA (0.47) is between those for anions and cations. Most compounds (with the exception of epinephrine) exhibit similar response peaks at the bare electrode, with $i_{p,x}/i_{p,cat.}$ values of 0.85–1.11. Overall, the film coverage results with only modest (25–40%) attenuations of the FIA response for cationic and neutral species (compared to ca. 85–95% diminutions of the response of anionic ones). The permselective transport is strongly affected by the film thickness (Table II). Low-thickness films that offer improved rejection of anionic species and enhanced response of cationic ones (relative to the neutral catechol), as well as modest attenuations of the peaks of interest (relative to the bare surface), were used throughout. The Eastman-AQ coated electrode exhibits a rapid response to dynamic changes in concentration that characterize FIA systems. For example, a response time (to reach 90% of the maximum signal) of 1 s and peak width (at 0.6 C_{max}) of 2 s were observed for injections of 1×10^{-4} M dopamine solutions (20 μL). High injection rates (of about 120 samples/h) are thus feasible. Slower response characteristics were reported at Nafion-based FIA detectors (*15*). Repetitive preparations of the film result in relatively reproducible transport characteristics. For example, a series of eight different films yielded a mean $i_{p,AA}$(coated)/$i_{p,AA}$(bare) value of 0.17, with a range of 0.15–0.21 and a relative standard deviation of 11%.

Table I. Relative Response of Various Compounds Compared to That of Catechol[a]

compound	$i_{p,x}/i_{p,cat.}$[b] coated electrode	bare electrode
acetaminophen	0.65	0.91
ascorbic acid	0.18	0.85
caffeic acid	0.04	0.85
L-DOPA	0.47	1.08
DOPAC	0.12	0.96
dopamine	1.29	0.89
epinephrine	1.52	1.53
norepinephrine	1.34	1.11
4-methylcatechol	1.08	1.00
uric acid	0.18	1.02

[a] Conditions: flow injection measurements at the 1×10^{-4} M level; applied potential, +0.7 V; flow rate, 1.0 mL/min. [b] Ratio between the current of each compound over that of catechol.

Table II. Effect of Film Thickness on the Permselective Response[a]

coating	$i_{p,AA}/i_{p,cat.}$[b]	$i_{p,DA}/i_{ip,cat.}$[c]	$i_{p,cat(coated)}/i_{p,cat(bare)}$[d]
low thickness	0.18	1.29	0.62
medium thickness	0.43	0.98	0.46
high thickness	0.90	0.55	0.05

[a] Low-, medium-, and high-thickness films were prepared by using different dilutions of the polymer solution, 1:20, 1:10, and 1:5 (v/v), respectively. Flow injection operation, as in Table I. [b] Ratio between the current of ascorbic acid over that of catechol. [c] Ratio between the current of dopamine over that of catechol. [d] Ratio between the current of catechol at the coated electrode over that at the bare surface.

The potential of the Eastman-AQ electrode to overcome surfactant adsorption problems is illustrated in Figure 2, which compares the stability of the response for successive injections of sample containing 1×10^{-4} M acetaminophen and 500 ppm albumin. A rapid loss of the electrode activity is observed at the bare surface (A), with up to a 20% decrease in the response for the 24 repetitive injections shown. The coated electrode, in contrast, is resistant to fouling and exhibits a highly stable analytical response (B). The rapid and stable response is important for the utility of Eastman-AQ coated electrodes as in vivo probes.

Ion-Exchange Properties. Ion-exchange voltammetry, based on the electrostatic partitioning of ionic species at film-coated electrodes, is of great significance for both electroanalysis and electrocatalysis (*6*, *17*). Cyclic voltammograms representing the partition of $Ru(bpy)_3^{2+}$, $Ru(NH_3)_6^{3+}$, and MV^{2+} into the Eastman-AQ film upon repetitive cycling gave

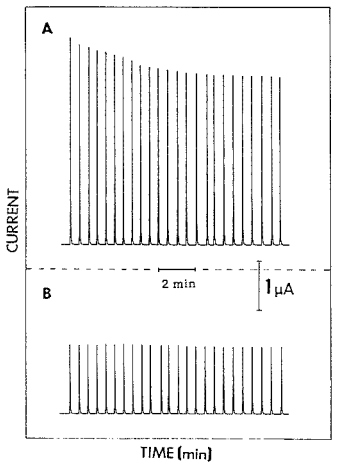

Figure 2. Detection peaks for repetitive injections of a 1×10^{-4} M acetaminophen solution, containing 500 ppm bovine albumin: (A) bare electrode, (B) coated electrode; flow rate, 1.0 mL/min; applied potential, +0.7 V; electrolyte and carrier, 0.05 M phosphate buffer (pH 7.4).

Table III. Partition Characteristics of Various Cations[a]

cation	$10^8\Gamma$,[b] mol/cm^2	t_{eq},[c] min	Γ_{45}/Γ_0[d]
MV^{2+}	5.9	50	0.68
$Ru(NH_3)_6^{3+}$	4.9	36	0.65
$Ru(bpy)_3^{2+}$	0.49	150	0.79
FA^+	0.47	43	0.52

[a] Conditions as in Figure 4. [b] Surface coverage obtained by integrating the peak area. [c] Equilibration time. [d] Retention ratio is the fraction of the initially incorporated ion that was retained 45 min after the coated electrode was transferred to a blank (electrolyte) solution.

increasing peak currents, reflecting the incorporation of these cationic species (Figure 3). Such incorporation is attributed to electrostatic interaction with anionic sulfonated exchange sites. The voltammograms reached steady state after ca. 150 (A), 36 (B), and 150 (C) min. The steady-state peak currents are significantly (50–70-fold) larger than those of the solution species alone (estimated from the first scan). These and other data of the charge trapping experiment are listed in Table III. This behavior is similar to that reported for the incorporation of the same cationic redox species at Nafion-coated glassy carbon electrodes (*6*). Faster attainment of equilibrium was observed at higher concentrations of exchanging ions (equilibration times of 30, 150, and 180 min for 10^{-3}, 10^{-4}, and 10^{-5} M MV^{2+}, respectively). A similar trend was observed for FA^+ (not shown). Hence, a facile incorporation of organic counterions can be attained from dilute solutions (in the presence of a large excess concentration of simple inorganic cations, e.g. those of the supporting electrolyte). This feature is attributed to the structural characteristics of Eastman-AQ polymers, and particularly to the relatively hydrophobic nature of the polyester backbone (*14*). The scan rate dependence of the cyclic voltammetric peak current was evaluated after equilibration from 1×10^{-4} M $Ru(NH_3)_6^{3+}$ and $Ru(bpy)_3^{2+}$ solutions. The resulting log–log plots of peak current against scan rate were linear, with slopes of 0.47 and 0.43, respectively. Such values indicate diffusion control of the electrolysis of trapped ions. Significant incorporation of cationic species was observed also in acidic media (e.g. $\Gamma(Ru(NH_3)_6^{3+})$ of 2.9×10^{-8} mol/cm^2 at pH 2.1). This observation suggests that factors

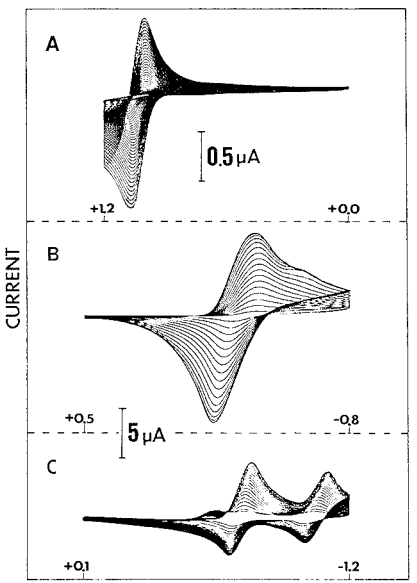

Figure 3. Cyclic voltammograms for 1×10^{-4} M $Ru(bpy)_3^{2+}$ (A), $Ru(NH_3)_6^{3+}$ (B), and MV^{2+} (C) recorded continuously at a glassy carbon electrode coated with Eastman-AQ film. Scan rate is 20 mV/s; other conditions are as in Figure 1.

other than charge may control the extent of incorporation.

Cyclic voltammetric experiments were employed also for constructing partition isotherms (of Γ_{eq} vs C_{soln}). Such isotherms for MV^{2+} and $Ru(NH_3)_6^{3+}$ were linear at low-concentration regions (up to 7×10^{-5} and 4×10^{-5} M, respectively); a leveling off was observed at higher concentrations, suggesting a saturation phenomenon. Because of the facile incorporation from dilute solutions and the linear partition isotherms, Eastman-AQ polymers hold great potential for trace analysis of organic cations using the technique of ion-exchange voltammetry (*6*, *17*). For example, at the 10^{-5} M level, MV^{2+} and FA^+ were preconcentrated by factors of 50× and 35×, respectively, relative to the naked electrode. These observations point to the large partition coefficients involved.

Many of the incorporated ions remained in the Eastman-AQ film for long periods when the electrodes were removed from the incorporated solution and replaced in a pure supporting electrolyte solution. The retention capability of the Eastman-AQ coatings was estimated by measuring the retention ratio, Γ_{45}/Γ_0, after equilibrating the electrode from 10^{-4} M solutions of various cations (Γ_{45}/Γ_0 is the ratio of the coverage immediately after transfer to the pure electrolyte solution to that 45 min later). Γ_{45}/Γ_0 values of 0.79, 0.68, 0.65, and 0.52 were calculated for $Ru(bpy)_3^{2+}$, MV^{2+}, $Ru(NH_3)_6^{3+}$, and FA^+, respectively. Such retentions compare favorably with those observed with other ion-exchange films previously used in the field of polymer-coated electrodes (*17*).

The facile incorporation and prolonged survival of ionic metal complexes hold great promise for electrocatalysis. Catalysis of hydrogen peroxide was used to illustrate the ability of Eastman-AQ bound metal complexes to mediate electron exchange with redox species in solution. The oxidation of hydrogen peroxide at naked carbon surfaces requires a substantial overpotential (e.g., Figure 4A). However, with the Eastman-AQ/$Ru(bpy)_3^{2+}$ coated electrode the hydrogen

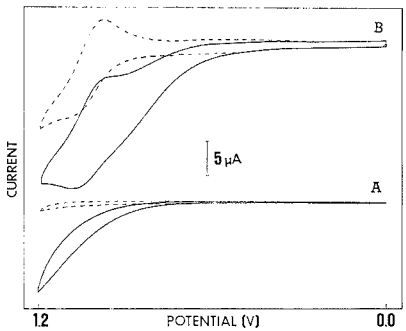

Figure 4. Cyclic voltammograms for 1 × 10^{-3} M hydrogen peroxide at bare (A) and coated (B) glassy carbon electrodes. The response at the coated electrode was obtained following equilibration from a 1 × 10^{-3} M $Ru(bpy)_3^{2+}$ solution. Other conditions are given in Figure 1. The dotted lines correspond to the response of the blank solution.

peroxide oxidation commences at a lower potential, where $Ru(bpy)_3^{2+}$ is electrooxidized to $Ru(bpy)_3^{3+}$ (Figure 4B). Coupled with the rejection of anionic species, such electrocatalysis of hydrogen peroxide oxidation can benefit various biosensing applications.

In conclusion, the experiments described above have indicated that the transport properties and ion-exchange characteristics of Eastman-AQ films make them well-suited for voltammetric sensing. In particular, the enhanced selectivity obtained as a result of excluding anionic species could be very valuable for in vivo brain electrochemistry. The preconcentration of counterions and their ability to mediate electron transfer may result with sensitive electrochemical sensors.

LITERATURE CITED

(1) Faulkner, L. R. *Chem. Eng. News* **1984**, Feb. 27, 31.
(2) Murray, R. W.; Ewing, A. G.; Durst, R. A. *Anal. Chem.* **1987**, *59*, 379A.
(3) Durst, R. A.; Blubaugh, E. A. *ACS Symp. Ser.* **1986**, No. 309, 245.
(4) Dong, S.; Wang, Y. *Electroanalysis* **1989**, *1*, 97.
(5) Wang, J.; Hutchins, L. D. *Anal. Chem.* **1985**, *57*, 1536.
(6) Szentirmay, M. N.; Martin, C. R. *Anal. Chem.* **1984**, *56*, 1898.
(7) Coury, L. A.; Birch, E. M.; Heineman, W. R. *Anal. Chem.* **1988**, *60*, 553.
(8) Oyama, N.; Ohsaka, T.; Shimizu, T. *Anal. Chem.* **1985**, *57*, 1526.
(9) Cox, J. A.; Kulkarni, K. P. *Analyst* **1986**, *111*, 1219.
(10) Ye, J.; Baldwin, R. P. *Anal. Chem.* **1988**, *60*, 1979.
(11) Sittampalam, G.; Wilson, G. S. *Anal. Chem.* **1983**, *55*, 1608.
(12) Wang, J.; Tuzhi, P. *Anal. Chem.* **1986**, *58*, 3257.
(13) Noonan, J. M. U.S. Patent 4,419,437, 1983.
(14) *Kodak Lab. Res. Prod. News* Eastman Kodak, Rochester, NY, August 1988.
(15) Wang, J.; Tuzhi, P.; Golden, T. *Anal. Chim. Acta* **1987**, *194*, 129.
(16) Ji, H.; Wang, E. *J. Chromatogr.* **1987**, *410*, 111.
(17) Wang, J. In *Electroanalytical Chemistry*; Bard, A. J., Ed.; Marcel Dekker: New York, 1989; Vol. 16, pp 1–88.

RECEIVED for review December 20, 1988. Accepted March 31, 1989. This work was supported by grants from the National Institutes of Health (GM 30913-06) and Battelle Pacific Northwest Laboratory.

Second Dissociation Constant and pH of *N*-(2-Hydroxyethyl)piperazine-*N'*-2-ethanesulfonic Acid from 0 to 50 °C

Daming Feng,[1] W. F. Koch,* and Y. C. Wu

National Institute of Standards and Technology, Gaithersburg, Maryland 20899

HEPES (*N*-2-hydroxyethylpiperazine-*N'*-2-ethanesulfonic acid) has been recommended as a pH buffer for physiological measurements. The pH values for this buffer system, at ionic strengths similar to those in physiological fluids, have been determined at temperatures from 0 to 50 °C by the emf method. The influence of NaCl on this buffer and the liquid junction potential associated with this salt have been evaluated. Thus, the practical, operational pH value can be ascertained. The second dissociation constant of HEPES has been determined, and the thermodynamic properties have been calculated.

INTRODUCTION

In recent years, HEPES (*N*-2-hydroxyethylpiperazine-*N'*-2-ethanesulfonic acid), $HOCH_2CH_2$–$NHCH_2CH_2$–$N(CH_2CH_2SO_3H)CH_2CH_2$, has attracted attention as a pH buffer of physiological interest. Good et al. first reported its preparation and pK_2 values in 1966 (*1*). Vegas and Bates have determined the pK_2 values and corresponding thermodynamic properties of HEPES from 5 to 50 °C (*2*). Taylor et al. (*3*) and Roy et al. (*4*) have determined the pK_2 values in DMSO–water and ethylene glycol–water mixtures. However, suitable pH buffer standards at an ionic strength of 0.16 mol/kg (*m*), for physiological application based on HEPES, have not yet been established.

This paper presents buffers for physiological pH standards: an equimolal 0.08 *m* mixture of HEPES and its sodium salt (NaHEPESate), buffer I; and the same mixture with 0.08 *m* sodium chloride added to match the ionic strength of the physiological media, buffer II. Both of the buffers have pH values of about 7.5 at 25 °C, close to the pH value of physiological fluids. In addition, an equimolal 0.05 *m* mixture of HEPES and NaHEPESate, buffer III, and an equimolal 0.05 *m* mixture of HEPES, NaHEPESate, and NaCl, buffer IV, are presented.

To determine pH values from 0 to 50 °C, values of electromotive force (emfs) for the following cell

Pt, H_2 (1 atm)|HEPES (m_1), NaHEPESate (m_1), NaCl (m_2)|AgCl, Ag

without lifquid junction, have been measured. From this data, the second dissociation constant may be evaluated with the

* Author to whom correspondence should be addressed.
[1] Current address: Guangzhou Institute of Non-ferrous Metals, Guangzhou, People's Republic of China.

assumption that the activity coefficient of an undissociated molecule is unity, as has been done previously (2–4). However, the undissociated molecule of HEPES is a zwitterion and has a large dipole moment, although the overall charge is neutral. The activity coefficient of this molecule is not equal to 1, but rather is a function of its own molality (5, 6). Moreover, the dipolar molecule also exerts influence on the activity coefficient of an added neutral salt (5, 6) such as NaCl. Both effects are small at low concentration, and hence the influence on the pK value is negligible. However, those effects on the pH value at 0.05 and 0.08 m are appreciable and are illustrated below.

The influence of a neutral salt, NaCl, on this zwitterionic buffer differs from that of an ionic buffer. This difference is demonstrated in flowing junction experiments.

THEORY

HEPES is generally in the form of a zwitterion, a dipolar molecule ($Z^{\pm}$). The first dissociation is from the sulfonic acidic group, and the second dissociation is from the protonated amino group. It is customary to add an equivalent amount of NaOH to the HEPES to form hydroxysodium HEPEsate (abbreviated ZOH^- or simply Z^-) to obtain the second dissociation constant, K_{2A}, which controls the ionization equilibrium. The thermodynamic process is described as follows:

$$ZOH^- = Z^{\pm} + OH^- \quad (1)$$

$$K_B = \frac{a_{Z^{\pm}} a_{OH^-}}{a_{ZOH^-}} = \frac{a_{Z^{\pm}} K_w}{a_{ZOH^-} a_{H^+}} = \frac{m_{Z^{\pm}} \gamma_{Z^{\pm}}}{m_{ZOH^-} \gamma_{ZOH^-}} \frac{K_w}{a_{H^+}} \quad (2)$$

and

$$-\log a_{H^+} = pK_w - pK_B - \log \frac{m_{Z^{\pm}}}{m_{Z^-}} - \log \frac{\gamma_{Z^{\pm}}}{\gamma_{Z^-}}$$

or

$$pH = pK_{2A} + \log \frac{m_{Z^-}}{m_{Z^{\pm}}} + \log \frac{\gamma_{Z^-}}{\gamma_{Z^{\pm}}} \quad (3a)$$

where $pK_{2A} = pK_w - pK_B$, m is concentration expressed as molality, a is activity, and γ is the molal activity coefficient. The emf obtained from cell I may be used to obtain K_{2A} as follows:

$$E = E^\circ - k \log a_H a_{Cl} \quad (4)$$

or

$$E' \equiv (E - E^\circ)/k + \log m_{Cl} = -\log a_{H^+} - \log \gamma_{Cl^-} \quad (5)$$

The substitution of eq 3 into eq 5 yields

$$E' = pK_{2A} + \log \frac{m_{Z^-}}{m_{Z^{\pm}}} + \log \frac{\gamma_{Z^-}}{\gamma_{Z^{\pm}} \gamma_{Cl^-}} \quad (6)$$

Since the dissociation of ZOH^- (Z^-) is small ($\sim 10^{-7}$ m), then $m_{Z^-} = m_1 - m_{OH} = m_1$; and $m_{Z^{\pm}} = m_1 + m_{OH^-} = m_1$. Equation 6 reduces to

$$E' = pK_{2A} - \log \gamma_{Z^{\pm}} + \log \gamma_{Z^-}/\gamma_{Cl^-} \quad (7)$$

where $\log \gamma_{Z^-}/\gamma_{Cl^-}$ is a function of the ionic strength (I). If $\gamma_{Z^{\pm}}$ is unity, as is customarily assumed for undissociated neutral molecules, then eq 7 may be used to obtain pK_{2A} by plotting E' vs I and extrapolating to $I = 0$. The intercept to the ordinate is pK_{2A}. On the other hand, if $\gamma_{Z^{\pm}}$ is not unity, then the intercept will be $pK_{2A} - \log \gamma_{Z^{\pm}}$.

The activity coefficient of a dipolar molecule as a function of its own concentration has been discussed by Cohn and Edsall (5) and analyzed theoretically by Scatchard and Kirkwood (6). Accordingly, it is necessary to measure the emf of another set of cells in which m_{NaCl} is varying but $m_{Z^-}/m_{Z^{\pm}}$ is constant. Thus, in each cell the total ionic strength is varied at a given $m_{Z^{\pm}}$. Equation 7 still applies. There will be one intercept for each $m_{Z^{\pm}}$, which is $pK_{2A} - \log \gamma_{Z^{\pm}}$ for that $m_{Z^{\pm}}$. If $\log \gamma_{Z^{\pm}} = 0$, all of the intercepts would converge into one, i.e., pK_{2A}. The unmerging intercepts indicate that $\log \gamma_{Z^{\pm}} = f(m_{Z^{\pm}})$; at low $m_{Z^{\pm}}$, a linear term of $m_{Z^{\pm}}$ is sufficient. A plot of ($pK_{2A} - \log \gamma_{Z^{\pm}}$) vs $m_{Z^{\pm}}$ extrapolated to $m_{Z^{\pm}} = 0$ will yield a true pK_{2A} at the intercept, and the slope is the linear term constant, α, i.e., $-\log \gamma_{Z^{\pm}} = \alpha m_{Z^{\pm}}$. By substitution of this quantity into eq 7, it becomes

$$E'' \equiv E' - \alpha m_{Z^{\pm}} = pK_{2A} + \log (\gamma_{Z^-}/\gamma_{Cl^-}) \quad (8)$$

E'' is a linear function of I at low ionic strength, and K_{2A} is the thermodynamic dissociation constant for HEPES. From this, the set of thermodynamic properties may be derived after determining the temperature coefficient of K_{2A}.

The Derived pH. Equation 3 shows that with $m_{Z^-} = m_{Z^{\pm}}$

$$pH = pK_{2A} - \log \gamma_{Z^{\pm}} + \log \gamma_{Z^-} \quad (3b)$$

for pure HEPES, or

$$pH - \log \gamma_{Cl} = pK_{2A} - \log \gamma_{Z^{\pm}} + \log (\gamma_{Z^-}/\gamma_{Cl^-}) \quad (9)$$

for HEPES with added sodium chloride to increase the ionic strength.

From eq 8, let

$$\log (\gamma_{Z^-}/\gamma_{Cl^-}) = \beta I \quad (10)$$

Since $\log \gamma_{\pm NaCl}$ is known to be influenced by the dipolar molecule, Cohn and Edsall (5) have demonstrated that the activity coefficient of NaCl in glycine solution is

$$m_{NaCl} = 0, \quad \log (\gamma_{NaCl}/\gamma_{NaCl}^\circ) = -0.14173 m_{Z^{\pm}} + 0.03234 m_{Z^{\pm}}^2 \quad (11)$$

$$m_{NaCl} = 0.5, \quad \log (\gamma_{NaCl}/\gamma_{NaCl}^\circ) = -0.04764 m_{Z^{\pm}} - 0.00002 m_{Z^{\pm}}^2 \quad (12)$$

where the superscript, o, indicates pure aqueous solution. No data for NaCl in HEPES was found. It is assumed that they are similar and that $\log \gamma_{Cl}/\gamma_{Cl}^\circ$ is the same as $\log \gamma_{NaCl}/\gamma_{NaCl}^\circ$. Also, a linear interpolation of the first terms on the right of eq 11 and 12 for $m_{NaCl} = 0.05$ is taken to be $-0.13 m_{Z^{\pm}}$, and for $m_{NaCl} = 0.08$, $-0.125 m_{Z^{\pm}}$. Then eq 10 becomes

$$\log \gamma_{Z^-} = \log \gamma_{Cl} + \beta I = \log \gamma_{Cl}^\circ - 0.125 m_{Z^{\pm}} \text{ (or } -0.13 m_{Z^{\pm}}) + \beta I \quad (13)$$

To evaluate $\log \gamma_{Cl}^\circ$, the Debye–Hückel extended equation is assumed; i.e.

$$\log \gamma_i^\circ = -\frac{AI^{1/2}}{1 + BaI^{1/2}} + bI \quad (14)$$

where A and B are Debye-Hückel constants; a and b are adjustable parameters. If $\gamma_{Cl} = \gamma_{\pm NaCl}$ is assumed, then $a = 4.2$ and $b = 0.032$ will fit the experimental data for $\gamma_{\pm NaCl}$ to within ±0.001 unit up to 1 m. The substitution of eq 13 and 14 into 3 and 9 will yield equations for evaluating a set of values of pH for HEPES and HEPES plus NaCl at the desired ionic strength.

EXPERIMENTAL SECTION

Materials. HEPES and sodium HEPESate were obtained from Sigma Co. (St. Louis, MO). A portion of HEPES was recrystallized twice from 80% ethanol. Both purified and unpurified materials were dried in a vacuum oven at 50 °C and assayed by titration with standard sodium hydroxide. The analyses of both samples of HEPES averaged 99.91% pure. NaHEPESate solution was made by neutralizing a portion of the purified HEPES solution with standard sodium hydroxide. SRM 185f, potassium hydrogen phthalate (KHph), SRM 186-I-d, potassium dihydrogen phosphate, SRM 186-II-d, disodium hydrogen phosphate, and sodium chloride (Mallinckrodt, AR) were dried at 120 °C before use. The laboratory distilled water used in this

Table I. emf of the Cell H_2, HEPES (m_1), NaHEPESate (m_2), NaCl (m_3), AgCl, Ag

		E, V						
$m_1 = m_2$	m_3	0 °C	10 °C	15 °C	20 °C	25 °C	37 °C	50 °C
0.02	0.01	0.772 88	0.779 95	0.783 15	0.786 12	0.789 08	0.795 22	0.800 61
	0.02	0.756 91	0.763 39	0.766 29	0.768 98	0.771 61	0.777 05	0.781 70
	0.05	0.736 35	0.742 04	0.744 56	0.746 86	0.749 03	0.753 55	0.757 23
	0.09	0.723 64	0.728 78	0.731 02	0.733 06	0.735 06	0.738 95	0.742 02
	0.14	0.714 52	0.719 27	0.721 32	0.723 14	0.724 95	0.728 34	0.730 95
0.05	0.01	0.774 46	0.781 47	0.784 62	0.787 58	0.790 32	0.796 45	0.801 77
	0.03	0.749 16	0.755 22	0.757 89	0.760 39	0.762 72	0.767 73	0.771 90
	0.05	0.737 77	0.743 39	0.745 85	0.748 16	0.750 23	0.754 72	0.758 36
	0.08	0.727 49	0.732 69	0.734 97	0.737 05	0.738 92	0.742 94	0.746 11
	0.11	0.720 64	0.725 57	0.727 70	0.729 65	0.731 50	0.735 06	0.737 90
0.065	0.065	0.732 45	0.737 72	0.740 10	0.742 24	0.744 31	0.748 33	0.751 67
0.08	0.01	0.775 76	0.782 65	0.785 78	0.788 69	0.791 44	0.797 57	0.802 92
	0.02	0.759 58	0.765 87	0.768 73	0.771 35	0.773 94	0.779 11	0.783 59
	0.04	0.743 97	0.749 69	0.752 24	0.754 59	0.756 84	0.761 36	0.765 22
	0.06	0.734 91	0.740 29	0.742 67	0.744 85	0.746 87	0.751 04	0.754 49
	0.08	0.728 59	0.733 71	0.735 98	0.738 03	0.739 92	0.743 77	0.746 91
0.09	0.09	0.726 34	0.731 26	0.733 44	0.735 42	0.737 37	0.740 89	0.743 94
m_1	$m_2 = m_3$							
0.02	0.01					0.770 88		
0.05	0.01					0.748 05		
0.08	0.01					0.736 56		

experiment was passed through a deionizing column and had a conductivity of less than 1 μS/cm. Stock solutions were prepared by weight. Buoyancy corrections were applied for all masses. The concentration of hydrochloric acid was standardized coulometrically.

Two series of experiments, one with the purified HEPES and NaHEPESate and the other without purification, were performed with the Harned type cell. Also, a series of experiments with flowing junction cell and combination glass electrode–pH meter was performed to compare pH values of HEPES/HEPESate with those of other standard buffers.

Apparatus. The Harned cell

Pt, H_2 (1 atm)|HEPES (m_1), NaHEPESate (m_2), NaCl (m_3)|AgCl, Ag (I)

was used for the emf measurements. The platinum black (hydrogen) electrodes and silver–silver chloride electrodes were identical with those previously used in this laboratory (*7*) and were tested prior to use by measuring their E° in 0.05 *m* hydrochloric acid with $\gamma = 0.8304$ at 25 °C (*8*). The deviations from the standard value for E° were usually less than 0.1 mV. The setup and the temperature control bath have been described in a previous paper (*9*). The temperature was controlled to ±0.01 °C. A flowing junction cell connected to the Harned cell was used to measure the liquid junction potentials and is described in detail elsewhere (*10*). An Orion 701A pH meter and Corning X-EL combination glass electrode were used to measure the pH values for the solutions, and these values were compared with those obtained from emf measurements.

Results. The emf values of cell I from 0 to 50 °C are listed in Table I. The emfs of the following cells with flowing junction were measured:

Pt, H_2 (1 atm)|HEPES (m_1), NaHEPESate (m_2), NaCl (m_3)||KCl (satd)|Hg_2Cl_2, Hg (II)

Pt, H_2 (1 atm)|phosphate buffer||KCl (satd)|Hg_2Cl_2, Hg (III)

and

Hg, Hg_2Cl_2|KCl (satd)||NaCl (*m*)|AgCl, Ag (IV)

The results will be discussed later.

Values for pK_{2A} and pH. pK_{2A}. The results listed in Table I can be used with eq 7 to determine pK_{2A} by extrapolating E' vs I to $I = 0$. The intercepts represent the quantity of $pK_{2A} - \log \gamma_{Z\pm}$, because $\log \gamma_{Z\pm}$, the activity coefficient of the undissociated dipolar molecule being zero charge, is not a function of I as discussed in the theory section. Then, by plotting of ($pK_{2A} - \log \gamma_{Z\pm}$) vs $m_{Z\pm}$ and extrapolation to $m_{Z\pm} = 0$, pK_{2A} is obtained at the intercept and $-\log \gamma_{Z\pm} = \alpha m$, where α is the slope of this plot. Both these plots are shown in Figure 1.

Table II. Second Dissociation Constants of HEPES and Parameters

t, °C	pK_{2A} (this work)	α	β	pK_{2A} (Vega and Bates)[a]
0	7.878	0.38	0.50	
10	7.747	0.30	0.49	7.751
15	7.683	0.27	0.48	7.690
20	7.622	0.22	0.47	7.629
25	7.562	0.20	0.46	7.565
37	7.427	0.15	0.45	
50	7.285	0.08	0.46	7.283

[a] Reference 2.

Table III. Thermodynamic Properties Corresponding to pK_{2A} at 25 °C

	this work	Vega and Bates[a]
ΔG°, kcal mol^{-1}	10.31	10.32
ΔH°, kcal mol^{-1}	4.79	4.87
ΔS°, cal mol^{-1} K^{-1}	−18.52	−18.3
ΔC_p°, cal mol^{-1} K^{-1}	6.26	11

[a] Reference 2.

It is interesting to note that, if those emf values at $m_1 = m_2 = m_3$ were selected, a linear plot of E' vs I of those points, where I is extrapolated to 0, will yield the same pK_{2A}, and $E' = pK_{2A} + bI$, where b is the slope. This process of experiments and treatment of data has been done for obtaining pK_{2A}, because as $I \to 0$, $m_{Z\pm} \to 0$ and therefore $\log \gamma_{Z\pm} = 0$. However, bI should contain the other quantity, $\alpha m_{Z\pm}$; i.e., $bI = \beta I + \alpha m_{Z\pm}$. In this case, by application of eq 8 to all the data listed in Table I and

$$E'' = E' - \alpha m_{Z\pm} = pK_{2A} + \log \gamma_{Z^-}/\gamma_{Cl^-} \quad (8)$$

plotting of E'' vs I, a straight line is obtained, as shown in Figure 2. All the above derived quantities are listed in Table II.

The thermodynamic properties related to the second dissociation of HEPES are shown in Table III.

pH. On the basis of the analyses developed in the theory section, eq 3b is employed to determine pH. The term $\log \gamma_{Z^-}$ of eq 3b is evaluated by eq 13 and 14. The term $\log (\gamma_{Cl}/\gamma_{Cl}^\circ) = -0.125 m_{Z\pm}$ for $m_{Z\pm} = 0.08$ and $-0.130 m_{Z\pm}$ for $m_{Z\pm} = 0.05$ is assumed to be temperature independent, similar to the system

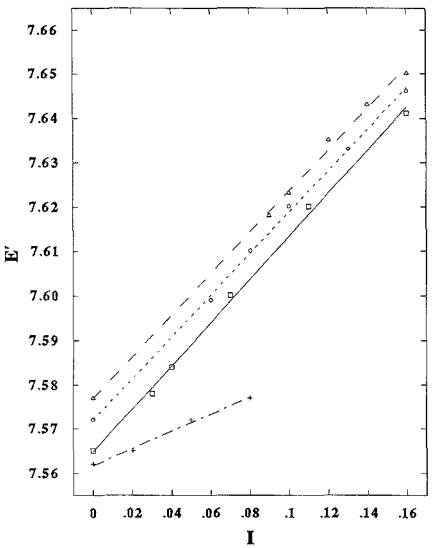

Figure 1. Plots of eq 7 at 25 °C: □, E' vs I for $m_{Z\pm} = 0.02$; ○, E' vs I for $m_{Z\pm} = 0.05$; Δ, E' vs I for $m_{Z\pm} = 0.08$; + (pK_{2A} – log $\gamma_{Z\pm}$ vs $m_{Z\pm}$ at $I = 0$.

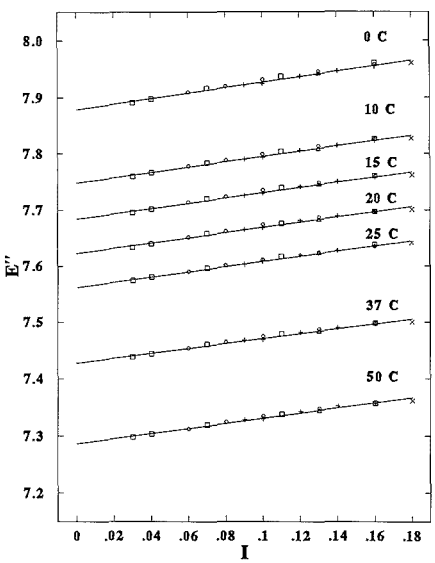

Figure 2. $E' - \alpha m_{Z\pm}$ vs I at temperatures from 0 to 50 °C: □, $m_1 = m_2 = 0.02$; ○, $m_1 = m_2 = 0.05$; Δ, $m_1 = m_2 = 0.065$; +, $m_1 = m_2 = 0.08$; ×, $m_1 = m_2 = 0.09$.

of NaCl–glycine. In eq 14 the term Ba is 1.38 for all the temperatures, 0–50 °C. In this study, however, the b parameter varies with temperature as

$$b = b_{25} + (6.2 \times 10^{-4})(t - 25) - (8.7 \times 10^{-6})(t - 25)^2 \quad (15)$$

These two parameters of eq 14 reproduce the activity coefficients of NaCl up to 1 m to within ±.001 of literature values (*8*). The pH values for the four buffers are computed as shown in Table IV.

Table IV. pH Values of HEPES Buffers at 0–50 °C Computed by Eq 3 and 9

	0.08 m		0.05 m	
t, °C	HEPES, NaHEPESate (buffer I)	HEPES, NaHEPESate, NaCl (buffer II)	HEPES, NaHEPESate (buffer III)	HEPES, NaHEPESate, NaCl (buffer IV)
0	7.839	7.853	7.832	7.834
10	7.700	7.713	7.696	7.697
15	7.633	7.646	7.630	7.631
20	7.568	7.580	7.566	7.566
25	7.504	7.516	7.504	7.503
37	7.359	7.370	7.361	7.360
50	7.213	7.223	7.217	7.215

The pH values are described as a function of temperature in the range 0–50 °C by the following equations:

0.08 m HEPES, 0.08 m NaHEPESate (buffer I):

$$pH = 7.504 - 0.01251(t - 25) + 0.0000348(t - 25)^2$$

0.08 m HEPES, 0.08 m NaHEPESate, 0.08 m NaCl (buffer II):

$$pH = 7.516 - 0.01260(t - 25) + 0.0000344(t - 25)^2$$

0.05 m HEPES, 0.05 m NaHEPESate (buffer III):

$$pH = 7.504 - 0.01229(t - 25) + 0.0000325(t - 25)^2$$

and

0.05 m HEPES, 0.05 m NaHEPESate, 0.05 m NaCl (buffer IV):

$$pH = 7.503 - 0.01237(t - 25) + 0.0000333(t - 25)^2$$

where t is the temperature in °C. The standard deviation for regression for these four equations is 0.0017, 0.0016, 0.0015, and 0.0013, respectively.

The measurement of pH is a practical matter in which the glass electrode–pH meter is commonly used. It is necessary to ascertain that the pH values determined with the Harned cell are compatible with the glass electrode–pH meter measurement. The latter is defined as an operational system, such that

$$pH = pH_S + [(E_X - E_S + \delta E_{J(pH)})/k] \quad (16)$$

with the subscripts X for unknown and S for standard; $k = 0.05916$ at 25 °C, a constant; and $\delta E_{J(pH)}$ is the residual liquid junction potential. The standard buffer used is the physiological phosphate (pH = 7.415). The E_J of this buffer is 2.5 mV, determined from cell III as shown in Table VI.

For the glass electrode–pH meter system, the term $\delta E_{J(pH)}$ is assumed to be zero. For the NBS pH standard buffers this assumption is valid to within ±0.005 pH unit, or ±0.3 mV, the claimed uncertainty. However, when NaCl is added to the phosphate buffer, the change in pH value is substantial (*11*). There is an apparent effect, other than the ionic strength change, of added salt to the pH of a buffer, which may be due to a change of E_J by the added NaCl. However, the influence of E_J by the added NaCl to the HEPES buffers is small. For this reason, a series of experiments with cell II and cell III with a flowing junction was conducted. Emfs of cell IV were measured for evaluating E_J; these results are shown in Table V.

The liquid junction potentials, E_J, are evaluated with the assumption that the single-ion activity coefficients obey the extended Debye–Hückel equation as follows:

from cell IV:

$$E_J = E - E^\circ_{SCE} + E^\circ_{Ag,AgCl} + k \log m_{Cl} + k \log \gamma_{Cl} \quad (17)$$

where

$$\log \gamma_{Cl} = -\frac{AI^{1/2}}{1 + 1.38I^{1/2}} + 0.032I \quad (18)$$

and $E^\circ_{SCE} = -0.2415$ (*12*); $E^\circ_{Ag,AgCl} = -0.22244$ (*9*)

from cell II

$$E_J = E + E^\circ_{SCE} - k\text{pH} \quad (19)$$

Table V. emf of Cells II–IV

Cell II

m_1	m_2	m_3	E, V 5 °C	15 °C	25 °C	37 °C	45 °C
0.08	0.08	0	0.683 69	0.686 07	0.687 60	0.689 04	0.689 20
0.08	0.08	0.08	0.683 40	0.685 30	0.686 65	0.687 99	0.688 37

Cell III

	E, V 5 °C	15 °C	25 °C	37 °C	45 °C
0.008 695 m KH_2PO_4 0.030 43 m Na_2HPO_4	0.670 20	0.676 26	0.682 72	0.691 40	0.697 26
+ 0.02 m NaCl			(0.681 42,[a] ΔpH = −0.022)		
+ 0.05 m NaCl			(0.679 70,[a] ΔpH = −0.051)		

Cell IV

m_{NaCl}	E, V 25 °C
0.005	0.115 91
0.015	0.089 99
0.03	0.073 52
0.05	0.061 89
0.1	0.046 07
0.3	0.021 87

[a] Estimated from ref 11.

where pH values are computed by eq 3 and 9 and are shown in Table IV. The values for E_J are shown in Table VI.

RESULTS AND DISCUSSION

The thermodynamic second dissociation constants of HEPES from 0 to 50 °C were determined with the unpurified materials and checked at a few points with material that was purified by recrystallization. The constants agreed to within ±0.005 pK_{2A} unit and also agreed well with the literature values. The values for thermodynamic properties are also in agreement, except $\Delta C_p°$, which is very sensitive to experimental errors.

To obtain values for pH, it is necessary to know the values of log $\gamma_{Z\pm}$, the activity coefficient of the undissociated HEPES, a dipolar molecule. The first series of measurements, in which $m_1 = m_2 = m_3$, yield values for pK_{2A} (eq 7), because the values for log $\gamma_{Z\pm}$ are concealed by the extrapolating process, due to the fact that when $I = 0$, $m_{Z\pm} = 0$, and therefore, log $\gamma_{Z\pm} = 0$. A second series of measurement were made in which the total ionic strength was varied, but $m_{Z\pm}$ was kept constant, so that when $I = 0$, $m_{Z\pm}$ remains finite. Figure 1 shows clearly that log $\gamma_{Z\pm}$ is a function of its own concentration, as predicted by the theory of Scatchard and Kirkwood (6).

To evaluate the term log γ_{Z^-}, the activity coefficient of the dissociated ion of HEPES, two assumptions have been made. First, the activity coefficient of Cl^- ion behaves the same way as that of NaCl; and second, this coefficient being influenced by the dipolar molecule of HEPES is the same as that of glycine. The first assumption is justifiable in that, if the term log γ_{Na}/γ_{Na} is added to log $\gamma_{Z^-}/\gamma_{Cl^-}$, it becomes log $\gamma_{\pm NaHEPESate}/\gamma_{\pm NaCl}$ by neglecting the small variation due to the dissociated ions. The second assumption is made for lack of data, but the correction is small, amounting at most to 0.01 in the pH at 25 °C.

The values for pH obtained through these treatments at 25 °C are shown in Table VII together with those measured from flowing junction experiments and the glass electrode–pH meter system. A glance at these values shows that there is an apparent discrepancy of about ±0.03 pH unit. However,

Table VI. Liquid Junction Potentials

system		E_J, mV 5 °C	15 °C	25 °C	37 °C	45 °C
physiological phosphate		1.8	2.3	2.5	2.9	3.1
HEPES m(HEPES) = m(NaHEPES)	m(NaCl)					
0.02	0			2.3		
	0.02			1.7		
	0.05			1.2		
	0.1			0.6		
0.05	0			2.2		
	0.02			1.9		
	0.05			1.4		
	0.08			1.0		
	0.1			0.7		
0.08	0	0.6	1.6	2.2	2.4	2.5
	0.02			1.7		
	0.04			1.4		
	0.08	−0.5	0.1	0.5	0.7	1.0
	0.1			0.5		
pure NaCl[a]	m					
	0.005			3.1		
	0.015			2.0		
	(0.02)			(1.9)		
	0.03			1.7		
	0.05			1.2		
	(0.08)			(0.7)		
	0.1			0.5		

[a] Values in parentheses are interpolated.

Table VII. Values for pH at 25 °C

Cell II $m_1 = m_2$	m_3	flowing junction before corr[a]	after corr[b]	glass el[c]	calcd[d]
0.02	0.0	7.509	7.512	7.515	7.513
	0.02	7.489	7.503	7.494	7.503
	0.05	7.477	7.499	7.481	7.499
	0.10	7.470	7.502	7.472	7.503
0.05	0.0	7.496	7.501	7.509	7.503
	0.02	7.491	7.501	7.501	7.501
	0.05	7.483	7.502	7.493	7.503
	0.08	7.481	7.506	7.491	7.507
	0.10	7.479	7.509	7.490	7.511
0.08	0.0	7.497	7.502	7.510	7.503
	0.02	7.490	7.504	7.507	7.505
	0.04	7.487	7.506	7.505	7.507
	0.08	7.480	7.514	7.502	7.515
	0.10	7.485	7.519	7.501	7.520

[a] pH = 7.415 + [(E − 0.68272)/0.05916] where 7.415 is the pH value for physiological phosphate at 25 °C and 0.68272 is the emf of cell III at 25 °C. [b] Calculated by eq 22. E_J values are listed in Table VI. [c] Physiological phosphate taken as standard. [d] Calculated by eq 3, 9, 13, and 14. The related parameters are listed in Table II.

the three sets of pH values were obtained by two different assumptions. The values obtained by the Harned cell without liquid junction are based on those assumptions for evaluating single-ion activity coefficients, as discussed above, and those by cell with flowing junction and by glass electrode–pH meter are based on $\delta E_{J(pH)} = 0$ of eq 16; i.e., the E_J of HEPES in the cell is the same as that of the reference solutions. However, if the pH values obtained from the Harned cell are used to evaluate the E_J from the flowing junction cell for buffers containing NaCl and are compared with the E_J of NaCl in the same cell, as shown in Table VI, they agree to within ±0.2 mV; hence a functional relationship of E_J with m_{NaCl} for HEPES is obtained from values in Table VI with least-squares fit as

$$E_J/\text{mV} = 2.2 - 17m_{\text{NaCl}} \pm 0.1\ \text{mV} \quad (20)$$

Since E_J for the physiological phosphate buffer is 2.5 mV, then the pH values obtained by the operational methods, i.e., the cell with flowing junction and the cell with glass electrode–pH meter, may be corrected by evaluating $\delta E_{J(pH)}$ as

$$\delta E_J = 2.5 - (2.2 - 17m_{\text{NaCl}}) \quad (21)$$

Equation 16 becomes

$$pH_X = pH_S + [(E_X - E_S + \delta E_J)/k] \quad (22)$$

With this δE_J correction, the pH values from the cell with flowing junction and those computed with eq 9 are in agreement to within ±0.005 pH unit, as shown in Table VII. The overall uncertainty is about ±0.015 pH unit, which is caused by the experimental error (about ±0.2 mV) and by the assumptions for the evaluation of the activity coefficients (about ±0.6 mV). The consistency of the three sets of experiments allows one to have confidence in the pH values of HEPES solutions.

LITERATURE CITED

(1) Good, N. E.; Winget, G. D.; Winter, W.; Connolly, T. N.; Izawa, S.; Singh, R. M. M. *Biochemistry* **1966**, *5*, 467.
(2) Vega, C. A.; Bates, R. G. *Anal. Chem.* **1976**, *48*, 1293.
(3) Taylor, M. J.; Pignat, Y. *Cryobiology* **1982**, *19*, 99.
(4) Roy, R. N.; Gibbons, J. J.; Baker, G. E. *Cryo-Lett.* **1985**, *6*, 285.
(5) Cohn, E. J.; Edsall, J. T. *Proteins, Amino Acids and Peptides*; Hafner Publishing Co.: New York, 1965.
(6) Scatchard, G.; Kirkwood, J. G. *Phys. Z.* **1932**, *33*, 297.
(7) Wu, Y. C.; Koch, W. F. *J. Solution Chem.* **1986**, *15*, 481.
(8) Harned, H. S.; Owen, B. B. *The Physical Chemistry of Electrolytic Solutions*; Reinhold Book Co.: New York, 1958.
(9) Wu, Y. C.; Koch, W. F.; Marinenko, G. *J. Solution Chem.* **1986**, *15*, 675.
(10) Wu, Y. C.; Feng, Daming; Koch, W. F. *J. Solution Chem.*, in press.
(11) Bates, R. G. *Determination of pH*; John Wiley & Sons, Inc.: New York, 1954.
(12) Latimer, W. M. *Oxidation Potentials*, 2nd ed.; Prentice-Hall, Inc.: Englewood Cliffs, NJ, 1952.

RECEIVED for review November 14, 1988. Accepted March 8, 1989. Certain commercial equipment, instruments, or materials are identified in this report to specify adequately the experimental procedure. Such identification does not imply recommendation or endorsement by the National Institute of Standards and Technology, nor does it imply that the materials or equipment identified is necessarily the best available for the purpose.

Fluorescence Studies of Energy Transfer in Sodium Taurocholate and Sodium Dodecyl Sulfate Micellar Solutions

Kasem Nithipatikom[1] and Linda B. McGown*

Department of Chemistry, P. M. Gross Chemical Laboratory, Duke University, Durham, North Carolina 27706

The use of micellar reagents to solubilize fluorescent molecules in solution can lead to determination errors if the solubilization is accompanied by promotion of photophysical interactions between the molecules. The fluorescence spectral studies of energy transfer between polycyclic aromatic hydrocarbons described here indicate that sodium taurocholate (NaTC) is less likely than sodium dodecyl sulfate (NaDS) to promote photophysical interactions. Fluorescence lifetime studies and vibronic band ratios of pyrene indicate that the probe microenvironments are less polar in NaTC than in NaDS. Interpretation of these results in terms of structural differences between the bile salt NaTC and the detergent NaDS suggests that (1) the NaTC interior is more closely packed, less permeable to external solution, and better able to isolate probes from each other and (2) NaTC is preferable to NaDS for the solubilization of analytes in direct fluorometric determinations.

INTRODUCTION

Micellar reagents have been used in fluorescence analysis to solubilize hydrophobic molecules in aqueous solution (*1–3*). At low concentrations of solubilized molecules, it is unlikely that more than one molecule will bind per micelle. Multiple occupancy may occur at higher concentrations, thereby increasing the probability of intermolecular interactions such as excited-state complex formation, complexation quenching, and nonradiative energy transfer. Inaccuracy in the determination of a fluorescent compound may arise from any of these processes. In the case of nonradiative energy transfer, error may occur if the analyte is located near another fluorescent molecule that has an excitation spectrum that overlaps with the emission spectrum of the analyte.

We have been investigating sodium taurocholate (NaTC), a trihydroxy bile salt, as a micellar reagent for fluorescence analysis. The aggregation properties and physical characteristics of NaTC are quite different from those of conventional detergents and may prove to be preferable for solubilization of analytes. Specifically, NaTC aggregates are smaller and have lower aggregation numbers than do common detergent micelles, and are therefore less likely to bind multiple probes per micelle. In addition, the structure of the NaTC monomer (*4*) suggests a higher concentration of mass in a more rigidly structured micellar interior, which could provide NaTC with a greater ability to isolate solubilized molecules from the aqueous solution and from each other. In this paper, we describe studies of energy transfer between polycyclic aromatic hydrocarbon (PAH) molecules in aqueous NaTC and sodium dodecyl sulfate (NaDS) solutions, in order to compare the extent of energy transfer in the two different micellar media.

EXPERIMENTAL SECTION

The NaTC (ULTROL grade, >98%) was purchased from Calbiochem, the NaDS (puriss, >99%) was from Fluka, perylene and NaCl (both gold label grade) were from Aldrich, phenanthrene, 9,10-dimethylanthracene (DMA), benzo[*k*]fluoranthene (B*k*F), and pyrene were from Ultra Scientific, and 9-methylanthracene (9MA) was from Molecular Probes. All of the compounds were used without further purification. Stock solutions

*Author to whom correspondence should be addressed.
[1]Present address: Department of Chemistry and Biochemistry, Texas Tech University, Lubbock, TX 79409.

0003-2700/89/0361-1405$01.50/0

Table I. Energy-Transfer Parameters (6) and Aqueous Solubilities (7) of the PAH Compounds

donor	acceptor	R_0, Å	C_0, mM	spectral overlap, 10^{-15} cm^6/mol	solubility,[a] μM
phenanthrene	DMA				7.2/0.27
phenanthrene	9MA	23	37	8.59	7.2/1.4
phenanthrene	9PA	24	32	11.20	
pyrene	perylene	33	12	31.34	0.72/0.0012
pyrene	B&F				0.72/0.003
9MA	perylene	36	9	46.46	1.4/0.0012
B&F	perylene				0.003/0.0012

[a] Aqueous solubilities of donor/acceptor.

of the PAH compounds were prepared in absolute ethanol. All aqueous solutions were prepared in demineralized, HPLC-grade water. Stock solutions of NaTC and NaDS in water, with or without NaCl, were prepared fresh each day. Solutions of the PAH compounds in NaTC or NaDS were prepared by gently evaporating the ethanol from the appropriate volume of the PAH stock solution, diluting with the NaTC or NaDS stock solution in a volumetric flask, and sonicating for at least 1 h. Solutions were not deoxygenated.

Fluorescence spectral and lifetime measurements were made with an SLM 48000S multifrequency, phase modulation spectrofluorometer (SLM Instruments, Inc., Urbana, IL), with a 450-W xenon arc lamp source and photomultiplier tube detectors. The sample chamber was maintained at 25.0 ± 0.1 °C. Fluorescence excitation and emission spectra were collected with 1-nm scanning intervals, in the "10-average" mode, in which each measurement is the average of 10 samplings made over a 3-s interval. For each donor/acceptor pair in NaTC or NaDS, spectra were recorded for the donor, the acceptor, and the donor/acceptor mixture. The individual spectra of the donor and the acceptor were subtracted from the spectrum of the donor/acceptor mixture, producing a fluorescence difference spectrum.

Fluorescence lifetimes were determined from the phase shift and demodulation of the emission signal, relative to the modulated excitation beam, at three or more modulation frequencies (5). Each lifetime was determined in the "100-average" mode (100 samplings averaged over a 30-s interval), and each reported lifetime is the average of five determinations.

RESULTS AND DISCUSSION

The donor/acceptor pairs were selected on the basis of nonradiative energy-transfer probability, which can be expressed in terms of several parameters, including R_0, which is the mean distance between donor and acceptor at which the probability for nonradiative energy transfer is equal to the probability of emission, C_0, which is the concentration of acceptor at which there is an average of one acceptor molecule within a sphere of radius R_0 about the donor, and the overlap between the emission spectrum of the donor and the excitation spectrum of the acceptor. The relative orientation of the transition dipoles of the donor and acceptor molecules is also an important factor. In micellar systems, the probability of energy transfer will depend upon the location and concentration of the donor and acceptor in the micelles and on their orientation and freedom of motion at the binding sites. Aqueous solubility of the donor and acceptor may be an important factor in determining their relative location and distribution within the micellar solutions and could therefore also affect the energy-transfer probability. Energy-transfer parameters (6) and aqueous solubilities (7) are listed in Table I for the donor/acceptor pairs used in our studies.

Energy Transfer in NaTC and NaDS and Dependence on Acceptor Concentration. Spectra are shown in Figure 1 for five different donor/acceptor pairs, each with a given donor concentration and three or more different acceptor concentrations, in NaTC and NaDS. The concentration of the micellar reagents, expressed in terms of total monomer added, is 30 mM for both NaDS and NaTC, which is well above the critical micelle concentration (cmc) for both reagents (8.1 mM for NaDS (8) and ca. 12 mM for the "quasi-cmc" of NaTC (9, 10)). The spectra for a given donor/acceptor pair are all normalized to the spectrum of the donor in NaDS to eliminate effects due to variations in quantum yield and molar absorptivity in the different media and are shown on the same intensity scale to permit direct comparisons between spectra in NaTC and those in NaDS. As discussed above, each spectrum is the difference between the mixture spectrum and the spectra of the individual components (donor and acceptor in NaTC or NaDS, at the same concentrations as in the mixture). The difference spectrum, therefore, indicates only those spectral features that result from mixing the donor and acceptor together and does not include any fluorescence produced by direct excitation of the acceptor at the wavelengths used to excite the donor. The subtraction also eliminates any contributions due to reagent impurities.

The difference spectra contain two different regions, corresponding to the emission spectrum of the donor and, at longer wavelengths, the emission spectrum of the acceptor. In the event of nonradiative energy transfer, the intensity of the emission spectrum of the donor decreases with increasing acceptor concentration, and this portion of the difference spectrum becomes increasingly negative. Other processes that may contribute to a negative difference include (1) a filtering effect, in which the acceptor exhibits significant absorption at the wavelengths used to excite the donor, resulting in a decrease in the exciting light available to the donor, (2) radiative transfer, i.e., reabsorption by the acceptor of light emitted by the donor, and (3) competition for micellar binding sites, resulting in displacement of donor molecules by acceptor molecules.

The region of the difference spectrum corresponding to the emission spectrum of the acceptor is zero in the absence of acceptor and, in the event of energy transfer, increases as acceptor concentration increases. It is interesting that all of the difference spectra have negative regions in the presence of acceptor, but not all of them have significant positive regions. For example, the 9MA/perylene system does not exhibit significant acceptor fluorescence, despite its having very favorable characteristics for energy transfer (long R_0, low C_0, and high spectral overlap) and a large negative difference at the emission wavelengths of 9MA. The absence of nonradiative energy transfer in this system could be due to (1) a large separation between the donor and acceptor molecules, especially in light of the 1000-fold difference between their aqueous solubilities, (2) an unfavorable relative orientation of their transition dipoles in the micellar aggregates, or (3) displacement of the donor from the micelle by the much less soluble acceptor.

In terms of analytical applications of micellar solubilization, the most significant observation from Figure 1 is that the magnitudes of both the negative and positive portions of the difference spectra are greater in NaDS than in NaTC, indicating that solubilization in NaDS is much more likely than in NaTC to promote energy transfer and other photophysical interactions between fluorescent molecules.

Effects of Micelle Concentration and NaCl. Parts a–d of Figure 2 show the difference spectra for the phenanthrene/9MA system at two postmicellar concentrations of both NaTC and NaDS. Significant energy transfer is observed in the phenanthrene–9MA system, despite relatively unfavorable R_0, C_0, and overlap parameters; perhaps the very similar solubilities of the donor and acceptor promote energy transfer in the micelles by locating the two molecules in close proximity. Again, as was the case for the systems shown in Figure 1, energy transfer is significantly greater in NaDS than in NaTC; this is true at both concentrations of NaTC and NaDS.

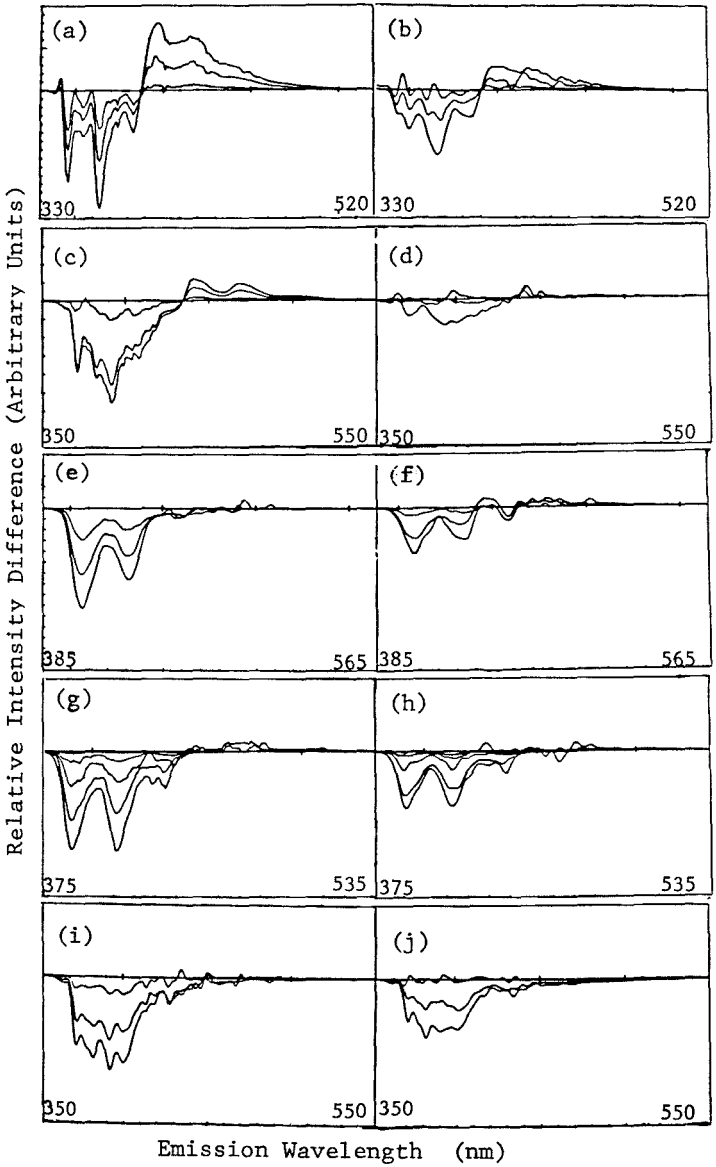

Figure 1. Difference spectra of donor/acceptor systems. Acceptor concentrations in the key correspond to spectra, listed in order of increasing negative/positive spectral magnitudes. Key: (a) phenanthrene (2.5 μM)/9PA (1, 5, 10 μM), in 30 mM NaDS; (b) donor/acceptor as in a, in 30 mM NaTC; (c) pyrene (10 μM)/perylene (2, 10, 20 μM), in 30 mM NaDS; (d) donor/acceptor as in c, in 30 mM NaTC; (e) BkF (2.5 μM)/perylene (1, 5, 10 μM), in 30 mM NaDS; (f) donor/acceptor as in e, in 30 mM NaTC; (g) 9MA (2.5 μM)/perylene (0.5, 1.0, 2.5, 5.0, 7.5 μM), in 30 mM NaDS; (h) donor/acceptor as in g, in 30 mM NaTC; (i) pyrene (5.0 μM)/BkF (1, 5, 10 μM), in 30 mM NaDS; (j) donor/acceptor as in i, in 30 mM NaTC.

For both NaDS and NaTC, the magnitude of the positive portion of the difference spectrum is smaller at the higher concentration of the micellar media, indicating a lower degree of energy transfer at the higher concentration. As micellar concentration increases, the number and/or size of the micelles increases, thereby reducing the number of molecules solubilized within a single micelle and increasing the average distance between donor and acceptor. The magnitudes of the negative portions of the difference spectra, which correspond to phenanthrene emission, are slightly less at the higher concentration. The spectral features in the negative regions are slightly different at the two concentrations, indicating a difference in donor microenvironment.

Figure 2e shows the phenanthrene/9MA system in absolute

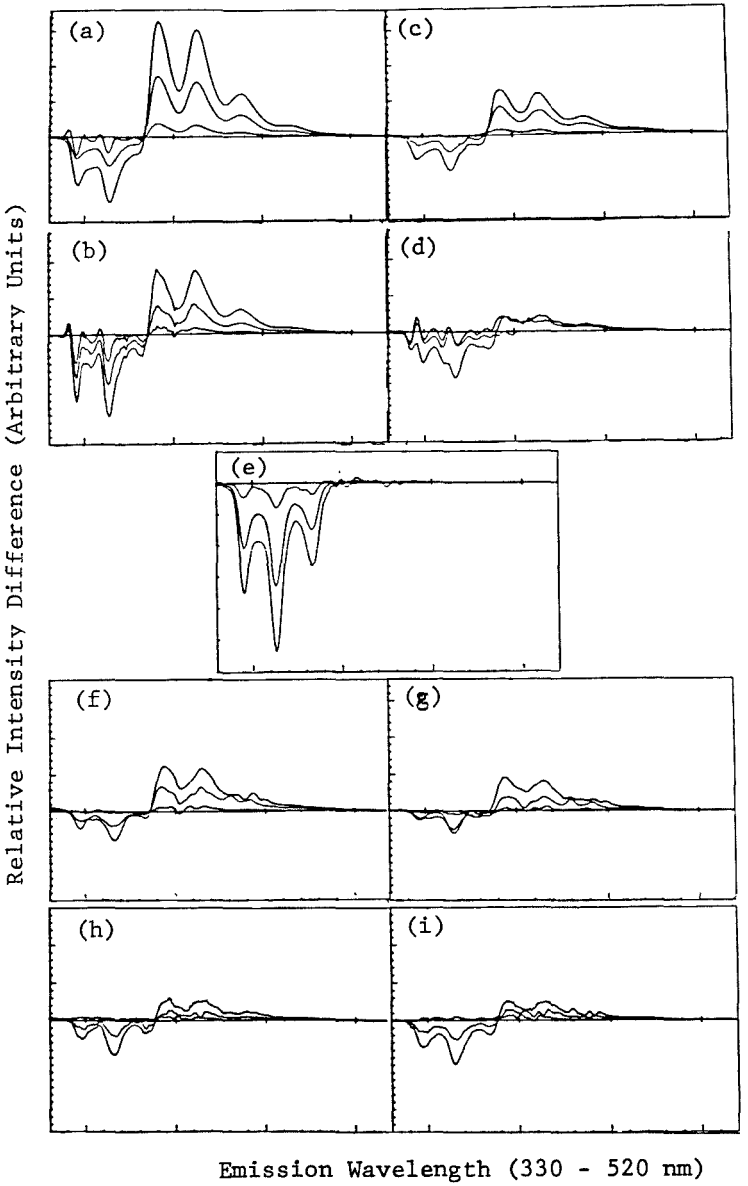

Figure 2. Difference spectra of phenanthrene donor (2.5 μM)/9MA acceptor (1, 5, 10 μM, in order of increasing spectral magnitude). Key: (a) 15 mM NaDS; (b) 30 mM NaDS; (c) 15 mM NaTC; (d) 30 mM NaTC; (e) ethanol; (f) 15 mM NaTC and 0.10 M NaCl; (g) 30 mM NaTC and 0.10 M NaCl; (h) 15 mM NaTC and 1.0 M NaCl; (i) 30 mM NaTC and 1.0 M NaCl.

ethanol, in the absence of micellar media. The magnitude of the negative difference is much greater in ethanol than in any of the micellar solutions, indicating that the acceptor is absorbing at the donor excitation wavelengths (the filter effect, discussed above). No energy transfer is evident in ethanol, which suggests that energy transfer in the micellar media is a nonradiative process.

Parts f–i of Figure 2 show the effect of NaCl on the phenanthrene/9MA system in NaTC. The stabilizing effect of NaCl on NaTC aggregation has been well-described (*11*) and is an important consideration for designing analytical experiments in which NaTC is used for solubilization. At 15 mM NaTC, which is just above the quasi-cmc region, NaCl significantly increases the number and/or size of the NaTC aggregates, thereby decreasing the probability of nonradiative energy transfer and reducing the magnitudes of both the negative and positive portions of the difference spectrum. This is different from the effect of increasing NaTC concentration

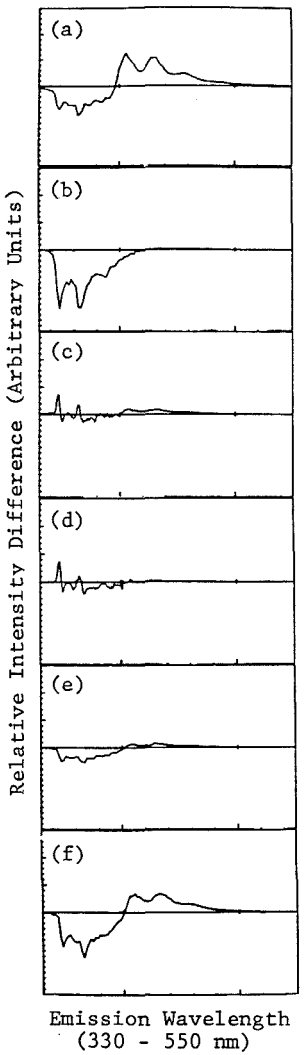

Figure 3. Difference spectra of phenanthrene donor/DMA acceptor (3 μM each, unless otherwise noted). Key: (a) 15 mM NaDS; (b) 15 mM NaTC; (c) 25 mM NaTC; (d) 50 mM NaTC; (e) 15 mM NaTC and 0.50 mM NaCl; (f) same as e but with 5 μM phenanthrene, 5 μM DMA.

in the absence of NaCl (Figure 2c,d), which decreased the magnitude of the positive portion only. It would appear that the aggregates formed in the 15 mM NaTC solution with NaCl are different from those formed in the 30 mM NaTC medium. Effects of NaCl are less noticeable in the 30 mM NaTC solution, which is well above the cmc and less susceptible to the influence of NaCl.

Figure 3 shows the difference spectra for phenanthrene/DMA in 15 mM NaDS, 15 mM NaTC, 25 mM NaTC, and 50 mM NaTC. Spectra are also shown for two concentrations of probe in 15 mM NaTC solutions containing NaCl. A high degree of energy transfer occurs in NaDS, while none is evident in the same concentration of NaTC. Either increasing NaTC to 25 mM or adding NaCl to the 15 mM solution produces

Table II. Fluorescence Lifetimes of Donor in the Presence of Acceptor in 30 mM Micellar Solutions

donor, μM	acceptor, μM	fluorescence lifetime, ns NaDS	NaTC
B*k*F	perylene		
2.5	–	10.6	11.2
	1.0	10.7	11.1
	5.0	10.7	11.5
	10.0	10.7	11.1
pyrene	perylene		
10.0	–	165	290
	2.0	161	290
	10.0	163	290
	20.0	164	291
pyrene	B*k*F		
5.0	–	162	292
	1.0	163	292
	5.0	161	292
	10.0	163	292

Table III. Vibronic Band Intensity Ratio of Pyrene in the Presence of Acceptor in 30 mM Micellar Solutions[a]

donor, μM	acceptor, μM	fluorescence lifetime, ns NaDS	NaTC
pyrene	perylene		
10.0	–	1.194	0.946
	2.0	1.206 (1.0)	0.952 (0.6)
	10.0	1.219 (2.1)	0.953 (0.7)
	20.0	1.221 (2.3)	0.946 (0.0)
pyrene	B*k*F		
5.0	–	1.136	0.940
	1.0	1.138 (0.2)	0.941 (0.1)
	5.0	1.150 (1.2)	0.949 (1.0)
	10.0	1.165 (2.6)	0.954 (1.5)

[a] Intensity ratio of band I (373 nm) to band III (384 nm). The percent change in the ratio, relative to the ratio in the absence of acceptor, is in parentheses.

a small amount of energy transfer, which is increased further in the latter case by increasing the probe concentration. No energy transfer is observed in 50 mM NaTC. Apparently, within a certain NaTC concentration range, or in the presence of NaCl, the NaTC aggregates are able to bind the donor and acceptor within the distance and orientation limits required for energy transfer.

Fluorescence Lifetimes and Vibronic Band Ratios. The fluorescence lifetimes of the donor are shown in Table II for three different donor/acceptor systems. For all three systems, the donor lifetimes are the same in the absence and presence of acceptor, over the entire range of acceptor concentrations studied. This is not surprising, since energy transfer does not occur in any of the systems except pyrene/perylene, which exhibits a small degree of energy transfer in NaDS. More importantly, the donor lifetimes are significantly longer in NaTC than in NaDS, indicating a difference in the microenvironment of the donor between the two micellar media.

A difference in microenvironment between NaTC and NaDS is also indicated by measurements of the vibronic band intensity ratio (band I to band III) of pyrene, which increases as the polarity of the pyrene microenvironment increases (*12*). The ratios, shown in Table III, indicate that the pyrene microenvironment is more polar in NaDS than in NaTC. In both micellar media, the band ratio increases as acceptor (perylene

or BkF) is added to the system. The percent increase is greater in NaDS than in NaTC, which is further evidence of the greater degree of interaction between donor and acceptor in NaDS than in NaTC.

CONCLUSIONS

Of the seven donor/acceptor systems studied in this work, four exhibited energy transfer; in all of the latter cases, energy transfer was promoted to a much greater degree in NaDS than in NaTC. Comparison of the structures of NaDS and NaTC monomers suggests an explanation for the difference between the two media. Typical detergents, such as NaDS, have a hydrophilic head group and a long, hydrophobic tail. Micelles formed by such detergents in aqueous solution are often spherical, with the head groups at the surface, in contact with the external solution, and the tails in the interior. The polarity of the interior depends on several factors, including the permeability of the micelle to the aqueous solution. One can imagine an interior of a large micelle that is only partially filled by the hydrophobic tails, in which the remaining space could be occupied by aqueous solution and solubilized molecules.

In contrast, the NaTC monomer has a relatively small, hydrophilic "head" group and a bulky hydrophobic region. It is reasonable to expect the micellar aggregates of NaTC to have very different structures than those of detergents, with the NaTC structures having a greater internal concentration of micellar bulk, which could decrease the internal capacity for solution from the outside. This supposition is consistent with the experimental results described in this paper, namely, that energy transfer is less likely to occur in NaTC than in NaDS and that the microenvironment of probes solubilized in NaTC is less polar than the corresponding microenvironment in NaDS.

Our results suggest that NaTC is preferable to conventional detergents such as NaDS for solubilization of analytes in direct fluorometric determinations, in order to minimize error due to energy transfer and other photophysical interactions. It is also important that NaCl has little effect on the energy-transfer systems in 30 mM NaTC, indicating that the salt content of a sample will not be an important factor in the determinations. Clearly, it is important to use a sufficiently high concentration of NaTC, in order to completely solubilize the probes and minimize the number of probes per micelle. The presence of NaTC monomer in these solutions should not affect the solubilization or energy-transfer processes. The 30 mM NaTC solutions used in these studies appear to be adequate for total probe concentrations as high as 30 μM.

LITERATURE CITED

(1) Love, L. J. C.; Habarta, J. G.; Dorsey, J. G. *Anal. Chem.* **1984**, *56*, 1133A.
(2) Pelizzetti, E.; Pramauro, E. *Anal. Chim. Acta* **1985**, *169*, 1.
(3) Ramis Ramos, G.; Garcia Alvarez-Coque, M. C.; Berthod, A.; Winefordner, J. D. *Anal. Chim. Acta* **1988**, *208*, 1.
(4) Small, D. M. In *Molecular Association in Biological and Related Systems*; Gould, R. F., Ed.; Advances in Chemistry Series 84; American Chemical Society: Washington, DC, 1968; pp 31–52.
(5) Spencer, R. D.; Weber, G. *Ann. N. Y. Acad. Sci.* **1969**, *158*, 361.
(6) Berlman, I. B. *Energy Transfer Parameters of Aromatic Compounds*; Academic Press: New York, 1973.
(7) Pearlman, R. S.; Yalkowsky, S. H.; Banerjee, S. *J. Phys. Chem. Ref. Data* **1984**, *13*, 555.
(8) Hinze, W. L. In *Ordered Media in Chemical Separations*; Hinze, W. L., Armstrong, D. W., Eds.; American Chemical Society: Washington, DC, 1987; p 4.
(9) Kallay, N.; Colic, M.; Simeon, V.; Kratochvil, J. P. *Croatica Chem. Acta* **1987**, *60*, 555.
(10) Meyerhoffer, S. M.; McGown, L. B., unpublished results.
(11) Kratohvil, J. P.; Hsu, W. P.; Jacobs, M. A.; Aminabhavi, T. M.; Mukunoki, Y. *Colloid Polym. Sci.* **1983**, *261*, 781.
(12) Kalyanasundaram, K.; Thomas, J. K. *J. Phys. Chem.* **1977**, *81*, 2176.

RECEIVED for review January 13, 1989. Accepted March 15, 1989. This work was supported by the United States Department of Energy (Grant No. DE-FG05-99ER13931).

Flow Injection Donnan Dialysis Preconcentration of Cations for Flame Atomic Absorption Spectrophotometry

John A. Koropchak* and Lori Allen

Department of Chemistry and Biochemistry, Southern Illinois University, Carbondale, Illinois 62901-4409

The sample loop of a conventional high-performance liquid chromatography injector is replaced by a coil of tubular cation-exchange tubing, enabling Donnan dialysis to be performed under static conditions while allowing enriched samples to be injected into a flame atomic absorption (FAA) spectrometer at optimum nebulizer flow rates. The receiver solution, containing a high percentage of dissolved solids, is only introduced into the flame for short times, which permits higher receiver concentrations to be used. Short tubing lengths provide higher enrichment, within the limits of sample dispersion, providing a compact dialysis cell. Decreasing the cation-exchange-membrane thickness reduces the dialysis time required for optimum enrichment. For the thin-wall tubing employed herein, 5-min dialyses provide 100-fold enrichment and limit-of-detection (LOD) improvement factors. The approach is demonstrated for the trace determination of lead in drinking water.

* Author to whom correspondence should be sent.

When an ion-exchange membrane separates a high ionic strength solution from a low ionic strength solution, ions of appropriate charge for the membrane are transported from the more concentrated solution to the more dilute solution. Since the membrane is impermeable to co-ions, ions from the dilute solution must diffuse to the more concentrated solution via a process termed Donnan dialysis in order to maintain electroneutrality (*1*). If the volume of the high ionic strength solution (receiver) is small compared to that of the low ionic strength solution (sample), enrichment of the dilute ions results (*2*). This process has been shown to provide essentially matrix independent cation enrichment for samples of low to moderate ionic strength (*2*, *3*) for both flat (*4*) and tubular (*5*) cation-exchange membranes.

Tubular membranes are particularly advantageous since they have high surface area to internal volume ratios and are readily interfaced to various detectors in on-line fashion. Modest success was initially reported for coupling tubular Donnan dialysis on-line with flame atomic absorption (FAA) (*6*); more recently, detailed charcterization of this approach

0003-2700/89/0361-1410$01.50/0

demonstrated signal enhancement factors exceeding 20 with 5-min dialyses for a variety of cations (7). Enrichment factors were shown to increase with tubing length, lower receiver pHs, and temperature (7). Further, the analyte was concentrated into a normalized matrix, in which easily ionizable elements (EIE) could be included for ionization suppression (7). Finally, since co-ions are rejected with Donnan dialysis, interferences such as PO_4^{3-} on Ca^{2+} could be alleviated in an on-line fashion (7). In a later study, this approach was employed with inductively coupled plasma atomic emission spectrometry (ICP-AES); high signal enhancement factors (>50) and alleviation of intra-alkali interferences were reported (8). A further characteristic of this approach was the minimal additional hardware requirements for conducting these experiments (i.e. the tubing, a peristaltic pump, and a stirrer) compared to that required for the normal FAA or ICP-AES experiments.

With either of these previous on-line experiments, receiver solution was continuously pumped through the tubing (bathed in sample solution) and into the nebulizer of the atomizer. Since typical receiver solutions contain 3–10% dissolved solids, this continuous introduction may periodically result in nebulizer, burner, or torch blockage (8). In addition, Donnan dialysis is optimized under static conditions while typical nebulizers are optimized at flow rates of 1–10 mL/min. Consequently, compromised flow rates were required for the on-line experiments (7, 8). In addition, enrichment factors increased with tubing length, which necessitated larger sample volumes and a bulky dialysis cell. Finally, typical turnaround analysis times were on the order of 20 min (7, 8).

Described herein is a flow injection approach to the Donnan dialysis FAA experiment, which is intended to overcome these less desirable characteristics. The coiled, tubular membrane is used as a direct replacement for the injection loop of a conventional sample injector. In this manner, the dialysis is conducted under static flow conditions, while the preconcentrated sample is injected at the optimum nebulizer flow rate and the receiver is introduced only during the injection. Characterization of relevant operating parameters and applications of the optimized experiment to drinking water analysis are described.

EXPERIMENTAL SECTION

The cation-exchange membrane employed for most of the Donnan dialysis experiments was 0.64 mm i.d. × 0.89 mm o.d. tubing of various lengths made of Nafion 811 (Du Pont Polymer Products, Wilmington, DE). For some experiments, a thin-wall Nafion membrane (0.33 mm i.d. × 0.48 mm o.d.) obtained from Perma-Pure Products (Farmingdale, NJ) was employed. The dimensions were for the dry tubing. In either case, the tubular membrane was affixed to a Rheodyne 7125 sample injector as depicted in Figure 1. The membranes were loosely coiled (to maximize solution contact) around a three-prong holder; the tubing ends were inserted into short lengths of 1.6 mm o.d. tetrafluoroethylene (TFE) tubing of appropriate inner diameter to fit snugly around the chosen membrane and were connected to the injector by using 1.6-mm Kel-F fingertight fittings from Upchurch Scientific (Oak Harbor, WA). When the compression type fittings are tightened, effective seals are made, preventing leakage at the operating pressures of the experiment, even with >5 mL/min of liquid flow.

Atomic absorption measurements were made by using a Varian AA-475 with the automatic gas control unit set at 13 L/min air and 1.7 L/min acetylene for Pb analyses and 13 L/min air and 1.4 L/min acetylene for Cu analyses. Analytical wavelengths were 217.0 nm for Pb and 324.7 nm for Cu.

To begin a dialysis experiment, the injector was placed in the LOAD mode and the tubular membrane was manually flushed and filled with the receiver solution (typically 0.5 M $Sr(NO_3)_2$, 1.20 mM $Al(NO_3)_3$, and 0.1 M HNO_3 in deionized, distilled water (DDW)) by using a syringe. The dialysis cell could then be lowered into the stirred sample solution and the dialysis conducted for the appropriate time prior to injection. Carrier solutions were metered with a pulse-dampened Beckman 110B pump. During a dialysis, pure carrier solution was provided to the FAA nebulizer; 5.4 mL/min was typically employed since this was close to the optimum flow rate for direct aspiration. In the INJECT mode the carrier solution was directed through the tubular membrane, flushing the dialysate into the FAA and preparing the membrane for the next dialysis. In general, the carrier solution was pumped through the membrane until the signal returned to the base line. During this flushing, the outside of the membrane was rinsed with DDW.

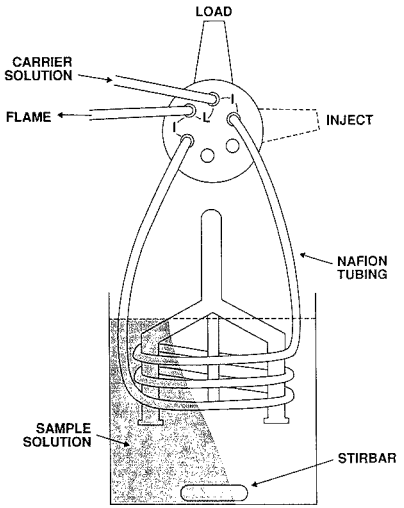

Figure 1. Diagram of the flow injection Donnan dialysis cell.

All solutions were prepared from analytical reagent grade (or better) salts or acids dissolved in DDW or dilute HNO_3. All glassware was scrupulously cleaned to include a final soak in dilute HNO_3 followed by a DDW rinse.

The criteria employed for the selection of cations comprising the receiver solution have been detailed earlier (7).

Limits of detection reported herein are based on $3 \times \sigma$ signal levels.

RESULTS AND DISCUSSION

The evaluation of the experiments described herein is typically reported in terms of enrichment factors (EFs), calculated as the ratio of the signal for the dialysis to the signal for the direct aspiration of the same sample. More precisely, an enrichment factor is defined as the ratio of the analyte concentration in the dialysate to that in the original sample (5). Since all of the EFs in this study were based on measurements of Cu^{2+}, for which signals were not affected by the receiver matrix, the more precise definition is maintained. For certain measurements where dispersion was shown to influence signals, the use of the EF term is less accurate. For consistency however, the EF term was employed throughout the study.

One of the early observations for the flow injection Donnan dialysis (FIDD) FAA experiment was that signals typically exhibited a bimodal peak shape with high time resolution, as shown in Figure 2. These different signals result from essentially two different analyte forms after dialysis: one corresponding to analyte in the receiver solution and a second corresponding to analyte that is affixed to the membrane. The solution-phase analyte is quickly flushed into the FAA upon injection, while ion-exchange reactions are required to remove the bound analyte fraction. If a low ionic strength receiver solution is employed (i.e. DDW), no Donnan dialysis can occur and the first peak disappears. However, the second peak,

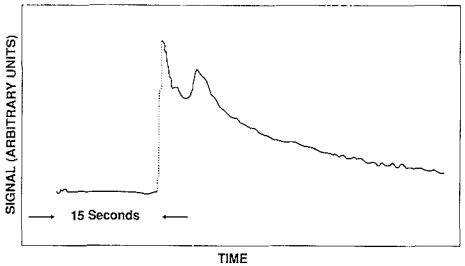

Figure 2. Raw data depicting bimodal signals for 5-min Donnan dialysis of 50 ng/mL Cu^{2+} using 3.25 m of thin-wall Nafion tubing: carrier, 5.4 mL/min 1.0 M HNO_3; receiver, 0.5 M $Sr(NO_3)_2$, 1.3 mM $Al(NO_3)_3$, 0.1 M HNO_3; 350-mL sample volume.

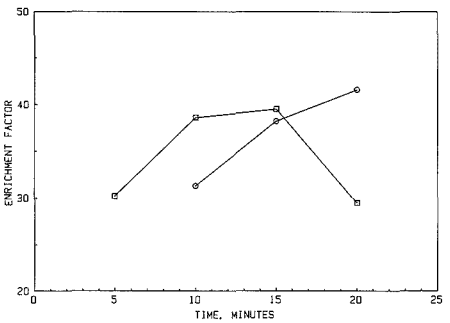

Figure 3. Enrichment factors versus dialysis time for first peak (□) and second peak (○); dialyses of 250 ng/mL Cu^{2+} with 5 m of thick-wall Nafion tubing; other conditions as in Figure 2.

which is largely independent of the receiver solution, remains.

The magnitudes of both peak signals were dependent on the time for the dialysis, as shown in Figure 3. As indicated, maximum signals for the first peak were observed for relatively short dialysis times (≤15 min), while those for the second peak were initially lower and began to exceed signals for the first peak at times greater than 15 min. Since one goal of this work was to provide relatively short analysis times, signals for the first peak were employed in the remainder of these studies for the calculation of enrichment factors. For short dialysis times, the second peak typically appeared as a shoulder to the first peak.

The time for which the maximum signal is achieved for the first peak likely corresponds to the attainment of ion exchange or Donnan equilibrium for the system. The decline in signal for the first peak at later times corresponds to the movement of the system toward the different state of chemical equilibrium. These two states have previously been described for similar solution and cation-exchange membrane systems by Blaedel and Haupert (*9*). The times prior to the achievement of Donnan equilibrium involve primarily the Donnan dialysis process, which has been shown to provide enrichment that is largely matrix independent (*2*), an additional reason to emphasize the signals for the first peak. Signals for the latter process (second peak) would rely on competition between cations for available ion-exchange sites within the membrane.

Since the flow injection approach offered an alternative to the continuous introduction of receiver solution to the FAA, it was felt that more concentrated receiver solution could be tolerated, ideally providing higher mass transport rates and reduced analysis times. Table I indicates the effect of receiver composition on EF for 5-min dialyses of 250 ng/mL Cu^{2+} solutions. The carrier flow rate (5.4 mL/min 1 M HNO_3) was

Table I. Receiver Composition Effects on Enrichment Factors for Cu^{2+}[a]

receiver solution composition	enrichment factor
0.20 M $Sr(NO_3)_2$, 0.5 mM $Al(NO_3)_3$, 0.1 M HNO_3	18.7
0.36 M $Sr(NO_3)_2$, 0.9 mM $Al(NO_3)_3$, 0.1 M HNO_3	28.0
0.52 M $Sr(NO_3)_2$, 1.3 7M $Al(NO_3)_3$, 0.1 M HNO_3	31.8
0.68 M $Sr(NO_3)_2$, 1.7 mM $Al(NO_3)_3$, 0.1 M HNO_3	31.7
0.5 M $Sr(NO_3)_2$, 1.3 mM $Al(NO_3)_3$, 0.1 M HNO_3	28.1
0.5 M $Sr(NO_3)_2$, 1.3 mM $Al(NO_3)_3$, 0.2 M HNO_3	28.2
0.5 M $Sr(NO_3)_2$, 1.3 mM $Al(NO_3)_3$, 0.3 M HNO_3	29.2
0.5 M $Sr(NO_3)_2$, 1.3 mM $Al(NO_3)_3$, 0.4 M HNO_3	25.5

[a] Five-minute dialyses of 250 ng/mL Cu^{2+} from 400-mL samples using a 5-m coil of thick-wall tubing; carrier flow was 5.4 mL/min 0.1 M HNO_3.

Table II. Carrier Stream and Receiver Effects on Enrichment Factors and Analysis Times[a]

carrier compn	receiver compn	enrichment factor	anal. time, min
0.2 M Sr^{2+}, 0.5 mM Al^{3+}, 0.1 M HNO_3	0.2 M Sr^{2+}, 0.5 mM Al^{3+}, 0.1 M HNO_3	38.7	≫8
0.1 M HNO_3	0.2 M Sr^{2+}, 0.5 mM Al^{3+}, 0.1 M HNO_3	25.9	≫8
1.0 M HNO_3	0.2 M Sr^{2+}, 0.5 mM Al^{3+}, 0.1 M HNO_3	22.5	8
1.0 M HNO_3	0.52 M Sr^{2+}, 1.3 mM Al^{3+}, 0.1 M HNO_3	46.7	<5

[a] Ten-minute dialysis of 250 ng/mL Cu^{2+} from 400-mL samples using a 5-m coil of thick-wall tubing; carrier flow rate was 5.4 mL/min.

the same as the aspiration rate for direct analyses. Varied in these experiments were the concentrations of $Sr(NO_3)_2$ and $Al(NO_3)_3$ (as multiples of our previous receiver—0.2 M $Sr(NO_3)_2$, 0.5 mM $Al(NO_3)_3$) and pH (as HNO_3 concentration). As shown in the table, increasing the receiver concentration about 2.6 times provided a 70% increase in signal while increases in receiver pH had little effect on the results for 5-min dialyses. Consequently, the receiver composition employed for the remainder of these studies was a 0.5 M $Sr(NO_3)_2$, 1.2 mM $Al(NO_3)_3$, 0.1 M HNO_3 solution. No problems of nebulizer or flame blockage were encountered with this concentration receiver (~11% dissolved solids) during any subsequent studies.

Although the signals resulting from the second peaks described earlier were considered of lesser analytical utility than those corresponding to Donnan dialysis, these signals represented a limitation to the turnaround time for the use of a particular membrane cell. In order to prepare the membrane for the next analysis, prevent contamination of the next sample, and reestablish a base-line signal, this residual analyte must be efficiently removed from the membrane. Since this removal is primarily dependent on exchange reactions with cations in the carrier stream, a variety of carrier stream compositions were evaluated as indicated in Table II. The analysis times indicated correspond to the times from injection to the reestablishment of the original base-line signal. For the combination of the 1.0 M HNO_3 carrier and the 0.5 M $Sr(NO_3)_2$, 1.2 mM $Al(NO_3)_3$, 0.1 M HNO_3 receiver, the turnaround times were on the order of 2–3 min. Further, no analyte carryover was indicated by the absence of any signal for the dialysis of blank solutions following the dialysis of standards. This combination was therefore employed for the remainder of these studies.

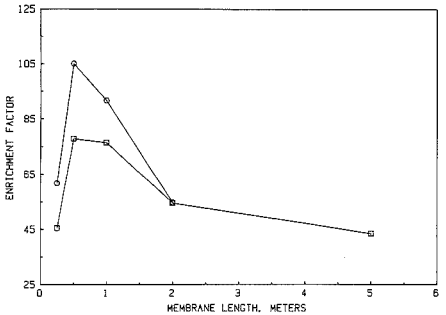

Figure 4. Enrichment factor versus Nafion tubing length for high-dead-volume (□) and low-dead-volume (○) sample transfer, 10-min dialyses of 50 ng/mL Cu^{2+} using thick-wall Nafion tubing; other conditions as in Figure 2.

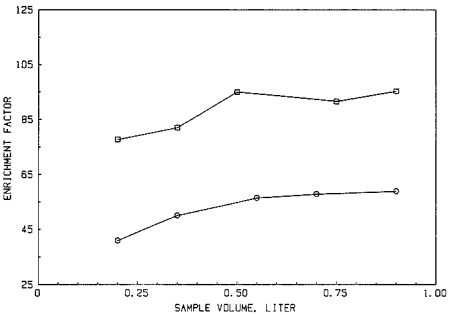

Figure 5. Enrichment factor versus sample volume for 1.0- (□) and 2.0-m (○) thick-wall Nafion tubing lengths; other conditions as in Figure 2.

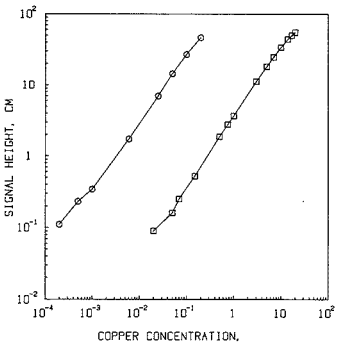

Figure 6. Calibration data for 10-min Donnan dialyses (○) and for direct aspiration (□); 1 m of thick-wall tubing; other conditions as in Figure 2.

Enrichment factors obtained for Cu^{2+} as a function of tubing length for 10-min dialyses of 50 ng/mL Cu^{2+} are indicated in Figure 4. The lower curve is data obtained for our initial experiment for which the dead volume between the injector and FAA was 0.35 mL. As indicated, enrichment factors improved as the tubing length decreased down to 1 m. The reason for this increase lies with the fact that the sample to receiver volume ratio increases as the tubing length decreases. This contrasts with data for continuous, on-line dialysis (*7, 8*) for which long tubing lengths provided the highest signal enhancement. In those cases, the effective residence time of a particular segment of receiver solution was increased as the length increased. For tubing lengths ≤2 m, the dialysis cell is quite compact.

The trend of enhanced enrichment for shorter tubing lengths was not continued below 1 m for the data in the lower curve of Figure 4. Since the internal volume of this tubing is approximately 320 μL/m, it was felt that dispersion effects might be substantial with tubing lengths less than 1 m. The data for the upper curve were obtained after the dead volume between the injector and FAA had been reduced to 0.013 mL. With this reduced dispersion, the trend for increased enrichment continued to 0.5 m of tubing, indicating the importance of dead volume to these experiments. Also indicated are enrichment factors exceeding 100, obtained with a 10-min dialysis with 0.5-m tubing lengths.

Another factor that can affect Donnan dialysis is the actual sample volume employed, since this affects the sample to receiver volume ratio and the total amount of analyte available. Figure 5 shows the effect of sample volume on EF for two lengths of tubing. In either case, a slight decline in EF for sample volumes less than 500 mL was observed. For highest EFs, sample volumes exceeding this value should be employed. Of further importance, errors in sample volume measurement may affect signal measurement precision and accuracy. Such effects would be small on the basis of Figure 5, especially for sample volumes greater than or equal to 500 mL. To reduce sample handling and preparation requirements, 350-mL sample volumes were used for the remainder of this study.

A limiting factor to the achievement of equilibrium with a membrane system is typically the rate of mass transfer across the membrane. For any membrane type, this rate will be determined by the ionic strength gradient across the membrane, as well as the membrane thickness and other factors (*2*). As indicated in Figure 3, dialysis times between 10 and 15 min provide optimum enrichment for tubing with a 0.25-mm wall thickness (dry). When a thinner wall tubing (0.15 mm) was employed, the optimum dialysis time was reduced to 5 min. All other characteristics of the experiment were essentially identical with those for the thicker membrane, except that 0.8 m of the thin-wall tubing provided the highest enrichment compared to 0.5 m for the thicker tubing. The fact that optimum enrichment was provided with a slightly longer tubing length can be attributed to the smaller internal volume of the thinner tubing (~100 μL/m) and the dispersion effects described earlier.

From the conditions established thus far, calibration data for the Donnan dialysis experiment were determined. Figure 6 compares results for direct aspiration (□) with those for 10-min Donnan dialyses (○) of copper standards. As indicated, the dialysis results were linear, and the primary effect was to shift the calibration curve to a lower concentration range. In this case, a decrease by a factor of about 100 in LOD for Cu^{2+} was demonstrated (down to 0.2 ng/mL). Similar data were typically obtained for other cations. Also indicated in Figure 6 is the independence of FIDD enrichment on sample concentration, as evidenced by the parallel nature of the two calibration curves. This allows calibration data for direct aspiration measurements to be used to calibrate FIDD measurements, with periodic determination of the enrichment factor. Precision for FIDD-FAA was typically 3–5% RSD compared to 1% RSD provided by direct aspiration.

Using a 1-m length of the thick-wall membrane and a dialysis time of 10 min, we studied the effect of sample ionic strength, using $NaNO_3$ or $Pb(NO_3)_2$ as ionic strength adjustors. As reported previously by Cox et al. (*2*) for flat membranes, enrichment factors for FIDD were found to be constant up to sample ionic strengths of 10^{-2}, independent of sample

composition for mixtures of cations. For higher ionic strength solutions, standard addition procedures are recommended (2).

The calculated LOD for Pb^{2+} with the use of FIDD-FAA was about 1 ng/mL. This LOD was of particular interest since the EPA limit on Pb in drinking water was recently lowered to 5 ng/mL. The LOD for direct aspiration FAA was typically 90 ng/mL. To test the applicability of the FIDD-FAA experiment to drinking water analysis, tap water samples were spiked at the 5 ng/mL level and acidified to pH ~3.5. The average recovery of Pb^{2+} was 103 ± 16%, indicating the usefulness of this approach to drinking water analysis.

CONCLUSIONS

Flow injection Donnan dialysis has been shown to be a simple, rapid means for obtaining large (>100) improvements in LOD for flame atomic absorption analysis. The degree of LOD enhancement can be controlled for a particular application through adjustment of the membrane tubing length, dialysis time, sample volume, carrier flow rate, and membrane thickness. Only about 8 min is required (dialysis time plus flush) to obtain near-optimum enrichment factors (~100) with the thin-wall membrane. By the use of multiple dialysis cells, the effective analysis time could be reduced to the time required for signal generation and cell flushing, thus providing high sample throughput (20–30 per hour). Based on the simple hardware requirements, the FIDD approach readily lends itself to automation, unlike more traditional enrichment techniques, such as precipitation or solvent extraction (10). The Donnan dialysis technique also has advantages over ion-exchange preconcentration since enrichment factors have been shown to be comparable for a wide range of cations (2, 4, 7), while those for flow injection ion-exchange procedures have been shown to vary substantially due to differences in cation selectivity coefficients (11). Like Donnan dialysis, ion-exchange preconcentration methods are effectively subject to sample ionic strength limitations (11).

Registry No. Cu, 7440-50-8; Pb, 7439-92-1; water, 7732-18-5.

LITERATURE CITED

(1) Wallace, R. M. *Ind. Eng. Chem. Process Des. Dev.* **1967**, *6*, 423.
(2) Cox, J. A.; Gray, T.; Yoon, K. S.; Kim, Y.; Twardowski, Z. *Analyst (London)* **1984**, *109*, 1603.
(3) Cox, J. A.; Twardowski, Z. *Anal. Chim. Acta* **1980**, *119*, 39.
(4) Cox, J. A.; DiNunzio, J. E. *Anal. Chem.* **1977**, *49*, 1272.
(5) Cox, J. A.; Twardowski, Z. *Anal. Chem.* **1980**, *52*, 1503.
(6) Cox, J. A.; Carnahan, J. W. *Appl. Spectrosc.* **1981**, *35*, 447.
(7) Koropchak, J. A.; Dabek-Zlotorzynska, E. *Appl. Spectrosc.* **1987**, *41*, 1231.
(8) Koropchak, J. A.; Dabek-Zlotorzynska, E. *Anal. Chem.* **1988**, *60*, 328.
(9) Blaedel, W. J.; Haupert, T. J. *Anal. Chem.* **1966**, *38*, 1305.
(10) Mizuike, A. *Enrichment Techniques for Inorganic Trace Analysis*; Springer-Verlag: New York, 1983.
(11) Hartenstein, S. D.; Christian, G. D.; Ruzicka, J. *Can. J. Spectrosc.* **1985**, *30*, 144.

RECEIVED for review January 17, 1989. Accepted March 24, 1989. This research was supported in part by a grant from the Office of Research Development and Administration, SIU-C.

Automated Slurry Sample Introduction for Analysis of a River Sediment by Graphite Furnace Atomic Absorption Spectrometry

M. S. Epstein,[1] G. R. Carnrick, and Walter Slavin*

The Perkin-Elmer Corporation, Norwalk, Connecticut 06859

N. J. Miller-Ihli

U.S. Department of Agriculture, Nutrient Composition Laboratory, Beltsville, Maryland 20705

A prototype automated slurry sample introduction (SSI) system is used with a graphite furnace atomic absorption spectrometer (GFAAS) and Zeeman-effect background correction to determine lead, manganese, arsenic, and iron in a standard reference material (SRM) river sediment (SRM 2704). Different methods of slurry preparation are tested, optimum analysis parameters are determined, and sources of variability in the GFAAS measurements are characterized. Measurement variability is found to increase in proportion to the percent of analyte not extracted into the aqueous phase of the slurry solution and is highly dependent on the homogeneity of analyte distribution in the sample. Analytical results for the four elements determined in SRM 2704 are in good agreement with certified values and confirm the utility of SSI combined with GFAAS for analysis of a complex matrix.

[1] On leave from the Center for Analytical Chemistry, National Institute of Standards and Technology (formerly the National Bureau of Standards), Gaithersburg, MD.

INTRODUCTION

The slurry sampling method of material introduction into a graphite furnace atomizer has been proposed as a rapid and effective technique to reduce the preparation requirements for samples to be analyzed by graphite furnace atomic absorption spectrometry (GFAAS) (1). This paper evaluates the application of an automated slurry sample introduction (SSI) device for the determination of arsenic, iron, manganese, and lead in a National Institute of Standards and Technology (NIST) standard reference material (SRM) river sediment (SRM 2704) (2, 3) by GFAAS, using stabilized temperature platform furnace (STPF) technology (4). The automated slurry sampling system (5) uses a retractable ultrasonic probe for mixing of slurry solutions prior to sampling and deposition into a graphite furnace. The accuracy and precision of the slurry sample introduction system are evaluated, and different methods to prepare the slurry are compared. Sources of experimental variability in slurry sampling are identified and quantitated.

0003-2700/89/0361-1414$01.50/0

Table I. Instrument Conditions Used for Slurry Sampling

parameters	element			
	As	Fe	Mn	Pb
sample size, (μL)	10	5	5	10
wavelength, nm	193.6	346.6	403.1	283.3
spectral bandpass, nm	0.7	0.2	0.2	0.7
radiation source	EDL (8 W)	HCL (12 mA)	HCL (20 mA)	HCL (12 mA)
integration time, s	10	10	10	5
furnace program steps				
drying, °C, s	120, 50	120, 50	120, 50	120, 50
pyrolysis	800, 30	1400, 30	1000, 30	650, 30
cooldown	20, 15	20, 15	20, 15	20, 15
atomize	2100, 10	2400, 10	2200, 10	1800, 5
cleanup	2600, 5	2600, 8	2600, 7	2600, 5
matrix modifier[a]	Ni	Pd, $MgNO_3$	PO_4, $MgNO_3$	PO_4, $MgNO_3$
sonification time, s	15	15	10	10
vortexing time, s[b]			30	30
concn of high std, mg/L[c]	0.1	150	1	0.3
M_0 (obsd)[d]	14	5700	24	17
M_0 (theoret)[d]	15		21[e]	12
measurement precision, %[f]				
std/sample supernate	1.5	4.0	0.9	0.6
slurry	4.5	8.8	4.3	1.2

[a] Composition of matrix modifier in sample solution: Ni = 0.3% nickel; Pd, $MgNO_3$ = 0.06% Pd + 0.04% $Mg(NO_3)_2$; PO_4, $MgNO_3$ = 0.8% $(NH_4)H_2PO_4$ + 0.04% $Mg(NO_3)_2$. [b] Vortexing was only used for slurry sampling of Pb and Mn. [c] Concentration of the highest standard used to establish the calibration curve. [d] Characteristic mass, picograms, for 0.0044 *A* s. [e] Estimated from relative sensitivities given for flame analysis. [f] Typical relative standard deviation of three replicate measurements at the concentration of analyte in the sample.

EXPERIMENTAL SECTION

Instrumentation. All determinations were made on a Perkin-Elmer Model Zeeman 5100 PC atomic absorption spectrometer equipped with an HGA-600 graphite furnace atomizer, AS-60 autosampler, and IBM PC-AT computer. A prototype ultrasonic probe mixer synchronized to the operation of the autosampler, after the design of Miller-Ihli (*5*), was used to suspend sediment particles in the sample cups. The graphite furnace used maximum power heating for atomization with pyrolytic graphite tubes and L'vov platforms. Peak area measurements were used for all analyses. Instrument parameters are summarized in Table I.

Slurry Preparation. Samples were either weighed directly (1–2 mg) into polyethylene autosampler cups or sampled from a vortexed suspension (10–50 mg), as described by Miller-Ihli (*1*). Both methods were employed for studies involving lead and manganese. Since no significant difference in results was observed between the two methods, the simpler method involving direct weighing into the autosampler cups was used for studies of arsenic and iron. Weighing of samples was done on an electronic balance to an accuracy of ±0.01 mg. Each sample was weighed into the appropriate container, and a diluent solution consisting of 5% HNO_3 and 0.04% Triton X-100 was added to the sample in a weight ratio of approximately 1 part sample to 500 parts diluent. Matrix modifiers were also added directly to the samples in the autosampler cups. Standards were prepared from NIST SRM spectrometric solutions or other commercial standards that were certified in weight/volume units (i.e., mg/L). All dilutions were made by using weight aliquots delivered with a micropipet and weighed on an electronic balance. When required for conversion to volume units, densities were determined by replicate measurements of the weight of solution in a calibrated (to contain) 1-mL vessel. The river sediment reference material (SRM 2704) was not dried, but analyzed as received, and corrected for moisture (0.8%) determined on separate samples.

When vortexing and aliquoting procedures were used to prepare slurries for sampling, two aliquots were removed from each slurry preparation and weighed into autosampler cups. Three replicate samples were taken from each autosampler cup for an analysis set, and one or two analysis sets were performed. The fraction of each element extracted into the solvent phase during preparation of the slurry was estimated by allowing the slurry to settle and adjusting the autopipetor tip so that only the solvent phase was sampled.

Design for Evaluation of Sources of Experimental Variability. An analysis of variance (ANOVA) nested design, which analyzes the effect of one or more factors on one response variable (the measured analyte concentration in this case), was used to examine all sources of variability in the GFAAS–SSI system. Figure 1 illustrates the experimental design for (a) the direct weighing procedure and (b) the vortexing and aliquoting procedure. The design was meant to separate sampling variability caused by analyte inhomogeneity from variability due to weighing errors, aliquoting errors, and instrument noise. In the direct weighing procedure, eight 2-mg samples of SRM 2704 were weighed from four different bottles (two samples from each bottle) directly into the autosampler cups. In the vortexing and aliquoting procedure, six 10-mg samples were weighed into plastic test tubes, and two aliquots of each slurry were removed and weighed into autosampler cups. Lead and manganese were chosen as the test elements, since lead was reported by isotope dilution mass spectrometry to be inhomogeneous in SRM 2704, while manganese had been shown to be homogeneous to better than 0.4% RSD for a 1-g sample size by X-ray fluorescence (XRF) (*2*, *3*).

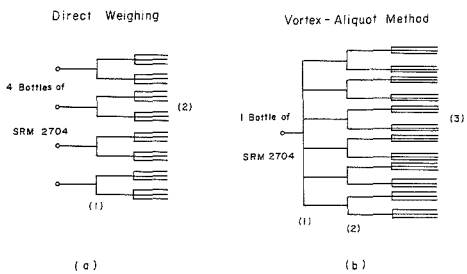

Figure 1. Experimental design for the analysis of variance. (A) Direct weighing: (1) two weighings from each bottle into autosampler cups; (2) three to six instrument measurements of each weighing. (B) Vortex–aliquot method: (1) six weighings into test tubes; (2) two aliquots from each vortexed slurry into autosampler cups; (3) three to six instrument measurements of each aliquot.

RESULTS AND DISCUSSION

Accuracy and Precision of the GFAAS–SSI System. The effect on measurement accuracy of SSI for the GFAAS determination of arsenic, iron, manganese, and lead in SRM 2704 can be assessed from the data in Table II. The analysis results for iron, lead, and manganese are in good agreement

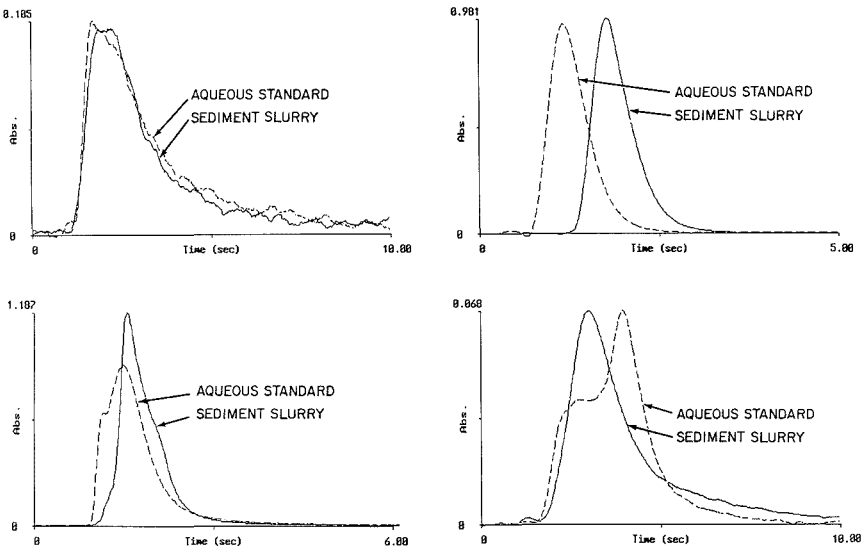

Figure 2. Absorbance versus time profiles for slurry and standard measurements, illustrating differences observed for release of analyte from the solid slurry matrix: upper left panel, Fe; upper right panel, Pb; lower left panel, Mn; lower right panel, As.

Table II. Analytical Results for Slurry Sampling of Sediment (SRM 2704)

elem.	conditions[a]	N^b	$\%E^c$	anal. val, $\mu g/g^d$	certfd val, $\mu g/g$
As	2, DW	8	68	21.7 ± 0.6	23.4 ± 0.8
Fe	2, DW	8	22	40600 ± 1700	41100 ± 1000
Mn	2, DW	8	64	558 ± 18	555 ± 19
	10, VTX	6		558 ± 19	
	50, VTX	3		522 ± 24	
Pb	2, DW	8	88	171 ± 24	161 ± 17
	10, VTX	6		171 ± 35	
	50, VTX	4		165 ± 11	

[a] Sample size is given in milligrams, and methods of preparation are as follows: DW, direct weighing into autosampler cup; VTX, vortex mixing and transfer of slurry into autosampler cup. Samples were diluted in a volume of solution (5% HNO_3 and 0.04% Triton X-100) corresponding to a weight ratio with the sample of 500:1. [b] Number of discrete samples of sediment weighed. [c] Percent of analyte extracted into diluent solution. [d] Uncertainty expressed as confidence limits at a 95% confidence level.

with the certified values for those elements. The analysis result for arsenic is slightly lower than and slightly outside the confidence limits for the certified value. Absorbance versus time profiles of samples and standards for all four elements are shown in Figure 2. Sample and standard peak profiles and appearance times are identical for iron. Profile shapes are identical for lead, but the slurry signal appears about 0.6 s after the standard signal. Manganese profiles vary somewhat in both shape and appearance time. For these elements the STPF conditions have been properly optimized to eliminate bias caused by sample matrix effects. The arsenic absorbance versus time profile for the sediment has not quite returned to the base line, which may cause the small bias observed in the analytical results. Alternatively, the bias may be caused by the loss of arsenic during the charring step, since the nickel matrix modifier cannot interact with the solid slurry component as well as with the solution component.

In general, the precision of results for the analytes that are known to be homogeneously dispersed in the sample (As, Fe, Mn) is equivalent to what might be expected from GFAAS using an acid digestion method of sample preparation. Relative precision, expressed as 95% confidence limits, is 3–4% of the analyte concentration for these elements. The inhomogeneous distribution of lead in SRM 2704 causes the measurement precision to vary from 7 to 15% of the analyte concentration. The inhomogeneity of lead distribution was reported by analysts participating in the certification of SRM 2704 (*4*) and has been suggested to be caused by segregation of lead in specific mineral fractions, such as zircon (*6*).

The precision of the lead measurements reported in Table II is a good indication of the degree of lead homogeneity at the weighed sample size (i.e., 2–50 mg), since almost 90% of lead in the sample is extracted into the solvent phase during the ultrasonic mixing step. When the analyte extraction efficiency is close to 100%, SSI measurement precision is largely determined by the degree of material homogeneity at an "effective" sample size (for homogeneity considerations) corresponding to the total amount of sample weighed to prepare the slurry. For a homogeneously distributed analyte in a finely ground sample, the SSI measurement precision would be expected to approach the precision defined by instrument noise. However, for most "real-world" samples, degree of analyte homogeneity is likely to limit measurement precision.

At low extraction efficiencies, the SSI measurement precision is determined by the degree of homogeneity at a sample size corresponding to only the amount of slurry introduced into the furnace. Since this "effective sample size" will be at least 2 orders of magnitude smaller than the amount of sample weighed into the autosampler cup, the measurement precision would be expected to be significantly poorer for analytes with low extraction efficiency and inhomogeneous distribution in the sample.

The precision of replicate measurements for standards of slurry supernate solutions is contrasted with measurements of the slurries at the bottom of Table I. In all cases, precision is poorer when the analyte is measured in the slurry samples. The difference in the measurement precision of standards compared to that of the slurry samples is a function of the

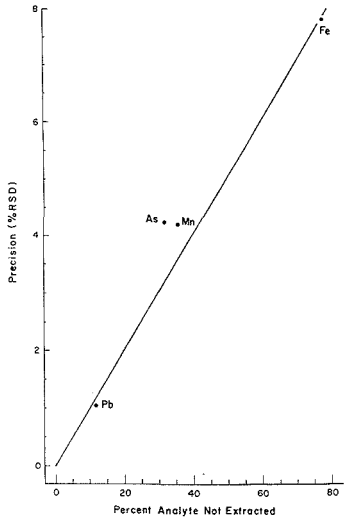

Figure 3. Correlation plot of the measurement precision of slurry sampling versus the percent analyte remaining unextracted after ultrasonic probe treatment of the sample.

amount of analyte extracted into solution, the degree of analyte homogeneity in the sample, and the level of instrument noise. The measurement precision for the standards or slurry supernate solutions shown in Table I can be deconvoluted from the slurry measurement precision by subtracting in quadrature (i.e., the square root of the difference of the squares), assuming the variability of the standard measurements is not related to the variability of the slurry sampling (i.e., independent sources of variability are involved). The resulting precision is due only to sampling of the slurry and is highly correlated with the fraction of unextracted analyte, as shown in Figure 3. This would be the case if the degree of homogeneity for all four elements in the sample was similar. This is not true at large "effective" sample sizes, as illustrated by the analysis results for lead in Table II. However, assuming the lead is distributed as a small number of discrete particles of high lead concentration, the probability of sampling a lead-containing mineral fraction is small at the effective sample size ($\sim$10 μg) aliquoted by the autosampler. Alternately, the lead-containing mineral fraction may be soluble in the HNO_3 diluent. Thus, the measurement variability observed for replicate aliquots from a single slurry preparation will be determined by the homogeneity of the analyte in the insoluble fraction of the sample (e.g. a silicate). In either case, the composition of the insoluble fraction of the slurry appears to be similar for the measured elements, and the degree of homogeneity of that fraction dominates the measurement process.

Direct Weighing versus Vortex Mixing/Sampling. Direct weighing of sample into autosampler cups is preferable to vortex mixing and aliquoting of the slurry into the cups, unless weighing to $\pm$0.01 mg or better is not possible. Vortex mixing and aliquoting will result in a negative bias of results if the extraction efficiency of analyte into the diluent solution is low and the analyte is associated with large particles that settle out of suspension before a representative sample can be taken (*1*). An example of this phenomenon is the low value for manganese in Table II at a 50-mg sample size. The test tube used for the 50-mg samples could not be sampled during vortexing without loss of sample. The slurry had to be aliquoted after vortexing, which resulted in a nonrepresentative sample of manganese. This was not a problem for lead because of the high extraction efficiency. It was also not a problem for the measurements of manganese when the smaller test tube and 10-mg sample weights were used, since that tube could be aliquoted during vortexing.

Table III. Evaluation of Sources of Measurement Variability in GFAAS–SSI

	percentage of the total variability resulting from				
conditions[a]	bulk sampling[b]	aliquoting[c]	instrum measmt	slurry sampling measmt[d]	total measmt
lead, VTX	99.7	0.1			0.2
lead, VTX[e]	96.5	1.2			2.3
manganese, VTX	23.5	7.4			69.1
lead, DW	92.8		1.8	5.4	7.2
manganese, DW	12.6		3.8	83.6	87.4
iron, DW	1.7		20.3	78.0	98.3
arsenic, DW	17.5		9.2	73.3	82.5

[a] Element and slurry preparation method (VTX is vortexing and aliquoting; DW is direct weighing into autosampler cups). [b] Replicate weighing of SRM 2704 into test tubes or autosampler cups. [c] Replicate volumes of RSM 2704 taken from vortexed test tube. [d] Replicate autosampler aliquots of slurry taken from autosampler cup. [e] One very high lead value was rejected in this sample set to note the effect on the ANOVA.

The vortex mixing method of slurry sample would be advantageous when material homogeneity is a critical concern. That method can provide a larger "effective" sample size if the extraction efficiency of analyte into the diluent solution is high. However, if the extraction efficiency is low, the "effective" sample size is the amount of sample aliquoted from the slurry by the autosampler. That "effective" sample size would be similar to one taken by direct weighing, so there would be no advantage to use of the vortex mixing method. Furthermore, the chance of error is also increased due to contamination or aliquoting errors resulting from the increased sample handling required by the vortex mixing method.

Evaluation of Sources of Experimental Variability Using an Analysis of Variance (ANOVA). All sources of variability in the SSI process were examined by using the ANOVA as described in the Experimental Section. Table III shows the percentage breakdown of the sources of variability from the ANOVA obtained for lead and manganese when both vortexing and direct weighing procedures were used and for arsenic and iron with only the direct weighing procedure. Sample-to-sample variability in the bulk sample weighing step is the dominant source of random error for all lead measurement methods, reflecting the material heterogeneity for lead. The principal source of variance in all other cases was the instrumental measurement process. However, the instrumental measurement process (i.e., replicate within-sample measurements) involves components of variance due to both the instrument "noise" *and* the variability in autosampler aliquoting of the slurry. The latter operation is a sampling procedure that depends on the degree of analyte homogeneity in the slurry and the percentage of analyte extracted into the diluent. If the analyte is completely extracted into the diluent, there is no inhomogeneity contribution to the variance of the replicate within-sample measurements. Only the precision of the delivered volume is significant. Alternately, if the analyte is not extracted into the diluent, analyte inhomogeneity will determine the variability of the replicate within-sample measurements, as was demonstrated in Figure 3. By deconvolution of the slurry sampling function from the instrument noise, as described previously, using the measurement precisions shown in Table I, the actual contribution of

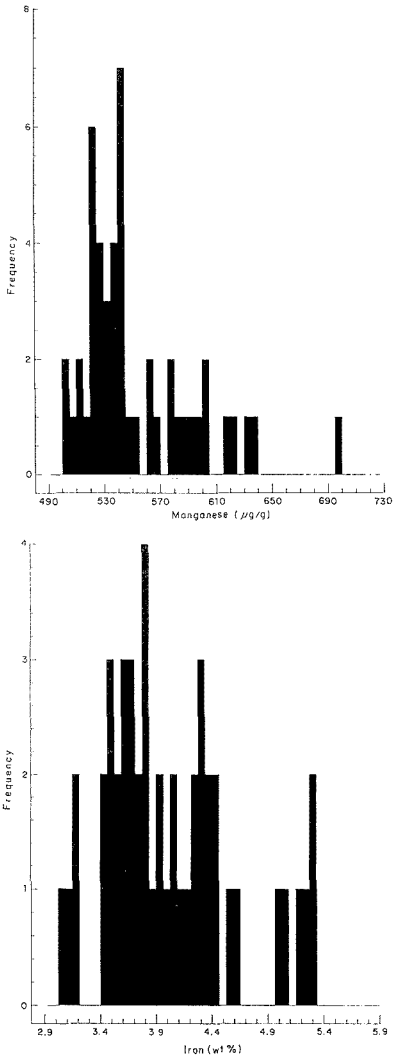

Figure 4. Frequency histograms of data from slurry sampling, illustrating the nonnormal distribution of the data, for (a) Mn (top) and (b) Fe.

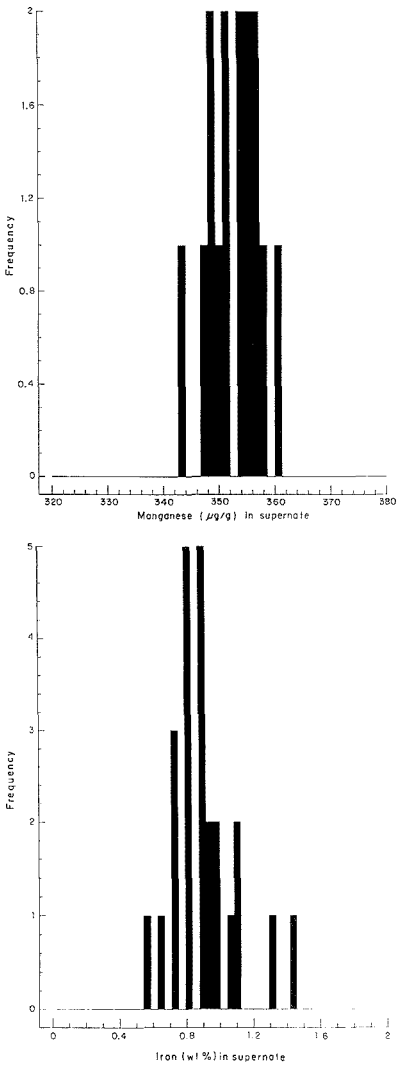

Figure 5. Frequency histograms of data taken by sampling from the supernate above the slurry after treatment with ultrasonic probe and settling of the particles, illustrating the normal distribution of the data, for (a) Mn (top) and (b) Fe.

material inhomogeneity to the total variance can be seen to be greater than 90% in all cases.

Frequency Distributions of Analysis Results from SSI. Figure 4 shows frequency histograms of results from the direct weighing experiments in slurry sampling. The manganese distribution in Figure 4a is severely skewed, and the iron distribution in Figure 4b appears slightly skewed. The distribution for lead was severely skewed, similar to that of manganese, while the arsenic distribution appeared normal. These distributions are similar to histograms of data from geochemical exploration of ore bodies (7). The skewed distributions are characteristic of inhomogeneous analyte distributions, and many of the same principles used in geostatistics may therefore be applicable to data treatment and evaluation in slurry sampling. In contrast to the skewed histograms from the slurry sampling, Figure 5 shows histograms of data from sampling of the supernate from the slurry after the particles have been allowed to settle. Both iron and manganese show normal distributions, which indicate the dominance of instrument noise and the random nature of the extraction process.

CONCLUSIONS

GFAAS–SSI has been shown to be a useful method for very rapid and quantitative evaluation of element concentrations in a complex sediment matrix. The ultrasonic probe mixer allows direct weighing of samples into autosampler cups and adequately suspends the solids for sampling into the graphite furnace. It is also clear that the precision and accuracy of

analytical results obtained by using SSI for GFAAS will be highly dependent on the analyte homogeneity in the sample material. Since this has been shown to be critical for a reference material that has been extensively sieved and blended, it may be a far more serious concern for real samples of more questionable homogeneity. Therefore, to obtain accurate analyses when SSI is used on a material of unknown homogeneity, particularly for elements of low extraction efficiency, a relatively large number of carefully chosen, discrete samples must be taken. A sampling protocol such as described by Ingamells (7) for geological samples will ensure that material homogeneity is properly evaluated and the measured analyte concentration and uncertainty reflect the true values. Such a protocol emphasizes that a relatively large number of discrete samples must be taken to obtain accurate analyses, and that "abnormally" high data points cannot be arbitrarily discarded, as might be done for conventional analytical work.

Registry No. As, 7440-38-2; Fe, 7439-89-6; Mn, 7439-96-5; Pb, 7439-92-1.

LITERATURE CITED

(1) Miller-Ihli, N. J. *J. Anal. At. Spectrom.* **1988**, *3*, 73.
(2) Standard Reference Material 2704 (River Sediment), NIST Certificate of Analysis, National Institute of Standards and Technology, Gaithersburg, MD, 1988.
(3) Epstein, M. S.; Diamondstone, B. I.; Gills, T. E. *Talanta* **1989**, *36*, 141.
(4) Slavin, W.; Carnrick, G. R.; Manning, D. C. *At. Spectrosc.* **1981**, *2*, 137.
(5) Miller-Ihli, N. J. Federation of Analytical Chemistry and Spectroscopy Societies Meeting, Paper 355, Oct. 1987.
(6) Barnes, I. L., National Institute of Standards and Technology, private communication.
(7) Ingamells, C. O.; Pitard, F. F. Applied Geochemical Analysis; John, Wiley and Sons: New York, 1986; Chapter 1.

RECEIVED for review December 27, 1988. Accepted March 23, 1989.

Measurement of Caustic and Caustic Brine Solutions by Spectroscopic Detection of the Hydroxide Ion in the Near-Infrared Region, 700–1150 nm

M. Kathleen Phelan, Clyde H. Barlow,[1] Jeffrey J. Kelly,[1] Thomas M. Jinguji, and James B. Callis*

Center for Process Analytical Chemistry, Department of Chemistry, BG-10, University of Washington, Seattle, Washington 98195

We have explored the feasibility of caustic measurement by direct detection of hydroxide ion using optical absorption spectroscopy in the near-infrared wavelength range 700–1150 nm. Unfortunately, the spectral features of the hydroxide ion are obscured by strong bulk water absorptions whose intensities and peak shapes are dependent upon temperature and the presence of electrolytes. Nevertheless, with the aid of difference spectra, second-derivative techniques, and multivariate spectral reconstruction, we have obtained a clear indication of the spectrum of the hydroxide ion. Its features include (a) a sharp absorption band at 965 nm that arises from the second overtone of the OH stretching motion localized on the hydroxide ion, (b) a broad absorption band centered at 1100 nm that arises from the binding of two water molecules to the hydroxide ion, and (c) a second sharp absorption band that is attributed to a combination stretch–bend transition arising from the concerted motion of the hydrated ion. Using this knowledge as a guide, we have developed multivariate analysis methods for determining hydroxide concentration of caustic brines in the range 0.01–5.0 M that are successful even in the presence of a large variable excess of NaCl. Such methods are suitable for implementation as process monitoring tools.

INTRODUCTION

Measurement of hydroxide concentration in caustic and caustic brine solutions is an important industrial problem. In the past, a number of techniques have been employed for caustic analysis (*1*). Among these methods, pH measurement by glass electrode is most common. However, at high pH, conventional glass electrodes become unstable and begin to suffer from interferences caused by the presence of other cations, most notably sodium (*2*). As a result, other techniques have been developed for caustic determination, such as index of refraction, conductivity, on-line titration, and flow injection analysis. All of the above methods have the drawback that they require physical invasion of the process with some sort of probe or sampling device. In a review on the current status of process analysis, the potential of remote, noninvasive methodologies was described (*3*). One particularly promising approach to noninvasive analysis involves the use of short-wavelength near-infrared (SW-NIR) spectroscopy in the wavelength region 700–1150 nm. This technique has the following advantages: (a) Measurements can be made remotely through quartz windows, using fiber optics to guide the light to and from the window; (b) path lengths can be long (many centimeters); (c) scanning fiber-optic spectrophotometers are available that are rugged, small, and relatively inexpensive (*4*); (d) signal-to-noise ratios are very high; and (e) good quantitative results are obtained on highly scattering samples. The major disadvantage of SW-NIR spectroscopy is low spectral resolution, which results in severe overlap of absorption spectra. This disadvantage is overcome with the aid of multivariate calibration methods (*5*), which usually work well in this spectral region due to the excellent signal-to-noise ratio.

Unfortunately, it is not straightforward to develop a spectroscopic method for determining hydroxide ion concentration because the major spectral features of this ion are expected to overlap the broad bands of water. To make

[1] Permanent address: Department of Chemistry, The Evergreen State College, Olympia, WA 98505.

0003-2700/89/0361-1419$01.50/0

Table I. Composition of Mixtures Analyzed

	set 1	set 2	set 3	set 4
salt				
NaOH, M	0–5.027	0–5.015	0–0.465	0–1.011
NaBr, M				0–1.031
NaCl, M			2.33–3.72	0–1.037
temp, °C	20.8 ± 0.6	25.5 ± 0.2	20 ± 1	26 ± 1
no. of samples	20	11	21	20
reference	air	water	air	water

matters worse, the exact details of the water absorption spectrum in the SW-NIR region remain a matter of some controversy (*6, 7*). In addition, the water spectrum is a strong function of temperature and is affected by the presence of dissolved ions (*8*).

Various types of qualitative studies have been carried out on ions in aqueous solutions (*9–11*). Most research relevant to the present work has been performed in the mid-infrared region and has shown that the symmetric OH vibration of aqueous alkali-metal hydroxide occurs around 3610 cm^{-1}, indicating strong hydrogen bonding from the hydroxide oxygen to a water hydrogen (*12, 13*). At the same time, as the hydroxide concentration rises, an intense continuous absorption grows in the 3000–2000-cm^{-1} region at the expense of the OH stretching vibration (3600–3000 cm^{-1}) of the bulk water (*14*).

Information provided by structural and ionic studies can provide a basis for developing quantitative methods. Hirschfeld (*15*) has used the effects of NaCl on the water bands in the long-wavelength region of the near-infrared (1200–2400 nm)—in particular, the effect of NaCl on the 1450- and 1900-nm water bands—to develop a quantitative method for salinity. Of greatest relevance here is the recent excellent work of Watson and Baughman (*16*), who explored the use of the near-IR spectral region from 1100 to 2500 nm for determining caustic concentration. In this paper, we have extended the spectroscopic approach of Watson and Baughman to a spectral region better suited to in situ measurement, used multivariate calibration methods to improve quantitation, and developed a rationale for the functional basis of the method.

EXPERIMENTAL SECTION

Materials. Sodium hydroxide, sodium chloride, and sodium bromide were all of reagent grade. Water was distilled in-house.

Spectroscopy. Absorption spectra were measured on a Pacific Scientific 6250 scanning near-infrared spectrophotometer equipped with a holographic grating and silicon detector for the spectral region 680–1235 nm. Subsequent manipulations of data sets were limited, however, to 700–1150 nm since excessive stray light interferences were noted above 1150 nm and severe noise increases were observed below 700 nm. Samples were held in a quartz sample cuvette that had a 1.00-cm path length. The spectra are referenced to an air or water blank as noted in Table I. All spectra are the result of an averaging of 50 scans that took approximately 30 s.

Data Analysis. Stagewise linear regression (SLR) (*17*), as supplied by Pacific Scientific Co. (Gardner/Neotec Instrument Division, Stage-Wise Regression Analysis, 1987), was performed to search for correlations between various features in the spectra and the independently measured constituent values, namely, molarity of the solutions. Further analysis was carried out by using the method of partial least squares (PLS), (Veltkamp, D.; Kowalski, B. R.; Center for Process Analytical Chemistry, BG-10, University of Washington, Seattle, 98195; PLS 2-Block Modeling Version 1.0 (IBM), 1986). The selection of the optimal number of latent variables was done by using predictive residual sum of squares plots as provided in the PLS package. The standard error of prediction is from a cross validation estimate (*18*), which uses all but one sample as a calibration set to form a prediction equation, and then a prediction is made of the remaining sample. This "leave-one-out" exercise was repeated for each sample in the training set, and the standard error of prediction was determined from the predicted and actual values for samples omitted. The software for spectral reconstruction was based on algorithms obtained from Lawson and Hanson (*19*) and was programmed by using Microsoft Fortran on IBM and IBM-compatible PC-AT computers.

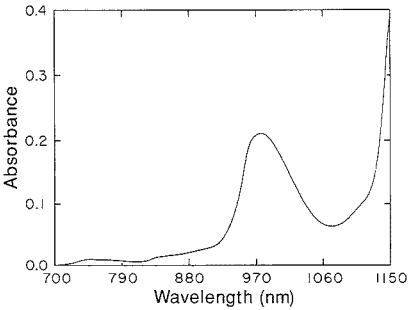

Figure 1. Short-wave near-infrared absorbance spectrum of distilled water referenced to air: path length, 1.00 cm; temperature, 22 °C. Absorption of water at 960 nm is assigned to $2\nu_1 + \nu_3$.

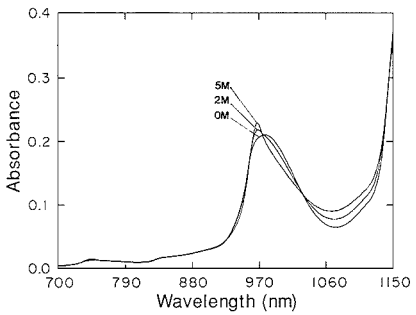

Figure 2. Short-wave near-infrared absorbance of 0.000, 2.040, and 5.027 M NaOH referenced to air: path length, 1.00 cm; temperature, 20 °C.

Solutions. Four sets of experiments were performed in which various combinations and concentrations of the reagents were dissolved in distilled water. In order to assure accurate concentration data, the mass of reagent and the mass of water were recorded to five significant figures. Table I lists the mixtures prepared. Samples were allowed to equilibrate to room temperature before spectra were taken. These temperatures are noted in Table I.

RESULTS AND DISCUSSION

Spectroscopic Assignment. Figure 1 is the short-wave near-infrared (SW-NIR) absorption spectrum of pure water referenced to an air blank. In the spectral region 700–1150 nm, the major feature is a broad asymmetric band centered at 960 nm. This absorption band has been assigned to the combination transition $2\nu_1 + \nu_3$, where ν_1 is the symmetric O–H stretch, ν_3 the antisymmetric O–H stretch, and ν_2 the O–H bending mode. Beginning at 1100 nm, in the pure water spectrum, is the onset of the combination band $\nu_1 + \nu_2 + \nu_3$. The final features that can be discerned are at 740 and 840 nm and are assigned to the combination bands $2\nu_1 + \nu_2 + \nu_3$ and $3\nu_1 + \nu_3$, respectively. These assignments are from ref 6 and 20.

Figure 2 shows three spectra of water with successive additions of sodium hydroxide in the range 0–5 M referenced to air (from data set 1). As the hydroxide concentration increases, one observes a change in shape of the 960-nm band and an increase in the valley region between 960 nm and the

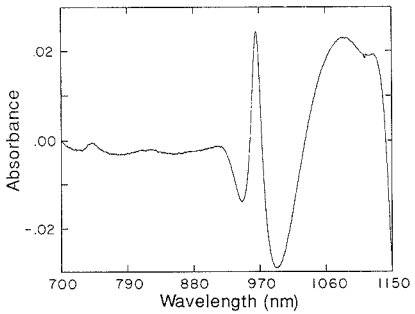

Figure 3. Short-wave near-infrared absorbance of 5.015 M NaOH solution referenced to water: path length, 1.00 cm; temperature, 25 °C. The sharp peak at 965 nm is assigned to the second overtone of the hydroxide stretching motion.

feature beginning at 1100 nm. Isosbestic points are noted at 980 and 1028 nm. However, no new, distinct bands are detectable by eye. This is not unexpected, since the O–H overtone stretching transitions of hydroxide ion are expected to strongly overlap those of water, as has been observed previously in the mid-infrared and near-infrared regions. To further elucidate the hydroxide spectrum, we present in Figure 3 the spectrum of 5.015 M NaOH, now referenced against pure water. This spectrum is from data set 2, which has samples of the same concentration range as data set 1. The spectrum of Figure 3 exhibits two kinds of features: (a) positive going bands, which are due to new absorptions contributed by hydroxide ions, and (b) negative going bands, which are due either to the physical displacement of water molecules by the ions and/or to disruption of bulk water structure. The most notable feature of the hydroxide ion absorption is the very sharp band at 965 nm, which is completely contained within the bulk water envelope. This is assigned to the second overtone of the O–H stretching motion (*21*). The third overtone can also be seen as a positive feature at approximately 740 nm. The broad positive feature in the region 1021–1050 nm is responsible for the "filling in" of the trough between the two major water peaks. It has previously been described as arising from the gradual disruption of the bulk water structure by the hydroxide ion (*12*).

Of interest are the negative absorption bands on either side of the hydroxide band at 965 nm due to the displacement of bulk water. By use of the absorption coefficient of the pure water solution, it was calculated that for every molecule of hydroxide added to the solution, two molecules of bulk water disappeared. This could not be explained by the change in volume of the solution, since the partial molal volume of sodium hydroxide is too small and the effect is of the wrong sign. Thus, we concluded that the two water molecules were no longer participating in the bulk structure, but instead had formed a complex with the hydroxide ion. This new structure could be observed by the increase in intensity in the 1100-nm region.

Since the spectra due to hydrated hydroxide ion and the spectra due to bulk water strongly overlap, we attempted to separate the two spectra by using multivariate statistics (*19*). We began by assembling the various spectra into a response matrix **R** as follows:

$$\mathbf{R} \equiv \{\mathbf{r}_{ij}\} \equiv \{\vec{r}_j\} \tag{1}$$

where the $\mathbf{r}_{ij}$ are the spectral elements indexed by wavelengths i and sample number j. The columns of **R** are the spectra $\vec{r}_j$ of the jth sample. We now assume that the water and hydroxide spectra add linearly and are unaffected by each other. In this case we can represent **R** as

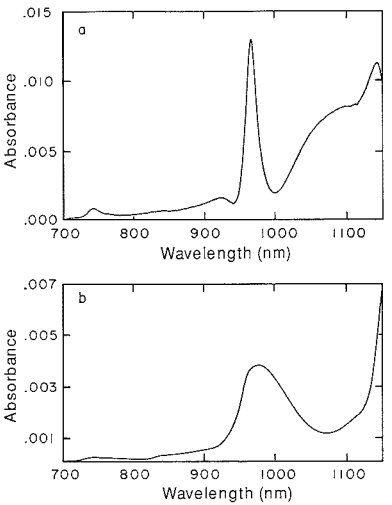

Figure 4. Reconstructed spectra of (a) NaOH and (b) water obtained by using the actual molar concentration of NaOH and the actual molar concentration of water minus 2 times the hydroxide concentration.

$$\mathbf{R} = \mathbf{SC} \tag{2}$$

where

$$\mathbf{S} \equiv \{\mathbf{s}_{ik}\} \equiv \{\vec{s}_k\},$$

and

$$\mathbf{C} \equiv \{\mathbf{c}_{kj}\} \equiv \{\vec{c}_j\} \tag{3}$$

The elements of **S** are the extinction coefficients at the ith wavelength for the kth component, while the elements of **C** are the concentration of the k components for the jth sample. The columns of **S** are the pure component spectra $\vec{s}_k$, while the rows of **C** are concentration of the components for the jth sample. From eq 2, the analytical problem can now be formulated as: Given **R** and **C**, recover **S**, the pure component spectra. In our case $i > j > k$, and the problem is overdetermined. Accordingly, we find an approximation to **S** from a least-squares procedure, i.e., such that

$$\|\mathbf{R} - \hat{\mathbf{S}}\mathbf{C}\|_{\min} \tag{4}$$

where $\hat{\mathbf{S}}$ is the maximum likelihood estimate for **S** (*19*). When eq 2 was solved for **S** under the condition of eq 4, the two spectra of Figure 4 were recovered. The lower spectrum is clearly that of bulk water; the upper spectrum is that of the hydrated hydroxide ion. In Figure 4a, the narrow absorption band at 960 nm is assigned to the second overtone OH stretch centered on the hydroxide ion. The broad feature centered at 1100 nm arises from the combination bands of less strongly bound water molecules.

Surprisingly, there is a second very sharp feature revealed at 1140 nm. This is assigned to a stretch–bend combination band mainly centered on the hydroxide ion, but clearly involving concerted motions of the complex as a whole.

Development of Analytical Method. With a better understanding of the features of the hydroxide ion spectrum, we are now ready to develop a spectroscopic method for hydroxide ion quantitation.

Multilinear Regression. The data set represented in Figure 2 was first analyzed by stagewise multilinear regression (SLR)

Table II. Regression Equation and Performance from Stagewise Regression

data set	math	analyte	α_0	λ_1, nm	α_1	λ_2, nm	α_2	mult R	SEE, M	SEP, M
1	none	NaOH	10.90	964	88.893	980	−138.23	0.999	0.051	0.068
1	2D	NaOH	−3.10	970	−104.89			0.999	0.020	0.044
2	none	NaOH	−0.009	965	110.702	980	−130.577	0.999	0.085	0.113
2	2D	NaOH	0.029	965	−90.011			0.998	0.123	0.146
3	none	NaOH	−12.60	964	170.024	951	−165.134	0.961	0.048	0.050
3	2D	NaOH	−7.202	970	−86.038	811	−241.098	0.981	0.033	0.041
3	2D	NaCl	−5.987	1025	515.116			0.985	0.085	0.0913
4	none	NaOH	0.05	966	25.67	998	−146.22	0.991	0.042	0.048
4	2D	NaOH	0.03	966	−58.56	1135	−57.65	0.998	0.022	0.044
4	2D	NaCl	−0.18	1111	−1530.64	1093	−1947.56	0.844	0.174	0.179
4	2D	NaBr	−0.18	1020	1109.06	896	−1449.37	0.904	0.137	0.141

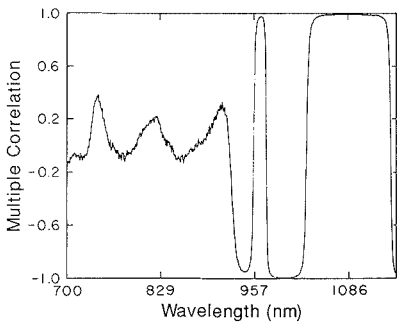

Figure 5. Correlation coefficient versus wavelength for data set 1.

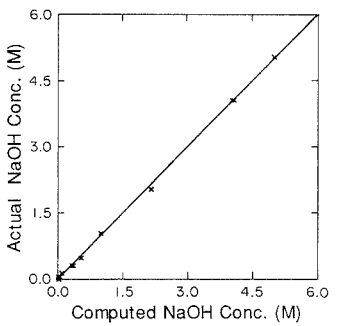

Figure 6. Actual NaOH molar concentration versus SLR predicted NaOH molar concentration for the raw spectra of data set 1.

because this method is rapid and provides "best wavelengths" for routine determination by fixed-wavelength instruments (filter photometers).

The wavelengths chosen also can be subject to a physical rationale for interpretation as to the basis of the analytical method. In determining how reasonable the chosen wavelengths are, we find it useful to display correlation coefficients (multiple R values) for each wavelength in graphical form. When this is done for data set 1, strong negative correlations are seen in those areas where bulk water predominates, and strong positive correlations are seen in the regions of the OH^- band (Figure 5). This data provides excellent supporting evidence for the assignment of the "continuum" region of the spectrum being due to water molecules that are lost from the bulk in binding to the hydroxide ion.

When the stagewise procedure was allowed to select wavelengths over the entire spectral range, the first wavelength selected was associated with the disappearance of bulk water (996 nm). This occurred because the spectral effect of bulk water dilution (or displacement) is larger than the spectral effect of hydroxide addition. However, real-world samples often contain more than two components. Since other solutes can also displace bulk water, this wavelength was rejected and wavelengths were searched for that were positively correlated with the hydroxide absorption band. We found that a more effective choice of wavelengths could be made by examining the reconstructed spectrum of the hydroxide ion (Figure 4). Using this information, we returned to data set 1 and constrained the SLR algorithm to choose a wavelength near the peak of the hydroxide ion (965 nm); in fact it chose 964 nm. The second wavelength selected corresponded to the displacement of water (980 nm). By this means a two-wavelength equation was developed for the data of set 1, which resulted in high correlation (multiple R = 0.999), a low standard error of estimation (SEE = 0.051 M), and excellent predictability by cross validation (SEP = 0.068 M) (see Figure 6). To analyze data set 2, we again constrained the algorithm to the

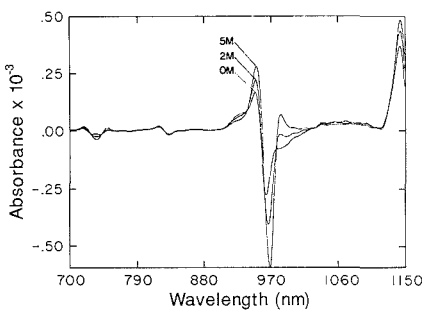

Figure 7. Second derivative of short-wave near-infrared absorbance spectra of 0.000, 2.028, and 5.015 M NaOH referenced to air: path length, 1.00 cm; temperature, 20 °C.

region near the absorption peak of the hydroxide ion. When the algorithm was forced to use the hydroxide overtone at 965 nm as the first wavelength and 980 nm (corresponding to the displacement of water) as the second wavelength, good correlation was again achieved (multiple R = 0.999; SEE = 0.085 M; SEP = 0.113 M). The results are summarized in Table II. The reader will note that the SEP for data set 2 is not as good as that for data set 1. First, referencing to water degrades the signal-to-noise ratio due to the marked temperature dependence of bulk water and problems with reproducing the cuvette position in a blank measurement. Second, the number of samples is small for data set 2. In analyzing these data sets, we noted that the second OH overtone absorption band of hydroxide was much sharper than the underlying water absorption band. Accordingly, we used a second-derivative transformation (segment 10 nm, 0 nm) on the spectra of data set 1 to see if the stagewise procedure would directly select wavelengths that corresponded to hy-

Table III. Regression Performance from PLS[a]

data set	analyte	no. of latent var	R	SEE, M	SEP, M
1	OH	4	1.000	0.014	0.019
2	OH	5	0.999	0.064	0.130
3	OH	4	0.997	0.014	0.024
3	Cl	5	1.00	0.007	0.014
4	OH	3	0.989	0.045	0.069
4	Cl	6	0.941	0.100	0.275
4	Br	5	0.917	0.114	0.194

[a] All data were preprocessed by mean centering.

droxide ion absorption. Figure 7 shows the second-derivative spectra of set 1. Second-derivative smoothing parameters were chosen to yield the greatest sensitivity to sharp spectral features at the expense of broad features. Unfortunately, this procedure did not eliminate the bulk water spectral features, as shown by the 0.0 M NaOH curve. Nevertheless, the first wavelength chosen by stagewise regression corresponded more directly to hydroxide concentration. Use of the second-derivative transformation did lead to a noticeably better prediction error with only a single wavelength.

Partial Least Squares. To supplement the foregoing results, data set 1 was also analyzed by PLS (see Table III). Initially, our conception was that the hydroxide ion–water system could be approximated by two noninteracting components. Accordingly, a PLS model was formed using two latent variables. This resulted in a good fit to the data of set 1 (multiple R = 0.994; SEE = 0.141 M). However, it was noted that the standard error of the estimate obtained with the PLS model with two latent variables was larger than the standard error of the estimate obtained with stagewise regression and two wavelengths. In order to achieve the same magnitude of standard error as that of stagewise regression, PLS required at least three components on mean-centered data, suggesting that the data contains an interaction effect or nonlinearity. Examination of the first three loading plots obtained from data set 1 is very informative (Figure 8). The first latent variable resembles the spectrum of Figure 3, which is essentially the difference between the hydroxide ion and water spectra. This result is exactly what would be expected for a mean-centered single-component linear noninteracting model. However, this model is inadequate, as can be readily seen by examining the second and third latent variables. These appear to be accounting for changes in the number of less tightly bound water molecules as a function of concentration.

Caustic Brine. In real-world analysis, other components are frequently present with caustic. One example is caustic brine. Here, a typical industrial problem is to neutralize the caustic sufficiently so that it can be disposed of safely. At first sight, the presence of variable amounts of sodium chloride might be seen to pose no problem for SW-NIR hydroxide analysis because solid NaCl has no absorption in this region. However, the sodium and chloride ions do exert considerable influence on the water absorption bands in the near-IR region due to rearrangement of the water molecules in the inner solvation sphere (8). In order to assess whether a caustic neutralization analysis could be performed in the presence of a large and varying sodium chloride background, a sample set was made up of 21 solutions where the sodium hydroxide concentration varied in the range 0–0.465 M, while that of sodium chloride varied from 2.33 to 3.72 M. Sample temperatures were allowed to equilibrate to room temperature and were run at 20 ± 1 °C. Figure 9 presents all 21 spectra referenced to the air blank (data set 3, Table I). These spectra are virtually identical. The major variance arises from the irreproducibility in the base line caused by an inability to precisely remove and replace the sample in the spectrophotometer. Nevertheless, with the use of second-derivative transformation, an excellent correlation to NaOH molar concentration was obtained by stagewise multilinear regression (see Figure 10). It should be noted that the wavelengths chosen for data set 3 were similar to those chosen for data set 1. With stagewise regression on the second-derivative spectra of data set 3, a two-wavelength equation resulted that gave a multiple R = 0.981, SEE = 0.033 M, and SEP = 0.041 M. PLS analysis was performed on the raw data, and a good correlation using four latent variables was attained (multiple R = 0.997; SEE = 0.014 M; SEP = 0.024 M).

One of the major benefits of multivariate data is that multicomponent analysis becomes possible. Accordingly, we attempted to correlate both the raw and second-derivative data with concentration of NaCl. Application of the stagewise regression algorithm on the second-derivative spectra gave a multiple R = 0.985 and a SEE = 0.085 M using a one-wavelength equation (see Figure 11). With five latent variables

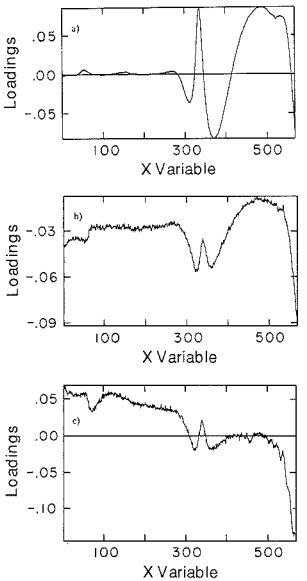

Figure 8. Loading plots of mean-centered data from data set 1 from PLS: (a) X-block loading for latent variable 1; (b) X-block loading for latent variable 2; (c) X-block loading for latent variable 3.

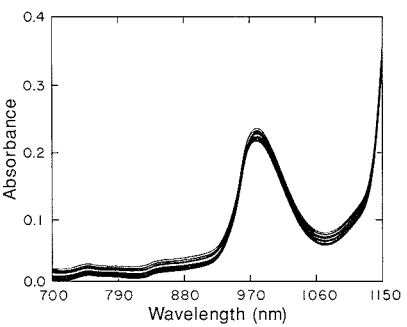

Figure 9. Twenty-one short-wave near-infrared spectra of NaOH and NaCl dissolved in water referenced to air. NaOH concentration ranged from 0 to 0.465 M, and NaCl concentration ranged from 2.33 to 3.72 M; pathlength, 1.00 cm; temperature, 20 °C.

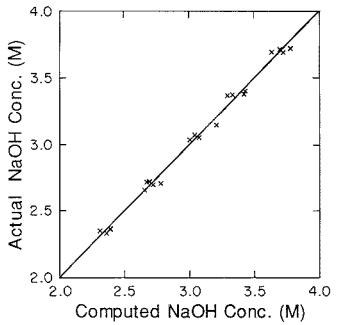

Figure 10. Actual NaOH molar concentration versus SLR predicted NaOH molar concentration from second-derivative data of data set 3.

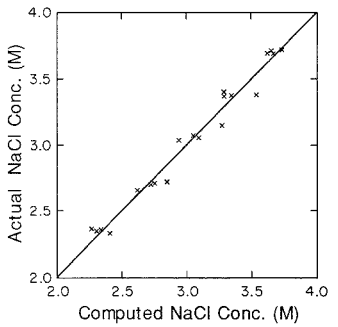

Figure 11. Actual NaCl molar concentration versus SLR predicted NaCl molar concentration from second-derivative data of data set 3.

on mean-centered data, PLS was able to achieve a multiple $R = 1.00$ and a SEE = 0.007 M. We attribute the poor performance of stagewise regression to its inability to confidently choose more than two wavelengths. This point is discussed by Draper and Smith (*17*). With PLS using a cross-validation approach, we could confidently use more latent variables to describe the phenomenon. As an extension of the above analysis, NaBr was added along with NaOH and NaCl to water (data set 4). NaOH concentration ranged from 0.0 to 1 M. Good correlation to hydroxide was attainable with both stagewise regression and PLS. With stagewise regression a two-wavelength equation was obtained for NaBr with a multiple R = 0.900; with PLS, five latent variables were used with mean-centered data to obtain a multiple $R = 0.917$ (see Tables II, III).

CONCLUSIONS

The results we have obtained are significant at several levels. The first is the use of the short-wavelength near-infrared spectral region. This region allows us to use very long path lengths (path lengths of 0.5–5 cm yield absorbancies of 0.1–1.0 at 960 nm) with attendant ease of sampling. Moreover, one can employ inexpensive optics and detectors, and the measurements can be made noninvasively and nondestructively.

The second is the advantage of direct detection of hydroxide ions by spectroscopy. Our method translates absorbance measurements directly into concentration, whereas the pH electrode actually measures activity and is plagued with interferences from other ions at high pH. In addition, one must address the issue of junction potentials and the problem of sampling when using the pH electrode. On the other hand, spectroscopy is not free of environmental effects. The extinction coefficient is not guaranteed to be independent of other analytes. Yet, with multivariate calibration, an analytical method can be developed that is at least robust to known interferences as properly accounted for in the training set. In spite of the apparent nonlinear interaction terms, the SW-NIR method provides excellent measurements of caustic concentration to ±0.05 M in the concentration range 0.0–5.0 M. In the case where full spectrum methods are used, residuals can be a powerful technique for determining whether an input spectrum is sufficiently similar to the original data set. Univariate methods do not have this feature. Multivariate methods also allowed us to reconstruct the hydroxide ion spectrum.

We wish to caution the reader that the water spectrum is temperature dependent and this source of variance must be adequately controlled. When this effect is studied and accounted for, one can not only correct for temperature variations, but measure the temperature accurately as well.

ACKNOWLEDGMENT

We thank Dr. David Burns, University of Washington, Department of Bioengineering, for his help with statistical analysis and Mrs. Louise Rose for her work on the graphic illustrations. We are also grateful to Avi Lorber for useful discussion.

LITERATURE CITED

(1) Clevitt, Kenneth J. *Process Analyzer Technology*; John Wiley and Sons: New York, 1986; pp 506–523.
(2) Christian, Gary. *Analytical Chemistry*; John Wiley and Sons: New York, 1980; p 304.
(3) Callis, J. B.; Illman, D. L.; Kowalski, B. R. *Anal. Chem.* **1987**, *56*, 624A–637A.
(4) Commercial vendors include Pacific Scientific Co., Silver Spring, MD; LT Industries, Rockville, MD. See also Mayes, D. M.; Callis, J. B. *Appl. Spectrosc.* **1989**, *43*, 27–32.
(5) Beebe, K. R.; Kowalski, B. R. *Anal. Chem.* **1987**, *59*, 1007A–1017A.
(6) Buijs, K.; Choppin, G. R. *J. Chem. Phys.* **1963**, *39*, 2035–2041.
(7) Horning, D. F. *J. Chem. Phys.* **1964**, *40*, 3119–3120.
(8) Paquette, J.; Jolicoeur, C. *J. Solution Chem.* **1977**, *6*, 403–428.
(9) Georgiev, G. M.; Kalkanjiev, T. K.; Petrov, V. P.; Nickolov, Zh. *Appl. Spectrosc.* **1984**, *38*, 593–595.
(10) Kleeberg, H.; Heinje, G.; Luck, W. A. P. *J. Phys. Chem.* **1986**, *90*, 4427–4430.
(11) Struis, R. P. W. J.; de Bleijser, J.; Leyte, J. C. *J. Phys. Chem.* **1987**, *91*, 6309–6315.
(12) Giguere, D. A. *Rev. Chim. Miner.* **1983**, *20*, 588.
(13) Busing, W. R.; Horning, D. F. *J. Phys. Chem.* **1961**, *65*, 284.
(14) Moskovits, M.; Michelian, K. H. *J. Am. Chem. Soc.* **1980**, *102*, 2207.
(15) Hirschfeld, T. *Appl. Spectrosc.* **1985**, *39*, 740–741.
(16) Watson, E., Jr.; Baughman, E. H. *Spectroscopy* **1987**, *2*, 44–48.
(17) Draper, N.; Smith, H. *Applied Regression Analysis*; John Wiley and Sons: New York, 1981; p 337.
(18) Sharaf, M. A.; Illman, D. L.; Kowalski, B. R. "Chemometrics". In *Chemical Analysis, A Series of Monographs on Analytical Chemistry and Its Applications*; Elving, P. J., Winefordner, James D., Eds.; Kolthoff, I. M., Ed. Emeritus; John Wiley and Sons: New York, 1986; Vol. 82.
(19) Lawson, C. L.; Hanson, R. J. *Solving Least Squares Problems*; Prentice-Hall, Inc.: Englewood Cliffs, NJ, 1974; p 290.
(20) Bayly, J. G.; Kartha, V. B.; Stevens, W. H. *Infrared Phys.* **1963**, *3*, 221–223.
(21) Wheeler, O. H. *Chem. Rev.* **1959**, *59*, 642–645.

RECEIVED for review September 12, 1988. Revised March 10, 1989. Accepted March 10, 1989. The authors thank the Center for Process Analytical Chemistry and the National Science Foundation for their financial support.

Near-Infrared Laser Diode Intracavity Absorption Spectrometry

Ed Unger and Gabor Patonay*

Department of Chemistry, Georgia State University, Atlanta, Georgia 30303

A simple and inexpensive laser diode intracavity spectrophotometer (LDIS) was constructed from off-the-shelf components. The design has significant advantages over other intracavity laser systems and has the potential to detect analytes at low concentrations compared to those detected with commercial spectrophotometers. The design and control of a compact laser diode intracavity spectrophotometer are discussed. Data are presented to indicate the advantages of intracavity operation.

INTRODUCTION

Laser intracavity spectrophotometry has had limited use in analytical chemistry since its introduction in the 1970s. Harris et al. described an intracavity dye laser in 1980 (*1*), in which intracavity absorbance was determined by an electrooptic cell placed in the cavity. As discussed by Harris and co-workers (*1*), the intracavity effect has three factors that increase its analytical sensitivity. First, there is a very large effective sample path length due to the multipass effect. Second, at the lasing threshold a large change in the laser output power results from a small sample absorption in the laser cavity. Third, there can be mode competition between modes affected by intracavity loss and other modes; if the sample absorbance line width is less than the laser gain bandwidth, the net effect can be reduced output intensity at the absorbed wavelength. Thus, comparing laser output power with an analyte within the cavity and a reference or blank within the cavity can result in analytical data.

Unfortunately, the use of intracavity spectrophotometers has been limited by instability and high cost. Several publications (*2–4*) over the last two decades have addressed the problems involved. While these reports demonstrate the potential of the intracavity method, no practical application has resulted from these early studies. Several methods were developed to obtain analytically useful signals. These methods varied from simple photographic light intensity determinations to more complicated photodiode measurement (*5, 6*). It was noted that the system operation was more reliable when the system operated at a stable lasing condition rather than close to the threshold of lasing.

With the development of laser diodes, a new approach to intracavity spectrometry has become possible, since increased cavity loss may be counterbalanced by simple electrical means. Laser diodes in addition have the advantages of low cost, compactness, light weight, low power consumption, fast direct modulation, and ease of integration with data acquisition systems.

Several analytical and spectroscopic uses of laser diodes and light-emitting diodes (LED) have recently been reported (*7–11*). Camparo and Klimak demonstrated the usefulness of laser diode instrumentation in determining hyperfine structures of atomic systems (*7*). PbSnTe and PbSnSe laser diodes were used by Kim and co-workers to record spectra of small molecules (*8*). Ishibashi and co-workers used laser diode fluorometry to detect very low concentrations of the cyanine dye DDTC (*10*), as well as to detect very low concentrations of human serum proteins by labeling them with cyanine dyes (*11*).

To our knowledge, no publication has described the application of the intracavity technique using laser diodes. It is our goal in this paper to demonstrate that ordinary spectrophotometric procedures can be improved for high-sensitivity determinations via laser diode intracavity spectrophotometry. We describe an LDIS that is compact, inexpensive, and capable of determining the analyte optical absorbance by simple electrical means. We will compare detectable absorbencies of the LDIS to those of commercial UV-visible spectrophotometers.

EXPERIMENTAL SECTION

Optics. A block diagram of the LDIS is shown in Figure 1. The laser diodes used in this study are emitting at 780 nm. Because laser diode beams are poorly collimated, a lens was needed. We chose a gradient index lens (GRIN), purchased from NSF America, SLW 3.0-0.11-C/BC-.78. The collimated beam was passed through a 1-cm quartz sample cell to a reflecting mirror and back through the sample cell and lens to the laser diode active layer. All optical components were secured to a Newport Corp. optical rail, MRL-12, which was secured to a Newport optical breadboard, LS-23. Thus the instrument is an extended double-cavity laser resonator in which the multipass enhancement is partially offset by the reflectivity of the front facet mirror of the laser diode.

Electronics. The laser diode output was measured by a Tenma Model 72-050 digital multimeter. This measured the output of the laser diode as voltage via a monitoring photodiode (PIN) incorporated into the laser diode package. Forward current to the laser diode was monitored by another Tenma multimeter. Power was suppled by a VIZ Model 708A regulated power supply. A drive circuit was constructed to protect the laser diode from excessive current and from transients caused by switching. A potentiometer incorporated into the circuit enabled us to null the PIN output, thus compensating for differences in sample and reference absorbencies. The system was grounded in order to protect the laser diode from static charges. An electronic schematic is shown in Figure 2.

Laser Diodes. Commercial laser diodes are available in low-, medium-, and high-power versions. The high-power versions are usually multistripe devices and therefore less suitable for intracavity applications since these lasers typically have as many as 5–40 cavity stripes. The low- and medium-power versions are usually single-stripe devices; i.e., there is only one active lasing cavity in the semiconductor material. Low-power laser diodes have a medium reflectivity coating ($R = 30\%$) at both facets and are made for consumer applications; optical feedback is intentionally minimized. Thus, low-power laser diodes are less suitable for intracavity applications.

Medium-power versions (30–40 mW) achieve higher optical output by coating the back reflecting surface with a highly reflective multilayer film composed of amorphous silicon and aluminum oxide, while the front facet is coated with a transparent dielectric film of aluminum oxide, which acts as a passivation coating and provides the required reflectivity. This chip structure efficiently directs the laser beam forward out of the chip. The back facet is highly reflective ($R = 95\%$), while the front surface has much lower reflectivity ($R = 5\%$). The medium-power laser diodes are more suitable for intracavity applications due to their highly transparent front reflecting surface. Since the back reflecting surface is only 5% transmissive, the multipass effect is enhanced. With our system, we would expect an enhancement factor of 20 (*12*), based on round trips of 20. We used a Sharp

* Author to whom correspondence should be addressed.

0003-2700/89/0361-1425$01.50/0

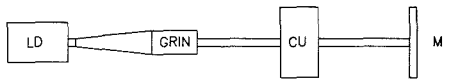

Figure 1. Schematic of the laser diode intracavity spectrometer: LD, laser diode; GRIN, gradient index lens; CU, sample cuvette; M, mirror.

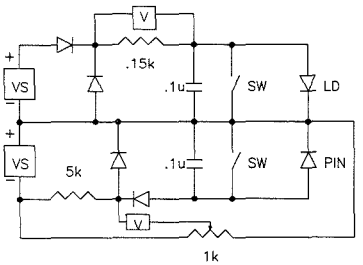

Figure 2. Electronic schematic of the laser diode intracavity spectrophotometer: VS, variable power supply; V, digital voltmeter; LD, laser diode; PIN, monitoring photodiode.

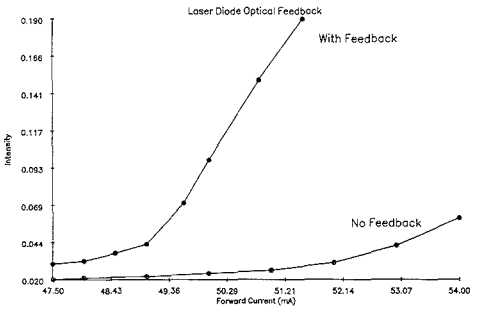

Figure 3. Effect of optical feedback obtained with low-power laser diode.

LTO23MFO as a low-power laser diode (5 mW) and a Sharp LTO24MFO as a medium-power device (30 mW).

Chemicals. Since the wavelength of the LDIS, in its present form, is fixed at 780 nm, we chose analytes that could be detected at this wavelength. We chose silica, tannic acid, phosphorus, and two cyanine dyes, indocyanine green, ICG (CAS 3599-32-4), and 1,1,1′,1′,3,3′-hexamethyl-4,4′,5,5′-dibenzo-2,2′-indotricarbocyanine perchlorate, HDITC (CAS 23178-67-8). The cyanine dyes were purchased from Kodak in laser grade and used as received. Silica was determined by Method 425D in ref 13, normally detected at 815 nm. Tannic acid was detected by Standard Method 513, normally detected at 700 nm. Phosphorus was detected by a variation of the molybdenum blue method first reported by Ishibashi and co-workers (*9*), using hydrazinium sulfate as a reducing agent. The cyanine dye ICG was detected in methanol, where it has an absorbance maximum at 795 nm. HDITC was detected in acidic ethanol, where the absorbance maximum is at 780 nm.

RESULTS AND DISCUSSION

We have observed the effect of optical feedback; i.e., the output intensity vs driving current curves are different when the external cavity mirror was in place. Figures 3 and 4 show the results obtained with the low-power LTO23MFO and the medium-power LTO24MFO laser diodes, respectively. As expected, an increase in the effect of optical feedback was observed as the power of the laser diode is increased, indicating the importance of the reflectivity of the front facet mirror of the laser diode. The integral monitoring photodiode (PIN) in the laser diode package responds to the differing back radiated light energy due to absorbing analytes placed in the extended cavity. A multimeter (Figure 2) interprets the PIN output as voltage. The greater the analyte absorption, the less the output voltage. The calibration curve for phosphorus determination was obtained by using a 1-cm-path-length cuvette and the 30-mW laser diode (Sharp LTO24MFO). The slope was calculated by using least square fit: $V = 9.96c$, where V is the voltage measured on the PIN diode in volts and c is the phosphorus concentration in mg/L. The range of linearity extends up to 0.4 mg/L. At 1 mg/L, there is a deviation of about 10% from linearity.

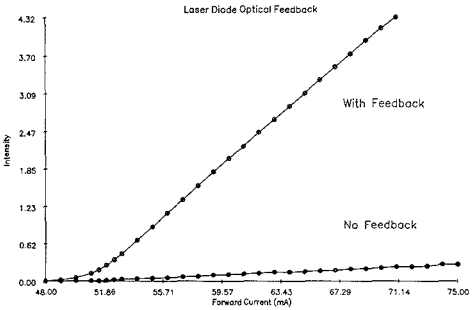

Figure 4. Effect of optical feedback obtained with medium-power laser diode.

Table I. Silica and Tannic Acid Determination Using a 30-mW Laser Diode

silica,[a] mg/L	output, V	tannic acid,[b] mg/L	output, V
0.0	0.06	0.0	0.31
0.001	0.08	0.05	0.38
0.01	0.50	0.25	0.68
		1.00	1.14
		2.00	2.02

[a] $s = 2.284$; $r = 0.998$. [b] $s = 0.0456$; $r = 0.0995$.

Table II. Intracavity Detection of Cyanine Dyes

HDITC,[a] nmol/L	output, V	ICG,[b] nmol/L	output, V
0.0	0.0	0.0	0.0
1.0	0.14	1.0	0.0
2.5	0.36	20.0	0.01
5.0	0.66	50.0	0.03
10.0	1.30		

[a] $s = 0.0020$; $r = 0.999$. [b] $s = 0.000284$; $r = 0.998$.

Table I provides information about the silica and tannic acid data obtained with the LDIS. The detection limits for silica and tannic acid were significantly lower than those reported in the literature (*10*). Table II summarizes the cyanine dye data obtained for the experiments performed in this study. On the commercial spectrophotometer we found an absorbance of 0.522 for a 4.49×10^{-6} molar solution of HDITC. The laser diode system was able to detect an absorbance of 1.06×10^{-4} for 1.0 nmol/L HDITC and gave an output voltage of 0.14 V. The noise level was below 0.01 V, resulting in a 1.2×10^{-5} absorbance noise level well below that of commercially available instruments. ICG could not be detected at concentrations similar to that of HDITC despite similar high extinction coefficients. These data show some disparity among the analytes detected by LDIS. We were able to determine that some of the mechanical perturbation caused by ordinary laboratory events contributed to signal noise. This resulted in the need for frequent readjustment of the optics. However, more research is needed to explain the remaining differences. There is reason to suspect that thermal effects

may occur in the sample cell; photodecomposition of the laser dyes is another possibility. Since the active layer of the laser diode is extremely small, minor changes in the refractive index of the solution can result in drifting of the reflected laser beam. Further studies are planned to determine the extent of this effect.

The described extended intracavity single-beam laser diode spectrophotometer can detect absorbencies as well as or better than many commercial double-beam absorption spectrophotometers. The commercial double-beam spectrophotometer was unable to distinguish between the 1 nmol/L HDITC solution and a 20 nmol/L solution of HDITC from the blank. It was observed that the major noise contributing factor is the optical noise generated by the mechanical instability of the optical mounts. When compared to commercial instruments, the laser diode system proved to be superior. Moreover, it should be noted that this simple arrangement is a single-beam instrument, using only a $160 laser diode as a light source and detector simultaneously.

The detectable absorbencies can be lowered by a number of improvements to the instrumentation. Less reflectivity of the front facet mirror of the laser diode will enhance the multipass effect and therefore increase the effective sample cell path length. If we can decrease the front facet's reflectivity to 1%, it would result in a much greater enhancement factor. Studies using special antireflective coated (AR) laser diodes are currently under development. Output stability can be improved by locking the optical components together. This will allow use of a more sensitive scale on the output multimeter, resulting in a lowering of the detection limits. Further improved detection limits can be expected from using an AR coated laser diode pair where one of the lasers can serve as a reference source. The use of a double-beam instrument as opposed to our present single-beam instrument will compensate for source and detector fluctuations and lower detection limits. The use of batteries instead of a regulated power supply can improve signal stability while reducing the size. The drive circuit can be put on a chip, further reducing the size. The instrument can be tuned to different wavelengths by changing the laser diode temperature or by subjecting it to an adjustable magnetic field. Using a 5- or 10-cm cell will allow for smaller detectable absorbencies. New laser diodes with lower emission wavelengths (a 680-nm device is now available) will extend the analytical utility of the instrument.

LITERATURE CITED

(1) Harris, T.; Mitchell, J.; Shirk, J. S. *Anal. Chem.* **1980**, *52*, 1701–1705.
(2) Peterson, N. C.; Kurylo, M. J.; Braun, W.; Bass, A. M.; Keller, R. A. *J. Opt. Soc. Am.* **1971**, *61*, 746–750.
(3) Klein, M. B. *Opt. Commun.* **1972**, *5*, 114–116.
(4) Thrash, R. J.; Weyssenhoff, H.; Shirk, J. S. *J. Chem. Phys.* **1971**, *55*, 4659–4660.
(5) Childs, W. J.; Fred, M. S.; Goodman, L. S. *Appl. Opt.* **1974**, *13*, 2297–2299.
(6) Green, R. B.; Latz, H. W. *Spectrosc. Lett.* **1974**, *7*, 419–430.
(7) Camparo, J.; Klimak, C. *Am. J. Phys.* **1983**, *51*(12), 1077–1081.
(8) Kim, K., et al. *Proc. Tech. Program, Int. Laser Expo.* Chicago, IL, **1975**, 191-5.
(9) Ishibashi, N.; Imasaka, T.; Kamikubo, T.; Kawabata, Y. *Anal. Chim. Acta* **1983**, *153*, 261–263.
(10) Ishibashi, N.; Imasaka, T.; Yoshitake, A. *Anal. Chem.* **1984**, *56*, 1077–1079.
(11) Ishibashi, N.; Imasaka, T.; Yoshitake, A. *Anal. Chem.* **1986**, *58*, 2649–2653.
(12) Demtroder, W. *Laser Spectroscopy*, 2nd ed.; Springer: Berlin, 1982; pp 389–390.
(13) *Standard Methods for the Examination of Water and Wastewater*, 16th ed.; American Public Health Association: Washington, DC, 1985; Method 425D, 513.

RECEIVED for review December 2, 1988. Accepted March 30, 1989. Acknowledgment is made to the donors of the Petroleum Research Fund, administered by the American Chemical Society, for the support of this research.

Atomic Absorption Determination of Copper in Silicate Rocks by Continuous Precipitation Preconcentration

Ricardo E. Santelli,[1] Mercedes Gallego, and Miguel Valcárcel*

Department of Analytical Chemistry, Faculty of Sciences, University of Córdoba, Córdoba-14004, Spain

A selective atomic absorption spectrophotometric method has been developed for the preconcentration and determination of copper after continuous precipitation with rubeanic acid. The precipitate is separated by continuous filtration and dissolved in potassium dichromate. A concentration factor of up to 500 is achieved. Several calibration graphs are used for the determination of copper(II) in the range 0.3–200 ng/mL with a sampling frequency between 1 and 20 h^{-1} and a relative standard deviation between 1.4 and 3.0%. The proposed method has been successfully applied to determination of copper at the μg/g level in silicate rocks.

INTRODUCTION

The precise determination of trace elements in rocks is usually hindered by the fact that they occur at levels beyond the typical detection limits of currently available instrumentation. Even with sensitive methods, constituents other than those of interest (whether major or minor elements) may hinder the detection of an element through secondary effects such as broadband absorption in electrothermal atomization atomic absorption or background radiation in neutron activation. Separation techniques have been used to overcome these problems, both by increasing concentrations above detection limits and by removing matrix constituents. Precipitation is one of the separation techniques most frequently used for enrichment purposes in inorganic analysis (*1*, *2*). Coprecipitation of trace elements with an unselective organic reagent is used quite frequently in the enrichment of trace elements (*3*), mainly in waters. Dithizone (*4*), 8-hydroxyquinoline (*5*), thionalide (*6*), α-benzildioxime (*7*), diethyldithiocarbamate (*8*), ammonium pyrrolidinecarbodithioate (*9*), and 8-hydroxyquinoline in combination with thionalide and tannic acid (*10*) are typical precipiate collectors and precipitants for copper. After collection of the desired trace elements, the precipitate collector is isolated from the sample

[1] Permanent address: Department of Geochemistry, University Federal Fluminense, Niterói-24020, Brazil.

0003-2700/89/0361-1427$01.50/0

solution by filtration or centrifugation, followed by washing, drying, or dissolution for trace determination by one of various techniques available. Carrier elements and organic matter are sometimes removed by different procedures prior to the determination. These operations result in low sampling frequencies and irreproducible recoveries; however, they afford enrichment factors of about 10^3.

The interest roused by automatic methods of analysis is ostensibly shown by the increased number of papers and monographs published on this topic in the last few years (*11–13*). The advantages of continuous automatic techniques become particularly evident when extensive manipulation is involved (e.g. when a separation technique is required). Continuous precipitation systems were recently approached by the authors. Our earliest endeavors in this respect were aimed at the study of continuous automatic precipitation–dissolution systems, coupled on-line with conventional atomic absorption instruments in implementing different methodologies such as indirect determinations of organic and inorganic anions and preconcentration of metal traces (*14*, *15*).

In this work, continuous precipitation–dissolution is used in conjunction with a flame atomic absorption spectrophotometer for the preconcentration and determination of μg/g quantities of copper in silicate rocks. Dithiooxamide (rubeanic acid) is used as an organic precipitating reagent, and no collector is required. The precipitate dissolution is effected by a solution of potassium dichromate in nitric acid. This concentration method allows the determination of copper in the range 0.3–200 ng/mL.

EXPERIMENTAL SECTION

Apparatus. A Perkin-Elmer 380 atomic absorption spectrometer equipped with a hollow-cathode copper lamp was used. The instrument was set at a wavelength of 324.7 nm, and the air/acetylene flame was adjusted according to standard recommendations. The peristaltic pump was a Gilson-Minipuls-2, furnished with poly(vinyl chloride) and Solvaflex tubing for aqueous and ethanol solutions, respectively. Two Rheodyne 5041 four-way valves connected to two channels were also used. A Scientific System 0.5-105 column with a removable screen-type stainless steel filter (pore size 0.5 μm, chamber inner volume 580 μL, and filtration area 3 cm^2), which was originally designed as a cleaning device for high-performance liquid chromatography, was employed for filtration purposes.

Reagents. A 1000 mg/L copper solution was prepared by dissolving 1.000 g of metal copper in a small volume of concentrated nitric acid and diluted to 1 L with 1% (v/v) nitric acid. A 0.1% (w/v) rubeanic acid solution was made in ethanol/water (60:40 (v/v)); this solution was stable for at least 1 week. A 0.083 M potassium dichromate solution was prepared in 1 N nitric acid. A 1 M acetic acid/1 M ammonium acetate buffer (pH 4.8) was also used. All other reagents were of analytical reagent grade.

Preparation of Standards and Samples. Copper standards in the range 0.1–2.0 μg in a 0.2 M acetic/acetate buffer (pH 4.8) were prepared in 10–250-mL calibrated flasks.

The silicate rock material was decomposed by the recommended method (*16*). An accurately weighed portion of finely powdered silicate rock was placed in a platinum crucible and moistened with some drops of water; then 10 mL of 48% hydrofluoric acid and 1 mL of 70% perchloric acid were added. After evaporation to perchloric acid fumes in a sand bath, the mass was allowed to cool, and a new portion of 5 mL of 48% hydrofluoric acid was added before evaporating next to dryness again. Once cool, the residue was extracted with several small portions of 1 M acetic acid/ammonium acetate, transferred to a volumetric flask, and diluted with water to a concentration of 0.2 M in the buffer. The remaining residue (e.g. iron, aluminum or silica) was removed by continuously filtering the solution through a microfilter. The solution was stored in polyethylene bottles. The amount of rock sample weighed ranged between 0.25 and 2.0 g, and the total volume of the rock solution depended on the copper content. The different solution volumes to be used in the determination (10–100 mL) contained about 1 μg of copper.

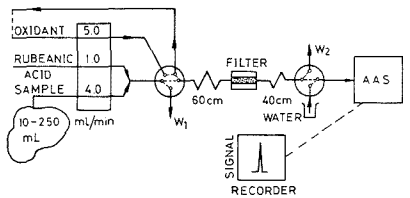

Figure 1. Schematic diagram of flow system for preconcentration of copper.

Procedure. The manifold used is illustrated in Figure 1. In the preconcentration step, 10–250 mL of sample containing 0.1–2.0 μg of Cu(II) in 0.2 M acetic acid/ammonium acetate buffer (pH 4.8) was continuously pumped into the system and mixed throughly with a 0.1% rubeanic acid solution. Precipitation was instantaneous and was followed by continuous filtration. In the dissolution step, the selecting valve was switched to pass a stream of 0.083 M potassium dichromate in 1 N nitric acid through the precipitate, which, once dissolved, gave a positive flow injection analysis (FIA) peak proportional to the amount of copper present in the sample volume introduced. No blank or precipitate washing was required. A second selecting valve was incorporated to directly aspirate a water stream intended to flush the nebulizer after each measurement. All reagents and instrumentation were kept at room temperature throughout the experiments.

RESULTS AND DISCUSSION

Continuous systems allow the precipitation of trace elements without the need for another precipitate collector as they permit one to deal with minute amounts of precipitates, which are not handled directly (*17*). Rubeanic acid can be used for the quantitative precipitation of copper, nickel, and cobalt in conventional methods (*18*). When a continuous preconcentration system (as shown in Figure 1) is used, neither nickel nor cobalt precipitates. The copper precipitate is dark green. There are no references to the use of this reagent for the preconcentration of metal traces, probably because of the insolubility of its precipitates.

Selection and Foundation of the Method. *Precipitating Reagent.* We assayed various organic reagents precipitating with dilute Cu(II) in acetic/acetate buffer. We also checked the potential precipitation of these reagents with other metal ions occurring as major or minor constituents in silicate rocks. The organic reagents in question were cupron (α-benzoinoxime), α-nitroso-β-naphthol, and rubeanic acid. Cupron and α-nitroso-β-naphthol were discarded, as they precipitated with Fe(III) at concentrations identical with that of Cu(II). Rubeanic acid was therefore chosen as the Cu(II) precipitant on account of its increased sensitivity and selectivity (it did not precipitate with Fe(III) or Al(III) at concentrations as high as 1 g/L).

Dissolving Reagent. Small amounts of the Cu(II)/rubeanate precipitate were subjected to the potential dissolving action of various solvents in test tubes. The solvents assayed were as follows: (1) acids (HCl, HNO_3) and bases (NaOH, NH_3) at different concentrations and organic solvents (acetone, acetonitrile, and dimethylformamide) (results dissatisfactory in every case); (2) complexing reagents such as 0.5 M ethylenediaminetetraacetic acid in 2 M ammonia and 5% (w/v) thioglycolic acid in 2 M ammonia (results also poor in this case); (3) oxidants such as H_2O_2 in NH_3 and $NaIO_4$, $KBrO_3$, KIO_3, $K_2Cr_2O_7$, $KMnO_4$, and $(NH_4)_2Ce(NO_3)_6$ at different concentrations in acid media (results satisfactory in all cases, but some oxidants dissolved the precipitate more rapidly than others). With an automated configuration similar to that depicted in Figure 1 and a 10-mL sample containing 0.2 μg/mL of Cu(II) in 0.2 M acetic acid/ammonium acetate buffer, the above oxidants were assayed at different concentrations in an acid medium in order to select the fastest. The

Table I. Characteristic Parameters of the Calibration Graphs and Analytical Features of the Determination of Copper in Different Sample Volumes

aliquot taken/mL	regression eq (absorbance vs μg/mL)	corr coeff	detection lim, ng/mL	RSD, %	sampling, freq/h^{-1}
10	$A = 0.003 + 1.023(Cu^{2+})$	0.999	5	1.4	20
25	$A = 0.001 + 2.519(Cu^{2+})$	0.999	2.5	1.2	10
50	$A = 0.001 + 5.204(Cu^{2+})$	0.998	1	1.6	5
100	$A = 0.002 + 10.510(Cu^{2+})$	0.997	0.5	2.0	2
250	$A = 0.003 + 26.060(Cu^{2+})$	0.998	0.3	3.0	1

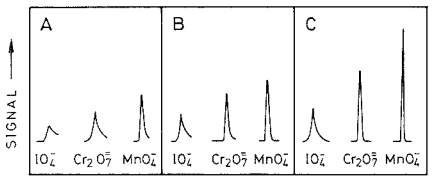

Figure 2. Influence of the nitric acid concentration on the precipitate dissolution process. A, B, and C: 0.1, 0.5, and 1–2 N nitric acid, respectively; oxidant concentration, 0.5 N.

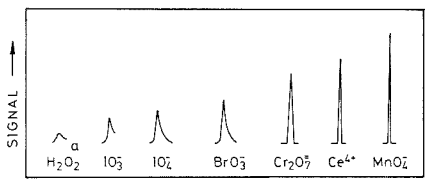

Figure 3. FIA peaks obtained with different oxidants in the dissolving solution. The concentrations of oxidants were 0.5 N in 1 N nitric acid; peak a, H_2O_2 in 2 M ammonia.

results obtained in these experiments are summarized in Figures 2 and 3. As can be seen, the best results were provided by $Cr_2O_7^{2-}$, Ce^{4+}, and MnO_4^- in 1 N nitric acid. Permanganate, which yielded the best results of all three oxidants, was discarded as it was unstable in the acid medium and gave rise to MnO_2, which clogged the filter and the nebulizer, after the redox reaction. The final choice was 0.083 M (0.5 N) potassium dichromate in 1 N nitric acid, which was stable and more economical than Ce^{4+} and dissolved the precipitate very rapidly.

Precipitate Dissolution Mechanism. Copper forms an uncharged chelate (CuL) with rubeanic acid. Polymeric chelates are probably formed through bonding of the metal to S at each end of the ligand (*19*). The mechanism of the redox reaction involved in the dissolution step could be as follows:

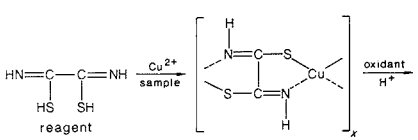

The presence of SO_4^{2-} and NO_3^- was confirmed by the Ba^{2+} and Griess reaction; gas bubbles (CO_2) were also detected in the dissolution step.

Optimization of Chemical Variables. This study was performed by continuously introducing into the system 10 mL of a solution containing 0.1 μg/mL of copper. As the organic reagent occurs in tautomeric forms, pH changes were bound to affect its reactivity. The maximum absorbances were obtained in the pH range 4.3–6.0. The absorbance decrease observed above pH 6.0 was probably a result of copper precipitating and being partially absorbed on the walls of the flask containing the sample. The effect of the concentration of the acetic acid/ammonium acetate buffer (pH 4.8) was examined up to 1 M; this variable did not affect the analytical signal over a wide range (0.1–1.0 M). A 0.2 M concentration of buffer was chosen as optimum. The influence of the ionic strength (adjusted with KNO_3 or NH_4Cl) was also tested; it had no effect, at least up to 3.5 M. When various concentrations of rubeanic acid solutions were used for a fixed concentration of copper, 0.002% of organic reagent solution was found to be sufficient for maximum response. Above this concentration, the absorbance remained constant up to 0.5%. A 0.1% concentration of rubeanic acid in (60:40 (v/v)) ethanol/water was used.

Precipitate dissolution must be instantaneous in order to obtain a transient signal rather than a plateau. Therefore, the precipitated copper rubeanate was dissolved by using a stream of potassium dichromate in nitric acid. Nitric acid concentrations below 1 N resulted in slow dissolution (Figure 2); above 1 N, the signal was virtually constant. Dissolution was complete at potassium dichromate concentrations above 0.35 N in 1 N nitric acid. According to the above considerations, we chose 0.5 N (0.083 M) potassium dichromate in 1 N nitric acid in order to achieve the best possible results in the dissolution step.

Optimization of FIA Variables. The variables studied were the length of the precipitation coil and flow rates of the sample, organic reagent, and dissolving reagent solutions. The influence of the precipitation coil length was investigated at constant flow rates in the range 20–300 cm (0.5-mm i.d.). This variable had no effect as precipitation was instantaneous. A coil length of 60 cm was chosen for further experiments. The tube length between the filter and the nebulizer (dissolution coil) did not influence the peak height below 50 cm, whereas longer lengths increased the dispersion of dissolved copper.

The sample flow rate (10 mL of a solution containing 0.1 μg/mL copper in the buffer) caused the smallest variations in the range 1–5 mL/min. As the preconcentration method required the aspiration of large sample volumes (up to 250 mL), the sampling time was rather long. A high flow rate (4.0 mL/min) was therefore selected in order to increase the sampling rate. The absorbance was maximum for rubeanic acid flow rates included within the interval studied (0.4–1.6 mL/min), so that a flow rate of 1.0 mL/min was chosen. The influence of the flow rate of the dissolving solution on the peak height was examined in the range 1–7 mL/min. The latter increased with increasing flow rate of the potassium dichromate solution and was constant above 3.5 mL/min. The peak height decreased below 3.5 mL/min; however, the peak width increased, and in all instances the area under the peak remained constant (a similar effect to that observed upon decreasing the dissolving reagent concentration). A flow rate of 5.0 mL/min was chosen in order to increase the sample throughput.

Determination of Copper. Figures of Merit. Under the optimum chemical conditions and by use of the manifold

Table II. Analysis for Copper in Silicate Rocks

sample	aliquot taken/mL	composition/%				copper content, μg/g	
		SiO_2	Al_2O_3	Fe_2O_3[a]	MnO	certfd	found[b]
marine mud, MAG-1 (USGS)	10	51.19	16.46	6.98	0.10	30 ± 3	27.3 ± 0.8
mica schist, SDC-1 (USGS)	10	66.15	15.75	6.85	0.12	30 ± 2	30.1 ± 0.8
granite, JG-2 (GSJ)	100	76.95	12.41	0.92	0.015	0.4	0.40 ± 0.05
granodiorite, JG-3 (GSJ)	25	67.10	15.52	3.73	0.072	6.0	5.6 ± 0.3
andesite, JA-3 (GSJ)	10	62.26	15.57	6.59	0.106	45.3	44 ± 1

[a] Percentage of total Fe_2O_3. [b] Average of three separate determinations.

depicted in Figure 1, several linear calibration graphs were run for copper with different sample volumes (between 10 and 250 mL). Table I lists the characteristic parameters of these graphs and the analytical features of the determination of copper(II) in the range 0.3–200 ng/mL. The detection limit was calculated as 3-fold the standard deviation of the peak height for 10 determinations of the same sample (*14*). The precision of the method (expressed as the relative standard deviation) was checked on 11 samples containing 1 μg each in different sample volumes.

Concentration factors of up to 500, calculated as the ratio between the slopes of the calibration graphs obtained by this method and by direct aspiration ($A = 0.002 + 0.0517(Cu^{2+})$), were readily achieved.

The effect of some components of silicate rocks was examined in order to detect potential interferences in the determination of copper. The cations assayed in this study of interferences can be classified in two groups: (a) major and minor elements commonly found in silicate rocks (e.g. Fe^{3+}, Al^{3+}, and Mn^{2+}), which can precipitate in the acid medium (pH 4.8) or with rubeanic acid and clog the filter; and (b) trace elements such as Co^{2+}, Ni^{2+}, and Zn^{2+}, which compete with copper for the reagent and give rise to poor results. Al^{3+}, Fe^{3+}, and Mn^{2+} caused no interference with the determination of 1 μg of copper (sample volumes of 50 mL) at concentrations of 15 000 μg; neither did 3000 μg of Fe^{3+} or Al^{3+} (sample volumes of 10 mL). Higher Fe^{3+} or Al^{3+} concentrations precipitated in the buffer of pH 4.8 and required the addition of tartrate (2% (w/v)) as a masking agent. As Co^{2+}, Ni^{2+}, and Zn^{2+} normally occur in silicate rocks at concentrations 5–20 times higher than that of copper, we only assayed concentrations up to 100-fold, which posed no interference. Finally, we prepared a synthetic silicate rock solution containing all the typical major and minor constituents at their maximum levels of occurrence. The copper recovery ranged between 98 and 101%, and the error made was rather small.

Determination of Trace Amounts of Copper in Silicate Rocks. The knowledge of the content and distribution of trace elements in rocks is of great interest to geochemical (particularly petrological and mineralogical) studies. The concentration of trace metals in silicate rocks varies with the silica content. Acidic rocks (higher silica content) generally contain small amounts of copper and other metals.

The applicability of the proposed copper/rubeanate method was studied by using silicate rocks in international reference samples from the United States Geological Survey (*20, 21*) (MAG-1 and SDC-1) and the Geological Survey of Japan (*22*) (JG-2, JG-3, and JA-3). The materials were dissolved as described in the Experimental Section, and the copper content of the resulting solutions was determined by the recommended procedure. The results obtained are listed in Table II.

CONCLUSIONS

Continuous preconcentration with rubeanic acid has proved to be an efficient and convenient method of overcoming the interference of relatively large amounts of some elements in the preconcentration and determination of copper in silicate rocks. The proposed automatic preconcentration method offers several major assets such as high sensitivity (a concentration factor of up to 500 is achieved), selectivity, and rapidity.

LITERATURE CITED

(1) Minczewski, J.; Chwastowska, J.; Dybczynski, R. *Separation and Preconcentration Methods in Inorganic Trace Analysis*; Ellis Horwood: Chichester, U.K., 1982.
(2) Mizuike, A. *Enrichment Techniques for Inorganic Trace Analysis*; Springer Verlag: Berlin and Heidelberg, 1983.
(3) Myasoedova, G. V. *Zh. Anal. Khim.* **1966**, *21*, 598.
(4) Zharikov, V. F.; Senyavin, M. M. *Tr. Gos. Okeanogr. Inst.* **1970**, *101*, 128.
(5) Scott, R. O.; Mitchell, R. L. *J. Soc. Chem. Ind.* **1943**, *62*, 4.
(6) Portmann, J. E.; Riley, J. P. *Anal. Chim. Acta* **1964**, *31*, 509.
(7) Jackwerth, E.; Salewski, S. *Fresenius' Z. Anal. Chem.* **1982**, *310*, 108.
(8) Watanabe, H. *Talanta* **1972**, *19*, 1363.
(9) Krishnamurty, K. V.; Reddy, M. M. *Anal. Chem.* **1977**, *49*, 222.
(10) Silvey, W. D., Brennan, R. *Anal. Chem.* **1962**, *34*, 784.
(11) Valcárcel, M.; Luque de Castro, M. D. *Automatic Methods of Analysis*; Elsevier: Amsterdam, 1988.
(12) Valcárcel, M.; Luque de Castro, M. D. *Flow Injection Analysis*: *Principles and Applications*; Ellis Horwood: Chichester, U.K., 1987.
(13) Ruzicka, J.; Hansen, E. *Flow Injection Analysis*, 2nd ed.; Wiley: New York, 1988.
(14) Martínez-Jiménez, P.; Gallego, M.; Valcárcel, M. *Anal. Chem.* **1987**, *59*, 69.
(15) Valcárcel, M.; Gallego, M. *TrAC, Trends Anal. Chem. (Pers. Ed.)* **1989**, *8*, 34.
(16) Jeffery, P. G. *Chemical Methods of Rock Analysis*, 2nd ed.; Pergamon Press: Oxford, U.K., 1975.
(17) Martínez-Jiménez, P.; Gallego, M.; Valcárcel, M. *Analyst* **1987**, *112*, 1233.
(18) Burger, K. *Organic Reagents in Metal Analysis*; Pergamon Press: Oxford, U.K., 1973.
(19) Sandell, E. B.; Onishi, H. *Photometric Determination of Traces of Metals. General Aspects*; John Wiley: New York, 1978.
(20) Gladney, E. S.; Goode, W. E. *Geostand. Newsl.* **1981**, *5*, 31.
(21) Flanagan, F. J. U.S. *Geol. Surv. Prof. Pap. (U.S.)* **1971**, No. 840.
(22) Ando, A.; Mita, N.; Terashima, S. *Geostand. Newsl.* **1987**, *11*, 159.

RECEIVED for review December 5, 1988. Accepted March 20, 1989. CICYT (Spain) is acknowledged for financial support (Grant No. PA86-0146). R. E. Santelli is also grateful to the Brazilian Government for financial support (CNPq-70.1898/87.9-PADCT/SPGTM).

Light Absorption and Mixed Micelle Composition as Factors in Determining Intensities of Room-Temperature Phosphorescence

N. E. Nugara and A. D. King, Jr.*

Department of Chemistry, School of Chemical Sciences, University of Georgia, Athens, Georgia 30602

A series of experiments have been performed that demonstrate (a) that problems arising from precipitation of Tl^+-alkyl sulfate salts at high Tl^+ concentrations in micelle-stabilized room-temperature phosphorescence (MS-RTP) solutions can be avoided by using mixed surfactant systems that include a short chain alkyl sulfate and (b) that in cases where the sulfite ion is used as a chemical deoxygenating agent, light absorption by a Tl^+–SO_3^{2-} complex can severely attenuate the exciting radiation, particularly at wavelengths below 275 nm, thus offsetting any gains derived from increasing the Tl^+ content of MS-RTP solutions through the use of mixed surfactants. The stoichiometry, formation constant, and molar absorptivity of this Tl^+–SO_3^{2-} complex are determined by using UV spectrometry. Fluorescence and thallium-induced phosphorescence intensity data derived from three aromatic compounds solubilized in a mixed micelle MS-RTP system containing Na_2SO_3 are included to illustrate the advantages of long wavelength excitation in such MS-RTP systems.

INTRODUCTION

Micelle-stabilized room-temperature phosphorescence (MS-RTP) is an interesting manifestation of the external heavy-atom effect, which shows great promise as a means of detection in liquid chromatography (*1–16*). Basically, MS-RTP achieves its effect by utilizing the amphiphilic character of micellized surfactant ions to compartmentalize solubilized lumiphore molecules, normally aromatics, in a submicroscopic region surrounded by a high concentration of heavy-atom counterions. This facilitates collisions between the two species and has the effect of increasing the flux of energy passing through the phosphorescence channel by increasing triplet quantum yields and perhaps phosphorescence efficiencies as well. Anionic micelles composed of dodecyl sulfate anions surrounded by a counterion sheath containing either Tl^+ or Ag^+ cations are commonly used to effect MS-RTP although micelles of the cationic type composed of cetyltrimethylammonium bromide have been shown to induce MS-RTP as well (*11*). While lumiphore concentration effects attributed to triplet–triplet annihilation and the inner-filter effect (*5*), as well as a specificity of Ag^+ relative to Tl^+ toward solubilized heterocyclic compounds (*15*) have been found to affect phosphorescence intensities in MS-RTP, there are two fundamental conditions that must be met in order to maximize the intensity of MS-RTP: (a) the relative concentration of heavy-atom ions relative to other counterions in the micellar solution must be as high as possible and (b) the concentration of O_2, a potent triplet quencher, must be minimized. In practice, however, the low solubilities of heavy-metal dodecyl sulfate salts at room temperature place a ceiling (approximately 30 mol % in the case of Tl^+) on the amount of heavy-metal ions that can be introduced into the commonly used MS-RTP systems based on sodium dodecyl sulfate. Likewise, the traditional method of using N_2 purging to remove O_2 from solution has been of limited utility because of foam generation and its concomitant problems. Because of this, the recent discovery that sulfite ions act as efficient O_2 scavengers in micellar solutions used for MS-RTP by Garcia and Sanz-Medel (*16*) represent a major technical advance in the use of MS-RTP.

The purpose of this paper is 2-fold. First, it will be shown that for MS-RTP systems that employ Tl^+, the solubility limitations encountered with sodium dodecyl sulfate (SDS) can be greatly ameliorated through the use of a mixed surfactant system composed of SDS blended with a shorter chain surfactant, sodium octyl sulfate (SOS). Secondly, evidence will be presented to show that light absorption by a 1:1 complex of Tl^+ with SO_3^{2-} acts to diminish the intensity of phosphorescence generated by micellar solutions which use Tl^+ as a heavy atom perturber and SO_3^{2-} as a chemical deoxygenating agent.

EXPERIMENTAL SECTION

Instrumentation. The UV absorption spectra of the micellar solutions of interest were obtained by using a Hewlett-Packard Model 8451-A diode array spectrophotometer. The emission spectra were measured with a Perkin-Elmer Model MPF-44B spectrofluorometer, equipped with a differential corrected spectral unit (DSCU) and a thermostated cell compartment that utilizes a Brinkmann-Lauda super K-2/R circulating constant temperature bath to control the temperature to 25 ± 0.5 °C for the work reported here. Surface tension measurements used to determine values for the critical micelle concentration (cmc) of purified SDS, SOS, and their mixtures were obtained by using a Fisher Autotensiomat, Model 215, automated duNouy tensiometer having a Haake Model FS constant temperature circulator to maintain solution temperature to ± 0.1 °C.

Chemicals and Reagents. The SDS and SOS used in this work were purchased from BDH Chemicals Ltd. (lot no. 9088113 C 500) and Eastman Kodak Co. (lot no. 16A), respectively. Each was recrystallized from 1:1 (for SDS) and 1:3 (for SOS) (v/v) ethanol/2-propanol mixtures and dried in vacuo prior to use. The purity of each surfactant with respect to alkyl group chain length was verified by comparing cmc values obtained with aqueous solutions of the recrystallized SOS and SDS with recommended literature values (*17*). Good agreement was found in each case. Thallium(I) nitrate, purchased from Fluka Chemie A.G., was recrystallized twice from H_2O and dried in vacuo. Sodium sulfite (anhydrous), purchased from J. T. Baker Chemical Co., was used as received. The naphthalene, Baker Analyzed Reagent Grade, purchased from J. T. Baker Chemical Co., was used as received while the phenanthrene and pyrene, both Eastman White Label Grade, were purchased from Eastman Kodak Co. and were recrystallized from ethanol prior to use. Doubly distilled water was used to prepare all solutions.

The luminescence intensities shown in Figures 1 and 4 are "uncorrected spectra" with no corrections being made for the wavelength dependence of instrument response. The 15-nm slits were used for both excitation and emission.

RESULTS AND DISCUSSION

Concentration–temperature phase diagrams for aqueous systems containing ionic surfactants have one feature in

0003-2700/89/0361-1431$01.50/0

common, namely that the solid solubility–temperature curves exhibit an abrupt increase in slope at a temperature known as the Krafft temperature, T_K (*18*). Short-chain surfactants have low Krafft temperatures and hence tend to be very soluble and readily form micellar solutions at ordinary temperatures. Long-chain surfactants on the other hand are characterized by high Krafft temperature and become quite insoluble whenever T_K exceeds ambient temperature. Mixtures of short- and long-chain surfactants have Krafft temperatures that are intermediate to those of the two pure species. Large polarizable counterions, such as Tl^+ in the case of SDS, have the effect of increasing T_K and hence reducing solubility. This effect is roughly proportional to the concentration of the large counterions and the addition of a salt containing such an ion will cause a surfactant to precipitate whenever the concentration of that counterion reaches a level sufficient to raise T_K above ambient temperature. As noted earlier, in the case of SDS, precipitation occurs when the Tl^+ content reaches approximately 30 mol % relative to Na^+, i.e.

$$(Tl^+/Na^+)\% = \frac{[Tl^+]}{[Tl^+] + [Na^+]}100 = 30\%$$

Since the addition of a short chain surfactant acts to lower T_K, one expects that a surfactant blend containing a short-chain and a long-chain surfactant of the same class will be more resistant to precipitation by polarizable counterions than the long-chain surfactant alone. This is found to be the case with MS-RTP systems based on SDS and Tl^+. Here one finds that the increased resistance to precipitation afforded by the addition of sodium octyl sulfate to make a 20 mol % SOS–80 mol % SDS blend allows one to obtain spectra with Tl^+ contents reaching $(Tl^+/Na^+)\% = 50\%$ without precipitation.

Figure 1 is derived from intensities of fluorescence, I_f, and phosphorescence, I_P, measured at 325 nm and 476 nm, respectively, for naphthalene solubilized in three different micellar solutions composed of SDS, a SDS/SOS blend (80% SDS), and pure SOS, each containing 0.005 M Na_2SO_3 and varying amounts of $TlNO_3$. The absorbance of naphthalene dissolved in each solution is 1.00 at the wavelength used for excitation, λ_{ex} = 276 nm. The cmc values measured in the absence of added salt at 25 °C for SDS, the 80% SDS/SOS blend, and pure SOS are 8.0×10^{-3} M, 9.0×10^{-3} M, and 0.13 M, respectively. Therefore, to a first approximation, each of these solutions contains the same concentration (0.1 M) of micellized alkyl sulfate ions.

Figure 1a shows the phosphorescence intensity measured with each of these solutions plotted as a function of Tl^+ content expressed as $(Tl^+/Na^+)\%$. While the intensities obtained by using the SDS/SOS blend do not differ appreciably from those obtained with pure SDS at low Tl^+ concentrations, one sees that I_p falls off sharply at higher concentrations so that little is gained by using the mixed surfactant system to achieve Tl^+ concentrations in excess of the precipitation limit for SDS, i.e. greater than $(Tl^+/Na^+)\% = 30\%$. The phosphorescence intensities observed with pure SOS under the same conditions are less intense and pass through a similar though less pronounced maximum at a thallium content of $(Tl^+/Na^+)\% = 30\%$.

The errors associated with the intensities of phosphorescence, I_p, and fluorescence, I_f, originate from instrumental error, uncertainties in thallium ion and sodium ion concentrations (hence $(Tl^+/Na^+)\%$), as well as errors in the concentrations of the solubilized aromatic lumiphore, sulfite ion, and residual O_2. The sensitivity of I_P (or I_f) to each of these factors is unknown although each of the chemically related sources of error is expected to become more severe at shorter excitation wavelengths. However, an error estimate based on replicate spectra obtained with naphthalene at two different

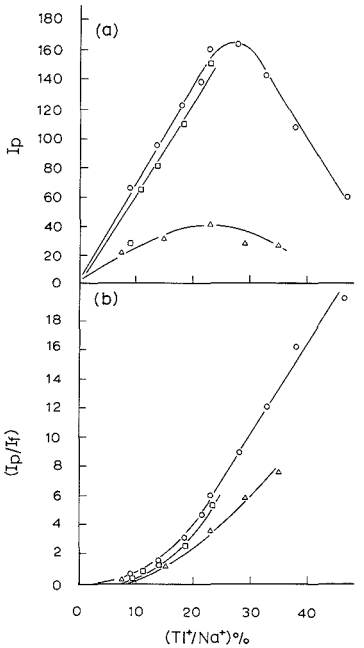

Figure 1. (a) Intensity (arbitrary units) of phosphorescence, I_P, at 476 nm for naphthalene solubilized in 0.10 M SDS (□), 0.23 M SOS (△), and 0.080 M SDS/0.020 M SOS (○), each with 0.005 M Na_2SO_3 and varying $TlNO_3$ concentrations at 25 °C, shown as a function of $(Tl^+/Na^+)\%$. λ_{ex} = 276 nm. [Naphthalene] = 1.67×10^{-4} M. (b) The ratio of intensities, (I_P/I_f), for naphthalene solubilized in the micellar solutions used in Figure 1a, as denoted by the same symbols, plotted as a function of $(Tl^+/Na^+)\%$.

$(Tl^+/Na^+)\%$ using 276 nm excitation indicates that I_P and I_f can be reproduced to within ±8% using a MS-RTP system based on a 0.10 M 20% SOS-80% SDS mixture. Since I_P and I_f used to calculate individual values of I_P/I_f are measured in the same experiment, only instrumental error, uncertainties in $(Tl^+/Na^+)\%$ and residual O_2 concentration contribute to the error associated with this ratio and the error limit for the ratio I_P/I_f based on this same set of experiments is found to be ±12%.

Two factors may be responsible for this fall off in phosphorescence intensity at high Tl^+ ion concentrations. First, Tl^+ ions concentrated about the alkyl sulfate micelles may act as quenching agents by increasing the rate of nonradiative energy loss from the lowest triplet state of the solubilized naphthalene molecules. Alternatively, the Tl^+ ions may cause a reduction in luminescence by simply reducing the intensity of light at the excitation frequency that reaches the solubilized naphthalene, presumably by forming a light absorbing complex with one or more of the species in solution.

The ratio of phosphorescence and fluorescence intensities, I_P/I_f, obtained with uncorrected emission spectra having constant band shapes can be shown to be a function solely of the various rate constants that govern the internal channels for energy flow within the lumiphore; i.e.

$$I_P/I_f = (\text{const})\frac{k_{TM}}{k_{FM}}\left\{\frac{k_{PT}}{k_{PT} + k_{GT}}\right\} \quad (1)$$

Here k_{TM} represents the rate constant for intersystem crossing between the lowest excited singlet (S_1) and triplet (T_1) states. The term k_{GT} is the rate constant governing nonradiative

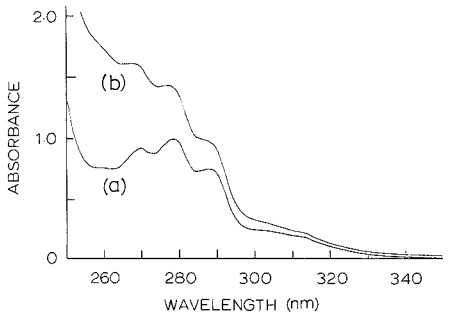

Figure 2. Absorption spectra of naphthalene solubilized in 0.23 M SOS and 0.019 M $TlNO_3$ (a) before and (b) after the addition of 0.005 M Na_2SO_3 at 25 °C: path length, 1 cm; [naphthalene] = 1.67×10^{-4} M.

decay of T_1 while k_{FM} and k_{PT} are rate constants governing the radiative decay of S_1 and T_1, respectively. Therefore, the fact that the experimentally determined ratios of I_P/I_f for naphthalene in the three different micellar solutions, shown plotted in Figure 1b, all follow a smooth, concave upward path over the full range of (Tl^+/Na^+)% concentrations available to each system indicates that the loss of phosphorescence intensity observed in Figure 1a is not due to a quenching process whereby Tl^+ accelerates the rate of nonradiative decay from T_1 by increasing k_{GT} but rather is caused by attenuation of the exciting radiation by either light scattering or light absorption by some complex formed by Tl^+ in solution.

The absorption spectra shown in Figure 2 taken with a Tl^+ based MS-RTP solution containing naphthalene solubilized in SOS support this conclusion. Here it is seen that a broad absorption band develops under the absorption band of naphthalene when Na_2SO_3 is added to the solution. This strongly suggests that a thallium(I)–sulfite complex is responsible for the light absorption, although the possibility exists that light scattering by large micelles produced by added sodium sulfite may be the cause of the observed attenuation.

Figure 3 compares the absorption spectra obtained with aqueous solutions containing (a) 0.010 M $TlNO_3$, (b) 0.010 M Na_2SO_3, and (c) a 1:1 mixture of these two solutions, all in the absence of any surfactant. Here it is seen that a strong structureless absorption band develops in the region between 250 nm and the weak NO_3^- band at 310 nm when the two salts are mixed. Since no surfactant is present in these solutions, one concludes that a Tl^+–SO_3^{2-} complex is responsible for the light absorption observed with the mixture in Figure 3 and, by inference, for the light absorption found with the MS-RTP solution shown in Figure 2 as well.

A series of spectral measurements were performed to determine the absorbance of binary solutions having various concentrations of $TlNO_3$ and Na_2SO_3 in order to characterize the Tl^+–SO_3^{2-} complex responsible for this light absorption. The first of these entailed using a method developed by Vosburgh and Cooper (*19*) in which a Job plot is used to determine the stoichiometry of the light-absorbing complex. Here equimolar solutions of $TlNO_3$ and Na_2SO_3 are mixed in different proportions to produce a series of solutions having the same total volume but different relative concentrations of the two salts. The absorbance values measured for these mixtures, when plotted against the relative concentration of one salt compared to the other, expressed as mole fraction, will yield a curve having negative curvature whose maximum corresponds to the mole fraction representing the stoichiometry of the light-absorbing complex. The upper-left inset of Figure 3 shows the results obtained with $TlNO_3$–Na_2SO_3

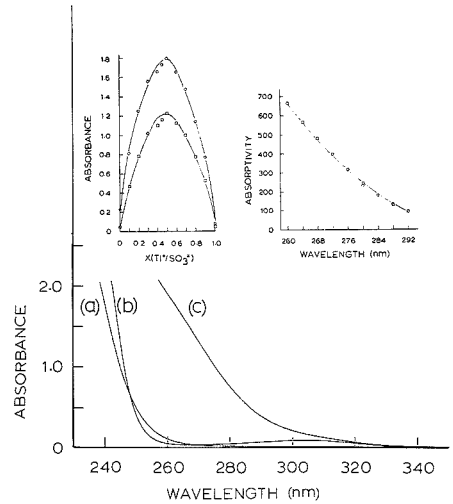

Figure 3. Absorption spectra of aqueous solutions containing (a) 0.010 M Na_2SO_3, (b) 0.010 M $TlNO_3$, and (c) a 1:1 mixture of 0.010 M $TlNO_3$ and 0.010 M Na_2SO_3. Path length, 1 cm. Upper left inset: Job plot showing absorbance values plotted as a function of $X_{Tl^+/SO_3^{2-}}$ for solutions containing different proportions of $TlNO_3$ and Na_2SO_3 at 25 °C. Upper curve, absorbance at 260 nm; lower curve, absorbance at 270 nm. Total concentration of Tl^+ and SO_3^{2+} is 0.02 M. Optical path length, 1 cm. Upper right inset: Absorptivity of the $TlSO_3^-$ complex in aqueous solution shown as a function of wavelength. (O) Absorptivities obtained directly from nonlinear least-squares fit of absorbance data taken over range 276–292 nm. (□) Absorptivities calculated by using the K_{sc} value obtained from nonlinear least-squares fit of 276–292 nm data with more dilute solutions of $TlNO_3$ and Na_2SO_3 having differing relative concentrations.

mixtures at two different wavelengths, 260 and 270 nm. Both maxima occur at a mole fraction of 0.5 indicating that a 1:1 complex between Tl^+ and SO_3^{2-} is responsible for light absorption over the range 260–290 nm seen in Figures 2 and 3.

Once the stoichiometry is known, one can utilize similar spectral data to determine the value of the stability constant, K_{sc}, for this Tl^+–SO_3^{2-} complex using a method developed by Yoneda (*20*). Here, absorbance values were measured at five different wavelengths over the range 276–292 nm for a series of solutions containing 0.0100 M $TlNO_3$ and varying amounts of Na_2SO_3. The results obtained at each wavelength were fitted to the equations derived by Yoneda using nonlinear least-squares methods to yield values for the absorptivity of the complex and K_{sc}. The values obtained for K_{sc} show no trend with wavelength and yield an average value for K_{sc} at 25 °C

$$K_{sc} = \frac{[TlSO_3^-]}{[Tl^+][SO_3^{2-}]} = 48 \pm 3$$

It is interesting to note that this value is quite similar to that found for the 1:1 complex of Tl(I) with sulfate ion which is $K_{sc} = 28$ at 25 °C (*21*).

Once the stoichiometry and formation constant are known, it becomes a simple matter to calculate values for the absorptivity of this Tl^+–SO_3^{2-} complex using the absorption spectra obtained with these solutions. The results calculated at 4-nm intervals are shown plotted as a function of wavelength in the upper-right inset of Figure 3 along with the values derived by the original least-squares fit. It is clear from these results that the absorbance due to this Tl^+–SO_3^{2-} complex can become quite large in MS-RTP solutions using

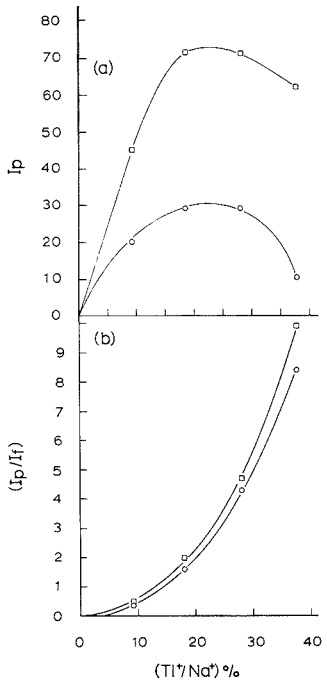

Figure 4. (a) Intensity (arbitrary units) of phosphorescence, I_P, at 470 nm obtained by using two different excitation wavelengths, for phenanthrene solubilized in solutions containing 0.080 M SDS, 0.020 M SOS, 0.005 M Na_2SO_3, and varying amounts of $TlNO_3$ at 25 °C, shown as a function of (Tl^+/Na^+)%. (O): λ_{ex} = 276 nm, (□): λ_{ex} = 296 nm. [Phenanthrene] = 5.3 × 10^{-5} M ca. Absorbance (276 nm) = 1.0, absorbance (296 nm) = 0.84, 1 cm path length. (b) The ratio of intensities, (I_P/I_f), for phenanthrene solubilized in the micellar solutions used in Figure 4a, as denoted by the same symbols, plotted as a function of (Tl^+/Na^+)%.

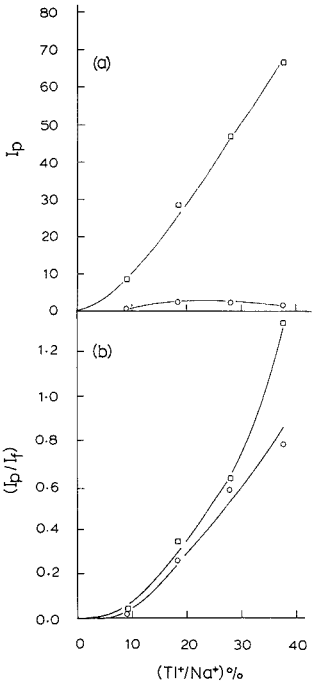

Figure 5. (a) Intensity (arbitrary units) of phosphorescence, I_P, at 575 nm obtained by using two different excitation wavelengths, for pyrene solubilized in solutions containing 0.080 M SDS, 0.020 M SOS, 0.005 M Na_2SO_3, and varying amounts of $TlNO_3$ at 25 °C, shown as a function of (Tl^+/Na^+)%: (O) λ_{ex} = 276 nm, (□) λ_{ex} = 338 nm; [pyrene] = 2.2 × 10^{-5} M. Absorbance (276 nm) = 1.0, absorbance (338 nm) = 1.1, 1 cm path length. (b) The ratio of intensities (I_P/I_f), for pyrene solubilized in the micellar solutions used in Figure 5a, as denoted by same symbols, plotted as a function of (Tl^+/Na^+)%.

Na_2SO_3 for deoxygenation, particularly at higher thallium concentrations. For example, ignoring ionic strength effects, one can use the experimentally determined value K_{sc} = 48 and the absorptivity values shown in Figure 3 to estimate that the absorbance over a 1-cm path length due to the Tl^+–SO_3^{2-} complex in the SOS–SDS MS-RTP solution used in Figure 1 will exceed unity at wavelengths less than 276 nm whenever the thallium ion content exceeds (Tl^+/Na^+)% = 30%. This situation, of course, becomes progressively worse at higher thallium concentrations.

The fact that the intensity of phosphorescence depends upon the relative concentrations of Tl^+ and Na^+ in these solutions while the concentration of light-absorbing complex depends upon the concentration of Tl^+ alone explains why the intensity of phosphorescence of naphthalene solubilized in SOS shown in Figure 1 is weak in comparison with that generated by the solutions containing SDS or the SOS–SDS mixture. The cmc of SOS is 0.13 M at 25 °C (*17*). Therefore, a surfactant concentration of 0.23 M is required to produce 0.1 mol of micellized surfactant ions per liter, the amount of micellized surfactant ions common to all the data shown in Figure 1. Including the Na_2SO_3, the sodium ion concentration in these SOS solutions is 0.24 M, roughly twice that in the solutions containing SDS or SOS mixed with SDS, both of which are 0.1 M with respect to surfactant. It follows that twice as much Tl^+ is required to produce a given (Tl^+/Na^+)% in the SOS solutions, which in turn produces increased concentrations of the light-absorbing Tl^+–SO_3^{2-} complex. One calculates that the 1 cm path length absorbance of the MS-RTP solution containing 0.23 M SOS used in Figure 1 will exceed unity whenever the thallium content exceeds (Tl^+/Na^+)% = 15%.

Finally, the absorptivity of the Tl^+–SO_3^{2-} complex shown in Figure 3 is seen to fall off rapidly with wavelength. This suggests that, where a choice is possible, much is to be gained by using long wavelength excitation. This is illustrated by phosphorescence data obtained with phenanthrene. The vibronic structure of the ^1L_a absorption band of phenanthrene contains two well-defined maxima having nearly the same absorptivity at 276 and 296 nm, respectively. Inspection of the absorptivities of the Tl^+–SO_3^{2-} complex shown in Figure 3 leads one to conclude that excitation at 276 nm will be attenuated to a much greater extent than that at 296 nm in MS-RTP solutions thus leading to reduced excitation and hence weaker phosphorescence when 276-nm excitation is used. The data in Figure 4 show this to be the case. A second and more exaggerated example illustrating this same effect is provided by MS-RTP spectra derived from solubilized pyrene shown in Figure 5a. Here, the combined effects of a low triplet quantum yield (k_{FM} is large relative to k_{TM} for the unperturbed molecule) and the high absorptivity of the Tl^+–SO_3^{2-} complex at 276 nm render excitation at 276 nm virtually ineffective. On the other hand, illumination at 338 nm, where no attenuation is expected, generates intense phosphorescence from the same solution. The pyrene ab-

sorption bands at 276 and 338 nm have nearly identical absorptivities but are derived from optical transitions to two entirely different excited electronic states. Although the experimental error associated with the extremely weak fluorescence and phosphorescence emissions obtained by using 276 nm excitation are quite large, the near identity of the I_P/I_f ratios shown in Figure 5b indicate that, as expected, rapid interconversion between the excited singlet states of pyrene prevails leaving the phosphorescence quantum yield insensitive to the fact that the excited singlet states resulting from excitation at 276 and 338 nm are different.

LITERATURE CITED

(1) Kalyanasundram, K.; Grieser, F.; Thomas, J. K. *Chem. Phys. Lett.* **1977**, *51*, 501–505.
(2) Humphry-Baker, R.; Moroi, Y.; Grätzel, M. *Chem. Phys. Lett.* **1978**, *58*, 207–210.
(3) Turro, N. J.; Liu, K.-C.; Chow, M.-F.; Lee, P. *Photochem. Photobiol.* **1978**, *27*, 523–529.
(4) Almgren, M.; Grieser, F.; Thomas, J. K. *J. Am. Chem. Soc.* **1979**, *101*, 279–291.
(5) Cline Love, L. J.; Skrilec, M.; Habarta, J. G. *Anal. Chem.* **1980**, *52*, 754–759.
(6) Skrilec, M.; Cline Love, L. J. *Anal. Chem.* **1980**, *52*, 1559–1564.
(7) Armstrong, D. W.; Hinze, W. L.; Bui, K. H.; Singh, H. N. *Anal. Lett.* **1981**, *14*(A19), 1659–1667.
(8) Skrilec, M.; Cline Love, L. J. *J. Phys. Chem.* **1981**, *85*, 2047–2050.
(9) Cline Love, L. J.; Habarta, J. G.; Skrilec, M. *Anal. Chem.* **1981**, *53*, 437–444.
(10) Cline Love, L. J.; Skrilec, M. *Anal. Chem.* **1981**, *53*, 1872–1875.
(11) Wolff, T. *Ber. Bunsen-Ges. Phys. Chem.* **1982**, *86*, 1132–1134.
(12) Weinberger, R.; Yarmchuk, P.; Cline Love, L. J. *Anal. Chem.* **1982**, *54*, 1552–1558.
(13) Cline Love, L. J.; Weinberger, R., *Spectrochim. Acta, Part B* **1983**, *38B*, 1421–1433.
(14) Femia, R. A.; Cline Love, L. J. *Anal. Chem.* **1984**, *56*, 327–331.
(15) Woods, R.; Cline Love, L. J. *Spectrochim. Acta, Part A* **1984**, *40A*, 643–650.
(16) Garcia, M. E. D.; Sanz-Medel, A. *Anal. Chem.* **1986**, *58*, 1436–1440.
(17) Mukerjee, P.; Mysels, K. J. Critical Micelle Concentrations of Aqueous Surfactant Systems. *Natl. Stand. Ref. Data Series (U.S., Natl. Bur. Stand.)* **1961**, *NSRD S-NBS 36*.
(18) Adamson, A. W. *Physical Chemistry of Surfaces*, 4th ed.; John Wiley & Sons: New York, 1982; Chapter XIII.
(19) Vosburgh, W. C.; Cooper, G. R. *J. Am. Chem. Soc.* **1941**, *63*, 437–442.
(20) Yoneda, H. *Bull. Chem. Soc. Jpn.* **1956**, *29*, 68–71.
(21) Sillen, L. G.; Martell, A. E. *Stability Constants of Metal Ion Complexes*, 2nd ed.; The Chemical Society of London: London, 1964; p 244.

RECEIVED for review December 21, 1988. Accepted March 27, 1989. The results reported here are taken from the M.S. Thesis of N. E. Nugara (University of Georgia, 1988). The authors express appreciation for support provided by the National Science Foundation (NSF) under Grant CHE-8218288.

Aromatic Bases as Eluent Components for Conductivity and Indirect Ultraviolet Absorption Detection of Inorganic Cations in Nonsuppressed Ion Chromatography

Paul R. Haddad* and Roy C. Foley

Department of Analytical Chemistry, University of New South Wales, P.O. Box 1, Kensington, New South Wales 2033, Australia

A range of protonated aromatic bases was investigated as eluents for the nonsuppressed ion chromatography of inorganic cations, using simultaneous direct conductivity and indirect UV absorption detection. When a low-capacity styrene–divinylbenzene cation-exchange column was used, methylpyridine isomers, dimethylpyridine isomers, benzylamine, 2-phenylethylamine, and 4-methylbenzylamine proved suitable for the separation of alkali-metal cations and ammonium. Detection limits were in the range 0.3–6.7 ppb for conductivity detection and 0.2–21.0 ppb for UV absorption detection. Alkaline-earth-metal cations could be separated by using higher concentrations of the same eluent species, giving detection limits of 9–917 and 1.3–1370 ppb for conductivity and UV absorption detection, respectively. Aromatic base eluents were applied to the separation of calcium and magnesium in seawater and are potentially suitable for the determination of aluminum.

INTRODUCTION

Detection modes in ion chromatography can be conveniently classified as direct or indirect by comparison of the detector signal occurring during elution of a solute species with the base-line detector signal occurring when no solute is eluted. When the base-line signal is less than that of the solute, the detection mode is direct, whereas indirect detection results when the base-line detector signal exceeds that of the solute. For example, the most common mode of conductivity detection for anions in ion chromatography is direct (that is, with the use of low-conductance eluents), while indirect UV absorption detection is commonly employed with the aid of strongly absorbing eluent ions. Moreover, use of an aromatic acid anion (such as phthalate) as eluent enables both of these detection modes to be employed simultaneously.

Detection modes applicable to nonsuppressed ion chromatography of cations are much more limited, with the general approaches being restricted to indirect conductivity or postcolumn derivatization. It is therefore of interest to determine whether direct conductivity and indirect UV detection using eluents of suitably high absorbance and low conductance can be applied successfully to inorganic cations. Eluent species that have been evaluated for indirect UV absorption detection of cations include copper(II) (*1–7*), mixtures of copper(II) and cobalt(II) (*4*, *5*), cerium(III) (*7*), pyridine (*2*), aniline (for indirect refractive index detection) (*8*), benzylamine (*9*), and benzyltrimethylammonium bromide (*2*). Copper *o*-sulfobenzoate has been shown to be a suitable eluent for the simultaneous detection of anions and cations using indirect UV absorption (*10*). Cerium(III) appears to be the most promising of the inorganic eluent ions, while the organic eluent ions studied to date have given only moderate sensitivity and poor chromatographic selectivity for alkali-metal solute ions. In this paper we provide a comprehensive assessment of the suitability of a range of aromatic bases as eluents for indirect UV absorption and direct conductivity detection of cations in nonsuppressed ion chromatography.

0003-2700/89/0361-1435$01.50/0

THEORY

Indirect UV absorbance detection of inorganic cations has been shown in principle to be a viable technique using aromatic bases as eluents (*9*). The principle of indirect detection, when applied to cations, relies on the premise that each solute cation eluting from the ion-exchange column displaces an equivalent number of eluent cations from the mobile phase so as to preserve electroneutrality.

The following relationship has been derived to describe the retention of cations on low-capacity ion-exchange columns:

$$\log k' = \text{constant} - (y/x) \log [\mathrm{E}]_m \qquad (1)$$

where k' is the capacity factor, $[\mathrm{E}]_m$ is the concentration of the eluting ion in the eluent, y is the charge on the solute ion, x is the charge on the eluent ion, and the constant term incorporates a number of factors such as the selectivity coefficient. The full derivation of this relationship has been presented elsewhere (*9*, *11*).

Equation 1 predicts a linear relationship between $\log k'$ and $\log [\mathrm{E}]_m$ with a negative slope equal to the ratio of the charges on the solute and eluent cations. A slope of −1.00 for a singly charged solute indicates that a singly charged eluent species is the eluting ion. Plots of $\log k'$ versus $\log [\mathrm{E}]_m$ are of fundamental importance in elucidating the nature of the eluting species in ion chromatography.

Two further important equations have been derived for the detector response occurring during elution of a solute. For conductivity detection, the change in conductance, ΔG, accompanying solute elution is given by (*12*)

$$\Delta G = \frac{(\lambda_{S^+} - \lambda_{E^+})C_{s^+}}{10^{-3}K} \qquad (2)$$

where λ_{S^+} and λ_{E^+} are the limiting equivalent ionic conductances (λ_+) of the solute and eluent ions, respectively, C_{S^+} is the concentration of ionized solute, and K is the cell constant, which accounts for the physical dimensions of the cell.

For UV absorption detection, the change in absorbance, ΔA, that accompanies elution of the solute is given by (*13*)

$$\Delta A = (\epsilon_{S^+} - \epsilon_{E^+})C_{S^+}l \qquad (3)$$

where l is the cell path length, C_{S^+} is the concentration of ionized solute, and ϵ_{S^+} and ϵ_{E^+} are the molar absorptivities of the solute and eluent ions, respectively.

EXPERIMENTAL SECTION

Apparatus. The liquid chromatograph consisted of a Millipore Waters (Milford, MA) Model M6000 pump, U6K injector, Model 430 conductivity detector, and a Model 481 variable wavelength UV–vis detector interfaced to a Houston Instruments (Austin, TX) Omnscribe Model B5217-1 dual pen chart recorder. The UV detector preceded the conductivity detector in the flow stream. A Waters IC-PAK C (50 × 4.6 mm i.d.) low-capacity polystyrene–divinylbenzene-based cation-exchange column was used, and the column was housed in a Waters Model 1122/WTC-120 column heater, operated at 35 °C. A Waters IC-PAK C cation concentrator column was used as a precolumn, and further protection of the analytical column from contamination by polyvalent metal ions was achieved by inserting a used IC-PAK C analytical column between the pump and injector.

The limiting equivalent ionic conductance determinations were performed on a homemade conductance meter connected to a Philips conductance cell, Model PW9510, and the UV spectral data were collected on a Hitachi U-3200 UV/vis spectrophotometer.

Reagents. Eluent solutions were prepared from 2-aminopyridine, 3,5-dimethylpyridine, 2-methylbenzylamine (EGA-Chemie, Steinheim/Albuch, West Germany), 4-aminopyridine, benzylamine hydrochloride, 2,4-dimethylpyridine, 2,3-dimethylpyridine, 1,4-phenylenediamine dihydrochloride (Aldrich, Milwaukee, WI), benzylamine (B.D.H. Chemicals, Ltd., Poole, England), 2-phenylethylamine hydrochloride, 2-methylpyridine, 3-methylpyridine, 4-methylpyridine, 3,4-dimethylpyridine, 2,6-dimethylpyridine, 4-methylbenzylamine, *N*-methylbenzylamine (Fluka AG, Buchs, Switzerland), disodium ethylenediaminetetraacetate (May and Baker, Ltd., Dagenham, England), ammonia gas, and nitric acid (Ajax, Sydney, Australia). These were used without further purification except for the nitric acid, which was distilled in a poly(tetrafluoroethylene) PTFE still. Water treated with a Millipore (Bedford, MA) Milli-Q water purification system was used to prepare eluent solutions.

Stock solutions of the individual alkali-metal ions, ammonium ion, alkaline-metal cations, and aluminum(III) were prepared with a polypropylene volumetric apparatus. The analytical grade chloride satls were used, with the exceptions of lithium, aluminum, rubidium, and magnesium, which were prepared from the respective sulfate, carbonate, and nitrate salts.

Procedures. Mobile phases were prepared by dissolution of the required amount of material in water, with the pH being adjusted if necessary with dilute nitric acid, followed by filtration through a 0.45-μm membrane filter and degassing in an ultrasonic bath. All eluents were operated at a flow rate of 1 mL/min.

The mobile phase used to periodically regenerate the cation-exchange column consisted of an aqueous solution of ethylenediaminetetraacetate (10 mM), buffered to pH 9.9 with ammonia/ammonium solution. The aqueous ammonia component of the buffer solution was prepared by bubbling ammonia gas through purified water and measuring the specific gravity to determine concentration. The resultant solution was diluted appropriately.

The seawater sample was pretreated prior to analysis by passage through a Waters Sep-Pak C18 filter cartridge that had been preconditioned with methanol and water.

RESULTS AND DISCUSSION

Selection of Suitable Eluents. Theoretical considerations suggest that bases to be used as eluent components for direct conductivity and indirect UV absorption detection of cations should have a $pK_a > 6$, a relatively large molar absorptivity, and a low limiting equivalent ionic conductance (*9*). The limitation on the value of the pK_a of the eluent base arises due to the necessity for a considerable fraction of the eluent to be protonated (so that it can function as a competing ion), without maintaining a significant concentration of hydrogen ions in the eluent. Hydrogen ions function as an effective ion-exchange displacing species for monovalent cations and can therefore interfere by competition with the protonated eluent ion during the ion-exchange process. When solute elution is influenced simultaneously by hydrogen ions and protonated eluent ions, the sensitivity of conductivity detection is reduced (*9*) because these two eluting species have opposite detection characteristics. In the conductivity detection mode, hydrogen ions provide indirect detection of solutes (i.e. decreasing conductance signals), whereas protonated eluent ions provide direct detection of solutes (i.e. increasing conductance signals). It is apparent that the composite change in conductance occurring on elution of a solute can be positive or negative, depending on the relative degrees to which retention is governed by hydrogen ions and protonated eluent ions. From this point of view, the free hydrogen ion concentration must be minimized, and this can be achieved by using a mobile phase of sufficiently high pH, typically around 6–7.

Table I lists the bases evaluated as eluents in this study, together with their pK_a values, measured limiting equivalent ionic conductances, measured molar absorptivities, and wavelength of maximum absorption. Table II shows the limiting equivalent ionic conductances of the solute cations used. It can be seen from Table I that all of the compounds considered were aromatic bases of appropriate pK_a values, with low limiting equivalent ionic conductances and moderate molar absorptivities in the mid-UV wavelength range. Comparison of Tables I and II suggests that direct conductivity detection should be possible for all solute ions except for

Table I. Properties of Aromatic Bases as Prospective Eluent Components

eluent component	λ_{max}, nm	ϵ, L mol^{-1} cm^{-1}	λ_+, S cm^2 equiv^{-1}	pK_{a1}	pK_{a2}
2,3-dimethylpyridine	266.4	6494	31.7	6.57	
2,4-dimethylpyridine	258.5	5460	32.8	6.99	
2,6-dimethylpyridine	269.2	7705	31.4	6.72	
3,4-dimethylpyridine	258.0	4619	36.9	6.49	
3,5-dimethylpyridine	267.5	5623	34.4	6.15	
2-methylpyridine	262.3	6449	29.8	5.92	
3-methylpyridine	262.3	7177	20.4	5.52	
4-methylpyridine	253.4	6516	36.7	6.08	
2-methylbenzylamine	263.3	492	34.9	9.19	
4-methylbenzylamine	261.6	276	36.3	9.36	
N-methylbenzylamine	255.8	509	34.5	9.54	
2-phenylethylamine	256.7	219	39.5	9.84	
benzylamine	255.9	249	31.6	9.33	
2-aminopyridine	290.0	4188	33.4	6.71	−7.6
3-aminopyridine	289.6	2717	34.1	6.03	−1.5
4-aminopyridine	260.5	14175	24.4	9.11	−6.55
1,4-phenylenediamine	284.1	12984	nd[a]	nd[a]	2.89

[a] Not determined.

Table II. Limiting Equivalent Ionic Conductances for the Inorganic Cations Investigated[a]

cation	λ_+, S cm^2 equiv^{-1}	cation	λ_+, S cm^2 equiv^{-1}
H^+	349.81	Li^+	38.68
Na^+	50.10	K^+	73.50
NH_4^+	73.50	Rb^+	77.81
Cs^+	77.26	Mg^{2+}	53.05
Ca^{2+}	59.50	Sr^{2+}	59.45
Ba^{2+}	63.63	Al^{3+}	61.00

[a] Data taken from ref 14 and 15.

lithium, which has a limiting equivalent ionic conductance very similar to those of the eluent ions.

Separation and Detection of Monovalent Cations. Each of the aromatic bases listed in Table I was used over a range of concentrations and pH values to form eluents suitable for the separation of monovalent cations. Table III lists the eluent conditions used for some of these eluents, together with the capacity factors observed. Elution characteristics for all the dimethylpyridine isomers were similar to those shown for 2,6-dimethylpyridine. Similarly, data for 2-methylpyridine are representative of those for other methylpyridine isomers. Plots of log k' versus log eluent concentration were constructed by varying the eluent concentration at fixed pH, and the slopes of these plots for the eluent

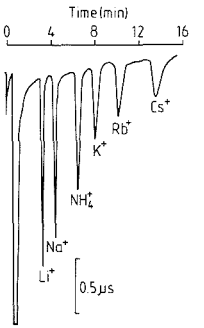

Figure 1. Chromatogram obtained with 2 mM nitric acid as eluent by use of indirect conductivity detection. Sample: 20 μL of a solution containing 10^{-5} M of each of the indicated ions.

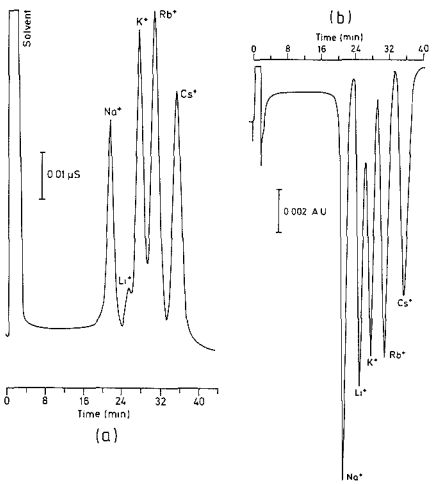

Figure 2. Chromatogram obtained with 0.2 mM 2,6-dimethylpyridine at pH 6.35 as eluent by use of (a) direct conductivity and (b) indirect UV absorption detection. Sample: 15 μL of a solution containing 2 × 10^{-5} M of each of the indicated ions.

species shown in Table III are listed in Table IV. All of the results shown were obtained from direct injection of 100-μL aliquots of a mixture containing 1.0 × 10^{-6} M of each of the solutes listed.

Nitric acid is a standard eluent used with conductivity detection of monovalent inorganic cations and was included in this study for comparison with the aromatic bases investigated. Figure 1 shows a typical chromatogram obtained with nitric acid and illustrates that indirect conductivity detection occurred as a result of the very high limiting ionic conductance of the hydrogen ion.

Table III. Capacity Factors of Monovalent Cations Obtained with Typical Eluents

eluent	concn, mM	pH	capacity factor Li^+	Na^+	NH_4^+	K^+	Rb^+	Cs^+
2,6-dimethylpyridine	0.20	6.35	35.9	32.8	42.1	42.4	47.6	54.4
2-methylpyridine	0.50	5.46	11.9	10.4	15.0	13.8	15.3	17.5
benzylamine	0.15	7.14	9.6	11.3	14.1	15.9	18.1	21.8
2-phenylethylamine	0.11	5.58	8.1	9.5	11.3	12.5	13.8	15.9
4-methylbenzylamine	0.10	6.92	6.8	8.2	10.2	11.6	13.2	15.0
nitric acid	2.0	2.70	3.8	5.6	9.0	11.3	14.5	19.8

Table IV. Slopes of Plots of log k' versus log Eluent Concentration for the Monovalent Inorganic Cations

eluent	pH	Li^+	Na^+	K^+	NH_4^+	Rb^+	Cs^+
2,6-dimethylpyridine	6.30	−0.83	−0.86	−0.87	−0.86	−0.86	−0.88
2-methylpyridine	5.95	−0.79	−0.82	−0.79	−0.78	−0.75	−0.77
benzylamine	7.00	nd[a]	−0.94	−0.93	−0.93	nd[a]	nd[a]
2-phenylethylamine	6.00	−1.15	−1.17	−1.14	−1.14	−1.24	−1.16
4-methylbenzylamine	6.20	−0.77	−0.77	−0.79	−0.77	−0.79	−0.79

[a] Not determined.

Figure 2 shows the chromatograms obtained by using 0.2 mM 2,6-dimethylpyridine at pH 6.35 as eluent, with both conductivity and UV absorption detection. Two points of interest emerge from Figure 2. First, the elution order of lithium and sodium was reversed in comparison to that obtained with the nitric acid eluent. No conclusive reason for this behavior was found, but it is possible that complexation effects between the eluent and the solute are responsible. A similar reversal of the conventional elution order for ammonium and potassium was noted for all of the dimethylpyridine isomers examined, except for 2,6-dimethylpyridine. The second point of interest from Figure 2 is the very small conductivity signal obtained for lithium, which is expected from the limiting equivalent ionic conductances for lithium and 2,6-dimethylpyridine listed in Tables I and II. It is noteworthy that potassium and ammonium could not be resolved under the chromatographic conditions used in Figure 2.

The slopes obtained for plots of log k' versus log eluent concentration (Table IV) can be used to ascertain the degree to which hydrogen ions contribute to the elution of the cations studied. Since the pH (and thus the hydrogen ion concentration) were constant for each eluent concentration used in the preparation of the above plots, the slope can be expected to range between zero (for the case where hydrogen ions are solely responsible for elution) and −1.0 (the theoretical slope for the case where the base exists as a monoprotonated cation and is solely responsible for elution of a singly charged solute). Knowledge of this slope provides an insight into the relative contributions to elution of the base cations and hydrogen ions and therefore into whether the chromatographic conditions in use provide optimal detection. It is noteworthy that the degree of protonation of the eluent does not affect the slope and is reflected as an increased intercept on the log k' axis as the degree of protonation decreases. These effects are illustrated schematically in Figure 3. The slopes shown in Table IV for 2,6-dimethylpyridine fall in the range −0.83 to −0.88. These results indicated that the contribution of hydrogen ions to elution was small. Similar results were observed for other dimethylpyridine isomers, with the exception of 2,4-dimethylpyridine, which gave an average slope of −1.25. This gives an effective charge for 2,4-dimethylpyridine eluent of 0.8, which for a univalent solute cation is calculated by taking the reciprocal of the observed slope. This low value for the effective charge on the eluent cation can possibly be explained by steric effects that prevent close approach of the cationic nitrogen atom to the sulfonate exchange site on the stationary phase (*16*).

The methylpyridine isomers also eluted the monovalent cations as a closely spaced group of peaks; however, the selectivity exhibited by these eluents was such that resolution of five solutes could be achieved with a shorter analysis time than that possible with the dimethylpyridine eluents. Figure 4 shows a typical separation obtained with 2-methylpyridine, using both conductivity and UV absorption detection. Slopes of the plots of log k' versus of eluent concentration for methylpyridine eluents were close to −1.0, except for 2-methylpyridine, which gave an average slope of −0.78 (see Table IV), indicating some competition by hydrogen ions under the chromatographic conditions employed. Once again, sodium eluted before lithium, but this effect was not observed for 4-methylpyridine. In all cases, lithium appeared as a small negative peak when conductivity detection was used.

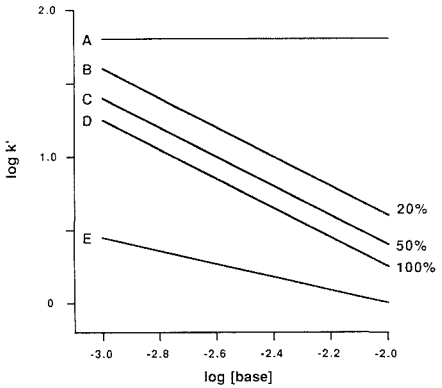

Figure 3. Schematic representation of plots of log k' versus log base concentration showing the effect of varying degrees of protonation of the eluent. In curve A, hydrogen ions are solely responsible for elution, while in curves B, C, and D, the aromatic base cation is solely responsible for elution. Curve E shows the case where the eluent is fully ionized and both species contribute to elution. A singly charged eluent and solute cation is assumed.

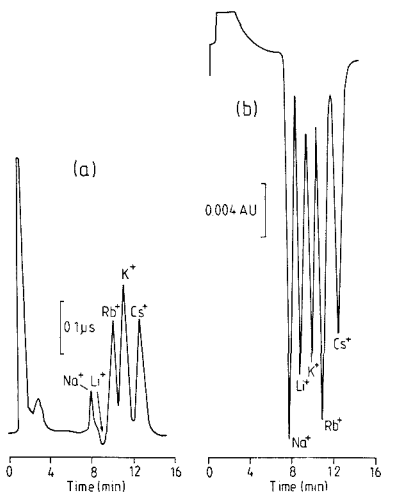

Figure 4. Chromatogram obtained with 0.5 mM 2-methylpyridine at pH 5.46 as eluent by use of (a) direct conductivity and (b) indirect UV absorption detection. Sample: 25 μL of a solution containing 2×10^{-5} M of each of the indicated ions.

Chromatograms obtained with the other aromatic bases studied, namely benzylamine, 2-phenylethylamine, and 4-methylbenzylamine, were all similar, and as a representative example, the chromatogram for 0.1 mM 4-methylbenzylamine at pH 6.92 is shown in Figure 5.

Resolution of all six monovalent cations could be achieved with these eluents, with lithium appearing as a small positive peak with conductivity detection. The slopes of plots of log k' versus log eluent concentration for these eluents are given

Table V. Detection Limits Obtained for Monovalent Cations with Typical Aromatic Base Eluents, Calculated for a 100-μL Injection

eluent	detection mode	detection limits, ppb					
		Li^+	Na^+	K^+	NH_4^+	Rb^+	Cs^+
2,6-dimethylpyridine	conductivity	*a*	2.1	0.6	1.4	2.9	6.7
	indirect UV	0.4	0.8	0.9	1.8	5.0	11.1
2-methylpyridine	conductivity	*a*	1.1	0.6	1.1	2.5	4.7
	indirect UV	0.4	1.2	3.0	1.9	5.7	11.1
2-phenylethylamine	conductivity	1.6	0.6	0.4	0.6	1.3	2.9
	indirect UV	0.7	2.0	1.8	3.4	6.6	14.3
4-methylbenzylamine	conductivity	0.3	0.8	0.4	0.6	1.3	2.5
	indirect UV	0.2	0.8	0.7	1.3	4.1	10.2
benzylamine	conductivity	0.8	0.4	0.4	0.5	1.4	2.9
	indirect UV	0.6	1.3	2.3	2.8	9.1	21.0
nitric acid	conductivity	0.1	0.4	0.4	1.4	2.4	5.3

[a] Negligible detection signal for lithium in the concentration range studied.

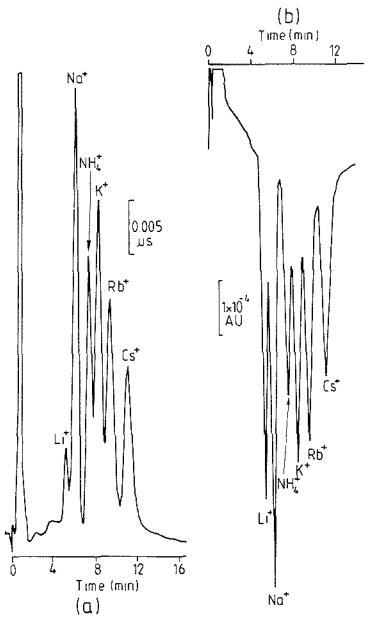

Figure 5. Chromatogram obtained with 0.1 mM 4-methylbenzylamine at pH 6.92 as eluent by use of (a) direct conductivity and (b) indirect UV absorption detection. Sample: 15 μL of a solution containing 2 × 10^{-5} M of each of the indicated ions.

in Table IV. The elution order of sodium and lithium for the eluents was identical with that observed for nitric acid, provided the column used was in good condition and had been adequately conditioned with eluent. A large system peak at a retention time of 35 min was observed for the 2-phenylethylamine eluent with both conductivity and UV absorption detection. System peaks were not found for any of the other eluents examined.

As a general trend, it was found that ortho and para isomers of the substituted aromatic bases provided superior chromatographic separation to that achieved with meta isomers. It is noteworthy that the direction of the lithium peak obtained by conductometric detection could not be predicted from the values of limiting equivalent ionic conductance listed in Tables I and II. For example, it was expected that a positive lithium peak would result when 4-methylpyridine was used as eluent, since the limiting equivalent ionic conductance for the eluent

Table VI. Capacity Factors of Polyvalent Solutes Obtained with Typical Eluents

eluent	concn, mM	pH	capacity factor			
			Mg^{2+}	Ca^{2+}	Sr^{2+}	Ba^{2+}
benzylamine	10	5.5	1.9	3.5	4.1	8.2
2-phenylethylamine	10	5.7	3.8	7.0	9.2	19.0
4-methylbenzylamine	8	7.2	5.8	10.4	12.5	26.1
4-aminopyridine	10	7.02	8.2	14.5	24.8	nd[a]

[a] Not detected.

cation was less than that for the lithium ion. In practice, a negative peak was observed. This discrepancy can be explained by considering the contribution to elution of hydrogen ions, which would produce a negative (i.e. indirect) conductivity peak. With all eluents tested, lithium was easily detectable by indirect UV absorption.

The detection limits (calculated for a signal to noise ratio of 2) attained for monovalent cations by using typical aromatic base eluents are listed in Table V. Nitric acid provided the highest sensitivity for lithium and sodium when conductivity detection was used, but for the remaining monovalent cations, the aromatic base eluents gave superior sensitivity. Examination of the limiting equivalent ionic conductances listed in Table I suggests that eluents based on the hydrogen ion should give the highest detection signals, but the requirement to offset the high background conductance of nitric acid eluents resulted in increased base-line noise. Direct conductivity detection with eluents of low background conductance did not suffer from this drawback, and good detection sensitivity was attained despite the fact that the difference in limiting equivalent ionic conductance between the eluent and solute cations was less for aromatic base cations than for hydrogen ions. Detection limits for indirect UV absorption detection were comparable to those for conductivity detection for lithium and sodium, but were somewhat worse for the remaining solute cations. Nevertheless, UV detection of cations can be performed at great sensitivity, and the detection limits obtained are superior to those reported for inorganic anions when aromatic carboxylic acids are used as eluents (*13*).

Separation and Detection of Polyvalent Cations. Several of the aromatic bases studied were found to be suitable for the separation of alkaline-earth-metal cations, and all showed the same selectivity for these solutes, giving an elution order of magnesium, calcium, strontium, and barium. Table VI shows retention times obtained for representative eluents of each type, and Table VII lists the slopes of plots of log k' versus log eluent concentration for alkaline-earth-metal cations obtained with the use of these eluents.

The alkaline-earth-metal cations are not eluted by hydrogen ions, even when relatively high concentrations of acid are

Table VII. Slopes of Plots of log k' versus log Eluent Concentration for Alkaline-Earth-Metal Cations

eluent	pH	Mg^{2+}	Ca^{2+}	Sr^{2+}	Ba^{2+}
benzylamine	5.50	−2.02	−2.02	−2.07	−1.97
2-phenylethylamine	5.70	−1.99	−1.88	−2.02	−2.00
4-methylbenzylamine	5.70	−2.00	−1.96	−1.97	−2.00
4-aminopyridine	5.30	−1.04	−0.95	−0.88	−0.87

Table VIII. Detection Limits Obtained for Alkaline-Earth-Metal Cations with Typical Aromatic Base Eluents, Calculated for a 100-μL Injection

eluent	detection mode	detection limits, ppb			
		Mg^{2+}	Ca^{2+}	Sr^{2+}	Ba^{2+}
2-phenylethylamine	conductivity	9	19	48	82
	indirect UV	1.3	3.8	12	58
benzylamine	conductivity	12	13	87	917
	indirect UV	11	63	290	1370
4-methylbenzylamine	conductivity	20	50	110	514
	indirect UV	5.1	16	47	147

present in the eluent. The detection interference problems caused by hydrogen ions that were encountered with monovalent solute cations were therefore no longer present. The pK_a of the eluent base and the pH of the eluent were not critical, and the only constraint was that an eluent pH that is too low resulted in a high background conductance, which was required to be electronically offset by the detector. This had the effect of increasing base-line noise and reducing the sensitivity of conductometric detection. For this reason, the eluents were used at a pH that ensured total protonation of the eluent base, leading to an effective eluent charge of +1.0 for all of the base cations (see Table VII), except for the difunctional 4-aminopyridine, which had an effective charge of +2.0. The slopes listed in Table VII and all close to the theoretical values predicted from eq 1.

Figure 6 shows chromatograms obtained for alkaline-earth-metal cations by using 10 mM phenylethylamine at pH 5.49 as eluent, with conductivity and UV absorption detection. These chromatograms are representative of those obtained with all of the eluents listed in Table VI. Detection limits for each cation, obtained by using three of the eluents examined, are listed in Table VIII, from which it can be seen that conductivity detection was generally inferior to indirect UV absorption detection. The phenylethylamine eluent was applied to the separation of calcium and magnesium in seawater by direct injection of a sample that had been diluted by a factor of 100. Figure 7 shows the chromatogram obtained and illustrates that the large excess of sodium in the sample did not cause any significant interference, presumably because the sodium ions were unretained with the eluent used.

More powerful eluents can be obtained by using bases that can carry two positive charges. Fortier and Fritz (*17*) have employed 1,4-phenylenediamine at pH 2.94 as an eluent for the determination of aluminum(III) using conductivity detection. Table I shows that this eluent has a considerable molar absorptivity, suggesting that indirect UV absorption detection should be possible. Figure 8 shows chromatograms obtained with both of the above forms of detection using an eluent prepared from the dihydrochloride salt of 1,4-phenylenediamine, and it illustrates that aluminum could be detected by either method. The detection limits for conductivity and UV detection were 100 and 270 ppb, respectively, and these values were limited by the high background signals produced by the eluent, which increased base-line noise and, in the case of UV detection, necessitated use of a detection wavelength giving decreased absorption.

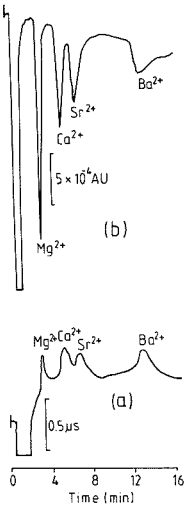

Figure 6. Chromatogram obtained with 10 mM phenylethylamine at pH 5.49 as eluent by use of (a) direct conductivity and (b) indirect UV absorption detection. Sample: 60 μL of a solution containing 10^{-5} M of each of the indicated ions.

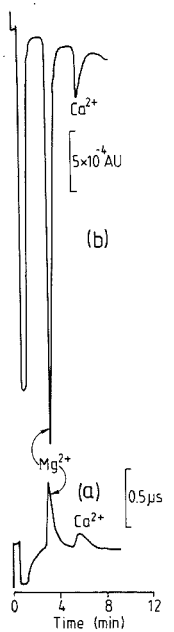

Figure 7. Separation of magnesium and calcium in seawater with use of (a) direct conductivity and (b) indirect UV absorption detection. Sample: 20 μL of a seawater sample diluted 100-fold. Chromatographic conditions are as for Figure 6.

CONCLUSIONS

This study has shown that indirect UV absorbance detection and direct conductivity detection of inorganic cations can be applied simultaneously in the separation of alkali-metal, ammonium, alkaline-earth-metal, or aluminum(III) cations

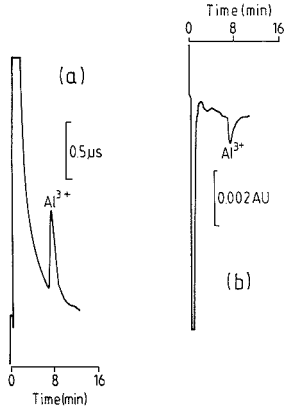

Figure 8. Chromatogram of aluminum(III) obtained with 5.48 mM 1,4-phenylenediamine at pH 2.68 as eluent and (a) direct conductivity and (b) indirect UV absorption detection. Sample: 100 μL of a 10^{-4} M solution of aluminum(III).

using protonated aromatic bases as eluent components. Adequate resolution of the six monovalent cations was obtained with eluents containing benzylamine, 2-phenylethylamine, or 4-methylbenzylamine, and these three eluent systems offered sensitive detection of the six ions by either form of detection. Eluents formed from any of the remaining aromatic bases could separate five of the six monovalent ions. However, the very low detection limits offered by these eluent systems for common ions such as sodium, ammonium, and potassium still make them attractive with indirect UV absorbance detection.

The separation and detection of alkaline-earth-metal ions was possible with many of these same eluent systems, provided they were used at higher concentrations, with the best results being obtained with 2-phenylethylamine when used with indirect UV absorbance detection.

Use of these aromatic bases as eluents for the simultaneous separation of monovalent and divalent cations does not appear feasible due to the large disparity in affinity for column sites between these two groups of solutes. However, it has been demonstrated that the same column and eluent type can be used for the determination of monovalent, divalent, or trivalent inorganic cations.

LITERATURE CITED

(1) Small, H.; Miller, T. E., Jr. *Anal. Chem.* **1982**, *54*, 462.
(2) Miller, T. E., Jr. *Adv. Instrum.* **1983**, *38*, 347.
(3) Miyazaki, M.; Hayakawa, K.; Choi, S. G. *J. Chromatogr.* **1985**, *323*, 443.
(4) Shintani, H. *J. Chromatogr.* **1985**, *341*, 53.
(5) Shintani, H.; Tsuji, K.; Oba, T. *Bunseki Kagaku* **1985**, *34*, 109.
(6) Hayakawa, K.; Ebina, R.; Matsumoto, M.; Miyazaki, M. *Bunseki Kagaku* **1984**, *33*, 390.
(7) Sherman, J. H.; Danielson, N. D. *Anal. Chem.* **1987**, *59*, 490.
(8) Haddad, P. R.; Heckenberg, A. L. *J. Chromatogr.* **1982**, *252*, 177.
(9) Foley, R. C.; Haddad, P. R. *J. Chromatogr.* **1986**, *366*, 13.
(10) Iskandarani, Z.; Miller, T. E., Jr. *Anal. Chem.* **1985**, *57*, 1591.
(11) Lederer, M.; Kertes, S. *Anal. Chim. Acta* **1956**, *15*, 226.
(12) Fritz, J. S.; Gjerde, D. T.; Pohlandt, C. *Ion Chromatography*; Huthig: Heidelberg, 1982; p 119.
(13) Haddad, P. R.; Jandik, P. Detection Methods for Ion Chromatography. In *Ion Chromatography*; Tarter, J. G., Ed.; Marcel Dekker: New York, 1986; p 87.
(14) Chang, R. *Physical Chemistry with Applications to Biological Systems*; Macmillan: New York, 1977; p 290.
(15) Alyward, G. H.; Findlay, T. J. V. *SI Chemical Data*, 2nd ed.; Wiley: Sydney, 1974; p 126.
(16) Lederer, M. *J. Chromatogr.* **1988**, *452*, 265.
(17) Fortier, N. E.; Fritz, J. S. *Talanta* **1985**, *32*, 1047.

RECEIVED for review December 19, 1988. Accepted March 20, 1989. We thank Millipore Waters for generous support provided for this project.

Fast Atom Bombardment Induced Reduction of Aromatic Oximes

M. Graca O. Santana-Marques and Antônio J. V. Ferrer-Correia

Department of Chemistry, University of Aveiro, 3800 Aveiro, Portugal

Michael L. Gross*

Midwest Center for Mass Spectrometry, Department of Chemistry, University of Nebraska, Lincoln, Nebraska 68588

Aromatic oximes and β-hydroxyoximes are reduced to their corresponding imines by interaction of their solutions in glycerol solvent with a 7-keV argon atom beam. Evidence that the reduction occurs for the protonated oximes comes from fast atom bombardment (FAB) mass spectrometry, tandem mass spectrometry, and time-resolved FAB studies. The requirement that the oxime be in solution was established by comparing the FAB results with those obtained by electron ionization, chemical ionization, and laser desorption. The time-dependent studies of the concentration of the protonated oxime and the reduced product, a protonated imine, were made with and without added anionic surfactant. The abundance of the reduced species depends on the concentration of the protonated oxime at the matrix surface, thus showing that the first step of the reduction mechanism is the protonation of the analyte, followed by reduction and eventual desorption of the reduced species. Surface reduction occurs for all the compounds containing an oxime group that were studied and is a useful characteristic for identifying oximes by fast atom bombardment mass spectrometry.

INTRODUCTION

Fast atom bombardment mass spectrometry is a useful technique especially for the analysis of polar and nonvolatile compounds. Mechanisms of desorption that occur upon fast atom bombardment are still the object of some controversy, and several interpretations of the ionization phenomena under fast atom bombardment conditions were advanced by different authors (*1–6*). A better understanding and a better utilization of this technique can be achieved through the investigation of the many facets of desorption ionization from a liquid matrix.

Reduction of the analyte under desorption ionization conditions has received considerable attention and occurs for different types of compounds (*7–10*). Evidence exists that reduction takes place for the same type of compound both in the absence (*11*) and in the presence of a liquid matrix (*12, 13*). Suggestions that radicals produced in the liquid matrix play a role in reduction phenomena were advanced by Field (*14*) and Ligon (*15*), whereas Cerny and Gross (*16*) proposed multiple protonation followed by one and two electron reductions. Williams et al. (*17*) attempted to generalize the mechanism for reduction under fast atom bombardment and secondary ion mass spectrometry by postulating that the electrons produced by the impact of kiloelectronvolt ionizing particles are the effective reducing agents. Reduction involves in part the capture of thermal or near thermal energy electrons by sample molecules.

Under fast atom bombardment conditions, reductions involving dehalogenation were observed (*18, 19*). For some *N*-hydroxy nitrogen compounds (benzohydroxamic acid, 1-hydroxybenzotriazole, and *N*-hydroxysuccinimide), reduction to their deoxygenated counterparts was also reported (*19*). Deoxygenation was observed for sulforhodamine B, a xanthane type dye (*10*). In all these studies, the mechanism and generality of the reduction processes were not established.

Table I. Aromatic Oximes of the General Formula $C_6H_5C(R)NOH$

	R	oxime	mol wt
I	H	benzaldoxime	121
II	CH_3	acetophenone oxime	135
III	C_2H_5	propiophenone oxime	149
IV	C_3H_7	butyrophenone oxime	163
V	C_6H_{13}	heptanophenone oxime	205
VI	$C_{11}H_{23}$	dodecanophenone oxime	275
VII	C_6H_5	benzophenone oxime	197

A substance that was extensively used for studying reduction is methylene blue (*11–13, 20*). A correlation of the extent of the reduction occurring in fast atom bombardment mass spectrometry and secondary ion mass spectrometry with its electrochemical potential in solution was established (*12, 13*), and it was concluded that the substance must be dissolved in a liquid matrix for reduction to occur (*12*). On the other hand, the same reduction processes were shown to occur in the absence of any protic solvent, due to self-hydrogenation by the analyte molecules, and the correlation mentioned above was suggested to be fortuitous (*11*). Thus, the requirements of fast atom bombardment mass spectrometry and the presence of a matrix for inducing reduction remain open questions. We will address these questions for oximes by studying their reduction to the corresponding imines under fast atom bombardment conditions.

Oximes are widely used in industry (*21, 22*) and in chemical analysis (*23–26*). Methods for structure proof and analysis of oximes are therefore needed. The reduction that we observe is common to all the compounds containing an oxime function group and is useful for establishing more clearly the mechanism of reduction induced by fast atom bombardment. Furthermore, reduction is a general feature of the fast atom bombardment (FAB) mass spectrometry of oximes and, as such, can be used in the identification and structure proof of this class of compounds, in either the pure or mixed state. The reader is directed to a recent review for a more detailed discussion of chemical reactions that accompany desorption ionization (*27*).

EXPERIMENTAL SECTION

All the oximes (Table I) and some of the hydroxyoximes (I to VI, Table II) were synthesized from their corresponding aldehydes and ketones by using standard procedures (*28*). Industrial hydroxyoximes (VII to X, Table II) were purified first by complexation with Cu(II) (*29*) and further by high-pressure liquid chromatography (*30*). Benzophenone imine was purchased from Aldrich (Milwaukee, WI).

0003-2700/89/0361-1442$01.50/0

Table II. Aromatic β-Hydroxyoximes of the General Formula $RC_6H_3OHC(R')$=NOH

	R	R′	hydroxyoxime
I	H	H	2-hydroxybenzaldoxime (salicylaldoxime)
II	H	CH_3	2-hydroxyacetophenone oxime
III	H	C_6H_5	2-hydroxybenzophenone oxime
IV	CH_3	H	2-hydroxy-5-methylbenzaldoxime
V	CH_3	CH_3	2-hydroxy-5-methylacetophenone oxime
VI	CH_3	C_6H_5	2-hydroxy-5-methylbenzophenone oxime
VII	C_8H_{17}	H	2-hydroxy-5-octylbenzaldoxime
VIII	$C_6H_{13}(CH_3)_2C$	H	2-hydroxy-5-(1′,1″-dimethyl-heptyl)benzaldoxime
IX	$C_6H_{13}(CH_3)_2C$	CH_3	2-hydroxy-5-(1′,1″-dimethyl-heptyl)acetophenone oxime
X	$C_6H_{13}(CH_3)_2C$	C_6H_5	2-hydroxy-5-(1′,1″-dimethyl-heptyl)benzophenone oxime

Fast atom bombardment mass spectra were obtained with a Kratos MS-50 triple analyzer mass spectrometer (Manchester, U.K.), which was described elsewhere (*31*). A standard Kratos FAB source equipped with an Ion Tech gun was used. The samples were dissolved in glycerol and bombarded with 7-keV argon atoms. For the time dependence studies, 0.01 M solutions of the oximes in glycerol and a 0.01 M solution of lithium dodecyl sulfate in glycerol were used. Ion abundances were measured by using the same calibration file (mass range from 99 to 282 amu) and doing the same number of successive scans, with the same instrumental parameters, for the selected mass range. Normal spectra were acquired at low mass resolution (ca. 3000).

Metastable ion and collisionally activated decomposition (CAD) mass analyzed ion kinetic energy spectra (MIKES) were obtained by scanning the second electrostatic analyzer. CAD spectra were obtained by using helium as collision gas (collision cell located between the magnetic sector and the second electrostatic analyzer), with 50% suppression of the intensity of the signal. The data were processed with a standard DS-55 data system by using software written at the Midwest Center for Mass Spectrometry.

Accurate mass measurements under FAB conditions were made by peak-matching with a Kelvin-Varley voltage divider, using selected ions from a desorption of a cesium iodide/glycerol sample as references.

Full scan, high resolution (R = 10 000) electron ionization (EI) mass spectra were obtained with a Kratos MS-50 double focusing mass spectrometer, interfaced to a Nova-4X computer and operating with DS-55 software. The source temperature was 250 °C, and the solids probe was heated sufficiently so that an ion beam was produced.

Laser desorption spectra were obtained with a Fourier transform mass spectrometer, constructed in the Midwest Center for Mass Spectrometry (*32*) and controlled with a Nicolet FTMS-1000 computer and data acquisition system. A Quanta-Ray DCR-2 Nd:YAG laser was used at two wavelengths and pulse intensities: 266 nm, 5 mJ and 1064 nm, 140 mJ.

RESULTS AND DISCUSSION

Fast Atom Bombardment and Fast Atom Bombardment Mass Analyzed Ion Kinetic Energy Spectra. Fast atom bombardment of all the compounds studied (aromatic oximes and β-hydroxyoximes) produces $[(M + H) - O]^+$ ions in the gas phase. The abundances of $[(M + H) - O]^+$ ions increase with increasing time, to the point where this ion is the most abundant. In Table III, the fast atom bombardment mass spectra of the oximes with the general formula $C_6H_5C(R)$=NOH, listed in Table I, are presented. The data were obtained from spectra recorded at the same elapsed time after sample introduction in all cases. Because the relative abundances of the $[M + H]^+$ and $[(M + H) - O]^+$ ions vary with time, the choice of the spectra was made after the time-dependent studies were analyzed. Spectra are reported at the point when the ratios of both the $[M + H]^+$ and $[(M + H) - O]^+$ ion abundances to their sum became constant within experimental error.

Table III. Relative Ion Abundances of Fast Atom Bombardment Mass Spectra of Oximes I to VII (% of Base peak)[a]

oxime	$[M + H]^+$	$M^{+\cdot}$	$[(M + H) - O]^+$	$[(M + H) - H_2O]^+$	$C_6H_5CNH^+$
I	28	25	100	50	49
II	34		100	49	13
III	27		55	26	19
IV	70		100	42	30
V	18		100	15	54
VI	30		74	11	17
VII	19		35	13	11

[a] "Plateau" values.

Besides the $[(M + H) - O]^+$ ions, the ions formed by a loss of one H_2O molecule are also significant for oximes. Formation of the molecular radical cation is only found in the case of the benzaldoxime. The ion of m/z = 104, probably having the formula $C_6H_5CNH^+$, is a common fragment for all the oximes.

To confirm that the $[(M + H) - O]^+$ ions are not the product of a gas-phase decomposition of the $[M + H]^+$ ions, but the result of an independent reduction process, metastable ion and collisionally activated MIKE spectra were obtained of the $[M + H]^+$ ions of all the oximes. The three most abundant ions for each of the oximes listed in Table I, are shown in Tables IV and V. The principal decompositions as registered in the metastable ion spectra are the loss of H_2O, the formation of ions of m/z = 104, m/z = 91, and m/z = 77, and alkene elimination in the case of oximes with larger alkyl groups (from C_3H_7 to $C_{11}H_{23}$). Upon collisional activation, the principal decompositions are the losses of H, ROH, and CRNHOH, the last two giving the ions of m/z = 104 and m/z = 77. Alkane elimination is only important for the heptanophenone oxime and dodecanophenone oxime. Loss of H_2O gives the most abundant fragment in the mass spectrum of benzophenone oxime.

From these results, the complete absence of a decomposition, either metastable or collisionally activated, giving rise to the loss of an oxygen atom from the protonated quasi-molecular action, is ascertained. Similar results were found in the case of the β-hydroxyoximes, so we can conclude that the $[(M + H) - O]^+$ ions are not formed by gas-phase decomposition of the $[M + H]^+$ ions but are probably produced in the matrix and then desorbed.

Identification of the Reduction Products. For the β-hydroxyoximes with the general formula $RC_6H_3OHC(R')$=NOH, listed in Table II from VII to X, the composition of the ions formed by the loss of 16 amu from the $[M + H]^+$ ions was established on the basis of accurate mass measurements. These are presented on Table VI. The correct composition is $[(M + H) - O]^+$, and other possible compositions such as $[(M + H) - NH_2]^+$ and $[(M + H) - CH_4]^+$ are ruled out because they give deviations in the range 67–97 and 106–151 ppm, respectively.

In addition, the iminium ion structure of the $[(M + H) - O]^+$ ions had to be checked. It is well-known that imines of the general formula RR′C=NH are often very unstable and highly reactive (*33*). Nevertheless, some aromatic imines such as the benzophenone imine are stable enough to be synthesized and stored. Therefore, we sought to compare the CAD spectrum of the protonated ion of the benzophenone imine and that of the $[(M + H) - O]^+$ ion of the benzophenone oxime (see Figure 1). On the basis of their near identity, the proposed iminium structure for the reduced form is confirmed.

It is interesting to note that an iminium type intermediate has been postulated for the electrochemical reduction of ox-

Table IV. Metastable Ion MIKE Spectra of $[M + H]^+$ Given as Decreasing Abundances[a]

oxime		fragments		
I	ion	$[(M + H) - H_2O]$	$C_6H_5^+$	$M^{+\bullet}$
	(*m/z*)	(104)	(77)	(121)
	rel abund	50%	34%	16%
II	ion	$[(M + H) - H_2O]^+$	$C_6H_5^+$	$C_7H_7^+$
	(*m/z*)	(118)	(77)	(91)
	rel abund	83%	4%	2%
III	ion	$[(M + H) - H_2O]^+$	$[(M + H) - ROH]^+$	$C_2H_5CNOH^+$
	(*m/z*)	(132)	(104)	(72)
	rel abund	46%	24%	17%
IV	ion	$[(M + H) - OH]^+$	$[(M + H) - C_3H_6]^+$	$[(M + H) - H_2O]^+$
	(*m/z*)	(147)	(122)	(146)
	rel abund	19%	18%	16%
V	ion	$[(M + H) - C_6H_{12}]^+$	$[(M + H) - H_2O]^+$	$C_7H_7^+$
	(*m/z*)	(122)	(188)	(91)
	rel abund	26%	10%	8%
VI	ion	$[(M + H) - H_2O]^+$	$[(M + H) - C_{11}H_{22}]^+$	$C_7H_7^+$
	(*m/z*)	(258)	(122)	(91)
	rel abund	31%	18%	9%
VII	ion	$[(M + H) - H_2O]^+$	$C_6H_5CNOH^+$	$C_6H_5^+$
	(*m/z*)	(180)	(120)	(77)
	rel abund	62%	9%	2%

[a] Ion abundances were normalized to 100.

Table V. CA MIKE Spectra of $[M + H]^+$ Given as Decreasing Abundances[a]

oxime		fragments		
I	ion	$[(M + H) - ROH]^+$	$M^{+\bullet}$	$C_6H_5^+$
	(*m/z*)	(104)	(121)	(77)
	rel abund	32%	24%	21%
II	ion	$[(M + H) - ROH]^+$	$M^{+\bullet}$	$C_6H_5^+$
	(*m/z*)	(104)	(135)	(77)
	rel abund	25%	16%	13%
III	ion	$[(M + H) - ROH]^+$	$M^{+\bullet}$	$C_6H_5^+$
	(*m/z*)	(104)	(149)	(77)
	rel abund	17%	16%	15%
IV	ion	$[(M + H) - ROH]^+$	$M^{+\bullet}$	$C_6H_5^+$
	(*m/z*)	(104)	(163)	(77)
	rel abund	22%	14%	10%
V	ion	$[(M + H) - ROH]^+$	$[(M + H) - C_4H_{10}]^+$	$M^{+\bullet}$
	(*m/z*)	(104)	(148)	(205)
	rel abund	18%	13%	10%
VI	ion	$[(M + H) - C_9H_{20}]^+$	$[(M + H) - C_{10}H_{21}]^+$	$[(M + H) - ROH]^+$
	(*m/z*)	(148)	(135)	(104)
	rel abund	17%	14%	12%
VII	ion	$[(M + H) - H_2O]^+$	$M^{+\bullet}$	$C_6H_5^+$
	(*m/z*)	(180)	(197)	(177)
	rel abund	39%	26%	15%

[a] Sum of abundances normalized to 100.

Table VI. Accurate Mass Measurements Establishing the Composition of $[(M + H) - 16]^+$ Ions

hydroxyoxime	calculated mass for $[(M + H) - O]^+$	found	error, ppm
VII	234.185 789	234.184 79	−4.3
VIII	248.201 439	248.200 66	−3.1
IX	262.217 089	262.216 14	−3.6
X	324.232 739	324.230 74	−6.2

imes in solution (*34*), where they are reduced, in some cases, to the corresponding amines via the imines in an overall two-step, four-electron process. These studies were mainly performed in an acidic or neutral media. Here we propose a two-electron process that will be discussed later.

FAB in Other Matrices and CI. We attempted to evaluate whether reduction occurs in a matrix-less FAB experiment. Unfortunately, the signals for $(M + H)^+$ were so

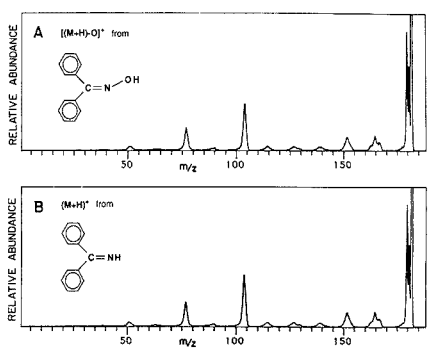

Figure 1. CAD MIKE spectra of ions $(C_6H_5)_2C{=}NH_2^+$ (m/z = 182): (A) ion obtained in FAB spectrum of benzophenone oxime; (B) ion obtained in FAB spectrum of the benzophenone imine.

transient, even at the lowest atom dosages we could arrange with a saddle field gun, that no conclusion can be drawn from these experiments.

Nevertheless, we are able to establish that the reduction is most facile in protic solvents. The fractions of the ion current of the $[(M + H) - O]^+$ ion with respect to the sum of the currents of $[(M + H) - O]^+$ and $(M + H)^+$ for tetradecylaldoxime are given as follows for four test matrices: 3-nitrobenzyl alcohol, 7%; *o*-nitrophenyloctyl ether, 18%; dithioerythritol/dithiothreitol, 34%; acidified glycerol, 52%.

The trend is evidence that a protic solvent is required for reduction to occur.

Under isobutane chemical ionization conditions, the relative abundance of the $[(M + H) - O]$ for the tetradecylaldoxime is 1% at best, also confirming the need for a protic matrix for the reduction.

High-Resolution Electron Ionization and Laser Desorption Fourier Transform Mass Spectra. Having established that the $[(M + H) - O]^+$ ions are iminium ions and that their formation is not a result of gas-phase decompositions, we wish to demonstrate that the iminium ions are formed almost exclusively as the result of a fast atom bombardment induced reduction. The absence of imine traces in the oxime samples was established. High-resolution EI mass spectra were obtained to ensure that even traces (<1%) were not present. The loss of an oxygen atom upon EI was reported for some oximes and oxime O-alkyl ethers (*35–40*) and was at first considered an unusual mass spectrometric fragmentation (*35–37*). Later it was explained as a thermal decomposition process (*38–40*), in agreement with the known fact that when oximes are subjected to intense heating, they can decompose to the corresponding imines (*41*). One source for the $[M - O]^+$ ion formation under EI conditions, other than a thermal reaction, was proposed to be the bimolecular reaction $2[M]^{+\bullet} \rightarrow [M - O]^+ + [M + O]^+$ (*42*). Because $[M - O]^+$ ions are not detected in the high-resolution EI mass spectra (the two most abundant ions are the $[M - OH]^+$ ion and the molecular radical cation), we conclude that neither thermal decomposition nor bimolecular processes give rise to the above mentioned ions.

Laser desorption is a desorption ionization (DI) method in which the tendency toward thermal degradation is greater (*43*) than for other DI methods. So, having excluded the possibilities of thermal decomposition and of trace impurities, we sought evidence for the possibility of a thermal decomposition under more vigorous conditions by obtaining the laser desorption Fourier transform mass spectra of the oximes in the absence and in the presence of a liquid matrix (1% acidic glycerol). In all the recorded spectra, the fragment ions $[(M + H) - H_2O]^+$ were observed in addition to ions formed by protonation or attachment of metal ions (i.e., $[M + H]^+$, $[M + Na]^+$, and $[M + K]^+$. The spectra were recorded at two different wavelengths and pulse energies.

The relative abundances of the ions under LD conditions vary; most abundant at 1064 nm is the $[(M + H) - H_2O]^+$ ion and at 266 nm the $[M + K]^+$ ion. The general spectral pattern, as far as the mass-to-charge ratios of the ions are concerned, remains the same, however. No detectable $[(M + H) - O]^+$ ions are produced. This suggests that the presence of the matrix is not the determining factor for the formation of the $[(M + H) - O]^+$ ions, nor is the desorption process by itself. In a previous study by solid secondary ion mass spectrometry of monoquaternary and diquaternary pyridine aldoximes, no reduction of an oxime to imine was observed (*44*). This is possibly due to the fact that the matrix, although not a determining factor by itself, has nevertheless an important role, either as a source of protons or by its "self-cleaning" characteristics (*4*).

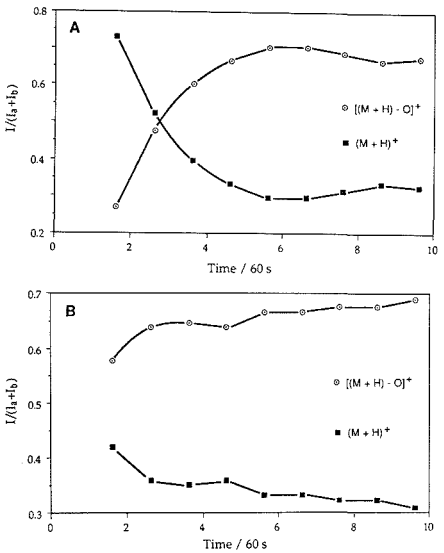

Figure 2. Relative abundances of $[(M + H) - O]^+$ and $[M + H]^+$ ions vs elapsed time: (O) $[(M + H) - O]^+/([(M + H) - O]^+ + [M + H]^+)$, (■) $[M + H]^+/([(M + H) - O]^+ + [M + H]^+)$; (A) FAB spectrum of dodecanophenone oxime in glycerol, (B) As A, but with added surfactant (lithium dodecyl sulfate).

An exclusive thermal formation of the reduced species can be ruled out because the matrix plays the role of buffer for the deposited energy, which is dissipated by losses of matrix molecules from ejected clusters (*45*). Furthermore, one of the processes giving rise to secondary quasi-molecular ions, the sputtering of low internal energy (vibrationally cold) ionic species into the gas phase, is said to be analogous to the cooling caused by an adiabatic expansion in the vacuum (*46*). Moreover, laser desorption is a thermally driven process, but it gives no reduced species. If a significant increase in temperature is sufficient to cause thermal formation of the $[(M + H) - O]^+$ ions under fast atom bombardment conditions, the lifetime of the oxime in the matrix is insufficient for decomposition to compete significantly with desorption.

Time Dependence Studies. Having ascertained that the reduction to the imine occurs under fast atom bombardment conditions, we seek more information about the kinetics of the reduction process. For that purpose, time dependence studies of the relative abundances of the protonated oxime cations and of the reduced forms were undertaken for the oximes listed in Table I. The $[M + H]^+$ and $[(M + H) - O]^+$ ion currents were recorded at different time intervals from the start of FAB. For all the oximes under study, the abundance of the $[(M + H) - O]^+$ ion increased, whereas the abundance of $[M + H]^+$ ion decreased with increasing time.

The general trend showed by the plots of the ratios $[M + H]^+/\{[M + H]^+ + [(M + H) - O]^+\}$ and $[(M + H) - O]^+/\{[M + H]^+ + [(M + H) - O]^+\}$ vs time is an initial steep increase of the abundance of the $[(M + H) - O]^+$ ion and a corresponding decrease of the $[M + H]^+$ ion. Following these regions of rapid change are zones where both ratios remain approximately constant. This can be observed in Figure 2A where the time dependence behavior for the two ions from dodecanophenone oxime is presented.

These "plateau" zones correspond to the stage where the concentration of the reduced species at the matrix surface exceeds the concentration of the protonated oxime at the same

surface. The basis for this state is that the relative abundances of their corresponding ions in the gas phase are a measure of their concentration at the matrix surface. The results point to the fact that, after an early stage where desorption to the gas phase of the protonated oxime dominates, reduction in the matrix becomes the main pathway for consumption of the protonated oxime at that surface. In that case, protonation precedes reduction, and a more favorable accumulation of the $[M + H]^+$ ion at the matrix surface in the early stage of the experiment will result in a more rapid attainment of the "plateau".

To test the last hypothesis, the experiments were repeated in the presence of an anionic surfactant, lithium dodecyl sulfate. Surfactants have been used in desorption ionization mass spectrometry experiments, either by what has been termed "hydrophobic reverse derivatization" (formation of a surface active intermediate) (*47*, *48*) or by binding analyte ions to a position near the surface where they can be efficiently desorbed (*49*). The plots of the same ratios for the same ion abundances recorded in the presence of the surfactant show that the initial increase of the $[(M + H) - O]^+$ is much more abrupt and the initial decrease of the $[M + H]^+$ is also more rapid. The "plateau" is attained sooner in each case. An example of this time-dependent behavior of the two ions from dodecanophenone oxime in the presence of the surfactant is shown in Figure 2B.

Chemical noise in the spectra obtained in the absence of surfactant is not considerable and becomes almost completely suppressed when the surfactant is added. This fact, taken in conjunction with the above mentioned results, points to the formation of the $[(M + H) - O]^+$ ion by reduction of the $[M + H]^+$ ions at the surface. This reduction is dependent on the extent of protonation within the matrix, the diffusion of the protonated species to the surface being the rate-determining step. The anionic surfactant causes a concentration gradient to develop, resulting in the surface enrichment of the $[M + H]^+$ ions. This enrichment is responsible not only for the observed initial changes but also for the higher "plateau" values of the $[(M + H) - O]^+/\{[M + H]^+ + [(M + H) - O]^+\}$ ratios observed under these conditions, when compared to the values obtained in the absence of surfactant. By plotting the $[M + H]^+/\{[M + H]^+ + [(M + H) - O]^+\}$ and $[(M + H) - O]^+/\{[M + H]^+ + [(M + H) - O]^+\}$ ratios for all the oximes at the same fixed times, it can be seen that, as a general rule, the difference in the "plateau" values, with and without the surfactant, becomes smaller with the increasing length of R (for those cases where R is a linear alkyl group in oximes of the general formula $C_6H_5C(R)=NOH$). The evidence for the surface formation of ion $[(M + H) - O]^+$ from the protonated cation is thus reinforced because the oximes with longer linear alkyl groups are themselves surfactants.

Reduction Mechanisms. For the reduction of oximes to imines under fast atom bombardment conditions in the positive ion mode, the possible mechanisms can be summarized in the scheme depicted by eq 1–3.

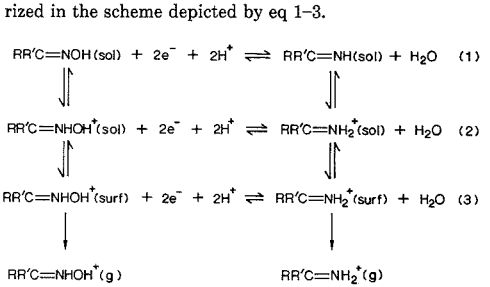

From the previous considerations, mechanism 3 (reduction at the surface of the condensed phase preceded by protonation and followed by desorption) is favored over mechanisms 1 and 2. The addition of the surfactant causes an enrichment of $RR'C=NHOH^+$ in a surface layer. Thus, the probability of the reduction process increases with respect to the desorption process as the concentration of the protonated oxime increases at the surface. The complete reduction to the amine, as it occurs in solution (*34*, *50*), is not observed, possibly because the reduction of the iminium ion is slow when compared to its desorption.

Further support for the mechanism is found in the polarographic behavior of compounds containing a carbon–nitrogen double bond (*34*, *50*). The protonated cation is reduced at a less negative potential than the corresponding conjugate base, the height of the polarographic wave being determined in a certain pH range by the rate of protonation.

ACKNOWLEDGMENT

We thank Ron Cerny and Paul Chiarelli (MCMS) for the studies of different FAB matrices and for the LD-FTMS data, respectively. We are also grateful to Paula M. C. Vieira and J. A. S. Cavaleiro (University of Aveiro), who were responsible for the synthesis of some of the oximes; P. O'Brien (Queen Mary College, London) and J. M. R. Carvalho (I.S.T., Lisbon) for the industrial β-hydroxyoxime samples; and Kenny Caldwell (MCMS) for helpful suggestions.

LITERATURE CITED

(1) Clayton, E.; Wakefield, A. J. C. *J. Chem. Soc., Chem. Commun.* **1984**, 969–970.
(2) Macfarlane, R. D. *Acc. Chem. Res.* **1982**, *15*, 268–275.
(3) Barber, M.; Bordoli, R. S.; Elliot, G. S.; Sedgwick, R. D.; Tyler, A. N. *J. Chem. Soc., Faraday Trans. 1* **1983**, *79*, 1249–1255.
(4) Wong, S. S.; Rolfgen, F. W.; Manz, I.; Przybylski, M. *Biomed. Mass Spectrom.* **1985**, *12*, 43–46.
(5) Cooks, R. G.; Busch, K. L. *Int. J. Mass Spectrom. Ion Phys.* **1983**, *53*, 111–124.
(6) Sunner, J. A.; Kulatunga, R.; Kebarle, P. *Anal. Chem.* **1986**, *58*, 2009–2014.
(7) Hand, O. W.; Scheifers, S. M.; Cooks, R. G. *Int. J. Mass Spectrom. Ion Processes* **1987**, *78*, 131–146.
(8) Fujita, Y.; Matsuo, T.; Sakuari, T.; Matsuda, H.; Katakuse, I. *Int. J. Mass Spectrom. Ion Processes* **1985**, *63*, 231–240.
(9) Cerny, R. L.; Sullivan, B. P.; Bursey, M. M.; Meyer, T. J. *Anal. Chem.* **1983**, *55*, 1954–1958.
(10) Brown, R. M.; Creaser, C. S.; Wright, H. J. *Org. Mass Spectrom.* **1984**, *19*, 311–314.
(11) Burinsky, D. J.; Dilliplane, R. L.; DiDonato, G. C.; Busch, K. L. *Org. Mass Spectrom.* **1988**, *23*, 231–235.
(12) Pelzer, G.; De Pauw, E.; Dung, D. V.; Marien, J. *J. Phys. Chem.* **1984**, *88*, 5065–5068.
(13) Gale, P. J.; Bentz, B. L.; Chait, B. T.; Field, F. H.; Cotter, R. J. *Anal. Chem.* **1986**, *58*, 1070–1076.
(14) Field, F. H. *J. Phys. Chem.* **1982**, *86*, 5115–5123.
(15) Ligon, W. V. *Int. J. Mass Spectrom. Ion Processes* **1983**, *52*, 189–193.
(16) Cerny, R. L.; Gross, M. L. *Anal. Chem.* **1985**, *57*, 1160–1163.
(17) Williams, D. H.; Findeis, A. F.; Naylor, S.; Gibson, B. W. *J. Am. Chem. Soc.* **1987**, *109*, 1980–1986.
(18) Sethi, S. K.; Nelson, C. C.; McCloskey, J. A. *Anal. Chem.* **1984**, *56*, 1975–1977.
(19) Nakamura, T.; Nagaki, H.; Kinoshita, T. *Bull. Chem. Soc. Jpn.* **1985**, *58*, 2798–2800.
(20) Pannell, L. K.; Sokoloski, E. A.; Fales, H. M.; Tate, R. L. *Anal. Chem.* **1985**, *57*, 1060–1067.
(21) Ashbrook. A. W. *Coord. Chem. Rev.* **1975**, *16*, 285–307.
(22) Cox, M.; Flett, D. *Chem. Ind.* **1987**, *6*, 188–193.
(23) Burkin, A. R.; Preston, J. S. *J. Inorg. Nucl. Chem.* **1975**, *37*, 2187–2195.
(24) Singh, R. B.; Garg, B. G.; Singh, R. D. *Talanta* **1979**, *26*, 425–444.
(25) Levine, S. P.; Harvey, T. M.; Waeghe, T. G.; Shapiro, R. H. *Anal. Chem.* **1981**, *53*, 805–809.
(26) Masse, R.; Laliberte, C.; Tremblay, L. *J. Chromatogr.* **1985**, *339*, 11–23.
(27) Detter, L. D.; Hand, O. W.; Cooks, R. G.; Walton, R. A. *Mass Spectrom. Rev.* **1988**, *7*, 465–502.
(28) Vogel, A. I. *Practical Organic Chemistry*; Longman: London, 1974; pp 345, 721.
(29) Preston, J. S.; Whewell, R. J. *J. Inorg. Nucl. Chem.* **1977**, *39*, 1675–1678.
(30) Sowa, W.; Licht, B. H.; Itzkovitch, I. J. *J. Chromatogr.* **1976**, *116*, 197–200.
(31) Gross, M. L.; Chess, E. K.; Lyon, P. A.; Crow, F. W.; Evans, S.; Tudge, H. *Int. J. Mass Spectrom. Ion Phys.* **1982**, *42*, 243–254.

(32) Ledford, E. B., Jr.; White, R. L.; Gadheri, S.; Wilkins, C. L.; Gross, M. L. *Anal. Chem.* **1980**, *52*, 2450–2451.
(33) Pine, S. H.; Hendrickson, J. B.; Cram, D. S.; Hammond, J. S. *Organic Chemistry*; McGraw-Hill International Book Co.: Tokyo, 1980; p 285.
(34) Lund, H. *Acta Chim. Scand.* **1959**, *13*, 249–267.
(35) Cooks, R. G.; Varvoglis, A. G. *Org. Mass Spectrom.* **1971**, *5*, 687–696.
(36) Leyshon, W. M.; Wilson, D. A. *Org. Mass Spectrom.* **1973**, *7*, 251–257.
(37) Thorstad, O.; Undheim, K.; El-Gendy, M. A. F. *Org. Mass Spectrom.* **1975**, *10*, 1155–1159.
(38) Vijfhuizen, P. C.; Heerma, W.; Dijkstra, G. *Org. Mass Spectrom.* **1975**, *10*, 919–929.
(39) Vijfhuizen, P. C.; Terlow, J. K. *Org. Mass Spectrom.* **1977**, *12*, 245–253.
(40) Kallury, R. K. M. R.; Rao, P. L. K. M. *Org. Mass Spectrom.* **1977**, *12*, 411–415.
(41) Lachman, A. *Organic Synthesis, Collective Volume II*; Wiley: New York, 1943; pp 234–236.
(42) Deem, M. L. *Org. Mass Spectrom.* **1980**, *15*, 573–577.
(43) Busch, K. L.; Cooks, R. G. *Science* **1982**, *218*, 247–254.
(44) Vincze, A.; Busch, K. L.; Cooks, R. G. *Anal. Chim. Acta* **1982**, *136*, 143–153.
(45) De Pauw, E. *Mass Spectrom. Rev.* **1986**, *5*, 191–212.
(46) Day, R. J.; Unger, S. E.; Cooks, R. G. *Anal. Chem.* **1980**, *52*, 557A–572A.
(47) De Pauw, E.; Pelzer, G.; Marien, J.; Piette, J. L.; Pardon, M. C. *Org. Mass Spectrom.* **1985**, *20*, 692–693.
(48) Ligon, W. V., Jr. *Anal. Chem.* **1986**, *58*, 487–490.
(49) Ligon, W. V., Jr.; Dorn, S. B. *Int. J. Mass Spectrom. Ion Processes* **1985**, *63*, 315–324.
(50) Gardner, H. J.; Georgans, W. P. *J. Chem. Soc.* **1956**, 4180–4186.

RECEIVED for review September 13, 1988. Accepted March 15, 1989. The authors are indebted to the INIC (Instituto Nacional de Investigacao Cientifica) for a scholarship given to M. G. Santana-Marques. This work was supported in part by the Midwest Center for Mass Spectrometry, a National Science Foundation facility (Grant No. CHE 8620177).

Ion Confinement in the Collision Cell of a Multiquadrupole Mass Spectrometer: Access to Chemical Equilibrium and Determination of Kinetic and Thermodynamic Parameters of an Ion–Molecule Reaction

Claude Beaugrand

SN Nermag, 49 quai du Halage, 92500 Rueil-Malmaison, France

Daniel Jaouen, Hélène Mestdagh, and Christian Rolando*

Ecole Normale Supérieure, Dépertement de Chimie, Laboratoire de l'Activation Moléculaire, UA 1110, 24 rue Lhomond, 7531 Paris Cedex 05, France

Ions can be confined in an rf-only collision cell of a tandem quadrupole mass spectrometer so that ion–molecule reactions can be studied for variable interaction times (0.05–250 ms). The chemical system studied (ammonium ion, pyrrolidine, piperidine) involved the following reactions: proton exchange, formation of proton-bound dimers, and amine exchange between dimers. Chemical equilibrium could be reached for the exchange reactions. The equilibrium constants of these reactions, as well as the rate constants of the different reactions involved, were thus easily determined from the variation of relative abundance of reactant and product ions versus confinement time.

Detailed kinetic and thermodynamic data concerning ion–molecule reactions are useful both from a fundamental point of view and as a basis for designing analytical uses of these reactions for mass spectrometry. The most direct way of obtaining such information is to provide for a variable reaction time under a given set of conditions and to observe the variation of reactant and product ion abundances. Numerous such experiments have been performed either in ICR (ion cyclotron resonance) cells (*1*) (reaction pressure: 10^{-8} to 10^{-5} Torr) or in high-pressure ion sources (see for example ref 2–5) and flow tube instruments (*6*) (reaction pressure: a few Torr). It is interesting to make this possibility available in the rf-only collision cell of a quadrupole spectrometer, which allows investigations in an intermediate pressure range (10^{-5} to 10^{-2} Torr). Quadrupole ion traps (reaction pressure: 10^{-7} to 10^{-4} Torr) have also been used in this way (*7*, *8*).

Thus, we modified the operation of a rf-only collision cell of our multiquadrupole MS/MS/MS instrument in order to control the duration of an ion–molecule reaction, i.e., to trap ions in the cell for a variable time. A similar trapping device has been used to improve the efficiency of reaction product detection in a MS/MS quadrupole spectrometer (*9*). Providing the interaction time is long enough, one can expect to reach chemical equilibrium for a reversible reaction and thus determine its equilibrium constant.

The ion confinement technique was first tested on a simple process: collisionally activated dissociation of the $FeCO^+$ ion leading to the Fe^+ fragment ion (*10*). We now wish to report its application to the study of ion–molecule reactions, showing that chemical equilibrium actually can be attained under ion confinement conditions.

In order to determine the efficiency of this method, we chose to confine NH_4^+ ions with a mixture of pyrrolidine and piperidine in the collision cell. The reactions involved are proton exchanges and formation of proton-bound dimers. This system seemed suitable for our purpose because (i) it is of reasonable complexity, having six different ions present in the reaction mixture; and (ii) such reactions were studied under ICR conditions, so that some of the kinetic and thermodynamic data obtained can be compared with literature values.

EXPERIMENTAL SECTION

The experiments were performed on a prototype MS/MS/MS multiquadrupole mass spectrometer described elsewhere (*11*). Briefly, it is composed of the following parts: source (electron

0003-2700/89/0361-1447$01.50/0

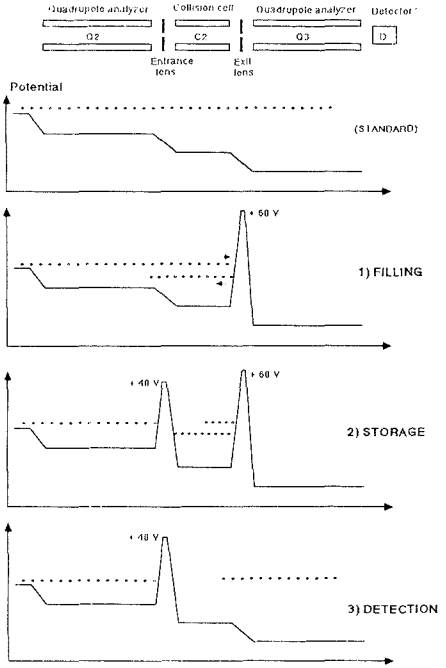

Figure 1. Successive stages of a confinement cycle.

impact, chemical ionization, or fast atom bombardment), first quadrupole analyzer, first rf-only collision cell, second analyzer, second rf-only collision cell, third analyzer, and detector. In all the experiments described here, the first collision cell contained no collision gas, and the second analyzer was left in the rf-only mode. Ion confinement was performed in the second collision cell, using the entrance and exit lenses of this cell as electrostatic mirrors. The potentials of the lenses were varied according to the confinement cycle described below. The corresponding potentials were generated by a two-channel fast rise power supply driven by an auxiliary microcomputer slave of the main data system. The power supply from SN Nermag has the following characteristics: continuously adjustable output voltage 0–100 V, input voltage 0–5 V; the maximum frequency allowed without distortion of the signal is 50 kHz. The auxiliary data system is a personal computer with a homemade 8-bit digital-to-analog interface. The confinement cycle is defined by the following parameters: filling time, storage time, and detection time. The minimum value allowed by the system for one operation is 50 μs. EMMA, the main data acquisition system, was modified so as to trigger the confinement cycle. This improvement allows one to record standard mass spectra in the confinement mode.

Ammonium ions were generated in the source by chemical ionization using ammonia. Piperidine and pyrrolidine were purified by distillation over calcium hydride. Equal weights of liquid piperidine and pyrrolidine were mixed in a flask connected to the cell via a controlled leak valve from Riber Co. (Rueil-Malmaison, France). The composition of the gas mixture was determined by ^1H and ^{13}C NMR after pumping a small amount of vapor over the liquid mixture and condensing it into a cold trap: The measured pyrrolidine to piperidine molar ratio was 1.9 ± 0.1. The absolute pressure in the collision cell was measured by using a Bayard-Alpert gauge, calibrated for the mixture to be studied with a capacitance manometer from MKS Instruments, Inc. (Andover, MA).

RESULTS AND DISCUSSION

The Confinement Cycle. The entrance and exit lenses of the collision cell were used as cell doors. At its normal low potential, a lens allows the ions through (open door), whereas at high potential it functions as an electrostatic mirror (closed door). Figure 1 displays the potentials applied to the lenses during the following successive stages of a confinement cycle:

(*1*) *Filling Stage* (*250 μs*). The entrance lens is at its normal low potential, and the exit lens is at a high potential, i.e., 2 or 3 times the average kinetic energy of the incoming ions.

(*2*) *Storage Stage* (*Variable Time*). Both lenses are at high potential.

(*3*) *Detection Stage* (*250 μs*). The exit lens is switched to low potential, while the entrance lens is kept at high potential; ions are thus allowed to reach the last analyzer.

The entire cycle is then repeated after a delay time.

The confinement time can be varied from a few hundredths of a millisecond to 250 ms. In order to scan a range of confinement time in a single experiment, the time can be automatically increased by a defined step. Figure 2 shows that in such an experiment the total ion current measured remained fairly independent of the confinement time. This means that little ion loss occurred during the storage step, showing the high efficiency of the confinement device.

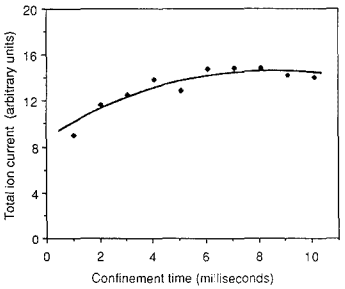

Figure 2. Variation of total ion current with confinement time in a given series of experiments.

Variation of Relative Abundances of Reagent and Product Ions versus Confinement Time. The reaction of ammonium ions with the pyrrolidine–piperidine mixture was followed at five different pressures (1.0×10^{-5} to 2.7×10^{-4} Torr), with the confinement time varying from 0.035 to 10.1 ms. For one pressure (5.3×10^{-5} Torr) the confinement time was increased up to 220 ms. The reaction mixtures consisted of the following six ions in variable proportions according to the different reaction periods: NH_4^+ (*m/z* 18), reagent ion; $C_4H_{10}N^+$ (*m/z* 72), protonated pyrrolidine (PyH^+); $C_5H_{12}N^+$ (*m/z* 86), protonated piperidine (PiH^+); $C_8H_{19}N_2^+$ (*m/z* 143), pyrrolidine proton-bound dimer ($PyHPy^+$); $C_9H_{21}N_2^+$ (*m/z* 157), pyrrolidine–piperidine proton-bound mixed dimer ($PyHPi^+$); $C_{10}H_{23}N_2^+$ (*m/z* 171), piperidine proton-bound dimer ($PiHPi^+$).

Figure 3 displays the variation of the relative abundance of each of these ions with confinement time at a 5.3×10^{-5} Torr pressure. The pattern of these abundance curves allows qualitative analysis of the successive processes occurring in the reaction mixture.

(*i*) *0–1 ms.* NH_4^+ decreases to 0; PyH^+ and PiH^+ increase because the initial reaction is protonation of the amines by NH_4^+ ions.

$$NH_4^+ + Py \xrightarrow{k_1} PyH^+ + NH_3 \quad (1)$$

$$NH_4^+ + Pi \xrightarrow{k_2} PiH^+ + NH_3 \quad (2)$$

The relative amounts of PyH^+ versus PiH^+ formed by these reactions are kinetically controlled, so that the mixture initially formed is not in equilibrium.

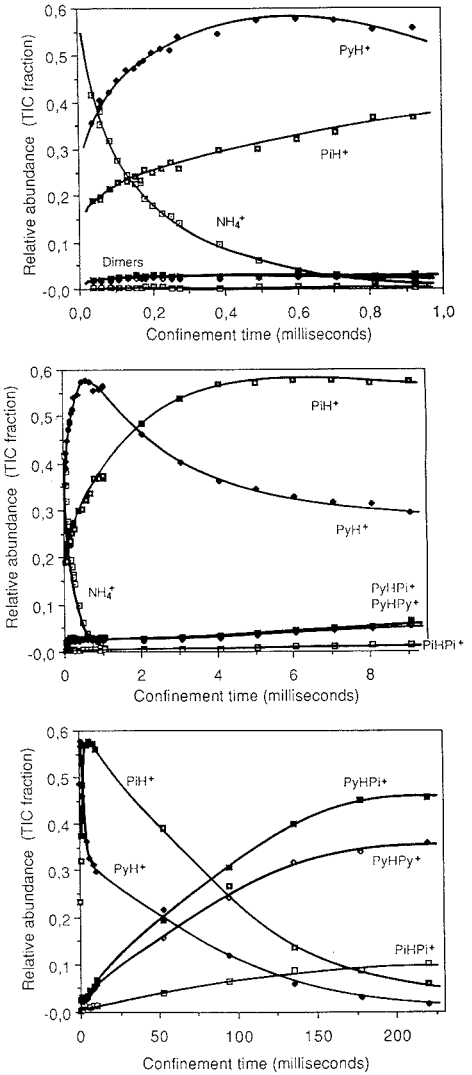

Figure 3. Variation of relative abundance of reactant and product ions with confinement time at a 0.053-mTorr pressure, for short (a, top), medium (b, middle), and long (c, bottom) confinement times.

(ii) 1–10 ms. PyH^+ decreases, PiH^+ increases; the dominant reaction is proton exchange leading to the acid–base equilibrium

$$PyH^+ + Pi \underset{k_-}{\overset{k_+}{\rightleftharpoons}} PiH^+ + Py \qquad K = k_+/k_- \qquad (3)$$

(iii) 1–220 ms. Concurrently with the preceding reaction and throughout the confinement period, a slow increase of dimer abundance ($PyHPy^+$, $PyHPi^+$, $PiHPi^+$) is observed. However, their abundance ratios relative to each other rapidly become independent of time (see Figures 5 and 6 for the corresponding curves), showing that equilibrium is achieved among the dimers. This means that the dimers undergo amine exchange much faster than they are formed from their monomer precursors, according to the following scheme:

$$PyH^+ + Py \longrightarrow PyHPy^+$$
$$Py \rightleftharpoons Pi \quad \text{fast equilibrium}$$
$$PyH^+ + Pi \longrightarrow PyHPi^+$$
$$PiH^+ + Py \longrightarrow PyHPi^+$$
$$Py \rightleftharpoons Pi \quad \text{fast equilibrium}$$
$$PiH^+ + Pi \longrightarrow PiHPi^+$$

The abundance curves obtained at other pressures display similar features. As expected, all the reaction rates increased with pressure. For the lowest pressure used (1.0×10^{-5} Torr) no significant amount of dimers had yet formed after 10 ms, and chemical equilibrium for reaction 3 had not yet been attained.

These results are entirely consistent with the ICR studies of amine protonation and dimerization; the shapes of the curves obtained are similar to those reported for protonation and dimerization of an azetidine–pyrrolidine mixture (*12*).

In the experiments performed, the dimer abundance had not reached a constant value for the longest (220 ms) confinement time studied, indicating that thermodynamic equilibrium had not been attained with regard to dimerization reactions. Our results indicate, however, that this equilibrium is shifted far toward dimerization, since in two cases ($P = 5.3 \times 10^{-5}$ Torr, confinement up to 220 ms, and $P = 2.7 \times 10^{-4}$ Torr, confinement up to 10 ms) dimers constituted, respectively, more than 92% and 96% of the final reaction mixture. The temperature dependence of the equilibrium constant of pyrrolidine dimerization was recently determined (*13*). Extrapolation to room temperature of the corresponding linear plot of ln K versus $1/T$ leads to an approximate K value of 10^8 $Torr^{-1}$, which means that within the pressure range used in our experiment (10^{-5} to 10^{-3} Torr) the remaining monomers would not be detectable if the equilibrium were completely achieved.

No significant amount of trimer was detected in our experiments. A minor amount of pyrrolidine trimer (ca. 10% at 10^{-4} Torr) should be present, however, at equilibrium (*13*). The trimerization reaction is likely far too slow to be detected under the conditions used.

These results illustrate the utility of ion confinement in characterizing the successive steps of a chemical process in the gas phase. Furthermore, knowledge of the relative concentrations of reactant and product ions as a function of reaction (confinement) time allows one to obtain quantitative thermodynamic and kinetic data concerning the reactions involved.

Determination of Equilibrium Constants. *Proton Exchange between Piperidine and Pyrrolidine (Reaction 3).* Figure 4 shows the variation of the PiH^+/PyH^+ ratio with confinement time. Except at the lowest pressure, this ratio clearly attains a constant equilibrium value, independent of pressure: $(PiH^+/PyH^+)_e = 1.85 \pm 0.15$.

The equilibrium constant of reaction 3 thus can be determined:

$$K = (PiH^+/PyH^+)(Py/Pi) = 3.5$$

corresponding to $\Delta G° = -3.1$ kJ mol^{-1} = -0.74 ± 0.10 kcal mol^{-1}

Although slightly lower than those determined by other workers, this value is in agreement with them within experimental uncertainties:

$$\Delta G° = GB(Py) - GB(Pi) = -1.1 \pm 0.2 \text{ kcal mol}^{-1} \text{ (14)}$$
$$= -0.9 \text{ kcal mol}^{-1} \text{ (15)}$$

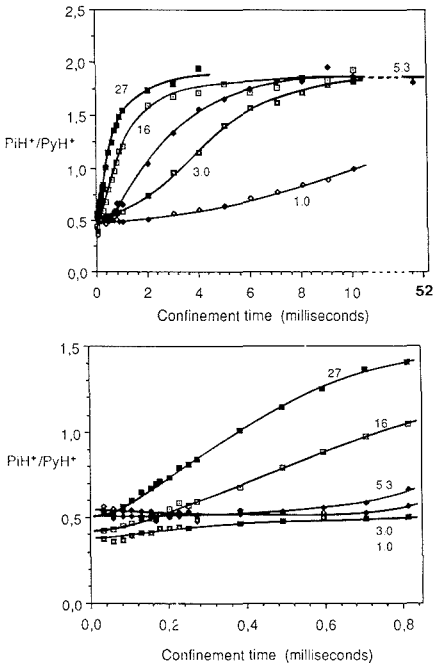

Figure 4. Variation of the PiH^+/PyH^+ ratio with confinement time for the different pressures used (pressures indicated in 10^{-5} Torr units): medium (a, top) and short (b, bottom) confinement times.

where GB(Pi) and GB(Py) are the gas-phase basicities of piperidine and pyrrolidine, relative to the same absolute scale.

It was pointed out by Bowers et al. that competitive dimerization may alter the measurement of proton-exchange equilibrium constants, the apparent equilibrium being shifted toward the more slowly dimerizing species (*16*). Because of the fast amine exchange between the three dimers, individual dimerization rates are not accessible from our experiments. However, comparison between the average dimerization rate and the proton-exchange rate (see below for determination of the corresponding rate constants) shows that even if one amine dimerizes much faster than the other, no significant error is introduced in the K value for the pressure range studied. This is supported by the fact that K is pressure-independent within experimental uncertainties.

Base Exchange between Dimers. These reactions correspond to eq 4 and 5:

$$PyHPy^+ + Pi \rightleftarrows PyHPi^+ + Py \quad K_4 \qquad (4)$$

$$PyHPi^+ + Pi \rightleftarrows PiHPi^+ + Py \quad K_5 \qquad (5)$$

Figures 5 and 6 show the variation of $PyHPi^+/PyHPy^+$ and $PiHPi^+/PyHPi^+$ ratios, respectively, with confinement time. Both of these ratios attain their equilibrium value at the four pressures used:

$$(PyHPi^+/PyHPy^+)_e = 1.2 \pm 0.2$$

$$(PiHPi^+/PyHPi^+)_e = 0.20 \pm 0.04$$

The dispersion of the results is slightly larger than in the preceding case, probably because in these experiments dimers

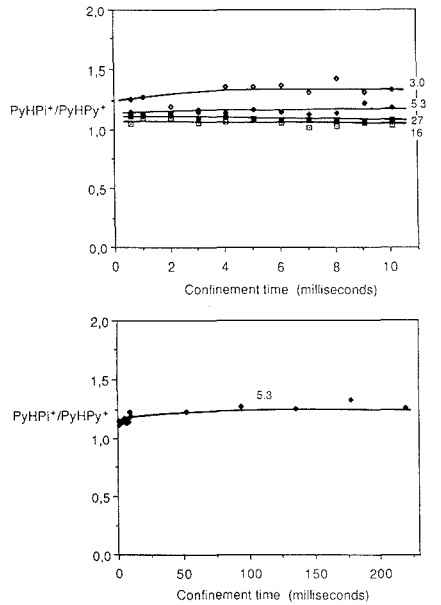

Figure 5. Variation of the $PyHPi^+/PyHPy^+$ ratio with confinement time for the different pressures used (pressures indicated in 10^{-5} Torr units): medium (a, top) and long (b, bottom) confinement times.

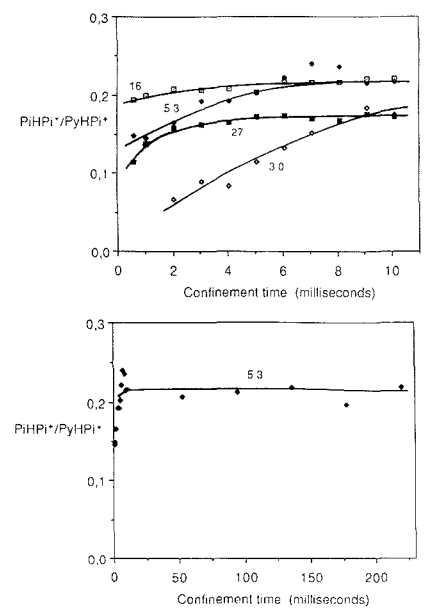

Figure 6. Variation of the $PiHPi^+/PyHPi^+$ ratio with confinement time for the different pressures used (pressures indicated in 10^{-5} Torr units): medium (a, top) and long (b, bottom) confinement times.

are very often minor components of the reaction mixture.

These ratios lead to the following equilibrium constants:

$$K_4 = (PyHPi^+/PyHPy^+)_e(Py/Pi) = 2.3$$

corresponding to $\Delta G°_4 = -2.0$ kJ mol^{-1} =
-0.48 ± 0.15 kcal mol^{-1}

$$K_5 = (\mathrm{PiHPi^+/PyHPi^+})_e(\mathrm{Py/Pi}) = 0.38$$

corresponding to $\Delta G°_5 = 2.4$ kJ mol^{-1} =
0.56 ± 0.20 kcal mol^{-1}

These values are close to those that can be calculated from reported molecule pair gas-phase basicities (MPGB) (*17*):

$\Delta G°_4$ = MPGB(PyHPy$^+$) − MPGB(PyHPi$^+$) =
−0.5 kcal mol^{-1}

$\Delta G°_5$ = MPGB(PyHPi$^+$) − MPGB(PiHPi$^+$) =
0.2 kcal mol^{-1}

The formation of a proton-bound dimer from an acid AH$^+$ and a base B was shown to be increasingly exoenergetic with increasing acidity of AH$^+$ and with increasing basicity of B (*18*, *19*). Consider the dimerization equilibria

$$\mathrm{PyH^+ + Py \rightleftarrows PyHPy^+} \qquad \Delta G°(\mathrm{PyPy})$$

$$\mathrm{PyH^+ + Pi \rightleftarrows PyHPi^+} \qquad \Delta G°(\mathrm{PyPi})$$

$$\mathrm{PiH^+ + Py \rightleftarrows PyHPi^+} \qquad \Delta G°(\mathrm{PiPy})$$

$$\mathrm{PiH^+ + Pi \rightleftarrows PiHPi^+} \qquad \Delta G°(\mathrm{PiPi})$$

As piperidine is more basic than pyrrolidine, these free energies should verify the following relationships:

$$\Delta G°(\mathrm{PyPi}) < \Delta G°(\mathrm{PyPy}) < \Delta G°(\mathrm{PiPy})$$

$$\Delta G°(\mathrm{PyPi}) < \Delta G°(\mathrm{PiPi}) < \Delta G°(\mathrm{PiPy})$$

The preceding free energies are related to the experimental free energies $\Delta G°$, $\Delta G°_4$, and $\Delta G°_5$:

$$\Delta G°(\mathrm{PyPi}) - \Delta G°(\mathrm{PyPy}) = \Delta G°_4 = -0.5 \text{ kcal/mol}$$

$\Delta G°(\mathrm{PyPy}) - \Delta G°(\mathrm{PiPy}) = \Delta G° - \Delta G°_4$ =
−0.3 kcal/mol

$\Delta G°(\mathrm{PyPi}) - \Delta G°(\mathrm{PiPi}) = \Delta G° - \Delta G°_5$ =
−1.3 kcal/mol

$$\Delta G°(\mathrm{PiPi}) - \Delta G°(\mathrm{PiPy}) = \Delta G°_5 = +0.6 \text{ kcal/mol}$$

The expected inequalities are therefore verified, with the exception of the last one. This may be interpreted as $\Delta G°$(PiPi) being slightly higher than expected, possibly because of steric interactions hindering piperidine dimerization more than formation of the other two proton-bound dimers. Since the basicities of piperidine and pyrrolidine are close to each other, even a slight steric effect may reverse the order of the free energy values under consideration.

Reaction Temperature. In the preceding considerations we have assumed a reaction temperature of 298 K, i.e. the temperature of the collision gas in the cell. However, the reacting ions may not be thermalized at this temperature, since their average translational energy may be modified by the variable electric field present in the collision cell. In order to check the validity of our initial assumption concerning temperature (this point was raised by a reviewer) two experiments were performed:

(i) Variation of the rf power of the cell quadrupole. The position of the piperidine–pyrrolidine proton-exchange equilibrium was observed to be insensitive to this variation.

(ii) Study of a known temperature-dependent equilibrium. Proton exchange between triethylamine and putresceine (*20*) was chosen for this purpose. Ammonium ions were reacted with mixtures of triethylamine and putresceine in the collision cell until the protonated triethylamine to protonated putresceine ratio attained its equilibrium value. In this experiment the collision cell was slightly heated (ca. 50 °C) due to the low volatility of putresceine. The equilibrium ratio, joined to the pressure ratio of the two amines, allowed us to determine the corresponding equilibrium constant: 1.16 ± 0.1. According to the temperature dependence reported in ref *20*, this corresponded to a temperature of 330 K, in fair agreement with the temperature of the gas in the cell. These measurements were performed at a total pressure of 10^{-5} to 10^{-4} Torr, i.e. in the same pressure range as with the pyrrolidine–piperidine mixture. However, experiments done in a wider pressure range on trimethylamine proton-bound dimer formation equilibrium (*18*) have shown that at the highest pressures usable in the cell (a few milliTorr) the apparent reaction temperature is much higher than the gas temperature. These phenomena are under investigation.

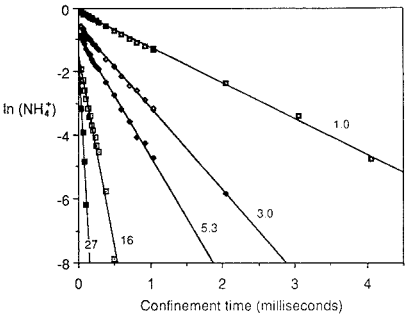

Figure 7. Variation of ln (NH_4^+) with confinement time for the different pressures used (pressures indicated in 10^{-5} Torr units).

Determination of Rate Constants. *Amine Protonation by Ammonium Ion (Reactions 1 and 2).* Figure 7 shows the variation of ln (NH_4^+) versus confinement time for the different pressures used. The corresponding curves are linear, in agreement with the expected rate law:

$$\mathrm{d(NH_4^+)}/dt = [k_1(\mathrm{Py}) + k_2(\mathrm{Pi})](\mathrm{NH_4^+})$$

$$\ln(\mathrm{NH_4^+}) = -[k_1(\mathrm{Py}) + k_2(\mathrm{Pi})]t = -k_p t$$

With $a = (\mathrm{Py})/(\mathrm{Pi}) = 1.9$ and P = total pressure

$$k_p = P(k_1 + k_2 a)/(1 + a)$$

Plotting k_p values (slopes of the different curves of Figure 7) versus pressure P showed that k_p is actually proportional to P. The corresponding slope is

$k_p° = 2.22 \times 10^{-9}$ s^{-1} molecule^{-1} cm^3 =
$(k_1 + k_2 a)/(1 + a)$

The second relationship needed to determine k_1 and k_2 is obtained by evaluating the k_1/k_2 ratio: For short reaction times the (PiH^+)/(PyH^+) ratio should tend to be constant and equal to k_2(Pi)/k_1(Py), since reaction 3 is much slower than reactions 1 and 2. Figure 4b shows that this is actually the case (as expected it is more apparent at the lowest pressures) and allows one to determine k_2/k_1:

$$k_2(\mathrm{Pi})/k_1(\mathrm{Py}) = [(\mathrm{PiH^+})/(\mathrm{PyH^+})]_0 = 0.48 \pm 0.1$$

$$k_2/k_1 = a[(\mathrm{PiH^+})/(\mathrm{PyH^+})]_0 = 0.91 \pm 0.25$$

The rate constants k_1 and k_2 are then derived from the values of $k_p°$ and k_2/k_1:

$$k_1 = (2.3 \pm 0.5) \times 10^{-9} \text{ s}^{-1} \text{ molecule}^{-1} \text{ cm}^3$$

$$k_2 = (2.1 \pm 0.5) \times 10^{-9} \text{ s}^{-1} \text{ molecule}^{-1} \text{ cm}^3$$

The values of k_1 and k_2 are close to each other, which is not surprising as piperidine and pyrrolidine are approximately the same size and are both much more basic than ammonia, so their proton-transfer cross sections with the ammonium

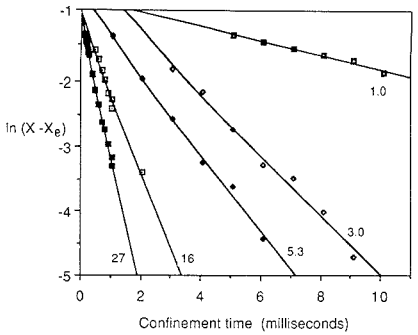

Figure 8. Variation of ln $(X - X_e)$ (see text for definition) with confinement time for the different pressures used (pressures indicated in 10^{-5} Torr units).

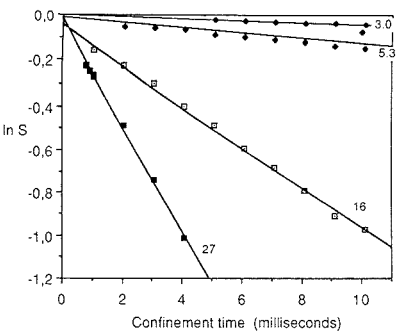

Figure 9. Variation of ln S = ln $[(PyH^+) + (PiH^+)]$ with confinement time for the different pressures used (pressures indicated in 10^{-5} Torr units), for medium confinement times. The points obtained for longer confinement times (up to 220 ms) at 5.3×10^{-5} Torr pressure are aligned with those shown here and are included in the represented linear regression.

ion have no reason to be very different. These rate constants are also of the same order of magnitude as those reported for protonation of piperidine and pyrrolidine by their respective radical cations (*21*). They are in good agreement with the values calculated from the ADO theory of Su and Bowers (*22*): 2.60×10^{-9} s^{-1} molecule^{-1} cm^3 for pyrrolidine and 2.46×10^{-9} s^{-1} molecule^{-1} cm^3 for piperidine.

Proton Exchange between Pyrrolidine and Piperidine (Reaction 3). Determination of the corresponding rate constants k_+ and k_- can be done after complete disappearance of ammonium ions, i.e. excluding short reaction times. As will be shown below, dimerization reactions are much slower than proton exchange (the largest k_d/k_e ratio, corresponding to the highest pressure used, is 0.23 ms^{-1}/2.1 ms^{-1} = 0.11). Thus it can be assumed that concurrent dimerization reactions have negligible rates versus proton-exchange rates. The following rate law can then be expected:

$$d(X - X_e)/dt = -[k_+(Pi) + k_-(Py)](X - X_e)$$

where $X = (PiH^+)/[(PiH^+) + (PyH^+)]$ and X_e is the equilibrium value of X.

$$\ln (X - X_e) = \ln (X_0 - X_e) - [k_+(Pi) + k_-(Py)]t$$
$$= \ln (X_0 - X_e) - k_e t$$
$$k_e = P(k_- + k_+ a)/(1 + a) = k_e^\circ P$$

Figure 8 displays ln $(X - X_e)$ versus confinement time, showing that the corresponding curves are linear. Their slopes k_e were plotted versus pressure P. The slope of the resulting linear curve is

$$k_e^\circ = 7.0 \text{ ms}^{-1} \text{ mTorr}^{-1} =$$
$$2.14 \times 10^{-10} \text{ s}^{-1} \text{ molecule}^{-1} \text{ cm}^3$$

k_+ and k_- are then easily determined, since $k_+/k_- = K = 3.5$.

$$k_+ = (2.8 \pm 0.5) \times 10^{-10} \text{ s}^{-1} \text{ molecule}^{-1} \text{ cm}^3$$

$$k_- = (8.1 \pm 2) \times 10^{-11} \text{ s}^{-1} \text{ molecule}^{-1} \text{ cm}^3$$

Dimerization Reactions. As already pointed out, these experiments do not give access to the individual dimerization rate constants, because of fast equilibration occurring among the dimers. An average dimerization rate constant k_d can be defined as follows:

$$d[(PyHPy^+) + (PyHPi^+) + (PiHPi^+)]/dt =$$
$$k_d[(PyH^+) + (PiH^+)]$$

As in the preceding case we consider only reaction times long enough so that no ammonium ion is present in the reaction mixture. With $S = (PyH^+) + (PiH^+)$

$$d(1 - S)/dt = k_d S$$

k_d will remain constant with reaction time providing equilibrium 3 is achieved, or if the individual dimerization rate constants have similar values. In that case we expect the following relationship:

$$\ln S = \ln S_0 - k_d t$$

Figure 9 displays ln S versus confinement time for the different pressures used, showing that the corresponding curves are linear. Their slopes, k_d, when plotted versus P and versus P^2, appeared to be proportional to P^2: $k_d = k_d^\circ P^2$.

$$k_d^\circ = 3.3 \text{ ms}^{-1} \text{ mTorr}^{-2} = 3.0 \times 10^{-24} \text{ s}^{-1} \text{ molecule}^{-2} \text{ cm}^6$$

k_d° is the average third-order dimerization rate constant for the considered pyrrolidine–piperidine mixture. Similar dimerization reactions have been shown to follow a rate law consistent with the likely mechanism involving collisional deactivation of the excited dimer initially formed (*23*, *24*):

$$AH^+ + A \underset{k_b}{\overset{k_f}{\rightleftharpoons}} (AHA^+)^*$$

$$(AHA^+)^* + A \xrightarrow{k_s} AHA^+ + A$$

$$d(AHA^+)/dt = k(AH^+)(A)$$

where $k = k_f k_s(A)/[k_b + k_s(A)]$.

This means that these reactions approach second order at high pressure and third order at low pressure.

The preceding results show that the considered dimerization reactions follow third-order kinetics implying rate-limiting collisional deactivation, which is also the case for similar amine systems in the same pressure range (*24*).

CONCLUSION

Ion confinement in the rf-only collision cell of a tandem quadrupole mass spectrometer allows the study of a reaction mixture for variable reaction times and thus gives access to reliable kinetic and thermodynamic data for the reactions involved. The described application of this method to quantitatively characterize competitive reactions between pyrrolidine and piperidine in the gas phase demonstrates that it has the potential for investigation of complex reaction mechanisms. Application of the ion confinement technique to various ion–molecule reactions, for instance in the area of gas-phase organometallic chemistry, is thus very promising.

ACKNOWLEDGMENT

We thank Abdelouahid Dahrouch for his contribution to the most recent experiments, Dr. Nicole Morin for helpful

technical assistance, and Professor J. T. Watson for useful discussions. The efficient technical assistance of the Nermag staff is gratefully acknowledged.

Registry No. Py, 123-75-1; Pi, 110-89-4; PyH, 55526-39-1; PiH, 17523-59-0; NH_4, 14798-03-9.

LITERATURE CITED

(1) Hartmann, H.; Wanczeck, K. P. *Ion Cyclotron Resonance Spectrometry II*; Lecture Notes in Chemistry 31; Springer-Verlag: Berlin, Heidelberg, New York, 1982.
(2) Cunningham, A. J.; Payzant, J. D.; Kebarle, P. *J. Am. Chem. Soc.* **1972**, *94*, 7627.
(3) Kebarle, P. *Annu. Rev. Phys. Chem.* **1977**, *28*, 445.
(4) Meisels, G. G.; Illies, A. J.; Stradling, R. S.; Jennings, K. R. *J. Chem. Phys.* **1978**, *68*, 866.
(5) Solomon, J. J.; Field, F. H. *J. Am. Chem. Soc.* **1975**, *97*, 2625.
(6) Smith, D.; Adams, N. G. In *Gas Phase Ion Chemistry*; Bowers, M. T., Ed.; Academic Press: New York, San Francisco, London, 1979; Vol. 1, p 1.
(7) Armitage, M. A.; Higgins, M. J.; Lewars, E. G.; March, R. E. *J. Am. Chem. Soc.* **1980**, *102*, 5064.
(8) Brodbelt-Lustig, J. S.; Cooks, R. G. *Talanta*, in press.
(9) Dolnikowski, G. G.; Kristo, M. J.; Enke, C. G.; Watson, J. T. *Int. J. Mass Spectrom. Ion Processes* **1988**, *82*, 1.
(10) Beaugrand, C.; Devant, G.; Jaouen, D.; Mestdagh, H.; Rolando, C. *Spectrosc. Int. J.* **1987**, *5*, 265.
(11) Beaugrand, C.; Devant, G.; Jaouen, D.; Rolando, C. *Int. J. Mass Spectrom. Ion Processes*, in press.
(12) Bowers, M. T.; Aue, D. H.; Webb, H. M. *J. Am. Chem. Soc.* **1971**, *93*, 4314.
(13) Hiraoka, K.; Takimoto, H.; Yamabe, S. *J. Am. Chem. Soc.* **1987**, *109*, 7346.
(14) Aue, D. H.; Webb, H. M.; Bowers, M. T. *J. Am. Chem. Soc.* **1976**, *98*, 311.
(15) Lias, S. G.; Liebman, J. F.; Levin, R. D. *J. Phys. Chem. Ref. Data* **1984**, *13*, 695.
(16) Davidson, W. A.; Bowers, M. T.; Su, T.; Aue, D. H. *Int. J. Mass Spectrom. Ion Phys.* **1977**, *24*, 83.
(17) Aue, D. H.; Bowers, M. T. In *Gas Phase Ion Chemistry*; Bowers, M. T., Ed.; Academic Press: New York, San Francisco, London, 1979; Vol. 2, p 1.
(18) Yamdagni, R.; Kebarle, P. *J. Am. Chem. Soc.* **1973**, *95*, 3504.
(19) Meot-Ner (Mautner), M. *J. Am. Chem. Soc.* **1984**, *106*, 1257.
(20) Wren, A. G.; Gilbert, P. T.; Bowers, M. T. *Rev. Sci. Instrum.* **1978**, *49*, 531.
(21) Scala, A. A.; Caputo, M. G.; Billings, D. *J. Heterocycl. Chem.* **1986**, *23*, 1027.
(22) Su, T.; Bowers, M. T. In *Gas Phase Ion Chemistry*; Bowers, M. T., Ed.; Academic Press: New York, San Francisco, London, 1979; Vol. 1, p 83 and references cited therein.
(23) Meot-Ner, M.; Field, F. H. *J. Am. Chem. Soc.* **1975**, *97*, 5339.
(24) Neilson, P. V.; Bowers, M. T.; Chau, M.; Davidson, W. R.; Aue, D. H. *J. Am. Chem. Soc.* **1978**, *100*, 3649.

RECEIVED for review July 6, 1988. Revised February 24, 1989. Accepted March 16, 1989. The authors are indebted to the Ministère de l'Education Nationale (Ecole Normale Supérieure and the grant Action Recherche Universitaire Entreprise) and to the Centre National de la Recherche Scientifique for their financial support of this work.

Sequence Analysis of Highly Sulfated, Heparin-Derived Oligosaccharides Using Fast Atom Bombardment Mass Spectrometry

Larry M. Mallis*

High Resolution Mass Spectrometry Facility, The University of Iowa, Iowa City, Iowa 52242

Hui M. Wang, Duraikkannu Loganathan, and Robert J. Linhardt

Division of Medicinal and Natural Products Chemistry, College of Pharmacy, The University of Iowa, Iowa City, Iowa 52242

Heparin, a polydisperse, sulfated copolymer of 1 → 4 linked glucosamine and uronic acid residues, has been used clinically as an anticoagulant for half a century. Despite a yearly use of over 50 million doses in the U.S. alone, heparin's exact chemical structure remains unclear. The negative ion fast atom bombardment mass spectrometry (FAB-MS) analysis is presented for a series of enzymatically prepared, homogeneous, structurally characterized, highly sulfated, heparin-derived oligosaccharides using triethanolamine as the FAB matrix. In addition to the clear presence of monoanionic sodiated molecular ions, structurally significant (sequence) fragment ions are observed and characterized with respect to the known structure for five of the heparin-derived oligosaccharides. The structure of a sixth oligosaccharide is predicted by using negative ion FAB-MS and subsequently confirmed by chemical, enzymatic, and NMR spectroscopic methods.

INTRODUCTION

Heparin, a polydisperse (having multiple sugar chain lengths), sulfated polysaccharide of 1 → 4 linked glucosamine and uronic acid residues, has been used clinically as an anticoagulant for half a century (*1*). Despite a yearly use of over 50 million doses in the U. S. alone (*1*), the exact chemical structure of heparin remains unclear. The role of heparin in anticoagulation involves the regulation of the coagulation cascade primarily through its potentiation of serine protease inhibitors (*2*) and is due to the presence of specific protein binding sites in the heparin chain (*3*, *4*). The heparin macromolecule is a proteoglycan (molecular weight approximately 1 000 000 amu) that consists of several polysaccharides having approximate molecular weight of 100 000 amu attached to a protein core (*5*). Although the structure–activity relationship of the heparin–serine protease inhibitor interaction has been explored in detail (*6*, *7*), considerably less is known about the structural requirements for heparin's other activities (*8*, *9*).

Glycosaminoglycan (GAG)-heparin results from the metabolic processing of proteoglycan heparin by proteases and a β-endoglucuronidase resulting in polydisperse polysaccharide chains of 5000–40000 amu (average of 13 000 amu). The sequence of the polysaccharide chains comprising GAG-heparin is of considerable interest (as this is heparin's drug form); thus heparin lyase is used to enzymatically depolymerize GAG-heparin into smaller oligosaccharides more suitable for structural analysis (*10*). In general, the structure and sequence of these heparin-derived oligosaccharides have been deter-

* Author to whom correspondence should be addressed.

0003-2700/89/0361-1453$01.50/0

mined by using an integrated approach involving enzymatic, chemical, electrophoretic (*11*) spectroscopic (including ^{13}C and ^{1}H NMR) (*12, 13*), and mass spectrometric methods.

Heparin is composed of polar, nonvolatile, and thermally labile oligosaccharides. Mass spectrometric (MS) methods that would result in detailed structure elucidation without the need for prior chemical degradation or derivatization have not yet been fully developed. For example, McNeal et al. reported on the ^{252}Cf plasma desorption (PD)-MS (*14*) analysis of a disaccharide, tetrasaccharide, and hexasaccharide enzymatically prepared from GAG-heparin. Due to the highly sulfated and carboxylated composition of these heparin-derived oligosaccharides, the possibility exists for these molecules to have several negative charge sites, making observation of a singly charged molecular ion and structurally significant fragment ions difficult. It was shown that by using the surfactant tridodecylmethylammonium chloride (TDMAC), these negative sites could be blocked by ion pairing and an intact positively charged molecular ion is observed (*14*). For a heparin-derived hexasaccharide, which contains seven sulfate and three carboxylate groups, the use of TDMAC resulted in an increase in molecular weight from 1603 to 7510 amu. Owing to the poor resolution of the time-of-flight MS experiment, the molecular ion of the ion-paired heparin-derived hexasaccharide was observed as an ion 400 mass units wide with the centroid calculated at approximately 7510 amu. It was also reported that structurally significant fragment ions were not observed and that the majority of fragment ions were assigned to the TDMAC surfactant (*14*). Interpretation of these results suggests that the use of PD-MS may be impractical for molecular ion analysis of even larger heparin-derived oligosaccharides.

Fast atom bombardment (FAB) ionization has proven to be a versatile and sensitive ionization method for many biological compounds (*15–21*). Several papers have been published dealing with the positive and negative ion MS analysis of polysaccharides (*22–25*); however, in most cases the analyzed polysaccharides were structurally simple, neutral oligosaccharides or were derivatized prior to analysis. Highly sulfated polysaccharides are more difficult to analyze with FAB ionization due to the possible presence of several negative charge sites. Recently, several papers dealing with the analysis of sulfated oligosaccharides have been published (*13, 26, 27*). For example, Reinhold et al. reported on the negative ion FAB-MS analysis of heparin-like oligosaccharides prepared by chemical synthesis (*27*). The dominant molecular ions observed were of the type $[M + Na_x - H_{x+1}]^-$ (where M is the fully protonated, acid form of the oligosaccharide and $x = 2–9$), and in all cases the observed spectra contained a molecular ion dispersion and little or no structurally significant fragment ions (*27*). More recently, Dell et al. described a strategy for sequencing sulfated oligosaccharide mixtures using positive ion FAB-MS, which required derivatization steps including permethylation, desulfation, and peracetylation (*28*).

In this paper, negative ion FAB-MS analysis is presented for a series of enzymatically prepared, homogeneous, structurally characterized, highly sulfated, heparin-derived oligosaccharides using triethanolamine as the FAB matrix. In addition to the clear presence of monoanionic sodiated molecular ions, structurally significant (sequence) fragment ions are observed and characterized with respect to the known structure for five of the heparin-derived oligosaccharides. The structure of a sixth oligosaccharide is predicted by using negative ion FAB-MS and subsequently confirmed by chemical, enzymatic, and NMR spectroscopic methods.

EXPERIMENTAL SECTION

Heparin sodium salt from porcine intestinal mucosa (145 units/mg) was obtained from Hepar Industries, Franklin, OH. Heparin sodium salt from bovine lung (145.7 units/mg) was obtained from Sigma Chemical Co., St. Louis, MO. Heparin lyase (heparinase, EC 4.2.2.7) was either purified from *Flavobacterium heparinum* (*29*) (5 units (μmol/min)/mg) or heparin lyase (1.5 units/mg) was obtained from Sigma.

Strong-anion-exchange high-performance liquid chromatography (SAX-HPLC) was performed on a Spherisorb (5-μm particle size) column of dimensions 2 cm × 25 cm from Phase Separations, Norwalk, CT. Sephadex G-10 was purchased from Pharmacia Biochemicals, Piscataway, NJ.

The triethanolamine used as the FAB-MS matrix was obtained from Sigma. All other chemicals utilized were of reagent grade.

Enzymatic Depolymerization of Heparin. A 750-μL aqueous solution containing 75 mIU of purified heparinase (*13*) or commercial heparin lyase was added to a 15-mL aqueous solution containing 120 mg of porcine mucosal heparin in 0.20 M sodium chloride/5 mM sodium phosphate, pH 7.0, and the mixture was incubated at 30 °C. The reaction was monitored (absorbance at 232 nm) by removal of 10-μL aliquots, which were then added to 990 μL of 0.03 M HCl. The reaction was complete within 24 h as determined by a constant absorbance. The addition of more enzyme caused no observable increase in absorbance.

Purification of Heparin-Derived Oligosaccharides DS-I, TS-I, TS-II, TS-III, and HS-I Using Strong-Anion-Exchange High-Performance Liquid Chromatography. SAX-HPLC was performed as described previously (*30*). Briefly, the column was equilibrated with 0.2 M NaCl, pH 3.5. Heparin oligosaccharides (100 mg in 2 mL), produced in a complete heparin lyase reaction, were applied to the SAX-HPLC column by using a 2-mL fixed-volume loop. The column was eluted with a linear gradient (concentration (y, in molarity) at any time (x, in seconds) = $0.0001x + 0.2$) of NaCl, pH 3.5, with a flow rate of 10 mL/min. The separation was monitored by UV absorbance at 232 nm at 2.0 absorbance units full scale. Fractions were collected, desalted twice by using a freshly prepared Sephadex G-10 gel permeation column, and quantified by UV absorbance at 232 nm (*31*). The SAX-HPLC purification and desalting was repeated to obtain heparin-derived disaccharide DS-I, tetrasaccharides TS-I, TS-II, and TS-III, and hexasaccharide HS-I, of greater than 90% purity (*31*).

Preparation and Characterization of Heparin-Derived Hexasaccharide HS-II. Bovine lung heparin was depolymerized as described above, but the reaction was terminated at 80% completion. This results in a variety of transient oligosaccharides (oligosaccharides still possessing linkages at which heparin lyase could act). Following SAX-HPLC and desalting steps, oligosaccharide HS-II is isolated, having a slightly shorter retention time than oligosaccharide HS-I on SAX-HPLC under the elution conditions described above.

Fast Atom Bombardment Mass Spectrometry. The studies reported here were performed with a VG ZAB-HF in the fast atom bombardment (FAB) ionization mode. The FAB ion source used for these studies was the standard VG Analytical, Inc., system equipped with a saddle field atom gun. Xenon was used for the bombarding fast atom beam; typical operating conditions were beam energies of 8 keV and neutral beam currents equivalent to 1.5 mA supplied by an ION TECH (Model B 50) current and voltage regulator–meter. Negative ion FAB spectra were obtained by signal adding four or eight scans with the use of the multichannel analysis (MCA) software of the VG 11-250 J data system.

The solutions of heparin-derived oligosaccharides were prepared for negative ion FAB-MS by dissolving the solid sample in doubly distilled–deionized water to a concentration of 10–20 $\mu g/\mu L$. Typically 1 μL of triethanolamine is placed on a standard VG stainless steel probe tip to which 1.5 μL of the oligosaccharide solution is added.

RESULTS AND DISCUSSION

In earlier papers, several experiments describing the mass spectrometric analysis of enzymatically (*12, 14*) and synthetically (*26*) prepared heparin oligosaccharides have been reported. Owing to the acidic nature of these highly sulfated and carboxylated compounds, negative ion fast atom bombardment mass spectrometry is used to provide molecular ion information (*12, 26*). Alkali-metal-attached molecular ions

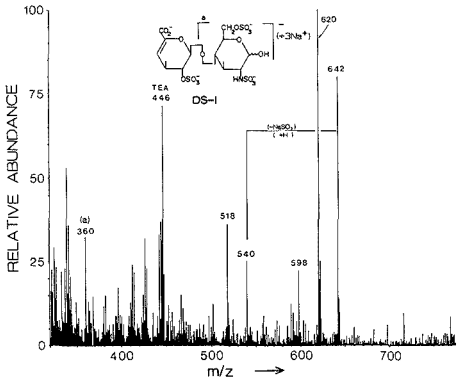

Figure 1. Negative ion fast atom bombardment (FAB) spectrum of disaccharide DS-I. For clarity only those ions that correspond to molecular or sequence fragment ions are labeled. The structure of DS-I is presented in the polyanionic form (M – 4H). The molecular ion is the trisodiated, monoanionic species $[M + 3Na - 4H]^-$ at m/z 642.

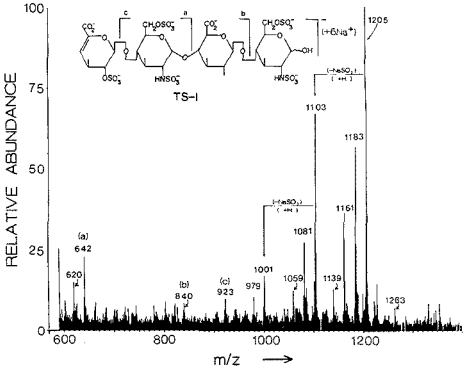

Figure 2. Negative ion FAB spectrum of tetrasaccharide TS-I. The structure of TS-I is presented in the polyanionic form (M – 7H). The molecular ion is the hexasodiated, monoanionic species [M + 6Na – 7H]⁻ at m/z 1205.

of the type $[M + Na_x - H_{x+1}]^-$ (M represents the fully protonated acid forms of di-, tetra-, and hexasaccharides; x = 2–9) were preferentially observed. For all previously reported experiments on the FAB-MS analysis of heparin oligosaccharides, thioglycerol was the FAB matrix of choice and structurally significant fragment ions were not observed (*12*, *22*, *23*).

It is interesting to note that thioglycerol has been reported to produce between a 5- and 10-fold increase in positive ion signal to noise ratio for a variety of polar organic molecules (*32*). For example, it was reported that sequence-specific fragment ions of oligopeptides, analyzed in the positive ion mode, were characterized by an increased signal to noise ratio facilitating the recognition of structurally significant fragment ions (*32*). Unlike oligopeptides, the sulfated oligosaccharides described in this paper are best analyzed in the negative ion mode. While the use of thioglycerol permits molecular ion determination of highly sulfated oligosaccharides, on the basis of the results stated above (*32*) it was anticipated that thioglycerol would not aid in the production of structurally significant sequence fragment ions in the negative ion mode. Analysis of these enzymatically prepared oligosaccharides, using thioglycerol as the FAB matrix, yielded satisfactory molecular and fragment ion information only for the disaccharide presented in this paper. Attempts at analysis of the tetra- and hexasaccharides, however, provided some molecular ion formation (with extremely high sample loading; 40 μg/mL), but structurally significant fragment ions were not observed (*13*, *33*).

Triethanolamine has been shown to provide an increase in overall sensitivity when FAB-MS analysis is performed in the negative ion mode (*34*). In this paper, the MS analysis of enzymatically prepared heparin oligosaccharides is reported using triethanolamine as the FAB-MS matrix. In all cases, molecular and structurally significant fragment ions are observed that correspond unambiguously to the known structures for these molecules.

The negative ion FAB-MS spectrum and structure of the heparin-derived disaccharide ΔIdoA2S(1 → 4)-α-D-GlcN2S6S, DS-I, (where ΔIdoA is 4-deoxy-α-L-threo-hex-4-enopyronosyluronic acid, *GlcN is glucosamine, and S is sulfate*) is shown in Figure 1. The ions at m/z 642, 620, and 598 correspond to molecular ions $[DS\text{-}I + 3Na - 4H]^-$, $[DS\text{-}I + 2Na - 3H]^-$, and $[DS\text{-}I + Na - 2H]^-$, respectively. The most prevalent fragment ion observed is loss of a $NaSO_3$ group (with addition of H^+) from the molecular ion, most likely resulting from a reaction between the matrix and the analyte. For example, the ions at m/z 540 and 518 correspond to loss of a $NaSO_3$ group from the previously described molecular ions at m/z 642 and 620 ($[DS\text{-}I + 3Na - 3H - NaSO_3]^-$ and $[DS\text{-}I + 2Na - 2H - NaSO_3]^-$, respectively; see structure in Figure 1). In contrast to previously reported results (*12*, *22*, *23*), structurally significant fragment ions are also observed. For example, in the spectrum of DS-I, the ion at m/z 360 assigned as the disulfated glucosamine fragment [D-GlcN2S6S + Na – 2H]⁻ represents a sequence fragment ion of this heparin-derived trisulfated disaccharide. Note that the ion at m/z 446 corresponds to the commonly observed triethanolamine (TEA) matrix ion of the type $[3TEA - H]^-$.

The negative ion FAB-MS spectrum and structure of the heparin-derived tetrasaccharide ΔIdoA2S(1 → 4)-α-D-GlcN2S6S(1 → 4)-β-D-GlcA(1 → 4)-α-D-GlcN2S6S, TS-I (where GlcA is glucuronic acid), are shown in Figure 2. The molecular ions for TS-I are observed at m/z 1205, 1183, and 1161. Structurally significant fragment ions corresponding to the loss of a $NaSO_3$ group are also observed in the negative ion FAB-MS spectrum of TS-I. For example, ions at m/z 1103 and 1001 are assigned to the loss of one and two $NaSO_3$ groups (with addition of H^+). Several sequence fragment ions are observed in the FAB-MS spectrum of TS-I. For example, the ion at m/z 923 is assigned as loss of the sugar residue from the nonreducing terminus of TS-I, whereas the ion at m/z 840 is assigned to loss of the sugar residue from the reducing terminus of TS-I ($[TS\text{-}I - (\Delta IdoA2S) + 4Na - 5H]^-$ and $[TS\text{-}I - (D\text{-}GlcN2S6S) + 5Na - 6H]^-$, respectively). The ion at m/z 642 is the result of loss of two sugar residues nearest the reducing end of TS-I and corresponds to the sodiated molecular ion observed for disaccharide DS-I ($[TS\text{-}I - (D\text{-}GlcA(1 \rightarrow 4)\text{-}\alpha\text{-}D\text{-}GlcN2S6S) + 2Na - 3H]^-$ or $[DS\text{-}I + 3Na - 4H]^-$).

ΔIdoA2S(1 → 4)-α-D-GlcN2S(1 → 4)-α-L-IdoA2S(1 → 4)-α-D-GlcN2S6S, TS-II (where IdoA is iduronic acid), is a structural isomer of TS-I differing only in the chirality of its internal uronic acid residue and the placement of a single sulfate group. The negative ion FAB-MS spectrum and structure of the heparin-derived tetrasaccharide TS-II are shown in Figure 3. Molecular ions at m/z 1205, 1183, and 1161 are identical with those observed for TS-I, corresponding to $[TS\text{-}II + 6Na - 7H]^-$, $[TS\text{-}II + 5Na - 6H]^-$, and $[TS\text{-}II + 4Na - 5H]^-$, respectively. Ions at m/z 1103 and 1001 correspond to loss of one and two molecules of $NaSO_3$ (with the addition of H^+) from the molecular ion at m/z 1205 ($[TS\text{-}II + 6Na - 6H - NaSO_3]^-$ and $[TS\text{-}II + 6Na - 5H - 2NaSO_3]^-$,

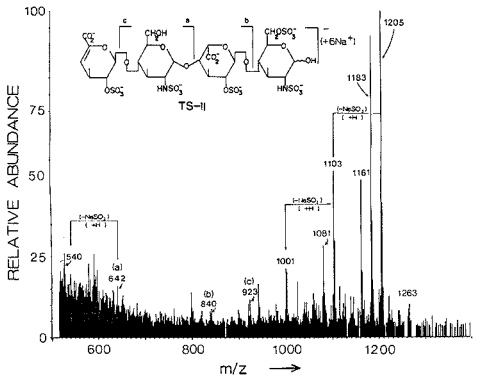

Figure 3. Negative ion FAB spectrum of tetrasaccharide TS-II. The structure of TS-II is presented in the polyanionic form (M – 7H). The molecular ion is the hexasodiated, monoanionic species $[M + 6Na - 7H]^-$ at m/z 1205.

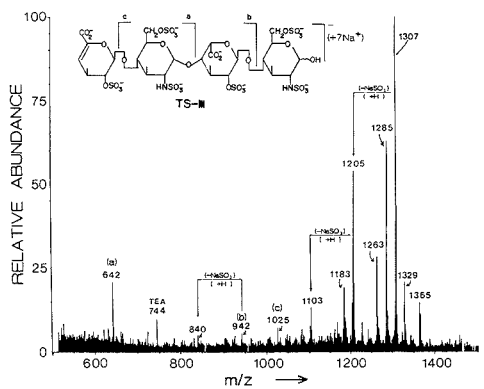

Figure 4. Negative ion FAB spectrum of tetrasaccharide TS-III. The structure of TS-III is presented in the polyanionic form (M – 8H). The molecular ion is the heptasodiated, monoanionic species $[M + 7Na - 8H]^-$ at m/z 1307.

respectively). Ions at m/z 923 due to the loss of a single sugar residue at the nonreducing terminus of TS-II and m/z 840 assigned as loss of the sugar residue at the reducing end of TS-II are observed. In addition, a fragment ion at m/z 642 due to the loss of two sugars from the reducing terminus of TS-II and corresponding to the sodiated molecular ion of DS-I is observed. Finally, the ion at m/z 540 corresponds to loss of $NaSO_3$ (with H^+ addition) from the fragment ion at m/z 642.

An abundance of structurally significant fragment ions is observed in the spectrum of the tetrasaccharide ΔIdoA2S(1 → 4)-α-D-GlcN2S6S(1 → 4)-α-L-IdoA2S(1 → 4)-α-D-GlcN2S6S, TS-III, shown in Figure 4. Molecular ions are observed at m/z 1329, 1307, 1285, and 1263, which correspond to $[TS\text{-}III + 8Na - 9H]^-$, $[TS\text{-}III + 7Na - 8H]^-$, $[TS\text{-}III + 6Na - 7H]^-$, and $[TS\text{-}III + 5Na - 6H]^-$, respectively. Structurally significant fragment ions assigned to loss of a $NaSO_3$ group are also observed in the negative ion FAB-MS spectrum of TS-III at m/z 1205 and 1103, corresponding to $[TS\text{-}III + 7Na - 7H - NaSO_3]^-$ and $[TS\text{-}III + 7Na - 6H - 2NaSO_3]^-$. Although these compounds are thoroughly desalted, by use of repetitive gel permeation chromatography, an ion at m/z 1365 is observed that corresponds to a sodium chloride adduct of the molecular ion at m/z 1307 ($[TS\text{-}III + 7Na - 8H + NaCl]^-$).

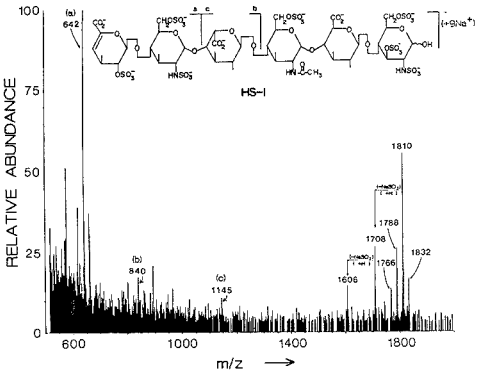

Figure 5. Negative ion FAB spectrum of hexasaccharide HS-I. The structure of HS-I is presented in the polyanionic form (M – 10H). The molecular ion is the nonasodiated, monoanionic species $[M + 9Na - 10H]^-$ at m/z 1810.

Experiments to elucidate the chemical nature of the interaction between NaCl and these heparin oligosaccharides are currently under way.

Several sequence elucidating fragment ions are observed in the negative ion FAB-MS spectrum of TS-III. The ion at m/z 1025 is assigned as loss of one sugar residue from the nonreducing end of TS-III ($[TS\text{-}III + 5Na - 6H - (\Delta IdoA2S)]^-$) while the ion at m/z 942 corresponds to loss of the reducing terminal sugar, ($[TS\text{-}III + 5Na - 6H - (D\text{-}GlcN2S6S)]^-$). In fact the ion at m/z 840 is assigned as corresponding to loss of a $NaSO_3$ group from the sequence fragment ion at m/z 942 ($[TS\text{-}III + 5Na - 5H - (D\text{-}GlcN2S6S) - NaSO_3]^-$). The ion at m/z 744 corresponds to the triethanolamine (TEA) matrix complex $[5TEA - H]^-$.

It is interesting to note that when TS-I, TS-II, and TS-III are exhaustively treated with either heparin monosulfate lyase or heparin lyase, they each form 1 mol of DS-I (TS-III gives 2 mol of DS-I) (*35*). It is not surprising, therefore, that each spectrum contains an ion at m/z 642 corresponding to the sodiated molecular ion of DS-I ($[DS\text{-}I + 3Na - 4H]^-$).

The ability to produce fragment ions corresponding to the sequence of these highly sulfated polysaccharides is much more difficult in the analysis of larger heparin-derived oligosaccharides. The structure of hexasaccharide ΔIdoA2S(1 → 4)-α-D-GlcN2S6S(1 → 4)-α-L-IdoA(1 → 4)-α-D-GlcNAc6S(1 → 4)-β-D-GlcA(1 → 4)-α-D-GlcN2S3S6S, HS-I, and its FAB-MS spectrum are shown in Figure 5. Molecular ions are observed at m/z 1810, 1788, and 1766 corresponding to $[HS\text{-}I + 9Na - 10H]^-$, $[HS\text{-}I + 8Na - 9H]^-$, and $[HS\text{-}I + 7Na - 8H]^-$, respectively. Loss of one and two $NaSO_3$ groups from the molecular ion at m/z 1810 results in the fragment ions observed at m/z 1708 and 1606 ($[HS\text{-}I + 9Na - 9H - NaSO_3]^-$ and $[HS\text{-}I + 9Na - 8H - 2NaSO_3]^-$, respectively). Three sequence elucidating fragments are observed at m/z 1145, 840, and 642. The first ion, at m/z 1145, is assigned to loss of two sugar residues from the nonreducing end of HS-I ($[HS\text{-}I - (\Delta IdoA2S(1 \rightarrow 4)\text{-}\alpha\text{-}D\text{-}GlcN2S6S) + 5Na - 6H]^-$). The second ion, at m/z 840, corresponds to the loss of three sugar residues from the reducing end of HS-I ($[HS\text{-}I - (\alpha\text{-}D\text{-}GlcNAc6S(1 \rightarrow 4)\text{-}\beta\text{-}D\text{-}GlcA(1 \rightarrow 4)\text{-}\alpha\text{-}D\text{-}GlcN2S3S6S) + 4Na - 5H]^-$). The third ion at m/z 642 corresponds, as described above, to the sodiated molecular ion of DS-I resulting from the loss of the four reducing terminal sugars from HS-I ($[HS\text{-}I - (L\text{-}IdoA(1 \rightarrow 4)\text{-}\alpha\text{-}D\text{-}GlcNAc6S(1 \rightarrow 4)\text{-}\beta\text{-}D\text{-}GlcA(1 \rightarrow 4)\text{-}\alpha\text{-}D\text{-}GlcN2S3S6S) + 3Na - 4H]^-$ or $[DS\text{-}I + 3Na - 4H]^-$).

Although sequence information for oligosaccharides DS-I, TS-I, TS-II, TS-III, and HS-I was obtained with negative ion

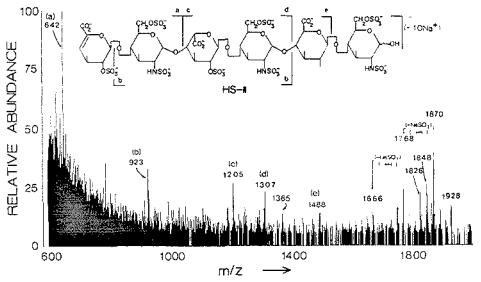

Figure 6. Negative ion FAB spectrum of structurally unknown hexasaccharide HS-II. The proposed structure of HS-II is presented in the polyanionic form (M – 11H). The molecular ion is the decasodiated, monoanionic species $[M + 10Na - 11H]^-$ at m/z 1870.

FAB-MS, these were all samples of known structure. The utility of this technique is clearly dependent on the ability to aid in the prediction of unknown sample structures. Oligosaccharide HS-II (Figure 6), isolated from a partial enzymatic depolymerization of bovine lung heparin, was originally thought to have the same structure as HS-I. Upon analysis, HS-II was observed to produce molecular ions that were 60 amu higher in mass than HS-I. The molecular ions at m/z 1870, 1848, and 1826 are assigned as nonacetylated octasulfated hexasaccharide with molecular ions $[HS\text{-}II + 10Na - 11H]^-$, $[HS\text{-}II + 9Na - 10H]^-$, and $[HS\text{-}II + 8Na - 9H]^-$, respectively. The ion at m/z 1928 results from addition of one molecule of sodium chloride to the molecular ion at m/z 1870 ($[HS\text{-}II + 10Na - 11H + NaCl]^-$). The loss of one and two $NaSO_3$ groups from the molecular ion at m/z 1870 is observed at m/z 1768 and 1666 ($[HS\text{-}II + 10Na - 10H - NaSO_3]^-$ and $[HS\text{-}II + 10Na - 9H - 2NaSO_3]^-$, respectively).

Owing to the fact that DS-I, TS-I, TS-II, TS-III, and HS-I comprise approximately 86% of the total oligosaccharide mass of heparin (*31*), it seems reasonable to suggest that HS-II would be composed of some combination of the di- and tetrasaccharides described above. Therefore, the fragment ions in the negative ion FAB-MS spectrum of HS-II at m/z 1307, 1205, and 642 provide structure information required to deduce the sequence of HS-II. These fragments correspond to the sodiated molecular ions of TS-III, TS-I (or TS-II), and DS-I, respectively. The fragment at m/z 1307 is assigned as the loss of the two sugar residues from HS-II ($[HS\text{-}II - (\beta\text{-D-GlcA}(1 \rightarrow 4)\text{-}\alpha\text{-D-GlcN2S6S}) + 7Na - 8H]^-$) and corresponds to the sodiated molecular ion of TS-III. The fragment ion at m/z 1205 can be assigned to three different structures, two corresponding to the sodiated molecular ions of TS-II or TS-I and the third corresponding to the loss of a $NaSO_3$ group from the TS-III fragment at m/z 1307 ($[TS\text{-}II + 6Na - 7H]^-$, $[TS\text{-}I + 6Na - 7H]^-$, and $[TS\text{-}III + 7Na - 7H - NaSO_3]^-$, respectively). Owing to the fact that formation of this fragment ion would require loss of two sugar residues and that this ion would have to be formed in accordance with the observation of the sodiated TS-III fragment (see structure of TS-III in Figure 4), it is proposed that the fragment ion at m/z 1205 corresponds to the sodiated TS-I residue only (see structure of TS-I in Figure 2). In either event, loss of a $NaSO_3$ group from TS-III could account for a significant portion of the abundance of the fragment ion at m/z 1205. The fragment ion at m/z 642 is once again assigned as the sodiated molecular ion of DS-I, which could be produced via loss of four nonreducing end sugar residues. Combining the interpretation of the fragment ions observed in the negative ion FAB-MS spectrum of HS-II, one could propose either DS-I(1 → 4)TS-I or TS-I(1 → 4)DS-I as structures for oligosaccharide HS-II. The fragment ion at m/z 923 is further assigned as the loss of one nonreducing end and two reducing end sugars from HS-II ($[HS\text{-}II - (\Delta IdoA2S)\text{-}(\beta\text{-D-GlcA}(1 \rightarrow 4)\text{-}\alpha\text{-D-GlcN2S6S}) + 4Na - 4H]^-$. Recall that a fragment ion at m/z 923 is observed in the negative ion FAB spectrum of TS-I and TS-II. It seems reasonable to suggest, therefore, that the structure of HS-II corresponds to DS-I(1 → 4)TS-I (fully sodiated molecular ion formed is $[DS\text{-}I(1 \rightarrow 4)TS\text{-}I + 10Na - 11H]^-$) from which the sodiated TS-III ion at m/z 1307 can be formed by loss of two reducing end sugars as described above.

Proposing DS-I(1 → 4)TS-I as the structure for HS-II by using negative ion FAB-MS analysis does not identify the chirality or the precise position of sulfate groups on each sugar residue. Therefore, enzymatic and NMR analyses were also used to aid in the interpretation of the structural information derived from the FAB-MS spectra. On exhaustive treatment with heparin lyase, oligosaccharide HS-II was broken down into 1 equiv each of two products that coeluted on SAX-HPLC with DS-I and TS-I, suggesting that oligosaccharide HS-II was simply DS-I(1 → 4)TS-I or TS-I(1 → 4)DS-I. Ozonolysis of HS-II followed by acidic workup (*35*) removes the unsaturated uronic acid residue on the nonreducing terminus of HS-II, affording a pentasaccharide with no UV chromaphore. On exhaustive treatment with heparin lyase this pentasaccharide afforded a single product (by SAX-HPLC using UV detection) that coeluted with TS-I. This experiment demonstrates that oligosaccharide DS-I is ozone-sensitive and must lie at the nonreducing terminus and thus establishes the sequence of oligosaccharide HS-II as DS-I(1 → 4)TS-I. Proton NMR at 360 MHz was also used to confirm the structure of HS-II. The chemical shifts for the anomeric signals starting at the nonreducing terminus are 5.57, 5.45, 5.21, 5.39, 4.62, and 5.50, consistent with the proposed sequence of the heparin-derived oligosaccharide HS-II (*12*, *13*).

This study further illustrates that the use of FAB-MS can aid in the unambiguous structural assignments of these and other heparin-derived oligosaccharides. Triethanolamine serves as an excellent FAB matrix in the negative ion mode, possibly enhancing the production of abundant molecular and structurally significant fragment ions of highly sulfated heparin-derived oligosaccharides. Since derivatization reactions are not required, analysis of larger heparin oligosaccharides can be performed. The use of enzymatic, chemical, and NMR spectroscopic methods to aid in the confirmation of the predicted structure (based on negative ion FAB-MS results) of HS-II for the first time establishes the predictive value of FAB-MS in obtaining structure and sequence information of unknown highly sulfated, heparin-derived oligosaccharides. Further studies into the sequence determination of larger biologically active heparin oligosaccharides are currently under way.

LITERATURE CITED

(1) Jacques, L. B. *Science* **1979**, *206*, 528–533.
(2) Rosenberg, R. D. *Fed. Proc.* **1977**, *36*, 10–18.
(3) Lindahl, U.; Backström, G.; Thumberg, L. *J. Biol. Chem.* **1983**, *258*, 9826–9830.
(4) Atha, D. H.; Stephens, A. W.; Rosenberg, R. D. *Proc. Natl. Acad. Sci. USA* **1984**, *81*, 1030–1034.
(5) Comper, W. D. In *Heparin (and Related Polysaccharides)*, *Polymer Monographs*; Huglin, M. B., Ed.; Gordon Breach: New York, 1981; Vol. 7.
(6) Atha, D. H.; Lormeau, J. C.; Petitou, M.; Rosenberg, R. D.; Choay, J. *Biochemistry* **1985**, *24*, 6723–6729.
(7) Villanueva, G. B. *J. Biol. Chem.* **1984**, *259*, 2531–2536.
(8) Folkman, J.; Langer, R.; Linhardt, R. J.; Haudenschild, C.; Taylor, S. *Science* **1983**, *221*, 719–725.
(9) Linhardt, R. J.; Rice, K. G.; Kim, Y. S.; Engelken, J. D.; Weiler, J. M. *J. Biol. Chem.* **1988**, *263*, 13090–13096.
(10) Linhardt, R. J.; Cooney, C. L.; Galliher, P. M. *Appl. Biochem. Biotechnol.* **1986**, *12*, 135–171.
(11) Rice, K. G.; Rottink, M. K.; Linhardt, R. J. *Biochem. J.* **1987**, *244*, 515–522.
(12) Linhardt, R. J.; Rice, K. G.; Merchant, Z. M.; Kim, Y. S.; Lohse, D. L. *J. Biol. Chem.* **1986**, *261*, 14448–14454.
(13) Merchant, Z. M.; Kim, Y. S.; Rice, K. G.; Linhardt, R. J. *Biochem. J.* **1985**, *299*, 369–377.

(14) McNeal, C. J.; Macfarlane, R. D.; Jardine, I. *Biochem. Biophys. Res. Commun.* **1986**, *139*, 18–24.
(15) Barber, M.; Bordoli, R. S.; Sedgwick, R. D.; Tyler, A. N. *J. Chem. Soc., Chem. Commun.* **1981**, 325–326.
(16) Fenselau, C. *Ion Formation from Organic Solids*; Benninghoven, A., Ed.; Springer Series in Chemical Physics 25; Springer: New York, 1983; p 90.
(17) Gaskell, S. J.; Brownsey, B. G.; Brooks, P. W.; Green, B. N. *Biomed. Mass Spectrom.* **1983**, *10*, 215.
(18) Williams, D. H.; Bradley, C.; Bojeson, G.; Santikarn, S.; Taylor, L. C. E. *J. Am. Chem. Soc.* **1981**, *103*, 5700.
(19) Williams, D. H.; Bradley, C. V.; Santikarn, S.; Bojeson, G. *Biochem. J.* **1982**, *201*, 105.
(20) Desiderio, D. M.; Katakuse, I. *Biomed. Mass Spectrom.* **1984**, *11*, 55.
(21) Barber, M.; Bordoli, R. S.; Sedgwick, R. D.; Tyler, A. N. *Biomed. Mass Spectrom.* **1982**, *9*, 208.
(22) Dell, A.; Morris, H. R.; Egge, H.; Von Nicolai, H.; Strecker, G. *Carbohydr. Res.* **1983**, *115*, 41–52.
(23) Dell, A.; Ballou, C. E. *Org. Mass Spectrom.* **1983**, *18*, 50–56.
(24) Dell, A.; Ballou, C. E. *Carbohydr. Res.* **1983**, *120*, 95–111.
(25) Ballou, C. E.; Dell, A. *Carbohydr. Res.* **1985**, *140*, 139–143.
(26) Strecker, G.; Wieruszeski, J. M.; Martel, C.; Montreuil, J. *Glycoconjugate J.* **1987**, *4*, 329–337.
(27) Reinhold, V. N.; Carr, S. A.; Green, B. N.; Petitou, M.; Choay, J., Sinay, P. *Carbohydr. Res.* **1987**, *161*, 305–313.
(28) Dell, A.; Rogers, M. E.; Thomas-Oates, J. E.; Huckerby, T. N.; Sanderson, P. N.; Nieduszynski, I. A. *Carbohydr. Res.* **1988**, *179*, 7–19.
(29) Yang, V. C.; Linhardt, R. J.; Bernstein, H.; Cooney, C. L.; Langer, R. *J. Biol. Chem.* **1985**, *260*, 1849–1857.
(30) Rice, K. G.; Kim, Y. S.; Grant, A. C.; Merchant, Z. M.; Linhardt, R. J. *Anal. Biochem.* **1985**, *150*, 325–331.
(31) Linhardt, R. J.; Rice, K. G.; Kim, Y. S.; Lohse, D. L.; Wang, H. M. Loganathan, D. *Biochem. J.* **1988**, *254*, 781–787.
(32) Lehmann, W. D.; Kessler, M.; Konig, W. A. *Biomed. Mass Spectrom.* **1984**, *11*, 217–222.
(33) Mallis, L. M.; Jardine, I.; Linhardt, R. J., unpublished results of experiments performed at the Mayo Clinic, Rochester, MN, 1984, and discussions with I. Jardine of Finnigan MAT, San Jose, CA, 1988.
(34) Gower, J. L. *Biomed. Mass Spectrom.* **1985**, *12*, 191–196.
(35) Rice, K. G.; Linhardt, R. J. *Carbohydr. Res.*, in press.

RECEIVED for review November 9, 1988. Accepted March 24, 1989. This work was supported by a grant from the National Institute of Health—General Medical Sciences (R.J.L., GM38060). Support for L.M.M., of the University of Iowa High Resolution Mass Spectrometry Facility, and funds for the purchase of mass spectrometry equipment for these studies were obtained from the University of Iowa Office of Educational Development and Research.

CORRESPONDENCE

Photodissociation in a Reflectron Time-of-Flight Mass Spectrometer: A Novel Mass Spectrometry/Mass Spectrometry Configuration for High-Mass Systems

Sir: The relative merits of time-of-flight (TOF) mass spectrometers have been discussed frequently. TOF instruments have the advantage of multichannel mass detection, high-frequency data acquisition, and high mass range. However, the applications of these instruments have been limited because of their low mass resolution. In recent developments, resolution limits on TOF instruments have been improved dramatically by the use of the "reflectron" configuration (*1–6*). Resolution in reflectron TOF systems has been demonstrated in the range of several thousand atomic mass units (*1–6*). This performance is now acceptable for many demanding applications. Nevertheless, TOF instruments have the remaining difficulty that they are not easily adaptable to tandem mass spectrometry experiments (i.e. MS/MS). In this correspondence, we describe a novel scheme involving a *reflectron tandem* instrument that overcomes many of the previous limitations on TOF systems for MS/MS experiments. This instrument configuration, and variations on this general theme, may have significant applications in a variety of mass spectrometry environments, particularly those involving large molecules.

Before we describe the new instrument, it is important to consider the problems inherent in MS/MS experiments using conventional TOF instruments. Collisionally activated dissociation (CAD) is fundamentally incompatible with TOF measurements because collisions destroy the required well-defined ion kinetic energy. Modified TOF instruments have been used for CAD studies, but with unsatisfactory results compared to those obtained with other instruments (*7, 8*). TOF instruments have been used successfully for *one* stage of analysis in MS/MS CAD experiments (*9, 10*). Additionally, new experiments have been described employing tandem TOF instruments with a solid surface for collisional activation (*11*). However, gas-phase CAD has not proven to be very useful for TOF/TOF experiments. In principle, laser radiation can be used instead of CAD for photodissociation with less distortion of the time-of-flight information. There have in fact been some successful examples of end-to-end tandem TOF experiments using laser dissociation (*12–14*). However, these experiments are difficult in practice because the fast ion beam must be overlapped in time and space with a pulsed (usually nanosecond) laser. Deceleration and reacceleration of the ion beam provides a partial solution to the problem, but the timing considerations are still critical. The reflectron configuration described below provides optimal laser overlap with the ion beam, while at the same time minimizing the uncertainties in the photodissociation laser firing time.

The schematic diagram of the reflectron system in our laboratory is shown in Figure 1. Sample species for photodissociation experiments in this system are introduced in a pulsed molecular beam. However, this sample introduction scheme is not critical for the operation of the reflectron system. Ions are formed by intersecting the collimated molecular beam with the unfocused output of an excimer laser operating at either 193 or 157 nm (ArF or F_2 mixtures, respectively). Ions are accelerated into the first arm of the flight with a two-stage acceleration plate configuration, imparting a constant kinetic energy to all species. Mass selection occurs at the end of the first flight tube (1.2 m from the ionization point). Parallel plates (3-cm spacing) at this position are biased with a positive voltage (typically 100 V), which deflects positive ions off the flight tube axis. The rise time of this pulse, which is about 1 μs in the present system, is the limiting factor in mass selection capability. At the precise arrival time of the ion packet to be selected, the deflection voltage pulses to ground, transmitting that ion packet to the reflection region. The

0003-2700/89/0361-1458$01.50/0

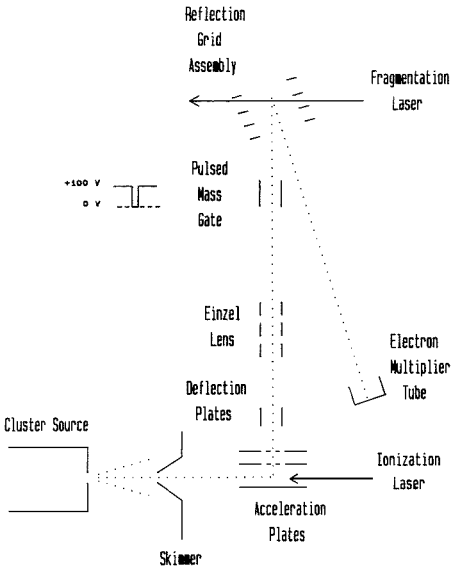

Figure 1. Apparatus configuration used for MS/MS experiments in the reflectron time-of-flight mass spectrometer.

reflection region of our instrument is constructed like those described previously (*1–6*). The angle between the two flight tubes is 12°, determined by other geometrical constraints in the molecular beam machine. However, windows are added to the vacuum system, allowing the introduction of a photodissociation laser in the reflection region. Specifically, the laser position and reflection voltages are adjusted so that the laser intersects the ion beam at the peak of its trajectory. At this point, the average vertical velocity component of the ion beam is zero, making it possible to fire the dissociation laser with the minimum timing uncertainty. Dissociation is accomplished with a second excimer laser. Residual parent ions and daughter fragment ions resulting from photodissociation are reaccelerated and mass analyzed by their flight time through the second arm of the flight tube (1.0-m length). The lasers and pulsed nozzle for this experiment are synchronized with a digital delay generator (Stanford Research Systems). Arrival time spectra are recorded with a transient digitizer system (Transiac Model 2101), triggered so that time zero is the fragment laser firing. Computer differences are accumulated for a sequence of 20 cycles with the fragment laser on and off for 20 laser shots each per cycle (800 total shots). The final spectrum presented is the resulting difference (laser on–laser off), indicating depletion in the parent ion channel and positive-going daughter fragments.

An example of the performance of this instrument is shown in Figure 2 for the metal cluster ion Pb_{17}^+ at m/z 3522. This species was produced by pulsed vaporization of a solid lead sample with a Nd:YAG laser at 532 nm, followed by photoionization at 193 nm. The 17-atom ion was size-selected out of a distribution containing clusters from two to 20 atoms in size and dissociated at 308 nm (XeCl excimer laser). The depletion in the parent ion channel represents approximately 5% of the available parent ion density per shot for a dissociation laser power of 1 mJ/cm². Higher laser powers produce greater depletion, but at the expense of multiphoton rather than single-photon absorption. Mass spectral studies of these cluster systems have been discussed in detail in previous reports from our laboratory (*15*). As shown, in this experiment

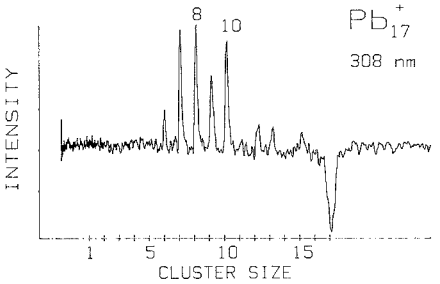

Figure 2. Representative photodissociation spectrum obtained with the reflectron system. In this spectrum, the parent ion is a 17-atom cluster of lead atoms. Dissociation at 308 nm produces fragment ions containing from six to 13 atoms.

the primary charged fragments are in the size range of six to 10 atoms. In principle, the integrated intensity of the fragment ions should add up exactly to the parent ion depletion, but this is not exactly the case in Figure 2. In part, this nonadditive effect is caused by the poor shot-to-shot reproducibility of our experiment (primarily due to the laser vaporization cluster source), amplified by the difference technique used in data acquisition. Another more interesting effect is caused by the ion optics of the reflectron itself. Trajectory calculations show that the corresponding parent and fragment ions do not follow exactly the same trajectory and are laterally displaced from each other on the detector. Our present detector has a small acceptance aperture (1 cm²), making it difficult to achieve optimum focusing for both parent and fragment ion beams. An increased area detector (e.g. 1-in. diameter) would eliminate this problem. Under the typical operating conditions used here, the first-stage acceleration voltages total 1700 V, and the delay between the ionization and dissociation laser pulses is 179 μs. The time interval within which the dissociation laser beam can be made to intersect the parent ion beam is 3.0 μs. This same experimental configuration without the fragmentation laser can be used to detect unimolecularly produced, or metastable, fragment ions resulting from the laser photoionization process. While we have detected metastables for other cluster systems (e.g. benzene clusters), we have not detected metastable lead cluster fragments.

It should be noted that laser dissociation experiments in reflectron spectrometers have been described previously (*16, 17*). However, this is the first such experiment in which dissociation occurs in the reflection field at the turning point in the ion trajectory. We have tried experiments with dissociation at other positions just prior to the reflection field or within the field prior to the turning point and find that the timing considerations are quite severe in these configurations.

Although the timing is convenient for dissociation at the turning point, it is important to consider the possible effects of mass discrimination in this geometry. To do this we have used trajectory calculations on a variety of parent ion and fragment ion masses, with dissociation at different points along the trajectory. If there is no significant kinetic energy release in the lighter fragment ions, fragmentation at the turning point results in the least possible deviation between the parent ion and fragment ion trajectories. However, if there is significant kinetic energy release, fragment ion trajectories may be sufficiently displaced from the parent ion axis so that they will miss the dectector. Significant kinetic energy release is not expected for unimolecular decay of large molecules. However, the exact amount of energy release necessary to cause a fragment ion to miss the detector depends on the mass of the

fragment, the distance to the detector, the size of the detector, and the angular distribution of the fragment. In our instrument, even a few tenths of an electronvolt of energy is sufficient to cause fragment loss if the energy is directed exactly perpendicular to the ion beam axis. Fragment ejection parallel to the beam axis may cause broadening in the arrival time spectrum. While we have made preliminary observations of fragment ion loss from diatomic and triatomic metal parent ions, we have not measured any noticeable broadening in arrival time spectra.

One of the initial applications of reflectron instruments was in the study of metastable ion decay (*2, 5, 6*). These experiments used the slow overall time scale for ion drift in the first flight tube, deceleration, and reacceleration to probe microsecond metastable lifetimes. Unimolecular dissociation lifetimes are another common problem in photodissociation studies of large molecules. In the configuration described above, however, irradiated ions remain in the turning region for up to 3–4 μs (mass dependent) before reacceleration. This instrument is therefore sensitive to "slow" unimolecular fragmentation processes.

It should be emphasized that the present system is not yet fully optimized for the study of large molecules. The system described in Figure 1 is in fact equivalent to two low-resolution spectrometers connected by the reflection/dissociation region. Mass selection of parent ions and mass analysis of fragment ions are both limited to unit resolution at about m/z 200 (typical for a simple linear TOF). However, the same Pb_{17}^+ ion can be detected without photodissociation by its time of flight through the full reflectron instrument with a resolution of about 1000. To incorporate this general idea into the design of a genuine high-mass/high-resolution instrument, then, it should be possible to include a reflectron for high-resolution analysis prior to mass selection and another reflectron after the dissociation region for high-resolution analysis of fragments. This "triple reflectron" instrument would not be simple geometrically, but designs based on the linear reflectron (*3, 18*) concept could be used to achieve a more compact system.

The general design philosophy described here may have significant applications for the study of large molecules, particularly for biological systems. Kinematic effects associated with large mass differences between parent ions and collision partners make collisionally activated dissociation less attractive than high-energy laser dissociation for these systems (*19, 20*). In the reflectron configuration the timing problems associated with laser experiments are effectively eliminated, and the benefits of essentially unlimited mass range can be realized without sacrificing resolution. Additionally, the pulsed nature of these laser experiments lends them naturally to coupling with recently developed laser desorption sources (*21–25*) for the study of involatile species. These and other applications of reflectron systems are under current investigation in our laboratory.

ACKNOWLEDGMENT

We thank Fred McLafferty and Jon Amster for helpful discussions about these experiments.

LITERATURE CITED

(1) Mamyrin, B. A.; Karataev, V. I.; Shmikk, D. V.; Zagulin, V. A. *Zh. Eksp. Teor. Fiz.* **1973**, *64*, 82.
(2) Boesl, U.; Neusser, H. J.; Weinkauf, R.; Schlag, E. W. *J. Phys. Chem.* **1982**, *86*, 4857.
(3) Lubman, D. M.; Bell, W. E.; Kronick, M. N. *Anal. Chem.* **1983**, *55*, 1437.
(4) Kuehlwind, H.; Neusser, H. J.; Schlag, E. W. *Int. J. Mass Spectrom. Ion Phys.* **1983**, *51*, 25.
(5) Kuehlwind, H.; Neusser, H. J.; Schlag, E. W. *J. Phys. Chem.* **1984**, *88*, 6104.
(6) Kuejlwind, H.; Neusser, H. J.; Schlag, E. W. *J. Phys. Chem.* **1985**, *89*, 5600.
(7) Hadden, W. F.; McLafferty, F. W. *J. Am. Chem. Soc.* **1968**, *90*, 4745.
(8) Hadden, W. F.; McLafferty, F. W. *Anal. Chem.* **1969**, *41*, 31.
(9) Stults, J. T.; Enke, C. G.; Holland, J. F. *Anal. Chem.* **1983**, *55*, 1323.
(10) Glish, G. L.; Goeringer, D. E. *Anal. Chem.* **1984**, *56*, 2291.
(11) Cooks, G. L. 11th International Mass Spectrometry Conference, Bordeaux, 1988.
(12) Geusic, M. E.; Jarrold, M. F.; McIlrath, T. J.; Freeman, R. R.; Brown, W. L. *J. Chem. Phys.* **1987**, *86*, 3862.
(13) Brucat, P. J.; Zheng, L. S.; Tittel, F. K.; Curl, R. F.; Smalley, R. E. *J. Chem. Phys.* **1986**, *84*, 3078.
(14) Liu, Y.; Zhang, Q. L.; Tittel, F. K.; Curl, R. F.; Smalley, R. E. *J. Chem. Phys.* **1986**, *85*, 7434.
(15) LaiHing, K.; Wheeler, R. G.; Wilson, W. L.; Duncan, M. A. *J. Chem. Phys.* **1987**, *87*, 3401.
(16) Alexander, M. L.; Levinger, N. E.; Johnson, M. A.; Ray, D.; Lineberger, W. C. *J. Chem. Phys.* **1988**, *88*, 6200.
(17) Posey, L. A.; Johnson, M. A. *J. Chem. Phys.* **1988**, *89*, 4807.
(18) El-Sayed, M. A.; Tai, Tsong-Lin *J. Phys. Chem.* **1988**, *92*, 5333.
(19) Neumann, G. M.; Sheil, M. M.; Derrick, P. J. *Z. Naturforsch.* **1984**, *39a*, 584.
(20) Kiplinger, J. P.; Bursey, M. M. *Org. Mass Spectrum.* **1988**, *23*, 342.
(21) Grotemeyer, J.; Boesl, U.; Walter, K.; Schlag, E. W. *J. Am. Chem. Soc.* **1986**, *108*, 4233.
(22) Tembreull, R.; Lubman, D. M. *Anal. Chem.* **1986**, *58*, 1299.
(23) Engelke, F.; Hahn, J. H.; Henke, W.; Zare, R. N. *Anal. Chem.* **1987**, *59*, 909.
(24) Tembreull, R.; Lubman, D. M. *Anal. Chem.* **1987**, *59*, 1082.
(25) Spengler, B.; Karas, M.; Bahr, U.; Hillenkamp, F. *J. Phys. Chem.* **1987**, *91*, 6502.

K. LaiHing
P. Y. Cheng
T. G. Taylor
K. F. Willey
M. Peschke
M. A. Duncan*

Department of Chemistry
School of Chemical Sciences
University of Georgia
Athens, Georgia 30602

RECEIVED for review December 2, 1988. Accepted March 21, 1989.

Polishable Modified Carbon Fiber Composite Electrodes Containing Copolymers of Vinylferrocene or Vinylpyridine in a Cross-Linked Polystyrene Matrix

Sir: The carbon fiber composite electrodes described herein are polishable, random arrays of polymer-modified ultramicroelectrodes. These electrodes illustrate two new general approaches for obtaining modified electrodes that have renewable surfaces, but with electrochemical properties resembling those of their nonrenewable polymer-film counterparts. These new types of electrodes may be designed and fabricated to have the selectivity, sensitivity, and detection limit of surface-modified electrodes, the signal-to-charging-current ratio and steady-state behavior of ultramicroelectrodes (*1, 2*),

0003-2700/89/0361-1460$01.50/0

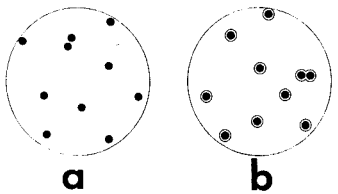

Figure 1. Cross sectional view of cylindrical modified carbon fiber composite electrodes. The black disks represent carbon fibers (7.2-μm diameters; not drawn to scale). (a) Matrix-modified electrode. The white area represents a copolymer of vinylferrocene or vinylpyridine with cross-linked polystyrene. (b) Ring-modified electrode. The rings surrounding the disks represent a coating of cross-linked poly(vinylferrocene) (also not to scale). The matrix (white area outside rings) is cross-linked polystyrene.

and the geometric current density and polishability of solid electrodes. Electrocatalysts may be incorporated into the composite matrix as well.

Both types of electrodes rely on bundles of carbon fibers dispersed in a cross-linked polystyrene matrix; the fibers are collinear within the cylinder that comprises the composite electrode. Carbon fiber microelectrodes (*3–6*) and arrays (*7, 8*) of carbon fibers have been used widely by electrochemists because of the useful physical properties of the carbon fibers themselves. Commercially available carbon fibers are typically less than 10 μm in diameter, are flexible, have electrical resistances from 1.0 to 4.0 kΩ/cm (*3*), and are inexpensive.

Modification of the carbon fiber electrodes was accomplished by one of two means: matrix modification or ring modification. Matrix-modified electrodes were prepared by copolymerizing vinylferrocene or vinylpyridine along with the styrene and divinylbenzene (DVB) that formed the composite matrix. For ring-modified electrodes, individual fibers in a bundle were coated with cross-linked poly(vinylferrocene) by electrocopolymerization of vinylferrocene and DVB. The coated fibers were then incorporated into a cross-linked polystyrene matrix as described above. A diagram of the cross section of the cylindrical electrodes is shown in Figure 1.

The general concept of ring-modified electrodes was modeled after the work of Subramanian (*9*) and of Bell and coworkers (*10, 11*), who used electropolymerization to form polymeric interlayers on carbon fibers used in epoxy composites, for improved mechanical properties.

Recently we reported carbon particle composites containing solids (*12*), vinylferrocene (*13*), and vinylpyridine (*14*) as modifiers. Also, Wang and co-workers used commercially available epoxy-bonded graphite to prepare bulk-modified electrodes containing a cation-exchange resin, poly(vinylpyridine), or cobalt phthalocyanine (*15*). Both particles and fibers have advantages as the conductive components of the composite, depending upon the application. The advantages of fibers used in electrodes described herein include improved conductivity, enhanced mass transport properties, and especially, ease of miniaturization (*16*). In addition, the uniform size of the microelectrodes will be easier to treat mathematically.

EXPERIMENTAL SECTION

Materials. Hercules AS4 carbon fibers were provided to us by James P. Bell, University of Connecticut. The fibers were packaged as a 3000-fiber bundle around a spool, and individual fibers had nominal diameters of 7.2 μm. Scanning electron microscopy showed that these fibers have uniform, circular cross sections.

Styrene, divinylbenzene (DVB), and vinylpyridine were purchased from Aldrich Chemicals and were vacuum-distilled. Vinylferrocene was also purchased from Aldrich and was purified by sublimation. Dimethylformamide (DMF), obtained from Baker Chemicals, was distilled and dried over activated alumina. Water was purified by using a Millipore reverse osmosis–ion-exchange system and had a measured resistivity of 18 MΩ cm. All other chemicals were of reagent grade and used as received.

Methods. Matrix-modified electrodes were prepared by mixing the modifying monomer (vinylferrocene or 4-vinylpyridine) with styrene, DVB, and azobis(isobutyronitrile) (AIBN) radical initiator and sonicating for 15 min to ensure dissolution of the AIBN and complete mixture of the monomers. An example composition for the vinylferrocene copolymer matrix-modified electrode was 67.8% styrene, 2.4% vinylferrocene, 26.9% DVB, and 2.9% AIBN. To minimize swelling (see below), while maintaining a high capacity for binding, the following composition was used for copoly(vinylpyridine) composites: 39.1% styrene, 39.9% vinylpyridine, 19.0% DVB, and 2.0% AIBN.

The carbon fibers were inserted into open-ended glass tubes (inner diameters of 1–5 mm). The tubes were placed upright in glass vials and were filled with the monomer mixture. After sonication for an additional 5 min, the vials were sealed with screw caps and heated in an oven at 65 °C for 3–10 h.

Vinylferrocene ring-modified composite materials were prepared by first electrocopolymerizing vinylferrocene and DVB to form films of the copolymer on individual fibers. This process was accomplished by maintaining a nominal potential of –2.5 V versus a Ag/Ag^+ (0.01 M) reference electrode for 30 min with carbon fiber bundles used as working electrodes in dry DMF solution that contained 10 mM vinylferrocene, 2 mM DVB, and 0.1 M tetrabutylammonium perchlorate (TBAP) (*17*). Alternatively, 64% dimethylacetamide (DMAC) in aqueous 0.1 M sulfuric acid was used as the solvent. Here, the minimum amount of DMAC was used to keep the solution clear, indicating dissolution of monomers. This approach minimized the solubility of oligomers and polymers produced at the surface of the electrode and allowed growth of thicker films.

After the electropolymerization process, the fibers were rinsed thoroughly with dry DMF, spread out, and hung to dry in an oven at 40 °C for 1 h. These modified fibers were placed in open-ended glass tubes that were filled with a solution of 70–78% styrene, 28–20% DVB, and 1–2% AIBN (weight percent) and sonicated for 5 min to disperse the fibers. After sonication, the tubes were placed in an oven and heated at 65 °C for 2–5 h.

The composite cylinders were sealed into glass tubes with epoxy and prepared for use as electrodes by first grinding with successively smaller grit (320, 400, and 600 grit) silicon carbide paper (3M Company). Polishing was performed with 6-μm and 1-μm diamond paste followed by 0.05-μm γ-alumina (all from Buehler). The electrodes were rinsed thoroughly with acetone and water after each successive polishing step. Glassy carbon electrodes were polished according to the same procedure.

Instrumentation. Scanning electron microscopy (SEM) and energy dispersive X-ray analysis were performed by using an Amray-1000 SEM instrument with an EDAX-9100 attachment. Fourier transform infrared (FTIR) spectra were obtained with a Mattson Cygnus 100 FTIR spectrometer. All electrochemical experiments were performed with a BAS-100 electrochemical analyzer. Electroanalytical experiments were carried out in aqueous 0.1 M KCl using a Ag/AgCl reference electrode unless noted otherwise.

RESULTS AND DISCUSSION

Preparation and Characterization of Composite Materials. *Composites as Materials.* The composite cylinders formed after polymerization of the matrix were hard and appeared dark and glasslike. In the case of ring-modified electrodes, the carbon fibers, normally quite flexible, became very rigid upon formation of the cross-linked poly(vinylferrocene) film via electrocopolymerization.

In order to estimate the thickness of the polymer films, electropolymerization was carried out using bundles of fibers as working electrodes under conditions similar to those described in the Experimental Section. The fibers were then dried in a vacuum oven at 40 °C for 15 h. The weight gained by the fibers was consistent with coatings in the range of 0.03–0.7 μm thick; the thicker coatings were obtained by using

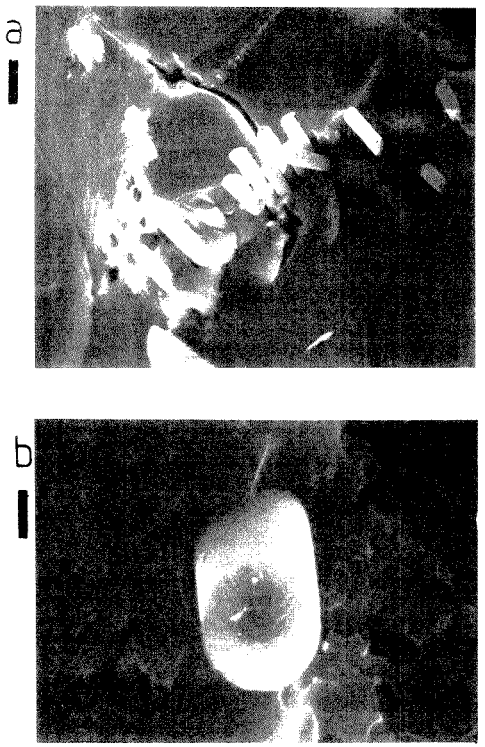

Figure 2. Scanning electron micrographs of cross section of vinylferrocene-modified composites. (a) Matrix-modified carbon fiber composite electrode magnified 480 times. Bar represents 20 μm. (b) Ring-modified carbon fiber composite electrode magnified 2600 times. Bar represents 2 μm.

the mixed solvent system (dimethylacetamide/sulfuric acid).

Evidence that the films remained intact upon incorporation into the cross-linked polystyrene composite is given below. The electrodes were evaluated as materials by using scanning electron microscopy. Bulk properties, i.e. adherence of the cross-linked polystyrene matrix to coated and uncoated fibers, and properties of the electrode surface after cleavage, polishing, and ultrasonication were of interest.

Figure 2 shows scanning electron micrographs of cross sections of the matrix- and ring-modified vinylferrocene composite materials. The samples were prepared by placing the composite cylinder in liquid nitrogen for 30 s and then breaking the material in two. The fractured surface of the matrix-modified electrode shown in Figure 2a shows that fibers protruding from the surface were oriented in a similar direction with respect to the fractured surface, and the fibers themselves were not evenly dispersed throughout the composite. Energy dispersive X-ray analysis (EDX) showed that iron from the ferrocene moieties was located throughout the polymer matrix, as expected.

The cross section of the vinylferrocene ring-modified fiber composite is shown in Figure 2b. This composite material was very similar to the matrix-modified electrode; the fibers were unevenly distributed and had a nearly uniform orientation with respect to the surface of the material. Energy dispersive X-ray analysis showed that roughly 20 times more iron was located on the poly(vinylferrocene) coating on the fibers than on ends of the carbon fibers; iron was not detected within the

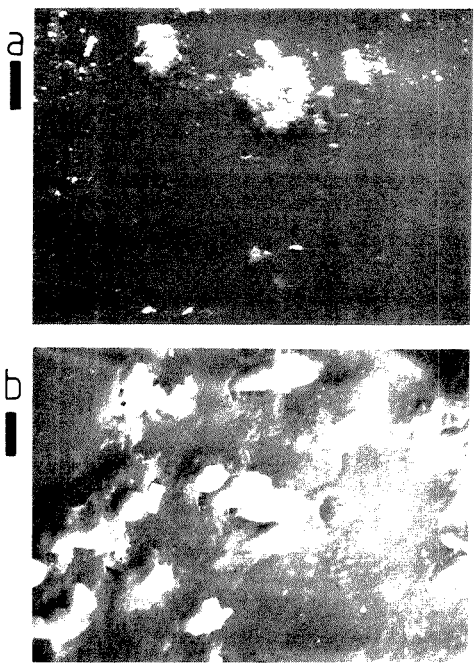

Figure 3. Scanning electron micrographs of polished matrix-modified composite electrode: (a) after 1 min of sonication, magnified 1000 times; (b) after 15 min of sonication, magnified 1100 times. The polishing procedure is described in text; bars represent 10 μm.

cross-linked polystyrene matrix of this composite. The sides of the poly(vinylferrocene)-coated ring-modified carbon fibers appeared much smoother in the SEM images than did those of uncoated fibers from the same batch (*10, 11*). These data suggest that the electropolymerized vinylferrocene coating was indeed cross-linked by copolymerization with DVB and remained intact, rather than dissolving in styrene and divinylbenzene used to form the surrounding matrix.

There was a marked difference between the degrees of fiber pull-out for the two materials. There appeared to be a strong bond between the uncoated fibers and cross-linked polystyrene that allowed fibers to pull out of the matrix only very slightly upon breakage of the composite rod. However, fibers coated with poly(vinylferrocene) pulled out much further and showed poorer binding between the poly(vinylferrocene) film and the surrounding cross-linked polystyrene matrix. The poor bonding led to improved mechanical strength since the fibers could slip within the matrix, but occasional fissures appeared as well (revealed upon polishing as discussed below).

Electrode Polishing. The procedure used to polish electrodes (described in the Experimental Section) left large amounts of alumina on the surface of the matrix-modified electrodes as shown by scanning electron microscopy (Figure 3a) and EDX. The surfaces of the carbon fibers were not directly visible anywhere on the surface of the composite, probably because they were obscured by alumina and diamond particles and polymeric debris that adhered to the ends of the carbon fibers and the polymer matrix surrounding them. Ultrasonication for 15 min removed the debris and revealed the ends of the carbon fibers (Figure 3b). The fibers protruded from the surface of the electrode, thereby increasing the active surface area of the electrode. Close inspection of the micrograph shows that even after sonication, some particles were

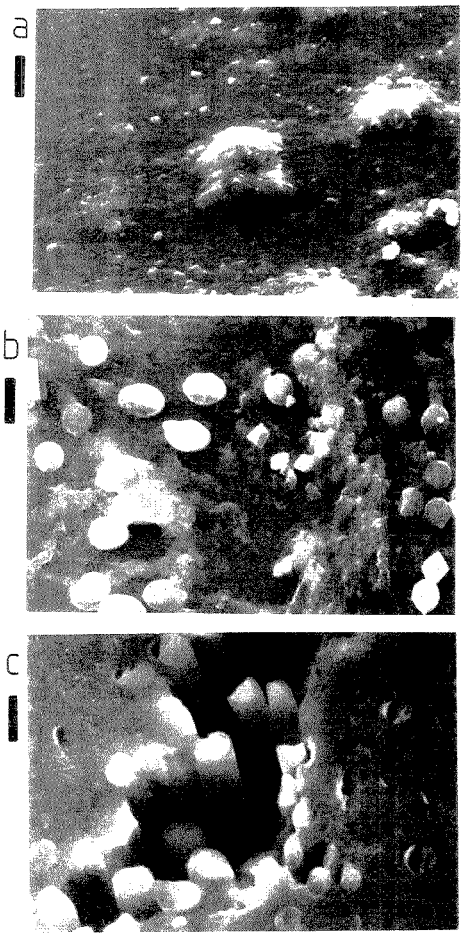

Figure 4. Scanning electron micrographs of polished ring-modified carbon fiber composite electrode: (a) after 1 min of sonication, magnified 1000 times; (b) after 15 min of sonication, magnified 1040 times; (c) same as b, different location on surface. Bars represent 10 μm.

still imbedded within the electrode's surface.

The polished surface of a poly(vinylferrocene) ring-modified electrode is shown in Figure 4a. EDX analysis again showed a large signal for aluminum, a result of polishing with alumina particles. The particles themselves are also visible. EDX analysis also showed that iron was distributed evenly across the surface as a result of polishing (recall that iron was associated only with the fibers when a cross section of the electrode was examined).

Although sonication for 15 min cleaned the surface of the electrode considerably, there were still many alumina and diamond particles imbedded in the surface of the electrode (Figure 4b). As discussed above, the poly(vinylferrocene)-coated fibers did not bind strongly to the composite matrix; this led to formation of rare fissures such as the one shown in the polished electrode in Figure 4c.

Electrochemical Behavior of Carbon Fiber Composite Electrodes. *Unmodified Composite Electrodes.* Unmodified

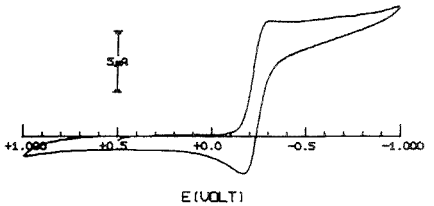

Figure 5. Cyclic voltammogram of 5 mM hexammineruthenium(III) chloride in aqueous 0.1 M KCl electrolyte solution on unmodified carbon fiber composite electrode containing 3000 fibers in a geometric area of 0.0707 cm^2. Scan rate was 50 mV/s.

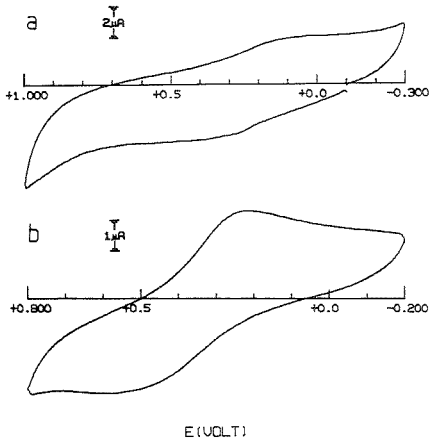

Figure 6. Cyclic voltammograms of vinylferrocene-modified carbon fiber composite electrodes (0.0314-cm^2 geometric area) in blank electrolyte (0.1 M KCl) solution at scan rates of 100 mV/s: (a) matrix-modified electrode, 3000 fibers; (b) ring-modified electrode, 6000 fibers.

carbon fiber composite electrodes were prepared to evaluate synthetic procedures and electrochemical performance of fibrous composite electrodes. Figure 5 shows a cyclic voltammogram for an aqueous solution containing 5 mM hexammineruthenium(III) chloride and 0.1 M KNO_3 on an unmodified carbon fiber composite electrode. This electrode had a diameter of 3 mm and contained 3000 fibers, which is 42 000 fibers/cm^2. The shape of the voltammogram suggests that both time-dependent planar diffusion and steady-state radial diffusion were important components of mass transport to the random array of microelectrodes. The voltammogram's shape is similar to that expected at a single microelectrode. However, the voltammogram was obtained with conventional instrumentation since the current was the sum of responses for 3000 carbon fibers.

Poly(vinylferrocene) Composite Electrodes. Previous work on modified particulate carbon composite electrodes showed that vinylferrocene could be incorporated into a composite material containing carbon black and that its properties were similar to those of poly(vinylferrocene) films on solid electrodes (*13*). Figure 6 shows cyclic voltammograms for (a) a matrix-modified poly(vinylferrocene) composite (3% vinylferrocene, 78% styrene, 18% DVB, 1% AIBN) and (b) a ring-modified poly(vinylferrocene) composite in blank electrolyte solution. The peak current densities were 0.7 and 0.6 mA/cm^2, respectively (geometric surface areas of all fibers were added to calculate current density).

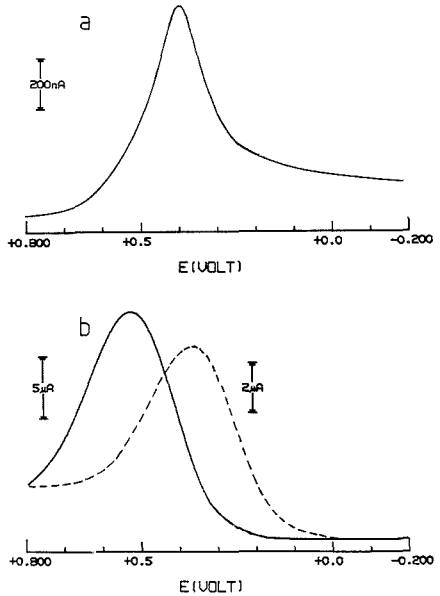

Figure 7. Square wave voltammograms of (a) poly(vinylferrocene) ring-modified carbon fiber composite (same electrode as in Figure 6b) in acetate buffer solution, pH 3.0, and (b) same solution as a with 2 mM ascorbic acid added. Conditions: composite electrode (---) and glassy carbon electrode with geometric surface area of 0.0855 cm^2 (—); square wave amplitude, 25 mV; frequency, 15 Hz; step potential, 4 mV.

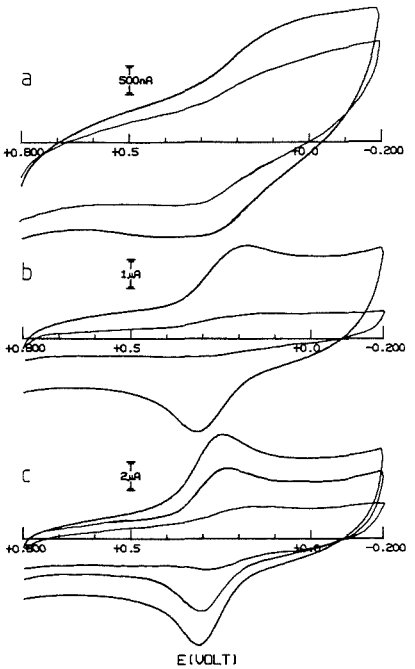

Figure 8. Cyclic voltammograms of 0.3 mM ferricyanide. The currents increase over time on vinylpyridine-modified carbon fiber composite electrodes: (a) 0 and 1 h at pH 3.0; (b) 0 and 1 h at pH 2.0; (c) 0, 1, and 2.5 h at pH 1.0. Scan rate was 250 mV/s.

Peak current density can probably be increased dramatically by improving the conditions under which the polymer film is formed. For example, a peak current density of 6.1 mA/cm^2 was obtained for ferrocene moieties at 50 mV/s for a single-fiber ring-modified electrode (*16*) prepared as follows. The fiber was held at −1.5 V vs SCE for 16 h in a solution containing 41 mM vinylferrocene, 11 mM DVB in 74% DMAC in 2% (v/v) sulfuric acid before fabrication of the single-fiber electrode. The ring-modified electrodes allow higher concentrations of ferrocene centers at the surface of the electrode than do matrix-modified electrodes because incorporation of too much vinylferrocene into the matrix yields a crumbly polymer.

Composite electrodes made without vinylferrocene showed no evidence of faradaic current in the range of potentials attributed to ferrocene moieties in modified electrodes. A Fourier transform infrared (FTIR) spectrum of a KBr pellet containing pulverized fibers coated with vinylferrocene copolymer showed peaks at 995, 815, and 1080 cm^{-1}, which have all been attributed to poly(vinylferrocene); the latter two peaks have been assigned to the cyclopentadienyl rings in the ferrocene moieties (*18*). No extraneous peaks that would have to be attributed to breakdown products of ferrocene were observed.

Electrode surfaces prepared by freezing the matrix- and ring-modified composite rods and then cleaving them showed electrochemical characteristics qualitatively similar to those of surfaces that were polished. However, peak currents were 2.2 and 3.7 times larger, respectively, which probably can be attributed to cleaner surfaces presented to electrolyte solution and the resulting increase in active electrode area.

The electrochemical behavior of these materials as modified electrodes for catalytic applications was investigated by using the the ferrocene moiety for oxidation of ascorbic acid (*19*, *20*). Figure 7 shows square wave voltammograms for (a) a ring-modified poly(vinylferrocene) fiber composite electrode in blank electrolyte solution (pH 3.0) and (b) the oxidation of ascorbic acid on a glassy carbon electrode and on a ring-modified composite electrode at pH 3.0.

A summary of peak potentials and peak currents appears in Table I. The peak current density at a ring-modified poly(vinylferrocene) composite electrode increased by a factor of 21 when 2 mM ascorbic acid was added to the pH 3.0 buffer solution. The peak potential was about 170 mV less positive in the presence of electrode-bound ferrocene, relative to an unmodified glassy carbon electrode. The improved efficiency of mass transport to the carbon fibers was largely responsible for the 32-fold increase in current density, relative to that for glassy carbon.

Poly(vinylpyridine) Composite Electrodes. Matrix-modified composite electrodes were made with fiber densities of 83 000 fibers/cm^2 in a polymer matrix containing 40% vinylpyridine, 39% styrene, 19% DVB, and 2% AIBN. These electrodes yielded clean background signals and good electrode responses for methyl viologen, hexammineruthenium(III), and ferricyanide in solutions buffered at pH 7. However, at more acidic pH values, the pyridine moieties within the polymeric matrix caused the polymer to swell via protonation and changed the electrode response toward ferricyanide, as reported for particulate carbon composite electrodes containing copoly(vinylpyridine) (*14*).

A series of voltammograms was recorded that illustrates the responses of a vinylpyridine copolymer electrode at different pH values as a function of time. The responses of this electrode for the reduction of 0.3 mM hexacyanoferrate(III) with pH buffered at values of 3.0, 2.0, and 1.0 are shown in

Table I. Square Wave Voltammetric Data for Oxidation of Ascorbic Acid

conditions[a]	peak potential, mV	peak current density, mA/cm^2
glassy carbon electrode; 2 mM ascorbic acid	529	0.2[b]
ring-modified poly(vinylferrocene) composite electrode; blank electrolyte, pH 3.0	391	0.3[c]
ring-modified poly(vinylferrocene) composite electrode; 2 mM ascorbic acid, pH 3.0	362	6.4[c]

[a] Other conditions are as in Figure 7. [b] Current density was calculated by using geometric surface area. [c] Current density was calculated by using the combined surface areas of all fibers.

Figure 8. Both charging and faradaic currents increased over the 1–2.5-h time periods shown.

The changes over time were more dramatic at lower pH's because as the hydronium ion activity increased, swelling of the pyridine-containing electrode surface became more extensive and occurred more rapidly. The higher charging currents indicate that increased active surface area was created as time passed. Since the faradaic current rose much more rapidly than the charging current, it is evident that the polymer, positively charged due to pyridine protonation, concentrated the highly charged ferricyanide ions.

ACKNOWLEDGMENT

We thank Jongman Park for advice on vinylpyridine copolymer matrices, Chia Lin Wang for data on the single-fiber ring-modified electrode, Andrew Garton for assistance with FTIR spectroscopy, and James P. Bell, Angel Wimolkiatasak, and Jemei Chang, Department of Chemical Engineering and Institute of Materials Science, for useful discussions related to electropolymerized interlayers in composites. Expertise in scanning electron microscopy offered by Carol Blouin, Institute of Materials Science, is acknowledged gratefully.

LITERATURE CITED

(1) Anderson, J. E.; Tallman, D. E.; Chesney, D. J.; Anderson, J. L. *Anal. Chem.* **1978**, *50*, 1051–1058.
(2) Weisshaar, D. E.; Tallman, D. E. *Anal. Chem.* **1983**, *55*, 1146–1151.
(3) Dayton, M. A.; Brown, J. C.; Stutts, K. J.; Wightman, R. M. *Anal. Chem.* **1980**, *52*, 946–950.
(4) Ponchon, J. L.; Cespuglio, R.; Gonon, F.; Jouvet, M.; Pujol, J. F. *Anal. Chem.* **1979**, *51*, 1483–1486.
(5) Wightman, R. M. *Anal. Chem.* **1981**, *53*, 1125A–1134A.
(6) Edmonds, T. E.; Guoliang, J. *Anal. Chim. Acta* **1983**, *151*, 99–108.
(7) Lipka, S. M.; Cahen, G. L., Jr.; Stoner, G. E.; Scribner, L. L., Jr.; Gileadi, E. *J. Electrochem. Soc.* **1988**, *135*, 368–372.
(8) Caudill, W. L.; Howell, J. O.; Wightman, R. M. *Anal. Chem.* **1982**, *54*, 2532–2535.
(9) Subramanian, R. V.; Crasto, A. S. *Polym. Compos.* **1986**, *7*, 201–218.
(10) Bell, J. P.; Chang, J.; Rhee, H. W.; Joseph, R. *Polym. Compos.* **1987**, *8*, 46–52.
(11) Chang, J.; Bell, J. P.; Shkolnik, S. *J. Appl. Polym. Sci.* **1987**, *34*, 2105–2124.
(12) Shaw, B. R.; Creasy, K. E. *J. Electroanal. Chem. Interfacial Electrochem.* **1988**, *243*, 209–217.
(13) Shaw, B. R.; Creasy, K. E. *Anal. Chem.* **1988**, *60*, 1241–1244.
(14) Park, J.; Shaw, B. R. *Anal. Chem.* **1989**, *61*, 848–852.
(15) Wang, J.; Golden, T.; Varughese, K.; El-Rayes, I. *Anal. Chem.* **1989**, *61*, 508–512.
(16) Creasy, K. E.; Wang, C. L.; Shaw, B. R. Pittsburgh Conference on Analytical Chemistry and Applied Spectroscopy, Atlanta, GA, March 6–10, 1989.
(17) Shaw, B. R.; Haight, G. P., Jr.; Faulkner, L. R. *J. Electroanal. Chem. Interfacial Electrochem.* **1982**, *140*, 147–153.
(18) Aso, C.; Kuhitake, T.; Nakashima, T. *Makromol. Chem.* **1969**, *124*, 232–240.
(19) Petersson, M. *Anal. Chim. Acta.* **1986**, *187*, 333–338.
(20) Cox, B. G.; Jedral, W.; Palou, J. *J. Chem. Soc., Dalton Trans.* **1988**, 733–740.

* To whom correspondence should be addressed.

Kenneth E. Creasy
Brenda R. Shaw*

Department of Chemistry U-60
University of Connecticut
215 Glenbrook Road
Storrs, Connecticut 06269-3060

RECEIVED for review July 5, 1988. Revised March 24, 1989. Accepted March 27, 1989. Acknowledgment is made to the donors of the Petroleum Research Fund, administered by the American Chemical Society, to the Research Corporation, and to support by the National Science Foundation under Grant No. CHE-8707973.

A Statistical Justification Relating Interlaboratory Coefficients of Variation with Concentration Levels

Sir: One of the most intriguing empirical relationships in modern analytical chemistry was published by Horwitz in 1980 (*1*, *2*); see for example Figure 1 of ref 2.

The graph results from an examination of over 50 interlaboratory collaborative studies conducted by the Association of Official Analytical Chemists on various commodities for numerous analytes over the last 100 years. Individual methods are tested by at least half a dozen laboratories on a series of blind samples. The results are analyzed for bias and interlaboratory variability. The graph relates the interlaboratory coefficients of variation (CV) found during proficiency testing with the concentration levels at which those particular analyses need to be carried out. The smooth relationship accomplishes this with no respect for the quite different methodologies and instrumentation used for the various analyses.

We have taken the liberty of labeling the graph as the "Horwitz Trumpet". The trumpet has profound implications for the level of detection and the precision that can be expected in setting legal controls in health-related legislation. The statistical techniques were developed to detect significant deviations from predetermined quality requirements and to provide a warning when this was no longer being fulfilled. The classical expectation of quality assurance is the production of identical interchangeable articles. However when an analytical laboratory produces results on a foodstuff, the results are not a series of identical measurements. The foodstuff varies in composition and there is no predetermined, absolute reference point from which to measure. Frequently a consensus value is established by adding a constituent and then recovering it. This somewhat artificial process is the closest that is obtained to a reference.

We now present a very simple theory that accounts very well for the experimental observations.

Let us postulate the following origin of the "trumpet curve". Suppose each laboratory result were the summation of many simple yes/no binomial components, each estimating the

0003-2700/89/0361-1465$01.50/0

concentration p. Then each point on the curve would be computed from a binomial distribution with parameters n and p, for some n. Each recorded sample result may be thought of as the mean of n binomial components. Of course we are not saying that all these experiments are carried out individually—only that the statistical accuracy of the results is such that the same coefficient of variation could hypothetically be achieved by carrying out n individual "yes–no" experiments. The yes–no experiments may be thought of as the individual quanta of which a large, sophisticated analytical scheme is composed.

The variance of the mean of a binomial value is $n^{-1}p(1 - p)$, while the expected value is p. Thus the coefficient of variation is

$$\mathrm{CV}(p) = [n^{-1}p(1 - p)]^{1/2}/p \approx (n^{-1}p)^{1/2}/p = (np)^{-1/2}$$

the approximation being valid for small p. For fixed n, a graph of $(np)^{-1/2}$ against p or $-\log p$, for p decreasing from 1 to zero, has the Horwitz trumpet shape. However, the fit of the calculated curve to the experimental curve at the center shows a positive deviation at high p and a negative deviation at low p.

To obtain a good fit, the number of "effective binomial components" that constitute a result must increase as p decreases. That is, at lower levels of detection as the experiment becomes more difficult, we postulate an increase in the number of "effective components" involved.

The increased difficulty at lower concentrations includes the increasing importance of extraction, cleanup, and contamination, as well as the increasing demands on the instrumentation and the operator.

The question now arises as to what dependence of p on n to assume. Zipf's law or the principle of least effort (*3*) argues that a geometric relation exists for the extra "effort" (in our case increase in $n \log n$) needed to cope with greater difficulty (in our case smaller p) for given cost of the experiment. In more detail, note that the effort or negative entropy associated with an n-component experiment is proportional to $n \log n$. The difficulty of each component is proportional to $\log p$, and so the total difficulty of the experiment is proportional to $n \log p$. The cost of an n-component experiment is proportional to n. Minimization of the effort for a given degree of difficulty and a given cost may be shown mathematically to produce $n = \beta p^{-\alpha}$, where α and β are constants whose values are determined by the given difficulty and cost. (Use the method of Lagrange multipliers.) Zipf's law may also be derived from Fermat's principle of least time (4).

Taking $n(p) = \beta p^{-\alpha}$ in the formula $\mathrm{CV}(p) = (np)^{-1/2}$, we obtain

$$\mathrm{CV}(p) = (\beta p^{-\alpha}p)^{-1/2} = (\beta p^{1-\alpha})^{-1/2},\ 0 < p < 1 \quad (1)$$

Equivalently, $\log_{10} \mathrm{CV}(p)$ and $\log_{10} p^{-1}$ admit the linear relationship

$$\log_{10} \mathrm{CV}(p) = (1/2)\ (1 - \alpha)\ \log_{10} p^{-1} - (1/2)\ \log_{10} \beta,\ 0 < p < 1$$

Approximate values $\alpha = 0.7$ and $\beta = 2\ 500$ are obtainable by nonlinear regression from data in ref 2.

Equation 1 then becomes

$$\mathrm{CV}(p) = p^{-0.15}/50 \quad (2)$$

which is very close to the formula $100\,\mathrm{CV}(p) = 2p^{-0.5} \log_{10} 2$.

To test the suitability of this formula, we interpolated from Figure 1 at $p = 10^{-3}$, $10^{-4.8}$, 10^{-6}, $10^{-7.5}$, $10^{-9.0}$, and $10^{-10.0}$, read off values of $\mathrm{CV}(p)$, and compared these with the values of $\mathrm{CV}(p)$ given by formula 2.

The curve obtained from formula 2 lies almost directly on top of the trumpet curve; see Figure 1.

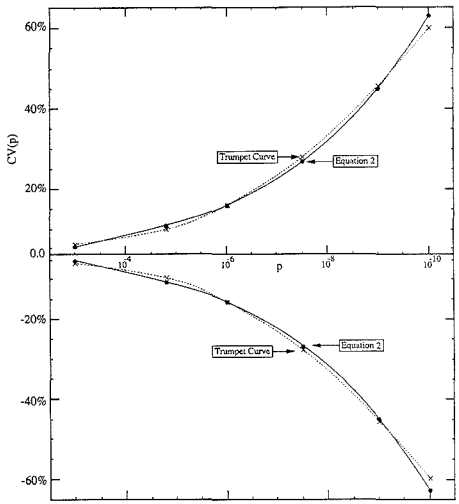

Figure 1. A comparison between the empirical Horwitz trumpet and the theoretical equation (2).

The fit is good. It supports the idea that the effort put into detecting lower concentrations increases in such a way that the "precision" changes as though sample size increased inversely with the concentration p. The actual relationship is as $p^{-0.7}$. Therefore the precision keeps pace to some extent with increasing "intrinsic error", although α would have to equal 1.0 rather than 0.7 before the precision would be equal at all concentrations. Conversely, one could argue that the effort put into measuring at high concentrations is correspondingly reduced because the high precision in that region is unwarranted.

The value of α is as approximate as the Horwitz trumpet curve itself. However it is the very resilience of the trumpet that is its attraction. We believe that the utter simplicity of our model and its good fit make it attractive in turn.

The analytical chemist at work appears to provide a beautiful example of Zipf's "Principle of Least Effort"—no offence meant!

LITERATURE CITED

(1) Horwitz, W. Evaluation of Analytical Methods Used for Regulation of Food and Drugs. *Anal. Chem.* **1982**, *54*(1), 67A.
(2) Horwitz, W.; Laverne, R. K.; Boyer, W. K. Quality Assurance in the Analysis of Foods for Trace Constituents. *J. Assoc. Off. Anal. Chem.* **1980**, *63*(6), 1344.
(3) Zipf, G. H. *Human Behaviour and the Principle of Least Effort*; Hafner: New York, 1965.
(4) Feynman, R. P. *The Feynman Lectures on Physics*; Addison Wesley Publishing Co.: Reading, MA, 1973; Vol 1, Part 2 [Optics 26-4].

Peter Hall

Department of Statistics
The Australian National University
G.P.O. Box 4
Canberra 2601, Australia

Ben Selinger*

Department of Chemistry
The Australian National University
G.P.O. Box 4
Canberra 2601, Australia

RECEIVED for review October 17, 1988. Accepted March 16, 1989.

TECHNICAL NOTES

Determination of Antioxidants in Lubricating Oils Using Ultramicroelectrodes

Graham T. Cheek*

Chemistry Department, United States Naval Academy, Annapolis, Maryland 21402

Robert Mowery

Chemistry Division, Code 6170, Naval Research Laboratory, Washington, D.C. 20375

INTRODUCTION

Recent studies have shown that the ester-based lubricants used in naval applications (*1*) degrade rapidly as antioxidant levels decrease (*2*), emphasizing the importance of monitoring antioxidant levels in the oils as operating time progresses. The methods presently used for antioxidant monitoring in these systems include thin-layer chromatography (*3*) and visible spectroscopy (*4*), both of which are used in a laboratory setting and can be time-consuming when used to acquire quantitative information. Considering that antioxidants are themselves oxidized in providing stability to oil formulations, it was decided to employ a related phenomenon, electrochemical oxidation, to determine antioxidant levels in these media. In recent years, the use of ultramicroelectrodes has revolutionized the practice of voltammetry in poorly conducting media (*5–8*) so that the application of this technology to the monitoring of antioxidants in lubricating oils seems very appropriate. Within this general strategy, several approaches can be taken, including addition of long-chain supporting electrolytes to the oils to provide conductivity and use of extremely small (submicrometer) electrodes so that addition of supporting electrolytes is not necessary. Given that such small electrodes are difficult to fabricate and that oil solutions are difficult to handle in voltammetric operations, it was deemed necessary to investigate other methods of voltammetric determination of antioxidants. We have found that a particularly convenient procedure involves the addition of the oil/antioxidant solution to acetonitrile, the resulting solution having sufficient conductivity to allow meaningful voltammetric measurements of antioxidant concentrations. The results of our investigations, including some considerations on the use of ultramicroelectrodes for these measurements, are presented here.

EXPERIMENTAL SECTION

Phenothiazine (PTZ), diphenylamine (DPA), and phenyl-1-naphthylamine (PANA) were purified by sublimation. The oils investigated were Hercolube (pentaerythritol tetra-*n*-hexanoate, NRL preparation) and TMP (a trimethylolpropane-based lubricant with acyl chain length distribution of 7,7,5 carbon atoms; Stauffer base stock 707) which were used as received. Standards were prepared on a weight percent basis, the manner customary in antioxidant/lubricating oil investigations.

The cell system employed in this work was deliberately kept very simple and involved a two-electrode system composed of a platinum ultramicroelectrode and a suitable reference/counter electrode. The ultramicroelectrode was constructed by sealing closed a length of Pyrex capillary tubing (6 mm o.d., 1 mm i.d.), inserting a 1–2 cm length of platinum wire (10–50 μm diameter; Goodfellow Metals Ltd.) above the sealed area, and sealing the wire into the tubing under vacuum. Cutting the sealed end of the tube midway along the wire seal exposed a microdisk electrode. After the electrode was polished with successively finer grades of alumina (final polish, 0.05 μm), electrical contact with the microdisk was made by using a small amount of Ga/In eutectic mixture (Alfa Products, 89180) in the tube. Three types of cells were used in this investigation (Figure 1):

[1] Initially, a simple glass vial cell with a close-fitting top equipped with a platinum wire (0.5 mm diameter) counter electrode (Bioanalytical Systems) was used. The counter electrode wire could be positioned within 1–2 mm of the ultramicroelectrode.

[2] The above cell was improved by using an inverted-configuration counter electrode (exposed platinum disk, 1.0 mm diameter), which allowed positioning of the counter electrode to within less than 1 mm of the ultramicroelectrode.

[3] Most of the results in this study were obtained with a cell of fundamentally different design. A fritted glass tube (Ace Glass Co., Inc.; porosity E) was simply bent into a "U" configuration, with the ultramicroelectrode and a Ag/AgCl reference electrode (Bioanalytical Systems, Inc.) placed in the resulting arms of the cell. The solution under investigation was placed in the ultramicroelectrode arm of the cell and an aqueous 0.1 M $NaClO_4$ solution was placed in the other arm. This cell was found to be most satisfactory for this investigation and most of the results were obtained from its use.

The instrumentation was similar to that described in other reports (*7*), involving application of a linear potential sweep to the cell with a simple triangular wave potential generator (Bioanalytical Systems, Model CV-1B) and measurement of the resulting current with a picoammeter (Keithley Model 617). The potential and current outputs were recorded on a Houston Model 2000 XY recorder.

The analytical method finally adopted involved adding 5.00 mL of acetonitrile (Burdick and Jackson) to a weighed amount (0.250–1.000 g) of the antioxidant/oil solution whose antioxidant concentration ranged from 0.10% to 2.00%. The acetonitrile/lubricant mixture was introduced into the cell, deoxygenated for 10 min with presaturated (acetonitrile) nitrogen, and then scanned in the positive direction from an initial potential of 0.00 V. Curves were recorded at a scan rate of 25 mV/s. The best results were obtained when the ultramicroelectrodes were polished (0.05 μm alumina, followed by ultrasonication) after each scan.

RESULTS AND DISCUSSION

To describe the method of choice in this investigation, it is of interest to mention the evolution of electrochemical cell design which led to the development of the final method. The results of previous approaches give some insight into the problems encountered in making electrochemical measurements in these highly resistive systems.

The first approach taken was perhaps the most obvious and involved the attempted measurement of phenothiazine concentration (1.00%) in Hercolube (a commercial ester-based lubricant) using cell configuration 1. Even with the counter electrode wire positioned 1 mm away from the ultramicroelectrode tip, very little (<10 pA) current was observed upon application of a potential scan to the cell. Addition of a supporting electrolyte (0.3 M tetra-*n*-hexylammonium benzoate) to the Hercolube solution resulted in a very broad oxidation wave for phenothiazine oxidation. Some filming of the electrode surface was evident as a gradual decrease of the current plateau for phenothiazine oxidation as scanning proceeded. In addition, a lessened oxidation current was

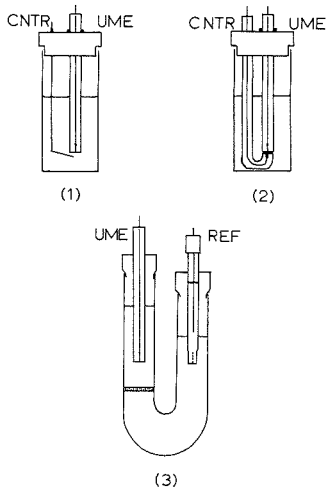

Figure 1. Cell configurations used in this work. Abbreviations are as follows: UME, ultramicroelectrode; CNTR, counter electrode (platinum); REF, reference/counter electrode (Ag/AgCl type).

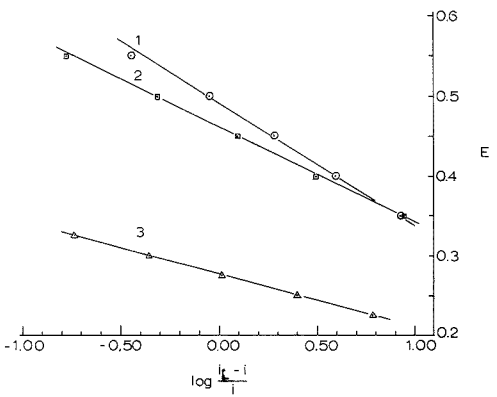

Figure 2. Plot of potential vs log $(i_L - i)/i$ for oxidation of 1 mM ferrocene in acetonitrile solution. Numbers refer to cell configurations given in the Experimental Section. Scan rate was 25 mV/s. Potentials are measured with respect to Ag/AgCl reference electrode.

observed during successive scans. The purification and handling of the supporting electrolyte were difficult and solutions of it in Hercolube were very viscous, making cleaning of the electrode very tedious. It was therefore decided to seek another approach to these measurements.

Recent research by other groups has shown that voltammetric measurements can be carried out at ultramicroelectrodes in acetonitrile solutions containing no intentionally added supporting electrolyte (*7*, *8*). This suggested that the determination of antioxidants in lubricating oils could be carried out simply by mixing the oils with acetonitrile and making electrochemical measurements on the resulting solution. The effectiveness of the various cell configurations mentioned in the Experimental Section was evaluated by obtaining current–potential curves for ferrocene oxidation in acetonitrile solutions with no added supporting electrolyte. Figure 2 shows the resulting plots of log $(i_L - i)/i$ vs potential, in which i_L is the limiting current. The slopes are quite high for configurations 1 and 2 (158 and 148 mV, respectively). Use

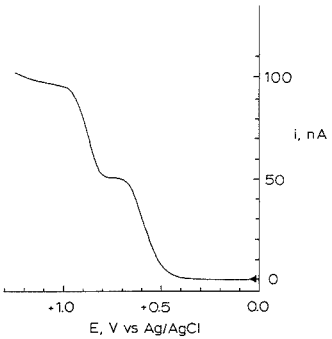

Figure 3. Voltammogram of a mixture of 1.00% PTZ/1.00% PANA in TMP, after addition of 0.250 g of antioxidant/oil mixture to 5.00 mL of acetonitrile. A 50-μm (diameter) platinum ultramicroelectrode in cell configuration 3 was used. Scan rate was 25 mV/s.

of configuration 3 gives a value of 65 mV, close to the theoretical slope (*7*). Independent experiments in a cell of type 2 showed that addition of $NaClO_4$ at the 10^{-3}–10^{-4} M level is sufficient to produce a wave slope of 60 mV, indicating that at least this amount of electrolyte is provided by leakage across the fritted barrier in cell configuration 3. This finding is in general agreement with the results of a similar study in acetonitrile/tetra-*n*-butylammonium fluoroborate (*7*).

To investigate the cell configurations for actual determination of antioxidants in lubricating oil (TMP), solutions were prepared as described in the Experimental Section. When the potential was scanned from an initial value of 0.00 V to +1.50 V, two oxidation waves were observed for a mixture of PTZ and PANA using cell configuration 1. As expected from the results with ferrocene oxidation, these oxidation waves were rather broad, having wave slopes of 150 mV ($E_{3/4} - E_{1/4}$). Great improvement was found upon making the measurements in a cell of configuration 2, which generally gave wave slopes of less than 100 mV. With this improved apparatus, calibration curves were linear over the range of 0.1–2.0% in antioxidant (both PTZ and PANA) concentration. This approach showed that this type of measurement was indeed feasible; however, this particular cell design does not provide for a potential reference, a feature that was deemed very desirable for automated workup of the current–potential curves.

The final cell configuration, 3, addresses the above deficiency by providing a potential reference. A Ag/AgCl reference electrode is placed in one arm of the cell. By use of an aqueous electrolyte solution in this arm, increased conductivity is provided to the acetonitrile solution through the leakage of a small amount of the aqueous solution across the fritted barrier. To use the cell, the aqueous solution side is first filled to within 2 cm of the top of the arm, followed by placement of the reference electrode into the top of the arm through a small plastic cap. Following the removal (by pipet) of any aqueous solution from the ultramicroelectrode arm of the cell, the acetonitrile solution of the lubricating oil/additives mixture is then placed in this arm of the cell. The sample volume is adjusted to a level slightly above that of the aqueous solution. Responses for the electrochemical oxidation of 1% PTZ and 1% PANA solutions in TMP are shown in Figure 3. The first wave corresponds to PTZ oxidation, followed by PANA oxidation at more positive potentials. The wave slopes are characteristic of one-electron oxidations (60–70 mV) and resulted in $E_{1/2}$ values which were constant with concentration of the antioxidants. This indicates that iR drops are minimal. Calibration curves over the range 0.1–2.0% for

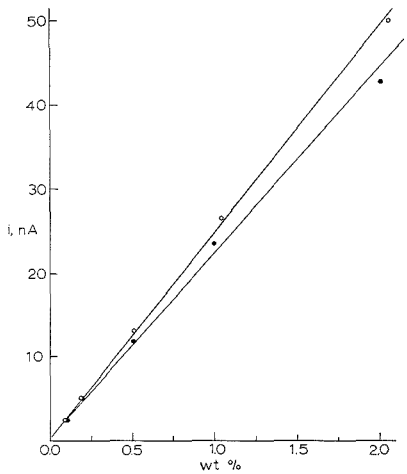

Figure 4. Calibration curve for PTZ and PANA in TMP. Data were collected for solutions prepared by addition of 1.000 g of antioxidant/TMP oil mixture to 5.00 mL of acetonitrile. A 10-μm (diameter) platinum ultramicroelectrode in cell configuration 3 was used. Scan rate was 25 mV/s. PTZ data points, open circles; PANA data points, filled circles. Slope/intercept information (units as given on figure): PTZ (24.39 ± 0.40; 0.45 ± 0.43) PANA (20.99 ± 0.83; 1.09 ± 0.86).

both PTZ and PANA were linear (Figure 4), giving r values of 0.9996 and 0.997, respectively. The method is characterized by rather good precision (1.2% relative standard deviation), leading to detection limits of approximately 0.010% (as expressed for antioxidants in actual oil samples). Continuing studies have shown that interferences encountered in used oil samples are slight and occur as an increase in background current at potentials more positive than +0.95 V.

CONCLUSIONS

This work demonstrates the feasibility of electrochemical determination of antioxidants in lubricating oils. The procedure is greatly simplified by mixing the oil with a suitable cosolvent, thereby providing sufficient conductivity to obtain voltammetric measurements on the solution. Further improvement can be achieved through the use of a compartmented cell which provides small amounts of additional electrolyte by leakage into the ultramicroelectrode compartment. Ultramicroelectrodes allow the use of very simple measuring equipment and will allow construction of a reliable unit for field determination of additives in lubricating oils. In addition, the steady-state responses obtained with ultramicroelectrodes are easily measured and interpreted.

Registry No. PTZ, 92-84-2; DPA, 122-39-4; PANA, 90-30-2; NRL, 7445-47-8; TMP, 77-99-6; Pt, 7440-06-4; acetonitrile, 75-05-8.

LITERATURE CITED

(1) Cohen, G.; Murphy, C. M.; O'Rear, J. G.; Ravner, H.; Zisman, W. A. *Ind. Eng. Chem.* **1953**, *45*, 1766.
(2) Ravner, H.; Wohltjen, H. *Lubr. Eng.* **1986**, *39*, 701.
(3) Sniegowski, P. J. *J. Chromatogr. Sci.* **1977**, *15*, 328.
(4) Mowery, R. L. "Helicopter Lubricant Sensors"; NRL Prob.#61-2236-0-5, 2 June 1986.
(5) Geng, L.; Ewing, A. G.; Jernigan, J. C.; Murray, R. W. *Anal. Chem.* **1986**, *58*, 852.
(6) Amatore, C.; Deakin, M. R.; Wightman, R. M. *J. Electroanal. Chem.* **1987**, *220*, 49.
(7) Pena, M. J.; Fleischmann, M.; Garrard, N. *J. Electroanal. Chem.* **1987**, *220*, 31.
(8) Ciszkowska, M.; Stojek, Z. *J. Electroanal. Chem.* **1986**, *213*, 189.

RECEIVED for review September 27, 1988. Accepted February 1, 1989.

Carbon Fiber Electrode Cell for Square Wave Voltammetric Detection of Biogenic Amines in High-Performance Liquid Chromatography

Samuel P. Kounaves*,[1] and James B. Young

Charles A. Dana Research Institute and Harvard University, Thorndike Laboratory, Department of Medicine, Beth Israel Hospital, Boston, Massachusetts 02215

INTRODUCTION

Application of voltammetric fast-scan techniques to high-performance liquid chromatography (HPLC) has been investigated by several groups (*1–4*). Samuelsson et al. (*1*) were the first to describe the use of square wave voltammetry (SWV) with HPLC. SWV is an electrochemical technique that allows the rapid scanning of a voltage range with a minimal contribution of charging current to the output signal (*5*). Using *N*-nitrosodiethanolamine and *N*-nitrosoproline, they showed the advantages and possibilities of the technique. Detection was limited by flow pulsation noise, the geometry of the cell, and the computer-controlled sampling interval for both the time and potential domains (ca. 200 s × 400 mV with sampling at 2-s and 10-mV intervals). More recently Goto and Shimada (*4*), using SWV in combination with a carbon fiber electrode (CFE) and HPLC, described the analysis of several catecholamines by three-dimensional HPLC–SWV. The results presented, even though of qualitative value, were of very low temporal resolution (4 scans/min or 3–4 peak data points/chromatographic peak) and thus of questionable quantitative value. Insufficient data was given to make a valid estimate of sensitivity or detection limits, and the authors did not provide any information on reproducibility. Even though both of the above studies suggested potential qualitative uses of three-dimensional HPLC–SWV, neither demonstrated its actual practical qualitative and quantitative use.

The use of single graphite fibers as working electrodes in HPLC has been reported by several groups. Recently Jorgenson et al. (*2, 6*) have used a micropositioner to insert and hold a carbon fiber electrode at the outlet of an HPLC column. Attempts to use a similar system in this laboratory found that, even though this system provides some versatility for research, it is rather bulky and highly susceptible to mechanical vibrations. Goto and Shimada (*4*) have fabricated an electrode by inserting and sealing the carbon fiber into a fused silica tube. We found it difficult, however, to duplicate the electrode since construction details were not adequately described.

[1] Permanent address: Department of Chemistry, Tufts University, Medford, MA 02155.

0003-2700/89/0361-1469$01.50/0

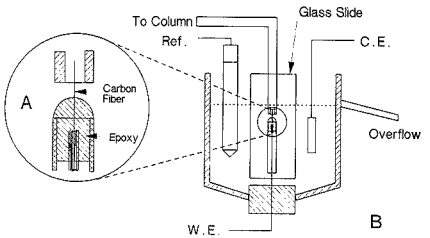

Figure 1. Construction details of (A) the carbon fiber electrode and (B) the flowthrough cell assembly.

Several electrodes made to their approximate specifications presented problems with mechanical instability and large background noise.

In attempting to use a fast-scan technique such as SWV for the detection scheme in HPLC, one must take into consideration several important factors when designing the electrochemical cell. Most carbon electrode flowthrough cells are designed for amperometric detection and, as such, have extremely poor transient response characteristics (i.e. RC > 5 ms). High-frequency SWV requires a cell configuration with an RC of about 0.1 ms or less. Another critical point to consider is the positioning of the electrode within the cell. The cell must permit the growth of the diffusion layer and the flux lines without any hindrance, otherwise the resistance will increase and so will the time constant.

In this paper we describe a chromatovoltammographic (HPLC–SWV) system using a commercially available potentiostat and microcomputer and a custom-fabricated working electrode consisting of a combination carbon fiber (permanently mounted at the HPLC column outlet on a glass slide) and flowthrough cell. The system is used to obtain qualitative and quantitative data from a solution containing a mixture of biogenic amines, with the results being presented in the form of contour and isochromic plots. We also look at the effect of electrode pretreatment on the position and intensity of the SW net-current peak for several biogenic amines. Combining SWV with HPLC provides a new "dimension" in the collection and analysis of chromatographic data in that both the chromatographic domain (time vs concentration signal) and the electrochemical domain (potential vs current) can be viewed simultaneously, allowing peaks that overlap in either technique to be resolved and detected separately.

EXPERIMENTAL SECTION

Apparatus. Square wave voltammetry was carried out with an EG&G potentiostat/galvanostat Model 273 (EG&G Princeton Applied Research, Princeton, NJ) controlled by a Vectra PC (Hewlett-Packard, Sunnyvale, CA) with 640K memory, 40-MB hard disk, 10-MHz clock, and a GPIB-488 interface card. Generation of square waveforms through the EG&G Model 273, data acquisition from the EG&G Model 273, and display of the resulting three-dimensional chromatovoltammographic data were accomplished by software written and compiled with QuickBASIC V.4 (Microsoft, Redmond, WA).

The liquid chromatography system consisted of a Model 196 minipump (Milton Roy, Riviera Beach, FL), a 50-μL loop injection valve (Model 7125, Rheodyne, Berkeley, CA), a pulse dampener, and a 150 mm × 4 mm Bio-Sil ODS.5S reversed-phase column (Bio-Rad, Richmond, CA). The mobile phase contained 0.1 M sodium acetate (Fisher), 0.04 M citric acid (Mallinckrodt), 0.8 mM sodium octyl sulfate (Kodak), 0.1 mM ethylenediaminetetraacetic acid (EDTA) (Fisher), and 5% methanol (Fisher) and was adjusted to a pH of 5.2 with sodium hydroxide. The flow rate was 1 mL/min.

Electrodes. The carbon fiber electrode and cell assembly are shown in Figure 1. The carbon fiber electrodes were constructed by threading a bundle of the 7-μm carbon fibers (ca. 70–80 mm long, Avco/Textron, Lowell, MA) through a 0.8 mm × 30 mm capillary tube (Kimax-51, Kimble, Vineland, NJ). The bundle was pulled through in such a way as to allow one fiber to protrude at least 4–6 mm from one end. This end was then sealed with a bead of fast-drying epoxy (2R:1H, DURO-Master Mend, Loctite Corp., Cleveland, OH) with some of the epoxy being drawn 2–3 mm into the tube (Figure 1A). After about a half-hour was allowed for hardening, the bundle of fibers at the other end was tightly wound around a copper stranded wire (ca. 20 mm striped wire 20 cm long) and twisted into the capillary. Any excess fibers were cut off, and this end was also sealed with epoxy and allowed to dry; then ca. 1 cm of heat-shrinkable tubing was placed over the capillary/wire joint. The electrode was then mounted with epoxy onto a slide (7.5 mm × 25 mm × 1 mm) on which Teflon capillary tubing (0.3 mm i.d. × ca. 20 cm long) had been previously mounted, by inserting the fiber into the end of the Teflon tubing to within ca. 0.5 mm of the seal (Figure 1A), and held in place till dry (ca. 4 min). The entire assembly was cured at 70 °C for 3 h. The complete electrochemical detector, shown in Figure 1B, consists of the above electrode assembly mounted in a modified high-density polyethylene (HDPE) bottle along with a Pt-wire counter electrode and saturated NaCl calomel reference electrode. The cell is filled with mobile-phase solution and kept at constant volume by suction. Unless otherwise indicated, the carbon fiber electrode was pretreated only once at the very beginning before being used. The pretreatment consisted of applying a 1-Hz triangular waveform potential varying between 0 and +1500 mV for 60 s with a mobile-phase flow rate of 1 mL/min.

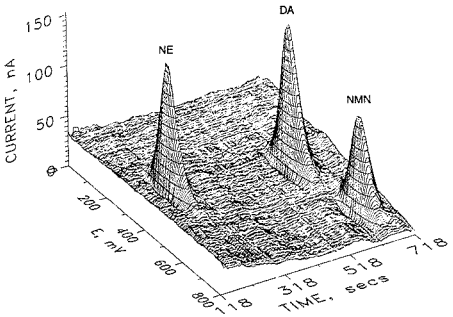

Figure 2. Square wave chromatovoltammogram of NE, DA, and NM, all at 1 × 10^{-5} M, represented as a three-dimensional *XYZ* plot. Chromatographic and voltammetric conditions are given in text.

Reagents. All solutions were prepared with 18-MΩ water from an ion-exchange system (Millipore) fed from a singly distilled source. Epinephrine (E), norepinephrine (NE), dopamine (DA), 5-hydroxytryptophan (5-HTP), 3,4-dihydroxybenzylamine (DHBA), and normetanephrine (NM) were obtained from Sigma Chemical Co., St. Louis, MO. Standard solutions were made up containing 1.0 mM concentrations of each amine in 0.1 M perchloric acid and stored at 4 °C.

RESULTS AND DISCUSSION

A three-dimensional chromatovoltammograph of a mixture of biogenic amines is shown in Figure 2. The sample contained 1 × 10^{-5} M NE, DA, and NM in 0.1 M $HClO_4$, 50 μL of which was injected onto the column with a mobile-phase flow rate of 1 mL/min. The SWV potential was scanned every 2 s from 0 to 800 mV with a step height (ΔE_S) of 5 mV, square wave amplitude (E_S) of 25 mV, and square wave frequency (f) of 100 Hz. The raw SWV data collected consisted of forward (i_f) and reverse (i_r) current as a function of potential and elution time. The data shown in Figure 2 is the resulting net current ($i_n = i_f - i_r$) after background subtraction and smoothing. For this sample, with relatively few peaks, we can clearly identify each component in the three-dimensional plot. A contour plot is displayed immediately after the analysis as an isochromic plot (current signal displayed in 15 different

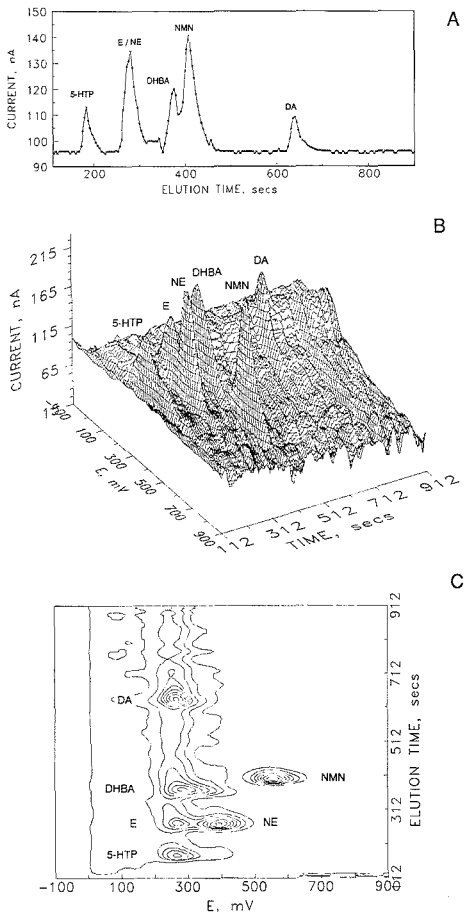

Figure 3. (A) Standard chromatogram of sample containing 5-HTP, E, NE, DHBA, NM, and DA, all at 1×10^{-6} M, with the CFE detector potentiostated at 650 mV. (B) Same sample analyzed with the chromatovoltammographic technique as a three-dimensional plot and (C) as a isogalvanic contour plot.

colors) on the computer monitor. The program allows the user to select (via hairline cursors) and read the current/concentration signal at any time–potential coordinates. The utility of this system becomes more evident during analysis of samples containing a large number of components at lower concentrations.

Figure 3A shows a standard chromatogram of a 50-μL injection of a sample containing 5-HTP, E, NE, DHBA, NM, and DA, all at 1×10^{-6} M, with the chromatographic conditions the same as before, except that the potential was fixed at 650 mV for the entire run. As can be seen, the peaks for E and NE are completely overlapping and those for DHBA and NM are partially overlapping. A 50-μL injection of the same sample run under the same conditions, except with a SWV potential scan range of −100 to 900 mV, scan interval = 2 s, ΔE_S = 5 mV, E_{SW} = 25 mV, and f = 600 Hz, shows the dramatic improvement in both the qualitative and quantitative information obtained (Figure 3B,C). With a larger number of components and lower concentrations, the three-dimensional chromatovoltammograph (Figure 3B) is useful only for a "qualitative feeling" of the results, with all of the biogenic amines in the sample being clearly resolved and quantified in the contour plot (Figure 3C).

The detection limit for these amines is between 6 and 4 pmol with a 2:1 signal/noise ratio. This limit was obtained without using a Faraday cage or a nonpulsating pump. The detection limit for a "slice" at 650 mV was ca. 5–2 pmol. These limits are an order of magnitude higher than obtained with the same detector in the amperometric mode but are several orders of magnitude lower than previously obtained with other scan voltammetric techniques (*2–4*).

The detector's linearity was assessed by injecting 50-μL samples containing 10^{-7} to 10^{-4} M epinephrine. The log–log plot of concentrations vs i_{np} gave a slope of 0.983, relative standard deviation of 0.020%, and correlation coefficient of 0.998.

Effect of Electrode Pretreatment on SWV Current Response. Previous research by several groups (*7–9*) has shown that the voltammetric sensitivity of carbon fiber electrodes to catechol- and indole-based compounds is significantly increased after "modification" of their surface by electrochemical pretreatments. Our studies, using SWV, have shown a similar behavior with these electrodes. However, care must be taken in making comparisons since SWV operates under a different set of assumptions and conditions (especially in terms of scan rate). As expected, pretreatment caused an increase in the SWV peak current response. However, an optimum time was reached for all the amines after approximately 50–60 s (except DA, 125 s). Unlike previous results (*7–9*), which showed a 10-fold increase in sensitivity, the difference in this case between treated and untreated electrodes was about 2-fold and the same for all the amines. However, it is interesting to note that the background current between the untreated and treated electrodes decreased by about 50%. No significant difference from the above results was seen with the use of a higher pretreatment frequency (up to 100 Hz) or potential excursion (up to 3.0 V). Electrochemical pretreatments have also been shown to cause a shift in the oxidation potentials of catecholamines (*8*). We found only a slight shift in the peak potentials between the treated and untreated electrodes of about 10 mV and no significant shift in peak net currents after any of the pretreatment electrolysis times (0–300 s).

This lack of improved sensitivity and shift in the oxidation potentials is in contrast to that obtained in several previous studies (*7–9*). There are several possible reasons for these discrepancies, such as the following: the lower current densities used during our electrolysis pretreatments; the composition of the buffer solution; the source and/or fabrication process of the carbon fibers; or factors intrinsic to the SWV technique, which uses comparatively high scan rates such that the usual adsorption equilibrium (*7*) may not reached. Since the exact nature of the pretreatment effects on the carbon fiber surface is not well understood (*9*), it is difficult to venture a guess as to the specific reason for these discrepancies at this point. We are currently looking at the SWV response of carbon fibers in greater detail, the results of which will be published in the near future.

The treated electrodes retained their properties for several weeks and did not seem to be affected by the number of times they were used for three-dimensional HPLC–SWV analysis.

Electrochemistry of Biogenic Amines with SWV. Two interesting aspects of using SWV for the electroanalysis of catecholamines are that no electrode-fouling products appear to be generated during the oxidation steps and only single-peak SW voltammograms are obtained at pHs >3. It has been previously shown (*10*) that for cyclic voltammetry (CV) at pHs >3 the unprotonated oxidation product of epinephrine (ep-

inephrine–quinone, EQ) is available in sufficient concentration to allow a rapid cyclization reaction to take place (k_{cyc} = 0.6 s^{-1}, t = 1.2 s), converting it to the indole (5,6-dihydroxyindoline). The indole however is more easily oxidized than epinephrine so that it is oxidized by the EQ to the respective aminochrome, which then proceeds to polymerize. This complex ECC mechanism (electrochemical reaction followed by two chemical reactions) is responsible for the multiple peaks normally seen in linear scan voltammograms of catecholamines and for the fouling of electrode surfaces under amperometric conditions. With SWV, using a frequency of 600 Hz and scanning from 0 to 1000 mV (0.2 s), the rate of reduction of the quinone back to the catecholamine is an order of magnitude greater than the rate of cyclization reaction. Thus, the cyclization reaction occurs to an insignificant degree so that the SW voltammogram shows only one peak and there is no chance for polymerization (fouling) to occur on the electrode surface. In addition, by changing the frequency of the SW, one could use the above situation to advantage to determine the heterogeneous electron-transfer rates of catecholamines and indoleamines.

In conclusion, it seems evident that many of the factors involved in using SWV with CFEs are only partially understood at this time. The pretreatment and configuration of the CFE is crucial to the signal response when one is using SWV. We feel that with proper cell configurations and conditions, SWV will prove to have much greater sensitivity and resolution than the other voltammetric techniques currently used.

ACKNOWLEDGMENT

The expert technical assistance of S. Gunn is gratefully acknowledged. This work was supported in part by the National Institutes of Health, Grant No. HL-37871.

Registry No. E, 51-43-4; NE, 51-41-2; DA, 51-61-6; 5-HTP, 56-69-9; DHBA, 37491-68-2; NM, 97-31-4.

LITERATURE CITED

(1) Samuelsson, R.; O'Dea, J. J.; Osteryoung, J. *Anal. Chem.* **1980**, *52*, 2215–2216.
(2) White, J. G.; St. Clair, R. L.; Jorgenson, J. W. *Anal. Chem.* **1986**, *58*, 293–298.
(3) Caudill, W. L.; Ewing, A. G.; Jones, S.; Wightman, R. M. *Anal. Chem.* **1983**, *55*, 1877–1881.
(4) Goto, M.; Shimada, K. *Chromatographia* **1986**, *21*, 631–634.
(5) Osteryoung, J.; Osteryoung, R. A. *Anal. Chem.* **1985**, *57*, 101A–110A.
(6) Knecht, L. A.; Guthrie, E. J.; Jorgenson, J. W. *Anal. Chem.* **1984**, *56*, 479–482.
(7) Gonon, F. G.; Fombarlet, C. M.; Buda, M. J.; Pujol, J. F. *Anal. Chem.* **1981**, *53*, 1386–1389.
(8) Kovach, P. M.; Deakin, M. R.; Wightman, R. M. *J. Phys. Chem.* **1986**, *90*, 4612–4617.
(9) Feng, J. X.; Brazell, M.; Renner, K.; Kasser, R.; Adams, R. N. *Anal. Chem.* **1987**, *59*, 1863–1867.
(10) Hawley, M. D.; Tatawawadi, S. V.; Piekarski, S.; Adams, R. N. *J. Am. Chem. Soc.* **1967**, *89*, 447–450.

RECEIVED for review October 17, 1988. Accepted March 28, 1989.

CORRECTIONS

Bienzymatic Electrode for the Determination of Aspartame in Dietary Products

Orlando Fatibello-Filho, Ahmad A. Suleiman, George G. Guilbault, and Glenn J. Lubrano (*Anal. Chem.* 1988, *60*, 2397–2399).

Equation 1 on page 2397 should read

$$\text{aspartame} \xrightarrow{\text{carboxypeptidase A}} \text{L-aspartic acid} + \text{L-phenylalanine}$$

Multifrequency Phase Fluorescence Study of Hapten-Antibody Complexation

Frank V. Bright (*Anal. Chem.* **1989**, *61*, 309–313).

Equation 12 on page 310 should read

$$\frac{r_0}{r} = \frac{1}{F_f}\{1 + (\tau_F/\phi_f)\} + \frac{1}{F_b F_L}\{1 + (\tau_L/\phi_L)\} + \frac{1}{F_b F_G}\{1 + (\tau_G/\phi_G)\}$$

As a result, Figure 1 should appear as

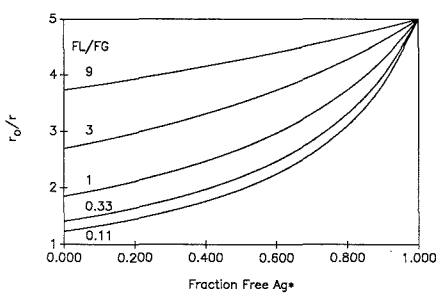

For Over Six Decades...

The Leader in the Field.

ANALYTICAL CHEMISTRY, the world's foremost publication in the vital field of measurement science, comes to you semi-monthly packed with *more* research articles, special features and application papers.

Keeping pace with the changes has continued to make *ANALYTICAL CHEMISTRY* the pinnacle of publications in the field . . . for over 6 decades.

For your personal subscription:

CALL TOLL FREE (800) 227-5558 (U.S. only)
Outside U.S. (202) 872-4363

Telex: 440159 UI
89 2582 ACSPUBS

American Chemical Society
1155 16th St., NW
Washington, DC 20036

A MODULAR TITRATION SYSTEM DESIGNED TO MEET YOUR NEEDS TODAY AND FAR INTO THE FUTURE.

TIM90 Titration Manager: *Manages up to 3 burettes. Stores 40 methods.*

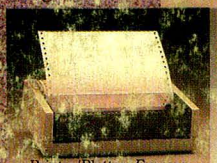

Printer/Plotter: *For your complete documentation needs.*

Plug-in modules *for pK, TAN/TBN, ion concentration and other methods.*

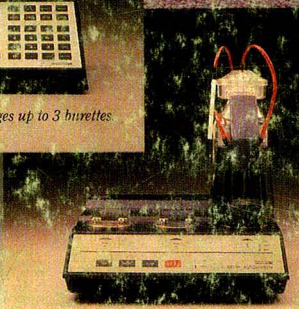

ABU91 Autoburette: *One burette (1,5,10, & 25 ml).*

SAM90 Sample Station: *Accepts one sample (500 ml to 1000 ml.) and 4 electrodes.*

SAC80 Sample Changer: *Accepts up to 20 samples (8 to 300 ml) and 4 electrodes.*

VIT90 Video Titrator: *Manages up to 12 burettes. Stores 60 methods.*

ABU93 Triburette: *Three burettes (1,5,10 & 25 ml).*

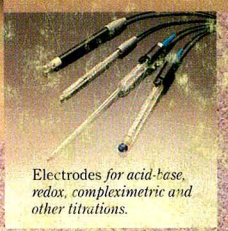

Electrodes *for acid-base, redox, complexometric and other titrations.*

Introducing TitraLab®, a family of compatible components for implementing "real world" titration applications in R&D, QA/QC or compliance testing laboratories.

With these components, you can configure an automatic titration system which meets today's needs, but does not strain today's budget. And you can add to that system as your needs change in the future.

We would like to tell you more.

For a demonstration, call David Perrin at (800) 321-9484 or (216) 871-8900. For a copy of the TitraLab brochure and our extensive published notes on environmental, food, petrochemical, pharmaceutical, plating and other applications, fill out the coupon and return it to Radiometer America Inc., 811 Sharon Drive, Westlake, OH 44145.

CIRCLE 140 ON READER SERVICE CARD

RADIOMETER COPENHAGEN

Please send literature on the new TitraLab® system to:

Name: _____

Title: _____

Organization: _____

Street & No.: _____

City: _____

State: _____ Zip: _____

Phone: _____

Application: _____